

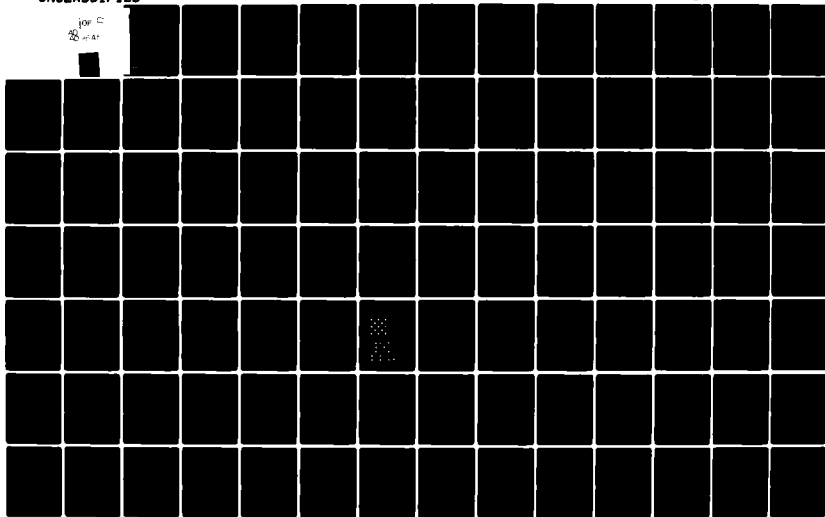
AD-A096 451

PENNSYLVANIA STATE UNIV UNIVERSITY PARK MATERIALS RE--ETC F/6 9/1
TARGETED BASIC STUDIES OF FERROELECTRIC AND FERROELASTIC MATERIALS--ETC(U)
DEC 80 L E CROSS, R E NEWNHAM, G R BARSCH N00014-78-C-0291

UNCLASSIFIED

NL

TOP C
25-01-01



AD A 096451

DBF FILE COPY

DEL

12

TARGETED BASIC STUDIES OF FERROELECTRIC AND FERROELASTIC
MATERIALS FOR PIEZOELECTRIC TRANSDUCER APPLICATIONS

Period December 1, 1979 to November 30, 1980

Annual Report

OFFICE OF NAVAL RESEARCH

Contract No. N00014-78-C-0291

APPROVED FOR PUBLIC RELEASE—DISTRIBUTION UNLIMITED

Reproduction in whole or in part is permitted for
any purpose of the United States Government

L.E. Cross
R.E. Newnham
G.R. Barsch
J.V. Biggers

DECEMBER 1980

DTIC
S
MAR 17 1981
A



THE MATERIALS RESEARCH LABORATORY
THE PENNSYLVANIA STATE UNIVERSITY
UNIVERSITY PARK, PENNSYLVANIA

81 3 17 213

6
TARGETED BASIC STUDIES OF FERROELECTRIC AND FERROELASTIC
MATERIALS FOR PIEZOELECTRIC TRANSDUCER APPLICATIONS.

Period December 1, 1979 to November 30, 1980

Annual Report 1 1 7 1 1

OFFICE OF NAVAL RESEARCH

Contract No. ~~N00014-78-C-0291~~

APPROVED FOR PUBLIC RELEASE—DISTRIBUTION UNLIMITED

Reproduction in whole or in part is permitted for
any purpose of the United States Government

10
L.E. Cross
R.E. Newnham
G.R. Barsch
J.V. Biggers

11
DECEMBER 1980

44

Accession For		
NTIS	GRA&I	✓
DTIC	TAB	
Unannounced		
Justification		
For		
Distribution/		
Availability Codes		
Avail and/or		
Dist	Special	
A		

57 15

Contents

	<u>Page</u>
1.0 INTRODUCTION-----	1
2.0 ELECTROSTRICTION-----	6
2.1 Introduction-----	6
2.2 Instrumentation-----	7
2.3 Electrostriction in Perovskites-----	7
2.4 Theory of Electrostriction-----	8
2.4.1 Temperature dependence of electrostriction of ferroelectric crystals in the paraelectric phase--	8
2.4.2 Lattice theory of the nonlinear elastic dielectric in the shell model-----	9
2.4.3 Shell model calculation of electrostriction coefficients of rocksalt-type alkali halides-----	9
2.4.4 Electrostriction, optic mode gammas and third order elastic constants of SrTiO ₃ in the shell model-----	10
2.5 Ferroelectric Relaxors-----	10
3.0 COMPOSITE TRANSDUCERS-----	11
3.1 Introduction-----	11
3.2 Fabrication Techniques-----	11
3.3 Hydrophone Materials-----	11
3.4 Higher Frequency Applications-----	12
3.5 Ceramic: Metal Composites-----	12
4.0 Grain Oriented Ceramics-----	14
5.0 Crystal Growth-----	15
6.0 PROCESSING STUDIES-----	16
7.0 PHENOMENOLOGICAL STUDIES-----	17
8.0 FERROELECTRIC BICRYSTALS-----	18
9.0 FERROELASTICS-----	19
10.0 PROGRAM ORGANIZATION: PERSONNEL AND EQUIPMENT-----	20
10.1 Personnel-----	20
10.2 Equipment-----	20
10.3 Advisory Committee-----	22
APPENDICES-----	24

UNCLASSIFIED

SECURITY CLASSIFICATION OF THIS PAGE (When Data Entered)

REPORT DOCUMENTATION PAGE		READ INSTRUCTIONS BEFORE COMPLETING FORM
1. REPORT NUMBER	2. GOVT ACCESSION NO.	3. RECIPIENT'S CATALOG NUMBER
	AD A096451	
4. TITLE (and Subtitle) TARGETED BASIC STUDIES OF FERROELECTRIC AND FERROELASTIC MATERIALS FOR PIEZOELECTRIC TRANSDUCER APPLICATIONS		5. TYPE OF REPORT & PERIOD COVERED Annual Dec 1, 1979 to Nov 30, 1980
		6. PERFORMING ORG. REPORT NUMBER
7. AUTHOR(s) L.E. Cross, R.E. Newnham, G.R. Barsch, J.V. Biggers		8. CONTRACT OR GRANT NUMBER(s) N00014-78-C-0291
9. PERFORMING ORGANIZATION NAME AND ADDRESS Materials Research Laboratory The Pennsylvania State University University Park, PA 16802		10. PROGRAM ELEMENT, PROJECT, TASK AREA & WORK UNIT NUMBERS
11. CONTROLLING OFFICE NAME AND ADDRESS Office of Naval Research, Room 619 Ballston Tower, 800 N. Quincy Street Arlington, VA 22217		12. REPORT DATE December 1980
		13. NUMBER OF PAGES 509
14. MONITORING AGENCY NAME & ADDRESS (if different from Controlling Office)		15. SECURITY CLASS. (of this report) UNCLASSIFIED
		15a. DECLASSIFICATION/DOWNGRADING SCHEDULE
16. DISTRIBUTION STATEMENT (of this Report) Reproduction in whole or in part is permitted for any purpose of the United States Government		
<div style="border: 1px solid black; padding: 5px; display: inline-block;"> This document has been approved for public release and sale; its distribution is unlimited. </div>		
17. DISTRIBUTION STATEMENT (of the abstract entered in Block 20, if different from Report)		
18. SUPPLEMENTARY NOTES		
19. KEY WORDS (Continue on reverse side if necessary and identify by block number)		
20. ABSTRACT (Continue on reverse side if necessary and identify by block number) This report covers work which was carried out over the period from December 1, 1979 to November 30, 1980 in the Materials Research Laboratory of The Pennsylvania State University under ONR contract N00014-78-C-0291. This contract is for a five year program of "Targeted Basic Studies of Ferroelectric and Ferroelastic Materials for Transducer Applications." The period covered by this report is the third year of operation of the program. Over this past year 31 technical papers have been published or submitted for publication. Reprints		

DD FORM 1 JAN 73 1473

EDITION OF 1 NOV 65 IS OBSOLETE
S/N 0102-014-6601

UNCLASSIFIED

SECURITY CLASSIFICATION OF THIS PAGE (When Data Entered)

UNCLASSIFIED

SECURITY CLASSIFICATION OF THIS PAGE(When Data Entered)

and preprints of these completed studies are submitted as technical appendices and form the bulk of the present report. Since the present work is a logical extension of studies initiated earlier on the contract, the technical appendices are numbered serially following on from those in the 1978-79 report, i.e., articles 20 through 50. The report itself has been kept to a very brief narrative description of current activities, which stresses the highlights of achievements in each area of study, and the basic interconnections between each of the different activities on the program.

For convenience, the headings used earlier are retained and the work is described under the following headings:

- A. Electrostriction
- B. Piezoelectric Composites
- C. Grain Oriented Ceramics
- D. Crystal Growth
- E. Processing Studies
- F. Phenomenological Theory
- G. Ferroelectric Bicrystals
- H. Ferroelastics

The topic H discusses new work on ferroelastic crystals which was initiated towards the end of the year.

Highlights of the current year's work have been:

- (1) The development of a refined shell model for electrostriction in strontium titanate (Appendix 27).
- (2) The initiation of a new phenomenological approach to electrostriction and spontaneous strains in antiferroelectric crystals (Appendices 21, 24, 28, 29, 30).
- (3) Delineation of the role of disorder in the B-site cation arrangement upon the relaxor-ferroelectric properties in lead scandium tantalate $[\text{Pb}(\text{Sc}_{1/2}\text{Ta}_{1/2})\text{O}_3]$ and lead scandium niobate $[\text{Pb}(\text{Sc}_{1/2}\text{Nb}_{1/2})\text{O}_3]$ (Appendices 31, 32, 33, 34, 35).
- (4) A new understanding of the role of the Poisson ratio of the polymer phase in modifying the piezoelectric properties of 3:1 connected PZT polymer composites which has lead to the evolution of new very high sensitivity materials for hydrophase applications.
- (5) The development of simple processing to produce strongly textured grain oriented ceramics from anisotropic ferroelectrics in the bismuth oxide layer structure, and in the tungsten bronze structure families. Initial work on lead metaniobate promise significant improvement in d_{33} and d_h without losing the low mechanical quality factor which is such a useful feature of the conventional ceramic.
- (6) The installation of three major new facilities for material processing:
 - (a) A complete Crystalox model MCGS3 crystal growth and materials preparation system.
 - (b) A Mepco plasma: flame spray equipment for ceramic film and coating applications.
 - (c) A Coherent Radiation 500 Watt CO_2 "everlase" laser system for surface treatment of sputtered, evaporated CVD and plasma sprayed ceramic films.

SECURITY CLASSIFICATION OF THIS PAGE(When Data Entered)

1.0 INTRODUCTION

This report covers work which was carried out over the period from December 1, 1979 to November 30, 1980 in the Materials Research Laboratory of The Pennsylvania State University under ONR contract N00014-78-C-0291. This contract is for a five year program of Targeted Basic Studies of Ferroelectric and Ferroelastic Materials for Transducer Applications. The period covered by this report is the third year of operation of the program. Over this past year 31 technical papers have been published or submitted for publication. Reprints and preprints of these completed studies are submitted as technical appendices and form the bulk of the present report. Since the present work is a logical extension of studies initiated earlier on the contract, the technical appendices are numbered serially following on from those in the 1978-79 report, i.e., articles 20 through 50. The report itself has been kept to a very brief narrative description of current activities, which stresses the highlights of achievements in each area of study, and the basic interconnections between each of the different activities on the program.

For convenience, the headings used earlier are retained and the work is described under the following headings:

- A. Electrostriction;
- B. Piezoelectric Composites;
- C. Grain Oriented Ceramics;
- D. Crystal Growth;
- E. Processing Studies;
- F. Phenomenological Theory;
- G. Ferroelectric Bicrystals; and
- H. Ferroelastics.

The topic H discusses new work on ferroelastic crystals which was initiated towards the end of the year.

Highlights of the current year's work have been:

(1) The development of a refined shell model for electrostriction in strontium titanate (Appendix 27).

(2) The initiation of a new phenomenological approach to electrostriction and spontaneous strains in antiferroelectric crystals (Appendices 21, 24, 28, 29, 30).

(3) Delineation of the role of disorder in the B-site cation arrangement

upon the relaxor-ferroelectric properties in lead scandium tantalate $[\text{Pb}(\text{Sc}_{1/2}\text{Ta}_{1/2})\text{O}_3]$ and lead scandium niobate $[\text{Pb}(\text{Sc}_{1/2}\text{Nb}_{1/2})\text{O}_3]$ (Appendices 31, 32, 33, 34, 35).

(4) A new understanding of the role of the Poisson ratio of the polymer phase in modifying the piezoelectric properties of 3:1 connected PZT polymer composites which has lead to the evolution of new very high sensitivity materials for hydrophase applications.

(5) The development of simple processing to produce strongly textured grain oriented ceramics from anisotropic ferroelectrics in the bismuth oxide layer structure, and in the tungsten bronze structure families. Initial work on lead metaniobate promise significant improvement in d_{33} and d_h without losing the low mechanical quality factor which is such a useful feature of the conventional ceramic.

(6) The installation of three major new facilities for material processing:

- (a) A complete Crystalox model MCGS3 crystal growth and materials preparation system.
- (b) A Mepco plasma: flame spray equipment for ceramic film and coating applications.
- (c) A Coherent Radiation 500 Watt CO_2 "everlase" laser system for surface treatment of sputtered, evaporated CVD and plasma sprayed ceramic films.

Based upon work on the current program, the following papers have been presented at National and International Meetings:

82nd Annual Meeting, American Ceramic Society, Chicago, April 1980

1. N. Setter and L.E. Cross, Investigation of the Mechanism of Phase Transition in Ferroelectric Relaxors.
2. K.A. Klicker, J.V. Biggers and W.A. Schulze, Effect of Polymer Matrix on Hydrostatic Response of PZT-Polymer Transducers.
3. T.R. Shrout, K. Rittenmyer, W.A. Schulze and J.V. Biggers, Simplified Fabrication of PZT/Polymer Composites.
4. K. Uchino and L.E. Cross, Electrostriction: Measurements and Applications.
5. L.J. Bowen, T.R. Shrout and J.V. Biggers, Inhomogeneous Densification During Sintering of PZT Ceramics.
6. D.L. Hankey, J.V. Biggers and T.R. Shrout, Investigation of Processing Parameters on Reaction Kinetics and Properties of PZT Compacts.

Electronics Division, American Ceramic Society, Fall Meeting, San Francisco, October 1980

7. L.E. Cross, Effects of Some Macro-, Micro-, and Nanostructural Features on the Properties of Electronic Ceramics.
8. S. Venkataramani, D. Hankey, A. Safari, L.J. Bowen, and J.V. Biggers, Densification in PZT.
9. N. Setter and L.E. Cross, Subgrain Ordering in Relaxor Ferroelectrics.
10. R.E. Newnham, K.A. Klicker, S.Y. Lynn, A. Safari, and H. Savakus, Ceramic-Polymer Composites for Hydrophones.
11. L.J. Bowen and T.R. Gururaja, High Frequency Properties of Ceramic/Polymer Piezoelectric Composites.
12. L.E. Cross and K. Uchino, Electrostriction in Perovskites.
13. S. Venkataramani, T.A. Shrout, J.V. Biggers and W.A. Schulze, Low Temperature Fired PZT.

International Summer School on Ferroelectrics, Erice, Sicily, July 1980

14. L.E. Cross, General Introduction to Ferroelectricity
15. L.E. Cross, Dielectrics and Electrostriction
16. L.E. Cross, Piezoelectric Composites

Physics of Dielectric Solids, Canterbury, UK, September 1980

17. L.E. Cross, R.E. Newnham, and S.J. Jang, Electrostriction in Perovskite Crystals.
18. R.E. Newnham, L.J. Bowen, K.A. Klicker, and L.E. Cross, Composite Paraelectric Transducers.

Other

19. K. Uchino, S. Nomura, R.E. Newnham, and L.E. Cross, Electrostriction in Perovskite Crystals and its Application in Transducers. Joint Soviet:Japan Seminar on Ferroelectrics, Kyoto, Japan, September 1980.
20. T. Gururaja, R.E. Newnham, K.A. Klicker, S.Y. Lynn, W.A. Schulze, T.R. Shrout, and L.J. Bowen, Composite Piezoelectric Transducers. Ultrasonics Symposium IEEE, Boston, November 1980.
21. R.E. Newnham and A.S. Bhalla, Holey Crystals. American Cryst. Assoc. Annual Meeting, Calgary, Canada, August 1980.
22. R.E. Newnham. Ferroic Crystals. Solid State Physics Meeting, Warwick University, England, January 1980.

Patent disclosures were submitted upon the following topics:

<u>PSU Disclosure Number</u>	<u>Title and Authors</u>
79-435	A New Type of Ultrasensitive AC Capacitance Dilatometer (L.E. Cross, K. Uchino)
79-447	A Single Step Hot Isostatic Pressing Process for Powder Densification (J.V. Biggers, L. Bowen, W. Schulze)

<u>PSU Disclosure Number</u>	<u>Title and Authors</u>
79-448	Lead Germanate Bonded PZT Composite Piezoelectrics (J.V. Biggers, L. Bowen, W. Schulze)
79-450	Simplified Fabrication of PZT/Polymer Composites (T.R. Shrout, W.A. Schulze, J.V. Biggers)
80-455	3:1 Connected PZT-Polymer Composites for Transducer Applications (K. Klicker, L.E. Cross, R.E. Newnham, J.V. Biggers)
80-456	Continuous Poling Technique for Piezoelectric Fibers (T.R. Gururaja, L.E. Cross, R.E. Newnham, L.J. Bowen)
80-457	Broad Band Composite Transducers for Resonant Applications (K. Klicker, R.E. Newnham, L.E. Cross, L.J. Bowen)
80-458	Internally Electroded Ceramic Piezoelectric Transformers (J.V. Biggers, W. Schulze, L. Bowen, T. Shrout)
80-461	Pressure Gauge Using Relaxor Ferroelectrics (K. Uchino, S.J. Jang, L.E. Cross, R.E. Newnham)

The following students who have been supported fully or partially upon ONR funds graduated during the year.

Ph.D.

S.J. Jang*	Electrostrictive Ceramics for Transducer Applications	Solid State Science November 1979
A.H. Amin	Phenomenological and Structural Studies of Lead Zirconate	Solid State Science November 1979
K.A. Klicker	Piezoelectric Composites with 3:1 Connectivity for Transducer Applications	Solid State Science May 1980
D.L. Hankey	Calcination Reaction Mechanisms and Kinetics in Lead Zirconate Titanate Powder Compacts	Solid State Science May 1980
N. Setter	The Role of Positional Disorder in Ferroelectric Relaxors	Solid State Science August 1980

M.S.

M.B. Holmes	Grain Oriented Ferroelectric Ceramics	Ceramic Science November 1980
J.F. Hauris	A Sensitive Capacitor Dilatometer for Electromechanical Strain Measurements	Solid State Science November 1979

*S.J. Jang - Xerox Research Award, 1980.

We are very pleased to report that the work performed by Dr. S.J. Jang in support of his Ph.D. in Solid State Science was judged by an independent University committee drawn from all materials related faculty at Penn State to be one of the two best efforts for Ph.D. in the whole University, and that S.J. Jang was in receipt of one of the Xerox Company Research Awards for 1980.

Mr. K.A. Klicker was awarded first prize in a University-wide speaking contest sponsored by the Central Pennsylvania Branch of the American Chemical Society. He spoke on piezoelectric composites.

2.0 ELECTROSTRICTION

2.1 Introduction

The experimental and phenomenological studies of electrostriction in perovskite type crystals has been summarized in three review articles (Appendices 28, 29, and 30). These articles summarize work upon the general interrelations of the electrostrictive Q parameters to other anharmonic properties (A20), electrostriction in non-polar perovskites (A23), some unusual inverse hysteresis effects in the lead magnesium niobate:lead titanate relaxor ferroelectrics (A25), and the initiation of a new phenomenological theoretical approach to the spontaneous strain effects in antiferroelectric perovskites (A21, A24).

In the more basic theoretical work, analysis of inter-relations to the stress dependence of the dielectric permittivity cast some doubt on the heretofore general assumption of only weak temperature dependence of the polarization related Q constants, which is supported by recent indirect measurements of Q_{ijkl} in BaTiO_3 above T_c . Conflict with the good agreement obtained using temperature independent constants to calculate spontaneous strains below T_c stresses the urgent need for better data on the constants in paraelectric perovskites.

Lattice theories of electrostriction in the shell model give a consistent description of the extrapolated zero temperature experimental data for SrTiO_3 (A27) but in alkali halides where the fit would be expected to be better, the disagreement with accepted experimental values casts further doubt upon the validity of the present experimental numbers for Q constants.

Work is now progressing well upon a full quantum theoretical treatment for zero point and thermal motions in the perovskites.

Studies of the dielectric characteristics in single crystals of lead scandium niobate (PSN) and lead scandium tantalate (PST) (A31) have progressed to the point where the role of disorder in the Sc:Ta and Sc:Nb cations upon the diffuse nature of the phase change at T_c has been clearly established (A32, A33). Unexpectedly, disorder in PST does not give rise to anomalously low values of the electrostrictive Q constants (A34) but does account rather nicely for the earlier divergences in experimental measurement of the phase change in PSN which had not taken account of possible differences occurring in the cation order as a result of the different processing conditions.

2.2 Instrumentation

Using the new phase locked drift compensated AC dilatometer, more precise values of d coefficients have been obtained for a number of crystals, and for PVF_2 polymers of different poling level. For several systems, linearity of the piezoelectric relations has been checked down to exceedingly low strain levels ($\sim 10^{-10}$). Though the proven AC sensitivity is entirely adequate, it has not yet proven possible to measure the electrostriction parameters for alkali halides. We believe that the problem may be associated with the higher level of Maxwell stress at the high voltage (field) levels which are necessary for the weakly electrostrictive solids. It appears that these surface applied forces may give rise to inhomogeneous stresses which produce larger deformations which again scale accurately with E^2 . It is hoped that this problem can be relieved by improving the mode of mounting the electrostrictive samples so that bending forces do not perturb the location of the sensing patterns.

Work is now progressing on the design of a simpler lower sensitivity AC dilatometer based on the same principles which would permit direct measurements of d coefficients for crystals and ceramics over a wide temperature range to supplement and check data from the very useful Berlincourt d_{33} meter.

2.3 Electrostriction in Perovskites

Studies have been made of the electrostriction effects in a wide range of perovskite type ferroelectrics including Skanavi type non-polar relaxors, Smolensky type cation disordered structures, crystals in which the cation order can be controlled, simple proper ferroelectrics, and antiferroelectric systems. Qualitatively it appears that the state of ordering in the B site cations may play a more important role in determining both the general level of electrostriction and the temperature dependence of the paraelectric polarizability than the nature of the lower temperature coupling whether it be ferro- or antiferroelectric. It appears that as a good "rule of thumb" the product of the Curie constant C and the hydrostatic Q constant ($Q_h = Q_{11} + 2Q_{12}$) is almost constant for all perovskites.

The fact that the polarizability (which is linearly related to C) appears to the second power in electrostrictive applications while Q is only a linear term, suggests the clear practical advantage in the cation disordered perovskites which has been verified by studies in the $\text{Pb}(\text{Mg}_{1/3}\text{Nb}_{2/3})\text{O}_3\text{:PbTiO}_3$ solid solution family.

To explore the spontaneous deformations accompanying antiferroelectric ordering, the simple two sublattice Kittel model for the system has been extended to include an effective electrostrictive interaction. It is shown that by including a symmetry permitted term to take account of the elastic interaction associated with coupling between the two sub-lattice polarizations it is possible to account satisfactorily for the volume changes which occur in the antiferroelectric transitions in PbZrO_3 and in $\text{Pb}(\text{Mg}_{1/2}\text{W}_{1/2})\text{O}_3$, and thus for the pressure dependence of the transition behavior in these systems.

Work is now proceeding to extend the phenomenology to a full three dimensional analysis, so that both shape and volume changes can be accounted for.

2.4 Theory of Electrostriction

The objective of this work is to investigate theoretically the magnitude and temperature variation of the electrostriction coefficients of ionic crystals in order to account for, and ultimately predict, tendencies in the effect of crystal structure and of the properties of the constituent ions. Progress during the previous year is summarized under the following subject headings.

2.4.1 Temperature dependence of electrostriction of ferroelectric crystals in the paraelectric phase

Rigorous phenomenological expressions for the temperature variation of the electrostriction coefficients of ferroelectric crystals in the paraelectric phase have been derived from the Curie-Weiss law pertaining to a stressed crystal. For the cubic prototype phase the coefficients $Q_{ijkl} = (\partial^2 \eta_{kl} / \partial P_i \partial P_j)$, where η_{kl} and P_i denote, respectively, the components of the strain tensor and of the polarization, depend linearly on temperature, in agreement with available experimental data. For a second order ferroelectric transition the electrostriction coefficients pertaining to shear deformations vanish at the Curie temperature T_c . For a uniaxial ferroelectric some components of the electrostriction tensor Q_{ijkl} exhibit a linear temperature variation, whereas for other components singular terms of the form $(T-T_c)^{-1}$ and $(T-T_c)^{-2}$ occur, in satisfactory agreement with experimental data. The implications of these results for the common procedure of determining electrostriction coefficients from the spontaneous polarization and strain in the ferroelectric phase are that the underlying assumption of constant coefficients in the Taylor expansion of the

Landau-Devonshire free energy, with the exception of the coefficient pertaining to the term quadratic in the polarization, is not fully justified.

2.4.2 Lattice theory of the nonlinear elastic dielectric in the shell model

Expressions for the first order anharmonic coefficients in the effective constitutive relations of the nonlinear elastic dielectric pertaining to a small deformation and electric field superimposed on a finite initial deformation and electric field have been derived for the static shell model by means of the method of long waves. They comprise the electrostriction, nonlinear dielectric, elasto-optic, and electro-optic coefficients and the strain- and electric-field derivatives of the piezoelectric and second order elastic constants and may easily be generalized for any anharmonic shell model in which both inter-ionic and intra-ionic anharmonicity is included.

2.4.3 Shell model calculation of electrostriction coefficients of rocksalt-type alkali halides

The electrostriction constants and the photoelastic constants of rocksalt-type alkali halides have been calculated for a variety of rigid ion models and shell models, with and without many-body interactions, and with and without intra-ionic anharmonicity included. For the electrostriction constants none of the models considered can account satisfactorily for the experimental data of Bohaty and Haussühl, especially for f_{12} and f_{44} . Moreover, in spite of the inclusion of intra-ionic anharmonicity the calculated electrostriction constants do not differ drastically from values calculated on the basis of a rigid-shell model with many-body forces included, although a perfect fit of the photoelastic constants can be obtained in this case. One may therefore conclude (a) that inclusion of intra-ionic anharmonicity, while essential for the photoelastic constants, is only of minor importance for the electrostriction constants; (b) that the effect of many-body forces, while apparent in the second and third order elastic constants, is only small for the electrostriction constants, at least in alkali halides, and/or (c) that the experimental electrostriction data for the alkali halides could be seriously in error.

To substantiate conclusion (b) we have applied Keating's model of angle bending forces up to third order in the four anion-cation-anion angles of the rocksalt structure. The results indicate that as a result of the crystal symmetry these angle bending forces do not contribute to the anharmonic potential

energy in the rocksalt structure. Thus the many-body forces present in the rock-salt structure must be of a more general nature. Furthermore, the role of thermal effects on the electrostriction constants in alkali halides is unknown.

2.4.4 Electrostriction, optic mode gammas and third order elastic constants of SrTiO_3 in the shell model

Lattice dynamical calculations of harmonic and first order anharmonic properties at the zone center have been performed for the perovskite structure on the basis of a shell model. The harmonic part of the model is equivalent to Cowley's model, with the 14 parameters determined from zone center properties only. Anharmonic interactions arising from Coulomb and short range repulsion are included and are characterized by three parameters. Numerical application to SrTiO_3 shows that the model gives a consistent description of third order elastic and electrostriction constants, provided that the higher than first order anharmonic contributions arising from zero point and thermal motion are eliminated from the experimental data by extrapolation to absolute zero.

2.5 Ferroelectric Relaxors

Studies have continued of the order:disorder of the B site cations in the perovskites $\text{Pb}(\text{Sc}_{1/2}\text{Ta}_{1/2})\text{O}_3$ and $\text{Pb}(\text{Sc}_{1/2}\text{Nb}_{1/2})\text{O}_3$. In the case of the tantalate the ordering process can be studied straightforwardly by x-ray methods and both the fractional order and the size of ordered domains established. For the niobate the B cations are too similar in atomic number for such a simple test, but Raman measurements on single crystals again have established the ordering phenomenon and serve to explain some of the wide property differences reported in this compound. For these earlier studies it was evident that different modes of preparation lead to different degrees of order (in the same chemical compound) and thus different Curie points and degree of diffuseness in transition behavior.

Possible utilization of the PST and PSN compositions in pyroelectric, piezoelectric, and electrostrictive transducers is now under study.

3.0 COMPOSITE TRANSDUCERS

3.1 Introduction

A major program area encompasses the application of ceramic:ceramic, ceramic:plastic, and ceramic:metal composites as new materials for piezoelectric transducers. Excellent success has been achieved in the area of hydrophone transducers where the ceramic:plastic composites with appropriately tailored microstructures yield figures of merit over 100 times larger than the single phase ceramic. New processing fabrication and poling techniques have been developed for these composite systems, and work is now proceeding on potential higher frequency applications which can make special use of the periodicity and the viscoelastic character of the microstructure and phase make-up.

3.2 Fabrication Techniques

Work has continued refining the extrusion and firing of very fine PZT fibers for ceramic:plastic composite structures. A post-sinter hot isostatic pressing (HIP) process has now been developed which yields excellent fiber characteristics down to diameters of 100 μ meters.

A new continuous poling process is being applied to the fibers before fabrication into the composite. Pre-poling in this manner permits the assembling of composites with more than one polar axis and with symmetry properties which are not permitted in single phase systems.

Following work on the replamineform replication method a new simpler technique has been evolved for developing 3:3 connected composites using a loading of micron sized plastic spheres in the PZT slip which burn out during firing to form a three dimensionally porous PZT sponge. The sponge can be vacuum impregnated with a suitable plastic to form a polable rigid composite closely comparable to the original replamineform material but much less expensive.

3.3 Hydrophone Materials

3:1 connected PZT:epoxy composites have been developed which show figure of merit ($d_h g_h$ product) up to $4,000 \times 10^{-12} \text{ m}^2/\text{N}$. Structures with softer elastomer as the plastic component proved initially disappointing. The reduced sensitivity was traced to an effect of the poisson ratio which is close to 0.5 in these elastomers. Modification of the poisson ratio was effected by foaming

the plastic and by incorporating hollow glass microspheres (ekospheres).

In both families of these new 3:1:0 3-phase composites it has proved possible to achieve $d_h g_h$ products greater than $50,000 \times 10^{-12} \text{ m}^2/\text{N}$, more than 100 times larger than the single phase PZT.

In the impregnated PZT sponge, transverse reinforcement is provided by the connected PZT so that Poisson ratio modification is unnecessary and sensitivities of order $d_h g_h \simeq 20,000 \times 10^{-12} \text{ m}^2/\text{N}$ can be achieved with a solid silicone rubber second phase.

3.4 Higher Frequency Applications

When the wavelength of the acoustic wave becomes comparable to the composite phase separation a new regime of operation occurs in the composites and averaged materials parameters are no longer adequate to describe the behavior. For 3:1 ceramic:plastic composites it would appear that even in the hard epoxy second phase the acoustic attenuation and reflection losses at interfaces are so large that the PZT fibers behave to a first approximation as isolated resonators. Thus for some broader band applications surface contour can be used to control bandwidth. For simple NDE applications in liquid media, acoustic matching is much superior to more dense PZT transducers and conformal profiles can be readily achieved by simple moulding techniques.

So far only the simplest configurations have been studied, but work is moving forward to explore more complex geometries for the component phases, possible impedance transformers using tube and sheet structures, and elements in which transmit and receive functions can be separated in the single element.

3.5 Ceramic:Metal Composites

Studies are under way to test the efficacy of implanted electrode structures made by the conventional tape casting and cofiring techniques widely used in capacitor manufacture. Platinum electrodes have been incorporated in both hard and soft PZTs and in several lead magnesium niobate (PMN) based electrostrictor compositions. Stacked elements designed to produce large displacements have been constructed for low voltages to test the reproducibility and hysteresis in the strain:field curves for piezoelectric and electrostrictive formulations.

In general the newer relaxor based electrostriction materials show superior reproducibility at low frequencies due, it is believed, to the absence of domain aging effects and to their very low thermal expansion.

4.0 GRAIN ORIENTED CERAMICS

A method for producing grain-oriented electroceramics of the bismuth titanate family has been developed which takes advantage of their mica-like morphology. Discrete plate-like grains of the compounds were produced by reacting the oxides in a NaCl-KCl bath. Tape casting was used to align the grains, and subsequent sintering resulted in a grain-oriented ceramic. Orientation was verified by scanning electron microscopy, x-ray diffraction, and dielectric measurements. The compounds produced by this method were Bi_2WO_6 , $\text{PbBi}_2\text{Nb}_2\text{O}_9$, and $\text{Bi}_4\text{Ti}_3\text{O}_{12}$. Investigations are now under way to densify the ceramics.

Similar experiments have been performed on lead metaniobate, PbNb_2O_6 . Flat elongated crystallites of the ferroelectric orthorhombic form were prepared by the molten salt and then tape-cast. An orthorhombic texture was obtained after sintering with the short axis of the crystallites perpendicular to the tape, and the long axis parallel to the casting direction. Piezoelectric coefficients of grain-oriented PbNb_2O_6 are superior to those of the randomly oriented ceramics used in hydrophones.

5.0 CRYSTAL GROWTH

Work has continued over the year on the flux growth of the complex perovskites lead scandium niobate (PSN) and lead scandium tantalate (PST) and is described in detail in Appendix 31. Crystals of a size and quality suitable for optical domain studies, dielectric measurements and ferroelectric switching studies have been produced. Attempts to grow PZT crystals at compositions close to morphotropy using flux methods have proven exceedingly difficult with only very heavily strained small samples being obtained. This effort has for the present been suspended pending the introduction of equipment for other methods.

During 1980 the group was delighted to be able to acquire a Crystalox Model MCGS3 Crystal Growth and Material Preparation System, and to be able to have Dr. D. Hukin from the Clarendon Laboratory in Oxford who is the designer of the system spend a six-month sabbatical working with the system.

The MCGS3 is of modular design, and the Penn State unit incorporates equipment for Czochralski, Bridgeman-Stockbarger, floating zone, and horizontal zone melting methods. Horizontal zone refining can be carried out in conventional and in cold boats with precisely controlled heat treatment and annealing schedules. Operating environments are available from vacua of 10^{-7} mbar to 4 bars of inert or active gases, at temperatures up to 2,500°C.

The 30 Kw Stanelco Hyforce RF generator unit is equipped for precise control by feedback from a temperature or a power level sensor and incorporates a microprocessor unit for program control.

It is anticipated that the full system will be in operation early in January 1981. Initial "proof testing" of the system will be concerned with the growth of a number of perovskite halide compounds for electrostrictive and ferroelastic studies, with larger single crystals of the PSN and PST, and with other members of the perovskite and tungsten bronze relaxor ferroelectric families.

6.0 PROCESSING STUDIES

Extensive studies of the calcination mechanisms in PZT ceramic powder compacts were carried out using the matrix flushing technique for x-ray diffraction analysis. Kinetic data obtained and the influences of incompletely reacted PbO solid solution phase have been carefully documented in the dissertation studies of D. Hankey.

This work is now being followed up by a more complete analysis of the sintering behavior of oxide powders calcined to different phase assemblages. The important role of the PbO solid solution phase in generating a preliminary dilation before proper shrinkage has been discussed in papers presented at the American Ceramic Society and will form the basis for the thesis work of S. Venkataramani.

The expertise which has been fostered in the group by continuing basic studies of the PZT family materials has proved of exceptional value in permitting the effective processing of materials for a wide range of composite structures and the possibility for fabricating limited batches of the more exotic perovskite and bronze structure compounds and solid solutions needed for other studies on the contract.

7.0 PHENOMENOLOGICAL STUDIES

Perovskites: Work has continued to improve and refine the elastic Gibbs function describing the PZT family. Present emphasis is upon a careful remeasurement of the heats of transition at T_c for a range of organically prepared, carefully homogenized pure PZTs. Comparison of the measured and calculated heats give a method of checking the Curie Weiss constant C_0 which will be compared to VHF dielectric data. A developing interest is to explore, using the known electrostrictive constants, the fourth order parameters in the Helmholtz function with particular reference to compositions close to pure PbZrO_3 which apparently show tricritical behavior.

8.0 FERROELECTRIC BICRYSTALS

Work on the lithium niobate bicrystals is being continued. Studies on the original samples bonded at 1100°C below the Curie temperature reveal that inserts of opposing domain configuration often occur adjacent to the bonded 'c' surfaces, and higher magnification SEM pictures reveal a measure of secondary recrystallization on the bonded surface.

Present studies are concerned with developing a suite of single domain samples bonded with clean interfaces so that the dielectric and pyroelectric spectra may be related to the orientation of the interface pairs.

In parallel with the single crystal work, preliminary experiments are being conducted to explore the possibility of generating polar grain oriented ceramics by field orienting powder from LiNbO_3 crystal offcuts in an organic liquid, then hot-pressing the compact to densify at temperatures below T_c .

9.0 FERROELASTICS

To initiate work in the topic of ferroelastics, studies on two new topics have been begun.

1. Data are being compiled of the ferroelastic Curie temperature, melting temperature and maximum spontaneous strain for a wide range of known ferroelastic solids. We wish to discern whether in ferroelastics there are relations similar to the Abrahams:Kurtz relations for ferroelectrics which give general formulae to relate P_s , T_c , and the soft mode displacements.

2. To explore the possibility of using the ferroelastic phase change and its associated twinning as a toughening mechanism for mechanical properties as with tetragonal zirconia, work has been begun on the mineral leucite as a model material.

Leucite $K[AlSi_2O_6]$ undergoes a phase change $m3m \rightarrow F4/m$ at $630^\circ C$ to a twinned ferroelastic form. At higher temperature the crystal has a high temperature cubic zeolite cage structure and extensive solid substitution is possible.

The leucite composition can also be easily quenched to a glass, and techniques are known for initiating and controlling the recrystallization process.

We propose to explore the ferroelastic coercivity in leucite crystals, the control of twinning and phase transition temperature by elastic constraints, and the possibility of suppression of the phase change in fine particle ceramic and glass ceramic samples.

10.0 PROGRAM ORGANIZATION: PERSONNEL AND EQUIPMENT

10.1 Personnel

The people directly responsible for work in this program are summarized in Figure 1. Major changes which have occurred during the year are indicated in the boxes on the figure. We are very pleased to report that Dr. V. Wadhawan joined us from the Clarendon Laboratory in Oxford to head up work on the ferro-elastic topic and that Dr. N. Setter assumed primary responsibility for relaxor ferroelectric studies as a postdoctoral fellow after completing her PhD work.

Dr. K. Uchino returned to take up his studies at the Tokyo Institute of Technology, Dr. L. Bowen accepted an appointment at GTE Waltham, and Dr. A. Amin joined Texas Instruments in Attleboro, Mass. Dr. B. Hardiman is planning to relocate in Europe. We are also delighted that several students who completed their studies have obtained excellent positions in industrial and government laboratories.

10.2 Equipment

Over the past year major pieces of equipment have been added for crystal growth and preparation. As indicated in the crystal growth section, a Crystalox MCGS3 growth and preparation system has been acquired and should be in full operation early in 1981.

A Mepco plasma:flame spray device has also been purchased on joint ONR:University funds and is presently being installed. This equipment requires rather extensive sound insulation with a special spray booth and baffle structure. Together with the very high electric power and cooling water requirement, extensive refurbishing of one of the laboratories has been required for these services.

A Coherent Everlase 500 watt CO_2 laser has also been installed and is now undergoing preliminary testing. Rather extensive accessories in the form of specimen tables, traverses, lens systems and other backup equipment are required for the fullest use of the system and these accessories are being built up over the next two years.

In measuring equipment, the frequency spectrum for dielectric studies has been dramatically extended by the acquisition of an HP Model 4191A impedance analyzer. This instrument sweeps the frequency range from 1 MHz to 1,000 MHz and provides direct reading of both real and imaginary components of sample

DN BASIC (PEOPLE)FACULTY

L.E. CROSS, PROFESSOR OF ELECTRICAL ENGINEERING
 R.E. NEWNHAM, PROFESSOR OF SOLID STATE SCIENCE
 G.R. BARSCH, PROFESSOR OF PHYSICS
 J.V. BIGGERS, SENIOR RESEARCH ASSOCIATE MRL
 W.A. SCHULZE, RESEARCH ASSOCIATE MRL

ASSOCIATES

B.N. ACHAR N. SETTER (PSU)
 A. BHALLA V. WADHAWAN (OXFORD)

L. BOWEN (GTE WALTHAM)	K. UCHINO (T.I.T. TOKYO)
B. HARDIMAN	A. AMIN (T.I. MASS.)

GRADUATE ASSISTANTS

T. GURURAJA
 S. LYNN
 K. RITTENMYER
 A. SAFARI
 S. SWARTZ
 S. VENKATARAMANI
 D. VOSS

D. HANKEY (SANDIA)
M. HOLMES (?)
J. JANG (WESTERN ELECTRIC)
K. KLICKER (BELL LABS)

TECHNICAL AIDES

R. BRENNEMAN, R. ORMSBY, S. LeFRANCOIS

impedance. Together with existing present equipment, we are now able to cover the range from 10^{-3} to 10^{+9} Hz in our dielectric studies.

In surface characterization tools the Laboratory has added new equipment for scanning ion mass spectroscopy and for simulated ion photon spectroscopy (SIMS:SIPS). This unique equipment provides unrivaled facility for identifying and profiling light ions incorporated in ceramic surfaces.

10.3 Advisory Committee

The third meeting for the ONR Advisory Committee on this program was held at Penn State on Wednesday and Thursday, October 8 and 9, 1980. Participants at the meeting were

A. Advisory Committee Members

A. Glass, Bell Telephone Laboratories, Holmdel NJ
 H. Anderson, University of Missouri-Rolla, Rolla MO
 W. Smith, North American Philips Laboratories, Briarcliff Manor NY
 B. Auld, Stanford University, Stanford CA
 W. Harrison, Honeywell Ceramics Center, Golden Valley MN

Unable to attend:

B. Jaffe, Vernitron Corporation, Bedford OH
 D. Berlincourt, Channel Products, Chesterland OH

B. Navy Representatives

A. Diness, ONR Washington DC
 R. Pohanka, ONR Washington DC
 A. Gilmore, ONR Washington DC
 S. Meeks, NRL Orlando FL
 D. Siegel, ONR Washington DC
 P. Smith, NRL Washington DC
 H. Savage, NSW Silver Springs MD
 C. LeBlanc, NURC New London CT
 R. Woollett, NURC New London CT

C. Guests

J. Deen Brown, General Dynamics, Groton CT
 F. Recny, Undersea Electronics Program Department, Syracuse NY
 R. Teza, Undersea Electronics Program Department, Syracuse NY
 A. Streater, Ocean Systems, Nashua NH
 T. Gerken, General Dynamics, Groton CT
 F. Johnson, Honeywell, Seattle WA
 J. Dougherty, Gulton Industries, Metuchen NJ
 D. Buckner, Gulton Industries, Fullerton CA
 M. Pedinoff, Hughes Corporation, Malibu CA
 R. Neurgaonkar, Rockwell International, Thousand Oaks CA
 G. Goodman, Johnson Controls, Milwaukee WI

D. Penn State

L. Cross
R. Newnham
J. Biggers
G. Barsch
B. Achar
W. Schulze

A. Bhalla
N. Setter
T. Gururaja
K. Rittenmyer
T. Shrout

The program of the meeting is outlined below.

WEDNESDAY 8th OCTOBER 1980

Room 250, Materials Research Laboratory

ONR PROGRAM REVIEW

9:00	R.C. Pohanka	Introduction
9:25	L.E. Cross	Program Outline Objectives and Achievements
10:00	L.E. Cross N. Setter K. Rittenmyer	ELECTROSTRICTION Experimental Measurements Perovskite Relaxors, Applications
11:00	G.R. Barsch N. Achar	Theoretical Work on Electro- striction
12:00	LUNCH	(Room 189 MRL)
1:00	New Equipment	
1:30	J.V. Biggers W.A. Schulze	PROCESSING Grain Oriented Ceramics
2:30	R.E. Newnham T. Gururaja	PIEZOELECTRIC COMPOSITES Higher Frequency Responses
3:30	L.E. Cross	New Starts; spinoffs
4:00	DISCUSSION	

THURSDAY 9th OCTOBER 1980

Room 250, Materials Research Laboratory

9:00 DISCUSSION (R.C. Pohanka, moderator)
Developing opportunities for technology transfer
1. Hydrophone composites
2. Electrostrictors
3. Grain oriented ceramics

Proceedings of this group are reported separately.

APPENDICES

20. K. Uchino, L.E. Cross. Electrostriction and its Interrelation with Other Anharmonic Properties of Materials. Jpn. J. Appl. Phys. 19, L171 (1980).
21. K. Uchino, L.E. Cross, R.E. Newnham. Electrostrictive Effects in Paraelectric-Ferroelectric-Antiferroelectric Phase Transitions. Jpn. J. Appl. Phys. 19, L425 (1980).
22. K. Uchino, S. Nomura, A. Amin, Z.P. Chang, L.E. Cross, R.E. Newnham. Elastic Constants and Thermal Expansion in Cation Disordered Perovskites. Jpn. J. Appl. Phys. 19, L398 (1980).
23. K. Uchino, L.E. Cross, R.E. Newnham, S. Nomura. Electrostriction Effects in Nonpolar Perovskites. J. Phase Trans. (accepted).
24. K. Uchino, L.E. Cross, R.E. Newnham, S. Nomura. Electrostrictive Effects in Antiferroelectric Perovskites. J. Appl. Phys. (accepted).
25. K. Uchino, L.E. Cross, S. Nomura. Inverse Hysteresis of Field Induced Elastic Deformation in the Solid Solution $0.9\text{Pb}(\text{Mg}_{1/3}\text{Nb}_{2/3})\text{O}_3:0.1\text{PbTiO}_3$. J. Mat. Sci. (accepted).
26. W. Schulze, T.R. Shrout, S.J. Jang, S. Sharp, L.E. Cross. Monolithic Multilayer Transducers for Optical Applications. J. Amer. Ceram. Soc. 63, 596 (1980).
27. B.N. Achar, G.R. Barsch, L.E. Cross. Electrostriction, Optic Mode Gammas and Third Order Elastic Constants of SrTiO_3 in the Shell Model. Phys. Rev. B (submitted).
28. K. Uchino, S. Nomura, L.E. Cross, R.E. Newnham. New Electrostrictive Materials. I. Elect. Ceram. 11 (summer) 57 (1980) (in Japanese).
29. K. Uchino, S. Nomura, L.E. Cross, R.E. Newnham. New Electrostrictive Materials. II. Elect. Ceram. 11 (autumn) (1980, in press) (in Japanese).
30. K. Uchino, S. Nomura, L.E. Cross, R.E. Newnham. Electrostriction in Perovskite Crystals and its Application to Transducers. J. Mat. Sci. (accepted).
31. N. Setter, L.E. Cross. Flux Growth of Lead Scandium Tantalate $\text{Pb}(\text{Sc}_{0.5}\text{Ta}_{0.5})\text{O}_3$ and Lead Magnesium Niobate $\text{Pb}(\text{Mg}_{1/3}\text{Nb}_{2/3})\text{O}_3$ Single Crystals. J. Cryst. Growth (accepted).
32. N. Setter, L.E. Cross. The Contribution of Structural Disorder to Diffuse Transitions in Ferroelectrics. J. Mat. Sci. 15, 2478 (1980).
33. N. Setter, L.E. Cross. The Role of B-Site Cation Disorder in Diffuse Phase Transition Behavior of Perovskite Ferroelectrics. J. Appl. Phys. 51, 4356 (1980).
34. N. Setter, L.E. Cross. Pressure Dependence of the Dielectric Properties of $\text{Pb}(\text{Sc}_{1/2}\text{Ta}_{1/2})\text{O}_3$. Phys. Stat. Sol. A61, K71 (1980).

35. N. Setter, L.E. Cross. Ferroelectric Transition Characteristics in $\text{Pb}(\text{Sc}_{0.5}\text{Nb}_{0.5})\text{O}_3$. Mat. Res. Bull. (submitted).
36. S.J. Jang, L.E. Cross, K. Uchino, S. Nomura. Dielectric and Electrostrictive Properties of Ferroelectric Relaxors in the System $\text{PbMg}_{1/3}\text{Nb}_{2/3}\text{O}_3$: PbTiO_3 : $\text{BaZn}_{1/3}\text{Nb}_{2/3}\text{O}_3$. J. Amer. Ceram. Soc. (accepted).
37. S.J. Jang, W.A. Schulze, J.V. Biggers. Low Firing Capacitor Dielectrics in the System $\text{Pb}(\text{Fe}_{2/3}\text{W}_{1/3})\text{O}_3$ - $\text{Pb}(\text{Fe}_{1/2}\text{Nb}_{1/2})\text{O}_3$ - $\text{Pb}_5\text{Ge}_3\text{O}_{11}$. J. Amer. Ceram. Soc. (submitted).
38. R.E. Newnham, L.J. Bowen, K.A. Klicker, L.E. Cross. Composite Piezoelectric Transducers (review). Int. J. Mats. in Eng. Appl. (accepted).
39. T.R. Gururaja, R.E. Newnham, K.A. Klicker, S.Y. Lynn, W.A. Schulze, T.R. Shrout, L.J. Bowen. Composite Piezoelectric Transducers. IEEE Ultrasonics Symposium, Nov. 5-7, 1980, Boston, MA. (accepted).
40. T.R. Shrout, L.J. Bowen, W.A. Schulze. Extruded PZT/Polymer Composites for Electromechanical Transducer Applications. Mat. Res. Bull. 15, 1371 (1980).
41. L.J. Bowen, T. Gururaja. High Frequency Electromechanical Properties of Ceramic/Polymer Composites in Broadband Applications. J. Appl. Phys. 51 (11), 5661 (1980).
42. T.R. Shrout, W.A. Schulze, J.V. Biggers, L.J. Bowen. Resonance Behavior of Internally Electroded PZT Devices. Mat. Res. Bull. 15, 551 (1980).
43. T.R. Gururaja, L.E. Cross, R.E. Newnham. Continuous Poling Technique for PZT Fibers. Bull. Amer. Ceram. Soc. (accepted).
44. L.J. Bowen, T.R. Shrout, S. Venkataramani, J.V. Biggers. Inhomogeneous Densification During Sintering of PZT. J. Amer. Ceram. Soc. (submitted).
45. H.P. Savakus, K.A. Klicker, R.E. Newnham. PZT:Epoxy Piezoelectric Transducers: A Simplified Fabrication Procedure. Phys. Stat. Sol. (submitted).
46. K.A. Klicker, J.V. Biggers, R.E. Newnham. Composites of PZT and Epoxy for Hydrostatic Transducer Applications. J. Amer. Ceram. Soc. (submitted).
47. M. Granahan, M. Holmes, W.A. Schulze, R.E. Newnham. Grain-Oriented PbNb_2O_6 Ceramics. J. Amer. Ceram. Soc. (submitted).
48. A. Amin, R.E. Newnham, L.E. Cross. Atom Shifts, Polarization Levels, and Curie Temperatures in Ferroelectric PbZrO_3 : PbTiO_3 Solid Solutions. Mat. Res. Bull. 15, 721 (1980).
49. A. Amin, L.E. Cross, R.E. Newnham. Effects of Elastic and Electric Boundary Conditions on the Morphotropic Phase Boundary in PZT. J. Mat. Sci. (accepted).
50. L.E. Cross, K.H. Hardtl. Ferroelectrics. Kirk Othmer Encyclopedia of Chemical Technology, Vol. 10, 1980, John Wiley and Sons, NY.

[APPENDICES 1 THROUGH 19 APPEARED IN LAST YEAR'S REPORT (DEC 1979)]

APPENDIX 20

K. Uchino, L.E. Cross. Electrostriction and its Interrelation with Other Anharmonic Properties of Materials. Jpn. J. Appl. Phys. 19, L171 (1980).

Electrostriction and Its Interrelation with Other Anharmonic Properties of Materials

Kenji UCHINO and Leslie E. CROSS

Materials Research Laboratory, The Pennsylvania State University,
University Park, Pennsylvania 16802, U.S.A.

(Received February 7, 1980)

Accumulating data upon the magnitudes of the hydrostatic electrostriction constants Q_h in a wide range of solids have been used to demonstrate several simple empirical relationships to other thermo-elastic and dielectric properties. i.e. $Q_h \propto 1/\epsilon$, $Q_h \propto \alpha^2$, $Q_h \propto \chi_T$ where ϵ is the dielectric permittivity, α the coefficient of thermal expansion and χ_T the isothermal compressibility. A very simple Born model is used to derive inter-relationships between the required properties, however, to obtain quantitative agreement, the reverse power in the repulsion term must be unrealistically small, indicating the need for a more realistic model.

Electrostriction is the basic secondary electro-mechanical coupling effect which can be observed in every type of non-conducting solid material. It is a measure of the electric field (or polarization) induced shifts of the atoms or ions away from their natural equilibrium positions. The electrostriction coefficients Q (or M , are defined as coefficients in the relationship between electric polarization P (or field E) and observed elastic strain $\Delta l/l$, in terms of $\Delta l/l = QP^2$ (or ME^2). Clearly, since the strain is a second rank polar tensor and the E and P are polar vectors, the Q or M are in general fourth rank polar tensors.

In a somewhat similar manner, we may regard the thermal expansion coefficient α and the isothermal compressibility χ_T as 'compliance' coefficients defined by the relations with respect to temperature T and hydrostatic pressure p , respectively ($\Delta l/l = \alpha T$, $\Delta V/V = -\chi_T p$).

It is thus not unreasonable, even for a simple rigid ion model, to expect that these 'compliance' coefficients will be interrelated. In Figs. 1, 2, and 3, plots of the dielectric permittivity ϵ , the thermal expansion α and the isothermal compressibility χ_T respectively, have been made against the polarization related electrostriction constant Q_h ($= Q_{11} + 2Q_{12}$) for materials of isotropic or cubic symmetry.

The experimental data used are from the following sources.

- I) Polymer [PVDF-unoriented KYNAR 7200 (1)]

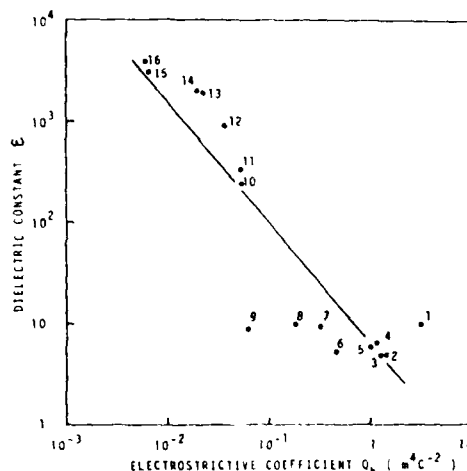


Fig. 1. Dielectric constant ϵ plotted as a function of hydrostatic electrostrictive coefficient Q_h for various materials with cubic or isotropic symmetry. The straight line has slope -1.2 .

Q_h , ϵ : K. Uchino, L. E. Cross and J. C. Hicks: to be published.

α : Kureha Chemical Co. data sheet.

χ_T : J. Brandrup and E. H. Immergut: *Polymer Handbook* (Interscience Pub., NY, 1966).

- II) Alkali Halide [KBr(2), KCl(3), NaBr(4), NaCl(5), NaF(6), LiF(7)]

Q_h , ϵ , α , χ_T : J. Fontanella, C. Andeen and D. Schuele: *Phys. Rev. B6* (1972) 582.

- III) MgO (8)

Q_h : G. R. Barsch: Private communica-

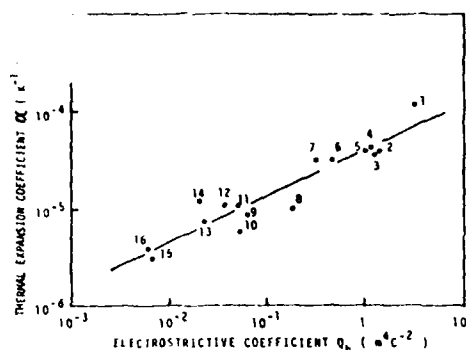


Fig. 2. Thermal expansion coefficient α plotted as a function of hydrostatic electrostrictive coefficient Q_h for various materials. The straight line has slope 0.5.

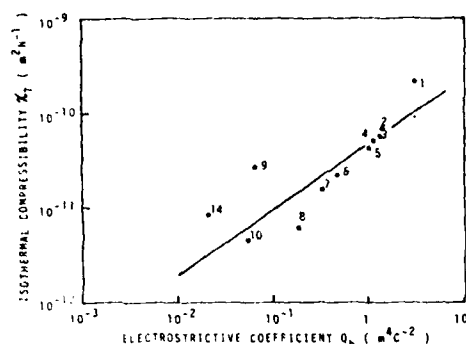


Fig. 3. Isothermal compressibility χ_T plotted as a function of hydrostatic electrostrictive coefficient Q_h for various materials. The straight line has slope 0.7.

tion.

ϵ : W. H. Gourdin and W. D. Kingery: *J. Mater. Sci.* **14** (1979) 2053.

α : B. Yates: *Thermal Expansion* (Plenum Press, London, 1972).

χ_T : K. Vedam and E. D. D. Schmidt: *Phys. Rev.* **146** (1966) 548.

IV) Glass [Pyrex (9)]

Q_h, ϵ : K. Uchino: unpublished.

α : C. L. Mantell: *Engineering Materials Handbook* (McGraw-Hill, N.Y., 1958).

χ_T : K. Vedam, E. D. D. Schmidt and R. Roy: *J. Am. Ceram. Soc.* **49** (1966) 531.

V) Simple Perovskites [KTaO₃(10), SrTiO₃(11), KNbO₃(12), PbTiO₃(13), BaTiO₃(14)]

Q_h, ϵ : Landolt-Börnstein: (Springer-Verlag, Berlin, 1979) Group III, Vol. II.

α : Landolt-Börnstein: (Springer-Verlag, Berlin, 1969) Group III, Vol. 3.

χ_T : M. E. Lines and A. M. Glass: *Principles and Applications of Ferroelectrics and Related Materials* (Oxford, London, 1977).

VI) Complex Perovskites [Pb(Zn_{1/3}Nb_{2/3})O₃ (15), Pb(Mg_{1/3}Nb_{2/3})O₃(16)]

Q_h, ϵ : S. Nomura, J. Kuwata, S. J. Jang, L. E. Cross and R. E. Newnham: *Mater. Res. Bull.* **14** (1979) 769.

K. Uchino, S. Nomura, L. E. Cross, S. J. Jang and R. E. Newnham: to be published in *J. Appl. Phys.* **51** (1980).

α : S. Nomura, M. Abe, F. Kojima and K. Uchino: *Jpn. J. Appl. Phys.* **14** (1975) 1881.

S. J. Jang, K. Uchino, S. Nomura and L. E. Cross: to be published in *Ferroelectrics* (1980).

χ_T : No reference.

The best fitting power curves for the three cases are described as follows:

$$\epsilon = 6.3 Q_h^{-1.2} \quad (\text{correlation coefficient } r=0.91), \quad (1)$$

$$\alpha = 4.2 \times 10^{-5} Q_h^{0.5} \quad (r=0.94), \quad (2)$$

$$\chi_T = 4.7 \times 10^{-11} Q_h^{0.7} \quad (r=0.89). \quad (3)$$

To explain these power relations between the electrostrictive coefficient and other physical properties we shall here use the theory of cohesive forces in ionic crystals, which was worked out mainly by Born.¹¹ In the interests of simplicity we shall derive formulae for the rock-salt structure only. For the average potential energy per ion pair, we may now use a potential function involving an inverse power type of repulsive energy of the form

$$U = -\frac{Mq^2}{r} + \frac{Nb}{r^n}, \quad (4)$$

where M is the Madelung constant, N the coordination number and b is a potential constant. Expanding the potential function around the equilibrium position ($r_0^{-1} = nNb/Mq^2$), we obtain the form as a function of $\Delta r (=r-r_0)$.

$$\Delta U = U(r) - U(r_0) = f(\Delta r)^2 - g(\Delta r)^3, \quad (5)$$

where $f = (n-1)Mq^2/2r_0^3$ and $g = (n+4)(n-1)Mq^2/6r_0^4$.

Using the Boltzmann distribution, the average equilibrium separation at high temperatures under an applied electric field, is as follows:

$$\begin{aligned} \langle \Delta r_{\pm} \rangle &\sim \int_{-\infty}^{\infty} \Delta r \exp(-\Delta V_{\pm}/kT) d\Delta r \\ &\quad \bigg/ \int_{-\infty}^{\infty} \exp(-\Delta V_{\pm}/kT) d\Delta r \\ &\sim \frac{3gk}{4f^2} T \pm \frac{q}{2f} E + \frac{3gq^2}{4f^3} E^2, \end{aligned} \quad (6)$$

where subscripts \pm denote the ion pairs in the positive and negative directions of the electric field respectively, and $\Delta V_{\pm} = \Delta U \pm qE\Delta r$. The strain is therefore given by:

$$\frac{\langle \Delta r_{+} \rangle + \langle \Delta r_{-} \rangle}{2r_0} = \frac{3gk}{4f^2 r_0} T + \frac{3gq^2}{4f^3 r_0} E^2, \quad (7)$$

where the first term represents thermal expansion and the second term, electrostriction.

Using the first law of thermodynamics of $dU = -p dV$, the isothermal compressibility χ_T becomes:

$$1/\chi_T = -V(\partial p/\partial V)_T = V(\partial^2 U/\partial V^2)_T. \quad (8)$$

Changing the variable from V to r and developing the result leads to the equation

$$\chi_T = 18r_0^4/(n-1)Mq^2. \quad (9)$$

Considering that the polarization P is given by

$$P = \frac{q\langle \Delta r \rangle}{2r^3} = \frac{q^2}{4fr_0^3} E, \quad (10)$$

the final forms of the coefficients Q , ϵ , α and χ_T are as follows:

$$Q = \frac{4(n+4)M}{nNb} r_0^{n+3}, \quad (11)$$

$$\epsilon = \frac{1}{2(n-1)M}, \quad (12)$$

$$\alpha = \frac{(n+4)k}{2n(n-1)Nb} r_0^n, \quad (13)$$

$$\chi_T = \frac{18}{n(n-1)Nb} r_0^{n+3}. \quad (14)$$

Note that the hydrostatic Q_h is related to the Q described above using the Poisson ratio σ :

$$Q_h = (1-2\sigma)Q. \quad (15)$$

If we suppose that the Madelung constant²⁾ M and the potential constant b are relatively insensitive to materials and that r_0 is the only variable, we obtain the next relationships:

$$\alpha \propto Q^{n/(n+3)}, \quad (16)$$

$$\chi_T \propto Q, \quad (17)$$

which give reasonable agreement with the experimental eqs. (2) and (3) for a relatively small n ($\sim 3-4$). This result, however, is inconsistent with the usually accepted n value ($\sim 9-11$).³⁾ Also, the result of the almost constant dielectric constant written in eq. (12) is consistent with the experimental dielectric data, especially for ferroelectric materials. More advanced models will clearly be desired to explain the observed relationships consistently.

Acknowledgment

We wish to thank the Office of Naval Research for their support of this work.

References

- 1) M. Born and M. Göppert-Mayer: *Handbuch der Physik* (Springer, Berlin, 1933) Vol. 24, p. 623.
- 2) J. Sherman: *Chem. Rev.* 11 (1932) 93.
- 3) F. Seitz: *The Modern Theory of Solids* (McGraw-Hill, New York, 1940).

APPENDIX 21

K. Uchino, L.E. Cross, R.E. Newnham. Electrostrictive Effects in Para-electric-Ferroelectric-Antiferroelectric Phase Transitions. Jpn. J. Appl. Phys. 19, L425 (1980).

Electrostrictive Effects in Paraelectric-Ferroelectric-Antiferroelectric Phase Transitions

Kenji UCHINO, Leslie E. CROSS and Robert E. NEWNHAM

*Materials Research Laboratory, The Pennsylvania State University,
University Park, Pennsylvania 16801, U.S.A.*

(Received May 23, 1980)

Electrostrictive terms have been introduced into the Kittel free energy expression by means of a fourth-order cross term of the two-sublattice polarizations, giving rise to multiple phase transitions. Schematic p - T diagrams of the nonpolar, polar and antipolar phases are classified by the electrostrictive Ω coefficient. Spontaneous strain curves are derived for each of the four types of phase diagrams.

Phenomenological treatments of antiferroelectrics have been developed by several investigators.¹⁻³⁾ Extended theories based on fourth order cross terms with two-sublattice polarizations are capable of characterizing antiferroelectric-ferroelectric transitions.^{4,5)} These treatments generally describe the electric field dependence of the polarization states, but *not* the pressure dependence.

In a preceding paper,⁶⁾ electrostrictive terms have been introduced into the Kittel free energy function for antiferroelectrics. This paper describes a phenomenological analysis of successive phase transitions under hydrostatic pressure, treating the second-order phase transition for mathematical simplicity. PbZrO_3 which exhibits paraelectric-ferroelectric-antiferroelectric phase transitions, is a possible example.

To start with, electrostrictive terms are introduced into Kittel's free energy expression for a linear ferro- or antiferroelectric crystal:

$$G_1 = \frac{1}{2} \alpha (T) (P_a^2 + P_b^2) + \frac{1}{4} \beta (P_a^4 + P_b^4) + \eta P_a P_b + \zeta (P_a^2 + P_b^2) P_a P_b - \frac{1}{2} \chi_T p^2 + Q (P_a^2 + P_b^2 + 2\Omega P_a P_b) p. \quad (1)$$

Here, P_a and P_b denote the two-sublattice polarizations, p hydrostatic pressure, χ_T compressibility, while Q and Ω are electrostrictive coefficients. The $P_a^2 P_b^2$ and $(P_a^2 + P_b^2)$ terms are omitted for simplicity. Introducing the Cross transformation²⁾ $P_1 = (P_a + P_b)/\sqrt{2}$ and $P_A =$

$(P_a - P_b)/\sqrt{2}$, and using simple mathematical procedures leads to three types of stable states for zero electric field ($E=0$). Each can give rise to minima in free energy in the P_F - P_A plane. Detailed calculations have been developed in our previous paper including η and ζ terms.⁷⁾

I Nonpolar; $P_F=0$, $P_A=0$

$$T_0(p) = T_0 - 2QC(1 + \Omega)p \quad (2)$$

$$1/\epsilon_n = (T - T_0(p))/C \quad (3)$$

$$(\Delta V/V)_n = -\chi_T p \quad (4)$$

$$G_n = -\frac{1}{2} \chi_T p^2 \quad (5)$$

II Polar; $P_F^2 = -2(T - T_c(p))/C(\beta + 4\zeta)$, $P_A=0$

$$T_c(p) = T_c - 2QC(1 + \Omega)p \quad (6)$$

$$1/\epsilon_p = -2(T - T_c(p))/C \quad (7)$$

$$(\Delta V/V)_p = -\chi_T p + Q(1 + \Omega)P_F^2 \quad (8)$$

$$G_p = -\frac{1}{2} \chi_T p^2 - \frac{1}{2} (T - T_c(p))^2 / C^2 (\beta + 4\zeta) \quad (9)$$

III Antipolar; $P_1=0$, $P_A^2 = -2(T - T_N(p))/C(\beta - 4\zeta)$

$$T_N(p) = T_N - 2QC(1 - \Omega)p \quad (10)$$

$$1/\epsilon_a = -\frac{2(\beta + 2\zeta)}{C(\beta - 4\zeta)} \left[T - \frac{3\beta}{2(\beta + 2\zeta)} T_N(p) + \frac{(\beta - 4\zeta)}{2(\beta + 2\zeta)} T_c(p) \right] \quad (11)$$

$$(\Delta V/V)_0 = -\chi_T p + Q(1-\Omega)P_A^2 \quad (12)$$

$$G_0 = -\frac{1}{2}\chi_T p^2 - \frac{1}{2}(T - T_N(p))^2/C^2(\beta - 4\zeta) \quad (13)$$

Here, $1/\epsilon$ is the reciprocal permittivity, $(\Delta V/V)$ the bulk strain, G the minimum energy, and C the Curie-Weiss constant. T_0 , T_C and T_N are related to the free energy coefficients as follows:

$$\alpha + \eta = (T - T_0)/C = (T - T_C)/C, \quad (14)$$

$$\alpha - \eta = (T - T_N)/C. \quad (15)$$

If $\eta < 0$ and $\zeta > 0$, successive paraelectric-ferroelectric-antiferroelectric phase transitions occur, and the paraelectric-ferroelectric transition temperature is given by eq. (6). The ferroelectric-antiferroelectric transition temperature $T_i(p)$ can be calculated from the condition $G_p = G_a$ (see eqs. (9) and (13)), as

$$T_i(p) = \frac{1}{2}(T_C + T_N) - \eta C \kappa - 2QC(1 + \Omega \kappa)p, \quad (16)$$

where

$$\kappa = \left(1 + \sqrt{\frac{\beta + 4\zeta}{\beta - 4\zeta}}\right) / \left(1 - \sqrt{\frac{\beta + 4\zeta}{\beta - 4\zeta}}\right). \quad (17)$$

If $\eta > 0$ and $\zeta < 0$, paraelectric-antiferroelectric-ferroelectric transitions occur, and the upper and lower transition temperatures are given by eqs. (10) and (16), respectively.

Assuming that a phase transition takes place at the point where two minima of the free energies are equally deep, a phase diagram of the three states (nonpolar, polar and antipolar states) can be calculated in the pressure-temperature plane. The hysteresis during a temperature or a pressure cycle cannot be predicted under this assumption. Considering the variation of the transition temperatures

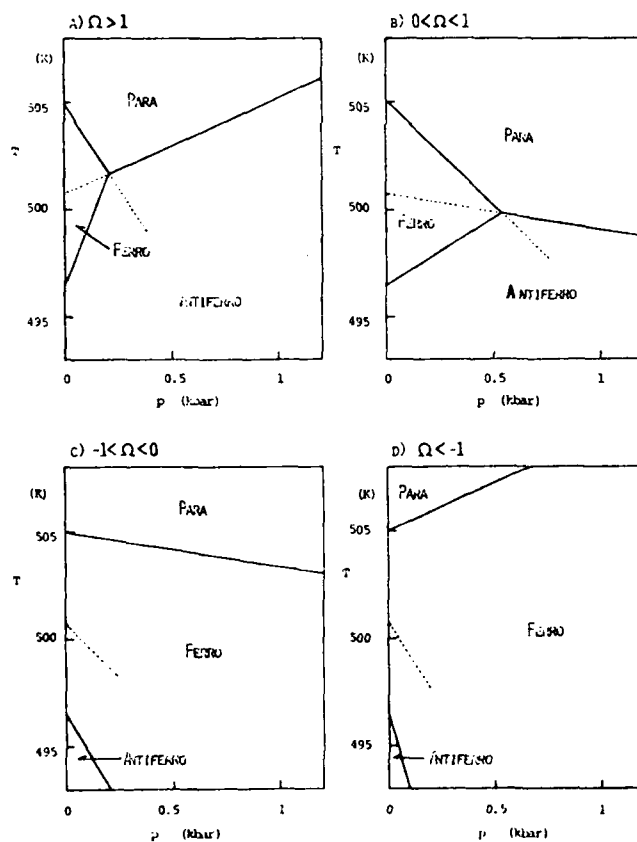


Fig. 1. Phase diagrams for $\eta < 0$ and $\zeta > 0$, (a) $\Omega > 1$, (b) $0 < \Omega < 1$, (c) $-1 < \Omega < 0$, and (d) $\Omega < -1$.

with hydrostatic pressure represented by eqs. (2), (6), (10) and (16), schematic phase diagrams are classified into four categories by the electrostrictive Ω coefficient. Figures 1(a)–(d) illustrate these four types in the case of $\eta < 0$ and $\zeta > 0$, calculated for $\Omega > 1$, $0 < \Omega < 1$, $-1 < \Omega < 0$, and $\Omega < -1$, respectively. Based on the data for PbZrO_3 , the parameters used in the calculation were selected as follows: $T_c = 505$ (K); $Q = 2 \times 10^{-2}$ ($\text{m}^4 \text{C}^{-2}$); $C = 1.6 \times 10^5 \text{ K} \text{Cm}^{-1} \text{V}^{-1}$; $\eta = -1.5 \times 10^6$ (mVC^{-1}); $\kappa = -3$ (or $\zeta/\beta = 0.15$); $\Omega = 1.8, 0.7, -0.7$, and -1.8 for Figs. (a), (b), (c), and (d), respectively.

If $\Omega > 0$, a triple point between paraelectric, ferroelectric, and antiferroelectric phases exists in the pressure-temperature plane. The critical pressure p° and temperature T° are then given by

$$p^\circ = -\eta/2Q\Omega, \quad (18)$$

$$T^\circ = T_c + \eta C(1 + \Omega)/\Omega. \quad (19)$$

Samara reported the pressure and temperature dependence of phase transitions of PbZrO_3 ,⁸⁾ and suggested a phase diagram similar to Fig. 1(a). The ferroelectric phase is "squeezed out" at pressures below 1 kbar, and only the paraelectric-antiferroelectric transition is observed at higher pressures.

Spontaneous strains (volume changes) are also derived from eqs. (4), (8) and (12), without considering thermal strain. Figures 2(a)–(d) show spontaneous volume changes at pressure $p = 0$ kbar, plotted as a function of temperature. Calculations are made for four types of phase diagrams using the value of $\beta = 2 \times 10^9$ ($\text{m}^5 \text{VC}^{-3}$), selected to give a reasonable temperature change of the spontaneous strain.

Precise thermal expansion measurements of PbZrO_3 ceramics by Tennery⁹⁾ and Goulpeau¹⁰⁾ have shown that discontinuous volume changes of $+(0.12 \text{ to } 0.16\%)$ and $-(0.5 \text{ to } 0.6\%)$ occur at the paraelectric-ferroelectric and ferroelectric-antiferroelectric transitions, respectively. Figure 2(a) shows a similarity to the experimental results, although the absolute values of spontaneous strains are different, probably because of the second-order transition treatment neglecting the term $(P_a^6 + P_b^6)$.

In conclusion, the electrostrictive terms introduced into the Kittel free energy expression with a fourth-order cross term of two-sublattice polarizations, can explain qualitatively the

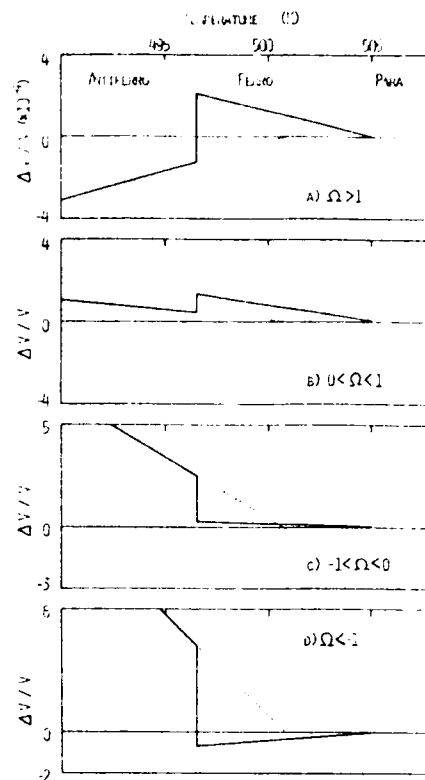


Fig. 2. Spontaneous volume changes at pressure $p = 0$ kbar, calculated for $\eta < 0$ and $\zeta > 0$, (a) $\Omega > 1$, (b) $0 < \Omega < 1$, (c) $-1 < \Omega < 0$, and (d) $\Omega < -1$.

spontaneous strains associated with the successive paraelectric-ferroelectric-antiferroelectric phase transitions of PbZrO_3 . The phase diagram of nonpolar, polar and antipolar states in the pressure-temperature plane may also be reasonably understood. Further development of the theory to include first-order transitions is clearly required to obtain quantitative comparisons with the experimental results. Precise measurements of the hydrostatic pressure dependence of phase transitions are also needed for other materials with multiple phase transitions (for example, $\text{Pb}(\text{Co}_{1/2}\text{W}_{1/2})\text{O}_3$ and $\text{Pb}(\text{Ni}_{1/2}\text{W}_{1/2})\text{O}_3$ with paraelectric-antiferroelectric-ferroelectric phase transitions^{7,11)}).

References

- 1) C. Kittel: *Phys. Rev.* **82** (1951) 729.
- 2) L. E. Cross: *J. Phys. Soc. Jpn.* **23** (1967) 77.
- 3) K. Okada: *J. Phys. Soc. Jpn.* **37** (1974) 1226.
- 4) L. Benguigui: *Phys. Lett.* **33A** (1970) 79.
- 5) I. Suzuki and K. Okada: *J. Phys. Soc. Jpn.* **45** (1978) 1302.
- 6) K. Uchino, L. E. Cross, R. F. Newnham and S. Nomura: *J. Appl. Phys.* to be published.
- 7) K. Uchino and S. Nomura: *Jpn. J. Appl. Phys.* **18** (1979) 1493.
- 8) G. A. Samara: *Phys. Rev. B1* (1970) 3777.
- 9) V. J. Tennery: *J. Am. Cer. Soc.* **49** (1966) 483.
- 10) L. Goulpeau: *Sov. Phys. Solid State* **8** (1967) 1970.
- 11) K. Uchino and S. Nomura: *Ferroelectrics* **17** (1978) 505.

APPENDIX 22

K. Uchino, S. Nomura, A. Amin, Z.P. Chang, L.E. Cross, R.E. Newnham.
Elastic Constants and Thermal Expansion in Cation Disordered Perovskites.
Jpn. J. Appl. Phys. 19, L398 (1980).

Elastic Constants and Thermal Expansion of Cation Disordered Perovskites

Kenji UCHINO, Shoichiro NOMURA, Ahmed AMIN,[†]
Zung P. CHANG,[†] Leslie E. CROSS[†] and Robert E. NEWNHAM[†]

Department of Physical Electronics, Tokyo Institute of Technology,
Ookayama, Meguro-ku, Tokyo 152

[†]Materials Research Laboratory, The Pennsylvania State University,
University Park, Pennsylvania 16802, U.S.A.

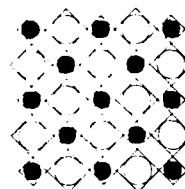
(Received May 23, 1980)

The elastic constants of the cation disordered perovskites $\text{Pb}(\text{Mg}_{1/3}\text{Nb}_{2/3})\text{O}_3$, $\text{Pb}(\text{Zn}_{1/3}\text{Nb}_{2/3})\text{O}_3$ and $(\text{K}_{3/4}\text{Bi}_{1/4})(\text{Zn}_{1/6}\text{Nb}_{5/6})\text{O}_3$ have been measured by the ultrasonic pulse superposition method, and the thermal expansion of $(\text{K}_{3/4}\text{Bi}_{1/4})(\text{Zn}_{1/6}\text{Nb}_{5/6})\text{O}_3$ has been determined from 300 K to 800 K by X-ray powder diffraction. Both the elastic stiffness and the thermal expansion coefficients of cation disordered perovskites are somewhat smaller than those of simple perovskites. Consistent with previously reported electrostrictive and dielectric properties, the results can be explained by an intuitive ion "rattling" space model.

In earlier papers on electrostriction in ferroelectrics,¹⁻⁵⁾ antiferroelectrics,* and non-polar perovskite crystals,⁶⁾ we have shown that the magnitude of the polarization related electrostriction coefficient Q is insensitive to ferroelectricity, antiferroelectricity, or non-polar behavior, but depends markedly on the degree of order in the cation arrangement. The Q values tend to increase with increasing order, from disordered, through simple and then ordered perovskite crystals. To explain the relationship between electrostrictive Q coefficient and cation order, we have proposed an intuitive crystallographic model. Figures 1(a) and (b) show the ordered and disordered structures for an $\text{A}(\text{B}_{1/2}\text{B}_{1/2})\text{O}_3$ perovskite crystal. Assuming a rigid ion model, a large "rattling" space is expected for the smaller B ions in the disordered structure because the larger B ions prop open the lattice framework. Much less "rattling" space is expected in the ordered arrangement where neighboring atoms collapse systematically around the small B ions. When an electric field is applied to a disordered perovskite, the B ion with large rattling space can shift easily without distorting the oxygen framework. Smaller strain is expected for unit magnitude of polarization, resulting in low electrostriction coefficients. On the other hand,

$\text{A}(\text{B}_{1/2}\text{B}_{1/2})\text{O}_3$ type perovskite

a) Ordered



b) Disordered

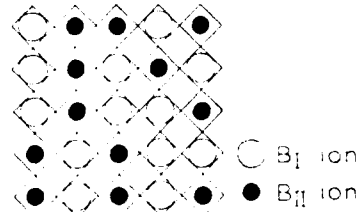


Fig. 1. Crystal structure models of the $\text{A}(\text{B}_{1/2}\text{B}_{1/2})\text{O}_3$ type perovskite:

- (a) Ordered structure with small rattling space,
- (b) Disordered structure with large rattling space.

in ordered perovskites with very small rattling space, larger electrostriction coefficients are expected.

Based on the "ion rattling space" model, disordered perovskites should also have smaller elastic stiffness coefficients and smaller thermal expansion coefficients than simple or ordered perovskites. A disordered perovskite crystal with large rattling space may easily be com-

*K. Uchino, L. E. Cross, R. E. Newnham and S. Nomura: unpublished.

pressed when pressure is applied, and the thermal strain at elevated temperatures may be cancelled by internal rearrangements in the rattling space.

In this paper we present experimental data regarding the elastic constants and thermal expansion coefficients of disordered perovskite ferroelectrics $\text{Pb}(\text{Mg}_{1/3}\text{Nb}_{2/3})\text{O}_3$ and $\text{Pb}(\text{Zn}_{1/3}\text{Nb}_{2/3})\text{O}_3$ and the non-polar dielectric $(\text{K}_{3/4}\text{Bi}_{1/4})(\text{Zn}_{1/6}\text{Nb}_{5/6})\text{O}_3$. The results are compared with data for simple perovskites in support of the "rattling space" model.

Single crystals of $\text{Pb}(\text{Mg}_{1/3}\text{Nb}_{2/3})\text{O}_3$, $\text{Pb}(\text{Zn}_{1/3}\text{Nb}_{2/3})\text{O}_3$ and $(\text{K}_{3/4}\text{Bi}_{1/4})(\text{Zn}_{1/6}\text{Nb}_{5/6})\text{O}_3$ were grown by a flux technique.^{7,8)}

Thermal expansion data were reported in previous papers,^{2,9)} for $\text{Pb}(\text{Mg}_{1/3}\text{Nb}_{2/3})\text{O}_3$ and $\text{Pb}(\text{Zn}_{1/3}\text{Nb}_{2/3})\text{O}_3$. An analytical formula has been developed for thermal expansion in disordered perovskites which exhibit diffuse phase transitions.¹⁰⁾ The model assumes that a disordered crystal is composed of microregions, each with a different local Curie temperature θ_c , and an unbroadened microstrain given by

$$\Delta l/l = a_i + b_i(T - \theta_c) + c_i(T - \theta_c)^2 \quad (1)$$

where $i=1$ corresponds to the ferroelectric phase and $i=2$ corresponds to the paraelectric phase. The distribution function for the local Curie point is represented by

$$f(\theta_c) = \exp \left[-\frac{(\theta_c - T_c)^2}{2\sigma^2} \right], \quad (2)$$

where T_c is the mean value of local Curie temperature, and σ is the standard deviation. The average value of the microstrain $\Delta l/l$ gives the measurable macrostrain $\Delta L/L$ which may be calculated from

$$\Delta L/L = \int_0^\infty (\Delta l/l) f(\theta_c) d\theta_c / \int_0^\infty f(\theta_c) d\theta_c \quad (3)$$

From the linear thermal expansion $\partial(\Delta L/L)/\partial T$ as a function of temperature measured in the dominantly paraelectric region above the Curie maximum, the linear thermal expansion coefficient appropriate for the individual micro region may be derived by curve fitting. The linear thermal expansion coefficient α for the individual micro region ($\partial \Delta l/l / \partial T$) for $\text{Pb}(\text{Mg}_{1/3}\text{Nb}_{2/3})\text{O}_3$ and $\text{Pb}(\text{Zn}_{1/3}\text{Nb}_{2/3})\text{O}_3$ listed in Table I are clearly significantly smaller than the α coefficients for normal simple ferroelectric perovskites.

The lattice parameter of a cubic non-polar $(\text{K}_{3/4}\text{Bi}_{1/4})(\text{Zn}_{1/6}\text{Nb}_{5/6})\text{O}_3$ crystals was determined by the X-ray powder diffraction at several temperatures between 300 K and 800 K. The results are shown in Fig. 2. An almost linear relation between the lattice parameter and temperature was obtained, yielding a thermal expansion coefficient of $7.9 (\pm 0.3) \times 10^{-6} \text{ K}^{-1}$, comparable to the smallest values in simple perovskites. In summary then it would appear that for disordered relaxor ferroelectrics at temperatures near the relaxation range α is significantly smaller than in simple perovskites, and that this lowering of α also appears in the non-polar relaxors with disordered cation

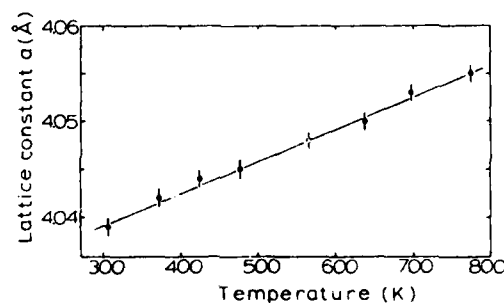


Fig. 2. Lattice constant of $(\text{K}_{3/4}\text{Bi}_{1/4})(\text{Zn}_{1/6}\text{Nb}_{5/6})\text{O}_3$ plotted as a function of temperature.

Table I. Electrostriction coefficients, linear thermal expansion coefficients and elastic constants for several disordered and simple perovskite-type crystals.

Order type	Substance	$(\times 10^{-2} Q_h \text{ m}^2 \text{ C}^{-2})$	$(\times 10^{-6} \alpha \text{ K}^{-1})$	C_{11} (GPa)	C_{44} (GPa)
Disordered	$\text{Pb}(\text{Mg}_{1/3}\text{Nb}_{2/3})\text{O}_3$	0.60 ³⁾	4 ²⁾	—	76 (RT)
	$\text{Pb}(\text{Zn}_{1/3}\text{Nb}_{2/3})\text{O}_3$	0.66 ³⁾	3.0 ^{9, 10)}	131 (RT)	56 (RT)
	$(\text{K}_{3/4}\text{Bi}_{1/4})(\text{Zn}_{1/6}\text{Nb}_{5/6})\text{O}_3$	0.55–1.15 ⁶⁾	7.9 (700 K)	172 (RT)	69 (RT)
Simple	BaTiO_3	2.0 ¹²⁾	12 (423 K) ¹³⁾	255 (423 K) ¹⁸⁾	108 (423 K) ¹⁸⁾
	SrTiO_3	4.7 ¹³⁾	11 (350 K) ¹⁶⁾	316 (RT) ¹⁹⁾	123 (RT) ¹⁹⁾
	KTaO_3	5.2 ¹⁴⁾	7 (375 K) ¹⁷⁾	431 (RT) ¹⁴⁾	109 (RT) ¹⁴⁾

arrangements.

Perovskite crystals in the cubic paraelectric phase belong to crystal class $m\bar{3}m$ with three independent elastic constants c_{11} , c_{12} , and c_{44} . Elastic constants of three disordered perovskites have been measured by the ultrasonic pulse superposition method.¹¹⁾ X-cut and AC-cut quartz transducers with a fundamental frequency of 20 MHz were bonded with Nonaq stopcock grease to the crystal surface and used to generate longitudinal and shear waves, respectively. The transit time of an ultrasonic wave between a pair of parallel faces of the sample was measured at room temperature. Using the velocity v calculated from the sample thickness and measured transit time, the elastic constant is expressed as

$$c = \rho v^2 \quad (4)$$

where ρ is the density of the crystal.

The results for $\text{Pb}(\text{Mg}_{1/3}\text{Nb}_{2/3})\text{O}_3$, $\text{Pb}(\text{Zn}_{1/3}\text{Nb}_{2/3})\text{O}_3$ and $(\text{K}_{3/4}\text{Bi}_{1/4})(\text{Zn}_{1/6}\text{Nb}_{5/6})\text{O}_3$ are summarized in Table I. For $\text{Pb}(\text{Zn}_{1/3}\text{Nb}_{2/3})\text{O}_3$, we have neglected the crystal distortion and the piezoelectric stiffening effect in the ferroelectric phase at room temperature. Certain stiffness coefficients could not be measured because of limitations on the crystal size. The error associated with the stiffness values is $\pm 15\%$. The elastic constants in disordered perovskites appear to be significantly smaller than in simple perovskites. It should be noted, however, that lead-containing crystals generally have somewhat smaller elastic constants than normal oxide crystals.

In conclusion, the predictions based on the intuitive "rattling" space model, that "both the elastic stiffnesses and the thermal expansion coefficient in cation disordered perovskites are

generally smaller than in simple or ordered perovskites" is confirmed experimentally. Further elastic constant measurements on ordered perovskites are clearly desirable, as well as measurements of the elastic constants of disordered perovskites across the diffuse transition range.

References

- 1) L. E. Cross, S. J. Jang, R. E. Newnham, S. Nomura and K. Uchino: *Ferroelectrics* **23** (1980) 187.
- 2) S. J. Jang, K. Uchino, S. Nomura and L. E. Cross: *Ferroelectrics* **27** (1980) 31.
- 3) S. Nomura, J. Kuwata, S. J. Jang, L. E. Cross and R. E. Newnham: *Mater. Res. Bull.* **14** (1979) 769.
- 4) S. Nomura, J. Kuwata, K. Uchino, S. J. Jang, L. E. Cross and R. E. Newnham: *Phys. Status Solidi (a)* **57** (1980) 317.
- 5) K. Uchino, S. Nomura, L. E. Cross, S. J. Jang and R. E. Newnham: *J. Appl. Phys.* **51** (1980) 1142.
- 6) K. Uchino, L. E. Cross, R. E. Newnham and S. Nomura: *J. Phase Transitions*, in press.
- 7) S. Nomura, T. Takahashi and Y. Yokomizo: *J. Phys. Soc. Jpn.* **27** (1969) 262.
- 8) S. Nomura and F. Kojima: *Jpn. J. Appl. Phys.* **12** (1973) 205.
- 9) S. Nomura, M. Abe, F. Kojima and K. Uchino: *Jpn. J. Appl. Phys.* **14** (1975) 1881.
- 10) J. Kuwata, K. Uchino and S. Nomura: *Ferroelectrics* **22** (1979) 863.
- 11) H. J. McSkimin: *J. Acoust. Soc. Am.* **33** (1961) 12.
- 12) T. Yamada: *J. Appl. Phys.* **43** (1972) 328.
- 13) G. A. Samara: *Phys. Rev.* **151** (1966) 378.
- 14) H. Uwe and T. Sakudo: *J. Phys. Soc. Jpn.* **38** (1975) 183.
- 15) G. Shirane and A. Takeda: *J. Phys. Soc. Jpn.* **7** (1952) 1.
- 16) F. W. Lytle: *J. Appl. Phys.* **35** (1964) 2212.
- 17) G. A. Samara and B. Morosin: *Phys. Rev.* **B8** (1973) 1256.
- 18) D. Berlincourt and H. Jaffe: *Phys. Rev.* **111** (1958) 143.
- 19) D. Y. Chung and Y. Li: *Phys. Lett.* **A58** (1976) 133.

APPENDIX 23

K. Uchino, L.E. Cross, R.E. Newnham, S. Nomura. Electrostriction Effects
in Nonpolar Perovskites. J. Phase Trans. (accepted).

Electrostrictive Effects in Non-Polar Perovskites

K. Uchino, L. E. Cross, and R. E. Newnham
Materials Research Laboratory
The Pennsylvania State University
University Park, PA 16802

and

S. Nomura
Department of Physical Electronics
Tokyo Institute of Technology
Ookayama, Meguro-ku, Tokyo 152

Abstract

Polarization-related electrostrictive coefficients Q_h have been determined for relaxation dielectrics $0.856\text{SrTiO}_3\text{-}0.144\text{Bi}_{2/3}\text{TiO}_3$ and $(\text{K}_{3/4}\text{Bi}_{1/4})(\text{Zn}_{1/6}\text{Nb}_{5/6})\text{O}_3$, and for a simple non-polar perovskite BaZrO_3 by measuring the hydrostatic pressure dependence of the dielectric permittivity. Anomalous variation in the electrostrictive coefficient with temperature and frequency were observed in $(\text{K}_{3/4}\text{Bi}_{1/4})(\text{Zn}_{1/6}\text{Nb}_{5/6})\text{O}_3$ in the relaxation temperature region. This behavior can be explained qualitatively with the simple model based on the potential barriers separating alternative cation sites. The empirical rule noted previously for ferroelectric perovskites that the electrostrictive Q coefficient increases with cation order from disordered, through simple and then order perovskites is confirmed again in non-polar perovskites.

INTRODUCTION

In earlier papers on the electrostriction in ferroelectrics [Uchino et al. 1980a; Nomura et al. 1979, 1980; Cross et al. 1980; Jang et al. 1980] and antiferroelectric perovskite crystals [Uchino et al. 1980b], we have suggested that the magnitude of the polarization-related electrostrictive coefficient Q is not affected strongly by ferro- or antiferroelectricity, but depends markedly on the degree of order in the cation arrangement. The Q value tends to increase with order from disordered, through simple and then ordered perovskite crystals.

In this paper this empirical rule is explored for non-polar perovskites. The hydrostatic Q_h values are determined by measuring the hydrostatic pressure dependence of the electric permittivity in two disordered relaxor dielectrics $0.856\text{SrTiO}_3\text{-}0.144\text{Bi}_{2/3}\text{TiO}_3$ and $(\text{K}_{3/4}\text{Bi}_{1/4})(\text{Zn}_{1/6}\text{Nb}_{5/6})\text{O}_3$, and in the simple non-polar perovskite BaZrO_3 . The empirical rule is obeyed in these non-polar perovskites, and explained in terms of a simple rigid-ion model for disordered perovskites.

EXPERIMENTAL RESULTS

Sample Preparation

Single crystals of the $\text{SrTiO}_3\text{-Bi}_{2/3}\text{TiO}_3$ solid solution were prepared by a flux technique using KF [Cross 1962]. The composition determined by chemical analysis was $0.856\text{SrTiO}_3\text{-}0.144\text{Bi}_{2/3}\text{TiO}_3$. The relative permittivity at room temperature is about 1450 at 10 kHz, and on cooling passes through a maximum at temperatures between -140°C and -60°C , depending on frequency.

Single crystals of $(K_{3/4}Bi_{1/4})(Zn_{1/6}Nb_{5/6})O_3$ were prepared using excess Bi_2O_3 as a flux [Nomura and Kojima 1973]. The permittivity maxima occur in the temperature range of $0^\circ C$ to $80^\circ C$, and the relative permittivity at room temperature is 440 at 10 kHz.

Polycrystalline ceramics of $BaZrO_3$ were prepared by solid state reaction. The dielectric constant at room temperature is about 31 at 10 kHz, with no observable dispersion.

Pressure Dependence of Permittivity

The polarization related electrostrictive coefficients of a cubic perovskite type crystal are defined by the equations,

$$Q_{11} = 1/2 \left(\frac{\partial^2 x_1}{\partial P_1^2} \right) \quad (1)$$

and

$$Q_{12} = 1/2 \left(\frac{\partial^2 x_2}{\partial P_1^2} \right) , \quad (2)$$

where x_1 and x_2 are the longitudinal and transverse induced strains, respectively. By using a Maxwell relation, eqs. (1) and (2) are transformed as follows:

$$Q_{11} = -1/2 \left(\frac{\partial^2 E_1}{\partial x_1 \partial P_1} \right) = -1/2 \left(\frac{\partial x_1}{\partial P_1} \right) \quad (3)$$

and

$$Q_{12} = -1/2 \left(\frac{\partial^2 E_1}{\partial x_2 \partial P_1} \right) = -1/2 \left(\frac{\partial x_2}{\partial P_1} \right) . \quad (4)$$

These equations indicate that the electrostrictive coefficients can be obtained by measuring stress X dependence of the reciprocal susceptibility

χ . When a hydrostatic pressure p is applied to a paraelectric crystal, the pressure dependence of the reciprocal susceptibility χ is represented by

$$\frac{\partial \chi_1}{\partial p} = 2Q_h, \quad (5)$$

where $Q_h = Q_{11} + 2Q_{12}$.

The effect of hydrostatic pressure on the electric permittivity was investigated up to 5 kbar for rectangular specimens with gold-sputtered electrodes. Capacitance was measured with an automatic capacitance bridge (Hewlett-Packard, 4270A) in the frequency range from 1 kHz to 1 MHz, and with a Q bridge (Boonton, Model 35A) from 300 kHz to 5 MHz. Hydrostatic pressure was generated by an air-driven intensifier pump (Pressure Products Industries), with plexol as the pressure medium. The value of pressure was monitored by a Heise gauge with the accuracy of ± 5 bar. Using a simple cryostat temperature was varied from -40°C to 40°C , as monitored with an A-C thermocouple set inside the cell.

Figures 1(a) and 2(a) show the relative capacitance change of $0.856\text{SrTiO}_3-0.144\text{Bi}_{2/3}\text{TiO}_3$ and $(\text{K}_{3/4}\text{Bi}_{1/4})(\text{Zn}_{1/6}\text{Nb}_{5/6})\text{O}_3$, respectively, measured at room temperature as a function of hydrostatic pressure. For $0.856\text{SrTiO}_3-0.144\text{Bi}_{2/3}\text{TiO}_3$, the slope of the capacitance versus pressure curve does not depend significantly on frequency, but in $(\text{K}_{3/4}\text{Bi}_{1/4})(\text{Zn}_{1/6}\text{Nb}_{5/6})\text{O}_3$ a rapid decrease in slope is observed with increasing frequency. From the values of the slope and from eq. (5), electrostrictive coefficients Q_h are calculated as a function of frequency [Figs. 1(b) and 2(b)]. The compressibility [Beattie and Samara 1971] is such that the very small change of dimension under pressure has negligible effect on the capacitance

change, and finite strain corrections have been neglected. The electrostrictive Q_h coefficient of $0.856\text{SrTiO}_3-0.144\text{Bi}_{2/3}\text{TiO}_3$ is almost frequency-independent and is about $1.3 \times 10^{-2} \text{ m}^4 \text{ C}^{-2}$, several times smaller than typical values for simple perovskites (Table I). On the other hand, the Q_h value of $(\text{K}_{3/4}\text{Bi}_{1/4})(\text{Zn}_{1/6}\text{Nb}_{5/6})\text{O}_3$ varies markedly with frequency in the range between 10^5 and 10^6 Hz, from $Q_h \sim 1.2 \times 10^{-2} \text{ m}^4 \text{ C}^{-2}$ at low frequencies to $Q_h \sim 0.5 \times 10^{-2} \text{ m}^4 \text{ C}^{-2}$ at high frequencies. It is very suggestive that this frequency range corresponds exactly with the frequency at which the permittivity versus temperature curve shows a maximum at room temperature.

Skanavi et al. [1958] proposed a model for $\text{SrTiO}_3\text{-Bi}_{2/3}\text{TiO}_3$ solid solutions in which A site cation vacancies are produced by the substitution of two Bi^{3+} ions for three Sr^{2+} ions. The presence of A site lattice vacancies leads to a shift of the equilibrium positions of the oxygen ions and consequently creates several local minima in the potential energy of Ti^{4+} ions in the distorted octahedral sites. A similar situation arises in $(\text{K}_{3/4}\text{Bi}_{1/4})(\text{Zn}_{1/6}\text{Nb}_{5/6})\text{O}_3$, where ions of different chemical valencies are randomly distributed on the B sites, as well as on the A sites of perovskite lattice [Nomura and Kojima 1973]. Dielectric relaxation arises from thermal hopping over the potential barriers separating these alternative sites. At low temperatures (or high frequencies) the B ion is assumed to be trapped in one local potential minimum and with increasing temperature (or decreasing frequency), hopping between minima commences. This situation resembles a ferroelectric order-disorder transition, but the ions do not have cooperative interaction between each other in the long range even below the "freezing-in" temperature.

Different electrostrictive Q_h coefficients may, therefore, be expected for the "trapped" and "untrapped" states, since the effective anharmonicity of the ionic thermal vibration can be different for each state [Uchino and Cross 1980]. This probably explains the electrostrictive data for $(K_{3/4}Bi_{1/4})(Zn_{1/6}Nb_{5/6})O_3$ shown in Fig. 2(a). Frequency dependence of the Q_h value in $0.856SrTiO_3-0.144Bi_{2/3}TiO_3$ is expected if measurements are made in the relaxation temperature range of $-140^\circ C$ to $-60^\circ C$.

The temperature dependence of the permittivity at 1 kHz in $(K_{3/4}Bi_{1/4})(Zn_{1/6}Nb_{5/6})O_3$ at 0 kbar and 3.5 kbar is shown in Fig. 3. A shift of the permittivity peak toward lower temperatures is observed with increasing pressure at a rate of about $1.3^\circ C/kbar$, much smaller than the usual value of $-(\partial T_c/\partial p)$ in ferroelectric perovskites ($\sim 5^\circ C/kbar$). The frequency dependence of the electrostrictive coefficient of $(K_{3/4}Bi_{1/4})(Zn_{1/6}Nb_{5/6})O_3$ at $-32^\circ C$ is also given in Fig. 2(b). The changes can be explained by the simple potential barrier model just described.

In the case of $BaZrO_3$, no variation in the electrostrictive coefficient with temperature or frequency are observed, and the Q_h value of about $2.3 \times 10^{-2} m^4 C^{-2}$ is almost the same as the coefficients for simple ferro- or antiferroelectric perovskites.

DISCUSSION

Electrostrictive coefficients $Q_h (=Q_{11} + 2Q_{12})$ for a number of oxide perovskites are summarized in Table I. The magnitude of the electrostrictive coefficient is not affected strongly by ferroelectricity, antiferroelectricity, or non-polar behavior, but is very dependent on the degree of order in the cation arrangement. The empirical rule suggested

for ferroelectric perovskites that the electrostrictive Q coefficient increases with cation order from disordered, through simple and then ordered perovskites is reconfirmed in non-polar perovskites.

The substitution of Bi^{3+} for Sr^{2+} causes a remarkable decrease in the electrostrictive coefficient: from $Q_h \sim 5.0 \times 10^{-2} \text{ m}^4 \text{ C}^{-2}$ in SrTiO_3 to $Q_h \sim 1.3 \times 10^{-2} \text{ m}^4 \text{ C}^{-2}$ in $0.856\text{SrTiO}_3-0.144\text{Bi}_{2/3}\text{TiO}_3$. The results of the electrostriction measurements in other solid solution systems $\text{Pb}(\text{Mg}_{1/3}\text{Nb}_{2/3})\text{O}_3$ - PbTiO_3 [Jang et al. 1980] and $\text{Pb}(\text{Mg}_{1/3}\text{Nb}_{2/3})\text{O}_3$ - $\text{Pb}(\text{Mg}_{1/2}\text{W}_{1/2})\text{O}_3$ [Nomura et al. 1980] are also very suggestive. In both systems, the small Q_h value of $\text{Pb}(\text{Mg}_{1/3}\text{Nb}_{2/3})\text{O}_3$ increases with increasing PbTiO_3 or $\text{Pb}(\text{Mg}_{1/2}\text{W}_{1/2})\text{O}_3$ content. A larger rate of increase was observed for the $\text{Pb}(\text{Mg}_{1/3}\text{Nb}_{2/3})\text{O}_3$ - $\text{Pb}(\text{Mg}_{1/2}\text{W}_{1/2})\text{O}_3$ system than for the $\text{Pb}(\text{Mg}_{1/3}\text{Nb}_{2/3})\text{O}_3$ - PbTiO_3 system because of the tendency of Mg and W ions to order.

An intuitive crystallographic model explaining the relationship between electrostrictive Q coefficient and cation order will now be described. Figures 4(a) and (b) show the ordered and disordered structures for an $\text{A}(\text{B}_{1/2}\text{I}\text{B}_{1/2}\text{II})\text{O}_3$ perovskite crystal. Assuming a rigid ion model, a large "rattling" space is expected for the smaller B ions in the disordered structure because the larger B ions prop open the lattice framework. Much less "rattling" space is expected in the ordered arrangement where neighboring atoms collapse systematically around the small B ions. The densely-packed structure of B ions in the ordered perovskite as shown in Fig. 4(b) has been observed for $0.9\text{Pb}(\text{Mg}_{1/2}\text{W}_{1/2})\text{O}_3-0.1\text{Pb}(\text{Mg}_{1/3}\text{Nb}_{2/3})\text{O}_3$ by Amin et al. [1980]. When an electric field is applied to a disordered perovskite, the B ion with large rattling space can shift easily without distorting the oxygen framework. Smaller strain is expected for unit

magnitude of polarization, resulting in low electrostrictive coefficients. On the other hand, in ordered perovskites with very small rattling space, the B ions cannot move easily without distorting the octahedron. A larger electrostrictive coefficient Q is expected.

ACKNOWLEDGMENT

We wish to thank the Office of Naval Research for their support of our work, through Contract No. N00014-78-C-0291.

REFERENCES

- Amin, A., R. E. Newnham, L. E. Cross and S. Nomura (1980). J. Solid State Chem. 35 (in press).
- Beattie, A. G. and G. A. Samara (1971). J. Appl. Phys. 42, 2376.
- Cross, L. E., S. J. Jang, R. E. Newnham, S. Nomura and K. Uchino (1980). Ferroelectrics (in press).
- Cross, L. E. (1962). The British Electrical and Allied Industries Research Association Reference L/T415, P. 5.
- Gavrilyachenko, V. G. and E. G. Fesenko (1971). Soviet Phys. - Cryst. 16, 54.
- Jang, S. J., K. Uchino, S. Nomura and L. E. Cross (1980). Ferroelectrics (in press).
- Nomura, S. and F. Kojima (1973). Japan. J. Appl. Phys. 12, 205.
- Nomura, S., J. Kuwata, S. J. Jang, L. E. Cross and R. E. Newnham (1979). Mat. Res. Bull. 14, 769.
- Nomura, S., J. Kuwata, K. Uchino, S. J. Jang, L. E. Cross and R. E. Newnham (1980). Phys. Stat. Sol. (a) 57 (in press).
- Samara, G. A. (1966). Phys. Rev. 151, 378.
- Samara, G. A. and B. Morosin (1973). Phys. Rev. B8, 1256.
- Schmidt, G. and E. Hegenbarth (1963). Phys. Stat. Sol. 3, 329.
- Skanavi, G. I., I. M. Ksendzov, V. A. Trigubenko and V. G. Prokhvatilov (1958). Soviet Phys. - JETP 6, 250.
- Uchino, K. S. Nomura, L. E. Cross, S. J. Jang and R. E. Newnham (1980a). J. Appl. Phys. 51 (in press).
- Uchino, K., L. E. Cross, R. E. Newnham and S. Nomura (1980b). Unpublished.
- Uchino, K. and L. E. Cross (1980). Unpublished.

Uwe, H. and T. Sakudo (1975). J. Phys. Soc. Japan 38, 183.

Yamada, T. (1972). J. Appl. Phys. 43, 328.

Yoshimoto, J., B. Okai and S. Nomura (1971). J. Phys. Soc. Japan 31, 307.

TABLE I. ELECTROSTRICTIVE COEFFICIENTS Q_H FOR ORDERED, SIMPLE AND DISORDERED PEROVSKITE CRYSTALS

ORDER-TYPE	POLAR-TYPE*	SUBSTANCE	Q_H ($\times 10^{-2} \text{ m}^4 \text{ C}^{-2}$)	REFERENCES
ORDERED	AF	$\text{Pb}(\text{Mg}_{1/2}\text{W}_{1/2})\text{O}_3$	6.2	UCHINO ET AL. (1980B)
	F	KTAO_3	5.2	UWE ET AL. (1975)
SIMPLE	FL	SrTiO_3	4.4	SAMARA ET AL. (1973)
			5.0	SCHMIDT ET AL. (1965)
			4.7	SAMARA (1966)
	NP	BAZrO_3	2.3	PRESENT WORK
	F	PbTiO_3	2.2	GAVRILYACHENKO (1971)
	F	BaTiO_3	2.0	YAMADA (1972)
			2.0	SAMARA (1966)
	AF	PbZrO_3	2.0	UCHINO ET AL. (1980B)
DISORDERED	NP	$0.856\text{SrTiO}_3-0.144\text{Bi}_{2/3}\text{TiO}_3$	1.3	PRESENT WORK
	NP	$(\text{K}_{3/4}\text{Bi}_{1/4})(\text{Zn}_{1/6}\text{Nb}_{5/6})\text{O}_3$	0.55 - 1.15	PRESENT WORK
	F	$\text{Pb}(\text{Zn}_{1/3}\text{Nb}_{2/3})\text{O}_3$	0.66	YOSHIMOTO ET AL. (1971) NOMURA ET AL. (1979)
	F	$\text{Pb}(\text{Mg}_{1/3}\text{Nb}_{2/3})\text{O}_3$	0.60	UCHINO ET AL. (1980A)

*F(L): FERROELECTRIC (-LIKE); AF: ANTIFERROELECTRIC; NP: NON-POLAR.

FIGURE CAPTIONS

Fig. 1(a) Capacitance change as a function of hydrostatic pressure measured in $0.856\text{SrTiO}_3\text{-}0.144\text{Bi}_{2/3}\text{TiO}_3$ at room temperature.

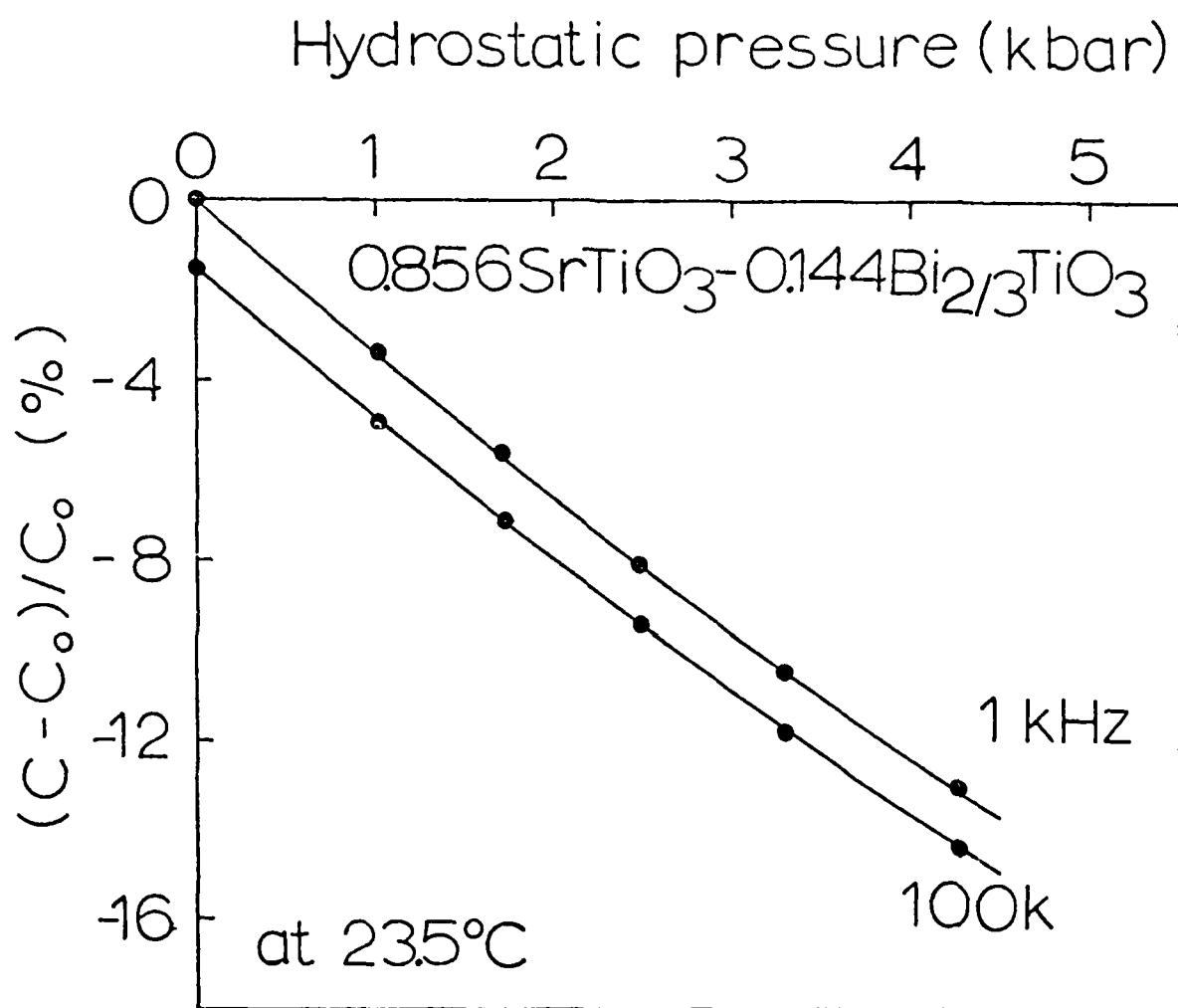
(b) Electrostrictive coefficient Q_h as a function of frequency measured at room temperature.

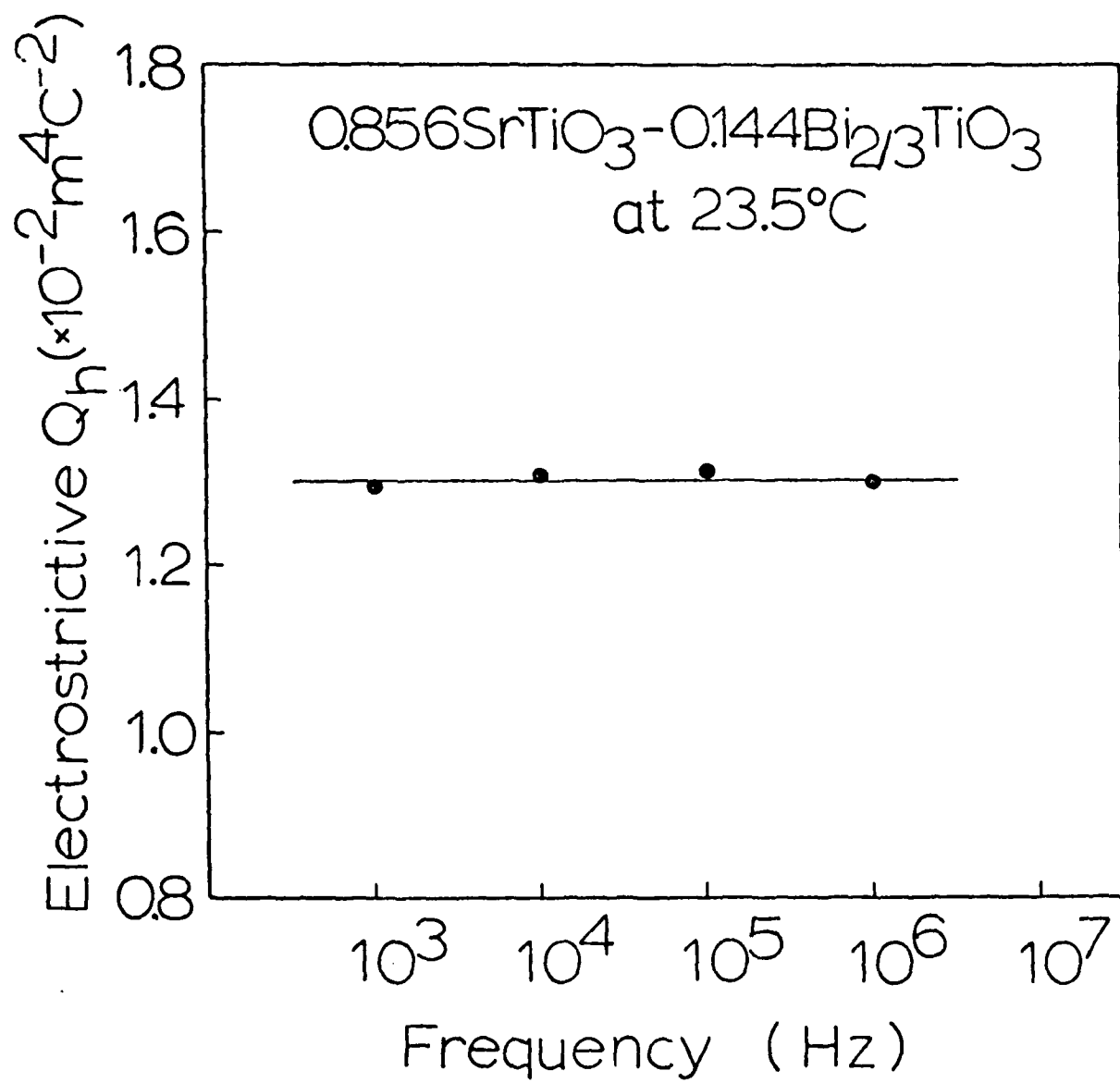
Fig. 2(a) Capacitance change as a function of hydrostatic pressure measured in $(\text{K}_{3/4}\text{Bi}_{1/4})(\text{Zn}_{1/6}\text{Nb}_{5/6})\text{O}_3$ at room temperature.

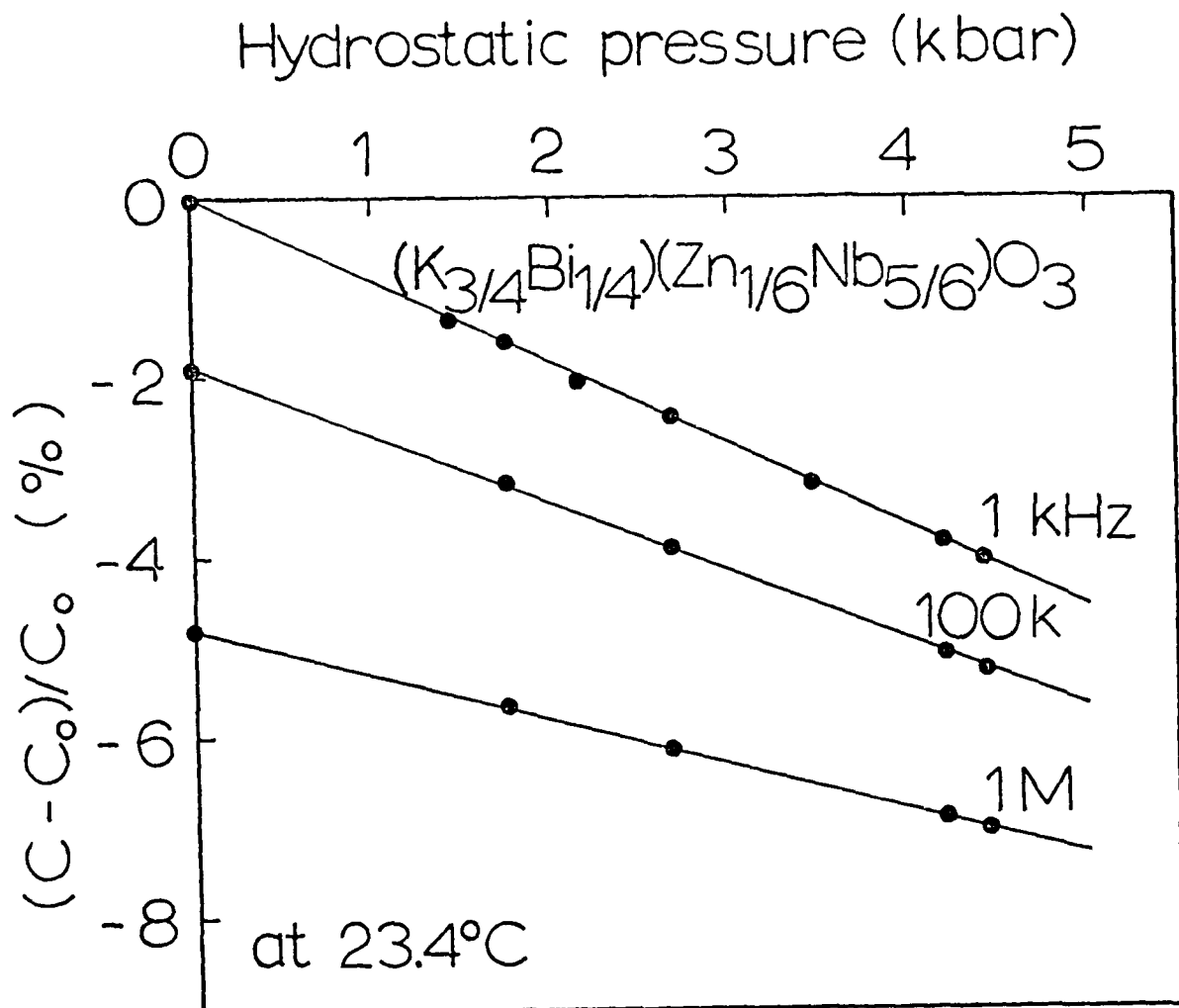
(b) Electrostrictive coefficient Q_h as a function of frequency measured at 23.4°C and -32.0°C .

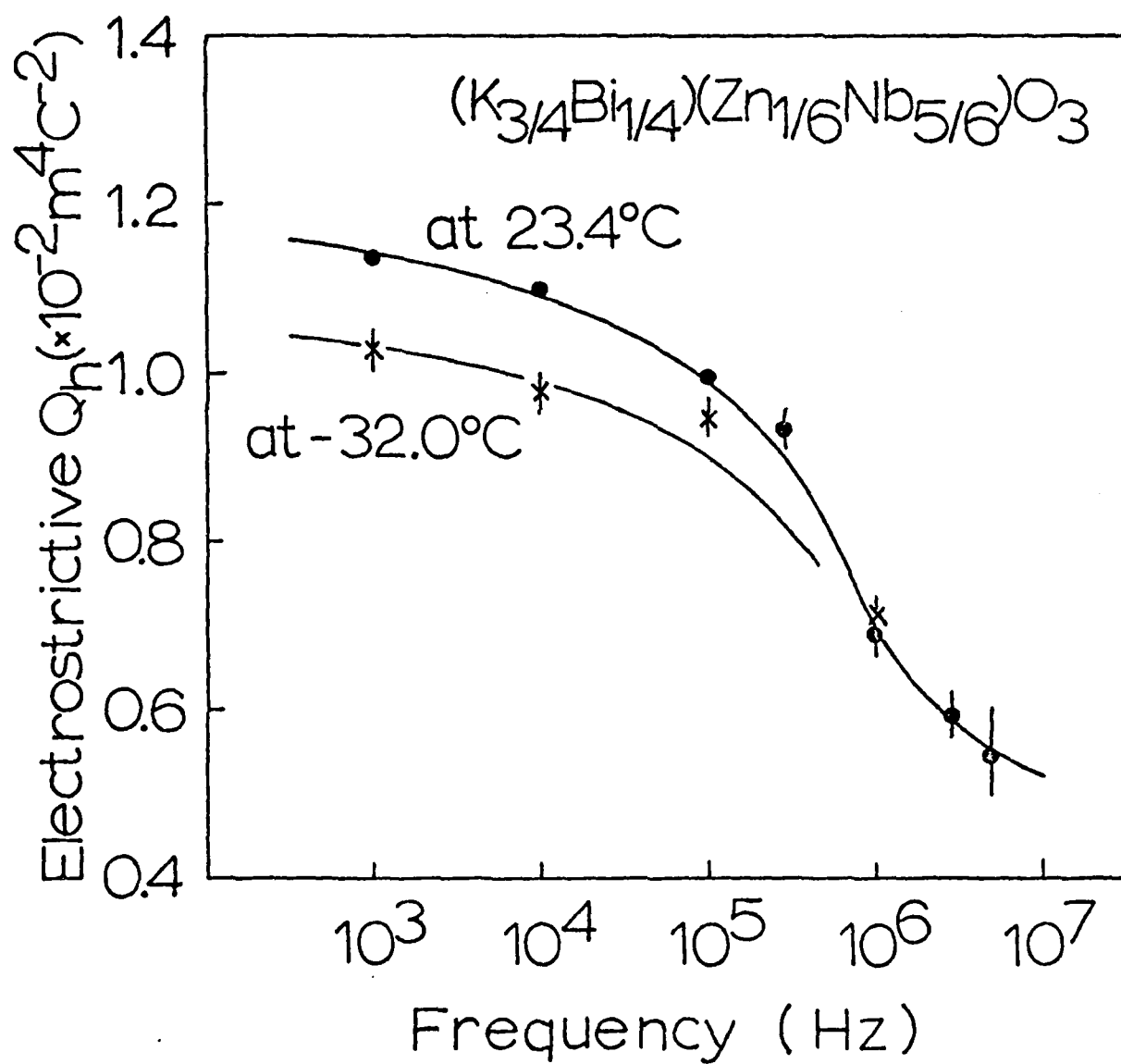
Fig. 3 Temperature dependence of the permittivity (at 1 kHz) in $(\text{K}_{3/4}\text{Bi}_{1/4})(\text{Zn}_{1/6}\text{Nb}_{5/6})\text{O}_3$ at 0 kbar and 3.5 kbar.

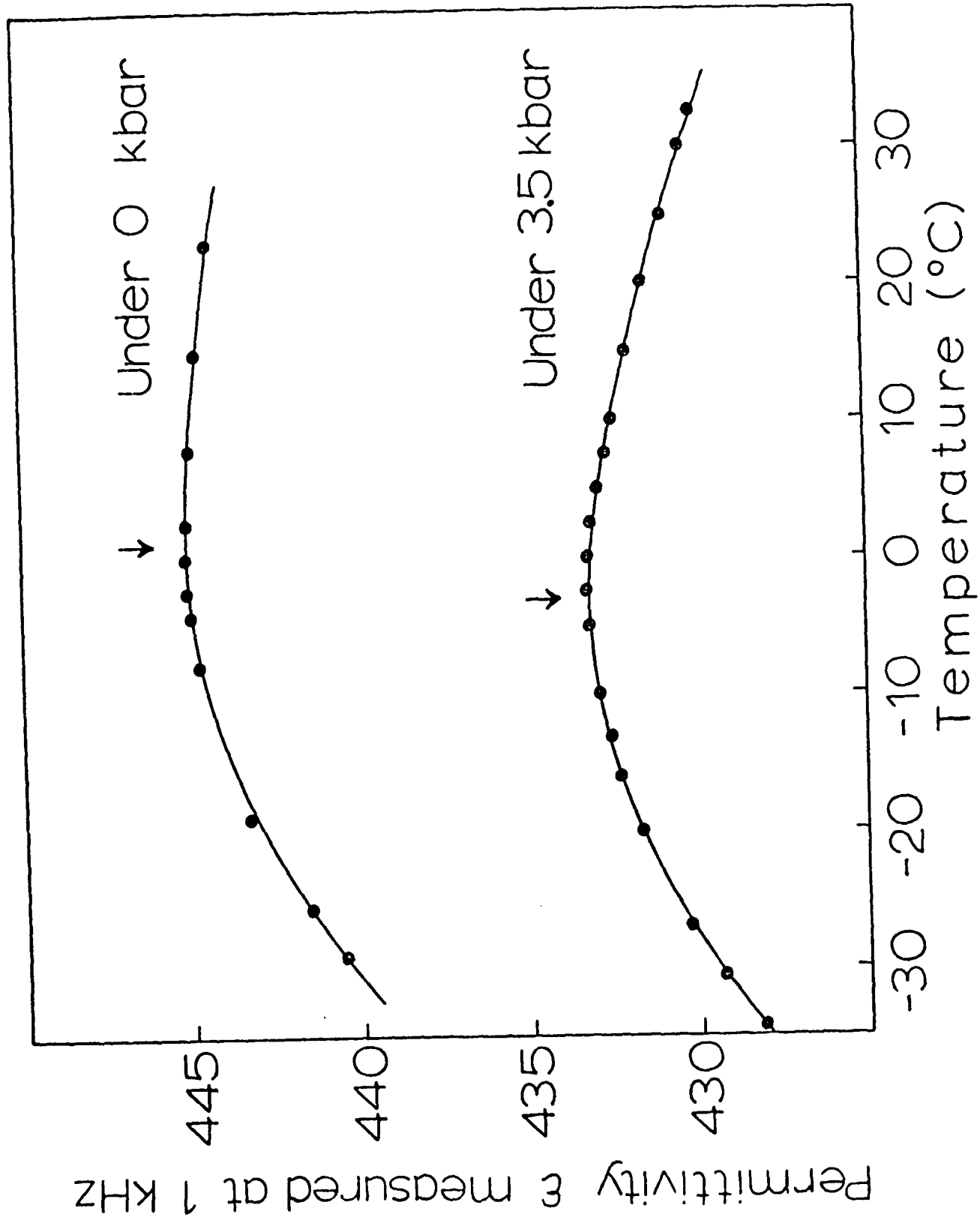
Fig. 4 Crystal structure models of the $\text{A}(\text{B}_{\text{I}1/2}\text{B}_{\text{II}1/2})\text{O}_3$ type perovskite: (a) ordered structure with a small rattling space and (b) disordered structure with a large rattling space.





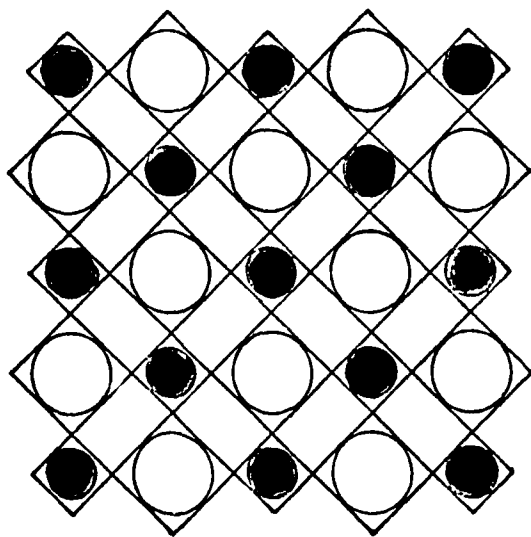




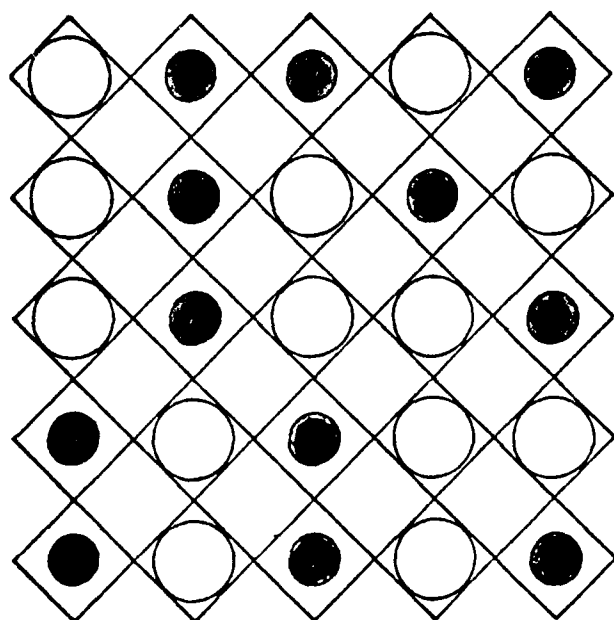


$A(B_{I1/2} B_{II1/2})O_3$ type perovskite

a) Ordered



b) Disordered



○ B_I ion
● B_{II} ion

APPENDIX 24

K. Uchino, L.E. Cross, R.E. Newnham, S. Nomura. Electrostrictive Effects
in Antiferroelectric Perovskites. J. Appl. Phys. (accepted).

Electrostrictive effects in Antiferroelectric Perovskites

K. Uchino, L. E. Cross, R. E. Newnham
Materials Research Laboratory
The Pennsylvania State University
University Park, PA 16802

and

S. Nomura
Department of Physical Electronics
Tokyo Institute of Technology
Ookayama, Meguro-ku, Tokyo 152

ABSTRACT

Electrostrictive terms have been introduced into the simple Kittel free energy function for antiferroelectrics. An additional coefficient Ω is found to be required to take account of the interaction with the sublattice polarizations, and Q and Ω values have been calculated from experimental data for typical antiferroelectric perovskites PbZrO_3 and $\text{Pb}(\text{Mg}_{1/2}\text{W}_{1/2})\text{O}_3$. Consideration of several ferro- and antiferroelectric perovskites suggests that the magnitude of Q is not affected strongly by ferro- or antiferroelectricity, but that it does depend quite strongly upon any disorder in the cation arrangement. An empirical rule that the product of the electrostrictive Q coefficient and the Curie Weiss Constant C is almost the same for all ferro- and antiferroelectric perovskites is proposed ($Q_h \cdot C = 3.1 \pm 0.4 \times 10^3 \text{ m}^4 \text{ C}^{-2} \text{ K}$). A very simple 'rattling ion' model is shown to give a simple intuitive explanation of the observed results.

1. INTRODUCTION

In earlier papers concerned with the electrostrictive effects in $\text{Pb}(\text{Mg}_{1/3}\text{Nb}_{2/3})\text{O}_3$ ⁽¹⁾ and $\text{Pb}(\text{Zn}_{1/3}\text{Nb}_{2/3})\text{O}_3$ ^(2,3) it has been shown that the polarization related electrostrictive coefficient Q in these relaxor type ferroelectrics are almost an order of magnitude smaller than in most 'normal' simple ferroelectric perovskites. On the other hand, the Curie-Weiss constants C in these relaxor crystals are several times larger⁽⁴⁾ and consequently the products QC are almost the same for both relaxor and normal materials (see Table II).

In this paper the QC product is explored for several antiferroelectric perovskites. The phenomenological relations defining the Q constants are developed, and values for the constants derived from known experimental data on PbZrO_3 (a simple perovskite) and on $\text{Pb}(\text{Mg}_{1/2}\text{W}_{1/2})\text{O}_3$ (an ordered antiferroelectric perovskite). The constancy of the QC product is established, and finally, a very simple intuitive 'rattling ion' model presented which explains qualitatively the observed behaviour.

2. THE PHENOMENOLOGICAL ANALYSIS OF ELECTROSTRICTION IN ANTIFERROELECTRICS

The two-sublattice model as a phenomenological description of antiferroelectricity was first introduced by Kittel⁽⁵⁾ and has been subsequently developed by many other authors⁽⁶⁻⁹⁾. Treatments of the elasto-electric interactions such as those by Devonshire⁽¹⁰⁾ and Kay⁽¹¹⁾ have been largely confined to simple proper ferroelectrics, with few attempts to explore the elasto-dielectric correlations in antiferroelectrics. Very recently, Fujimoto and Yasuda report a preliminary phenomenological attempt to correlate behaviour of antiferroelectrics under hydrostatic pressure⁽¹²⁾ but their treatment is unable to explain either the pressure dependence of the antiferroelectric Néel temperature T_N or the pressure dependence of

the Curie-Weiss temperature T_0 observed in simple perovskite antiferroelectrics PbZrO_3 , PbHfO_3 (17).

We believe that this inadequacy is due to their neglect of the coupling term Ω developed in the following analysis.

2.1 Free Energy Expression

By analogy to the phenomenological description of two-dimensional improper ferroelectrics (these studies are reviewed in texts such as those by Blinc and Žekš⁽¹³⁾ and by Lines and Glass⁽¹⁴⁾) the electrostrictive terms have been introduced into Kittel's free energy expression for linear antiferroelectrics using the two-sublattice model.

$$G_1 = 1/2\alpha(T)(P_a^2 + P_b^2) + 1/4\beta(P_a^4 + P_b^4) + 1/6\gamma(P_a^6 + P_b^6) + \eta P_a P_b - 1/2\chi_T p^2 + Qp(P_a^2 + P_b^2 + 2\Omega P_a P_b) \quad (1)$$

Here, P_a and P_b denote the two-sublattice polarizations, p hydrostatic pressure, χ_T compressibility, Q and Ω are the electrostrictive coefficients. Note that in the case of ferroelectrics with $\Omega = 0$, Q is equivalent to the hydrostatic electrostrictive coefficient Q_h ($= Q_{11} + 2Q_{12}$ in cubic phases). Other ferroelectric and antiferroelectric terms are omitted for simplicity.

We assume $\beta < 0$, $\gamma > 0$, $\eta > 0$ for a first-order antiferroelectric transition and α is the only temperature-dependent coefficient. Introducing the transformations $P_F = (P_a + P_b)/\sqrt{2}$, $P_A = (P_a - P_b)/\sqrt{2}$ (15) leads to the following expression:

$$G_1 = 1/2\alpha(P_F^2 + P_A^2) + 1/8\beta(P_F^4 + P_A^4 + 6P_F^2 P_A^2) + 1/24\gamma(P_F^6 + P_A^6 + 15P_F^4 P_A^2 + 15P_F^2 P_A^4) + 1/2\eta(P_F^2 - P_A^2) - 1/2\chi_T p^2 + Qp(P_F^2 + P_A^2 + \Omega(P_F^2 - P_A^2)) \quad (2)$$

The dielectric and elastic equations of state follow as

$$\left(\frac{\partial G_1}{\partial P_F}\right) = E = P_F[\alpha + \eta + 2Q(1 + \Omega)p + 1/2\beta P_F^2 + 1/4\gamma P_F^4 + 3/2\beta P_A^2 + 5/4\gamma P_A^4 + 5/2\gamma P_F^2 P_A^2], \quad (3)$$

$$\left(\frac{\partial G_1}{\partial P_A}\right) = 0 = P_A[\alpha - \eta + 2Q(1 - \Omega)p + 1/2\beta P_A^2 + 1/4\gamma P_A^4 + 3/2\beta P_F^2 + 5/4\gamma P_F^4 + 5/2\gamma P_F^2 P_A^2], \quad (4)$$

$$\left(\frac{\partial G_1}{\partial p}\right) = \frac{\Delta V}{V} = -\chi_T p + Q(1 + \Omega)P_F^2 + Q(1 - \Omega)P_A^2. \quad (5)$$

2.2 Stable States for $E = 0$

Three types of stable state which can give minima in free energy in the $P_F - P_A$ plane are given for $E = 0$ by simple mathematical procedures.

I Nonpolar; $P_F = 0, P_A = 0$

$$T_O(p) = T_O - 2QC(1 + \Omega)p \quad (6)$$

$$1/\epsilon_n = (T - T_O(p))/C \quad (7)$$

$$(\Delta V/V)_n = -\chi_T p \quad (8)$$

$$G_n = -1/2\chi_T p^2 \quad (9)$$

II Antipolar; $P_F = 0; P_A^2 = [-\beta + \sqrt{1/4\beta^2 - 4\gamma(T - T_N(p))/C}]/\gamma$

$$T_N(p) = T_N - 2QC(1 - \Omega)p \quad (10)$$

$$(\Delta V/V)_a = -\chi_T p + Q(1 - \Omega)P_A^2 \quad (11)$$

$$G_a = -1/2\chi_T p^2 + 1/2(\alpha - \eta + 2Q(1 - \Omega)p)P_A^2 + 1/8\beta P_A^4 + 1/24\gamma P_A^6 \quad (12)$$

III Polar; $P_F^2 = [-\beta + \sqrt{1/4\beta^2 - 4\gamma(T - T_C(p))/C}]/\gamma, P_A = 0$

$$T_C(p) = T_C - 2QC(1 + \Omega)p \quad (13)$$

$$(\Delta V/V)_p = -\chi_T p + Q(1 + \Omega)P_F^2 \quad (14)$$

$$G_p = -\chi_T p^2 + 1/2(\alpha + \eta + 2Q(1 + \Omega)p)P_F^2$$

Here, C is the Curie-Weiss constant and T_0 , T_N and T_C are given respectively as follows:

$$(\text{Curie-Weiss temperature}) \quad \alpha + \eta = (T - T_0)/C, \quad (16)$$

$$(\text{Néel temperature}) \quad \alpha - \eta - \frac{3}{16}(\beta^2/\gamma) = (T - T_N)/C, \quad (17)$$

$$(\text{Curie temperature}) \quad \alpha + \eta - \frac{3}{16}(\beta^2/\gamma) = (T - T_C)/C. \quad (18)$$

In the case of $\eta > 0$, the antipolar (antiferroelectric) state is more stable than the polar (ferroelectric) state if the pressure is not very high.

2.3 Effects of Hydrostatic Pressure

From Eq. (10) a linear shift of the Néel temperature is expected with increasing pressure; a decrease for $\Omega < 1$ and an increase for $\Omega > 1$, since $Q > 0$ in usual perovskite type crystals. The change in spontaneous antiferroelectric polarization is due to the displacement of the Néel point.

It is important to note the possibility of an antiferroelectric-ferroelectric phase transition with increasing pressure. The equation derived from Eqs. (10) and (13),

$$T_N(p) - T_C(p) = 2\eta C + 4QC\Omega p \quad (19)$$

suggests such a phase transition if $\Omega < 0$. The critical pressure is then given by

$$P_{\text{crit.}} = \eta/2Q|\Omega|. \quad (20)$$

For a first-order transition in the ferroelectric perovskites the difference $T_C - T_0$ is found experimentally to tend to decrease with increasing pressure. This suggests that there is a tendency toward second-order characteristics at higher pressures⁽¹⁶⁾. To explain such a tendency it would be necessary to introduce additional higher-order terms ($p(P_a^4 + P_b^4)$) to the free energy expression of Eq. (1).

3. COMPARISON WITH EXPERIMENTAL RESULTS

Direct electrostriction (strain induced by an applied electric field)

measurements have not been reported in antiferroelectric perovskites. We have calculated the electrostrictive coefficients Q and Ω for typical antiferroelectric perovskites PbZrO_3 (simple perovskite) and $\text{Pb}(\text{Mg}_{1/2}\text{W}_{1/2})\text{O}_3$ (ordered perovskite), using the data of the effects of hydrostatic pressure on antiferroelectric properties.

3.1 PbZrO_3

Samara reported complete data on the hydrostatic pressure dependence of the phase transition in PbZrO_3 ⁽¹⁷⁾. As is expected from the proposed theory, the Néel temperature increases linearly with increasing pressure. At constant temperature, the dielectric constant ϵ_n in the cubic phase obeys the relationship $\epsilon_n = C^*/(p - p_0)$. The Q and Ω values can be calculated from the experimental data of $(\partial T_N/\partial p)$, $(\partial(1/\epsilon_n)/\partial p)$ and the Curie-Weiss constant C , using Eqs. (7) and (10) (Table I). It is notable that the Q value ($2.03 \times 10^{-2} \text{ m}^4 \text{ C}^{-2}$) is almost the same value as the hydrostatic electrostrictive coefficients Q_h in simple perovskite ferroelectrics such as BaTiO_3 , PbTiO_3 , etc. The theoretical $(\partial T_0/\partial p)$ value calculated from Eq. (6) is exactly the same as the experimental value.

Using Eq. (11) and the volume change $(\Delta V/V)_s$ at the transition temperature, we obtain the P_A value or the sublattice polarization ($P_{as} = -P_{bs} = 35 \mu\text{Ccm}^{-2}$). The magnitude of this value is larger than the experimental spontaneous polarization in the field-induced ferroelectric phase observed in the double hysteresis loop ($\sim 10 \mu\text{Ccm}^{-2}$)⁽¹⁹⁾.

The entropy $S = -(\partial G_1/\partial T)$ is related in a simple way to the spontaneous polarization within the Devonshire approximation. The entropy change at the Néel temperature is given as follows:

$$\Delta S = \frac{1}{2C} P_A^2. \quad (21)$$

Very good agreement was obtained between the calculated and experimental data.

3.2 $\text{Pb}(\text{Mg}_{1/2}\text{W}_{1/2})\text{O}_3$

Polandov reported the effect of hydrostatic pressure on $\text{Pb}(\text{Mg}_{1/2}\text{W}_{1/2})\text{O}_3$. Although data are not reliable at higher pressures, Q and Ω can be calculated from the experimental data of $(\partial T_N/\partial p)$ and $(\partial(1/\epsilon_n)/\partial p)$ at lower pressures. The Q value obtained is several times larger than the values in simple perovskite crystals, while the Curie-Weiss constant of $\text{Pb}(\text{Mg}_{1/2}\text{W}_{1/2})\text{O}_3$ is several times smaller⁽²¹⁾.

The sublattice polarization is estimated from the volume change at the Néel point as $P_{as} = -P_{bs} = 16 \mu\text{Ccm}^{-2}$. Reasonable agreement was also obtained between the experimental entropy change data and the calculated value at the transition temperature.

It is interesting that since $\Omega < 0$, $\text{Pb}(\text{Mg}_{1/2}\text{W}_{1/2})\text{O}_3$ is an example which has the capability of an antiferroelectric-ferroelectric phase transition with increasing pressure.

4. DISCUSSIONS

The hydrostatic electrostrictive coefficients Q_h and the Curie-Weiss constants C are summarized in Table II for several kinds of perovskite type crystals: simple, disordered, partially-ordered and ordered ferroelectrics and antiferroelectrics.

The experimental rule proposed for perovskite ferroelectrics, that is, "the product value of the electrostrictive coefficient Q and the Curie-Weiss constant C is almost constant for all ferroelectric perovskites" is also true for antiferroelectric perovskites ($Q_h C = 3.1 \pm 0.4 \times 10^3 \text{ m}^3 \text{ C}^{-2} \text{ K}$).

Considering that the Q value of PbZrO_3 is of the same order of magnitude as the values for simple perovskite ferroelectrics, it appears probable that the magnitude of the electrostrictive coefficient Q is not strongly

affected by the tendency to ferroelectric or antiferroelectric order, but is much more strongly affected by the degree of order in the cation arrangement. The Q value tends to increase from disordered, through simple and then ordered perovskite crystals. The decreasing tendency of the Curie-Weiss constant from its highest values in disordered, through partially-ordered, and simple and ordered perovskites is also very suggestive.

We propose a simple intuitive model that explains the "constant QC rule." Figure 1(a) and (b) show two exaggerated B-ion surroundings of the perovskite structure. In the case of (a) with a large "rattling" space for a relatively small B ion, the ion can move easily without distortion of the oxygen octahedron when an electric field is applied. Larger polarization can be expected for unit magnitude of electric field; in other words, larger dielectric constant or larger Curie-Weiss constant. Also, smaller strain is expected for unit magnitude of polarization. On the other hand, in the case of (b) with a small "rattling" space for a relatively large B ion, it can not move easily without making distortion of the octahedron. Smaller Curie-Weiss constant and larger electrostrictive coefficient are expected in this case. A numerical description of the ion rattling model will be given in a subsequent paper. The results of the electrostriction in the solid solution systems $\text{Pb}(\text{Mg}_{1/3}\text{Nb}_{2/3})\text{O}_3 - \text{PbTiO}_3$ ⁽³⁴⁾ and $\text{Pb}(\text{Mg}_{1/3}\text{Nb}_{2/3})\text{O}_3 - \text{Pb}(\text{Mg}_{1/2}\text{W}_{1/2})\text{O}_3$ ⁽³⁵⁾ are also very suggestive. In both systems, the small Q -coefficient value of $\text{Pb}(\text{Mg}_{1/3}\text{Nb}_{2/3})\text{O}_3$ increases with increasing PbTiO_3 or $\text{Pb}(\text{Mg}_{1/2}\text{W}_{1/2})\text{O}_3$ content. An even larger rate of increasing was obtained for the $\text{Pb}(\text{Mg}_{1/3}\text{Nb}_{2/3})\text{O}_3 - \text{Pb}(\text{Mg}_{1/2}\text{W}_{1/2})\text{O}_3$ system than for the $\text{Pb}(\text{Mg}_{1/3}\text{Nb}_{2/3})\text{O}_3 - \text{PbTiO}_3$ system, due to the tendency of Mg and W ions to order. The densely-packed structure of B ions has been observed for $0.1\text{Pb}(\text{Mg}_{1/3}\text{Nb}_{2/3})\text{O}_3 - 0.9\text{Pb}(\text{Mg}_{1/2}\text{W}_{1/2})\text{O}_3$ by Amin et al.⁽³⁶⁾, which suggests the very small rattling space.

Further studies involving direct electrostriction measurements of PbZrO_3 and $\text{Pb}(\text{Mg}_{1/2}\text{W}_{1/2})\text{O}_3$ in the paraelectric phase are obviously desirable. The electrostrictive effects of non-ferroelectric relaxor perovskites will be also an interesting subject for study.

Acknowledgment

We wish to thank the Office of Naval Research for their support of our work, through Contract No. N00014-78-C-0291.

REFERENCES

1. K. Uchino, S. Nomura, L. E. Cross, S. J. Jang and R. E. Newnham, J. Appl. Phys. 51 (1980) in press.
2. J. Yoshimoto, B. Okai and S. Nomura, J. Phys. Soc. Japan 31, 307 (1971).
3. S. Nomura, J. Kuwata, S. J. Jang, L. E. Cross and R. E. Newnham, Mat. Res. Bull. 14, 769 (1979).
4. J. Kuwata, K. Uchino and S. Nomura, Ferroelectrics 22, 863 (1979).
5. C. Kittel, Phys. Rev. 82, 729 (1951).
6. Y. Takagi, Phys. Rev. 85, 315 (1952).
7. G. A. Smolenskii and V. Kozlovskii, Zh. eksp. teor. Fiz. 26, 684 (1954).
8. L. E. Cross, J. Phys. Soc. Japan 23, 77 (1967).
9. K. Okada, J. Phys. Soc. Japan 28S, 58 (1970).
10. A. F. Devonshire, Theory of Ferroelectrics, Phil. Mag. Suppl. 3, 85 (1954).
11. H. F. Kay, Rep. Progr. in Phys. 43, 230 (1955).
12. S. Fujimoto and N. Yasuda, Japan. J. Appl. Phys., 15, 595 (1976).
13. R. Blinc and B. Žekš, Soft Modes in Ferroelectrics and Antiferroelectrics, North-Holland Publishing Co., Amsterdam (1974).
14. M. E. Lines and A. M. Glass, Principles and Applications of Ferroelectrics and Related Materials, Clarendon Press, Oxford (1977).
15. L. E. Cross, J. Phys. Soc. Japan 23, 77 (1967).
16. G. A. Samara, Advances in high pressure research (ed. R. S. Bradley), Vol. 3, Chap. 3, Academic Press, New York (1969).
17. G. A. Samara, Phys. Rev. B1, 3777 (1970).
18. E. Sawaguchi, G. Shirane and Y. Takagi, J. Phys. Soc. Japan 7, 110 (1952).
19. G. Shirane, E. Sawaguchi and Y. Takagi, Phys. Rev. 84, 476 (1951).
20. I. N. Polandov, Soviet Phys. - Solid State, 5, 838 (1963).

21. S. Nomura, S. J. Jang, L. E. Cross and R. E. Newnham, J. Amer. Cer. Soc. 62, 485 (1979).
22. G. A. Smolenskii, N. N. Krainik and A. I. Agranovskaya, Soviet Phys. - Solid State, 3, 714 (1961).
23. B. A. Strukov, K. A. Minaeva, T. L. Skomorokhova and V. A. Isupov, Soviet Phys. - Solid State, 8, 781 (1966).
24. T. Yamada, J. Appl. Phys. 43, 328 (1972).
25. C. J. Johnson, Appl. Phys. Lett. 7, 221 (1965).
26. V. G. Gavril'yachenko and E. G. Fesenko, Soviet Phys. - Cryst. 16, 549 (1971).
27. E. G. Fesenko, V. G. Gavril'yachenko and E. V. Zarochentsev, Bull. Acad. Sci. USSR, Phys. Ser. 34, 2262 (1970).
28. G. Schmidt and E. Hegenbarth, Phys. Stat. Sol. 3, 329 (1963).
29. R. O. Bell and G. Rupprecht, Phys. Rev. 129, 90 (1963).
30. H. Uwe and T. Sakudo, J. Phys. Soc. Japan 38, 183 (1975).
31. H. Uwe, H. Unoki, Y. Fujii and T. Sakudo, Commun. Solid State Phys. 13, 737 (1973).
32. K. Uchino, F. Kojima and S. Nomura, Ferroelectrics, 15, 69 (1977).
33. V. A. Bokov, S. A. Kizhaev, I. E. Myl'nikova and A. G. Tutov, Soviet Phys. - Solid State 6, 2419 (1965).
34. S. J. Jang, K. Uchino, S. Nomura and L. E. Cross, Ferroelectrics (in press).
35. S. Norura, J. Kuwata, K. Uchino, S. J. Jang, L. E. Cross and R. E. Newnham, Phys. Stat. Sol. (a) 57, (1980) (in press).
36. A. Amin, R. E. Newnham, L. E. Cross and S. Nomura, (unpublished).

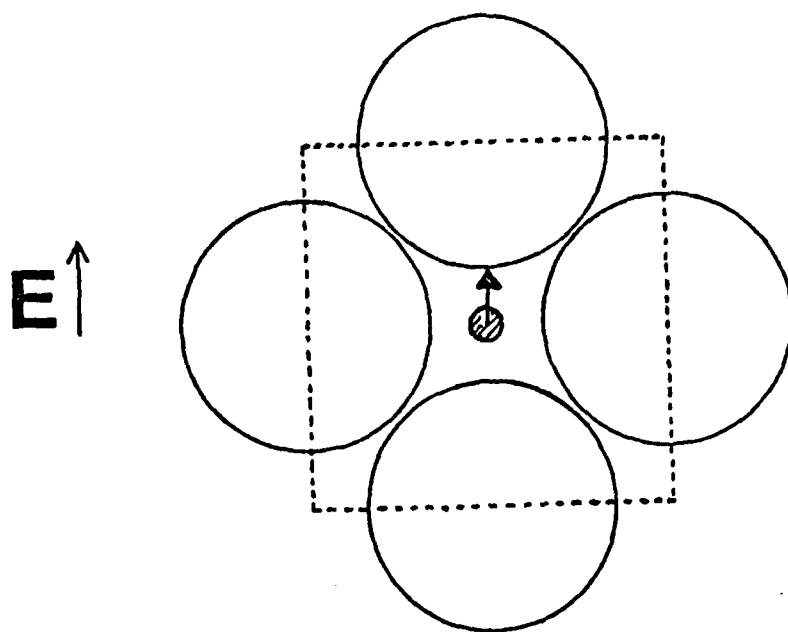
Table I Values of the transition parameters for PbZrO_3 and $\text{Pb}(\text{Mg}_{1/2}\text{W}_{1/2})\text{O}_3$ which are used in calculating electrostrictive coefficients. $(\Delta V/V)_s$, P_A and ΔS are the accompanying volume change, spontaneous antiferroelectric polarization change and transition entropy change.

Parameter	Substance	PbZrO_3		$\text{Pb}(\text{Mg}_{1/2}\text{W}_{1/2})\text{O}_3$	
		expt.	calc.	expt.	calc.
T_N (K)	(K)	507	17)	311	20)
T_O (K)	(K)	475	17)	100	21)
$(\partial T_N / \partial p)$ (K kbar ⁻¹)	(K kbar ⁻¹)	4.5	17)	-5.84	20)
$(\partial(1/En)/\partial p)$ (kbar ⁻¹)	(kbar ⁻¹)	1.0×10^{-4}	17)	8.0×10^{-5}	20)
C (K)	(K)	1.6×10^5	17)	0.42×10^5	21)
$(\Delta V/V)_s$		-4.06×10^{-3}	18)	3.93×10^{-3}	22)
Q (m C ⁻²)		-		-	6.19×10^{-2}
Ω		-		-	-0.27
P_A (Cm ⁻²)		-		-	0.224
$(\partial T_O / \partial p)$ (K kbar ⁻¹)	(K kbar ⁻¹)	-16.0	17)	-	-3.36
ΔS (cal K ⁻¹ mol ⁻¹)	(cal K ⁻¹ mol ⁻¹)	0.88	18)	0.88	23)
					0.63

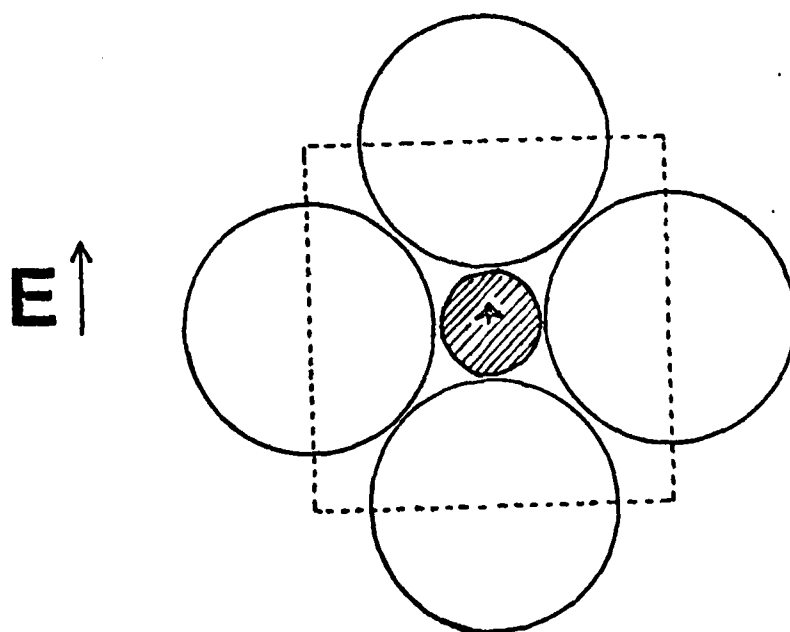
Table II Electrostrictive coefficients, Curie-Weiss constants and their product values for various perovskite-type ferroelectrics and antiferroelectrics.

Order-type	Substance	Q_h ($\times 10^{-2} \text{ m}^4 \text{ C}^{-2}$)	C ($\times 10^5 \text{ K}$)	$Q_h C$ ($\times 10^3 \text{ m}^4 \text{ C}^{-2} \text{ K}$)
disordered	$\text{Pb}(\text{Mg}_{1/3}\text{Nb}_{2/3})\text{O}_3$	0.60 1)	4.7 21)	2.8
	$\text{Pb}(\text{Zn}_{1/3}\text{Nb}_{2/3})\text{O}_3$	0.66 3)	4.7 4)	3.1
	BaTiO_3	2.0 24)	1.5 25)	3.0
	PbTiO_3	2.2 26)	1.7 27)	3.7
simple	SrTiO_3	5.0 28)	0.77 29)	3.8
	KTaO_3	5.2 30)	0.5 31)	2.6
partially-ordered	$\text{Pb}(\text{Fe}_{2/3}\text{U}_{1/3})\text{O}_3$	-	2.3 32)	-
simple	PbZrO_3	2.0*	1.6 17)	3.2
ordered	$\text{Pb}(\text{Co}_{1/2}\text{W}_{1/2})\text{O}_3$	-	1.2 33)	-
	$\text{Pb}(\text{Mg}_{1/2}\text{W}_{1/2})\text{O}_3$	6.2*	0.42 21)	2.6

*Calculated values



(a)



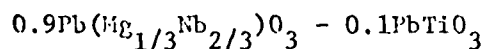
(b)

Figure 1. B-ion surroundings of the perovskite structure.
 (a) Large rattling space; (b) Small rattling space.

APPENDIX 25

K. Uchino, L.E. Cross, S. Nomura. Inverse Hysteresis of Field Induced
Elastic Deformation in the Solid Solution $0.9\text{Pb}(\text{Mg}_{1/3}\text{Nb}_{2/3})\text{O}_3:0.1\text{PbTiO}_3$.
J. Mat. Sci. (accepted).

INVERSE HYSTERESIS OF FIELD INDUCED ELASTIC DEFORMATION
IN THE SOLID SOLUTION



K. Uchino and L. E. Cross

Materials Research Laboratory
The Pennsylvania State University
University Park, Pennsylvania 16802

and

S. Numura

Department of Physical Electronics
Tokyo Institute of Technology
Ookayama, Megure-ku, Tokyo 152

ABSTRACT

Elastic deformations induced by high electric field in the solid solution system $\text{Pb}(\text{Mg}_{1/3}\text{Nb}_{2/3})\text{O}_3 - \text{PbTiO}_3$ has been measured using a strain gauge method at temperatures in the relaxation range. Unusual inverse hysteretic curves have been observed in the relation between the deformation and electric field in $0.9\text{Pb}(\text{Mg}_{1/3}\text{Nb}_{2/3})\text{O}_3 - 0.1\text{PbTiO}_3$ at temperatures outside the range where they would be of practical use in electrostrictive displacement control.

1. Introduction

Dielectric properties and electrostriction of materials in the solid solution systems $\text{Pb}(\text{Mg}_{1/3}\text{Nb}_{2/3})\text{O}_3 - \text{PbTiO}_3$ have been reported in our recent papers [1-4]. In pure $\text{Pb}(\text{Mg}_{1/3}\text{Nb}_{2/3})\text{O}_3$ and $\text{Pb}(\text{Mg}_{1/3}\text{Nb}_{2/3})\text{O}_3$ - rich compositions, a most unusual inverse hysteresis in the relation between the weak-field permittivity and the cyclic bias field has been observed at temperatures in the relaxation range.

Uchida and Ikeda reported rather similar bias characteristics of the weak-field permittivity in $\text{Pb}(\text{Zr}, \text{Ti})\text{O}_3$ families ceramics [5]. They explained the effects qualitatively by making specific assumptions as to the behavior of 180° -domain reversals and non 180° - rotations of domains as a function of the applied field [6]. On the other hand, they observed normal hysteresis in the biasing field characteristics of elastic deformation for BaTiO_3 and PZT families as are predicted by their theoretical model.

Concerning $\text{Pb}(\text{Mg}_{1/3}\text{Nb}_{2/3})\text{O}_3 - \text{PbTiO}_3$ ceramics, however, we observed also the peculiar inverse hysteresis in the bias characteristics of strain. We describe in this paper preliminary experimental data of temperature and frequency dependence of longitudinal and transverse strain measured in $0.9\text{Pb}(\text{Mg}_{1/3}\text{Nb}_{2/3})\text{O}_3 - 0.1 \text{PbTiO}_3$ ceramics, which reveals the largest inverse hysteretic effect among the samples with compositions containing less than 20 mol % of PbTiO_3 .

2. Sample Preparations

Ceramic specimens were prepared from reagent grade PbO , MgO , Nb_2O_5 and TiO_2 . The constituent oxides were mixed in appropriate proportions, ball-milled in alcohol, then dried and calcined in air at 800°C for 15 hours in a closed alumina crucible. The resulting calcine was ground

and refired for two additional 15-hour periods to ensure complete reaction.

For the transverse strain measurement, samples were prepared by cold pressing into disks and firing on platinum setters in air at 1000°C for 2 hours. Gold electrodes were sputtered onto the faces. For the longitudinal effect, internally electroded multilayer samples were prepared by standard type casting techniques using calcined $\text{Pb}(\text{Mg}_{1/3}\text{Nb}_{2/3})\text{O}_3 - \text{PbTiO}_3$ powder and a commercial doctor blade media (Cladan Inc., San Diego, CA, type B42) [7]. Internal electrodes were applied by screen printing platinum ink (Englehard Industries, East Newark, NJ, type E-305-A) onto the dried cast tape. Ten layer devices with thickness of 2.5mm were prepared by firing under the same conditions as described above.

The field-induced strain was measured by a strain gauge method. A polyimide foil strain gauge (Kyowa, KFR-02-C1-11) was bonded with a cement (Kyowa, PC-6) on the electroded face of the sample for the transverse measurement, or on the edge face of the multilayer sample for longitudinal measurements.

3. Experiments and Discussions

Measurements were carried out by a DC method using a double bridge technique. The longitudinally (S_1) and transeversely induced strains (S_2) were measured as a function of the applied electric field (0.001 ~ 0.1 Hz) at various temperatures (-80 ~ 70°C).

3.1 Temperature and Field Dependence of Strain

Figure 1(a) and (b) show the dependence of the longitudinal (S_1) and transverse strains (S_2) on the cyclic electric field at 0.002Hz for $0.9\text{Pb}(\text{Mg}_{1/3}\text{Nb}_{2/3})\text{O}_3 - 0.1\text{PbTiO}_3$ ceramics at various temperatures. In the longitudinal effect the inverse hysteresis can be observed even above the mean Curie temperature (~25°C). Below that temperature, the normal

hysteresis is dominant and the inverse hysteresis is observed only at high electric field, where it gradually disappears with decreasing temperature. In the transverse effect, the normal hysteresis is dominant for all temperatures. Below -10°C , however, the inverse effect appears at high electric field. It is notable that the magnitude of the strain change decreases with decreasing temperature below -10°C . The initial strain curves are also shown in Fig. 1(b), by dashed lines.

Figure 2(a) shows the maximum longitudinal strain at $E = 10\text{kV/cm}$ and the maximum transverse strain at $E = 8.5\text{kV/cm}$ plotted as a function of temperature. The initial strains of the transverse effect are also plotted for comparison. The temperature dependence curves are very similar to the curve for the polarization. Compared with the value of the transverse strain, the longitudinal strain is relatively smaller than the expected value ($S_1 \sim -3S_2$), which may be explained by the effect of the multilayer configuration due to two separate electrode systems and insulated electrode edges reducing the measured displacement [7]. The large strain difference between the initial and cyclic states in the transverse effect suggests that part of the non 180° -rotations of domain switching may be quenched by the initial field application and do not subsequently contribute to the cyclic domain switching. This quenching effect is not observed in the longitudinal effect.

Figure 2(b) shows the plots of the critical electric field of the inverse hysteresis as a function of temperature. The critical field shows a minimum at a temperature near the mean Curie temperature.

3.2 Frequency Dependence of Strain

Figure 3 shows the frequency dependence of the transverse strain (S_2) curve measured at -17.0°C . The critical field E_{cr} of the inverse

hysteresis increases with increasing frequency, which is clearly evident in Fig. 4. It is notable that the slope of the E_{cr} -log f curve tends to increase with decreasing temperature.

It is not possible to explain the inverse hysteresis in the elastic strain by the model proposed by Uchida and Ikeda [6]. It appears probable that consideration must be given to the possible interaction between 180° and non- 180° reorientations which are ignored in the Uchida-Ikeda model. Another possibility is the effect of the superposed giant quadratic electrostriction which is typically observed in relaxor ferro-electrics. Further investigation will be desired to elucidate between these possible models.

The authors wish to express their sincere thanks to Dr. S. J. Jang for his sample preparations. This work was supported by the Department of the Navy through the Office of Naval Research.

References

1. S. NOMURA, S. J. JANG, L. E. CROSS and R. E. NEWNHAM, J. Amer. Cer. Soc. 62, (1979) 485.
2. S. NOMURA, J. KUWATA, K. UCHINO, S. J. JANG, L. E. CROSS and R. E. NEWNHAM, Phys. Stat. Sol. (a) 57 (1980) to be published.
3. L. E. CROSS, S. J. JANG, R. E. NEWNHAM, S. NOMURA and K. UCHINO, Ferroelectrics, (in press).
4. S. J. JANG, K. UCHINO, S. NOMURA, L. E. CROSS, Ferroelectrics (in press).
5. N. UCHIDA and T. IKEDA, Japan. J. Appl. Phys. 4 (1965) 867.
6. N. UCHIDA and T. IKEDA, Japan. J. Appl. Phys. 6 (1967) 1079.
7. L. J. BOWNE, T. SHROUT, W. A. SCHULZE and J. V. BIGGERS, Ferroelectrics (in press).

Figure Captions

- Fig. 1. (a) longitudinal electrostriction and (b) transverse electrostriction as a function of electric field (0.002Hz) at various temperatures for $0.9\text{Pb}(\text{Mg}_{1/3}\text{Nb}_{2/3})\text{O}_3 - 0.1\text{PbTiO}_3$.
- Fig. 2. (a) maximum longitudinal electrostriction at $E = 10\text{kV/cm}$ and maximum transverse electrostriction at $E = 8.5\text{kV/cm}$ as a function of temperature. Initial strains are also plotted by dashed lines; (b) critical field of the inverse hysteresis as a function of temperature.
- Fig. 3. Frequency dependence of the transverse electrostriction curve measured at -17.0°C .
- Fig. 4. The dependence of the critical field of the inverse hysteresis on frequency and temperature.

Fig. 1(a)

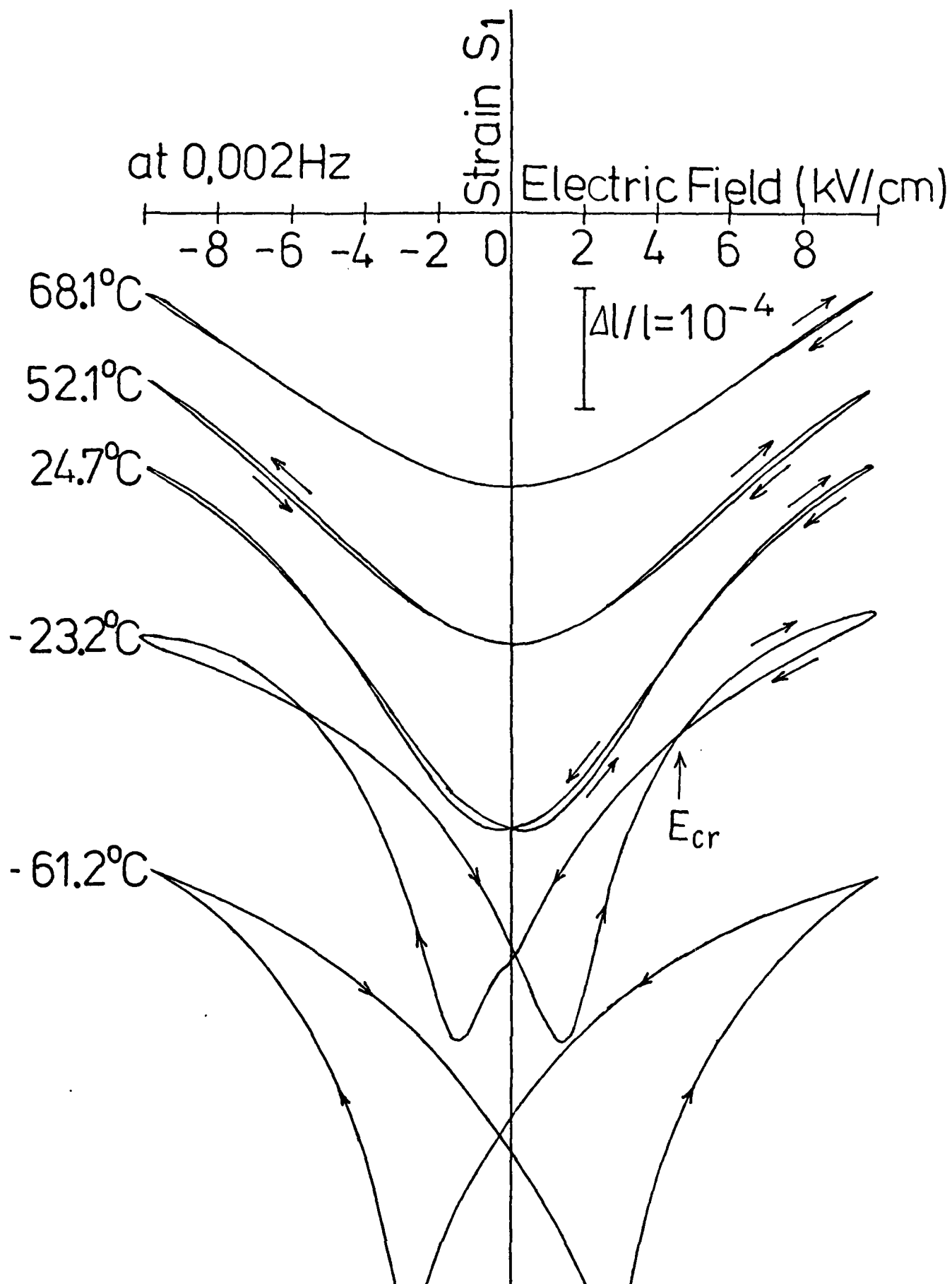


Fig. 1(b)

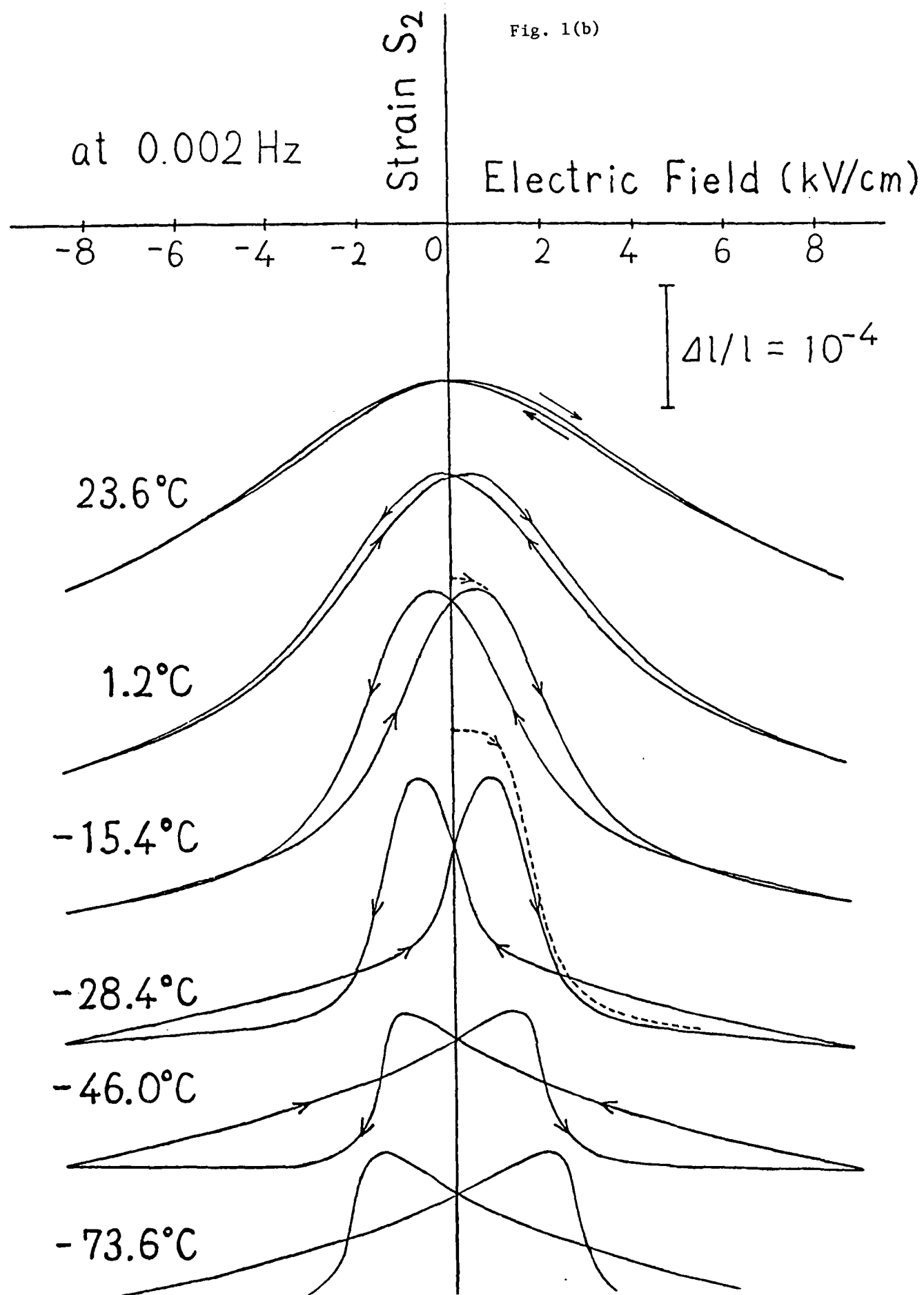


Fig. 2

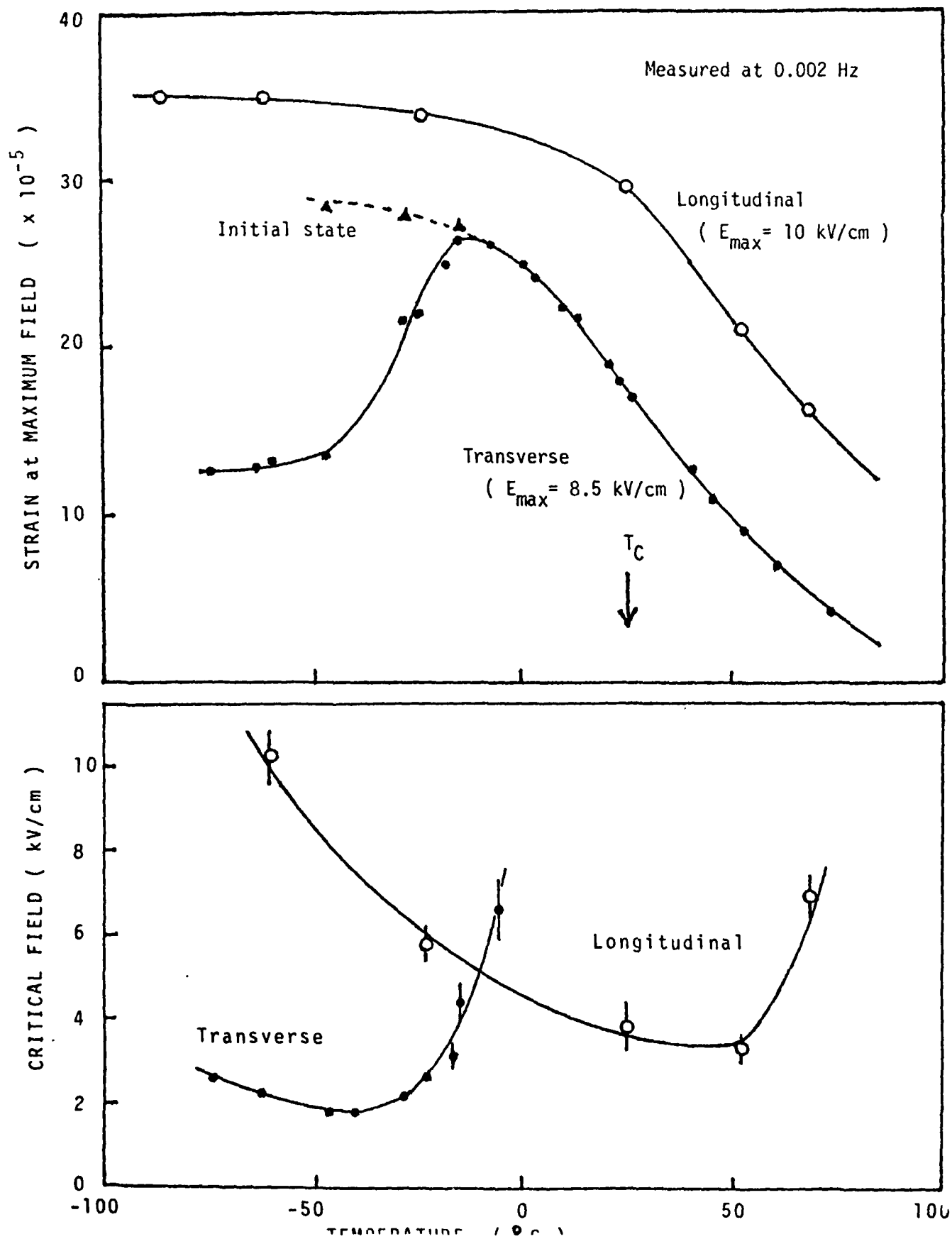


Fig. 3

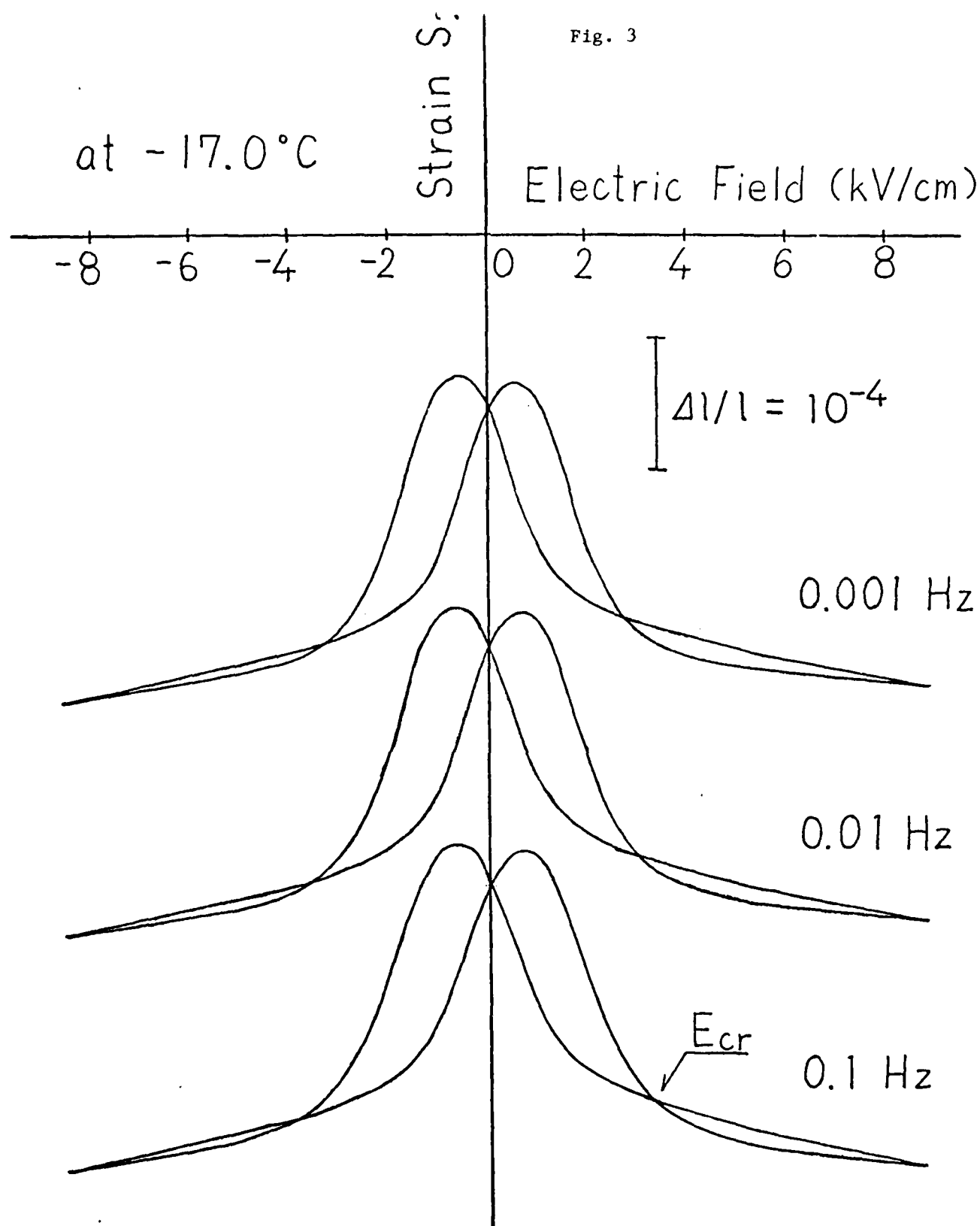
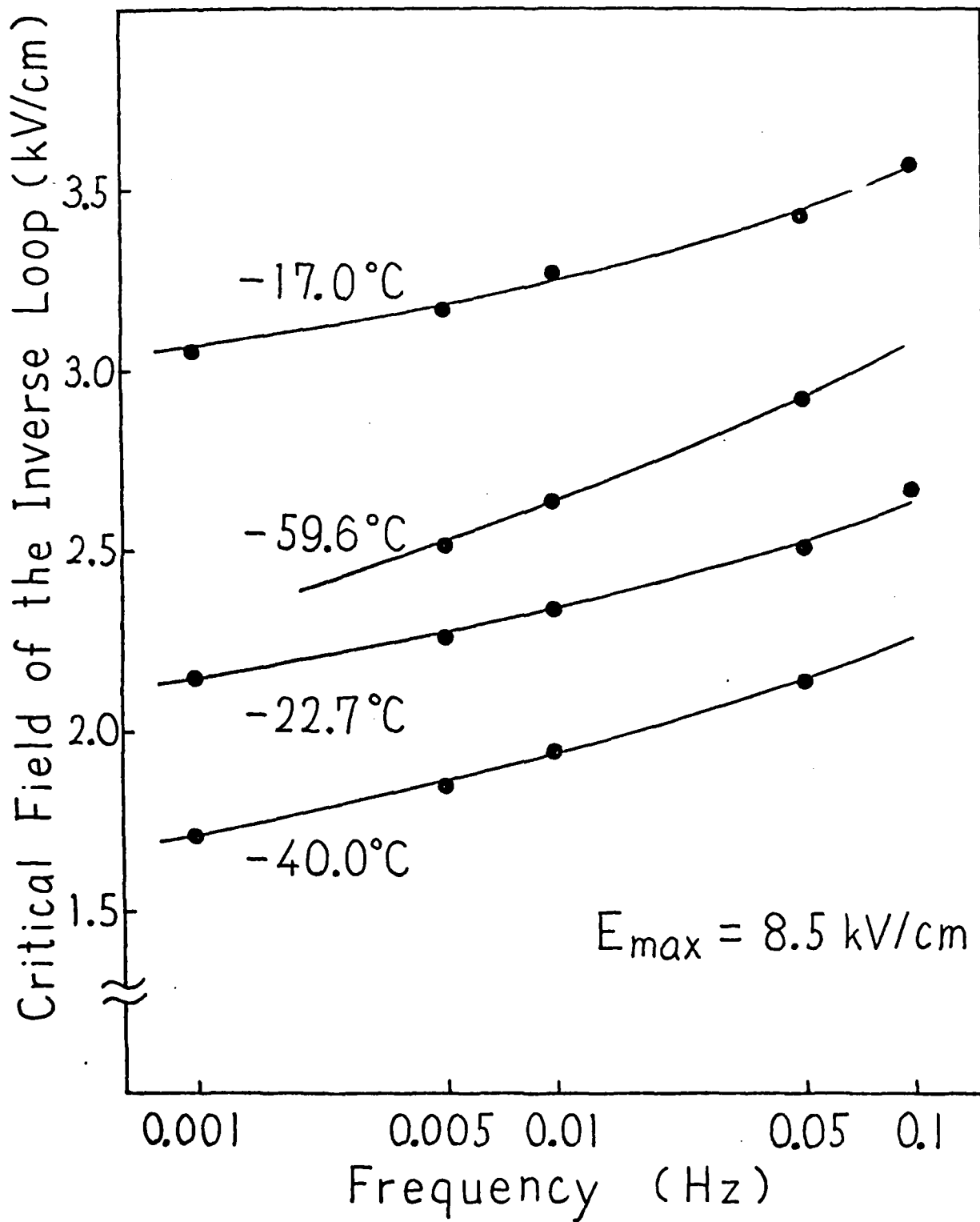


Fig. 4



APPENDIX 26

W. Schulze, T.R. Shrout, S.J. Jang, S. Sharp, L.E. Cross. Monolithic Multilayer Transducers for Optical Applications. J. Amer. Ceram. Soc. 63, 596 (1980).

Monolithic Multilayer Electromechanical Transducers for Optical Applications

W. A. SCHULZE,* T. R. SHROUT,* S. J. JANG, S. SHARP, and L. E. CROSS*

LASER-COMMUNICATION and information-processing systems have increased the need for simple electrically controllable micropositioners. Several of these needs have been met by using conventional piezoceramic materials; however, these materials often need very high driving voltages to develop the required displacements. They also lead to zero point drift due to aging and deaging under repeated field cycling.

Integral noble metal electrodes can be used to reduce the high driving voltage requirements in conventional piezoceramics. To explore this possibility, multilayer elements were fabricated from a low-hysteresis commercial PZT by using normal tape casting techniques.¹ The individual units consisted of 10 active layers

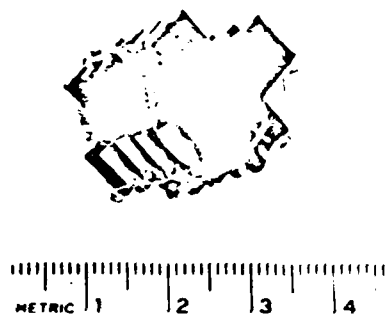


Fig. 1. Displacement transducer consisting of stack of PZT multilayers.

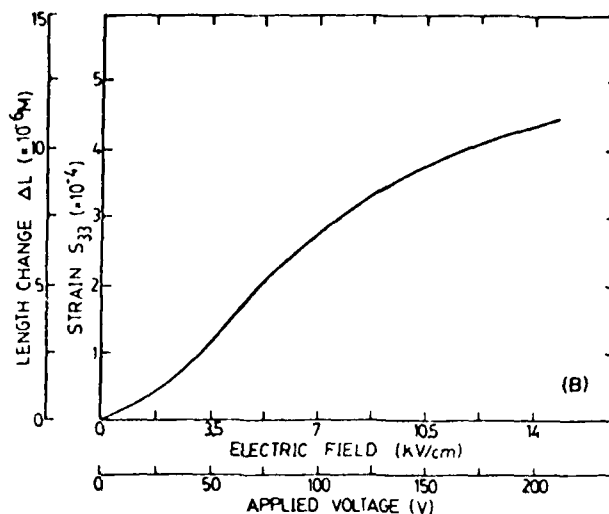
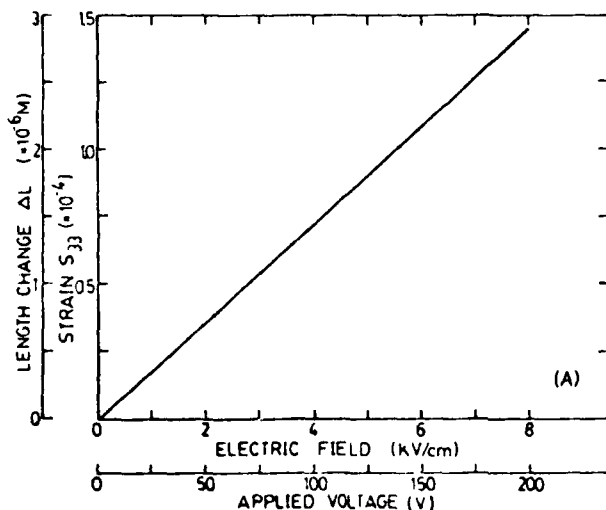


Fig. 2. Displacement and strain as a function of applied field or voltage for (A) PZT displacement transducer and (B) $0.9\text{Pb}(\text{Mg}_{1/3}\text{Nb}_{2/3})\text{O}_3:0.1\text{PbTiO}_3$ displacement transducer.

(1.8×10^{-4} m (7 mils) thick) with two passive screening layers acting as covers for the outer electrodes. Ten of these multilayers were epoxy-bonded and connected electrically in parallel to produce a stack 2.5×10^{-2} mm long (Fig. 1). This configuration permits displacements of $\approx 10 \mu\text{m}$, required for the laser system, at reasonable drive levels.

The displacement response as a function of applied field, after initial deaging, is shown in Fig. 2(A). The slope corresponds to an average piezoelectric coefficient of 220×10^{-12} C/N, near that of the bulk material. The internal electrode structure appears to have little effect on drift due to aging and deaging. With present commercial tape casting techniques, layer thicknesses of $< 2.5 \times 10^{-3}$ m (1 mil) are practical and would further reduce the drive voltage requirements by a factor of 7 from that of these experimental units.

To overcome the problems associated with aging and deaging, which are necessary features of any poled piezoceramic, experimental multilayers have been constructed from compositions in a newly developed family of electrostrictive ceramics in the $\text{Pb}(\text{Mg}_{1/3}\text{Nb}_{2/3})\text{O}_3:\text{PbTiO}_3$ family.² Electrostriction does not depend on the electrical prehistory (poling) of the sample and should not change with field cycling.

A device similar to the PZT stack (Fig. 1) was constructed by tape casting ceramic of composition $0.9\text{Pb}(\text{Mg}_{1/3}\text{Nb}_{2/3})\text{O}_3:0.1\text{PbTiO}_3$ with layers 1.5×10^{-4} m thick (6 mils). The displacement vs voltage curve is shown in Fig. 2(B). In this case, the response is nonlinear, as would be expected for electrostriction, but is reproducible for repeated cycling within the limits of the strain-measuring system ($\pm 0.1 \mu\text{m}$).²

Projecting the multilayer electrostrictor to a 2.5×10^{-3} m (one mil) layer spacing suggests that at 50 V strains of 10^{-3} should be achieved, i.e. a $25 \mu\text{m}$ strain on a 2.5×10^{-2} m element under 50 V drive with zero point drift, much less than any presently available PZT. Additional measurements have shown² that the thermal expansion at room temperature is $< 1 \times 10^{-6} \text{ } ^\circ\text{C}^{-1}$ in this ceramic, almost an order of magnitude less than PZT.

Received April 11, 1980; revised copy received May 23, 1980.
The writers are with the Materials Research Laboratory, The Pennsylvania State University, University Park, Pennsylvania 16802.
*Member, the American Ceramic Society.

¹J. C. Williams, pp. 173-98 in *Treatise on Materials Science and Technology*, Vol. 9, Ceramic Fabrication Processes, Edited by F. A. Wang, Academic Press, New York, 1979.

²S. J. Jang, "Electrostrictive Ceramics for Transducer Applications," Ph. D. Thesis, The Pennsylvania State University, University Park, Pa., November 1979.

APPENDIX 27

B.N. Achar, G.R. Barsch, L.E. Cross. Electrostriction, Optic Mode Gammas and Third Order Elastic Constants of SrTiO_3 in the Shell Model. Phys. Rev. B (submitted).

Electrostriction, Optic Mode Gammas and Third Order
Elastic Constants of SrTiO_3 in the Shell Model

B.N.N. Achar, G.R. Barsch* and L.E. Cross[†]
Materials Research Laboratory
The Pennsylvania State University
University Park, Pennsylvania 16802

Lattice dynamical calculations of harmonic and first order anharmonic properties at the zone center have been performed for the perovskite structure on the basis of a shell model. The harmonic part of the model is equivalent to Cowley's model, with the 14 parameters determined from zone center properties only. Anharmonic interactions arising from Coulomb and short range repulsion are included and are characterized by three parameters. Numerical application to SrTiO_3 shows that the model gives a consistent description of third order elastic and of electrostriction constants, provided that the higher than first order anharmonic contributions arising from zero point and thermal motion are eliminated from the experimental data by extrapolation to absolute zero.

PACS Numbers: 77.60. + V 62.20.Dc 63.20. - c

*Also affiliated with the Department of Physics.

[†]Also affiliated with the Department of Electrical Engineering.

I. Introduction

The ferroelectric and ferroelastic phase transformations occurring in many perovskite-type oxides and halides are well understood in terms of the experimentally observed softening of the zone-center Γ_{15} mode and the zone-corner R_{25} mode¹⁻³, respectively. In SrTiO_3 , one of the most extensively studied perovskites, the softening of both these modes has been investigated by means of infrared⁴⁻⁶, field-induced Raman scattering^{7,8} and inelastic neutron scattering techniques⁹⁻¹⁴ and explained theoretically on the basis of anharmonic phonon interactions¹⁵⁻²⁰. Issues not fully resolved at present include critical and transformation precursor phenomena and the actual microscopic origin of the large anharmonicity.

It is the purpose of the present paper to consider first order anharmonic properties at the zone center in order to investigate the anharmonicity of SrTiO_3 on the basis of a consistent model. The anharmonic properties considered here are the electrostriction constants, the third order elastic (T.O.E.) constants, and the optic mode gammas.

The experimental data available for SrTiO_3 consist of the complete set of six T.O.E. constants,^{21,22} two electrostriction constants,²³ and a semiempirical value for the soft mode gamma.^{24,25}

The available theoretical calculations of the electrostriction constants for ferroelectrics are based on a heuristic linear chain model²⁶ or on a point ion model with polarizable ions²⁷ which is known to be inadequate even for alkali halides²⁸. Electrostriction constants for SrTiO_3 at room temperature have also been calculated by Bruce and Cowley,²⁰ but as will be discussed below, are based on inconsistent model parameters. Thus a proper lattice dynamical treatment of electrostriction is not yet available for the perovskite structure. Third order elastic constants for the perovskite compound RbMnF_3 have been treated

theoretically by Naimon,²⁹ but no calculations of the mode gammas in perovskites have been made. Furthermore, the question of the consistency of the model parameters describing all first order anharmonic effects with the electrostriction constants has not yet been addressed.

While previous theories¹⁵⁻²⁰ consider anharmonicity mostly in the context of mode softening and take into account only the anharmonicity from the interionic interactions it has recently been shown by Migoni et al^{30,31} that for SrTiO_3 and KTaO_3 the intra-ionic anharmonicity arising from the nonlinear anisotropic polarizability of the oxygen ions could also be of major importance. It seems, therefore, necessary to use a rather general model for interatomic forces with a set of well-defined and mutually consistent parameters that can account for a sufficiently wide range of both harmonic and anharmonic properties. Since the intra-ionic anharmonicity proposed by Migoni et al^{30,31} is inconsequential for the first order anharmonic effects of the static crystal considered here it will not be further pursued.

A well-known difficulty in determining a consistent set of model parameters arises from the temperature dependence of the phonon frequencies and the properties in question. Within the framework of many-body perturbation theory, this temperature dependence is described by the temperature dependence of the anharmonic phonon self energy which can be calculated from the phonon Green's function.^{32,33} Although strictly, the frequencies which enter the Green's function are the unrenormalized frequencies pertaining to the static crystal they may to a good approximation be replaced by the renormalized frequencies which correspond to the experimentally measured frequencies for finite temperature.³³ This is the approach found "most satisfactory" and used by Cowley¹⁶ and Bruce and Cowley.²⁰ While this procedure may be a sufficiently good approximation for treating the renormalization of the harmonic properties it

becomes questionable when extended even to first order anharmonic properties of strongly anharmonic solids. For example, electrostriction of soft-mode materials at finite temperature is determined by higher than first order anharmonic contributions and lowest order anharmonic perturbation theory may not be adequate.

In order to circumvent these difficulties, in the present paper the effects of thermal and zero point motion will be eliminated from the experimental data for both harmonic and anharmonic properties by linear extrapolation from the high temperature region to absolute zero.^{34,35} The data so obtained will be regarded as pertaining to the static crystal. For comparison, lattice dynamical calculations pertaining to a quasistatic crystal have also been carried out by neglecting zero point and thermal motion and fitting the results to experimental room temperature data. As expected, no consistent fit even of first order anharmonic properties can be obtained in this case.

A further aspect of the present work is the inclusion of the Coulomb contributions to the anharmonic properties, neglected in previous theories.^{16,20} This is essential because of the near-cancellation of the Coulomb and the repulsive contributions to the soft mode frequency, which also occurs for the electrostriction coefficients. Moreover, for some of the T.O.E. constants both types of contributions are comparable.

Since the model considered here refers to the static soft-mode crystal, it is inherently unstable and could therefore provide a suitable starting point for a complete calculation of the anharmonic stabilization of both the Γ_{15} and R_{25} modes for SrTiO_3 occurring with increasing temperature. Work in this direction is in progress.

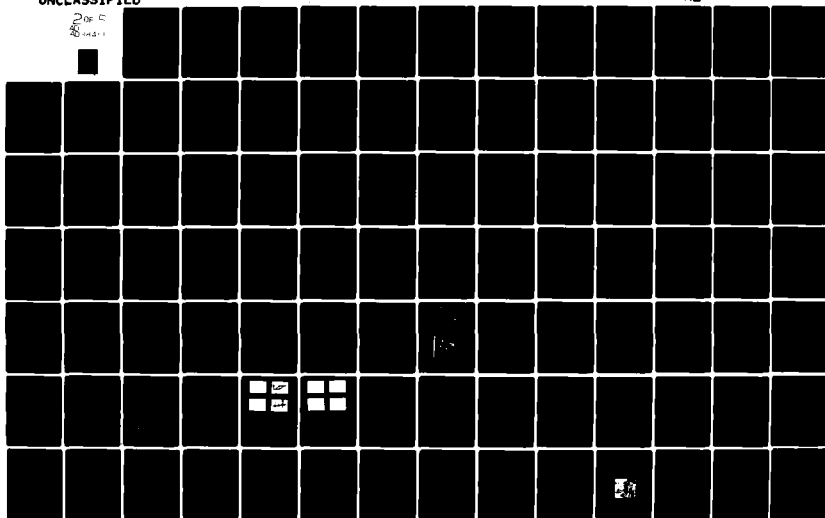
AD-A096 451

PENNSYLVANIA STATE UNIV UNIVERSITY PARK MATERIALS RE--ETC F/G 9/1
TARGETED BASIC STUDIES OF FERROELECTRIC AND FERROELASTIC MATERIALS--ETC(U)
DEC 80 L E CROSS, R E NEWNHAM, G R BARSCH N00014-78-C-0291

UNCLASSIFIED

NL

2 OF 5
84-0-1



II. LATTICE DYNAMICAL FRAMEWORK

A. Shell Model

The present paper employs the rigid shell model of Cowley¹⁰ for the cubic perovskite structure and takes into account the long range Coulomb interaction, the polarizability of all three ions, and the axially symmetric short range repulsive interaction between "nearest neighbor" Sr-O, Ti-O, and O-O ion pairs. In order to limit the number of parameters, the Sr-Ti interaction is neglected. This model has been tested extensively by Stirling¹⁴ in fitting experimental inelastic neutron scattering data, but in the present paper the model parameters are fitted to zone center properties. The model is characterized by 14 independent parameters. In the notation of Cowley,¹⁰ they consist of the dimensionless second derivatives of the repulsive potential A_i, B_i ($i = 1, 2, 3$ for Sr-O, Ti-O, O-O, respectively), the effective ionic charges Z_β , the electronic polarizabilities α_β , and the short-range polarization d_β of the ions labelled by $\beta = 1, 2, 3$ for Sr, Ti, O, respectively. Because of the charge neutrality condition only two of the three charges Z_β are independent. If the repulsive parameters A_i, B_i are regarded as the dimensionless second and first derivatives of a central force potential $\phi_i(r_i)$ the equilibrium condition must be imposed, thereby reducing the number of independent parameters by one.

The above harmonic shell model is extended to include inter-ionic anharmonicity by incorporating the third derivatives of both Coulomb and repulsive potentials. In the present work the latter are assumed to be of central force type and are described by the three dimensionless parameters $C_i = (a^4/e^2)(\partial^3\phi_i/\partial r_i^3)_0$ ($i = 1, 2, 3$; a = lattice constant).

B. Lattice Dynamics at Zone Center for Quasistatic Crystals

For the cubic perovskite structure, the harmonic lattice dynamical quantities at the zone center consist of the three elastic constants c_{11} , c_{12} , c_{44} , the two dielectric constants ϵ , ϵ_∞ , the six i.r. frequencies belonging to the Γ_{15} mode. Explicit expressions for the elements of the dynamical matrix and for the elastic constants pertaining to the above shell model for the perovskite structure have been given by Cowley.^{10,36} The dielectric constants may be calculated from the general shell model expressions given by Cowley.³⁷

The first order anharmonic zone center properties consist of the six T.O.E. constants c_{111} , c_{112} , c_{123} , c_{144} , c_{166} , c_{456} , the three electrostriction constants Q_{1111} , Q_{1122} , Q_{1212} , the three photoelastic constants P_{1111} , P_{1122} , P_{1212} , and the seven optic mode gammas. The electrostriction constants are defined (tensor notation) by $Q_{ijkl} = (\frac{1}{2})(\partial^2 \eta_{ij}) / \partial P_k \partial P_l$ where η_{ij} are the components of the strain tensor, and P_k the vector components of the electric polarization. General lattice theoretical expressions for the T.O.E. constants, for the electrostriction constants and for the photoelastic constants for non-primitive crystals have been given by Srinivasan.³⁸ Alternative expressions for these quantities more suitable for application to shell models have also been derived and will be given elsewhere.³⁹ Mode gammas may be calculated from first order perturbation theory by using expressions as given, for example in Ref. 40.

With the exception of a calculation of T.O.E. constants for RbMnF_3 by Naimon²⁹ these general theoretical expressions have not yet been applied to perovskites. However, the Coulomb sums given by Naimon represent the total Coulomb contribution to the T.O.E. constants and are given only for specific integer values of the ionic charges. Therefore in the Appendix, we tabulate the Coulomb sums representing the sublattice contributions to the T.O.E. constants that are required for the case of general sublattice charges. In addition, the repulsive contributions to

the T.O.E. constants from the three kinds of interactions discussed in Section A are given explicitly.

In Section III, the equations pertaining to the quasistatic crystals are applied to the calculation of the first order anharmonic properties for two different types of models, which differ in the manner of the determination of the parameters. For the models labelled "static", the parameters are fitted to data obtained by extrapolation to absolute zero, as described in Section IIC, and for the models labelled "R.T." they are directly fitted to the room temperature data.

C. Extrapolation of Experimental Input Data to Static Crystal

In this section, the procedure for eliminating the thermal and zero point effects from room temperature experimental data is discussed for those quantities that will be used to fit model parameters for the "static" type models.

In the paraelectric phase, the temperature dependence of the low frequency dielectric constant of ferroelectric crystals is described by the Curie-Weiss law:

$$\epsilon = C/(T-T_c) \quad (2.1)$$

According to the soft mode picture of Anderson¹ and Cochran², this law follows from the linear temperature dependence of the squared TO soft mode frequency

$$(\omega_1^{TO})^2 = A(T-T_c) \quad (2.2)$$

in connection with the Lyddane-Sachs-Teller (LST) relation

$$\epsilon/\epsilon_\infty = \prod_i (\omega_i^{LO}/\omega_i^{TO})^2 \quad (2.3)$$

provided that the temperature dependence of all polar modes i , other than the soft TO mode $i=1$ may be neglected.

In the case of the incipient ferroelectric SrTiO_3 , both $1/\epsilon$ and $(\omega_1^{TO})^2$ have been observed^{13,41} to vary linearly from room temperature down to 50K,

with a Curie temperature $T_c = 35.5K$. Below 50K, $1/\epsilon$ levels off because of stabilization of the paraelectric phase via quantum mechanical effects.^{41,42} The linear temperature dependence in the high temperature range can be explained theoretically on the basis of first order anharmonic perturbation theory.²⁰ The values of the dielectric constant and the squared soft mode frequency pertaining to the "static" crystal can therefore be obtained by extrapolating linearly from the high temperature region to absolute zero and are given by

$$\epsilon_{\text{stat}} = -C/T_c \quad (2.4)$$

$$(\omega_{\text{stat}}^{\text{TO}})^2 = -AT_c \quad (2.5)$$

These quantities are strictly harmonic quantities and are negative for SrTiO_3 . All other harmonic quantities at the Γ point such as the elastic constants $c_{\mu\nu}$ and the optic mode frequencies are weakly temperature dependent and in the high temperature limit, vary linearly with temperature. In order to obtain quantities pertaining to the static crystal, they must also be extrapolated to absolute zero.^{34,35}

Other input quantities required for fitting the anharmonic parameters are the pressure derivative of the dielectric constant $(\partial\epsilon/\partial p)_T$ and the T.O.E. constants $c_{\mu\nu\lambda}$. $(\partial\epsilon/\partial p)_T$ has been measured by Samara^{24,25} as a function of temperature for SrTiO_3 and the quantity referred to the static crystal $(\partial\epsilon_{\text{stat}}/\partial p)_T$ may be obtained from equations (2.1) and (2.4) as

$$\left(\frac{\partial \ln \epsilon_{\text{stat}}}{\partial p}\right) = \left(\frac{\partial \ln \epsilon}{\partial p}\right)_T - \frac{T}{T-T_c} \left(\frac{\partial \ln T_c}{\partial p}\right)_T \quad (2.6)$$

SrTiO_3 exhibits a structural transformation at 105K which arises from a condensation of a zone-corner R_{25} mode representing the rotations of the oxygen octahedra.^{12,43} Near the transformation, the second and third order elastic constants each exhibit a discontinuity.^{21,44,45} For the second order

elastic constants, the discontinuity has been explained as arising from the coupling of the acoustic modes to the soft R_{25} zone corner mode^{17,18,46} and the same explanation may be expected to hold for the T.O.E. constants also. The effect of the soft R_{25} mode may be neglected for the purposes of the present paper since a static model of SrTiO_3 for the Γ point properties is considered and since the parameters of the model can be determined by fitting to the zone center properties, linearly extrapolated to absolute zero from the high temperature region.

The extrapolation procedure introduces some uncertainty in the static values so obtained. However, these uncertainties appear to be small compared with the uncertainties resulting from the approximations usually made in performing theoretical calculations of the temperature effects via first order perturbation theory^{16,20} or via the self-consistent phonon approximation.¹⁹

III. RESULTS

A. Model Parameters

The shell models used here are characterized by 14 harmonic and three anharmonic parameters as introduced in Section II.A and as listed in Tables 1 and 2, respectively. Two types of models are considered and labelled "R.T." and "Stat." depending on whether the parameters are obtained by fitting to the experimental room temperature data, or to extrapolated data pertaining to the static crystal, respectively. The harmonic parameters are fitted to the 3 elastic constants, to the dielectric constants ϵ and ϵ_∞ , and to the seven zone center optic frequencies, with additional input and/or assumptions as discussed below. For each of the two types of models, three individual models, labelled A, B, and C, with common harmonic parameters can be distinguished

according to the input used for the determination of the anharmonic parameters. The input data for models A, B, and C consist of $(\partial \ln \epsilon / \partial p)$, c_{111} , and the set of the three quantities $(\partial \ln \epsilon / \partial p)$, c_{111} , and the "Cauchy average" $(c_{112} + c_{166})/2$, respectively. As discussed below, models A and B are subject to additional constraints.

The values of the harmonic parameters for the two models obtained by a least squares fit to the experimental data are given in Table I. For model "R.T.", the starting values of the parameters in the least squares fit procedure were taken from model 4 of Stirling,¹⁴ as this model gave the best agreement with Γ point data. Further, the values of 0-0 interaction parameters A_3 and B_3 and the electronic polarizabilities of Sr and Ti ions α_1 and α_2 , were held fixed at the values given by Stirling.¹⁴ The remaining 10 parameters were fitted to 11 experimental quantities. Assuming a common error of 3 percent for all input data a χ^2 value of 33 was obtained. As the equilibrium condition was not invoked, model "R.T." consists of axially symmetric forces and adequately reproduces the Cauchy deviation in the elastic constants.

For the model "Stat", the input quantities are the extrapolated quantities. of which the values of the low frequency dielectric constant and the squared soft mode frequency are both negative. The equilibrium condition was used to eliminate one of the short range parameters. It was not possible to get a least squares fit with starting values from any of the models given by Stirling.¹⁴ Similarly, it was not possible to get a good fit when the TKS values of ionic polarizability⁴⁷ were used. The model now has 13 parameters and there are not enough experimental data to fit all of these. A priori there is no way of fixing the values of any of these parameters. Therefore, the values of some parameters two at a time, and in turn were held constant, while the remaining 11 parameters were allowed to vary. After several runs it was found that the values of the

parameters α_1 and α_2 were stable. Subsequently, they were held constant, and the remaining parameters were fitted to the experimental data. In general, it was not possible to get a good least squares fit with all the data. A reasonable fit was obtained only within a small range of values of the ionic charges Z_1 and Z_2 . Assuming that the extrapolation to the static crystal introduces an error of 10 percent for all input data a χ^2 value of 26 is obtained for the static model.

Table II lists the values of the anharmonic parameters of the models A, B, and C. The parameters C_1 and C_3 in models A and B were determined by assuming the Born-Mayer form for the interatomic potential, which leads to $C_1 = -\sqrt{2}A_1^2/|B_1|$ and $C_3 = -\sqrt{2}A_3^2/|B_3|$. The least squares fits were excellent in all the cases except for model "R.T.-C", where a simultaneous fit of quantities $\partial \ln \epsilon / \partial p$, c_{111} , and $(c_{112} + c_{166})/2$ could not be obtained with reasonable values for the parameters C_1 , C_2 , and C_3 . Therefore, model "R.T.-C" is not included in Table II.

It can be seen from Table I that the values of the harmonic parameters of model "R.T." are very similar to those for Stirling's¹⁴ model 4. The value of A_2 is about 40 times larger than either A_1 or A_3 , indicating very strong Ti-O interaction. The parameter values for the static model differ considerably from those of model R-T. In the static model, the Ti-O interaction is still strong but is only 10 times larger than A_1 or only 3 times larger than A_3 . The O-O interaction is stronger in the static model than in the R.T. model. In fact, A_3 is 2.5 times larger than A_1 . On the basis of the ionic radii of Shannon and Prewitt⁴⁸ in relation to the interionic distances one would expect that the Ti-O repulsive interaction is smaller than the Sr-O and the O-O interactions, and that the latter two are of comparable magnitude. Thus it appears that the small values of A_3 and C_3 obtained in the room temperature models results from the fact that by fitting to a

harmonic model the large thermal effects present in the soft-mode frequency are lumped together with the cohesive contribution. The static and the room temperature models differ considerably in the values of the ionic charges and polarizabilities of the ions as well. Both harmonic models are characterized by large polarizabilities for the positive ions, larger than those of the oxygen ion. In addition, some of the short range polarizabilities are negative. These characteristics were present in the models described both by Cowley¹⁰ and by Stirling¹⁴ and may arise from the inadequacies of the simple shell model employed. The negative short range polarizability could be attributed to exchange charges produced by ionic overlap.⁴⁹

From Table II, it can be seen that there is a large difference between models "R.T.-A" and "R.T.-B", but all the static models "Stat-A", "Stat-B", and "Stat-C" are similar among themselves. The values of C_1 and C_2 could perhaps be compared with the values given by Bruce and Cowley²⁰ for the repulsive part of the interaction ϕ^{III} and ψ^{III} (in their notation), -230 and -1600 respectively, that were obtained after correcting for the Coulomb part based on formal ionic charges. Although they are of the same order of magnitude, these authors neglect the 0-0 interaction, and their method of obtaining the anharmonic parameters is not fully consistent.⁵⁰

The anharmonicity of the short range interactions $\phi_i(R_i)$ is characterized by the dimensionless ratio $R_i \phi_i''' / \phi_i''$. For the Sr-O interaction in the static models this ratio has the value of about 5, for the Ti-O interaction the value is 15 to 17, and for the O-O interaction a value of about 3.5 is obtained. Thus the Ti-O anharmonicity is largest, and the O-O anharmonicity is comparable to that of the Sr-O interaction.

B. Comparison With Experimental Data

1. Harmonic Quantities

In Table III, the harmonic properties at the zone center calculated on the basis of the model "R.T." and the models "Stat" are compared with experimental room temperature values and extrapolated static values, respectively. It is apparent that the agreement with room temperature data for the model "R.T." is excellent and is much better than that obtained by Stirling¹⁴ for his model 4, in which discrepancies of up to 50% occur for the elastic constants and for the dielectric constant. For the static model, the agreement with the extrapolated values is still good, but the deviation from the Cauchy relation is unaccounted for and the calculated value of the dielectric constant is about 25% too small.

In Table IV, calculated frequencies of the optic modes other than the soft mode are compared with experimental data at room temperature. It is apparent that for most of the frequencies the agreement is good at room temperature, and the assumption that these frequencies do not change with temperature is fairly well reproduced by the static model.

2. Anharmonic Quantities at Room Temperature

In Table V, the T.O.E. constants, the pressure derivative $(\partial \ln \epsilon / \partial p)$, the electrostriction constants and the mode gamma $\gamma_{T_1} = -(\partial \ln \omega_{T_1} / \partial \ln V)$ for the soft mode as calculated for the quasistatic models R.T.-A and R.T.-B are compared with the available experimental room temperature values. The electrostriction constant calculated from the pressure coefficient of the dielectric constant²⁴ according to $Q_h = -[2\epsilon_0(\epsilon-1)^2]^{-1}(\partial \epsilon / \partial p)_T$ (SI units) is $0.045 \text{ (m}^4/\text{C}^2)$ and agrees well with the directly determined value.²³ The "experimental" value of the soft-mode gamma γ_{T_1} has been calculated from $(\partial \ln \epsilon / \partial p)_T$ by Samara²⁵ from the

assumption that the product $\epsilon(\omega_1^{T0})^2$ is independent of volume and does not therefore provide an independent check of the theoretical results. The calculated mode gammas of the other optic mode gammas are listed in Table IV, but for lack of experimental data no comparison can be made.

It can be seen from Table V that for model R.T-A, the calculated values of Q_h , Q_s and γ_{T_1} are in reasonably good agreement, but c_{111} differs by about 45%. For model R.T-B, there is excellent agreement for c_{111} , which is fitted, but there is very poor agreement with all other quantities. There appears to be a basic difficulty in fitting the T.O.E. constants and $(\partial \ln \epsilon / \partial p)$ simultaneously by three anharmonic parameters for the room temperature model. As mentioned before, model R.T-C did not yield a good least squares fit for physically reasonable values of the parameters.

3. Anharmonic Properties for Static Crystal

In Table V, the T.O.E. constants, the pressure derivative of the dielectric constant $(\partial \ln \epsilon / \partial p)$, the electrostriction constants and the soft-mode gammas γ_{T_1} as calculated from the static models A, B, and C are compared with the corresponding extrapolated experimental data pertaining to the static crystal. Following Samara²⁵, the extrapolated experimental value shown for the soft-mode gamma γ_{T_1} has been calculated from the extrapolated static value of $(\partial \ln \epsilon / \partial p)$ on the basis of the assumption that in the static limit the product $\epsilon(\omega_1^{T0})^2$ is independent of volume.

Since the temperature dependence of the T.O.E. constants is small, for simplicity the R.T. values are used as the static values. The extrapolated static value of $(\partial \ln \epsilon / \partial p)$ is obtained from equation (2.6) by using the room temperature values of Samara^{24,25} $(\partial \ln \epsilon / \partial p)_T = -0.244 \times 10^{-2}/N$, $(\partial \ln T_c / \partial p) = -3.9 \times 10^{-9} \text{ m}^2/N$, and $T_c = 36K$.

It is apparent that all results for the three models are in much better agreement among themselves than for the R.T. models, and that good agreement is obtained even for those quantities that were not fitted, i.e. c_{111} for model A and $(\partial \ln \epsilon / \partial p)$ for model B. The largest discrepancies among the three models occur for Q_s . This reflects in part the fact that this quantity is almost ten times smaller than Q_h , and in part the greater sensitivity of Q_s to changes in the model parameters. For Q_h , the agreement between calculated and experimental values is best for models A and C, for which $(\partial \ln \epsilon / \partial p)$ was fitted. However, for Q_s the best agreement is found for model B, for which c_{111} , but not $(\partial \ln \epsilon / \partial p)$ was fitted. However, in view of the larger spread of the calculated results for the three models not too much significance should be attached to this agreement. Moreover, the calculated values of Q_h and Q_s contain a factor ϵ^{-2} . Since according to Table III, the calculated static value of ϵ is 20 percent too small it seems that part of the discrepancy between calculated and experimental values of Q_h and Q_s arises from the limitations already present in the harmonic model.

These limitations could arise from the neglect of many-body noncentral forces. This is consistent with the occurrence of a 0.9 percent deviation of the elastic constants c_{12} and c_{44} from their average value. For the T.O.E. constants even larger deviations from the Cauchy relations⁵⁴

$$c_{112} = c_{166} \quad (3.1a)$$

and

$$c_{123} = c_{144} = c_{456} \quad (3.1b)$$

are observed.²² The experimental values for c_{112} and c_{166} are ²²(in 10^{11} N/m^2) - -7.7 ± 1.6 and -3.0 ± 1.2 , respectively, and the calculated value of c_{112} agrees well with the fitted average -5.4 of the experimental values for c_{112} and c_{166} . The situation is similar for c_{123} , c_{144} and c_{456} , for which the experimental values

are ²²(in 10^{11}N/m^2) $+ 0.2 \pm 4.3$, -8.1 ± 2.4 , $+0.9 \pm 2.7$, respectively. The importance of three-body forces for the theoretical explanation of the photoelastic constants has recently been demonstrated for the alkali halides.⁵⁵ The photoelastic constants calculated from the present models show considerable deviation from the experimental data⁵⁶ for SrTiO_3 . However, as will be shown in Section III.C, the contribution from the photoelastic constants to the electrostriction constants amounts to at most a few percent and is therefore negligible for the purposes of the present paper.

It should be noted that the Coulomb contribution to the T.O.E. constants is quite significant and e.g. for model C amounts to 27, 34, and 100 percent of the total values for c_{111} , c_{112} , and c_{123} , respectively.

C. Pressure Derivative of LST Relation

By differentiating the LST relation (2.3) with respect to pressure, one obtains the relation

$$\frac{B}{2\epsilon^2} \left(\frac{\partial \epsilon}{\partial p} \right) = \frac{B}{2(\epsilon^\infty)^2} \left(\frac{\partial \epsilon^\infty}{\partial p} \right) + \sum_i (\gamma_i^{\text{LO}} - \gamma_i^{\text{TO}}) \quad (3.2)$$

where B denotes the bulk modulus. On the other hand, Samara²⁵ has calculated the soft mode gamma $\gamma_{T_1} = \gamma_1^{\text{TO}}$ from an equivalent form of the approximate relation

$$\frac{B}{2\epsilon^2} \left(\frac{\partial \epsilon}{\partial p} \right) = \gamma_{T_1} \quad (3.3)$$

This relation follows from the assumption that the product $\epsilon(\omega_1^{\text{TO}})^2$ is independent of volume.²⁵ Comparison with equation (3.2) shows that this assumption is justified if the first term on the RHS of (3.2) and all mode gammas other than the soft mode gamma γ_1^{TO} may be neglected. For SrTiO_3 at 300K, the first term on the RHS of (3.2) has the numerical value⁵⁶ 0.0122, which is 4 percent of the LHS. With the exception of γ_{15}^{LO} the calculated static mode gammas in Table IV

are less than 2 percent of the calculated soft-mode gamma. Surprisingly, however, for the static crystal the calculated mode gamma associated with the highest L0 frequency has the large positive value of 49.1 or 16 percent of the soft-mode gamma. Thus it appears that for the static crystal Samara's assumption²⁵ leading to (3.3) is only roughly justified.

V. Summary and Conclusions

The objective of the present paper is to investigate whether for SrTiO_3 the available first order anharmonic properties (T.O.E. and electrostriction constants) can be accounted for on the basis of a simple shell model with Coulomb and short range central force interactions. Since for soft-mode materials, the low frequency dielectric constant at finite temperature contains anharmonic contributions arising from the self energy of the soft-mode frequency the electrostriction constants are determined by higher than first order anharmonic terms. Therefore, the harmonic and anharmonic experimental data, especially the strongly T-dependent dielectric constant and electrostriction data were extrapolated to absolute zero in order to investigate within the framework of the model the consistency of the first order anharmonic quantities. Whereas for the static crystal, the T.O.E. constant c_{111} and the hydrostatic electrostriction constant Q_h are found to be compatible within experimental error, for the remaining T.O.E. constants and the shear electrostriction constant Q_s deviations occur which are attributed mostly to the neglect of many body noncentral forces. On the contrary, no consistent fit of the model to the room temperature data for c_{111} and Q_h could be obtained, obviously because of substantial higher than first order anharmonic contributions to Q_h .

The particular models considered are characterized by parameters fitted to the zone center properties only. Verification of the adequacy of these

parameters for describing the finite-temperature renormalized phonon frequencies and mode gammas in the dispersive range remains a future task. Some noteworthy, probably only weakly model dependent features of the models considered are

- (i) that the Ti-O short range interaction is the dominant interaction,
- (ii) that the harmonic part of the O-O interaction (neglected previously^{16,20}) is even larger than the Sr-O interaction;
- (iii) that for the Ti-O interaction the anharmonicity is about three times larger than for the Sr-O and O-O interactions.

ACKNOWLEDGMENT

This work has been supported by the Office of Naval Research under Contract No. N 00014-78-C-0291.

APPENDIX

In the following, the general equations for the T.O.E. constants are given for the perovskite structure, ABO_3 , in a form suitable for arbitrary valency of the constituent ions, and with short range interactions of the type A-O, B-O, and O-O included.

The T.O.E. constants are additively composed of the Coulomb and short range contributions according to (Brugger's definition⁵⁷ in Voigt notation):

$$c_{\mu\nu\lambda} = c_{\mu\nu\lambda}^{\text{Coul}} + c_{\mu\nu\lambda}^{\text{S.R.}} \quad (\mu, \nu, \lambda = 1, 2, \dots, 6) \quad (\text{A.1})$$

The Coulomb contribution can be expressed as a quadratic form in the effective charges $Z_\alpha e$ associated with the ion of type α ($\alpha = 1, 2, 3$ denotes A, B, O, respectively),

$$c_{\mu\nu\lambda}^{\text{Coul}} = (e^2/a^4) \sum_{\alpha, \beta=1}^3 \gamma_{\mu\nu\lambda}^{\alpha\beta} Z_\alpha Z_\beta \quad (\text{A.2})$$

Here a denotes the lattice constant. The charges Z_α satisfy the neutrality condition:

$$Z_1 + Z_2 + 3Z_3 = 0 \quad (\text{A.3})$$

The coefficients $\gamma_{\mu\nu\lambda}^{\alpha\beta}$ have been evaluated by Ewald's method and are listed in Table A.1. It should be noted that because of the constraint (A.3) for each set $\mu\nu\lambda$ only three of the six coefficients $\gamma_{\mu\nu\lambda}^{\alpha\beta}$ are independent.

For the three types of short range interactions considered their contributions are given by:

$$c_{111}^{\text{S.R.}} = (e^2/4a^4) [\sqrt{2}(C_1+C_3)/2 + C_2/2 - 3(A_1+3B_1+A_2+A_3+3B_3)] \quad (\text{A.4a})$$

$$c_{112}^{\text{S.R.}} = (e^2/4a^4) [\sqrt{2}(C_1+C_3)/4 - 3(A_1+A_3)/2 + 11(B_1+B_3)/2 + B_2] \quad (\text{A.4b})$$

$$c_{123}^{S.R.} = -(e^2/4a^4) [B_1 + B_3 + B_2/4] \quad (A.4c)$$

$$c_{166}^{S.R.} = c_{112}^{S.R.} - (e^2/4a^4) [8(B_1 + B_3) + 2B_2] \quad (A.4d)$$

$$c_{144}^{S.R.} = -c_{456}^{S.R.} = -c_{123}^{S.R.} \quad (A.4e)$$

Furthermore, using the equilibrium condition

$$12(B_1 + B_3) + 3B_2 - 4\alpha_M = 0 \quad (A.5)$$

with the Madelung constant given by

$$\alpha_M = -2.837298(Z_1^2 + Z_2^2) - 12.007 Z_3^2 - 0.575595 Z_2 Z_3 - 1.603872 Z_1 Z_2 - 3.49513 Z_1 Z_3 \quad (A.6)$$

the Cauchy relation⁵⁴ equations (3.1a) and (3.1b) are obtained.

REFERENCES

- ¹W. Sturrock, *Physics of the Solid State*, edited by G.I. Skanavi (Akad. Nauk. SSSR, Moscow, 1969), p. 29.
- ²W. Cochran, *Adv. Phys.* 9, 387 (1960).
- ³W. Cochran and A. Zia, *Phys. Status Solidi* 25, 273 (1968).
- ⁴W.G. Spitzer, R.C. Miller, D.A. Kleinman and L.E. Howarth, *Phys. Rev.* 126, 1710 (1962).
- ⁵A.S. Barker, Jr. and M. Tinkham, *Phys. Rev.* 125, 1527 (1962).
- ⁶A.S. Barker, Jr., *Phys. Rev.* 145, 391 (1966).
- ⁷P.A. Fleury, J.F. Scott, and J.M. Worlock, *Phys. Rev. Lett.* 21, 16 (1968).
- ⁸P.A. Fleury and J.M. Worlock, *Phys. Rev.* 174, 613 (1968).
- ⁹R.A. Cowley, *Phys. Rev. Lett.* 9, 159 (1962).
- ¹⁰R.A. Cowley, *Phys. Rev.* 134, A981 (1964).
- ¹¹R.A. Cowley, W.J.L. Buyers and G. Dolling, *Solid St. Commun.* 7, 181 (1969).
- ¹²G. Shirane and Y. Yamada, *Phys. Rev.* 177, 858 (1969).
- ¹³Y. Yamada and G. Shirane, *J. Phys. Soc. Jap.* 26, 396 (1969).
- ¹⁴W.G. Stirling, *J. Phys. C: Solid State Phys.* 5, 2711 (1972).
- ¹⁵B.D. Silverman and R.I. Joseph, *Phys. Rev.* 133, A207 (1964).
- ¹⁶R.A. Cowley, *Phil. Mag.* 11, 673 (1965).
- ¹⁷E. Pytte and J. Feder, *Phys. Rev.* 187, 1077 (1969).
- ¹⁸J. Feder and E. Pytte, *Phys. Rev.* B1, 4803 (1970).
- ¹⁹N.S. Gillis and T.R. Koehler, *Phys. Rev.* B4, 3971 (1971).
- ²⁰A.D. Bruce and R. Cowley, *J. Phys. C: Solid State Phys.* 6, 2422 (1973).
- ²¹E.L. Meeks and R.T. Arnold, *Phys. Rev.* B1, 982 (1970).
- ²²A.G. Beattie and G.A. Samara, *J. App. Phys.* 42, 2376 (1971).
- ²³G. Schmidt and E. Hegenbarth, *Phys. Status Solidi*, 3 329 (1963).
- ²⁴G.A. Samara, *Phys. Rev.* 151, 378 (1966).

- ²⁵G.A. Samara, *Ferroelectrics*, 2, 177 (1971).
- ²⁶B.D. Silverman, *Phys. Rev.* 131, 2478 (1963).
- ²⁷W. Kinase, S. Yokohama and K.N. Pak, *Ferroelectrics* 7, 243 (1974).
- ²⁸R.H. Lyddane and K.R. Herzfeld, *Phys. Rev.* 54, 846 (1938).
- ²⁹E.R. Naimon, *Phys. Rev.* B9, 737 (1974).
- ³⁰R. Migoni, H. Bilz and D. Bäuerle, *Phys. Rev. Lett.* 37, 1155 (1976).
- ³¹R. Migoni, H. Bilz and D. Bäuerle in *Lattice Dynamics*, edited by M. Balkanski (Flammarion, Paris, 1978), p. 650.
- ³²A.A. Maradudin and A.E. Fein, *Phys. Rev.* 128, 2589 (1962).
- ³³R.A. Cowley, *Adv. Phys.* 12, 421 (1963).
- ³⁴G. Leibfried and W. Ludwig in *Solid State Physics*, edited by F. Seitz and D. Turnbull (Academic, New York, 1961), Vol. 12, p. 275.
- ³⁵H. Hahn in *Inelastic Scattering of Slow Neutrons from Solids and Liquids*, (I.A.E.A., Vienna, 1963), Vol. I., p. 37.
- ³⁶The expressions for the elastic constants given in Ref. 10 contain a redundant factor of 2.
- ³⁷R.A. Cowley, *Proc. Roy. Soc.* A268, 121 (1962).
- ³⁸R. Srinivasan, *Phys. Rev.* 165, 1041 (1968).
- ³⁹B.N.N. Achar and G.R. Barsch. (To be published).
- ⁴⁰B.N.N. Achar and G.R. Barsch, *Phys. Rev.* B3, 4352 (1971).
- ⁴¹K.A. Müller and H. Burkard, *Phys. Rev.* B19, 3593 (1979).
- ⁴²J.H. Barrett, *Phys. Rev.* 86, 118 (1952).
- ⁴³H. Unoki and T. Sakudo, *J. Phys. Soc. Jap.* 23, 546 (1967).
- ⁴⁴R.O. Bell and G. Rupprecht, *Phys. Rev.* 129, 90 (1963).
- ⁴⁵A. Laubereau and R. Zurek. *Z. Naturforsch.* 25a, 391 (1970).
- ⁴⁶J.C. Slonczweski and H. Thomas, *Phys. Rev.* B1, 3599 (1970).
- ⁴⁷J.R. Tessman, A.H. Kahn and W. Schockley, *Phys. Rev.* 92, 890 (1953).

- ⁴⁸R.D. Shannon and C.T. Prewitt, Acta Cryst. B25, 925 (1969).
- ⁴⁹H. Bilz, M. Buchanan, K. Fischer, R. Haberkorn and U. Schröder, Solid State Comm. 16, 1023 (1975).
- ⁵⁰Although the parameters ψ^{II} , ψ^{III} , ψ^{IV} ; ψ^{II} , ψ^{III} , and ψ^{IV} of Bruce and Cowley²⁰ introduced as pertaining to short range interactions they are fitted to the empirically determined Landau-expansion coefficients of Ref. 46, which naturally also include Coulomb contributions. Moreover, the harmonic quantities ψ^{II} and ψ^{III} are redundantly and inconsistently determined from the empirical Landau-expansion coefficients⁴⁶ although they are in principle already determined by the harmonic parameters of Stirling's model¹⁴ taken over by Bruce and Cowley for the calculation of all harmonic quantities.
- ⁵¹T. Mitsui and W.B. Westphal, Phys. Rev. 124, 1354 (1961).
- ⁵²S.B. Levin, N.J. Field, F.M. Plock and L. Merker, J. Opt. Soc. Am. 45, 737 (1955).
- ⁵³G.R. Barsch, B.N.N. Achar and L.E. Cross, Ferroelectrics (to be published).
- ⁵⁴P.B. Ghatge, Phys. Rev. 139, A1666 (1965).
- ⁵⁵S.C. Goyal, R. Prakash and S.P. Tripathi, Phys. Stat. Sol. (b) 85, 477 (1978); Sol. State Commun. 25, 1105 (1978).
- ⁵⁶J.L. Kirk, Ph.D. Thesis in Solid State Science, The Pennsylvania State University (1972); K. Vedam and J.L. Kirk, to be published.
- ⁵⁷K. Brugger, Phys. Rev. 133, A1611 (1964).

TABLE I

Parameters for the Room Temperature (R.T.) and the Static (Stat.) Harmonic Models (in Standard Shell Model Notation).

Parameter	Model 2	
	(R.T.)	(Stat.)
A_1	7.18	11.44
B_1	2.74	-2.18
A_2	334.31	111.07
B_2	-74.39	-47.40 ^c
A_3	8.60 ^a	27.36
B_3	-1.32 ^a	7.92
Z_1	0.82	1.24
Z_2	4.95	2.42
α_1	0.025 ^a	0.179 ^b
α_2	0.068 ^a	0.068 ^b
α_3	0.015	0.026
d_1	-0.062	-1.040
d_2	-1.916	-0.162
d_3	0.430	0.937

a Values taken from Ref. 14.

b Values read in as explained in text.

c Fixed by equilibrium condition.

TABLE II
Parameters for Anharmonic Models.

Parameter	R.T.		Stat.		
	A	B	A	B	C
c_1	-26.58	-26.58	-84.95	-84.95	-80.29 ^c
c_2	-2910.5 ^a	-4693.5 ^b	-3565.0 ^a	-3764.5 ^b	-3779.1 ^c
c_3	-79.24	-79.24	-133.64	-133.64	-127.94 ^c

a Fitted to $\partial \ln \epsilon / \partial p$.

b Fitted to c_{111} .

c Fitted to $\partial \ln \epsilon / \partial p$, c_{111} and $(c_{112} + c_{166})/2$.

TABLE III

Comparison of Experimental Extrapolated and Calculated Values of Elastic Constants (10^{11} N/m²), Relative Dielectric Constants and Soft Mode Frequency (10^{13} rad/sec).

Constant	R.T.		Stat.	
	Experimental	Calculated	Extrapolated	Calculated
c_{11}	3.30^a	3.86	3.337^e	3.15
c_{12}	1.01^a	1.01	1.050^e	1.12
c_{44}	1.24^a	1.29	1.265^e	1.12
ϵ	301^b	304.5	$-2297.^e$	-1852.
ϵ_{∞}	5.5^c	5.71	5.5	5.36
$\omega_{T_1}(\Gamma_{15})$	1.652^d	1.66	$i \times 0.605^e$	$i \times 0.542$

a Ref. 44.

b Ref. 51.

c Ref. 52.

d Ref. 6.

e Extrapolated according to the procedure explained in text.

TABLE IV

Frequencies (10^{13} rad/sec) and Mode Gammas for Temperature Independent Optic Modes. Experimental Data for the Frequencies Refer to Room Temperature.

Mode Assignment		ω_i			γ_i	
Barker ^a	Stirling ^b	Exp.	R.T.	Stat.	R.T.-A	Stat.-C
L ₁	Γ_{15}	3.30 ^a	3.27	1.95	0.3	0.33
T ₂	Γ_{15}	3.355 ^a	3.34	2.61	1.48	-0.02
L ₂	Γ_{25}	5.026 ^b	5.01	5.20	-1.19	-0.43
T ₃	Γ_{25}	5.026 ^b	5.01	5.20	-1.19	-0.43
L ₃	Γ_{15}	8.67 ^a	9.08	8.70	0.10	3.88
T ₄	Γ_{15}	10.242 ^a	10.54	9.12	1.82	2.42
L ₄	Γ_{15}	15.394 ^a	15.29	15.09	0.61	49.14

a Ref. 6.

b Ref. 14.

TABLE V

T.O.E. Constants (10^{11} N/m²), Logarithmic Pressure Derivative of the Dielectric Constant (10^{-9} m²/N), Electrostriction Constants (m⁴/C²) and Soft-Mode Gamma.

Quantity	R.T.			Stat.			
	Exp.	A	B	Extrap.	A	B	C
c_{111}	-49.6 ± 4.3^a	-27.50	-49.6	-49.6	-47.1	-49.6	-49.6
c_{112}	-7.7 ± 1.6^a	-5.96	-5.96	-7.7	-4.7	-4.7	-4.6
c_{123}	0.2 ± 4.3^a	-1.93	-1.93	0.2	-1.2	-1.2	-1.2
$(\partial \ln \epsilon / \partial p)$	-0.244^b	-0.244	-1.86	4.08^e	4.08	4.71	4.08
Q_h^*	$0.050^{c \pm 0.01}$	0.046	0.99	0.103^e	0.125	0.143	0.125
Q_s^+	0.095^c	0.076	0.51	-0.013^e	-0.076	-0.031	-0.039
Q_{1212}	--	0.001	0.001	--	0.011	0.011	0.011
γ_{T_1}	21.5	20.1	182.0	-368.0	-306.2	-366.6	-307.8

$$^*Q_h = Q_{1111} + 2Q_{1122}$$

$$^+Q_s = Q_{1111} - Q_{1122}$$

a Ref. 22.

b Ref. 24.

c Ref. 23.

d Ref. 25

e Ref. 53 (calculated from R.T. values of Ref. 23).

TABLE A.1

Coulomb Sums $\gamma_{\mu\nu\lambda}^{\alpha\beta}$ Representing Sublattice Contributions to T.O.E. Constants.

$\mu\nu\lambda$	$\alpha\beta$	11=22	33	23	13	12
111		-13.49607	-1.14830	-68.28874	38.62021	30.91960
112		1.48934	-2.99360	5.78015	-1.47442	-0.46522
123		0.24310	1.45298	3.39776	0.72366	-3.60030
166		0.54361	-1.00868	5.58816	-2.63941	-0.99990
144		1.18889	5.45512	3.58984	1.88844	-3.06570

$$\gamma_{123}^{\alpha\beta} = \gamma_{456}^{\alpha\beta}$$

APPENDIX 28

K. Uchino, S. Nomura, L.E. Cross, R.E. Newnham. New Electrostrictive Materials. I. Elect. Ceram. 11 (summer) 57 (1980) (in Japanese).

新しい電歪材料 (1)

●内野 研二

●野村昭一郎

●L.E. Cross

●R.E. Newnham

1. 緒 言

電歪効果 (electrostrictive effect) は基本的な電気機械結合の一種であるにもかかわらず、実験的研究は遅れている。その原因は、2 次的な効果であるために通常誘起される歪は非常に小さく実験的な困難さをもたらしている点にある。信頼のおける単結晶の電歪定数がほとんど決められていない現在、その理論的 (微視的) 解明も望むのが難しい。

ところが近年、天文学、光学の分野において、光角度、光路長を微妙にコントロールする変位素子 (displacement transducer) が所望されるようになった⁽¹⁾。応用面からの要請により初めて電歪が注目されるようになった。

ポジション・コントロール用素子として備えるべき性質を列記しておく。

- (1) 感度 (変位/電界)
- (2) 反復再現性 (ヒステリシス)
- (3) 安定性 (温度、エージング)
- (4) 応答時間、共振減衰
- (5) 絶縁破壊強度など
- (6) サイズ、重量

素子材料としてまず考えられるのが、磁歪材料あるいは圧電材料であろう。しかしながら磁歪

(magnetostriction) は大きさ ($d\ell/l$) が $10^{-4} \sim 10^{-3}$ と圧電歪 (piezoelectric strain) の $10^{-4} \sim 10^{-5}$ に比べて 1 桁以上小さく、その上コイル等の大きな駆動デバイス (大きな電力) を必要とするので使いにくい。圧電歪の問題点は、ヒステリシスとエージングである。非フェロ結晶における電歪 (electrostriction) においては、原理的にヒステリシス、エージングはなく、応答時間も強誘電体の分域回転に比べて速い。加えてめんどろなポーリング過程を必要としない。このような背景のもとに、大きな電歪効果 (従来の常識に反対する) をもつ物質を発見する動きが活発になってきた。それと同時に電歪の起源の理論的解明も必要となってきた。

本稿では、東京工大とペンシルバニア州立大との共同研究の内容を中心に、新しい電歪材料開発の背景、応用および展望について紹介したい。ペンシルバニア州立大学における研究は、Office of Naval Research の大きな財政援助 (数億円) に依存する 5 年プロジェクト「Targeted basic studies of ferroelectric and ferroelastic materials for piezoelectric transducer applications」の一環として行われており、Cross, Newnham 両教授の指導の下、内野と Jang (現在 Western Electric Company 所属) が従事している。日本との研究連絡は内野を通じて定期的に行われており、日本では野村教授の指導の下、桑田を中心とした大学院生が、電歪効果の補助的および追試的測定をしている。こうした大きな組織の、系統的

うちの けんじ、のむら しょういちろう/東京工業大学
工学部
L.E. Cross, R.E. Newnham/ペンシルバニア州立大学、
材料研究所

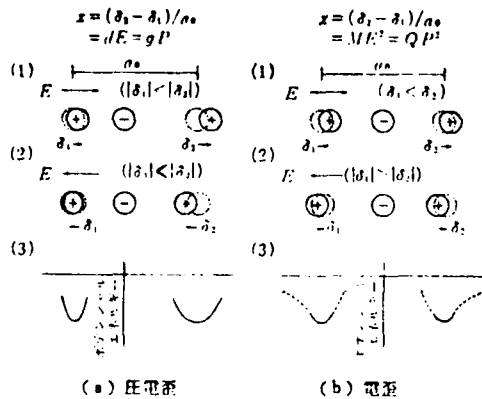


図1 電界下のイオン・シフト

な研究が、新しい材料の開発に成功をもたらしたといえる。

2. 電歪効果と非調和性

電歪は、電界（または分極）によって誘起される原子またはイオンの平衡位置からのシフトの尺度ではあるが、必ずしもシフトの大きさを表わしていない。図1は、圧電歪と電歪の起源を模式的に示している。対称性をもたない圧電体においては、あるイオンに対して左右のイオンは等価でなく、イオン対ポテンシャルの調和項は異なる。それによって印加電界に比例した歪が生ずる。中心対称をもつ場合には、あるイオンに対して左右のイオン対ポテンシャルの調和項は等しく、電界を印加しても（イオンシフトの大きさが圧電体と同程度であっても）ほとんど歪を生じない。しかし非調和項の存在により左右のイオンのシフト差が生ずる。それによって印加電界の向きによらない、電界の2乗に比例した歪が生ずる。電歪定数 Q （あるいは M ）は、分極 P （あるいは電界 E ）と歪 x との関係式 $x = QP^2$ （あるいは ME^2 ）によって定義される。

また熱膨張がポテンシャルの非調和性による歪であることはよく知られている（ $dL/L = \alpha T$ ）。したがって非調和項に由来する弾性コンプライアンス、電歪定数 Q と熱膨張係数 α との間に相関が

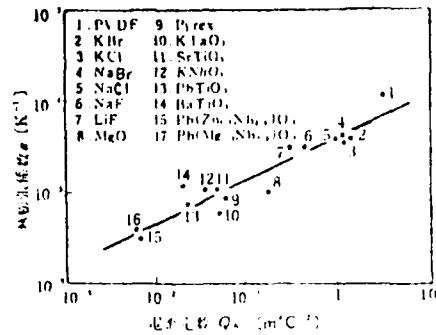


図2 電歪定数 Q と熱膨張係数 α の相関関係

期待されてもよい。図2は、立方晶あるいは等方性物質の熱膨張係数 α を電歪定数 Q （ $=Q_{11} + 2Q_{12}$ 、後述）に対してプロットしたものである。データの引用文献リストは、文献(2)にまとめてあるので参照されたい。グラフより、べき関係式

$$\alpha = 4.2 \times 10^{-5} Q^{0.5} \quad (1)$$

が得られた。

3. 電歪の現象論

3.1 強誘電体の場合

まず強誘電体における電歪の現象論を振り返っておこう。詳しくは、Jona and Shirane のテキストブック¹⁰などを参照されたい。

熱力学関数としては弾性ギブスエネルギー $G_1(X, P, T)$ （ $dG_1 = -x_{ij}dX_{ij} + E_m dP_m - SdT$ ）を用いるのが便利である。自由エネルギー G_1 は電気分極 P と応力 X の多項式で表現される。

$$G_1 = \frac{1}{2} \alpha_{ij} P_i P_j + \frac{1}{4} \beta_{ijkl} P_i P_j P_k P_l + \frac{1}{6} \gamma_{ijklmn} P_i P_j P_k P_l P_m P_n - \frac{1}{2} S_{ijkl} X_{ij} X_{kl} - Q_{ijkl} P_i P_j X_{kl} \quad (2)$$

Voigt 表示を用いて、無応力下の立方晶ペロブスカイト結晶の電歪定数テンソル Q_{ij} は、次の関係式で定義される。

$$\begin{pmatrix} x_1 \\ x_2 \\ x_3 \\ x_4 \\ x_5 \end{pmatrix} = \begin{pmatrix} Q_{11} & Q_{12} & Q_{13} & 0 & 0 & 0 \\ Q_{12} & Q_{22} & Q_{23} & 0 & 0 & 0 \\ Q_{13} & Q_{23} & Q_{33} & 0 & 0 & 0 \\ 0 & 0 & 0 & Q_{44} & 0 & 0 \\ 0 & 0 & 0 & 0 & Q_{55} & 0 \\ 0 & 0 & 0 & 0 & 0 & Q_{66} \end{pmatrix} \begin{pmatrix} P_1' \\ P_2' \\ P_3' \\ P_4' \\ P_5' \\ P_6' \end{pmatrix} \quad (3)$$

この関係式は電歪定数値決定の一方法、つまり電界あるいは分極とそれに伴う歪を比較する方法を示唆している。

ここで注意しておきたいのは、分極および歪が、誘起的のみならず自発的であってもかまわない点である。したがって相転移温度における自発体積変化 $(\Delta V/V)_s$ は、

$$(\Delta V/V)_s = Q_A P_s' \quad (4)$$

で表わされる。ただし

$$Q_A = Q_{11} + 2Q_{11} \quad (5)$$

で、 $P_s' (= \sqrt{P_1'^2 + P_2'^2 + P_3'^2})$ は、キュリー温度における自発分極である。

電歪定数値の別の決定法は以下の記述より示唆される。常誘電中心対称結晶に静水圧 p が加えられたとき、逆誘電率 χ は自由エネルギー G_1 から次のように求まる。

$$x_1 = \alpha_1 + 2Q_A p \quad (6)$$

ここで α_1 は通常のキュリー・ワイス則に従い、

$$\alpha_1 = (T - T_0)/C \quad (7)$$

T_0 はキュリー・ワイス温度で、 C はキュリー・ワイス定数である。電歪定数 Q_A は、逆誘電率 χ の静水圧依存性として求まる。

また、式(6)から導かれる、相転移温度 T_0 あるいはキュリー・ワイス温度 T_0 の静水圧によるシフトの大きさ、

$$(\partial T_0/\partial p) = (\partial T_c/\partial p) = -2Q_A C \quad (8)$$

からも定数 Q_A は吟味される。

3.2 反強誘電体の場合

反強誘電体のキッテル自由エネルギー表示⁽⁴⁾への電歪項の導入にふれておこう。詳しくは著者論文(5)を参照されたい。

1次元2副格子モデルを考えて、自由エネルギー G_1 を次のように展開する。

$$G_1 = \frac{1}{2} \alpha(T) (P_a'^2 + P_b'^2) + \frac{1}{4} \beta (P_a'^4 + P_b'^4) + \frac{1}{6} \gamma (P_a'^6 + P_b'^6) + \eta P_a' P_b'$$

$$- \frac{1}{2} \chi_T p' + Q_A (P_a'^2 + P_b'^2 + 2\eta P_a' P_b') p \quad (9)$$

ここで P_a' , P_b' は副格子分極、 p は静水圧、 χ_T は等温圧縮率、 Q_A と η は電歪定数を表わしている。付加電歪項 η は、副格子間の相互作用を表わしている。Cross の変換⁽⁶⁾

$$P_E = (P_a + P_b)/\sqrt{2},$$

$$P_A = (P_a - P_b)/\sqrt{2} \quad (10)$$

を導入して整理すると次の結果が得られる。相転移温度以上で、誘起体積変化は誘起強誘電分極と

$$(\Delta V/V)_{ind} = Q_A (1 + \eta) P_{E,ind}' \quad (11)$$

で関係づけられ、相転移温度以下で、自発体積変化は自発反強誘電分極と、

$$(\Delta V/V)_s = Q_A (1 - \eta) P_{A,s}' \quad (12)$$

で関係づけられる。ネール温度における自発体積変化が、 η 値に応じて正にも負にもなり得る点には、強誘電体の場合と著しく異なる。

ネール温度とキュリー・ワイス温度の静水圧依存性は、それぞれ

$$(\partial T_N/\partial p) = -2Q_A (1 - \eta) C \quad (13)$$

$$(\partial T_0/\partial p) = -2Q_A (1 + \eta) C \quad (14)$$

で与えられる。常誘電相における逆誘電率 χ の静水圧依存性は、

$$(\partial \chi/\partial p) = 2Q_A (1 + \eta) \quad (15)$$

で表わされる。反強誘電体ペロブスカイト結晶 PbZrO_3 と $\text{Pb}(\text{Mg}_{1/3}\text{V}_{2/3})\text{O}_3$ において、理論予測と実験結果^{(7),(8)} との見事な一致が確認されている。なお、反強誘電-強誘電-常誘電等の逐次相転移における電歪効果(相の静水圧安定性、自発歪等)については文献(9)を参照されたい。

4. 電歪の測定技術

前節でふれたように、電歪定数値決定にはいくつかの手段がある。

I. 歪直接測定法

- (1) 光学的方法(光干渉計、光てこ、光グリッド)
- (2) X線法
- (3) 電気的方法(容量型ディラトメータ、差

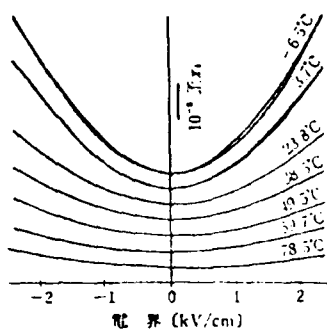


図3 歪ゲージ法による Pb(Mg_{1/3}Nb_{2/3})O₃ 単結晶の電歪測定

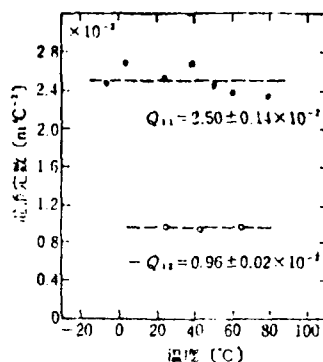


図4 Pb(Mg_{1/3}Nb_{2/3})O₃ の電歪定数の温度依存性

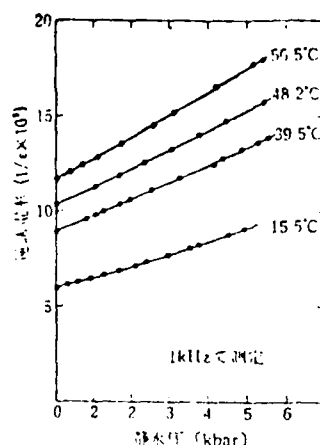


図5 Pb(Mg_{1/3}Nb_{2/3})O₃ の逆誘電率の静水圧依存性

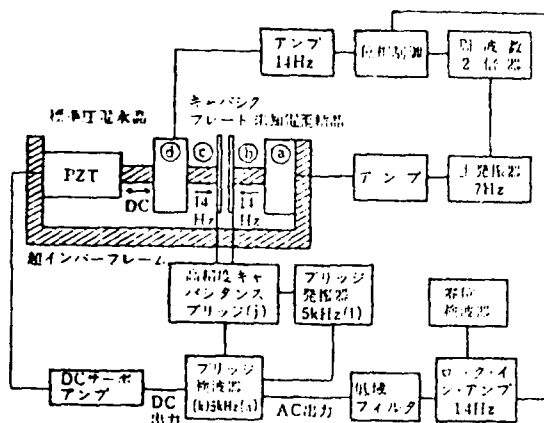


図6 高感度 AC キャパシタンス・ディラトメータのブロック・ダイアグラム

動トランス型)

(4) 歪ゲージ法

Ⅱ. 間接測定法

(1) 圧力ゲージ法

(2) 誘電率の圧力依存性

ここでは、緩和型強誘電体 (relaxor ferroelectrics) Pb(Mg_{1/3}Nb_{2/3})O₃ についての測定例をいくつか示しておこう。

4.1 歪ゲージ法⁽¹⁰⁾

図3は、歪ゲージによる電歪の測定例である。-10 から 80°C の温度範囲について電歪係数 d_{33} を電界 (0.002 kV) の関数としてプロットした。ソーヤ・タウフ回路により各温度の分極 P_r

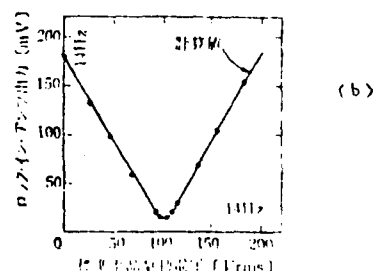
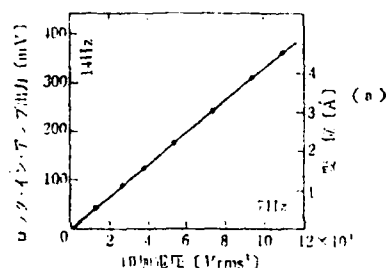


図7 ロック・イン・アンプ出力の印加電圧依存性

を測定し、式 (3) を用いて各温度の電歪定数を計算した (図4)。電歪定数がほとんど温度依存性をもたないことは明白である。($Q_{11} = 2.50 (\pm 0.14) \times 10^{-2} \text{ m}^2 \text{C}^{-1}$, $Q_{12} = -0.96 (\pm 0.02) \times 10^{-2} \text{ m}^2 \text{C}^{-1}$).

4.2 誘電率の圧力依存性⁽¹¹⁾

図5はいくつかの温度について測定した逆誘電率の静水圧依存性を示している。直線の傾きの温度依存性については、この物質の散漫相転移

(diffuse phase transition) に関する理論から理解される⁽¹⁰⁾。式(6)を用いて電歪定数 $Q_{11}=0.60 (\pm 0.08) \times 10^{-11} \text{ m}^2 \text{ C}^{-1}$ と計算され、この値は、4.1 で求められた $Q_{11}+2Q_{12}=0.58 (\pm 0.18) \times 10^{-11} \text{ m}^2 \text{ C}^{-1}$ と非常によい一致を示している。

4.3 AC キャパシタンス・ディラトメータ⁽¹¹⁾

図6に、新たに作製した高感度キャパシタンス・ディラトメータ(分解能 10^{-15} A)のブロック・ダイアグラムを示す。電歪定数を測定するには、まず 7 Hz の電圧を増幅器を通して試料結晶に印加する。これによって検出キャパシタの片プレートは 14 Hz で振動する。

一方、標準圧電結晶(水晶)に位相同期させた 14 Hz の電圧を印加する。やはり 14 Hz に位相同期させてあるロック・イン・アンプは、キャパシタ・プレート間隔変化に由来する、14 Hz で同期したキャパシタンス変化分を検出する。未知電歪結晶と標準水晶結晶に印加する電圧と位相を適当に調整して、両プレートの振動を同期させると、キャパシタンス変化(交流分)を零にすることが

できる。この零位状態(null condition)が実現できれば、両結晶の厚さ、印加電圧、水晶の圧電定数から、未知の電歪定数は簡単に計算される。

従来、感度を高める際に問題になったのは、熱揺動に伴うプレート間隔、キャパシタンスの変化であった。本装置においては、この変化はブリッジ検出部において DC アンバランス信号となり、増幅され、PZT 圧電素子に印加される。このサーボ機構によりプレート間隔は直流的に固定され、キャパシタンス・ブリッジの高い増幅レンジにおける安定な作動を可能にした。

$\text{Pb}(\text{Mg}_{1/3}\text{Nb}_{2/3})\text{O}_3$ セラミック試料だけに 7 Hz 正弦波を印加したときのロック・イン・アンプ出力を図 7(a) に示した。電圧と出力間の期待される 2 乗関係は満足されている。図 7(b)には零位法の例を示した。試料に適当な電圧を印加しておき、出力を水晶印加電圧の関数としてプロットした。電歪定数 M_{11} (セラミック) $= 8.46 \times 10^{-12} \text{ d}_{11}$ (水晶) あるいは $1.92 (\pm 0.02) \times 10^{-11} \text{ m}^2 \text{ V}^{-1}$ と求まり、歪ゲージ法による測定結果⁽¹¹⁾ とよい一致を示している。(つづく)

APPENDIX 29

K. Uchino, S. Nomura, L.E. Cross, R.E. Newnham. New Electrostrictive Materials. II. Elect. Ceram. 11 (autumn) (1980, in press).

5. ペロアスカイト結晶の電圧効果

[illegible]

6:6 昭和天皇強誘電体にふける巨大電圧効果 (13), (18)

電界印加下における電圧の大小より、 Q_2 (3=3000) による

[illegible]

固溶体に与りうる電測定結果は非常に興味深い(図9)。
 $\text{SrTi}_{1-x}\text{Fe}_x\text{O}_{3-\delta}$ 系においては、 $\text{Sr}_{1-x}\text{Fe}_x$ と空孔で置換するに従
 い電導率は急激に減少する(SrTiO_3 の $Q_{\text{H}} = 5.0 \times 10^{-2} \text{ m}^2 \text{ C}^{-2} \text{ s}^{-1}$ から
 $0.85 \times 10^{-2} \text{ m}^2 \text{ C}^{-2}$ 、 $0.14 \times 10^{-2} \text{ m}^2 \text{ C}^{-2}$ 、 $1.3 \times 10^{-3} \text{ m}^2 \text{ C}^{-2}$)

$Pb(0.495W_{0.505})O_3$ 、 $Pb(1.0 \frac{W_{0.505}}{Z_{0.505}})O_3$ と $Pb(0.495W_{0.505})O_3 - Pb(1.0 \frac{W_{0.505}}{Z_{0.505}})O_3$ 系 (15) において、 $Pb(0.495W_{0.505})O_3$ の $Q_H = 0.6 \times 10^{-2} \text{ kcal}^\circ\text{C}^{-1}$ である。

図 9 (a) と (b) に $(AB)_{1/2}Br_{1/2}O_3$ の結晶構造を示した。図 9 (a) は $(AB)_{1/2}Br_{1/2}O_3$ の結晶構造を示した。図 9 (b) は $(AB)_{1/2}Br_{1/2}O_3$ の結晶構造を示した。

[illegible]

見よう。それでは、 $\rho = 0.1$ 、 $P(\text{成功}) = 0.5$ 、 $P(\text{失敗}) = 0.5$ 、 $W_0 = 1000$ 、 $W_1 = 1000$ 、 $W_2 = 1000$ 、 $W_3 = 1000$ 、 $W_4 = 1000$ 、 $W_5 = 1000$ 、 $W_6 = 1000$ 、 $W_7 = 1000$ 、 $W_8 = 1000$ 、 $W_9 = 1000$ 、 $W_{10} = 1000$ 、 $W_{11} = 1000$ 、 $W_{12} = 1000$ 、 $W_{13} = 1000$ 、 $W_{14} = 1000$ 、 $W_{15} = 1000$ 、 $W_{16} = 1000$ 、 $W_{17} = 1000$ 、 $W_{18} = 1000$ 、 $W_{19} = 1000$ 、 $W_{20} = 1000$ 、 $W_{21} = 1000$ 、 $W_{22} = 1000$ 、 $W_{23} = 1000$ 、 $W_{24} = 1000$ 、 $W_{25} = 1000$ 、 $W_{26} = 1000$ 、 $W_{27} = 1000$ 、 $W_{28} = 1000$ 、 $W_{29} = 1000$ 、 $W_{30} = 1000$ 、 $W_{31} = 1000$ 、 $W_{32} = 1000$ 、 $W_{33} = 1000$ 、 $W_{34} = 1000$ 、 $W_{35} = 1000$ 、 $W_{36} = 1000$ 、 $W_{37} = 1000$ 、 $W_{38} = 1000$ 、 $W_{39} = 1000$ 、 $W_{40} = 1000$ 、 $W_{41} = 1000$ 、 $W_{42} = 1000$ 、 $W_{43} = 1000$ 、 $W_{44} = 1000$ 、 $W_{45} = 1000$ 、 $W_{46} = 1000$ 、 $W_{47} = 1000$ 、 $W_{48} = 1000$ 、 $W_{49} = 1000$ 、 $W_{50} = 1000$ 、 $W_{51} = 1000$ 、 $W_{52} = 1000$ 、 $W_{53} = 1000$ 、 $W_{54} = 1000$ 、 $W_{55} = 1000$ 、 $W_{56} = 1000$ 、 $W_{57} = 1000$ 、 $W_{58} = 1000$ 、 $W_{59} = 1000$ 、 $W_{60} = 1000$ 、 $W_{61} = 1000$ 、 $W_{62} = 1000$ 、 $W_{63} = 1000$ 、 $W_{64} = 1000$ 、 $W_{65} = 1000$ 、 $W_{66} = 1000$ 、 $W_{67} = 1000$ 、 $W_{68} = 1000$ 、 $W_{69} = 1000$ 、 $W_{70} = 1000$ 、 $W_{71} = 1000$ 、 $W_{72} = 1000$ 、 $W_{73} = 1000$ 、 $W_{74} = 1000$ 、 $W_{75} = 1000$ 、 $W_{76} = 1000$ 、 $W_{77} = 1000$ 、 $W_{78} = 1000$ 、 $W_{79} = 1000$ 、 $W_{80} = 1000$ 、 $W_{81} = 1000$ 、 $W_{82} = 1000$ 、 $W_{83} = 1000$ 、 $W_{84} = 1000$ 、 $W_{85} = 1000$ 、 $W_{86} = 1000$ 、 $W_{87} = 1000$ 、 $W_{88} = 1000$ 、 $W_{89} = 1000$ 、 $W_{90} = 1000$ 、 $W_{91} = 1000$ 、 $W_{92} = 1000$ 、 $W_{93} = 1000$ 、 $W_{94} = 1000$ 、 $W_{95} = 1000$ 、 $W_{96} = 1000$ 、 $W_{97} = 1000$ 、 $W_{98} = 1000$ 、 $W_{99} = 1000$ 、 $W_{100} = 1000$ 、 $W_{101} = 1000$ 、 $W_{102} = 1000$ 、 $W_{103} = 1000$ 、 $W_{104} = 1000$ 、 $W_{105} = 1000$ 、 $W_{106} = 1000$ 、 $W_{107} = 1000$ 、 $W_{108} = 1000$ 、 $W_{109} = 1000$ 、 $W_{110} = 1000$ 、 $W_{111} = 1000$ 、 $W_{112} = 1000$ 、 $W_{113} = 1000$ 、 $W_{114} = 1000$ 、 $W_{115} = 1000$ 、 $W_{116} = 1000$ 、 $W_{117} = 1000$ 、 $W_{118} = 1000$ 、 $W_{119} = 1000$ 、 $W_{120} = 1000$ 、 $W_{121} = 1000$ 、 $W_{122} = 1000$ 、 $W_{123} = 1000$ 、 $W_{124} = 1000$ 、 $W_{125} = 1000$ 、 $W_{126} = 1000$ 、 $W_{127} = 1000$ 、 $W_{128} = 1000$ 、 $W_{129} = 1000$ 、 $W_{130} = 1000$ 、 $W_{131} = 1000$ 、 $W_{132} = 1000$ 、 $W_{133} = 1000$ 、 $W_{134} = 1000$ 、 $W_{135} = 1000$ 、 $W_{136} = 1000$ 、 $W_{137} = 1000$ 、 $W_{138} = 1000$ 、 $W_{139} = 1000$ 、 $W_{140} = 1000$ 、 $W_{141} = 1000$ 、 $W_{142} = 1000$ 、 $W_{143} = 1000$ 、 $W_{144} = 1000$ 、 $W_{145} = 1000$ 、 $W_{146} = 1000$ 、 $W_{147} = 1000$ 、 $W_{148} = 1000$ 、 $W_{149} = 1000$ 、 $W_{150} = 1000$ 、 $W_{151} = 1000$ 、 $W_{152} = 1000$ 、 $W_{153} = 1000$ 、 $W_{154} = 1000$ 、 $W_{155} = 1000$ 、 $W_{156} = 1000$ 、 $W_{157} = 1000$ 、 $W_{158} = 1000$ 、 $W_{159} = 1000$ 、 $W_{160} = 1000$ 、 $W_{161} = 1000$ 、 $W_{162} = 1000$ 、 $W_{163} = 1000$ 、 $W_{164} = 1000$ 、 $W_{165} = 1000$ 、 $W_{166} = 1000$ 、 $W_{167} = 1000$ 、 $W_{168} = 1000$ 、 $W_{169} = 1000$ 、 $W_{170} = 1000$ 、 $W_{171} = 1000$ 、 $W_{172} = 1000$ 、 $W_{173} = 1000$ 、 $W_{174} = 1000$ 、 $W_{175} = 1000$ 、 $W_{176} = 1000$ 、 $W_{177} = 1000$ 、 $W_{178} = 1000$ 、 $W_{179} = 1000$ 、 $W_{180} = 1000$ 、 $W_{181} = 1000$ 、 $W_{182} = 1000$ 、 $W_{183} = 1000$ 、 $W_{184} = 1000$ 、 $W_{185} = 1000$ 、 $W_{186} = 1000$ 、 $W_{187} = 1000$ 、 $W_{188} = 1000$ 、 $W_{189} = 1000$ 、 $W_{190} = 1000$ 、 $W_{191} = 1000$ 、 $W_{192} = 1000$ 、 $W_{193} = 1000$ 、 $W_{194} = 1000$ 、 $W_{195} = 1000$ 、 $W_{196} = 1000$ 、 $W_{197} = 1000$ 、 $W_{198} = 1000$ 、 $W_{199} = 1000$ 、 $W_{200} = 1000$ 、 $W_{201} = 1000$ 、 $W_{202} = 1000$ 、 $W_{203} = 1000$ 、 $W_{204} = 1000$ 、 $W_{205} = 1000$ 、 $W_{206} = 1000$ 、 $W_{207} = 1000$ 、 $W_{208} = 1000$ 、 $W_{209} = 1000$ 、 $W_{210} = 1000$ 、 $W_{211} = 1000$ 、 $W_{212} = 1000$ 、 $W_{213} = 1000$ 、 $W_{214} = 1000$ 、 $W_{215} = 1000$ 、 $W_{216} = 1000$ 、 $W_{217} = 1000$ 、 $W_{218} = 1000</$

一、地方行政機構を、地方自治體として、
 二、地方自治體の組織を、地方自治體の
 三、地方自治體の組織を、地方自治體の
 四、地方自治體の組織を、地方自治體の
 五、地方自治體の組織を、地方自治體の
 六、地方自治體の組織を、地方自治體の
 七、地方自治體の組織を、地方自治體の
 八、地方自治體の組織を、地方自治體の
 九、地方自治體の組織を、地方自治體の
 十、地方自治體の組織を、地方自治體の

[illegible]

68 知能弾薬實體に於ける巨大電圧計置 (13), (18)
 69 以上 1) 7 被選されている (97)
 70 以上 2) 被選されている (97)

3. 球和エポキシ樹脂に於ける巨分子列本
電界印加工に於ける電圧の大小は、 $Q \cdot E^2$ (E は電界) である。

[illegible][illegible]

$$E_1 = \bar{Q}_1 \cdot P^2 \quad (9)$$

$$(\bar{Q}_1 = \text{多結晶体平均電圧定数}) \quad (10)$$

[illegible]

§7. 新ミラー・コントロール用デバイス

電子の技術の発展に伴って、半導体素子の性能は飛躍的に向上している。この中で、特に注目されているのは、シリコン素子である。シリコン素子は、その安定性、信頼性、そして低コストの製造が可能であることから、半導体素子として広く利用されている。シリコン素子の製造には、シリコンウェハの準備、回路の形成、そしてパッケージングの工程が必要である。シリコンウェハの準備には、シリコンの精製、ウェハの成長、そしてウェハの検査の工程がある。回路の形成には、フォトリソグラフィ技術、エッチング技術、そしてドープ技術が必要である。パッケージングには、ワイヤーボンディング技術、エポキシ樹脂封入技術、そして熱接着技術がある。シリコン素子の性能は、シリコンの純度、ウェハの品質、回路の設計、そして製造工程の制御によって決まる。シリコン素子の性能は、年々向上しており、現在では、10nm以下のプロセス技術が実現されている。シリコン素子の性能向上は、半導体産業の発展に大きく貢献している。

[illegible]

8. 結言

二 三 四 五 六 七 八 九 十 十一 十二 十三 十四 十五 十六 十七 十八 十九 二十 二十一 二十二 二十三 二十四 二十五 二十六 二十七 二十八 二十九 三十 三十一 三十二 三十三 三十四 三十五 三十六 三十七 三十八 三十九 四十 四十一 四十二 四十三 四十四 四十五 四十六 四十七 四十八 四十九 五十 五十一 五十二 五十三 五十四 五十五 五十六 五十七 五十八 五十九 六十 六十一 六十二 六十三 六十四 六十五 六十六 六十七 六十八 六十九 七十 七十一 七十二 七十三 七十四 七十五 七十六 七十七 七十八 七十九 八十 八十一 八十二 八十三 八十四 八十五 八十六 八十七 八十八 八十九 九十 九十一 九十二 九十三 九十四 九十五 九十六 九十七 九十八 九十九 一百

① 無欠力、計力欠力、半欠力、全欠力、F 領域の順に
 ② 差を Q とし、キュリー・ワイス定数 C の値はすべての座標
 ③ 反逆磁石体において一定である。 $(\alpha/C) = 3.1(\pm 0.4) \times 10^{-4}$
 ④ 差を Q とし、熱膨張係数 α の 12 乗に比例する $(\alpha/C) = 4.2 \times 10^{-5}$

1. 電圧降下を減らすために、電線の本数を増やす。
 2. 電圧降下を減らすために、電線の断面積を増やす。
 3. 電圧降下を減らすために、電線の長さを減らす。

[illegible]

以上、電位の正効果としての変位素子についての述べてきたが、同時に電位材料 ($0.3\text{Pb(Mg}_{0.15}\text{Nb}_{0.85})\text{O}_3 - 0.1\text{PbTiO}_3$) は、逆電位効果により、

[illegible]

文獻

- (1) Scientific American, Scientific American Inc. (New York), 239 (1979) 70
- (2) K. Uchino and L. E. Cross: Japan. J. Appl. Phys., 19 (1980) (EP 814P)
- (3) F. Jona and G. Shirane: Ferroelectric Crystals, Macmillan (New York) (1962)
- (4) C. Kittel: Phys. Rev., 82 (1951) 729
- (5) K. Uchino, L. E. Cross, R. E. Newham and S. Nomura: J. Appl. Phys. (in press)
- (6) L. E. Cross: J. Phys. Soc. Japan 33 (1967) 97
- (7) G. A. Sawada: Phys. Rev. B1 (1970) 3777
- (8) I. N. Pelandov: Soviet Phys. - Solid State 5 (1963) 838
- (9) K. Uchino, L. E. Cross and R. E. Newham: (in press)
- (10) K. Uchino, S. Nomura, L. E. Cross, S. J. Jang and R. E. Newham: J. Appl. Phys., 51 (1980) (EP 814P)
- (11) K. Uchino and L. E. Cross: Proc. 33rd Annual Symposium on Frequency Control, U.S. Army Electronics Command, Fort Monmouth, N.J. (1977) 110
- (12) K. Uchino and L. E. Cross: Ferroelectrics (EP 814P)
- (13) S. J. Jang, K. Uchino, S. Nomura and L. E. Cross: Ferroelectrics (EP 814P)
- (14) K. Uchino, L. E. Cross, R. E. Newham and S. Nomura: J. Phase Transitions (EP 814P)
- (15) S. Nomura, I. Kawada, K. Uchino, S. J. Jang, L. E. Cross and R. E. Newham: Phys. Stat. Sol. (a) 57 (1978) (EP 814P)
- (16) A. Amin, R. E. Newham, L. E. Cross, S. Nomura and D. E. Cox: J. Solid State Chemistry 35 (1980) (EP 814P)
- (17) K. Uchino, S. Nomura, A. Amin, L. E. Cross, R. E. Newham: (in press)
- (18) L. E. Cross, S. J. Jang, R. E. Newham, S. Nomura and K. Uchino: Ferroelectrics (EP 814P)
- (19) K. M. Lang, S. F. Liu and J. Kyriakou: Ferroelectrics (EP 814P)
- (20) V. A. Belyakov and I. E. Mylnikova: Fiz. Tverd. Tela, 3 (1961) 841
- (21) J. Frenkel, S. G. Lipson and P. F. Cove: Appl. Phys. Lett. 25 (1974) 311
- (22) S. J. Jang, K. Uchino, L. E. Cross and S. Nomura: J. Amer. Ceram. Soc. (in press)
- (23) L. J. Bowen, J. Shrieve, W. A. Schulze and J. V. Biegans: Ferroelectrics (EP 814P)

- (24) K. Uchida, L. E. Cross and S. Nomura, J. Mat. Sci. (研報中)
 (25) R. A. Levens and L. A. Coldren, Rev. Sci. Instrum. 49, (1978) 1650
 (26) K. Uchida, S. J. Jang, L. E. Cross and R. E. Muench, U.S.A. Patent (申請中)
 (27) H. Banno and H. Sobue, Proc. 2nd Meeting on Ferroelectric Mat. and Appl. (1979)
 61

図説明

- 図1 電界下のイオンシフト (a) 圧電歪と (b) 電歪
 電歪歪度と熱線歪係数の相関関係
 図2 電歪歪度と熱線歪係数の相関関係
 図3 電歪歪度と熱線歪係数の相関関係
 図4 $Pb_{0.99}Nb_{0.01}O_3$ の電歪歪度の温度依存性
 図5 $Pb_{0.99}Nb_{0.01}O_3$ の圧電歪度の温度依存性
 図6 電歪歪度と熱線歪係数の相関関係
 図7 ロックインアンプ出力の印加電圧依存性 (a) と、電位法の
 図8 各種国産セラミックスにおける電歪歪度の組成依存性
 図9 $A(B_{1-x}Ga_x)O_3$ ペロブスカイト型の積層配列 (a) と、無秩序
 配列 (b) の電歪歪度 (a) と、PZT 8 の圧電歪 (b)
 図10 $Gd_{0.9}Pb_{0.1}Nb_{0.9}O_3-0.1PbTiO_3$ の電歪 (a) と、PZT 8 の圧電歪 (b)
 図11 $0.9Pb(Nb_{0.9}Ga_{0.1})O_3-0.1PbTiO_3$ における、至一分極の関係
 図12 $0.9Pb(Nb_{0.9}Ga_{0.1})O_3-0.1PbTiO_3$ の熱膨張係数
 図13 ミラー・コンドロール・デハイス、ハニカム型 (弾頭果赤子)
 (a) 積層型 (弾頭果赤子) と、(b) ハニカム型 (弾頭果赤子)

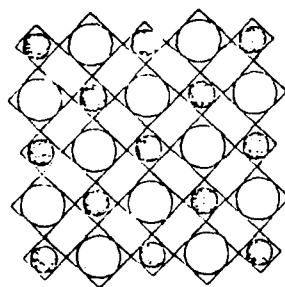
Table 1. Electrostrictive coefficients, Curie-Weiss constants and their product values for various perovskite-type crystals.

Polar-Type	Order-type	Substance	Q_h ($\times 10^{-2} \text{ m}^4 \text{ C}^{-2}$)	C ($\times 10^5 \text{ K}$)	$Q_h C$ ($\times 10^{-1} \text{ m}^4 \text{ C}^{-2} \text{ K}$)	References
Ferroelectric	Disordered	$\text{Pb}(\text{Mg}_{1/3}\text{Nb}_{2/3})\text{O}_3$	0.60	4.7	2.8	Uchino (1980a), Nomura (1979a)
		$\text{Pb}(\text{Zn}_{1/3}\text{Nb}_{2/3})\text{O}_3$	0.66	4.7	3.1	Nomura (1979b), Kuwata (1979)
	Partially ordered	$\text{Pb}(\text{Sc}_{1/2}\text{Nb}_{1/2})\text{O}_3$	0.83	3.5	2.9	Setter (1980)
	Simple	BaTiO_3	2.0	1.5	3.0	Yamada (1972), Johnson (1965)
		PbTiO_3	2.2	1.7	3.7	Gavril'yachenko (1970), Fesenko (1970)
		SrTiO_3	4.7	0.77	3.6	Samara (1963), Bell (1963)
		KTaO_3	5.2	0.5	2.6	Uwe (1975), Uwe (1973)
Antiferroelectric	Partially ordered	$\text{Pb}(\text{Fe}_{2/3}\text{U}_{1/3})\text{O}_3$	--	2.3	--	Uchino (1977)
	Simple	PbZrO_3	2.0	1.6	3.2	Uchino (1980b), Samara (1970)
	Ordered	$\text{Pb}(\text{Co}_{1/2}\text{Mn}_{1/2})\text{O}_3$ $\text{Pb}(\text{Mg}_{1/2}\text{Mn}_{1/2})\text{O}_3$	-- 6.2	1.2 0.42	-- 2.6	Bukov (1965) Uchino (1980b), Nomura (1979a)
Non-polar	Disordered	$(\text{Zr}_{1/4}\text{Ba}_{1/4})(\text{Zr}_{1/6}\text{Nb}_{5/6})\text{O}_3$	0.55 - 1.15	--	--	Uchino (1980c)
	Simple	BaZrO_3	2.3	--	--	Uchino (1980c)

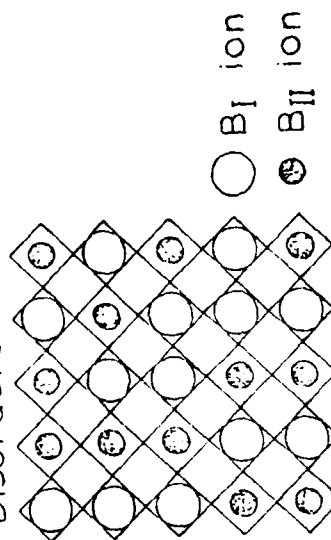
8 9

$A(B_{I1/2}B_{II1/2})O_3$ type perovskite

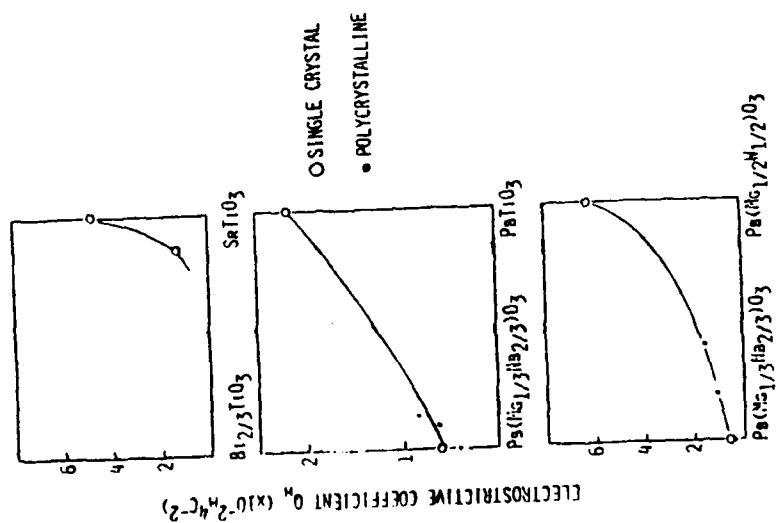
a) Ordered

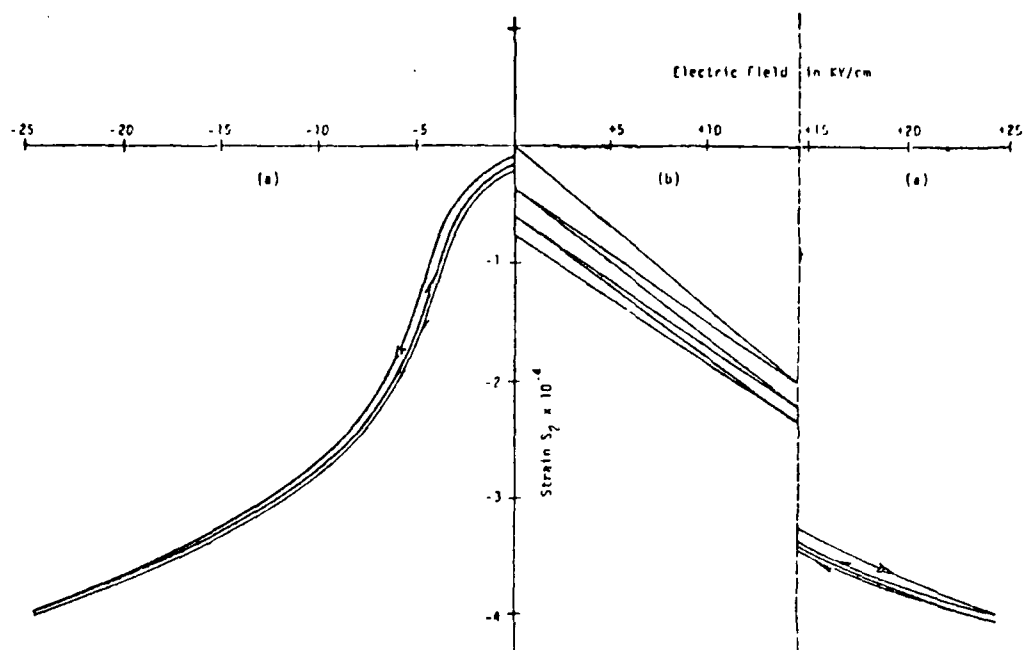


b) Disordered

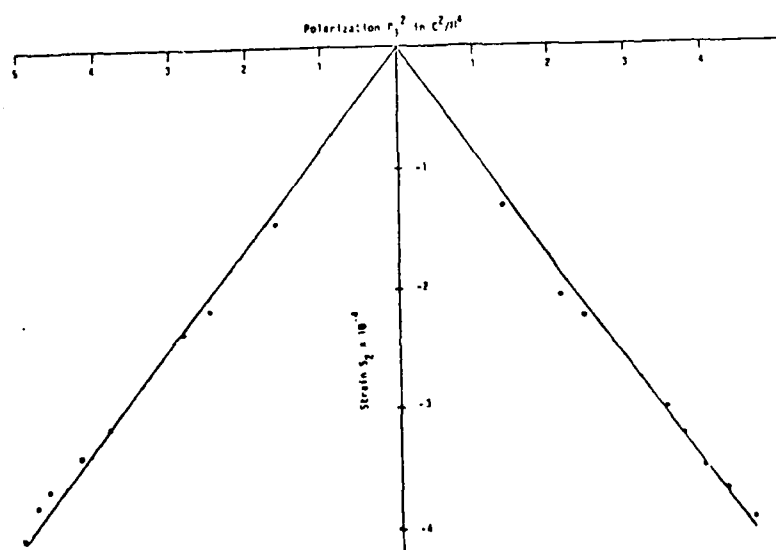


8 8

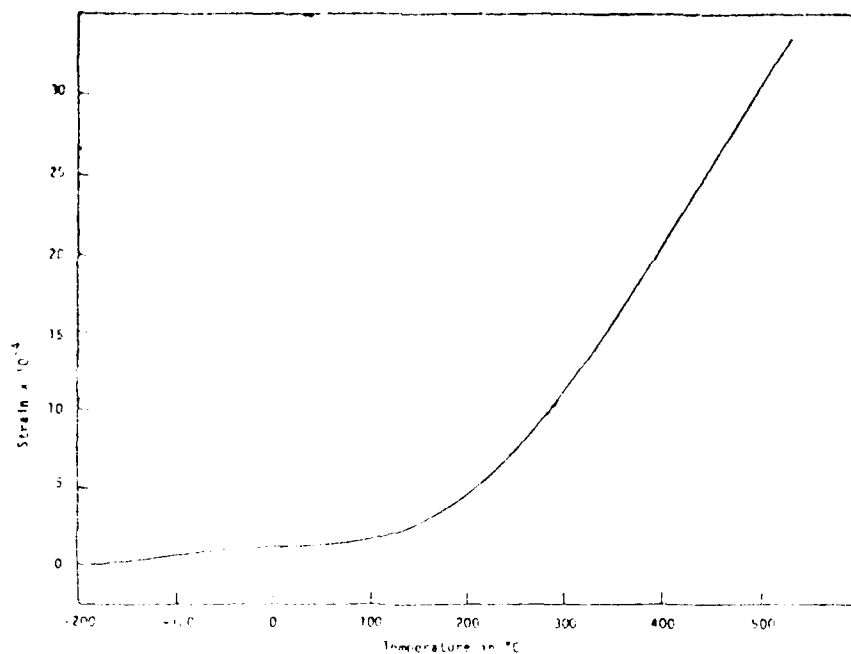




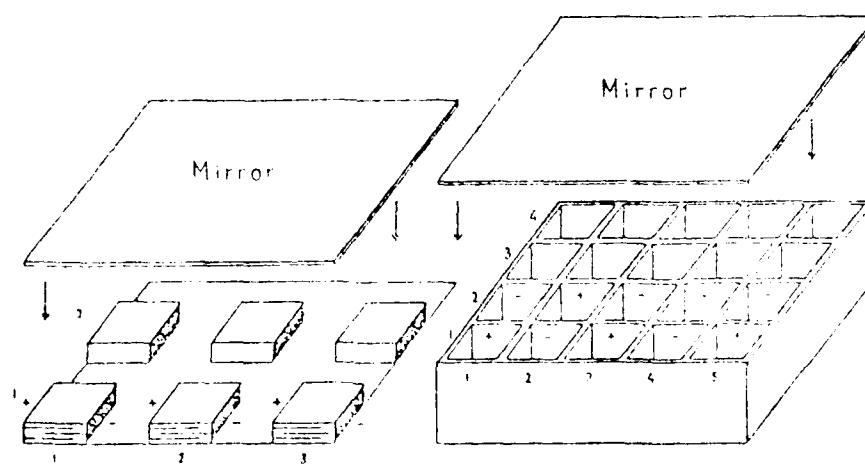
10



11



B 12



a) Multilayer transducer

b) Honeycomb-type transducer

B 13

APPENDIX 30

K. Uchino, S. Nomura, L.E. Cross, R.E. Newnham. Electrostriction in Perovskite Crystals and its Application to Transducers. J. Mat. Sci. (accepted).

Electrostriction in Perovskite Crystals and
Its Applications to Transducers

Kenji Uchino and Shoichiro Nomura

Department of Physical Electronics, Tokyo Institute of Technology
 Ookayama, Meguro-ku, Tokyo 152, Japan

and

Leslie E. Cross and Robert E. Newnham

Materials Research Laboratory, The Pennsylvania State University
 University Park, Pennsylvania 16802, USA

ABSTRACT

Electrostrictive materials for displacement transducers are reviewed, including preparative, theoretical, and design studies. Several empirical rules have been deduced from investigation of electrostrictive effects in ferroelectric, antiferroelectric, and non-polar perovskites. Consistent with these criteria, the relaxor ferroelectric $0.9\text{Pb}(\text{Mg}_{1/3}\text{Nb}_{2/3})\text{O}_3-0.1\text{PbTiO}_3$ has been shown to possess much larger strain with lower hysteresis, aging effects, and thermal expansion than commercial piezoelectric PZT. Using a multilayer configuration, we have developed a mirror-control device capable of large strains up to $\Delta L/L \sim 10^{-3}$ with only 200V applied.

Recent requirements for new displacive transducers with lower hysteresis and aging effects than conventional PZT based ceramics have prompted the development of a new family of electrostrictive ceramics for these applications.¹⁾ In this paper we review the properties of electrostrictive transducers, including recent experimental and theoretical studies.

Electrostriction is a measure of the strain resulting from ionic displacements caused by an applied electric field. In most centric crystals, the induced shifts of equivalent ions almost cancel one another, with only the differences arising from anharmonicity creating strain. It is thus not unreasonable to expect interrelations between anharmonic effects such as thermal expansion and electrostriction. Figure 1 shows the thermal expansion coefficient α plotted against the hydrostatic electrostriction coefficient $Q_h (=Q_{11}+2Q_{12})$ for materials of isotropic or cubic symmetry. The power relation

$$\alpha = 4.2 \times 10^{-5} Q_h^{0.5} \quad (1)$$

was obtained from this graph (empirical rule I).²⁾

There are several experimental methods for determining the electrostriction coefficients. Direct measurements of field-induced or spontaneous strain include optical methods (interferometer,³⁾ optical lever, optical grids), x-ray methods, electrical methods (capacitance dilatometer^{4),5)}, differential transformer dilatometer^{6),7)}) and strain gauge methods.^{8),9)} Pressure gauge methods, measurements of the permittivity variation with pressure^{8),10)} and induced-piezoelectric resonance techniques^{3),11)} are indirect methods. Figure 2 shows an example of a strain gauge determination of longitudinal electrostrictive strain in single crystals of the relaxor ferroelectric perovskite $\text{Pb}(\text{Mg}_{1/3}\text{Nb}_{2/3})\text{O}_3$, measured as a function of applied electric field at various temperatures above the Curie point.⁸⁾ Experimental values of the electrostriction coefficients

Q_{11} and Q_{12} are plotted as a function of temperature in Figure 3. It is evident that the electrostriction coefficients do not change significantly through the relaxation temperature range. The values of the coefficients obtained by different experimental techniques are in good agreement with each other.

In Table I, hydrostatic electrostriction coefficients Q_h and Curie-Weiss constants C are summarized for various kinds of oxide perovskite crystals: simple, disordered, partially ordered and ordered ferroelectrics, antiferroelectrics and non-polar dielectrics. Sources of the original experimental data are listed in references 8, 10, and 12. The magnitude of the electrostriction coefficient is not affected strongly by ferroelectricity, antiferroelectricity, or non-polar behavior, but is very dependent on the degree of order in the cation arrangement. An empirical rule II is proposed that states "the electrostrictive Q coefficient increases with cation order from disordered, through partially ordered, simple and then ordered perovskites." The decrease in the Curie-Weiss constant with increase in the degree of cation ordering is also correlated with electrostriction. This leads to empirical rule III, "the product of the electrostriction coefficient Q and the Curie-Weiss constant C is nearly constant for all ferroelectric and antiferroelectric perovskites ($Q_h C = 3.1 (\pm 0.4) \times 10^3 \text{ m}^4 \text{ C}^{-2} \text{ K}$)."

We have proposed an intuitive crystallographic model to explain the "constant QC rule." Figures 4(a) and (b) show the ordered and disordered structures for an $A(B_{I_{1/2}} B_{II_{1/2}})_3 \text{O}_3$ perovskite crystal.

Assuming a rigid ion model, a large "rattling" space is expected for the smaller B ions in the disordered structure because the larger B ions prop open the lattice framework. Much less rattling space is expected in the ordered arrangement where neighboring ions collapse systematically around the small B ions.¹³⁾ When an electric field is applied to a disordered perovskite, the B

ion with large rattling space can shift easily without distorting the oxygen framework. Larger polarization can be expected for unit magnitude of electric field, causing larger dielectric constants and larger Curie-Weiss constants. Under these circumstances, smaller strains are expected per unit magnitude of polarization, resulting in lower electrostriction coefficients. On the other hand, in ordered perovskites with very small rattling space, the B ions cannot move easily without distorting the oxygen octahedron. A smaller Curie-Weiss constant and a larger electrostriction coefficient are expected. The measurements on solid solution systems are also very suggestive. The results for $\text{Pb}(\text{Mg}_{1/3}\text{Nb}_{2/3})\text{O}_3$ - PbTiO_3 ,^{6),7)} $\text{Pb}(\text{Mg}_{1/3}\text{Nb}_{2/3})\text{O}_3$ - $\text{Pb}(\text{Mg}_{1/2}\text{W}_{1/2})\text{O}_3$ ⁹⁾ and SrTiO_3 - $\text{Bi}_{2/3}\text{TiO}_3$ ¹⁰⁾ indicate that the electrostriction coefficients decrease substantially with increasing rattling space.

Since the figure of merit for electrostrictive strain is $Q\epsilon^2$ (ϵ : permittivity) or QC^2 (eliminating temperature dependence), and the product QC is nearly constant for all ferroelectric perovskites, disordered perovskites with large Curie-Weiss constants, but small electrostriction coefficients, are preferred to the usual perovskites (e.g. $\text{Pb}(\text{Zr,Ti})\text{O}_3$ or BaTiO_3 based ceramics) for practical applications. The relaxor ferroelectric chosen for study is $\text{Pb}(\text{Mg}_{1/3}\text{Nb}_{2/3})\text{O}_3$, which itself is superior to conventional modified BaTiO_3 ceramics in its electrostrictive response.⁷⁾ The response can be further improved if the Curie range, which is below room temperature in $\text{Pb}(\text{Mg}_{1/3}\text{Nb}_{2/3})\text{O}_3$, is shifted to slightly higher temperature. The Curie range of the solid solution $0.9\text{Pb}(\text{Mg}_{1/3}\text{Nb}_{2/3})\text{O}_3$ - 0.1PbTiO_3 extends from 0°C to 40°C . Using a differential transformer dilatometer, the transverse electrostrictive strain was measured along the length of a thin ceramic rod, subject to DC bias fields applied in a perpendicular direction (Figure 5).⁶⁾ The relaxor ceramics are anhysteretic and retrace the same curve with rising and falling fields. For comparison the piezoelectric strain of a hard-PZT 8

under cyclic fields is also plotted in Figure 5. This material has often been used in the fabrication of active optical components.¹⁴⁾ Field-induced strains in $0.9\text{Pb}(\text{Mg}_{1/3}\text{Nb}_{2/3})\text{O}_3-0.1\text{PbTiO}_3$ are larger than those in PZT and far more reproducible under cyclic drive conditions. An additional merit is that electric poling is not required.

Another interesting property of relaxor ferroelectrics is the very small thermal expansion effect throughout the Curie range, as predicted from empirical rule I ($\alpha^2 \propto Q$). The thermal expansion coefficient of $0.9\text{Pb}(\text{Mg}_{1/3}\text{Nb}_{2/3})\text{O}_3-0.1\text{PbTiO}_3$ in the temperature range -100°C to $+100^\circ\text{C}$ is less than $1 \times 10^{-6} \text{ K}^{-1}$, comparable to the best low expansion ceramics or fused silica. The thermal strains are far smaller than the electrostrictive strains, which is extremely advantageous for micropositioner applications.

The multilayer technology used in the capacitor industry is one of the important factors prompting the development of new electrostrictive devices. The electric field across alternate layers is of opposite direction, but the displacive responses are additive. In a piezoelectric device of fixed total thickness, the total displacement for a given voltage is proportional to the number of layers. On the other hand, in an electrostrictive device the total displacement is proportional to the square of the number of layers, far more effective than in a piezoelectric material. Internally electroded ten-layer devices with a total thickness of 2.5 mm were prepared by standard tape casting techniques using calcined $0.9\text{Pb}(\text{Mg}_{1/3}\text{Nb}_{2/3})\text{O}_3-0.1\text{PbTiO}_3$ powder and a commercial doctor blade medium.^{15),16)} A mirror control device has been constructed from 10 ten-layer ceramics bonded together. With only 200V applied, the device develops large displacements up to $\Delta L \sim 25 \mu\text{m}$ ($\Delta L/L \sim 10^{-3}$) with very high reproducibility under cyclic fields. The total displacement of about 25 μm is an order of magnitude larger than that of commercial piezoelectric transducers (e.g. PZT-5H, 25 mm plate using d_{31}),¹⁷⁾ and may introduce a new class of

micropositioner devices. With further refinement of the tape casting process, it is probable that the driving voltage can be further reduced to less than 40V.

In the inverse electrostrictive effect, that is, the pressure dependence of dielectric constant, a sensitive pressure characteristic has also been observed in the same material. Applications of this electrostrictive material for pressure gauges and heavyweight detectors are also very promising.¹⁸⁾

References

1. K. Uchino, S. Nomura, L.E. Cross and R.E. Newnham: New Electrostrictive Materials, Electronic Ceramics (1980) (in Japanese)(in press).
2. K. Uchino and L.E. Cross: Jpn. J. Appl. Phys. Lett. 19 (1980) L171.
3. J. Kuwata, K. Uchino and S. Nomura: Jpn. J. Appl. Phys. (1980)(to be published).
4. K. Uchino and L.E. Cross: Proc. 33rd Annual Symposium on Frequency Control, U.S. Army Electronics Command, Fort Monmouth, NJ (1979) p. 110.
5. K. Uchino and L.E. Cross: Ferroelectrics 27 (1980) 35.
6. L.E. Cross, S.J. Jang, R.E. Newnham, S. Nomura and K. Uchino: Ferroelectrics 23 (1980) 187.
7. S.J. Jang, K. Uchino, S. Nomura and L.E. Cross: Ferroelectrics 27 (1980) 31.
8. K. Uchino, S. Nomura, L.E. Cross, S.J. Jang and R.E. Newnham: J. Appl. Phys. 51 (1980) 1142.
9. S. Nomura, J. Kuwata, K. Uchino, S.J. Jang, L.E. Cross and R.E. Newnham: Phys. Stat. Solidi (a) 57 (1980) 317.
10. K. Uchino, L.E. Cross, R.E. Newnham and S. Nomura: J. Phase Transitions (1980) (in press).
11. S. Nomura, K. Tonooka, J. Kuwata, L.E. Cross and R.E. Newnham: Proc. 2nd on Ferroelectric Mater. and Appl. (Kyoto, 1979) p. 133.
12. K. Uchino, L.E. Cross, R.E. Newnham and S. Nomura: J. Appl. Phys. (1980) (to be published).
13. A. Amin, R.E. Newnham, L.E. Cross, S. Nomura and D.E. Cox: J. Solid State Chemistry 35 (1980) (in press).
14. J. Feinleib, S.G. Lipson and P.F. Cone: Appl. Phys. Lett. 25 (1974) 311.
15. L.J. Bowen, T. Shrout, W.A. Schulze and J.V. Biggers: Ferroelectrics 27 (1980) 59.

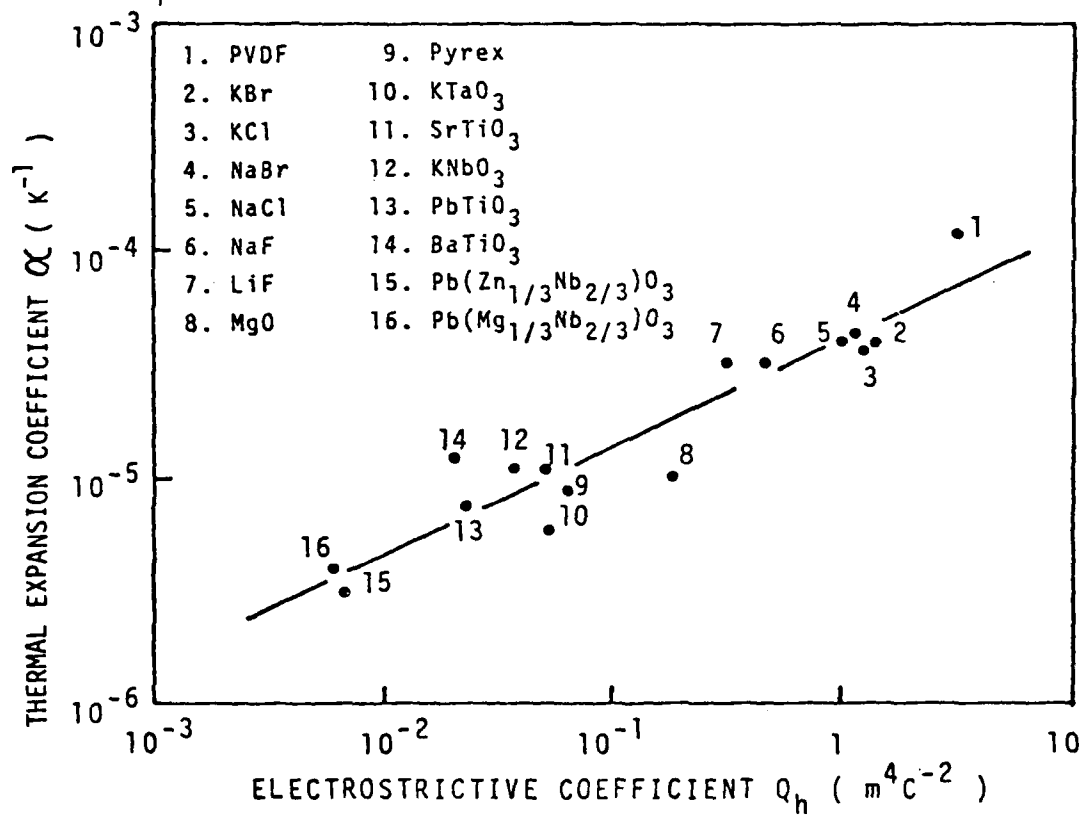
16. K. Uchino, L.E. Cross and S. Nomura: J. Mater. Sci. (1980) (in press).
17. R.A. Lemons and L.A. Coldren: Rev. Sci. Instrum. 49 (1978) 1650.
18. K. Uchino, S.J. Jang, L.E. Cross and R.E. Newnham: USA Patent (submitted in 1980).

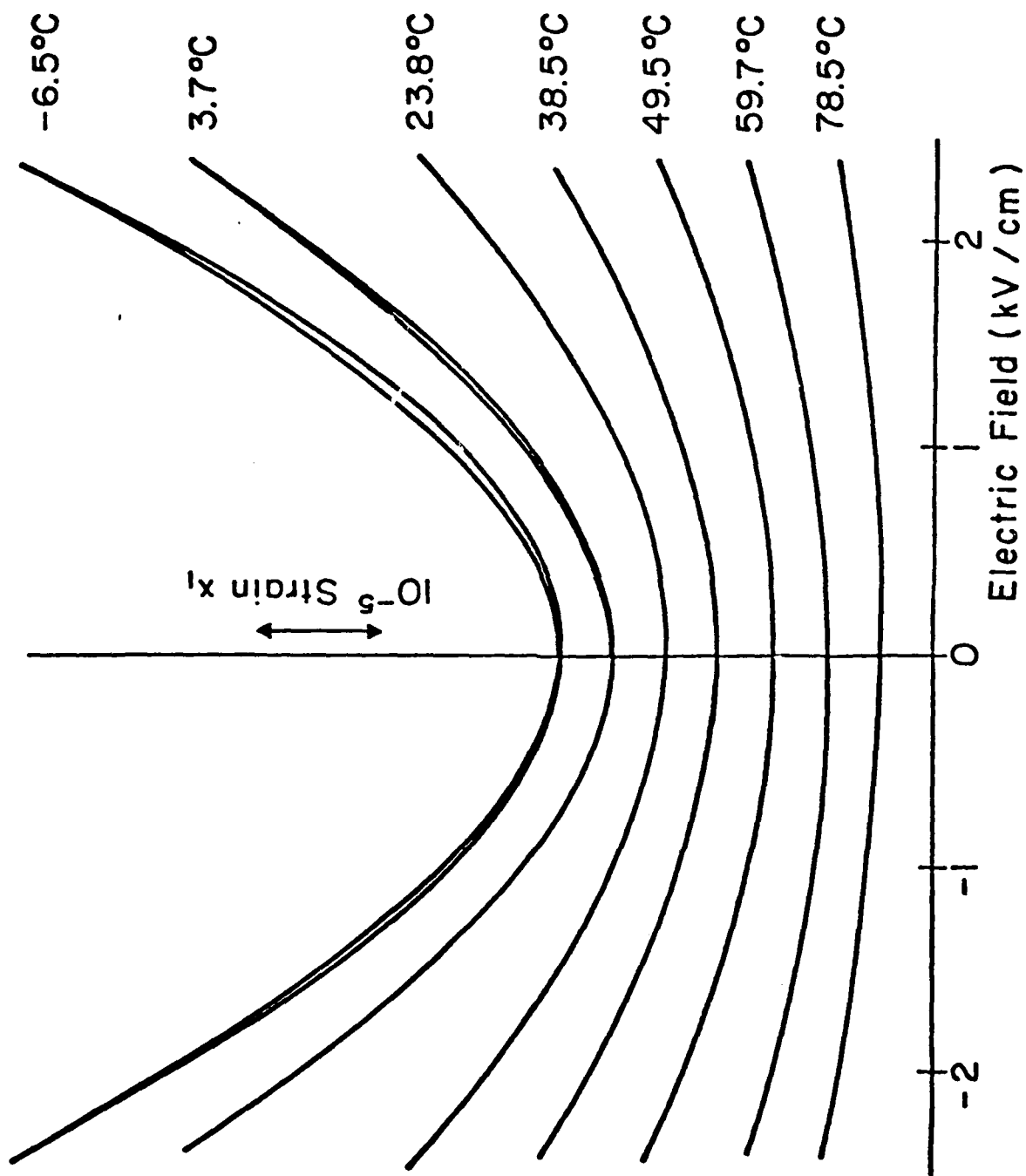
Table I. Electrostrictive coefficients, Curie-Weiss constants and their product values for various perovskite-type crystals.

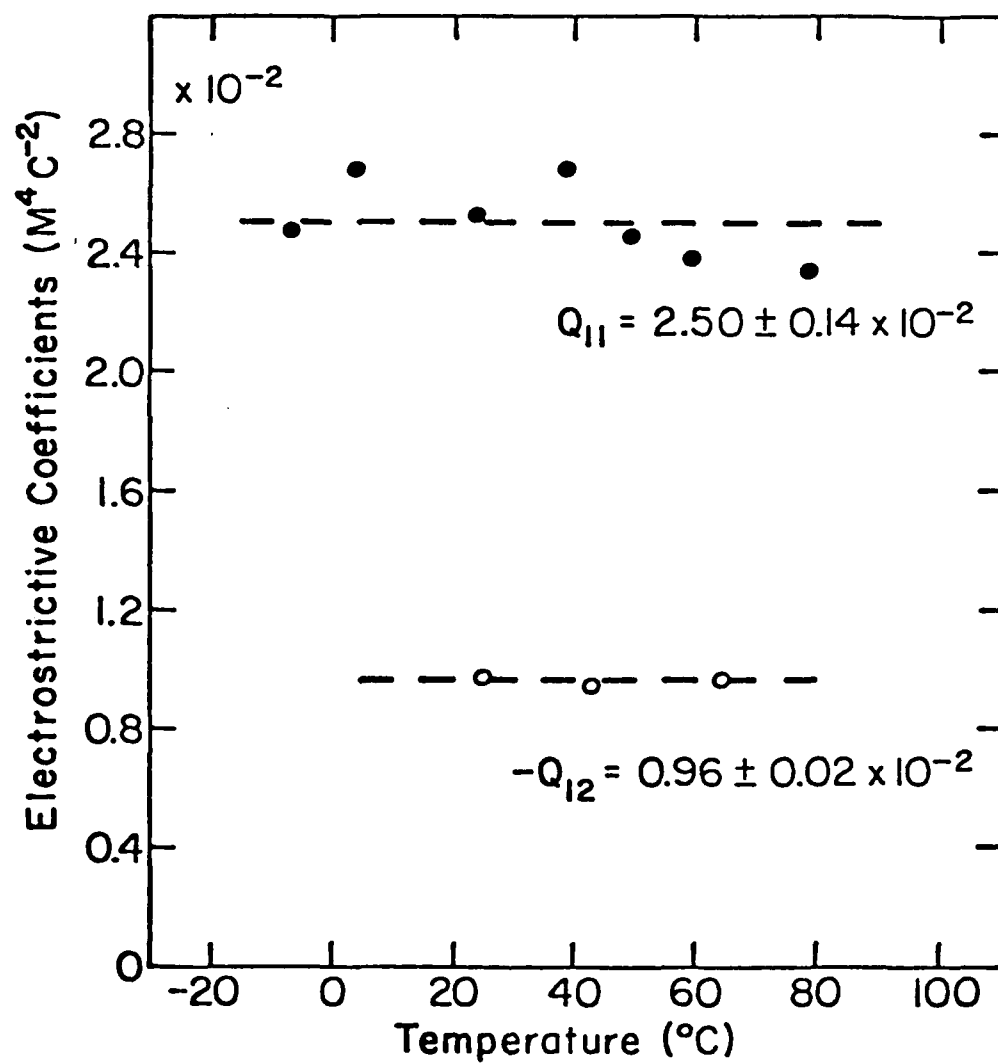
Polar-Type	Order-type	Substance	q_h ($\times 10^{-2} \text{ m}^4 \text{ C}^{-2}$)	C ($\times 10^5 \text{ K}$)	$q_h C$ ($\times 10^3 \text{ m}^4 \text{ C}^{-2} \text{ K}$)	References
Ferroelectric	Disordered	$\text{Pb}(\text{Mg}_{1/3}\text{Nb}_{2/3})\text{O}_3$	0.60	4.7	2.8	Uchino(1980a), Nomura (1979a)
		$\text{Pb}(\text{Zn}_{1/3}\text{Nb}_{2/3})\text{O}_3$	0.66	4.7	3.1	Nomura (1979b), Kuwata (1979)
	Partially ordered	$\text{Pb}(\text{Sc}_{1/2}\text{Nb}_{1/2})\text{O}_3$	0.83	3.5	2.9	Setter (1980)
	Simple	BaTiO_3	2.0	1.5	3.0	Yamada(1972), Johnson(1965)
		PbTiO_3	2.2	1.7	3.7	Gavrilyachenko (1970), Fesenko (1970)
SrTiO_3		4.7	0.77	3.6	Samara(1966), Bell(1963)	
KTaO_3		5.2	0.5	2.6	Uwe (1975), Uwe (1973)	
Antiferroelectric	Partially ordered	$\text{Pb}(\text{Fe}_{2/3}\text{U}_{1/3})\text{O}_3$	--	2.3	--	Uchino (1977)
	Simple	PbZrO_3	2.0	1.6	3.2	Uchino(1980b), Samara (1970)
		Ordered	$\text{Pb}(\text{Co}_{1/2}\text{W}_{1/2})\text{O}_3$	--	1.2	--
	$\text{Pb}(\text{Mg}_{1/2}\text{W}_{1/2})\text{O}_3$		6.2	0.42	2.6	Uchino(1980b), Nomura (1979a)
Non-polar	Disordered	$(\text{K}_{3/4}\text{B}_{1/4})(\text{Zn}_{1/6}\text{Nb}_{5/6})\text{O}_3$	0.55 - 1.15	--	--	Uchino (1980c)
	Simple	BaZrO_3	2.3	--	--	Uchino (1980c)

Figure Captions

- Figure 1. Thermal expansion coefficient α plotted as a function of hydrostatic electrostriction coefficient Q_h for various materials. The straight line has slope 0.5.
- Figure 2. Electric field dependence of the longitudinal electrostriction in $\text{Pb}(\text{Mg}_{1/3}\text{Nb}_{2/3})\text{O}_3$ at various temperatures (strain gauge methods).
- Figure 3. Temperature dependence of the electrostriction coefficients of $\text{Pb}(\text{Mg}_{1/3}\text{Nb}_{2/3})\text{O}_3$ single crystals.
- Figure 4. Crystal structure models of the $\text{A}(\text{B}_{\text{I}1/2}\text{B}_{\text{II}1/2})\text{O}_3$ type perovskite:
 (a) Ordered structure with a small rattling space.
 (b) Disordered structure with a large rattling space.
- Figure 5. Transverse strain in ceramic specimens of $0.9\text{Pb}(\text{Mg}_{1/3}\text{Nb}_{2/3})\text{O}_3-0.1\text{PbTiO}_3$:
 (a) And a typical hard PZT 8 piezoceramic.
 (b) Under slowly varying electric fields.

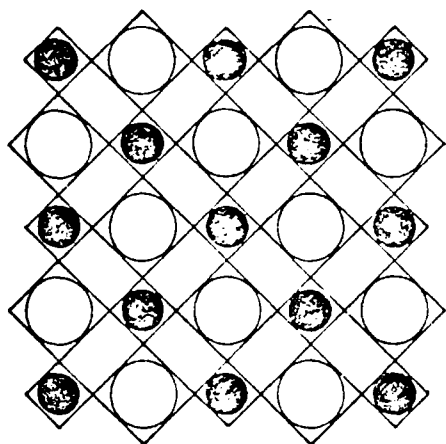




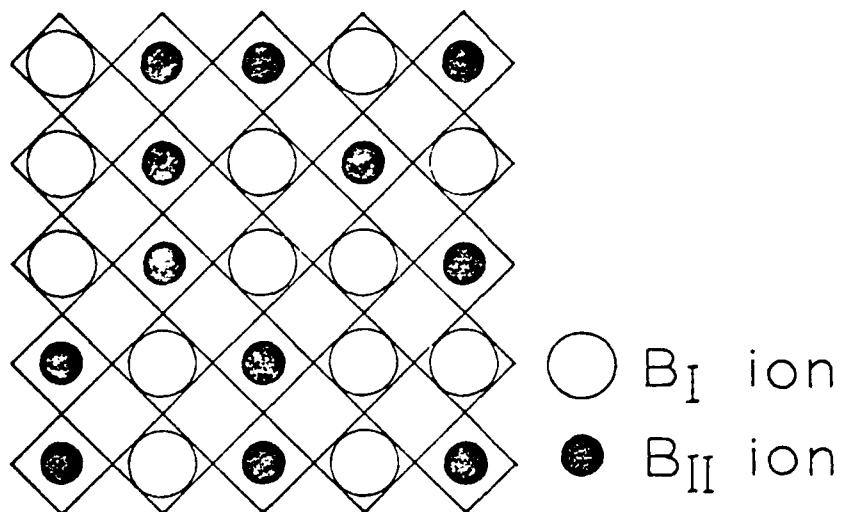


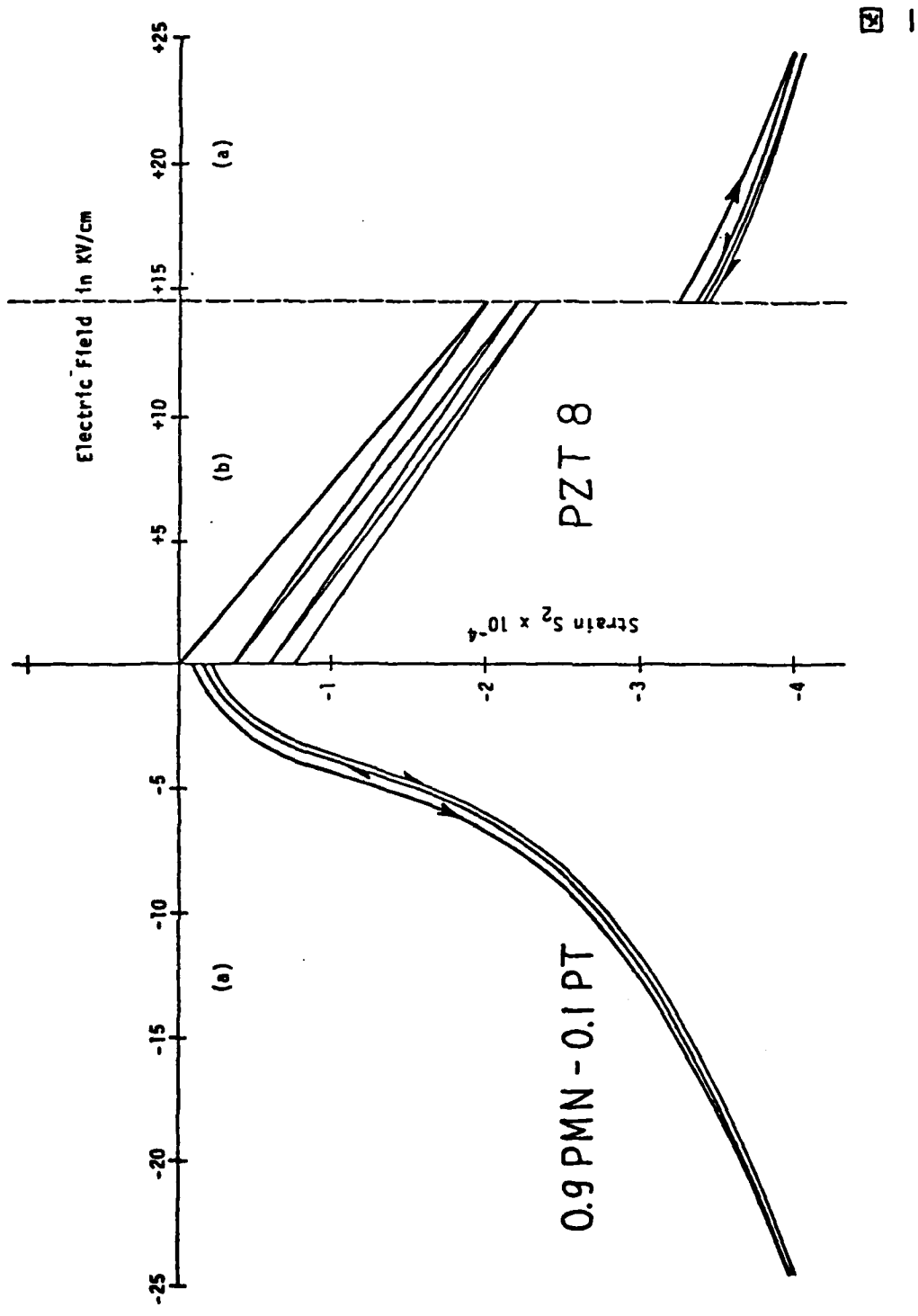
$A(B_{I1/2}B_{II1/2})O_3$ type perovskite

a) Ordered



b) Disordered





APPENDIX 31

N. Setter, L.E. Cross. Flux Growth of Lead Scandium Tantalate
 $\text{Pb}(\text{Sc}_{0.5}\text{Ta}_{0.5})\text{O}_3$ and Lead Magnesium Niobate $\text{Pb}(\text{Mg}_{1/3}\text{Nb}_{2/3})\text{O}_3$ Single
Crystals. J. Cryst. Growth (accepted).

Letter to the Editor

FLUX GROWTH OF LEAD SCANDIUM TANTALATE $\text{Pb}(\text{Sc}_{0.5}\text{Ta}_{0.5})\text{O}_3$ AND
LEAD MAGNESIUM NIOBATE $\text{Pb}(\text{Mg}_{1/3}\text{Nb}_{2/3})\text{O}_3$ SINGLE CRYSTALS

N. Setter and L.E. Cross

Materials Research Laboratory
The Pennsylvania State University
University Park, Pennsylvania 16802

Lead magnesium niobate and lead scandium tantalate are ferroelectric crystals which exhibit diffuse or broadened phase transitions and a ferroelectric Curie range^{1,2}. The tantalate crystal is of special interest, as it has been shown³ that the state of ordering of the two B site cations in the ABO_3 perovskite structure can be modified by suitable thermal treatment.

The growth procedure for the $\text{Pb}(\text{Sc}_{0.5}\text{Ta}_{0.5})\text{O}_3$ (PST) was as follows:

PST powder was first made by wet-mixing stoichiometric proportions of the constituent oxides (PbO , Sc_2O_3 , Ta_2O_5), ball milling for 20 hours under alcohol, drying, then calcining at 800°C for two hours. The calcined powder was then reground and fired at 1300°C for one hour to ensure complete reaction. X-ray diffraction of the final powder showed the expected perovskite structure with small traces of a pyrochlore structure phase.

The flux that proved most successful was a mixture of PbF_2 - PbO - B_2O_3 used in the ratio by weight $\text{PST}:\text{PbO}:\text{PbF}_2:\text{B}_2\text{O}_3 = 0.15:0.40:0.40:0.05$. The thermal cycle used was a rapid heating to 1250°C , soaking at that temperature for four hours, cooling at $3^\circ\text{C}/\text{hour}$ to $1,000^\circ\text{C}$, $5^\circ\text{C}/\text{hour}$ to 900°C and then $50^\circ\text{C}/\text{hour}$ back to room temperature.

For lead magnesium niobate (PMN), the growth procedure was rather similar as follows:

PMN powder was prepared from the mixed oxides. Again a low initial firing was found advantageous in limiting the formation of the undesired pyrochlore phase which can form in this system. The flux used was a $\text{PbO}:\text{B}_2\text{O}_3$ mixture and the ratios were similar to those chosen by Bonner and Van Uitert⁴ for pulling PMN by Kyropulos technique. The growth temperature cycle in our case was rapid heating to 1150°C soaking for two hours at that temperature, cooling at 3°C/hour to 950°C, 5°C/hour to 800°C followed by 50°C/hour back down to room temperature.

In this case the flux was not poured off after growth and the crystals were extracted from the matrix by dissolution in hot dilute nitric acid.

The furnace arrangement, which has been described in more detail elsewhere⁵, was an alumina tube type, heated by silicon carbide elements. The growth cycle was programmed by a 5600 μ Data Track Microprocessor based programmer with blend and master stations controlling a Research Inc. analogue power controller.

A listing of the general features of the grown crystals is given in Table 1. Rod-like PMN crystals have been previously grown from PbO flux (3:2PbO:PMN) by 25°/hr cooling in the 1200° - 900° range. Our crystals have the form of simple cubes with well developed 100 faces (Fig. 1a). The PST crystals have a similar morphology (Fig. 1b) but the unit cell is smaller than that reported earlier⁷ and is similar to that measured on PST powders formed by solid state reaction.

Dielectric constant was measured as a function of temperature as a means for evaluating the diffuseness of the phase transition (Figure 2). This was done by measuring the capacitance at frequencies of 1, 10, and 100 KHz with an automatic capacitance bridge (Hewlett Packard 4270A).

Table 1. General description of PST and PMN.

Property	PST	PMN
Color	Yellow	Yellow
Shape	Cube	Cube
Edge Size	1-3 mm	1-3 mm
Plane of Surface	(100)	(100)
Unit Cell Size	4.073A	4.020A
T _c	14°C	-8°C

The ϵ_{\max} of PST has a much higher value than the previously reported value of 1400 for polycrystalline samples². The transition temperature (T_c = 13°C) is also lower than the reported transition for ceramic PST.

The transition of PST is sharper than that of PMN, which is a classical relaxor. Also, the frequency dependence of the transition temperature is almost negligible for PST. There is, however, a strong suppression of the dielectric constant with increasing frequency. Curie constant as calculated far above the transition temperature is 2.5×10^5 for PST. This number is between the typical values for the order ferroelectric (1×10^5) and the values for ferroelectric relaxors (4.5×10^5 for PMN).

Acknowledgment

This work was supported by the Office of Naval Research, Grant No. N00014-78-C-0291.

REFERENCES

1. G.A. Smolenskii and A.I. Agranovskaja, Zh. Tech. Fiz. 28, 1791 (1958).
2. G.A. Smolenskii, et al., Soviet Physics-Solid State 1, 150-151 (1959).
3. N. Setter and L.E. Cross, J. Mat. Sci. (submitted).
4. W.A. Bonner and L.G. Van Uitret, Mat. Res. Bull. 2, 131-134 (1967).
5. L.E. Cross, J.V. Biggers, R.E. Newnham and G.R. Barsch, Annual Report Jan. 1 to Dec. 31, 1978, ONR Contract N00014-78-C-0291, "Targeted Basic Studies of Ferroelectric and Ferroelastic Crystals for Piezoelectric Transducer Applications."
6. J.W. Smith, Ph.D. Thesis, The Pennsylvania State University (1967).
7. F. Galasso and W. Darby, Inorg. Chem. 4, 71 (1965).

FIGURE CAPTIONS

Fig. 1. Crystals of PMN (a) and PST (b) as grown.

Fig. 2. Dielectric constant and dielectric loss of PMN (1,3) and PST (2,4) single crystals.

(a)



(b)

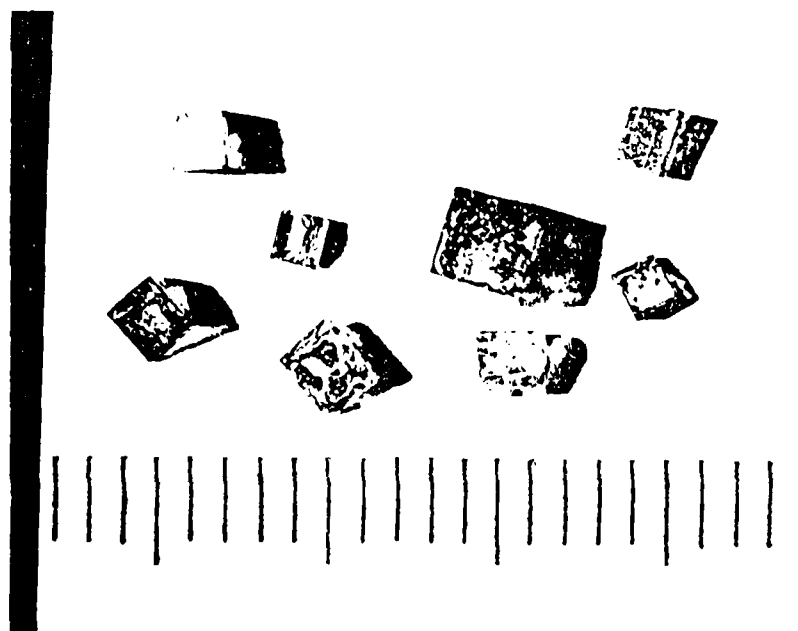


Fig. 1 Crystals of PMN (a) and PST (b) as grown.

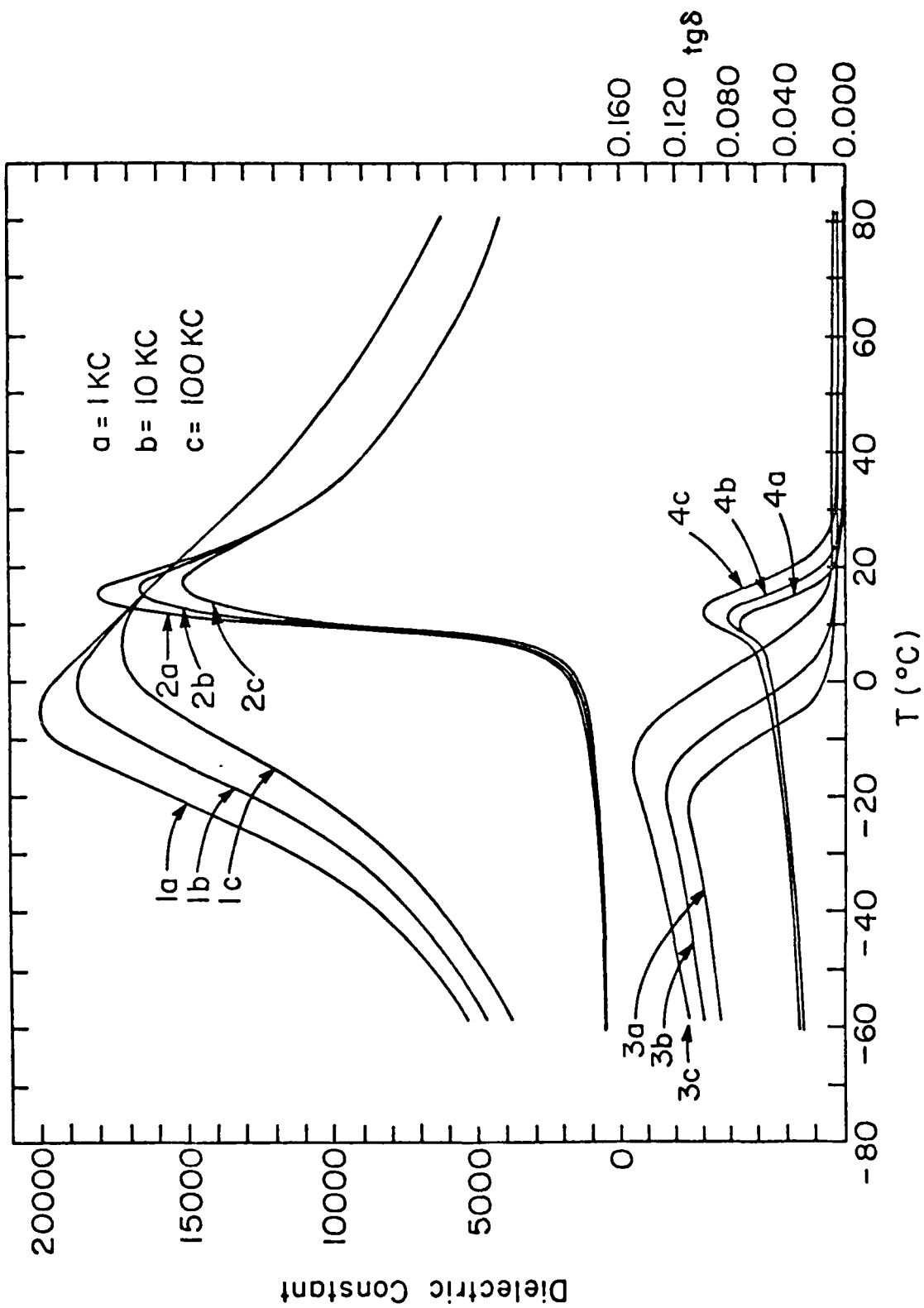


Figure 2. Dielectric constant and dielectric loss of PMN (1,3) and PST (2,4) single crystals.

APPENDIX 32

N. Setter, L.E. Cross. The Contribution of Structural Disorder to Diffuse Transitions in Ferroelectrics. J. Mat. Sci. 15, 2478 (1980).

The contribution of structural disorder to diffuse phase transitions in ferroelectrics

N. SETTER, L. E. CROSS

*Materials Research Laboratory, The Pennsylvania State University, University Park,
PA 16802, USA*

Simple crystal-chemical arguments were used to suggest that in the ferroelectric perovskite lead-scandium-tantalate ($\text{PbSc}_{0.5}\text{Ta}_{0.5}\text{O}_3$) the B-site cations in this simple ABO_3 structure should be close to the boundary between order and disorder. Both polycrystal ceramic and single crystal materials of this composition have been grown. In this study X-ray powder diffraction is used to identify the strong superlattice reflections associated with the ordering of scandium and tantalum ions in the B-site, and to demonstrate quantitatively how the degree of ordering can be modified by suitable thermal treatment. Thermal changes associated with the ferroelectric Curie temperature have been measured by differential scanning calorimetry and show very clearly the manner in which the diffuse (broadened) transition in this crystal is sharpened by increase in the B-cation ordering.

1. Introduction

A number of ferroelectric compounds and solid solutions of complex composition in the perovskite and tungsten bronze families exhibit a characteristic low-frequency dielectric dispersion and several unusual associated dielectric, optical and thermal properties [1-3]. Materials with this characteristic "relaxor-type" behaviour and associated properties are often referred to as ferroelectrics with diffuse or broadened phase transitions [4]. One possible explanation for the "smearing" of the normally sharp ferroelectric phase change [4] is in the statistical composition fluctuations which must occur if crystallographically equivalent sites are occupied randomly by different cations. A statistical treatment based on a postulated Gaussian distribution of local Curie temperatures associated with composition fluctuations has been given by Rolov [5] and does provide reasonable agreement with experiment. Some experimental support suggesting a sharpening of the transition with increasing order in the cation arrangement can be found from data on several different solid-solutions [3], but a clear resolution of the problem is masked by the changing compositions used in these studies.

In the following, simple crystal chemical principles have been used to suggest a compound, lead scandium tantalate (PST) which should be on the boundary between the ordered and disordered B-site cation arrangements. Powders, ceramics and single crystals of PST have been grown. This paper describes the crystal-chemical arguments used in selecting PST, and the X-ray diffraction studies which establish that the degree of disorder in the B-site cation arrangement can be controlled by suitable thermal treatment. To demonstrate that ordering of the B-cations does effect the sharpness of the ferroelectric transitions at the Curie temperature, differential scanning calorimetry has been used to delineate the associated thermal changes in samples with identical composition but different degrees of ordering.

In subsequent papers the influence of the ordering upon the dielectric, ferroelectric and elastoelectric properties of single crystals and ceramics will be discussed.

2. Crystal-chemical considerations

The simple crystal chemical arguments used to elaborate the structure and chemistry required may be briefly summarized as follows:

(1) Structure: In order to reduce the energy for ordering, a simple structure is preferred. There is some evidence in the literature [6] that the Curie temperature and the degree of ordering may be changed by annealing in some tungsten bronze structure ferroelectrics. However, the perovskite of the form $A(B'B'')O_3$ is a considerably simpler form and is therefore preferred.

(2) Cation ratio: The same argument of simplicity to reduce ordering energy would suggest a cation ratio $B'B'' = 1/1$ and thus eliminate the classical relaxors like $Pb(Mg_{1/3}Nb_{2/3})O_3$.

(3) Charge on B-site ions: Large differences in the valence between B' and B'' , as in $PbMg_{0.5}W_{0.5}O_3$, result in a very strong tendency to order through electrostatic forces. In the case of identical charges the correlation energy is related to cation size [7]. Thus, an appropriate compromise might suggest an $A(B_{0.5}^{2+}B_{0.5}^{3+})O_3$ composition.

(4) B-site ion size: Materials with large size differences in the B-cations are driven strongly towards ordering by electric forces, whilst materials with near identical cation size, for example $Ba(Fe_{0.5}Nb_{0.5})O_3$, may stay disordered even after long annealing. Gallaso and Darby [8] suggest for $Ba(M_{0.5}Nb_{0.5})O_3$ structures that the critical differences in Ahrens radius for ordering must lie between 7 and 17%.

(5) A-site ion size: The role of the A-site ion in modulating the interaction may be seen by comparing the disordered $Pb(Zn_{1/2}Nb_{1/2})O_3$ and $Ba(Zn_{1/2}Nb_{1/2})O_3$ with the corresponding ordered $Sr(Zn_{1/2}Nb_{1/2})O_3$. As would be expected, reducing the size of A-site cation enhances the elastic drive towards ordering on the B-site.

Similar arguments could be advanced in consideration of $(A'A'')BO_3$ perovskites, but the smaller base of available experimental data would make system selection more difficult.

To facilitate the selection of a suitable boundary composition, at the edge of stability for ordering, structural data were collected from the literature for about 150 compounds with the $AB_{0.5}B'_{0.5}O_3$ composition. A computer program tabulated the ionic radii R_A , R_B , $R_{B'}$, and the information on ordering. A small section of the tabulated data is given in Table I.

Taking consideration also of the known ferroelectric properties, the tabulation clearly suggested $Pb(Sc_{0.5}Nb_{0.5})O_3$ as a suitable starting candidate. Since, however, it would be desirable to be able to use X-ray diffraction to detect B-site order, a

composition with a larger difference in atomic number (scattering power) between B-site ions would be desirable. Since $Pb(Sc_{0.5}Ta_{0.5})O_3$ (PST) is also ferroelectric, with a convenient Curie range near room temperature and with very similar valence and size characteristics for its ions, this crystal was chosen for the initial study.

3. Experiment

3.1. Sample preparation

Powders of the PST composition were prepared from stoichiometric proportions of the constituent oxides: PbO , Sc_2O_3 and Ta_2O_5 using reagent or high purity grade chemicals. Following ball milling under alcohol for 20 hours, the milled powders were dried, then calcined at $800^\circ C$ for 2 hours. The calcined powder was then reground, pressed into pellets and fired at $1300^\circ C$ for 1 hour.

The degree of ordering in the Sc-Ta occupied B-sites was controlled by thermal annealing for different time periods at $1000^\circ C$. Disorder was induced by a short firing to between 1400 and $1560^\circ C$ followed by rapid quenching. It may be noted, however, that the ease with which the state of ordering could be changed depended markedly upon the thermal prehistory of the sample. To avoid chemical differences between samples, weight loss throughout all thermal treatments was kept below 1 wt%.

3.2. Ordering studies

X-ray diffraction was used to establish quantitatively the degree of ordering in the scandium and tantalum. In the ordered form, scandium and tantalum ions alternate in adjacent B-sites, forming two interpenetrating sublattices and giving an effective doubling of the primitive a -spacing. Thus the X-ray diffraction pattern is characterized by the appearance of superlattice reflections corresponding to half-integer spacing of the disordered structure.

X-ray diffraction patterns, scanned at a rate of $0.2^\circ \text{ min}^{-1}$, were taken using a General Electric diffractometer using $CuK\alpha$ radiation. Two superlattice reflections (111) and (311) were compared with adjacent normal lattice reflections (200) and (222) respectively (indices refer to the double-cell unit cell). The order parameter S for a particular sample was determined by comparing the ratio of the observed superlattice reflection to the base lattice reflection for that sample with the calculated ratio of intensities for perfect ordering

TABLE I The relation between ordering and ionic size of A and B ions in $A(B_{1/2}Nb_{1/2})O_3$

$A(B_{1/2}Nb_{1/2})O_3$	Ionic radii*			Order of phase	Reference
	A	B	B ⁺		
$Ca(NbAl)O_3$	1.49	0.78	0.67	ordered	[9]
$Sr(NbAl)O_3$	1.54	0.78	0.67	ordered	[10]
$Ba(NbAl)O_3$	1.74	0.78	0.67	ordered	[10]
$Pb(NbNi)O_3$	1.63	0.78	0.74	disordered	[11]
$Ba(NbNi)O_3$	1.74	0.78	0.74	disordered	[12]
$Ca(NbCr)O_3$	1.49	0.78	0.755	disordered	[9]
$Sr(NbCr)O_3$	1.54	0.78	0.755	ordered	[12]
$Ca(NbFe)O_3$	1.49	0.78	0.755	disordered	[9]
$Sr(NbFe)O_3$	1.53	0.78	0.755	disordered	[13]
$Pb(NbFe)O_3$	1.63	0.78	0.755	disordered	[14]
$Ba(NbFe)O_3$	1.74	0.78	0.755	disordered	[14]
$Pb(NbMn)O_3$	1.63	0.78	0.785	disordered	[15]
$Ba(NbMn)O_3$	1.74	0.78	0.785	disordered	[16]
$Sr(NbSc)O_3$	1.54	0.78	0.885	ordered	[10]
$Pb(NbSc)O_3$	1.63	0.78	0.885	{ partly ordered	[17]
				{ disordered	[14]
$Ba(NbSc)O_3$	1.74	0.78	0.885	{ disordered	[14]
				{ ordered	[10]
$Ca(NbIn)O_3$	1.49	0.78	0.94	ordered	[9]
$Sr(NbIn)O_3$	1.54	0.78	0.94	ordered	[9]
$Pb(NbIn)O_3$	1.63	0.78	0.94	disordered	[15]
$Ba(NbIn)O_3$	1.74	0.78	0.94	{ ordered	[18]
				{ partly ordered	
$Ca(NbYb)O_3$	1.49	0.78	1.008	ordered	[9]
$Pb(NbYb)O_3$	1.63	0.78	1.008	disordered	[14]
$Ba(NbYb)O_3$	1.74	0.78	1.008	{ partly ordered	[19]
				{ disordered	[14]
$Ca(NbHo)O_3$	1.49	0.78	1.041	ordered	[9]
$Pb(NbHo)O_3$	1.63	0.78	1.041	ordered?	[15]
$Ba(NbHo)O_3$	1.74	0.78	1.041	partly ordered	[19]

* Ionic radii according to R. D. Shannon and C. T. Prewitt [20].

That is

$$S^2 = \frac{\left(\begin{smallmatrix} 1 & 1 & 1 \\ 2 & 0 & 0 \end{smallmatrix} \right)_{\text{observed}}}{\left(\begin{smallmatrix} 1 & 1 & 1 \\ 2 & 0 & 0 \end{smallmatrix} \right)_{\text{calc. } S=1}}$$

and

$$S^2 = \frac{\left(\begin{smallmatrix} 1 & 3 & 1 \\ 2 & 2 & 2 \end{smallmatrix} \right)_{\text{observed}}}{\left(\begin{smallmatrix} 1 & 3 & 1 \\ 2 & 2 & 2 \end{smallmatrix} \right)_{\text{calc. } S=1}}$$

Development of the (111) superlattice line on extended thermal annealing is clearly evident in the X-ray patterns shown in Fig. 1. The corresponding calculated order parameters are shown on each picture.

3.3. Ferroelectric transitions

In ferroelectric perovskites the transitions in the degree of ordering which occurs at the Curie point critical temperature, T_c , is weakly a first order one: it is accompanied by a small latent heat and a peak in the specific heat. In the diffuse transition materials, since each microvolume transforms at a different temperature these heat changes are expected to be spread out, and the sharp peak reduced to a general rounded "hump". Thus, in samples where the degree of ordering can be controlled, it would be expected that the thermal change would sharpen and become larger with

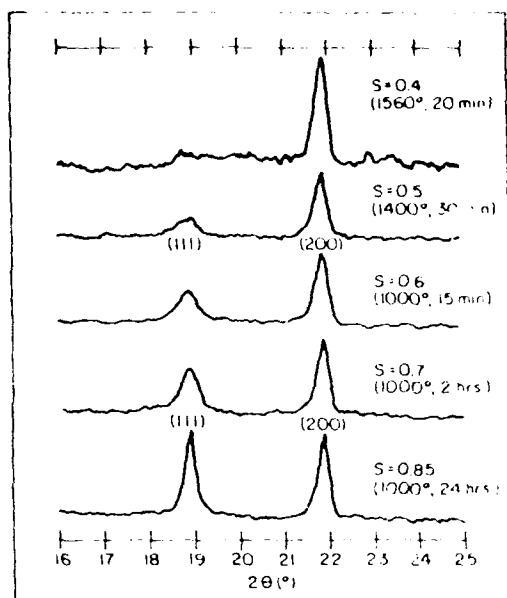


Figure 1 X-ray diffraction patterns of PST with varying degrees of ordering

increasing order better defining the local composition.

Heat capacities for samples with differing degrees of ordering, established by the X-ray measurements described above, were measured for temperatures around the transition range (see Fig. 2) using a duPont 900 thermal analyser with a differential scanning calorimetric cell (DSC). The cell was first cooled by liquid nitrogen to a temperature of about -77°C and then heated at a rate of $12^{\circ}\text{C min}^{-1}$ up to $+90^{\circ}\text{C}$. The heat of transition for each sample was calculated by extrapolating a base line from the region outside the transition range, and determining the area between this extrapolated base and the measured thermal curve.

4. Discussion

The X-ray diffraction measurements give clear evidence that $\text{Pb}(\text{Sc}_{0.5}\text{Ta}_{0.5})\text{O}_3$, as expected from the crystal chemistry, is near to the boundary between order and disorder in the Sc-Ta arrangement, and that the degree of ordering can be controlled over quite a wide range by suitable thermal annealing. The simple thermal measurements give a clear indication that the degree of ordering does have a strong effect upon the ferroelectric Curie temperature with the Curie range narrowing markedly as a high degree of order is established.

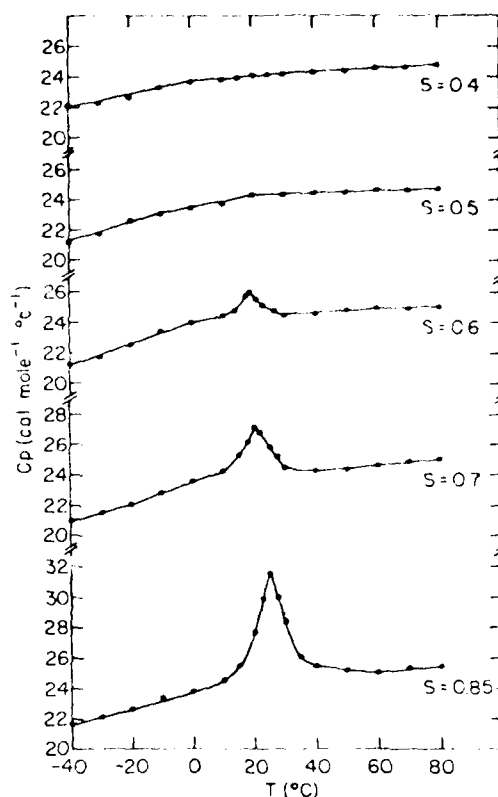


Figure 2 Variation of heat capacity of PST with degree of ordering

Burggraaf and Stenger [20] correlate ΔS and $\Delta S/T_c$ at the Curie transition with the probability of occurrence of heterophase fluctuations. Large values of the ratio $\Delta S/T_c$ giving sharp transitions, and lower values leading to more diffuse behaviour. In Table II we have added our data for the differently ordered PST samples to the earlier compilation. It is interesting to note that the values fit in well, and link continuously the sharp transitions of PbTiO_3 and BaTiO_3 , and those more diffuse transitions of the PLZTs.

The PST is apparently an excellent vehicle for study of the characteristics of ferroelectrics with diffuse phase transitions. In later papers we shall report dielectric, ferroelectric and elasto-electric measurements on both ceramic and single crystal specimens, and upon additional X-ray studies to determine the volume of the ordered regions and the manner in which this changes with increased ordering.

TABLE II Transition entropies and enthalpies of PST and other ferroelectrics

Compound	T_c (K)	ΔH (cal. mol ⁻¹)	ΔS (cal. mol ⁻¹ K ⁻¹)	$\frac{\Delta S}{T_c} \times 10^3$ (cal. mol ⁻¹ K ⁻²)	Type of transition	Reference
PbTiO ₃	763	1150	1.51	1.98	sharp	[22]
BaTiO ₃	393	47	0.12	0.30	sharp	[22]
PST ($S = 0.85$)	297	87	0.29	0.98	sharp	This work
PST ($S = 0.7$)	294	52	0.18	0.61	sharp	This work
PST ($S = 0.6$)	292	20	0.07	0.24	slightly diffused	This work
PST ($S = 0.5$)					diffused	This work
PST ($S = 0.4$)					strongly diffused	This work
PLZT 17/30/70	320	18	0.06	0.17	diffused	[21]
PLZT 11.1/55/45	325	11	0.03	0.10	strongly diffused	[21]

Acknowledgement

This work was carried out under contract No. N00014-78-C-0291 from the Office of Naval Research.

References

- V. A. BOKOV and I. E. MYLNIKOVA, *Fiz. Tverd. Tela* 3 (1961) 871, in Russian. For translation see *Soviet Physics Solid State* 3 (1961) 613.
- JUM KUWATA, K. UCHINO and S. NOMURA, *Ferroelectrics* 22 (1979) 863.
- A. M. GLASS, *J. Appl. Phys.* 40 (1969) 4699.
- G. A. SMOLENSKI, Proceedings of the 2nd International Meeting on Ferroelectricity, Kyoto (1969) (Phys. Soc. Japan, Tokyo, 1970) p. 26.
- B. N. ROLOV, *Fizika Tverd. Tela* 6 (1964) 2128, in Russian. For translation see *Soviet Physics Solid State* 6 (1976) 1676.
- G. BURNS and D. F. O'KANE, *Phys. Lett.* 28A (1969) 776.
- V. Va. FRIZBERG and B. A. ROLOV, *An. SSSR, Ser. Fiz. Giz.* 28 (1964) 649, in Russian. For translation see 28 (1964) 556.
- F. GALASSO and W. DARBY, *S. Phys. Chem.* 66 (1962) 131.
- V. S. FILIPEV and E. G. FRESENKO, *Kristallografiya* 10 (1965) 798, in Russian. For translation see *Kristallografiya* 10 (1965) 243.
- E. G. FRESENKO *et al.*, *Izv. An. SSSR, Ser. Fiz.* 28 (1964) 669, in Russian. For translation see *Izv. An. SSSR, Ser. Fiz.* 28 (1964) 576.
- L. I. SHUOVNEVA and Yu. N. VENEVSTEV, *JETP* 49 (1965) 1038, in Russian. For translation see 22 (1966) 722.
- G. B. BLASSE, *Inorg. Nucl. Chem.* 27 (1965) 993.
- F. S. GALASSO *et al.*, *J. Amer. Chem. Soc.* 81 (1959) 820.
- A. I. AGRANOVSKAYA, *Bull. Acad. Sci. USSR* 24 (1960) 1271.
- M. F. KUPRIYANOV and E. G. FRESENKO, *ibid.* 29 (1965) 930.
- V. S. FILIPEV *et al.*, *Kristallografiya* 6 (1962) 770, in Russian. For translation see *Kristallografiya* 6 (1962) 616.
- I. G. ISMAILZADE, *ibid.* 4 (1959) 417, in Russian. For translation see *Kristallografiya* 4 (1959) 389.
- F. C. GALASSO, "Structure, Properties and Preparation of Perovskite Type Compounds" (Pergamon Press, Oxford, 1969).
- R. D. SHANNON and C. T. PREWITT, *Acta Cryst.* B25 (1969) 925.
- A. J. BURGGRAAF and C. STENGER, *Ferroelectrics* 20 (1978) 185.
- J. C. BURFOOT, "Ferroelectrics" (Van Nostrand, London, 1967) p. 224.

Received 8 February and accepted 3 March 1980.

APPENDIX 33

N. Setter, L.E. Cross. The Role of B-Site Cation Disorder in Diffuse Phase Transition Behavior of Perovskite Ferroelectrics. J. Appl. Phys. 51, 4356 (1980).

The role of B-site cation disorder in diffuse phase transition behavior of perovskite ferroelectrics

N. Setter and L. E. Cross

Materials Research Laboratory, The Pennsylvania State University, University Park, Pennsylvania 16802

(Received 24 March 1980; accepted for publication 9 May 1980)

In $\text{Pb}(\text{Sc}_{0.5}\text{Ta}_{0.5})\text{O}_3$ it has been shown that the degree of order in the B-site Sc^{3+} , Ta^{5+} cations can be controlled by suitable thermal annealing. For samples which have been well-ordered by long annealing, dielectric measurements on single crystals show a normal first-order ferroelectric phase change at 13°C and a maximum low-temperature spontaneous polarization of $23.0\mu\text{C}/\text{cm}^2$. With increasing disorder, the crystals begin to exhibit the classical diffuse phase transition of a ferroelectric relaxor, with a broad Curie range and strong low-frequency dielectric dispersion in the transition range. X-ray diffraction measurements of the size of the ordered microregions suggest that ordering proceeds by different mechanisms in single-crystal versus ceramic samples, though the resulting effects upon the dielectric behavior are very similar.

PACS numbers: 77.80.-e, 71.55.Jv

I. INTRODUCTION

Structural disorder upon certain crystallographic sites has long been believed to be responsible for the diffuse phase transition (DPT) in a large group of ferroelectric oxides of complex composition with structures in the perovskite and tungsten bronze families. The diffuse phase transition is evidenced in many properties associated with the ferroelectric transition: slow change in dielectric permittivity, and very slow temperature dependence of the spontaneous electric polarization in the relaxation range are examples of the dielectric characteristics.

It is suggested that crystals exhibiting DPT can be viewed as having composition fluctuations on a microscopic scale and so of consisting of microvolumes each with slightly

different Curie temperature for the onset of ferroelectric polarization.¹ The overall properties result from the distribution of the Curie temperatures of these individual microvolumes. Expressions for the dielectric properties have been derived in a statistical treatment by Rolov,² and Clarke and Burfoot³ have expanded the model to include a composition dependent parameter. The model of Rolov predicts successfully the observed dielectric properties of ferroelectric relaxors such as lead magnesium niobate (PMN) and lead zinc niobate (PZN), but no verification appears yet to have been given for the direct role of composition fluctuations.

In solid solutions it has been observed that as the composition becomes close to that favoring a homogeneous distribution, the phase transition sharpens^{4,5} and an increase in structural ordering could explain the observed behavior but has not been verified. A difficulty in the interpretation of all earlier observations has been the changing chemical composition accompanying the changes observed in the solid solutions, which makes unequivocal interpretation impossible.

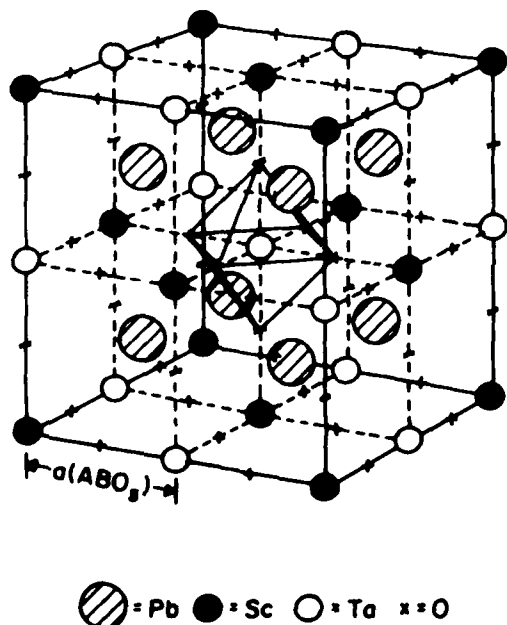


FIG. 1. Structure of ordered perovskite $\text{Pb}(\text{Sc}_{0.5}\text{Ta}_{0.5})\text{O}_3$ [after Galasso (7)]

TABLE I. Degree of ordering and size of ordered domains for PST of various annealing treatments.

Material	Heat treatment	Degree of order (S)	Approximate size of ordered domains
Ceramic PST	No annealing	0.37	100 Å
	15 min at 1000 °C	0.46	200 Å
	40 min at 1000 °C	0.51	300 Å
	65 min at 1000 °C	0.59	750 Å
	2 h at 1000 °C	0.72	900 Å
	4 h at 1000 °C	0.80	> 1000 Å
	6 h at 1000 °C	0.81	> 1000 Å
	9 h at 1000 °C	0.83	> 1000 Å
	24 h at 1000 °C	0.86	> 1000 Å
	103 h at 1000 °C	0.86	> 1000 Å
Single-crystal PST	As grown	0.80	100 Å
	1 h at 1400 °C	0.35	< 100 Å

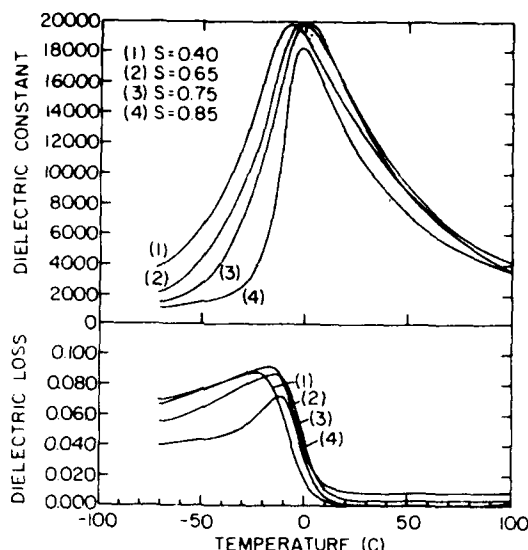


FIG. 2. Temperature dependence of dielectric permittivity and dielectric loss at 1 kHz of PST ceramics with different degree of order.

It has been shown⁶ that $\text{Pb}(\text{Sc}_{0.5}\text{Ta}_{0.5})\text{O}_3$ (PST) is close to the limit of stability between order and disorder for the B-site cations, and that the compound can exist at room temperature with different degrees of order. The influence of changing order upon the ferroelectric phase change can therefore be demonstrated very clearly in PST without any need to change the chemistry. The results of experiments upon both single crystal and ceramic samples with controlled degrees of ordering are presented in this paper.

II. EXPERIMENTS

Samples of the compound PST were prepared by reacting stoichiometric proportions of the mixed PbO , Sc_2O_3 , and

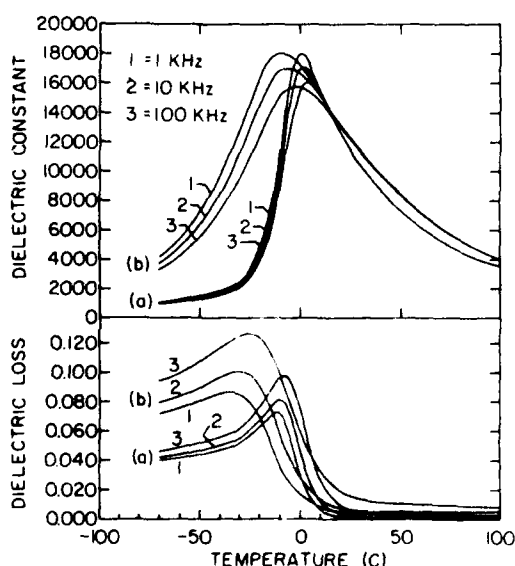


FIG. 3. Frequency dispersion of dielectric permittivity and dielectric loss of (a) mostly ordered ($S = 0.85$) ceramic and (b) disordered ($S = 0.40$) ceramic.

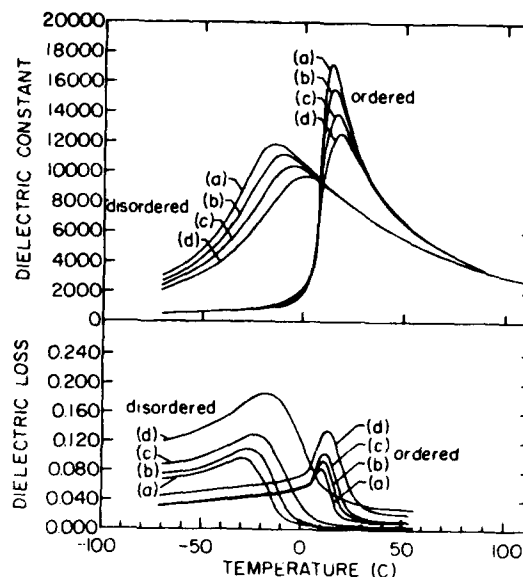


FIG. 4. Temperature dependence of dielectric constant and dielectric loss for ordered ($S = 0.80$) and disordered ($S = 0.35$) single crystals at (a) 1 kHz, (b) 10 kHz, (c) 100 kHz, (d) 1000 kHz.

Nb_2O_5 . The mixture was ball milled under alcohol to achieve intimate mixing, then fired for 2 h at 800 °C. The resulting cake was reground, pressed into pellets, and refired at 1300 °C for 1 h. Powder x-ray diffraction of this reacted powder showed a simple cubic perovskite structure with very small traces of a pyrochlore phase present.

To prepare ceramic disks for dielectric studies, the reacted powder was ground again to pass No. 400 mesh and pressed into 3/8-in-diam pellets, using a small amount of polyvinyl alcohol as a binder. The pellets were then sintered at 1560 °C in a closed alumina crucible using extra PST pellets with 20 wt. % added PbO to maintain a PbO -rich atmo-

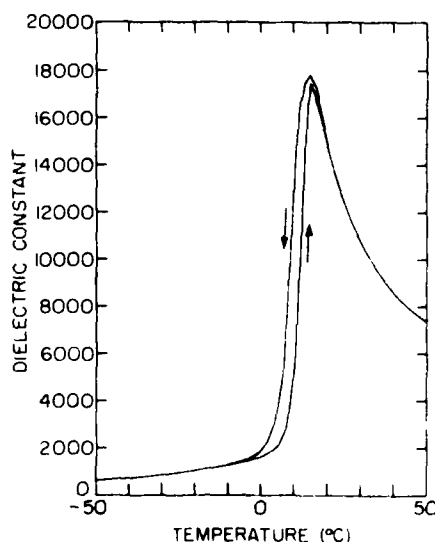
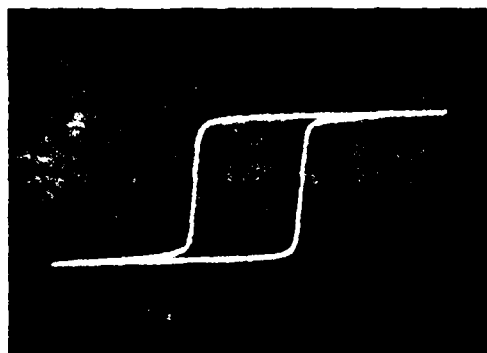


FIG. 5. Thermal hysteresis of an ordered crystal (1 kHz).



(a)



(b)



(c)



(d)

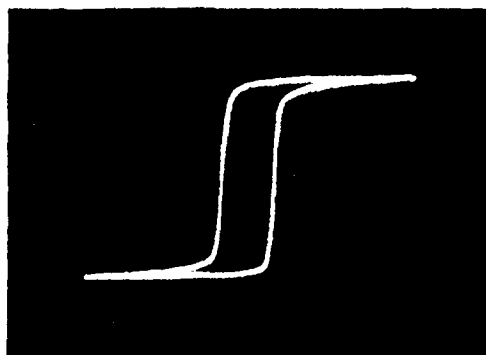
FIG. 6. Dielectric hysteresis of disordered PST single crystal. (a) -58°C , (b) -48°C , (c) -40°C , (d) -20°C .

sphere during firing. By this technique, weight loss during firing was kept to less than 2.5%, and final densities in the range 94–97% theoretical were achieved.

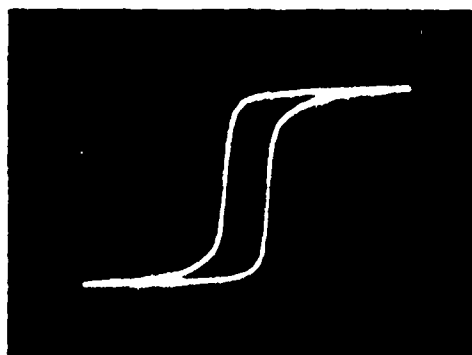
To establish the required degree of ordering, pellets were sliced and annealed at 1000°C for different lengths of time in the range from 10 min to 100 h. The degree of ordering and the size of the ordered domains were established by x-ray diffraction. In PST, ordering places Sc^{3+} and Ta^{5+} ions on adjacent B sites in a three-dimensional array, leads to an effective doubling of the a parameter of the original perovskite cell (Fig. 1), and thus to the appearance of superlattice lines in the x-ray diffractograms. The degree of ordering was determined by calculation from the ratio of the integrated intensities of pairs of base and superlattice reflections, and the ordered domain size determined by the broadening of the superlattice reflections with respect to the base lattice peaks. These data are summarized in Table I. It should be noted that the degree of ordering achieved is not just a function of the annealing time from the initial high-temperature quenched state, but does depend in a complex manner upon the previous thermal history of the individual sample. In these annealing studies no change was detected in the lattice spacing between ordered and disordered states.

Single crystals for dielectric study were grown by a flux technique which has been described elsewhere.⁸ In the as-grown condition, the B-site cations are well ordered. To establish a disordered condition, crystals were heated to 1400°C and air quenched. Stoichiometry of the single crystals was checked both before and after heat treatments using energy dispersive x-ray spectroscopy, and no stoichiometry change was detected.

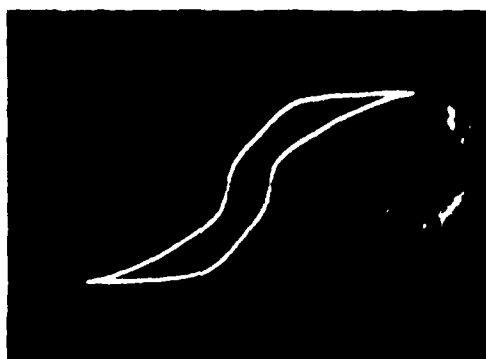
Dielectric permittivity and loss tangent under weak ac fields were measured at frequencies of 1, 10, 100, and 1,000 kHz using a Hewlett Packard 4270 A automatic capacitance bridge under full program control in a HP9825 bus-controlled system. The sharpening of the permittivity versus temperature curves measured at 1 kHz as a function of increasing order of B-site cations is clearly evident in Fig. 2. The strong control of the degree of ordering upon the dielectric dispersion in the transition region is evident in Fig. 3, which contrasts the behaviors of disordered and highly ordered ceramics. Weak-field permittivity data for single-crystal PST, measured with the E field applied along (001) is shown in Fig. 4. Again the highly dispersive character of the broadened transition in a 35% ordered sample is contrasted with the sharp transition in a crystal with 80% ordering. The



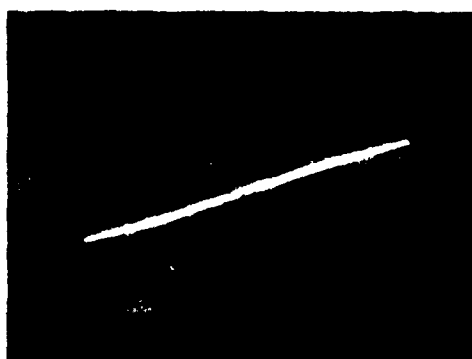
(a)



(b)



(c)



(d)

FIG. 7. Dielectric hysteresis of ordered PST single crystal. (a) 0 °C, (b) 7 °C, (c) 8 °C, (d) 14 °C.

first-order nature of the transition in the well-ordered crystal is further suggested by the obvious thermal hysteresis between heating and cooling curves (Fig. 5).

High-field behavior was explored using a balanced Sawyer-Tower Bridge. The dielectric hysteresis in the disordered single crystal shows the characteristic rounded curves and slow saturation for temperatures in the transition range [Figs. 6(a)–6(d)] in contrast to the sharp square lower coercivity behavior of the highly ordered crystals [Figs. 7(a)–7(d)]. The P_r values obtained by extrapolation of the saturation arms of the loops are shown in Fig. 8, where the major shift in Curie temperatures which accompanies ordering in the monocrystal is clearly evident, as is the sharper transition in the ordered sample.

III. DISCUSSION

The dielectric properties of the disordered crystals and ceramics of PST show all the characteristic features of a ferroelectric with DPT: (i) The dielectric peaks are rounded in the ϵ versus T curves; (ii) the temperature of peak permittivity shifts up with increasing frequency; (iii) strong dispersion in the radio frequency range occurs over the transition region; (iv) rounded dielectric hysteresis curves exhibit slow saturation and large effective coercivity.

With enhanced B-site cation ordering, however, crystals of the same composition show classical sharp transition behavior: (1) very sharp dielectric peaks, (2) almost no shift of T_m with frequency, (3) thermal hysteresis, and (4) square loops with low coercivity.

The dielectric behavior is qualitatively similar between ceramic and single crystals, and it is clear that the disorder

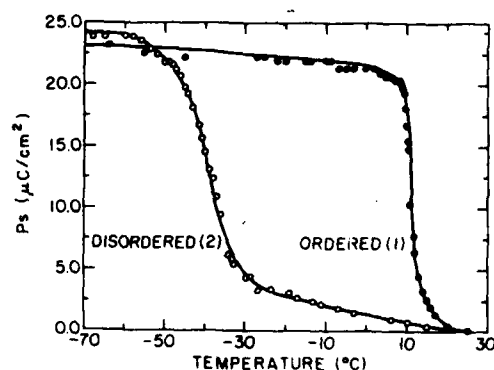


FIG. 8. Spontaneous polarization for ordered (1) and disordered (2) single crystals.

which contributes the local composition fluctuations responsible for the dispersion behavior is on a scale which is much below the ceramic grain size. The maximum P_r value $\sim 20 \mu\text{C}/\text{cm}^2$ is reasonable for a ferroelectric perovskite oxide with $T_c \sim 13^\circ\text{C}$.

A major difference between the ceramic and single-crystal samples appears to exist in the mode by which the Sc:Ta-cation ordering occurs under thermal annealing. In the ceramic it is evident from Table I that the ordered domains expand continuously in size up to macroscopic dimensions with continuous heat treatment. In the single crystal, however, the domain sizes are always small even in the highly ordered crystal.

Altogether, the dependence of DPT on positional disorder has been demonstrated unequivocally for perovskite ferroelectric relaxors, using PST as a suitable example. Indeed, the effect of other parameters such as thermal fluctuations,

defects, and internal stresses cannot be inferred from the above experimental results. However, the results strongly support the model of compositional fluctuation as correctly describing the diffused phase transition in ferroelectric relaxors.

This work was supported by the Office of Naval Research, Contract No. N00014-78-C-0291.

¹G. A. Smolenskii, J. Phys. Soc. Jpn. **28**, 26 (1970).

²B. N. Rolov, Fiz. Tverd. Tela. (Leningrad) **6**, 2128 (1964) [Sov. Phys. Solid State **6**, 1676 (1965)].

³R. Clark and J. C. Burfoot, Ferroelectrics **8**, 505 (1974).

⁴A. M. Glass, J. Appl. Phys. **40**, 4699 (1969).

⁵L. Benguigi, K. Bethe, J. Appl. Phys. **47**, 2787 (1976).

⁶N. Setter, L. E. Cross, J. Mater. Sci. (in press).

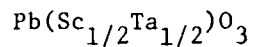
⁷F. S. Galasso, *Structure, Properties and Preparation of Perovskite-Type Compounds*, (Pergamon, New York, 1969).

⁸N. Setter, L. E. Cross, J. Cryst. Growth (in press).

APPENDIX 34

N. Setter, L.E. Cross. Pressure Dependence of the Dielectric Properties of $\text{Pb}(\text{Sc}_{1/2}\text{Ta}_{1/2})\text{O}_3$. Phys. Stat. Sol. A61, K71 (1980).

Pressure Dependence of the Dielectric Properties of



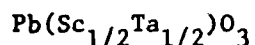
N. Setter, L.E. Cross

Materials Research Laboratory
The Pennsylvania State University
University Park, Pennsylvania 16802

Abstract

Pressure dependent dielectric properties were measured on a highly B-cation ordered $\text{Pb}(\text{Sc}_{.5}\text{Ta}_{.5})\text{O}_3$ (normal ferroelectric) and on a B-cation disordered $\text{Pb}(\text{Sc}_{.5}\text{Ta}_{.5})\text{O}_3$ (ferroelectric relaxor), using single crystals and ceramic samples. The hydrostatic electrostriction coefficient was found in this case to be insensitive to the degree of cation disorder. The value obtained, $Q_h = 0.87 \cdot 10^{-2} \text{ m}^4 \text{C}^{-2}$, is halfway between the value for simple perovskites and that for complex-perovskite relaxors.

Pressure Dependence of the Dielectric Properties of



Introduction

Ferroelectric relaxors of the perovskite family are known to have Curie constants (C) several times larger than those of normal perovskite ferroelectrics. Also, it has been shown that the electrostriction coefficients (Q_h) of ferroelectric relaxors are smaller than those of normal ferroelectrics (1). The observed high C and low Q_h are believed to be related to the disorder that exists on the B cation site of these relaxors.

$\text{Pb}(\text{Sc}_{1/2}\text{Ta}_{1/2})\text{O}_3$ (PST) has been shown to lie close to the limit of stability between order and disorder of the B cation site and to exist at room temperature in different degrees of order (2). It was found that the ordering of the B-site cations of PST changes its character from a diffuse transition to a normal first order ferroelectric type (3). This supports the composition-fluctuation model that is frequently used to explain diffused phase transition behavior (4).

The possibility to obtain both relaxor ferroelectric and normal ferroelectric behavior in the same chemical composition makes it simple to isolate the influence of the disorder alone on the Curie constant, on the electrostriction constant, and on other pressure dependent dielectric properties. As ferroelectric relaxors possess a potential for making excellent electrostrictive devices (5), this structure/property dependence of Q and C is of special interest.

Experimental Results

Both single crystals and polycrystalline materials were studied. The crystals were flux grown (6) ordered PST of 1.2-2.0 mm edge polished to 0.2-0.35 mm thickness with major (100) surface. Disorder was achieved by firing at 1400°C for one hour and rapid quenching. The crystals whose properties were compared had order parameter $S = 0.80$ and $S = 0.35$ for the ordered and the disordered crystals

respectively. The ceramic compared samples used in the experiments had order parameter $S = 0.85$ and $S = 0.40$ as determined by comparing x-ray diffraction superstructure lines. The preparation of the ceramic samples and delineation of the order parameter have been described elsewhere (3).

Hydrostatic pressure up to 5 kbar was generated by an air-driven intensifier pump and monitored by a Heize gauge. The pressure transmitting liquid was Plexol. The pressure vessel was held in an insulated box where temperature was varied by a resistive-tape heater and by dry-ice-cooled alcohol. The temperature was read by a chromel-alumel thermocouple placed adjacent to the sample. The temperature range which could be achieved was $+70^{\circ}\text{C}$ to -40°C . Each sample was first heated and the measurements were then taken upon cooling at a rate of about $2^{\circ}/\text{minute}$.

The capacitance was measured at frequencies of 1 kHz, 10 kHz, and 100 kHz (the small AC field applied along [001]) by a Hewlett-Packard 4270A automatic bridge.

The Curie constant C was calculated from dielectric data at temperatures far above the transition (70° - 120°C) measured at atmospheric pressure.

The dielectric constant around the transition for $p=0$, 1.46 and 3.64 kbars is shown in Figure 1 for the ordered crystal and the disordered crystal, and in Figure 2 for the ordered and the disordered ceramics. In the case of the disordered samples there is an apparent increase in the diffuseness of the transition with increasing pressure. This can be seen also to some extent for the ordered PST under the maximum pressure.

Figure 3(a) shows the dependence of the reciprocal permittivity upon pressure for the ordered crystal at temperatures in the range 22° - 52°C . From this graph Q_h is found to be $0.85 \cdot 10^{-2}$. Q_h does not vary with temperature within this range. In Figure 3(b) the same dependence is shown for the disordered

crystal, but in this case the dependence is nonlinear and Q_h must be derived.

For relaxor ferroelectrics of perovskite type, the dielectric permittivity dependence upon temperature and pressure has been shown (1) to take the form

$$\frac{1}{\epsilon} = \frac{1}{\epsilon_m} + \frac{(T-T_0)^2}{2 \epsilon_m \delta^2} \quad (1)$$

and

$$\frac{1}{\epsilon} = \frac{1}{\epsilon_m} + \frac{(2Q_h C)^2 (p-p_0(T))^2}{2 \epsilon_m \delta^2} \quad (2)$$

where δ is the diffuseness parameter and $P_0(T) = (T_0 - T)/2Q_h C$.

Applying (1) to disordered PST crystals gave $\delta = 52^\circ$ and $1/\epsilon_m = 9.6 \cdot 10^{-5}$. Plotting $(1/\epsilon - 1/\epsilon_m)^{1/2}$ vs $[p-p_0(T)]$ as shown in Figure 4 yields $Q_h = 0.88 \cdot 10^{-2}$ when taking $\delta = 45^\circ$ and $1/\epsilon_m = 8.6 \cdot 10^{-5}$ which is close to the above values. The Q_h value of the disordered ceramic was obtained by the same manner.

Table 1 summarizes the data obtained for this value at Q's and C's of ordered and disordered PST.

Discussion

Contrary to our expectation from earlier measurements on ferroelectrics with diffuse phase transitions (1), the electrostriction constant Q_h is of the same order in both ordered and disordered samples. The Curie constant appears as expected somewhat smaller in the ordered samples but the difference is not large.

As a very simple intuitive explanation for the low Q_h and higher C values in relaxor ferroelectric crystals with diffuse phase transitions, Uchino et al. (1) propose a simple "rattling ion" model in which it is proposed that in the disordered structure, the random distribution of larger lower valence cations prop open the oxygen octahedra permitting very high permittivities (large C) but uncoupling polarization and strain (low Q). While in the corresponding ordered structure, the octahedra readjust dimensions to suit the ordered cation

arrangement closer coupling the system for larger Q_h and lower C values.

It may be noted that to permit the order:disorder to be accomplished thermally in $\text{Pb}(\text{Sc}_{1/2}\text{Ta}_{1/2})\text{O}_3$, the system was deliberately selected for the similar size of the B site cations, and indeed x-ray measurements show no detectable difference in lattice parameter between ordered and disordered form. Thus on the basis of the simple model Q and C should not change markedly on ordering, and it is perhaps interesting to note that in magnitude they are indeed almost halfway between values measured for simple perovskites and those measured on relaxors like $\text{Pb}(\text{Mg}_{1/3}\text{Nb}_{2/3})\text{O}_3$ and $\text{Pb}(\text{Zn}_{1/3}\text{Nb}_{2/3})\text{O}_3$.

Unfortunately for the $\text{Pb}(\text{Sc}_{1/2}\text{Ta}_{1/2})\text{O}_3$ it was not possible to anneal to a completely ordered state, so that the results, though suggestive, are not completely definitive, and measurements on a completely ordered crystal would be desirable.

Acknowledgment

This work was supported by the Office of Naval Research, Contract No. N00014-78-C-0291.

References

1. K. Uchino, L.E. Cross, R.E. Newnham, S. Nomura, J. Appl. Phys. 51, 1142 (1980).
2. N. Setter, L.E. Cross, J. Mater. Sci. (in press).
3. N. Setter, L.E. Cross, J. Appl. Phys. (in press).
4. G.A. Smolenskii, Proc. 2nd International Meeting on Ferroelectricity, Kyoto, Japan, Suppl. J. Phys. Soc. Japan 28, 26 (1970).
5. S.J. Jang, K. Uchino, S. Nomura and L.E. Cross, Ferroelectrics 27, 31-34 (1980).
6. N. Setter, L.E. Cross, J. Cryst. Growth (in press).
7. K. Uchino, S. Nomura, L.E. Cross, R.E. Newnham, J. Phase Trans. (in press).

Table 1. C , Q_h , and $\frac{\Delta T}{\Delta p}$ for different PST samples.

$\text{Pb}(\text{Sc}_{1/2}\text{Ta}_{1/2})\text{O}_3$	Diffuseness Parameters	C	Q_h	$\frac{\Delta T}{\Delta p}$
		$\times 10^5 \text{ K}$	$\times 10^{-2} \text{ m}^2 \text{ C}^{-2}$	$^\circ\text{K-kbar}^{-1}$
Disordered crystal ($S = 0.35$)	$\delta = 45^\circ (52^\circ)$ $\frac{1}{\epsilon_m} = 8.6 \cdot 10^{-5}$	2.8	0.88	-3.6
Disordered ceramic ($S = 0.40$)	$\delta = 38^\circ (45^\circ)$ $\frac{1}{\epsilon_m} = 5.0 \cdot 10^{-5}$	3.0	0.95	-3.8
Ordered ceramic ($S = 0.85$)	---	2.9	0.80 ± 0.05	-3.1
Ordered crystal ($S = 0.80$)	---	2.4	0.85	-2.0
Average value for PST		2.80 ± 0.25	0.87 ± 0.06	

Figure Captions

Figure 1. $\epsilon(T, p)$ of (a) disordered ($S=0.35$) PST crystal (b) ordered ($S=0.80$) PST crystal ($f=1$ kHz).

1. $p = 0$
2. $p = 1.46$ kbar
3. $p = 3.64$ kbar

Figure 2. $\epsilon(T, p)$ of (a) disordered ($S=0.40$) and (b) ordered ($S=0.85$) PST ceramics ($f=100$ kHz).

1. $p = 0$
2. $p = 1.46$ kbar
3. $p = 3.64$ kbar

Figure 3. The dependence of ϵ upon pressure at various temperatures above the transition. (a) ordered PST crystal ($S=0.80$); (b) disordered crystal ($S=0.35$).

Figure 4. $(\epsilon - \epsilon_m)^{1/2}$ vs pressure at different temperatures of disordered PST single crystal.

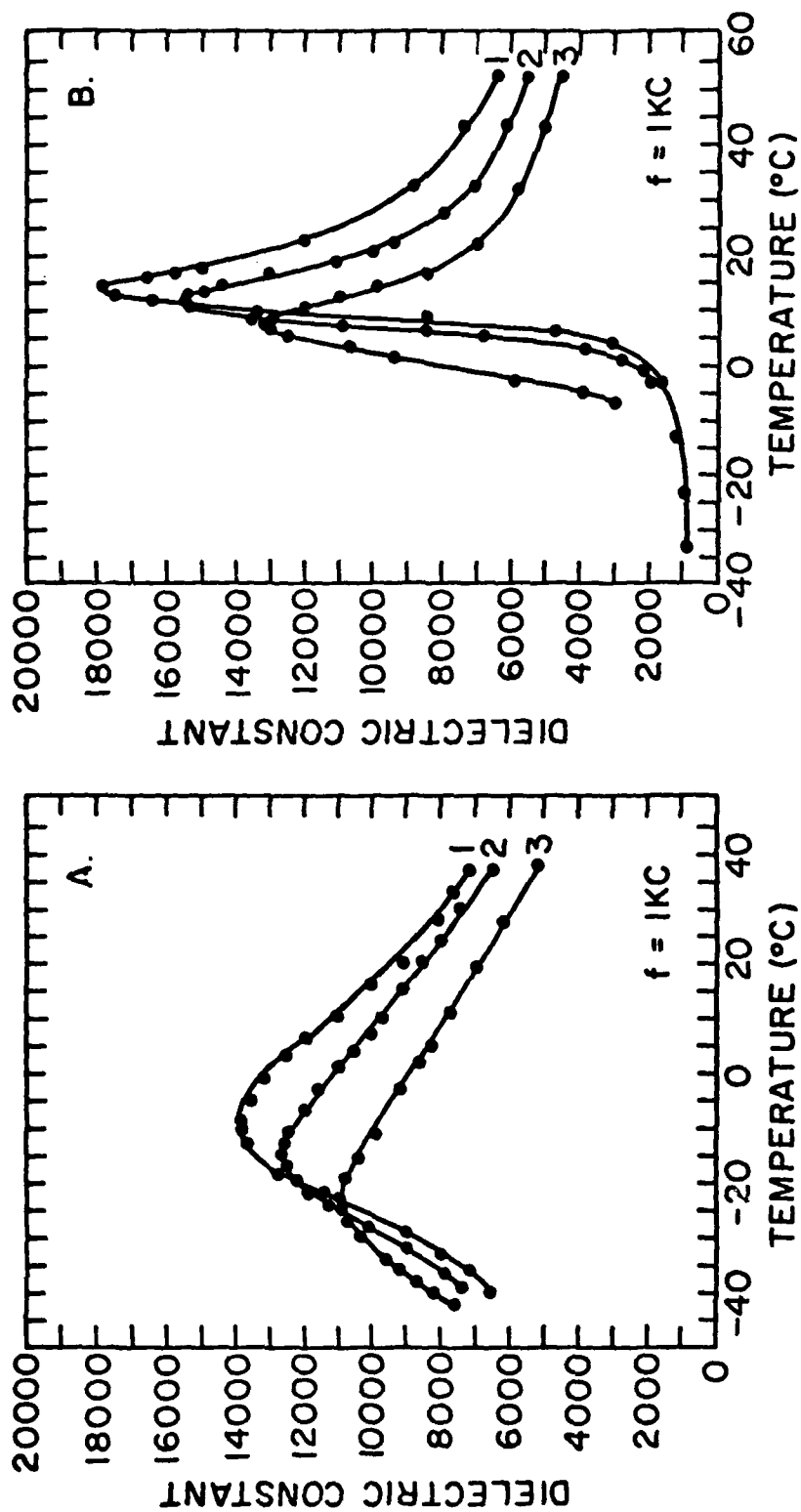


Figure 1

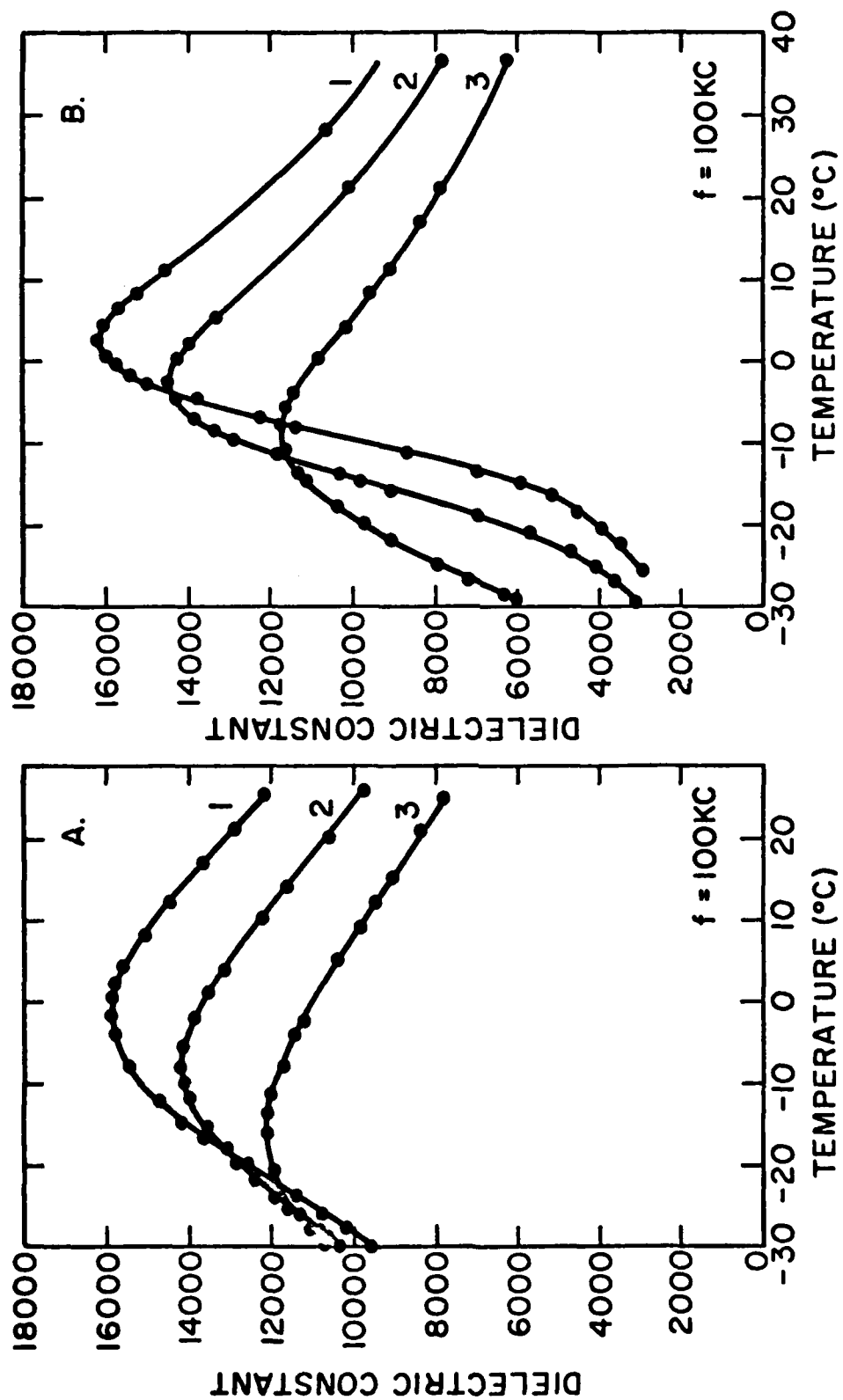


Figure 2

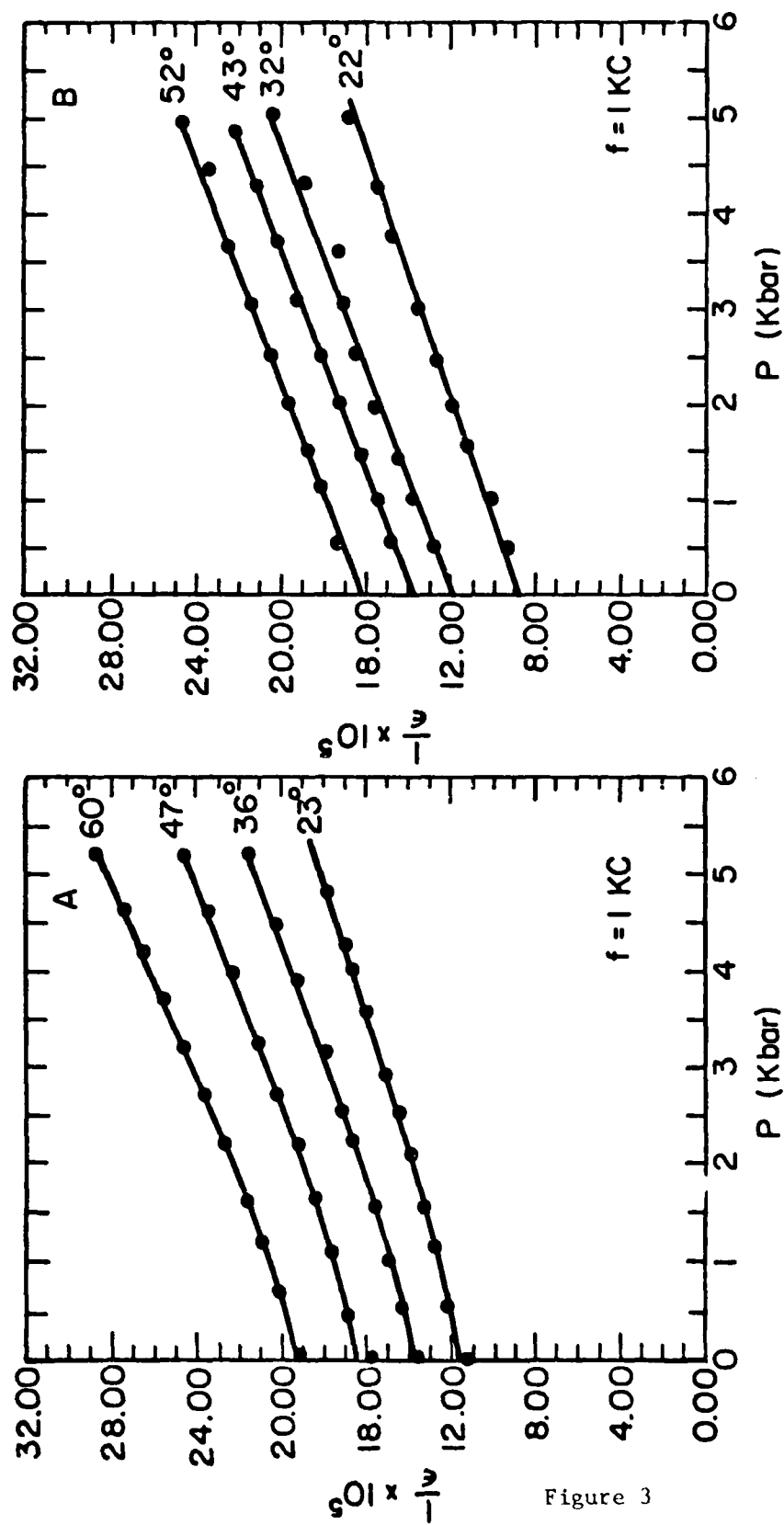


Figure 3

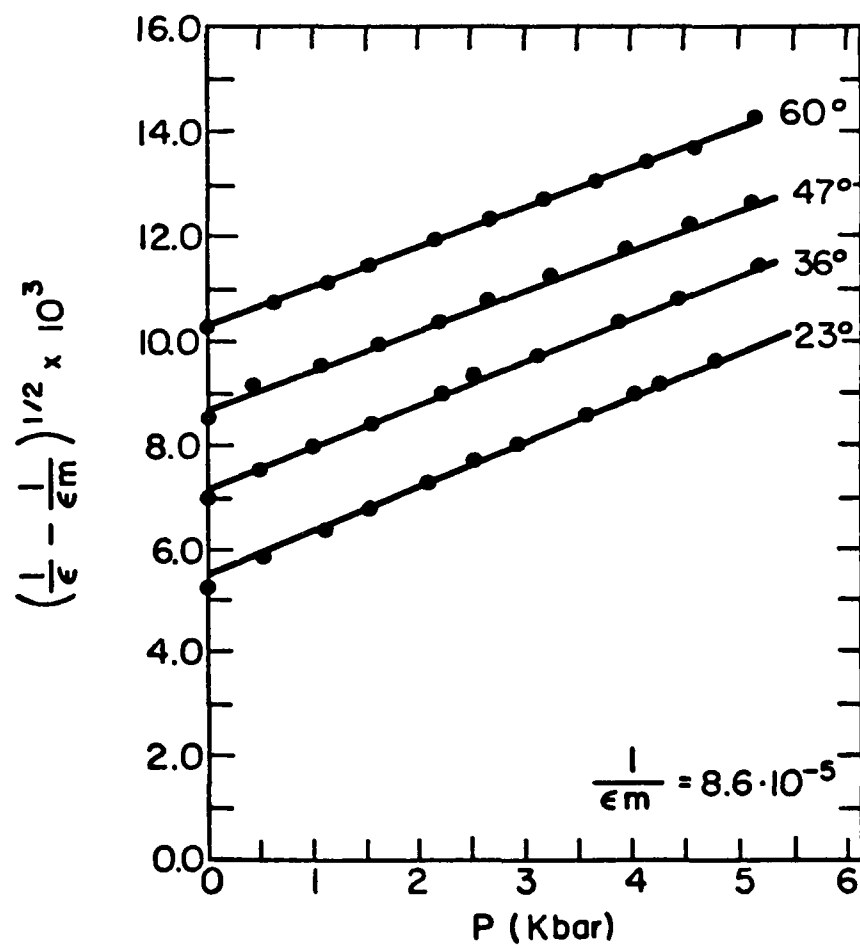


Figure 4

APPENDIX 35

N. Setter, L.E. Cross. Ferroelectric Transition Characteristics in
 $\text{Pb}(\text{Sc}_{0.5}\text{Nb}_{0.5})\text{O}_3$. Mat. Res. Bull. (submitted).

FERROELECTRIC-TRANSITION CHARACTERISTICS IN $\text{Pb}(\text{Sc}_{.5}\text{Nb}_{.5})\text{O}_3$

N. Setter and L. E. Cross
 Materials Research Laboratory
 The Pennsylvania State University
 University Park, PA 16802

ABSTRACT

Ferroelectric transition of $\text{Pb}(\text{Sc}_{.5}\text{Nb}_{.5})\text{O}_3$ can be either diffused or sharp depending upon the given heat treatment as verified by differential scanning calorimetry of single crystals and ceramic samples. Contradicting earlier reports of properties of $\text{Pb}(\text{Sc}_{.5}\text{Nb}_{.5})\text{O}_3$ are attributed therefore consistently to different preparation methods resulting in different degree of B-cation order.

Optical examination by polarized light determines that the ferroelectric phase of the 'as grown' single crystals is rhombohedral. Ferroelastic-ferroelectric domains have been observed.

Introduction

Since its first synthesis in 1961 (1) a number of investigations were made with regard to the dielectric properties of $\text{Pb}(\text{Sc}_{.5}\text{Nb}_{.5})\text{O}_3$ (PSN) (2-6). While reporting ferroelectric properties, these works differ markedly with regard to the transition related properties. The Curie temperature varies between 80° and 100°C. The dielectric permittivity is reported in some works to have a sharp peak at the transition but a round peak was observed in other cases. The structure of the ferroelectric phase is reported as either tetragonal (2,6) or rhombohedral (3-5). These contradictory reports have been noticed and further attempts have been made lately to unambiguously determine the structure and the transition related properties of PSN (7-9). These investigators still differ in conclusions about the nature of the ferroelectric transition in PSN.

In a recent work (10) crystal-chemical arguments were used to suggest that in PSN and also in $\text{Pb}(\text{Sc}_{.5}\text{Ta}_{.5})\text{O}_3$ (PST) the arrangement of the B-site cations, Sc^{+3} and Nb^{+5} or Sc^{+3} and Ta^{+5} , should be close to the bound between order and disorder. For PST it has been shown that the degree of order in the B-site can be modified by suitable thermal treatment. It has also been demonstrated (11) that for PST the ferroelectric behavior changes upon changing only the degree of order without changing the composition and that the material transforms from a ferroelectric relaxor in the disordered-cation arrangement to

a normal sharp first-order ferroelectric in the ordered cation arrangement. The decrease in order, as determined by x-ray diffraction, corresponded to a decrease in the heat of transition, to a rounding in the peak of the dielectric constant, to an increase in the low frequency dispersion of the dielectric properties and to other features that are associated with diffuse phase transition. Also, a consistent increase in T_c with the increase of the degree of B-site order has been observed.

With the above observation in mind, an attempt is made in the present work to sort out the reported dielectric properties of PSN and to relate them to the preparation method used showing that conflicting reports could have arisen from different preparation methods that produced PSN with different degrees of order in the cations and thus different transition behavior. The experimental results which are reported here support the argument.

Experimental

PSN powder was prepared by reacting stoichiometric proportions of the mixed oxides. Ball milling under alcohol for 20 hrs was followed by firing for 2 hrs at 800°C. The resulting cake was reground, pressed into pellets and refired at 1300°C for 1 hr. Pellets of PbZrO_3 + 20% PbO (by weight) were used to provide excess lead in the firing atmosphere. Powder x-ray diffraction of this reacted powder showed a simple cubic perovskite structure with no detected pyrochlore phase. Samples were annealed at different temperatures 700°-1180°C for different periods of time up to 72 hrs.

PSN single crystals were grown by a flux method. PSN reacted powder was used with flux of $\text{PbO-B}_2\text{O}_3$ with the ratio (by weight) $\text{PSN:PbO:B}_2\text{O}_3 = 0.15:0.80:0.05$. The growth cycle was: heating to 1150°C, soaking for 3 hrs at 1150°C, cooling at 3°C/hr to 850°C and at 50°C/hr to room temperature. The crystals were yellowish grey in color and had cubic shape with {100} surface and edges up to 2 mm. Unit cell size of the single crystal corresponded to 4.083 Å of a pseudo-cubic unit cell as determined by x-ray powder diffraction of ground up crystals taken using a General Electric diffractometer with $\text{CuK}\alpha$ radiation. No superlattice lines were observed for the single crystals.

Examination of the crystals by polarizing microscope was done on hot stage over the range of temperature from 20°C to 150°C.

Heat capacities were measured for single crystals as grown and for single crystals which were kept at 1370°C for 20 min and then air-quenched to room temperature (Figure 1). The heat capacity of the ceramic samples was measured for samples held at 1300°C for 1 hr and for samples held at 1180°C for 10 hrs (Figure 2). The heat capacity was measured for temperatures around the ferroelectric transition (330°-440°K) using a Perkin-Elmer Model DSC-2 differential scanning calorimeter. Heat of transition of the crystals as grown was calculated from the area under the peak of the heat capacity curve to be 17 cal/mole.

Discussion

(a) Transition Properties

The increase in order can be seen from the sharpening of the ferroelectric transition as detected by the sharpening of the peak of the specific heat curves.

The thermal measurements clearly show that the transition behavior is changed with proper heat treatment. As has been shown before for PST (9), increase in order results in sharpening of the transition.

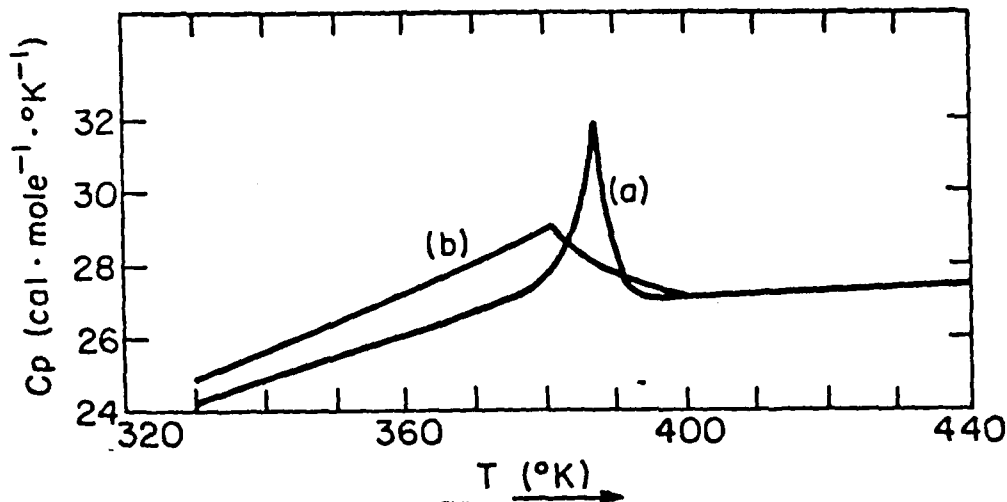


Fig. 1 Specific heat of $\text{Pb}(\text{Sc}_{.5}\text{Nb}_{.5})\text{O}_3$ single crystals

- (a) as grown
- (b) air quenching after firing at 1370°C for 1 hr

The heat of transition for a normal (fully ordered) first order PSN can be estimated from the phenomenological relation $\Delta H \approx P_{\text{So}}^2 T_0 / 2C$. Taking $P_{\text{So}} \approx 20 \mu\text{C}/\text{cm}^2$ (7) and $C \approx 4 \cdot 10^5$ (9) yields $\Delta H = 20 \text{ cal/mole}$, in good agreement with the measured heat of transition of the as-grown PSN single crystals. This, together with the observed sharp peak leads to the conclusion that these crystals are ordered to a high extent. Quenching to room temperature after short firing at 1370°C resulted in a diffused peak suggesting, as expected, decrease in the B-cation order. The specific heat of the polycrystalline powder prepared by 1 hr firing at 1370°C changes smoothly in the measured temperature range whereas annealing for 10 hrs at 1180°C yields a peak in the curve as expected when the degree of order is increased. The shape and the size of the peak suggest however that the full order was not achieved.

(b) Structure of PSN

Optical observation of the as-grown single-crystal in polarized white light shows at room temperature the existence of ferroelastic-ferroelectric domain walls (Figure 3). Upon heating, the domains disappear and the crystals become completely extinct for all orientation at the plane at polarization at 110°C . When cooling from the paraelectric phase, anisotropy and full ferroelectric domains are observed at 105°C . At room temperature the crystal extinguishes for nicols set at 45° to the $\langle 100 \rangle$ direction. It is therefore evident that the ferroelectric phase of the crystal as-grown is rhombohedral at room temperature.

X-ray diffraction failed to detect superlattice lines in the single crystals. In PST single crystal it has been shown (11) that the superlattice line is very strongly broadened. Unlike polycrystalline materials, the growth of the ordered domains in single crystals where grain boundaries do not exist proceeds by homogeneous nucleation only through the bulk. In the stable growth

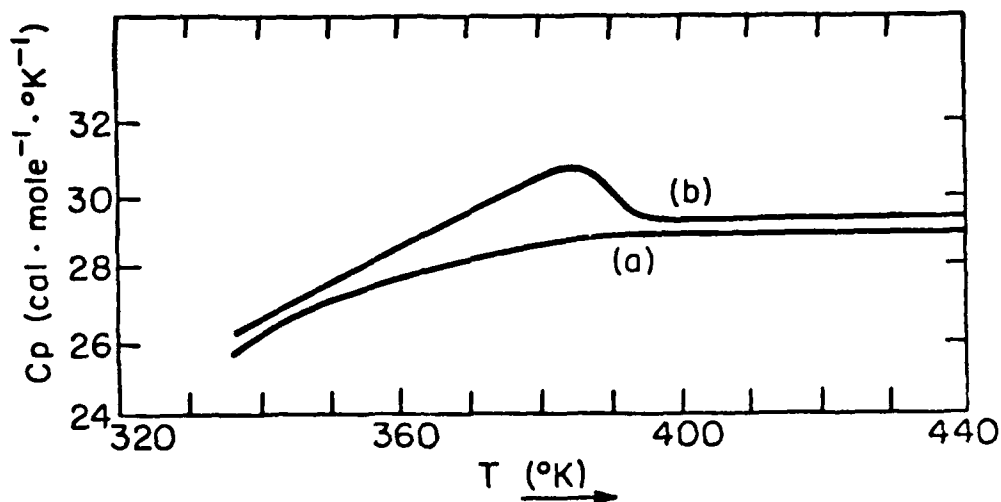


Fig. 2 Specific heat of $\text{Pb}(\text{Sc}_{.5}\text{Nb}_{.5})\text{O}_3$ ceramic samples

- (a) Firing at 1300°C for 1 hr
- (b) Annealing at 1180°C for 10 hrs

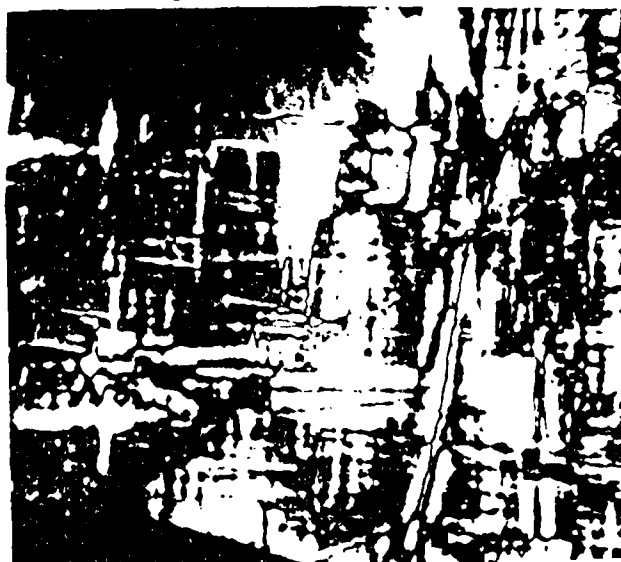


Fig. 3 'As grown' PSN crystal as observed by polarized light ($\times 150$)

condition of the single crystals, a high concentration of nuclei is expected. Therefore, the antiphase domain size is expected to be small and hence the broadening of the superlattice lines. In PSN single crystals, the same ordering growth mechanism is expected. This, combined with the initially weak intensity due to small differences in atomic number of Nb and Sc, prevent the detection of the superlattice lines. Therefore, x-ray diffraction fails to provide information on the degree of order in PSN.

(c) Structure-Property Relationship in PSN

The composition fluctuation model (12) correlating the ferroelectric-relaxor behavior with positional disorder in a certain crystallographic site is by now well established. The present study shows that like PST, PSN is also a

Table I

Preparation, structure and transition related properties of $\text{Pb}(\text{Sc}_{.5}\text{Nb}_{.5})\text{O}_3$

ref.	preparation method	transition related properties	T_c	lattice parameter change	structure	long range order	CONCLUSION about the transition
(3)	sintered ceramic firing at 1400°C	diffused transition	81			no superstructure observed	↑
(8)	transparent ceramic - hot pressed		85	'a' changes slowly above the transition	rhombo-hedral		↑
(5)	hot pressed ceramic	diffused ϵ and P_s frequency dependence	89				↑
(7)	1175°C, 1 hr. hot pressed ceramic	diffused transition frequency dependence $\frac{1}{\epsilon} \propto (T-T_0)^2$	90		tetragonal		↑
(1,2)	ceramic 1270, 1 hr	diffused	90		tetragonal	lines that were thought to be superstructure, are pyrochlore lines	↑
(4)	ceramic 1320-1385°C 2 hrs., slow cooling	$\Delta H = 40$ cal/mole for the transition			rhombo-hedral	weak superlattice lines	↑
(6)	single crystal, slow cooling 1100-750°C at 5-10°/hr	$-\epsilon$ sharp $-tg \delta$ sharp	91		tetragonal		↑
(9)	single crystal (growth procedure not reported)	transition sharp and non frequency $\frac{1}{\epsilon} \propto (T-T_0)$ in the range $T_0 < T < T_0+40$	97	'a' changes linearly with temperature above the transition	rhombo-hedral	no superlattice lines	↑

SHARP TRANSITION + INTERMEDIATE + DIFFUSED TRANSITION +

material whose degree of B-cation order and hence the ferroelectric transition behavior can be modified by proper heat treatment. Now, the conflicting properties reported earlier can be shown to be to a large extent the result of different preparation procedures which favored different degrees of order in the B-cation site.

In Table 1 the different reports are arranged according to methods of preparation, preparation favoring disorder (high temperature firing) at the top of the table and preparation methods favoring order (like single crystal growth by slow cooling) at the bottom. It is clear now that the different reported dielectric properties result to a large extent from differences in the degree of order in the B-cation site. Also the reported transition temperatures are consistent showing lower transition temperature for the less ordered, relaxor material. The single crystals as grown behave almost like a normal ferroelectric in accordance with the present study. The absence of superlattice lines in the single crystals which lead previously (9,13) to the conclusion that PSN is disordered or at least having only short-range order can be explained again by existence of small antiphase domains that caused strong broadening of the initial low intensity superlattice reflections. The only unresolved conflicting report is the structure of the ferroelectric phase and the present study determines unambiguously that the ferroelectric phase in the ordered single crystal PSN is rhombohedral.

This work was supported by the Office of Naval Research, Contract No. N00014-78-C-0291.

References

1. G.A. Snolenskii, V.I. Isupov, and A.I. Agranovskaya, *Fiz. tver. Tela.* 1, 170, (1959).
2. I.G. Ismailzade, *Kristallografiya* 4, 417, (1959).
3. V.S. Johnson, M.W. Valenta, J.F. Dougherty, R.M. Douglass and S.W. Meadows, *S. Phys. Chem. Solids* 24, 85, (1963).
4. V.J. Tennery, K.W. Hang and R.E. Novak, *J. Am. Cer. Soc.* 51, 671 (1968).
5. F. Kuchar, M.W. Valenta, *Phys. Stat. Sol. (a)* 6, 525, (1971).
6. E.G. Fesenko, E.A. Grigor'eva, A.Ya. Dantsiger, Yu.I. Golovko, and S.I. Dudkina, *Isv. Akad. Nauk SSSR Ser. Fiz.* 34, 2570 (1970).
7. R.A. Molchanova, E.I. Cheptsov, V.D. Komarov, and T.V. Mamerenko, *Isv. Akad. Nauk SSSR-Neorg. Mat.* 13, 1848, (1977).
8. A.R. Sternberg, E.A. Roberts, M.A. Knot, L.A. Stebanov, G.V. Lebertz, P.A. Fritzberg, K.A. Borman, A.A. Kapennyx, A.H. Burke, A.B. Zernaty, P.P. Kapostiyash, *Fiz. i. khim. Tu, Tela.* 9, 75, (1978).
9. A.V. Turik, N.B. Sheuchenko, M.F. Kuperiyanov, and S.M. Zaitsev, *Fiz. Tverd. Tela.* 21, 2484, (1979).
10. N. Setter, L.E. Cross, *J. Mat. Sci.* 15, 2478, (1980).
11. N. Setter and L.E. Cross, *J. Appl. Phys.* 51, 4336, (1980).
12. G.A. Smolenskii, *Proceedings of the 2nd International Meeting on Ferroelectricity, Kyoto (1969) (Phys. Soc. Japan, Tokyo, 1970) p. 26.*
13. F. Galasso, W. Darby, *Inorg. Chem.* 4, 71, (1965).

APPENDIX 36

S.J. Jang, L.E. Cross, K. Uchino, S. Nomura. Dielectric and Electrostrictive Properties of Ferroelectric Relaxors in the System $\text{PbMg}_{1/3}\text{Nb}_{2/3}\text{O}_3$: PbTiO_3 : $\text{BaZn}_{1/3}\text{Nb}_{2/3}\text{O}_3$. J. Amer. Ceram. Soc. (accepted).

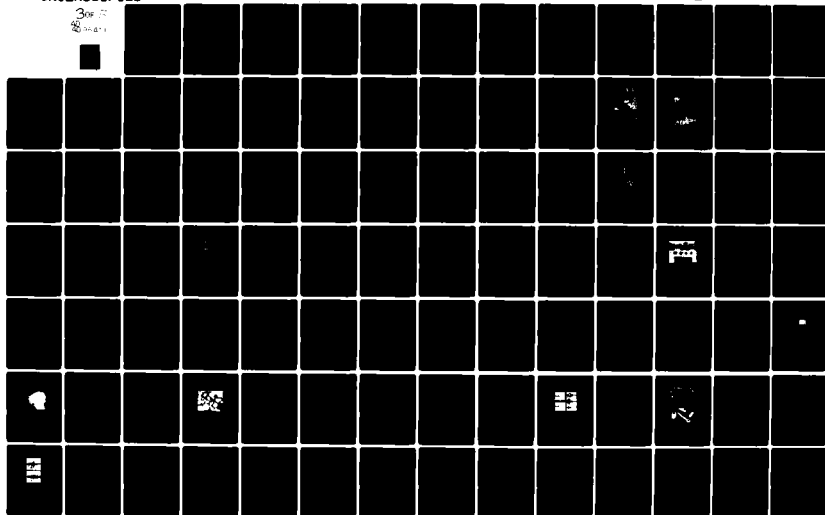
AD-A096 451

PENNSYLVANIA STATE UNIV UNIVERSITY PARK MATERIALS RE--ETC F/G 9/1
TARGETED BASIC STUDIES OF FERROELECTRIC AND FERROELASTIC MATERIALS--ETC(U)
DEC 80 L E CROSS, R E NEWNHAM, G R BARSCH N00014-78-C-0291

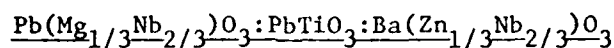
UNCLASSIFIED

NL

308 77
20-00014



Dielectric and electrostrictive properties of
ferroelectric relaxors in the system



S. J. Jang, L. E. Cross and K. Uchino
Materials Research Laboratory
The Pennsylvania State University
University Park, PA 16802

and

S. Nomura
Department of Physical Electronics
Tokyo Institute of Technology
Ookayama, Meguro-ku
Tokyo 152, Japan

ABSTRACT

Ceramic dielectrics which have been fabricated in the $\text{Pb}(\text{Mg}_{1/3}\text{Nb}_{2/3})\text{O}_3:\text{PbTiO}_3:\text{Ba}(\text{Zn}_{1/3}\text{Nb}_{2/3})\text{O}_3$ composition system are shown to exhibit two distinct dielectric maxima, both of which show the characteristic loss spectra of ferroelectrics with diffuse phase transitions. The height of the individual maxima can be controlled by the Zn:Mg ratio in the starting material, and in suitably chosen compositions a wide range of almost temperature independent high dielectric permittivity is possible. These dielectrics show strong electrostrictive deformations under high electric fields, but the electrostrictive strain is much less temperature sensitive than in other relaxors.

INTRODUCTION

Lead Magnesium Niobate $\text{PbMg}_{1/3}\text{Nb}_{2/3}\text{O}_3$ (PMN) is a ferroelectric with a diffuse phase transition near room temperature which has been associated with a range of Curie temperatures due to local composition fluctuations in the disordered B site cations in the ABO_3 perovskite structure (1,2). Lead zinc niobate $\text{PbZn}_{1/3}\text{Nb}_{2/3}\text{O}_3$ (PZN) has rather similar properties but with the Curie range in the vicinity of 140°C (3). It would be most interesting to explore the solid solution range between PMN and PZN, however, unfortunately PZN can not be made by solid state reaction under normal pressure in the required perovskite form, but forms instead a stable pyrochlore structure phase. Barium zinc niobate $\text{BaZn}_{1/3}\text{Nb}_{2/3}\text{O}_3$ (BZN) is also of perovskite structure (4) but does not exhibit any ferroelectric phase down to temperatures below 77°K . The solid solution between barium zinc niobate and lead titanate (PT) does, however, show interesting dielectric properties with a dielectric maximum near 100°C which changes in amplitude with composition (4). Unlike pure PZN, the BZN:PT solid solution can be fabricated by conventional solid state reaction, without contamination by the unwanted pyrochlore structure phase.

In this study, compositions in the ternary PMN:PT:BZN system have been explored. It is shown that in these solid solutions, unlike the normal sharp transition ferroelectric materials, the individual Curie ranges associated with the Mg and Zn local concentrations appear to retain their identity. This retention of two broad maxima in the permittivity whose heights can be controlled by the composition, gives the possibility of producing ceramics with very high permittivities and heretofore unrealizable temperature stabilities.

Electrostrictive measurements show that these dual relaxor compositions retain the large electrostrictive M constants of the more widely studied PMN:PT compositions but with very much reduced thermal instability.

We believe that these materials, and other possible dual relaxor compositions will find interesting application as capacitor dielectrics, electrostrictive position controls and stress gauges.

SAMPLE PREPARATION

Three compositions in the PMN:BZN:PT system were chosen for initial study,

0.45 PMN:0.3575 PT:0.1925 BZN

0.40 PMN:0.36 PT:0.24 BZN

0.15 PMN:0.50 PT:0.35 BZN

where the numbers give the mole fraction of each constituent. These compositions were synthesized from reagent grade PbO , MgO , Nb_2O_5 , TiO_2 , ZnO , and BaCO_3 .

The chemicals were mixed in appropriate proportions, ball milled in alcohol, then dried and calcined in air in a closed alumina crucible. Calcining conditions were 15 hours at 920°C , regrinding, followed by two more heat treatments at 950°C for 15 hours each. The resulting calcine was reground in agate, then cold pressed into disks 2.54 cm diameter using polyvinyl alcohol as a binder. The cold pressed disks were then stacked on platinum setters and fired in air.

X-ray powder patterns taken at room temperature using $\text{Cu K}\alpha$ radiation confirmed a single phase perovskite as the crystal structure of the ceramic. The lattice constants were determined from (200), (211), (220), (310) and (321) reflections, using the slow scan mode in a G. E. Diffractometer for enhanced precision.

Table 1 summarizes sintering behavior, calculated and measured densities and lattice parameters for the three compositions studied.

Grain size in the final ceramics was estimated from scanning electron microscope images of etched polished surfaces. A 5% HCl + 0.5% HF etching for 10 minutes was used to reveal the boundary structure: mean grain sizes determined by the linear intercept method were in the range 4 to 15 μ meters. The micrographs are suggestive of a liquid phase boundary region during sintering, but attempts to distinguish any composition change in the boundary region using microprobe techniques proved futile; no chemically distinct phase could be identified.

DIELECTRIC THERMAL AND ELECTROSTRICTIVE MEASUREMENT

Weak field dielectric permittivity ($E < 200$ V/cm) was measured as a function of temperature using a Hewlett Packard 4270A automatic bridge and a Delta Design model 2300 environment chamber. Samples were in the form of disks 0.5 cm diameter x 1 mm thick, equipped with fired-on silver electrodes on the major faces. The data (Fig. 1) suggest that in all three samples there are two separate relaxation regions, one always centered near 0°C, the second near to 110°C which shifts slightly towards higher temperature with increasing BZN concentrations. In the intermediate region, the permittivity is high but only weakly temperature dependent, and this dependence could probably be reduced by a proper tailoring of the composition.

Dielectric hysteresis for the three compositions (Fig. 2) was measured using a driving frequency of 0.1 Hz and a modified balanced Sawyer Tower circuit. All compositions show weak hysteresis, but the field induced polarization levels are not a strong function of temperature.

Thermal expansion was measured dilatometrically using bars of each composition 35 x 6 x 6 mm, and a Hewlett Packard 24 DCDT-250 linear displacement transducer. The runs shown in Fig. 3 were taken by cooling to nitrogen temperature, then heating at a constant rate of 0.5°C/minute to 500°C.

It is evident that as with other relaxor compositions (5) the thermal expansion is low in the Curie ranges, but increases to a normal value $\sim 11 \times 10^{-6}/^{\circ}\text{C}$ in the high temperature region above 300°C .

The transverse strain S_2 induced by electric fields along the axis of the disk was measured using a bonded strain gauge technique (6). The field was cycled at 0.002 Hz. Transverse contractions measured as a function of temperature on the three compositions are summarized in Fig. 4. Because of the minor dielectric hysteresis it is difficult to determine precise values of M_{12} , but it is clear from the general magnitude of induced strain that the M value is comparable to that of pure PMN. The major influence of the higher relaxation region is apparently to reduce the temperature dependence of the M coefficient.

DISCUSSION

The major point of interest in these ternary PMN:PT:BZN compositions is the manner in which the relaxation maximum in ϵ' associated with the BZN:PT solid solution is apparently little perturbed by the PMN addition which appears rather to contribute its own separate relaxation to the measured permittivity level. This behavior is in marked contrast to that of conventional perovskites' sharp Curie transition where the sharp transition character is largely retained but at a temperature intermediate between that of the two end member compositions. A possible explanation for this behavior might reside in poor solid solution formation; however, attempts to homogenize the ceramic by repeated firing and grinding were unsuccessful, and the continuous change of cubic lattice parameter suggests strongly that solid solution is in fact already achieved. A more likely explanation we believe is that this difference may be intrinsic to the mechanism of the diffuse transition. If, as Rolov (7) and Burfoot and Clarke (8) have suggested, the

Curie range depends upon fine scale (10 - 100 nm) fluctuations in the Mg:Nb and Zn:Nb distributions, it does appear possible, particularly in starting from the mixed oxide preparations, that the Zn-rich and Mg-rich regions may retain their local identities. Certainly, once the B site cation populations have been established it will be very difficult to effect rearrangement by any realizable thermal treatment.

Whatever the origin, however, the fact that a dual peak relaxor behavior can be retained for a wide range of different conventional forming conditions has real practical advantage. It is clear that with more careful selection of the proportions, very flat high K characteristics could be achieved. Further, if the generality of this type of behavior can be established in other relaxor ferroelectric compositions, the possibility exists of a more precise tailoring of the required properties over widely extended temperature ranges.

That the high electrostrictive constants are retained in their ternary compositions expands the possibility of using electrostriction for position control over wider temperature ranges, where the reduced thermal expansion is also advantageous. Finally, it must be remembered that electrostriction also represents the stress dependence of the dielectric stiffness. For the usual ferroelectrics close to T_c , the stress sensitivity can be very high, but practical utility is frustrated by the correspondingly high temperature sensitivity of stiffness. It would appear that in these ternary compositions, this temperature sensitivity can be largely suppressed, and further work is now in progress to determine the merits of this composition family for electrostrictive stress gauges.

REFERENCES

- (1) G.A. Smolensky, A.I. Agranovskaya. Soviet Phys.-Solid State 1, 1429 (1959).
- (2) V.A. Bokov, I.E. Mylnikova. Soviet Phys.-Solid State 3, 613 (1961).
- (3) V.A. Bokov, I.E. Mylnikova. Soviet Phys.-Solid State 2, 2428 (1961).
- (4) S. Nomura, H. Arima. Japanese J. Appl. Phys. 11, 358 (1972).
- (5) S.J. Jang, K. Uchino, S. Nomura, L.E. Cross. Ferroelectrics (to be published).
- (6) S. Nomura, J. Kuwata, S.J. Jang, L.E. Cross, R.E. Newnham. Mat. Res. Bull. 14, 769 (1979).
- (7) B.N. Rolov. Fiz. Tverd. Tela. 6, 2128 (1968).
- (8) R.A. Clark, J.C. Burfoot. Ferroelectrics 8, 505 (1974).

TABLE I

Composition (Mole Fraction PMN:PT:BZN)	Sintering (2 hrs)	Fired Density	Calculated Density	Lattice Constant
0.45:0.3575:0.1925	1,300°C	7.4 gm/cm ³	7.95 gm/cm ³	4.0227 Å
0.4:0.36:0.24	1,300	7.27	7.90	4.0244
0.15:0.5:0.35	1,280	7.24	7.79	4.0180

FIGURE CAPTIONS

- Fig. 1. Weak field dielectric permittivity (Fig. 1a) and tangents δ (Fig. 1b) as a function of temperature and frequency in several PMN:PT:BZN ceramics.
- Fig. 2. Dielectric hysteresis under a cycling frequency of 0.1 Hz for several compositions in the PMN:PT:BZN family.
- Fig. 3. Thermal dilatation in different compositions of PMN:PT:BZN ceramics.
- Fig. 4. Transverse electrostrictive strain S_2 as a function of cyclic driving field E_1 for several PMN:PT:BZN ceramics.

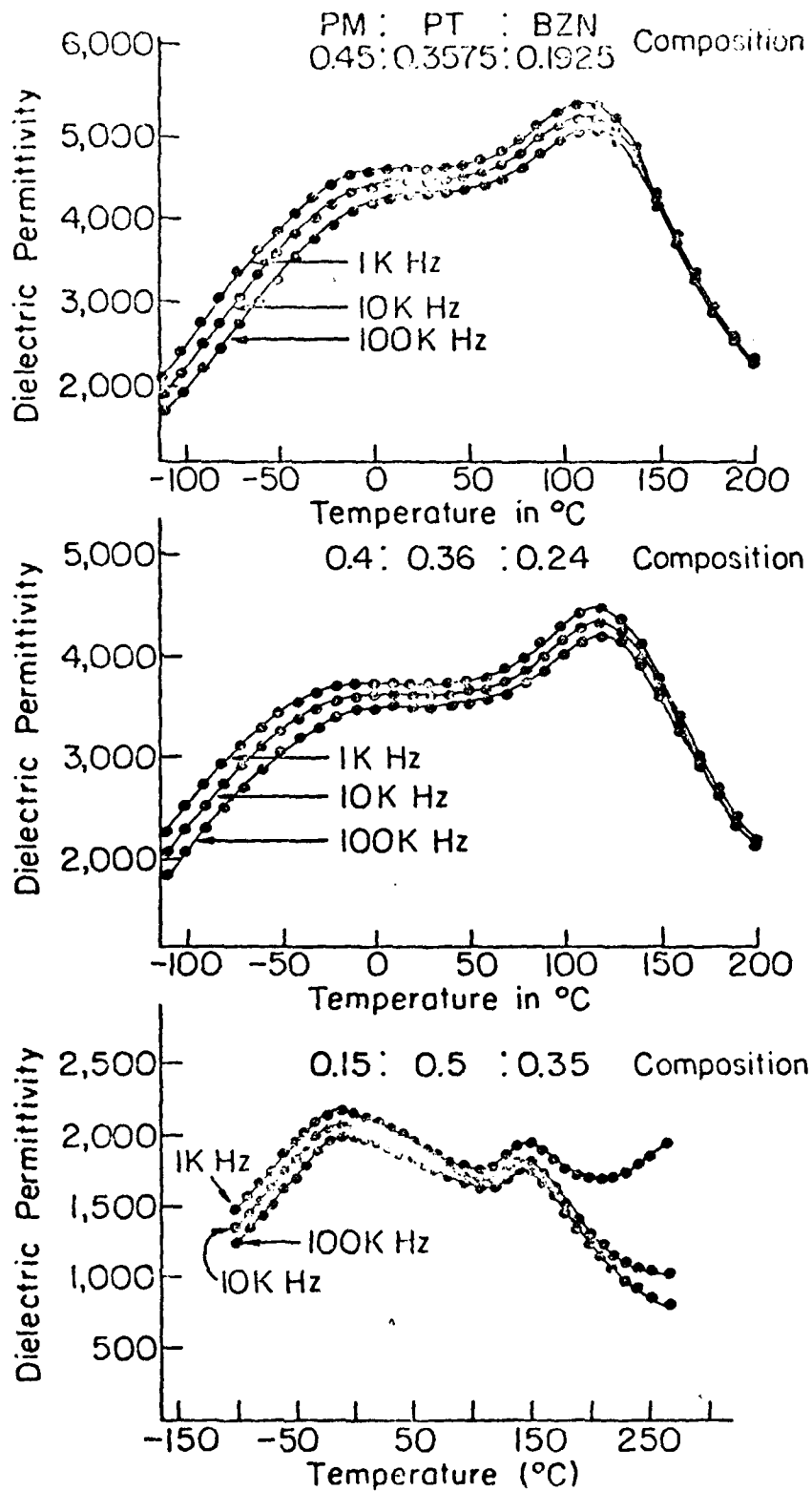


Figure 1a

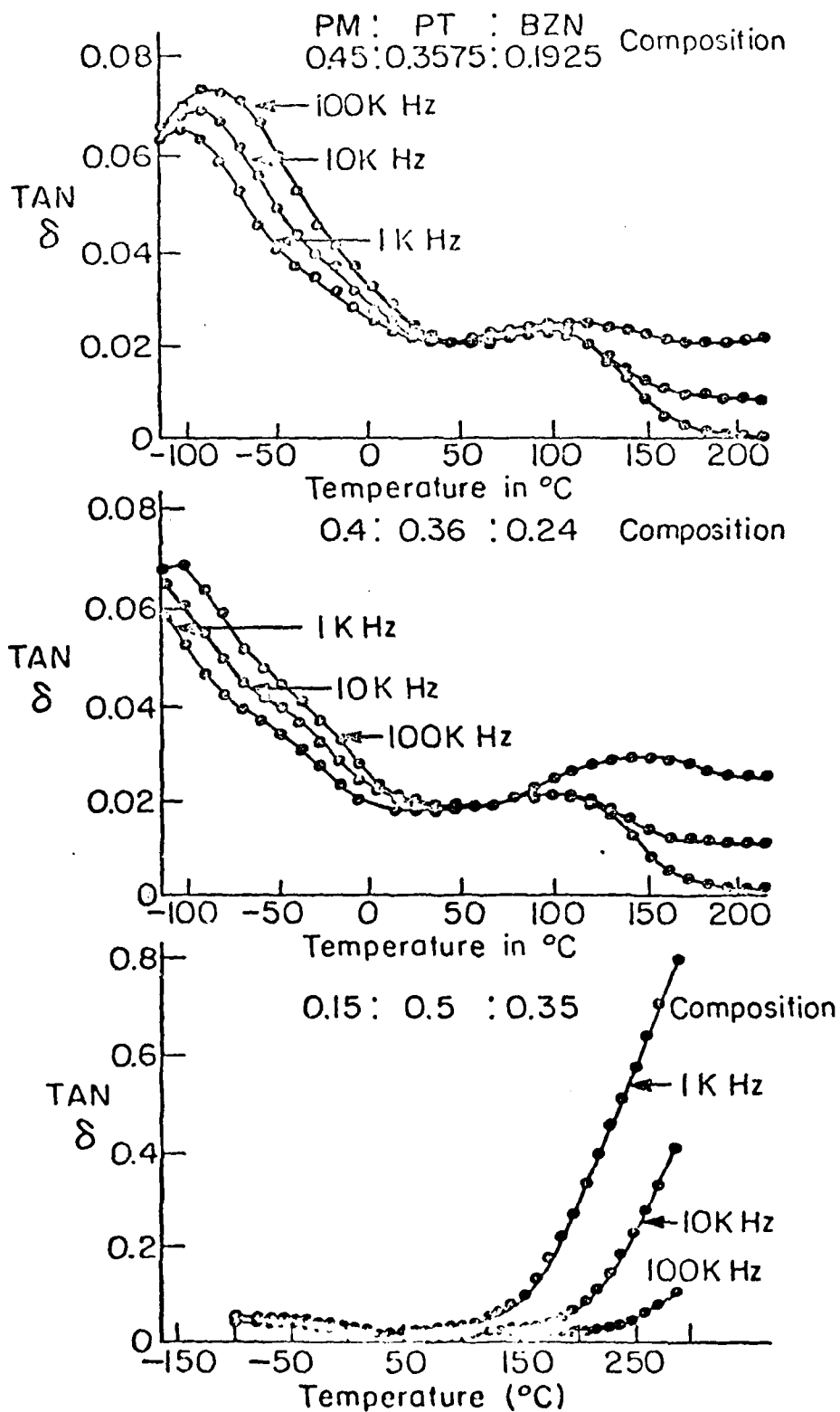
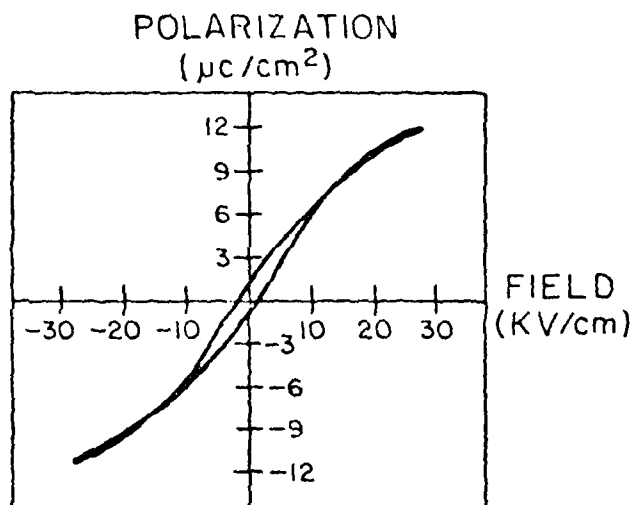
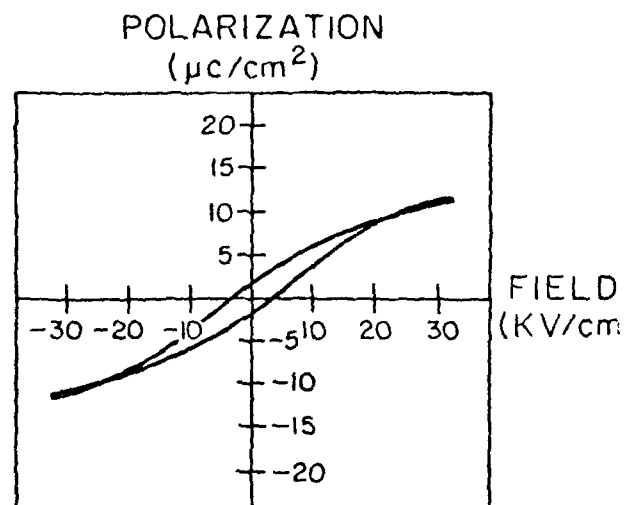


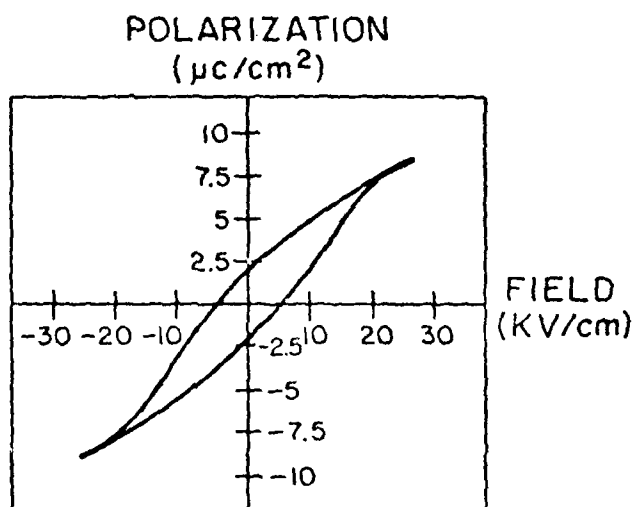
Figure 1 b



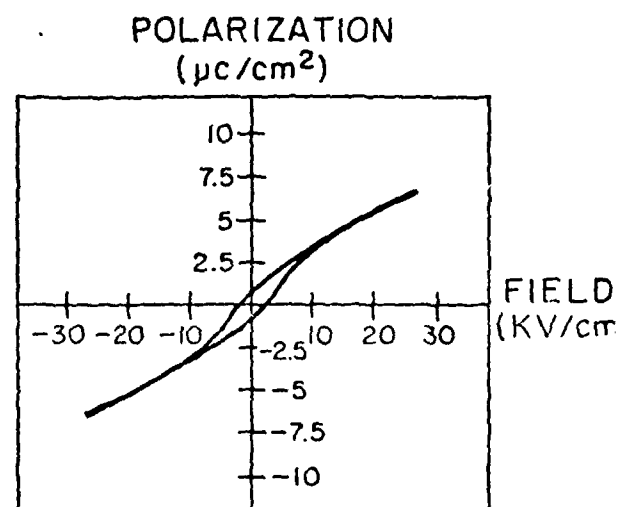
0.45 : 0.3575 : 0.1925
T = 25°C, f = 0.1 Hz



0.4 : 0.36 : 0.24
T = 22°C, f = 0.1 Hz



0.15 : 0.5 : 0.35
T = 23°C, f = 0.1 Hz



0.15 : 0.5 : 0.35
T = 122°C, f = 0.1 Hz

Figure 2

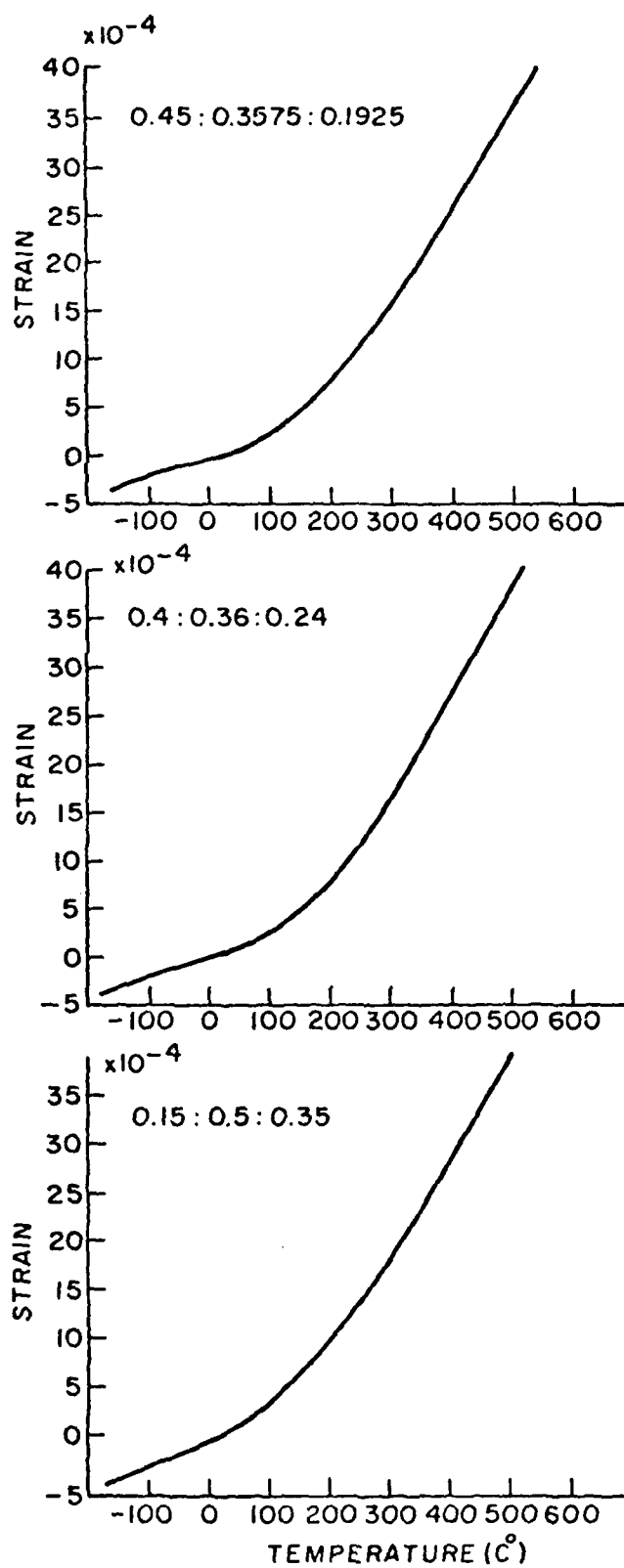


Figure 3

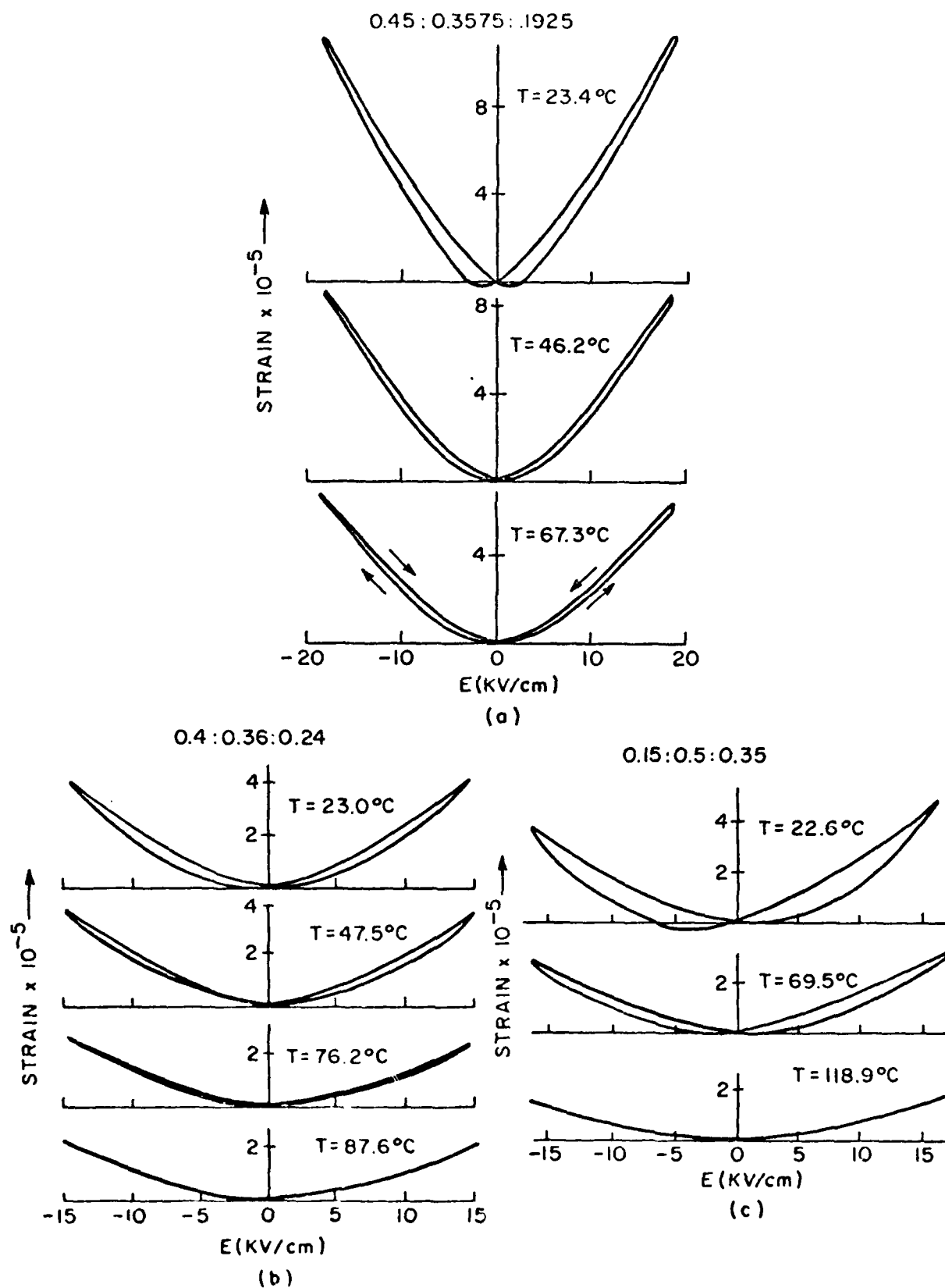
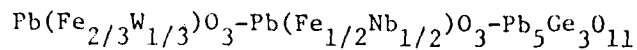


Figure 4

APPENDIX 37

S.J. Jang, W.A. Schulze, J.V. Biggers. Low Firing Capacitor Dielectrics
in the System $\text{Pb}(\text{Fe}_{2/3}\text{W}_{1/3})\text{O}_3$ - $\text{Pb}(\text{Fe}_{1/2}\text{Nb}_{1/2})\text{O}_3$ - $\text{Pb}_5\text{Ge}_3\text{O}_{11}$. J. Amer. Ceram.
Soc. (submitted).

Low Firing Capacitor Dielectrics in the System



S.J. Jang

Western Electric Company
Engineering Research Center
PO Box 900, Princeton, NJ 03540

W.A. Schulze and J.V. Biggers

Materials Research Laboratory
The Pennsylvania State University
University Park, Pennsylvania 16802

ABSTRACT

Lead germanate was used as a liquid phase sintering aid to lower the firing temperature of dielectrics from the solid solution system $\text{Pb}(\text{Fe}_{2/3}\text{W}_{1/3})\text{O}_3\text{-Pb}(\text{Fe}_{1/2}\text{Nb}_{1/2})\text{O}_3$ (PFW-PFN). A 10 w/o $\text{Pb}_5\text{Ge}_3\text{O}_{11}$ addition to a 0.3 x PFW-0.7 x PFN composition sintered to 90% of theoretical at 850°C. The ceramic had a weakfield K at 25°C of over 3000.

Introduction

Multilayer ceramic capacitors with their small size, high capacitance, electrical stability and low cost have become increasingly important as components in electronic devices.

Inherent in the present technology which uses dielectrics based on barium titanate is the need for precious metal internal electrodes.

It has been obvious from their inception that the capacitor cost could be significantly reduced if alternative less expensive electrode systems could be found. The current instability and rising prices of precious metals have underscored this problem. In some high capacitance parts with 50-70 internal electrodes, the precious metal may constitute 50-60% of the selling price of the capacitor.

Many different approaches have been tried in an effort to find less expensive electrodes. Current industry practice is to use BaTiO_3 dielectrics heavily fluxed with additions of Bi_2O_3 and/or PbO . These ceramics can be fired at temperatures around 1100°C and are compatible with 70 w/o Ag - 30 w/o Pd alloy electrodes.

Buessem and Prokopowicz (1) describe other alternative approaches that have not been used commercially. There are other interesting possibilities for reducing electrode costs. The earliest work was probably that of Herbert (2) who investigated the use of nickel electrodes, in the mid 1950s.

While Herbert succeeded in producing usable capacitors the devices were not marketed. The first commercially available nickel electroded multilayers were produced by the U.S. Capacitor Co. in the early 1970s. These capacitors had serious reliability problems and were soon withdrawn from the market.

While rumors of new nickel base electrodes persist, there are none presently available. The defect chemistry of dielectrics that can be fired in

the neutral or reducing atmospheres required for nickel is described by Daniels (3). The close control of composition necessary to produce dielectrics with good electrical properties and the ability to withstand reducing firing atmospheres is difficult to achieve in a production situation and may limit the usefulness of this approach.

Another possibility for using nonprecious metals in multilayers is to lower the sintering temperature of the dielectric into a range where reducing firing atmospheres are not necessary or where high silver content alloys can be used. Biggers et al. (4) describe a glass-bonded dielectric based on BaTiO_3 and low melting borosilicate glasses that sintered at 750°C .

Unfortunately the use of glass as a bonding phase has serious drawbacks. The dielectric mixing laws which apply to the two-phase composites with a dispersed high dielectric constant phase (BaTiO_3) in a continuous glass phase are very unfavorable and composites with as little as 3-5 w/o glass have dielectric constants of only 500-700.

In an attempt to achieve higher K's, Schulze and Biggers (5) have proposed the use of $\text{Pb}_5\text{Ge}_3\text{O}_{11}$ (PGO) and other low melting germanate phases as substitutes for glass. PGO has a melting point of 750°C and a dielectric constant of 70 (6). Composites of BaTiO_3 and PGO produced by Park (7) showed evidence of reaction and the dielectric constants were too low to be of commercial interest.

Schulze and Biggers (5) have shown that undesirable reactions did not occur with PGO and lead oxide containing phases, for example lead zirconate-lead titanate solid solution.

The work described in this paper is an attempt to use PGO as a bonding phase in a new series of dielectrics based on solid solutions of $\text{Pb}(\text{Fe}_{2/3}\text{W}_{1/2})\text{O}_3$ (PFW) and $\text{Pb}(\text{Fe}_{1/2}\text{Nb}_{1/2})\text{O}_3$ (PFN) developed by Yonezawa, et al (8). These ceramics have room temperature dielectric constants of over 2000 and sinter without appreciable liquid phase at 1000°C .

It was felt that combinations of PCO and PFW-PFN solid solutions might produce composites with high dielectric constants sintering below 850°C. These composites should be compatible with 100% Ag and possibly nickel electrodes.

Experimental Procedure

The compounds were prepared from reagent grade PbO , Fe_2O_3 , WO_3 , Nb_2O_5 , and GeO_2 . The oxides were mixed in appropriate proportions, ball milled in alcohol with alumina balls, then dried and calcined in air in a closed alumina crucible. Calcining temperatures for 0.3xPFW-0.7xPFN and PG were 750°C and 650°C respectively. The resulting masses were ground and recalined to ensure complete reaction. The PFN-PFW solid solutions and the $\text{Pb}_5\text{Ge}_3\text{O}_{11}$ were ball milled in alcohol for 20 hours, then dried and cold pressed into disks 1.7 μm in diameter. Sintering temperatures ranged from 800° to 900°C and times from 10 minutes to 100 minutes.

X-ray powder diffraction patterns of the solid solutions, taken at room temperature using Cu-K_α radiation, verified that the ceramics had a perovskite structure. To study melting and recrystallization of the liquid phase during the sintering process, a DuPont model 900 DTA was used for differential thermal analysis. Dielectric properties were measured using a Hewlett-Packard model 4270A automatic capacitance bridge and Delta model 2300 temperature chamber. The heating rate was approximately 2°C/minute.

Results and Discussion

The densities and room temperature dielectric constants of composites fired at various temperatures and times are shown in Figure 1. It appears that temperature is a stronger factor than time in densification, and after 30 minutes firing the densities were near maximum for all temperatures. With a small increase in

density, however, the dielectric constants improve quite significantly. The increase in K 's were much greater than would be expected from normal density corrections and suggests that the germanate phase surrounding the grains has changed in composition or structure causing the electric field distribution to change. The $\tan\delta$ are not plotted and were 0.04-0.05 for all compositions and firings.

SEM micrographs of the ceramics are shown in Figures 2 and 3. It can be seen that solid solution grains are coated by a lead germanate. With large grain size ($\sim 10 \mu\text{m}$), lead germanate accumulates in triple points between the grains as shown in Figure 2(c). It was found that the density is lower with very fine grain size ($< 1 \mu\text{m}$), and higher with 1-3 μm grains for the same firing conditions. This might be related to the grain surface area and volume of liquid phase.

Figure 4 shows differential thermal analysis run at a heating rate of $20^\circ\text{C}/\text{min}$ of a 20 wt% PGO composite. The endothermal peaks on heating at about 700°C , 750°C , and 790°C are probably melting of Pb_3GeO_5 (3:1), $\text{Pb}_5\text{Ge}_3\text{O}_{11}$ (5:3), and PbGeO_3 (1:1) respectively (9). This suggests that although the starting compound was the ferroelectric $\text{Pb}_5\text{Ge}_3\text{O}_{11}$ (5:3), a rapid reaction converted it to the ferroelastic PbGeO_3 (1:1), and Pb_3GeO_5 (3:1) as previously reported (5,7,10).

Conclusions

In our initial experiments we have shown that additions of $\text{Pb}_5\text{Ge}_3\text{O}_{11}$ to $\text{Pb}(\text{Fe}_{2/3}\text{W}_{1/3})\text{O}_3$ - $\text{Pb}(\text{Fe}_{1/2}\text{Nb}_{1/2})\text{O}_3$ can produce composites with sintering temperatures below 850°C . The composites with 10 w/o PGO have room temperature permittivities above 4000 and $\tan\delta$ below 0.05. Work in progress shows that this composition is compatible with 100% Ag internal electrodes.

While our evaluation of both the process and the compositional ranges of the germanate phase and the PFN-PFW solid solutions is not complete, it would seem that these combinations could be potentially useful in commercial applications.

REFERENCES

1. Buessem W. R., T. I. Prokopowicz. Electrde and Materials in Ceramic Capacitors Ferroelectrics. 10, 225-230 (1976).
2. Herbert J. M. Method of Making High Dielectric Constant Ceramic U. S. Pat. 2,934,442 (1959).
3. Daniels J. Detect Equilibrium in Acceptor Doped Barium Titanate. Philips Res. Repts. 31, 505-515 (1976).
4. Biggers J. V., G. L. Marshall, D. W. Strickler. Thick-film Glass-Ceramics Capacitors. Solid State Technology 13, 63-67 (1970).
5. Schulze W. A., J. V. Biggers. Piezoelectric Properties of $Pb_5Ge_3O_{11}$ Bonded PZT Compositions. Mat. Res. Bull. 14, 721-730 (1979).
6. Cline T. Domain Contributes to Dielectric Response in Ferroelectrics. Ph.D. Thesis, The Pennsylvania State University, University Park, PA (1977).
7. Park S. M. Liquid Phase Sintering of Heterophasic Dielectric in System Barium-Titanate-Lead (5) Germanium (3) Oxygen (11) Ph.D. Thesis, University of Illinois of at Urbana-Champaign (1977).
8. Yonezawa M, K. Utsumi, T. Ohno. Properties of $Pb(Fe_{2/3}W_{1/3})O_3$ - $Pb(Fe_{1/2}Nb_{1/2})O_3$ Ceramics. 1st Meeting Ferroelect. Mat. Appl. F-7, 297-302 (1978).
9. Zwicker, W. K., M. Delfino, J. P. Dougherty, A Sicignano, J. Lodell, J. A. Nicolosi. Formation of Secondary Phases During Crystal Growth of $Pb_5(Ge_3O_{11})$. J. Elec. Mat. 6(2), 125 (1977).

DENSITY AND DIELECTRIC CONSTANT OF $0.3 \times \text{Pb}(\text{Fe}_{0.00} \text{W}_{0.99})\text{O}_{3-}$
 $0.7 \times \text{Pb}(\text{Fe}_{0.5} \text{Nb}_{0.5})\text{O}_3$ WITH $\text{Pb}_3\text{Co}_2\text{O}_{11}$ AS A FUNCTION OF FIRING TIME

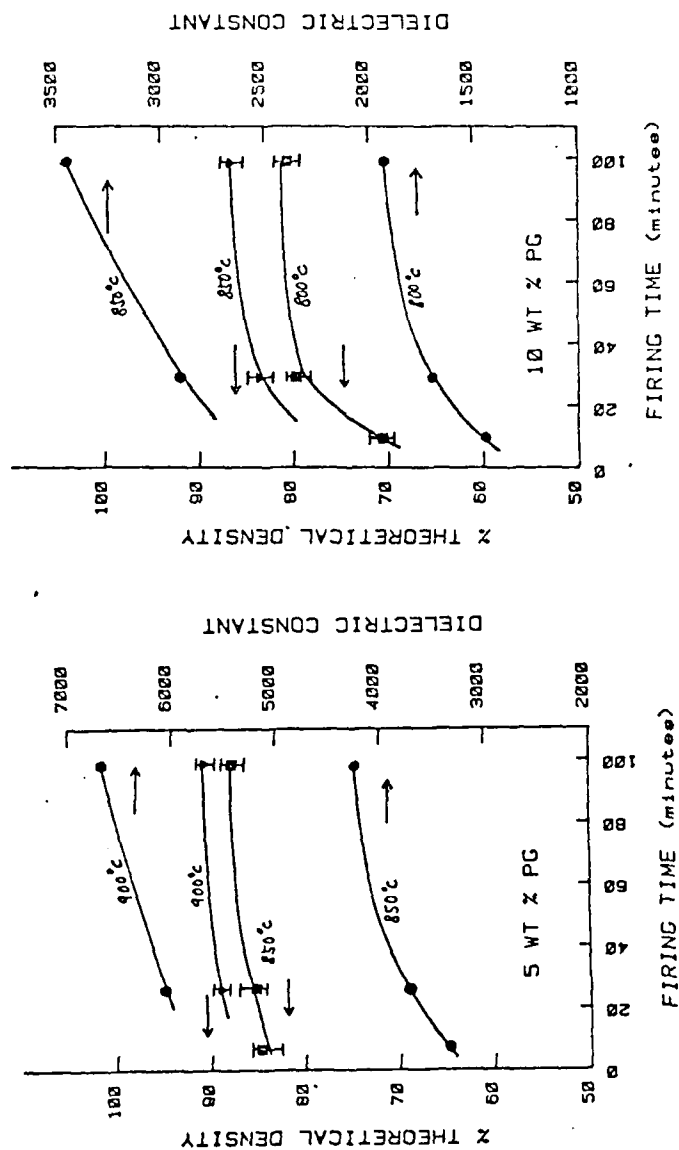
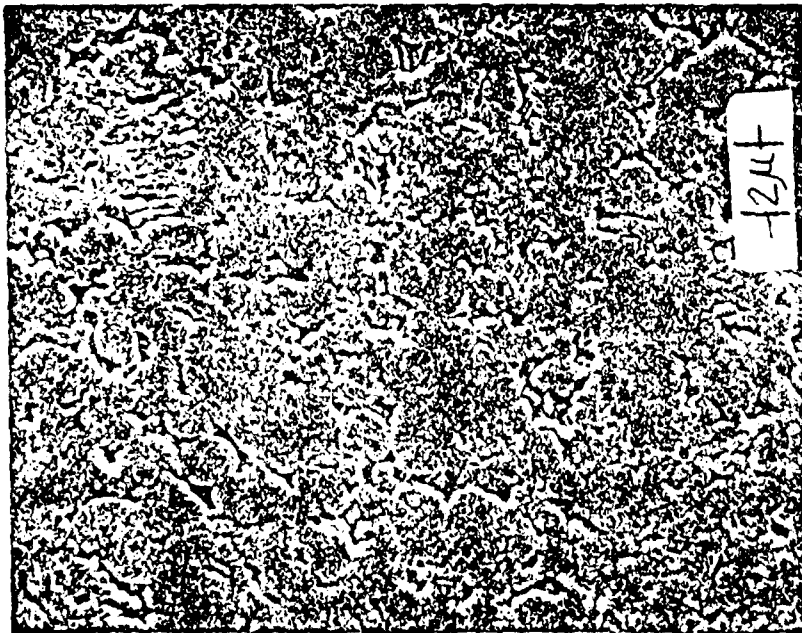
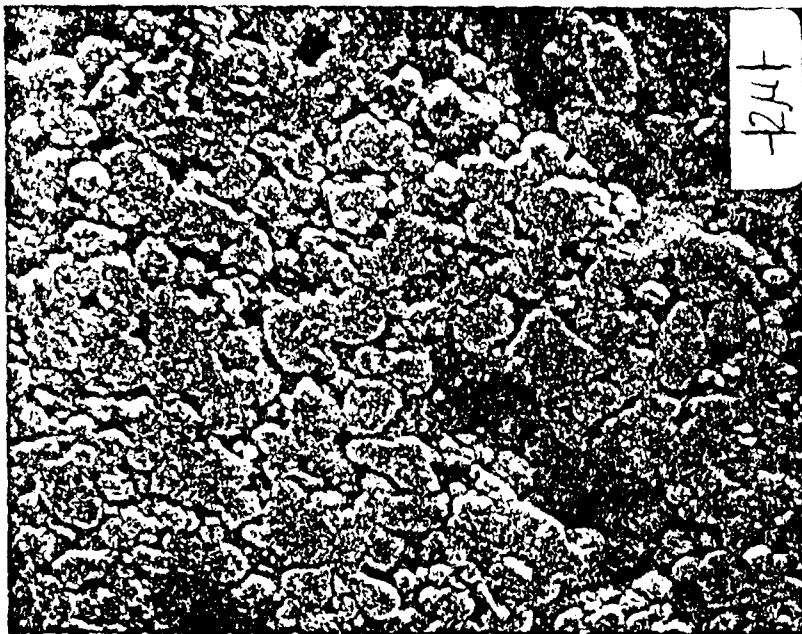


Figure 1



(A) ETCHED



(B) ETCHED

Figure 2. Microstructures of a $0.3 \times \text{Pb}(\text{Fe}_2/3\text{Mn}/3)\text{O}_3-0.7 \times \text{Pb}(\text{Fe}_1/3\text{Sb}_1/2)\text{O}_3$ and $10 \times 10 \times 10 \text{ mm}^3$ ceramic fired at 800°C for 100 minutes.



Figure 3. Microstructure of $0.3x \text{Pb}(\text{Fe}_{2/3}\text{W}_{1/3}\text{O}_3 - 0.7x \text{Pb}(\text{Fe}_{1/2}\text{Nb}_{1/2})\text{O}_3$ and 20 w/o ceramics fired at 850°C for 30 minutes.

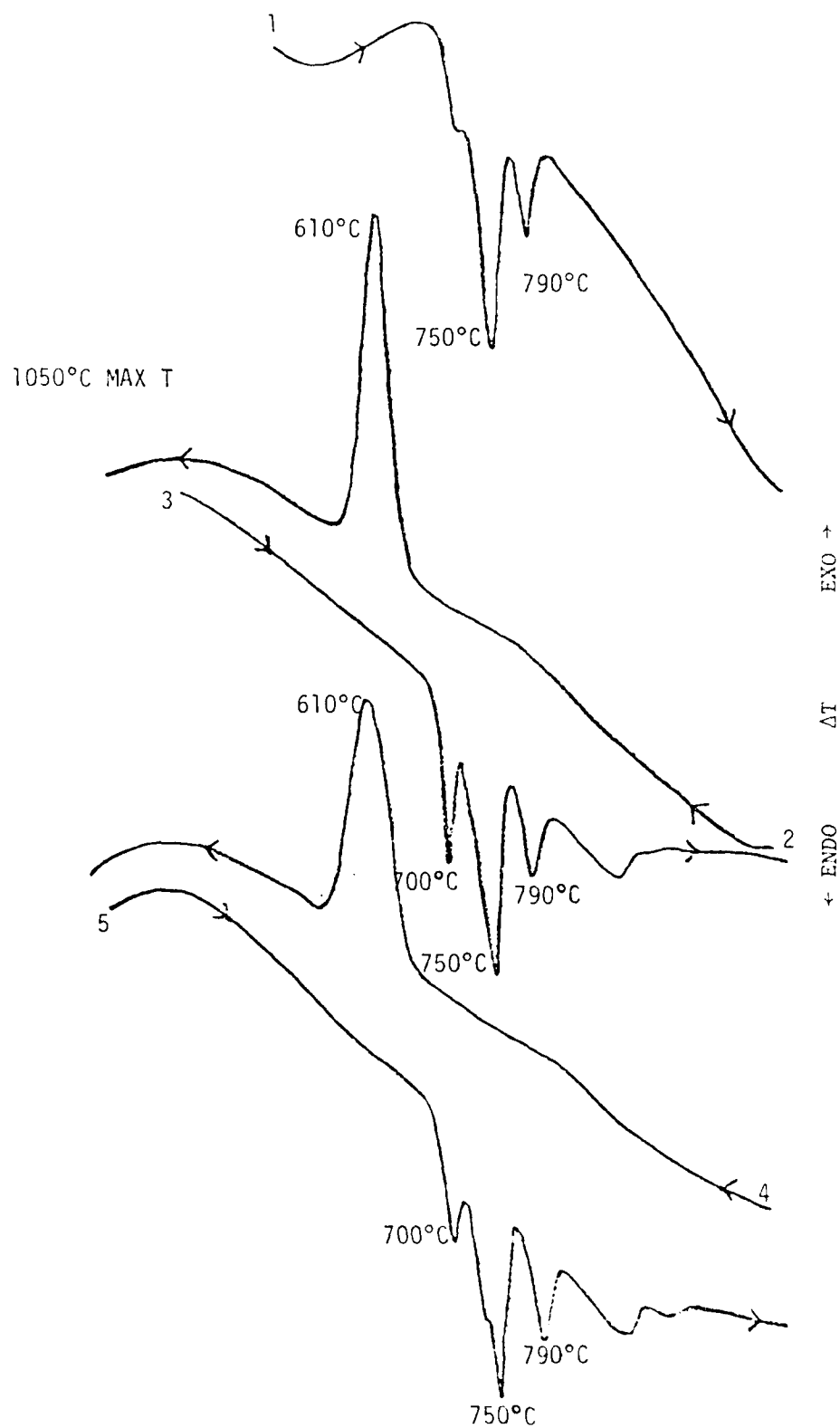


Figure 4. DTA curves for a $0.3 \times \text{Pb}(\text{F}_{2/3}\text{W}_{1/3})\text{O}_3 - 0.7 \times \text{Pb}(\text{Fe}_{1/2}\text{Nb}_{1/2})\text{O}_3$ and 20 weight % of $\text{Pb}_5\text{Ge}_3\text{O}_{11}$ composite materials.

APPENDIX 38

R.E. Newnham, L.J. Bowen, K.A. Klicker, L.E. Cross. Composite Piezoelectric Transducers (review). Int. J. Mats. in Eng. Appl. (accepted).

COMPOSITE PIEZOELECTRIC TRANSDUCERS

R. E. Newnham, L. J. Bowen, K. A. Klicker and L. E. Cross

Materials Research Laboratory

Pennsylvania State University

University Park, Pa., U.S.A. 16802

Considerations of the influence of crystal symmetry, macrosymmetry, and interphase connectivity have been used to explore possible macrostructures of interest as piezoelectric composites. Based on these design considerations, ceramic-plastic composites have been fabricated with 3-3 phase connectivity by the replication of natural template structures such as coral. Composites prepared in this way have piezoelectric g_{33} and g_h coefficients more than an order of magnitude higher than the coefficients of the homogeneously poled ferroelectric ceramic. A simplified fabrication technique has been developed by mixing volatilizable plastic spheres and PZT powder. When sintered and back-filled with epoxy, and poled, these composites give excellent piezoelectric voltage coefficients. Large voltage coefficients were also obtained from 3-1 piezoelectric composites made by embedding PZT fiber arrays in epoxy cement. A continuous poling method has been developed for these fibers which makes it possible to assemble complex composites from pre-poled PZT fibers in epoxy matrices. Multilayer composites with 2-2 connectivity have been produced for filters and other high-frequency applications. Processing methods for producing 3-1 and 2-2 connected composites are described.

1. Introduction

Progress in materials science—like progress in most fields—follows an S-shaped curve of history (Figure 1). When a new effect such as ferroelectricity is discovered, scientific development is rather slow at first, until its importance is recognized. Then follows a period of rapid growth when practical applications and new materials are discovered. During this period, rapid changes take place in selecting the "best" material for each application. Eventually the field matures as the choices are made, and the curve of history saturates.

We see this saturation effect in many branches of solid state research. In electroceramics, lead zirconate-titanate (PZT) has been the best transducer material, and barium titanate the best high-permittivity capacitor material for the past twenty years. Similar situations prevail in magnetic materials, semiconductors, ceramics, and metallurgy. Despite intensive search for new compounds, relatively few major changes have been made in the past decade.

Led by the semiconductor industry, materials science now appears to have entered a new era, the age of carefully patterned inhomogeneous solids designed to perform specific functions. Examples of heterogeneous systems optimized for particular applications include semiconductor integrated circuits, fiber-reinforced metals, and barrier-layer ferroelectric capacitors. No longer as much concerned with the properties of the best single-phase materials, many investigators now search for the best combination of materials and ways to process them. In a very real sense, the field has matured from materials science to materials engineering just as electrical science changed to electrical engineering many years ago.

In most electronic devices there are several phases involved and a number of material parameters to be optimized. An electromechanical transducer, for

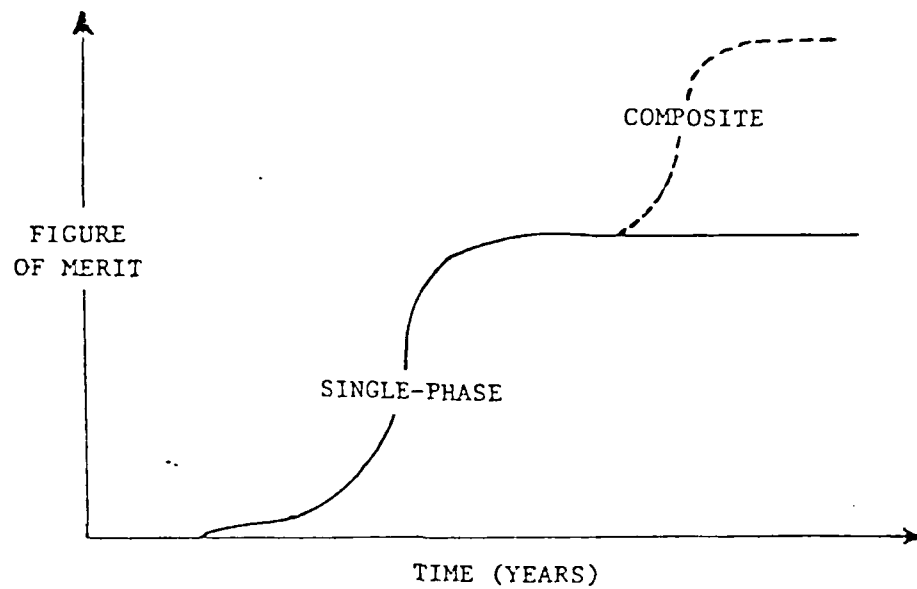


Figure 1. Curve of History for materials. Discovery is followed by a period of rapid development, and then a leveling off. The use of composites sometimes leads to further progress.

example, might require a combination of properties such as a large piezoelectric coefficient (d or g), low density, and high mechanical flexibility. A pyroelectric detector might require a large pyroelectric coefficient, low thermal capacity, and low dielectric constant. In general, the task of materials design may be considerably simplified if it is possible to devise a figure of merit which combines the most sensitive parameters in a form allowing simple intercomparison of the possible "trade offs" in property coefficients. In certain pyroelectric systems, for example, a useful figure of merit is p/ϵ where p is the pyroelectric coefficient and ϵ the electric permittivity.

Unfortunately, the figure of merit often involves property coefficients which are conflicting in nature. To make a flexible electromechanical transducer it would be desirable to have the large piezoelectric effects found in poled piezoelectric ceramics, but ceramics are brittle and stiff lacking the required flexibility, while polymers with the desired mechanical properties are at best very weak piezoelectrics. Thus, for such an application a composite material combining the desirable properties of two different phases might be vastly superior. The main problem is to effect the combination in such a manner as to exploit the desirable features of both components and thereby maximize the figure of merit.

During the past few years we have been experimenting with piezoelectric and pyroelectric composites made from plastics and ferroelectric ceramics, hoping to improve on some of the properties of homogeneous materials (1,2,3). Some of the results are summarized in this paper, along with a few design principles and potential applications.

2. Design Principles

Combining materials means not only choosing component phases with the right

properties, but also coupling them in the best manner. Connectivity of the individual phases is of utmost importance, because this controls the electric flux pattern as well as the mechanical properties. Symmetry is a second important consideration, since symmetry and properties are interrelated through tensor coefficients. In this regard there are several levels of symmetry to be considered: the crystallographic symmetry of each phase, the symmetry after processing, the combined symmetry of the composite, and the environmental influence on the total symmetry including electrodes and clamps.

The points of interest are schematically formalized in Figure 2 for a simple two-phase system. It is interesting to note that in some composites, not only are the properties of the separate phases modified (sum properties), but the composite may exhibit completely new couplings (product properties) not found in the separate phases.

2.1 Sum Properties and Product Properties

A physical property relates an input physical quantity X to an output physical quantity Y . The X - Y effect may be a linear relationship specified by a property coefficient $C = \partial Y / \partial X$, or it may be a more complicated effect. As pointed out by van Suchtelen (4), two classes of X - Y effects can be distinguished in composites.

Sum properties are those in which the X - Y effect of the composite is determined by the X - Y effects in phases 1 and 2. As an example, consider the stiffening of a matrix by strong parallel fibers. Young's modulus of the composite (\bar{E}) depends on the moduli of the matrix phase (1E) and the embedded fiber phase (2E). In the direction of the fibers, \bar{E} is given by $^1E v + ^2E(1-v)$, where v is the volume fraction (5). When measured in various directions, such properties often vary between the geometric and arithmetic mean of the properties associated with the constituent phases.

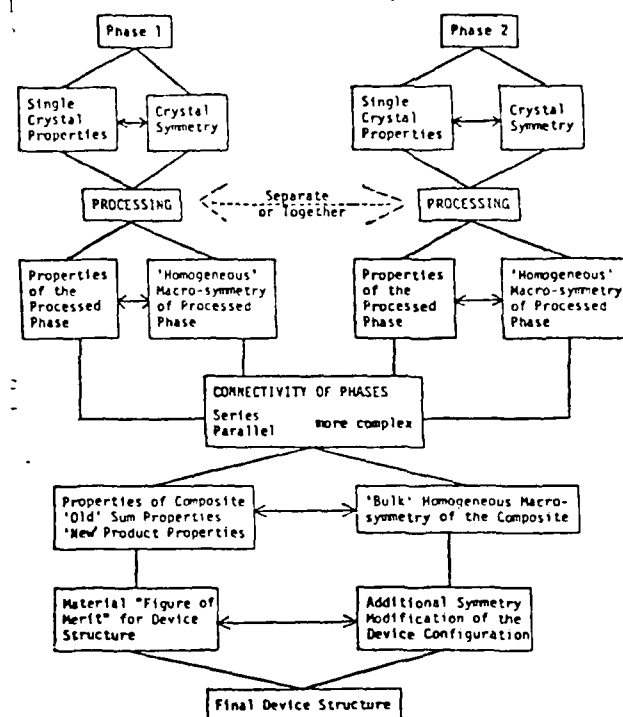


Figure 2. Flow chart illustrating design considerations for optimizing the performance of solid state devices. The task of the materials engineer is to find the materials, processing methods, and connectivity patterns which maximize the figure of merit.

Product properties are less expected and somewhat more complicated: An X-Y effect in the composite results from an X-Z effect in phase 1 and a Z-Y effect in phase 2. In other words, applying X to the composite causes Z to change in phase 1; a change in Z in phase 1 causes Z to change in phase 2, which then results in a change in Y in phase 2. The transfer of the quantity Z from 1 to 2 can be accomplished by several different kinds of coupling.

As an example of a product property, consider a magnetoelectric composite made from a ferroelectric (phase 1) and a ferromagnetic (phase 2). Crystallites of the two phases are assumed to be in good mechanical contact. The ferroelectric grains are poled near the ferroelectric Curie temperature in a strong electric field to make the composite piezoelectric. Magnetic poling of the ferromagnetic phase is accomplished in a similar way, by annealing the composite in a magnetic field.

When an electric field is applied to a magnetoelectric composite of this type the ferroelectric grains elongate parallel to the electric field. The change in shape of the ferroelectric grains causes the ferromagnetic grains to deform, resulting in a change in magnetization. Magnetoelectric measurements on $\text{BaTiO}_3\text{-CoFe}_2\text{O}_4$ composites prepared by unidirectional solidification at the eutectic composition show magnetoelectric coefficients two orders of magnitude larger than the best single phase material (6,7).

2.2 Connectivity

Connectivity is a key feature in property development in multiphase solids since physical properties can change by many orders of magnitude depending on the manner in which connections are made. Imagine, for instance, an electric wire in which the metallic conductor and its rubber insulation were connected in series rather than in parallel!

Each phase in a composite may be self-connected in zero, one, two, or three dimensions. It is natural to confine attention to three perpendicular axes because piezoelectricity and other property tensors are referred to such systems (8). If we limit the discussion to diphasic composites, there are ten connectivities designated as 0-0, 1-0, 2-0, 3-0, 1-1, 2-1, 3-1, 2-2, 3-2, and 3-3. The ten different connectivities are illustrated in Fig. 3, using a cube as the basic building block. A 2-1 connectivity pattern, for example, has one phase self-connected in two-dimensional layers, the other self-connected in one-dimensional chains or fibers. The connectivity patterns are not geometrically unique. In the case of a 2-1 pattern the fibers of the second phase might be perpendicular to the layers of the first phase, as in Figure 3, or they might be parallel to the layers.

In passing we note that connectivity patterns for more than two phases are basically similar to the diphasic patterns, but far more numerous. There are 20 three-phase patterns and 35 four-phase patterns compared to the 10 two-phase patterns in Figure 3. For n phases the number of connectivity patterns is $(n + 3)!/3!n!$. Triphasic connectivity patterns are important when electrode patterns are incorporated in the diphasic ceramic structures.

2.3 Processing Methods

During the past few years we have been developing processing techniques for making diphasic ceramic composites with different connectivities. Extrusion, tape-casting and replamine methods have been especially successful. The 3-1 connectivity pattern in Figure 3 is ideally suited to extrusion processing. A ceramic slip is extruded through a die giving a three-dimensionally connected pattern with one-dimensional holes, which can later be filled with a second phase.

Another type of connectivity well suited to processing is the 2-2

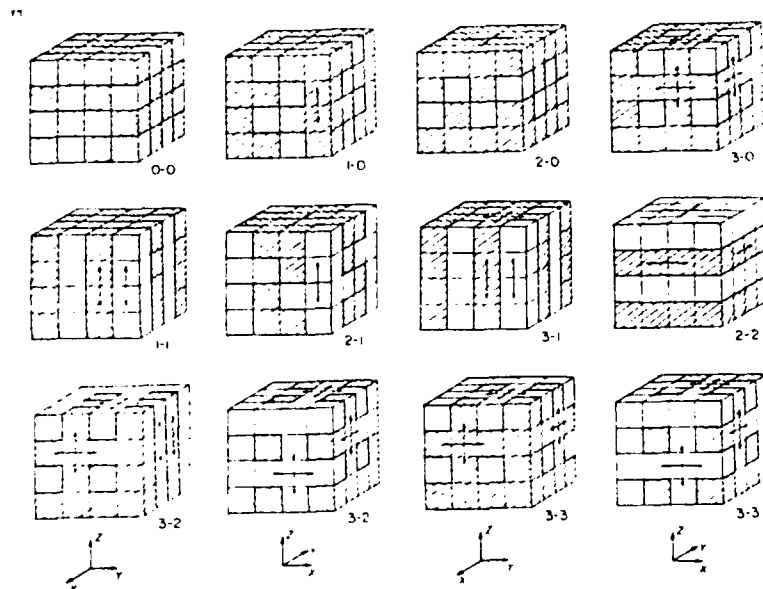


Figure 3. Ten connectivity patterns for a diphasic solid. Each phase has zero-, one-, two- or three-dimensional connectivity to itself. In the 3-1 composite, for instance, the shaded phase is three-dimensionally connected and the unshaded phase is one-dimensionally connected. Arrows are used to indicate the connected directions. Two views of the 3-3 and 3-2 patterns are given because the two interpenetrating networks are difficult to visualize on paper. The views are related by 90° counter-clockwise rotation about Z.

pattern made up of alternating layers of the two phases. The tape-casting of multilayer capacitors with alternating layers of metal and ceramic is a way of producing 2-2 connectivity. In this arrangement both phases are self-connected in the lateral X and Y directions but not connected perpendicular to the layers along Z.

In 3-2 connectivity, one phase is three-dimensionally connected, the other is two. This pattern can be considered a modified multilayer pattern with 2-2 connectivity. If holes are left in the layers of one phase, layers of the second phase can connect through the holes giving three-dimensional connectivity.

The most complicated and in many ways the most interesting pattern is 3-3 connectivity (Figure 2) in which the two phases form interpenetrating three-dimensional networks. Patterns of this type often occur in living systems such as coral where organic tissue and an inorganic skeleton interpenetrate one another. These structures can be replicated in other materials using the lost-wax method (9). The replamine process, as it is called, can also be used to duplicate the connectivity patterns found in foam, wood, and other porous materials.

Four examples of electroceramics with different connectivity patterns are shown in Figure 4. Diphasic ceramic capacitors have been made of BaTiO_3 grains separated by thin layers of NaNbO_3 in the grain boundary regions. The sodium niobate is three-dimensionally connected while the barium titanate grains are not in contact, making it a 3-0 connectivity pattern. The ceramic is manufactured by liquid phase sintering at temperatures above the melting point of NaNbO_3 but below that of BaTiO_3 . At these temperatures, sodium niobate melts and coats the BaTiO_3 grains but rapid cooling prevents reaction between the two phases. High dielectric constant

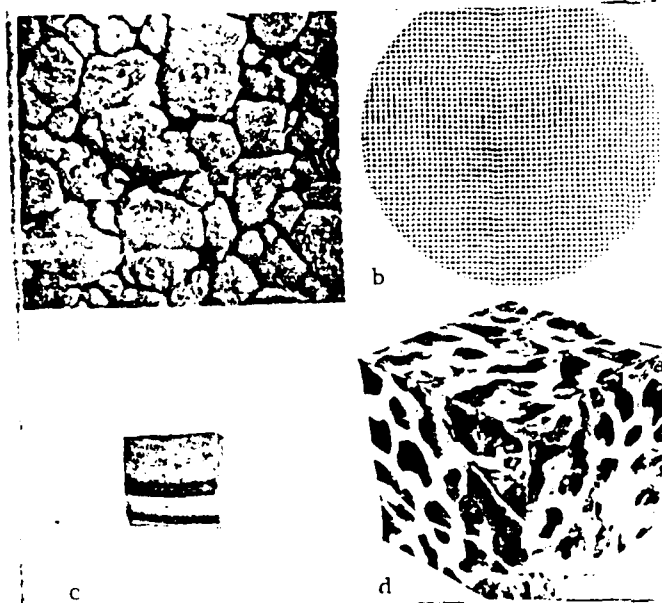


Figure 4. Four types of connectivity: (a) 3-0, (b) 3-1, (c) 2-2 and (d) 3-3 (replamine).

capacitors made with these microstructures show excellent high-voltage characteristics. Normally, the polarization of barium titanate capacitors saturates at high voltages, with the dielectric constant decreasing by as much as a factor of two; but separating the grains of ferroelectric BaTiO_3 with a thin layer of antiferroelectric NaNbO_3 compensates the saturation effect to give a flat voltage response (10).

PZT-plastic composites with 3-0 connectivity have been examined by Furukawa, Fujino and Fukada (11). Samples containing 10 to 30% PZT were made by embedding fine-grained powder in an epoxy resin then sliced into thin wafers, and electroded with silver. Limited poling was possible because of the conductivity of the epoxy, but the piezoelectric coefficients were small. Mixing rules were developed for spherical piezoelectric inclusions in a non-piezoelectric matrix. The calculated \bar{d}_{31} values gave reasonable agreement with experiment.

Connectivity patterns can be synthesized as macrostructures, as microstructures, or even as crystal structures. The BaTiO_3 - NaNbO_3 composite just considered had a 3-0 microstructure. The next three examples involve macrostructures with 3-1, 2-2, and 3-3 connectivities. Figure 4b shows an extruded BaTiO_3 honeycomb ceramic made by Dr. Irwin Lachman of the Corning Research Center. The ceramic is three-dimensionally connected with empty channels in one direction to provide the desired 3-1 connectivity. When the channels are filled with metal electrodes, sizable electric fields can be applied across the thin ceramic walls. The device is intended for use as an electrostrictive micropositioner for adaptive optic systems.

Two composite piezoelectric transducers are illustrated in Figures 4c and 4d. The multilayer composite of "hard" and "soft" PZT has 2-2 connectivity and properties superior to a single-phase piezoelectric. The

soft PZT has a large piezoelectric response and is kept in a poled state by the hard PZT. Figure 3d shows a silicone rubber-PZT composite made by the replamine process (2). The 3-3 connectivity provides mechanical strength and flexibility from the high polymer, and electric continuity and a large piezoelectric effect from PZT. The last two materials will be discussed in more detail later.

3. Piezoelectricity

A number of materials with acentric structure develop an electric polarization in response to mechanical stress. The magnitude of the charge is linearly proportional to the applied stress through the piezoelectric coefficient d , and the sign of the charge can be changed by reversing the direction of the stress.

Piezoelectric materials can be either single crystals or polycrystalline. Quartz is the most widely used single crystal piezoelectric and finds applications primarily in electronic frequency control as resonators and filters. Polycrystalline materials are generally isotropic after densification, but can be made piezoelectric if the material is ferroelectric. A polar axis is introduced by electroding the ceramic and applying a high electric field (typically about 3MVm^{-1}) at temperatures just below the Curie temperature. Polycrystalline ceramic piezoelectrics are easily fabricated in complex shapes and are considerably less expensive than single crystals. PZT ($\text{PbZr}_x\text{Ti}_{1-x}\text{O}_3$) is the most widely used piezoelectric ceramic.

The polarization (P_i) developed in a piezoelectric under applied stress T_j is

$$P_i = d_{ij} T_j \quad (1)$$

The converse piezoelectric effect is given by

$$S_i = d_{ji} E_j \quad (2)$$

where S_i is a strain component, E_j the applied electric field, and d_{ij} the piezoelectric coefficient expressed in coulombs per newton, or meters per volt. Subscripts i and j refer to orthogonal directions within the specimen (8). In ceramics, the poling direction is taken as X_3 .

Large d_{ij} coefficients are desirable in piezoelectric driver applications such as ultrasonic cleaners and sonar. For gramophone pick-ups and hydrophones a useful figure of merit is the piezoelectric voltage coefficient, g , defined by:

$$g_{ij} = \frac{d_{ij}}{\epsilon_i} \quad (3)$$

where ϵ_i is the dielectric permittivity of the material.

Typical single crystal and polycrystalline piezoelectrics and some of their relevant electromechanical properties are listed in Table 1.

3.1 Flexible Transducers

There is considerable practical interest in developing low-density, compliant, flexible piezoelectric transducers. A low-density piezoelectric would have better acoustic coupling to water and have more easily adjusted buoyancy than the high-density PZT ceramics now used for hydrophones. A compliant material would have better resistance to mechanical shock than a conventional ceramic transducer and a large compliance would also mean high damping, which is desirable in a passive device. A flexible material could be deformed to any desired profile. The development of a piezoelectric material which exhibits this combination of seemingly conflicting properties may be carried out in basically two different ways. The traditional approach is to look for a single homogeneous material possessing all the required properties. A material of current interest in this category is poly(vinylidene fluoride), generally referred to as PVF₂.

TABLE 1 Properties of Common Piezoelectric Materials (reference 12).

Piezoelectric Material	Property					
	Relative Permittivity		Elastic Compliance		Piezoelectric Coefficient	
	ϵ_1^T	ϵ_3^T	S_{11}^E pm^2N^{-1}	S_{33}^E pm^2N^{-1}	d_{31} pCN^{-1}	d_{33} pCN^{-1}
α -Quartz Single Crystal (Trigonal, 32)	4.5	4.6	12.8	9.6	$2.3(d_{11})$	—
BaTiO_3 Single Crystal (Tetragonal, 4mm)	2920	168	8.05	15.7	-34.5	85.6
BaTiO_3 Ceramic (γ mm)	1620	1900	8.55	8.93	-79.0	191.0
$\text{PbTi}_{0.48}\text{Zr}_{0.52}\text{O}_3$ Ceramic (γ mm)	1180	730	13.8	17.1	-93.5	223.0
PVF_2 ($\text{C}_2\text{H}_2\text{F}_2$) _n Polymer (ω mm) (Biaxially stretched and poled)	—	3.1	—	—	0.5	-7.5
Collagen (∞)	—	8	—	—	-2.6(d_{14})	—

Piezoelectricity was first reported in this material in 1969 by Kawai (13). In order to make PVF_2 piezoelectrically active, a film of the material, usually about 25 to 75 μm thick, is electroded and polarized under very large electric fields (about 10 to 100 MVm^{-1}) at elevated temperatures ($>100^\circ\text{C}$) for times up to several hours. The films are then cooled to room temperature before the field is turned off (14). PVF_2 has a dielectric constant of 15 which is high for normal organic materials but two orders of magnitude lower than a typical PZT ceramic. The longitudinal piezoelectric strain coefficients (d_{33}) of "poled" PVF_2 are quite high for polymers—on the order of 10 pCn^{-1} , but this is also significantly lower than the d_{33} values for PZT ceramics which range from about 100 to 600 pCn^{-1} . Although PVF_2 has a relatively small d_{33} , the permittivity of this material is low enough that a large figure of merit (g_{33}) is obtained ($140 \times 10^{-3} \text{ VmN}^{-1}$ compared to about $20 \times 10^{-3} \text{ VmN}^{-1}$ for a typical PZT ceramic) (15). The compliance and flexibility of PVF_2 is high and its density is low compared to conventional ceramic piezoelectrics. Overall, this combination of properties appears quite attractive and, in fact, PVF_2 has gained the attention of a number of investigators whose efforts have been directed toward developing devices based on piezoelectricity in PVF_2 (15,16). There are, however, problems associated with the use of PVF_2 . The low piezoelectric strain coefficient indicates that the material would not be of interest as an active device, and although its high voltage sensitivity means it may be good as a passive device, a problem arises here, too. When used as a hydrophone, the material must be fixed to a curved surface which can flex in response to pressure changes. The difficulty lies in designing a sealed flexible mount for the polymer which will function when exposed to the high pressures which exist deep in the ocean and still retain sensitivity

when near the surface. So we see, then, that the figure of merit g_{ij} is not the sole criterion, but that other aspects of the problem must be examined.

A second approach involves the design and use of a composite material. The composite should be designed to take maximal advantage of the useful properties of each phase. A logical choice is a composite made of a polymer and a PZT ceramic. The polymer phase would lower the density and permittivity and increase the elastic compliance. If an elastomer is used, the composite would be compliant and flexible. The properties of piezoelectric PZT are well known to electromechanical transducer designers, and these materials could impart large piezoelectric strain coefficients to the composite. A few attempts have been made at creating an elastomer/PZT composite for use as a flexible low-density transducer (17). The approach used in these attempts was to load a polymer film with particles of a piezoelectric material. The degree of flexibility and the magnitude of the d and g coefficients are primarily controlled by the size of the piezoelectric particles in the heavily loaded elastomer film.

Earlier flexible composites made at Gould were fabricated using 5 to 10 μm particles bound in a polyurethane matrix. A similar material (T-flex) was developed by Harrison (17) using 120 μm particles in a silicone rubber matrix. The longitudinal d values obtained in both cases were comparable to the piezoelectric PVF_2 material but the voltage sensitivities were lower because of the higher permittivities in the composites. The difficulty with this type of composite where the piezoelectric particles are smaller in diameter than the thickness of the polymer sheet (Figure 5a) is that low permittivity polymer layers interleave the piezoelectric particles

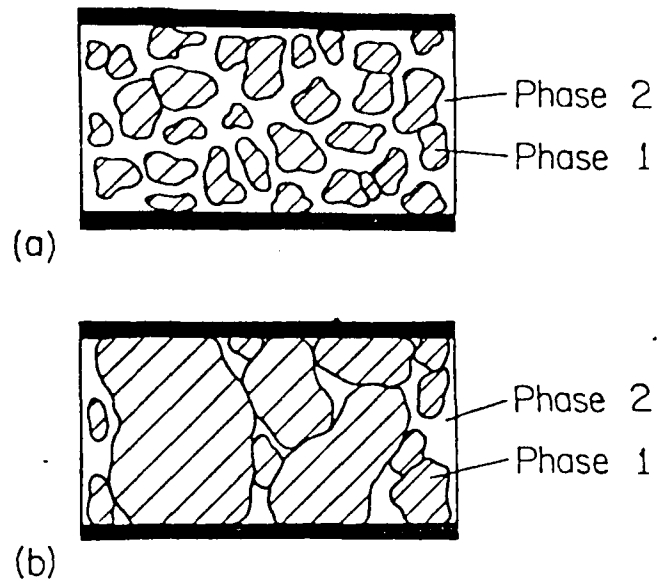


Figure 5. Two types of piezoelectric/polymer composites: (a) represents small piezoelectric particles suspended in a polymer film; (b) represents bound piezoelectric particles of a size comparable to the thickness of the polymer sheet.

preventing saturation poling after the composite is formed. After some poling has been achieved, the interleaved compliant polymer attenuates the piezoelectric response of the composite.

Composites are made at Honeywell (17) which contained much larger particles (up to 2.4 mm in diameter). A material of this type is shown schematically in Figure 5b. Here the particle size approaches the thickness of the composite. Since the piezoelectric particles run from electrode to electrode, near saturation poling can be achieved. The large rigid piezoelectric particles can transmit an applied stress well leading to high d values if d is measured across the particles. Permittivities in these materials are low compared to homogeneous PZT, resulting in high g coefficient. The problem here is that properties of the composite are extremely position sensitive.

To make an effective composite transducer, it can be seen that one cannot merely mix two materials together—some other consideration is necessary. Designing a composite entails not only choosing component phases with the right properties but also coupling the materials in the optimal manner. The connectivity of each phase is of major importance since this controls the electric flux pattern and the mechanical stress distribution.

3.2 Composites: Series Connection

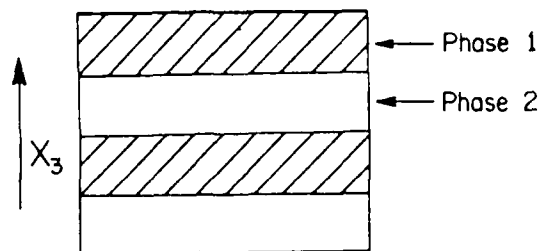
To illustrate the major modifications in ensemble properties which can be effected even in simple linear systems, one-dimensional solutions are presented for the piezoelectric and pyroelectric properties of heterogeneous two-phase structures (1,2).

Consider first the piezoelectric properties of lamellar diphasic composites. Longitudinal piezoelectric coefficient \bar{d}_{33} has been derived for a diphasic piezoelectric with the constituent phases arranged in alternating layers normal to the X_3 direction (Fig. 6a). Designating phase 1 with a superscript 1, and phase 2 with superscript 2, phase 1 has volume fraction 1v , piezoelectric coefficient $^1d_{33}$ and permittivity $^1\epsilon_{33}$, and phase 2 has 2v , $^2d_{33}$, and $^2\epsilon_{33}$, respectively. Solving for the piezoelectric coefficient of the composite gives

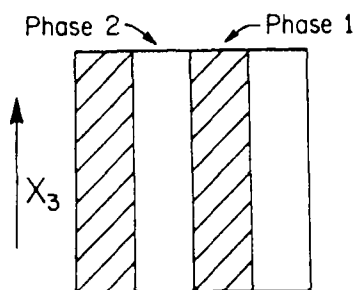
$$\bar{d}_{33} = \frac{^1v^1d_{33}^2\epsilon_{33} + ^2v^2d_{33}^1\epsilon_{33}}{^1v^2\epsilon_{33} + ^2v^1\epsilon_{33}} \quad (1)$$

Using the relation $\bar{g}_{33} = \bar{d}_{33}/\bar{\epsilon}_{33}$ yields the piezoelectric voltage coefficient

$$\bar{g}_{33} = \frac{^1v^1d_{33}}{^1\epsilon_{33}} + \frac{^2v^2d_{33}}{^2\epsilon_{33}} = ^1v^1g_{33} + ^2v^2g_{33} \quad (2)$$



(a)



(b)

Figure 6. The series (a) and parallel (b) models used in estimating the piezoelectric and pyroelectric effects of diphasic solids.

It is interesting to note that for series connection even a very thin low-permittivity layer rapidly lowers the d-coefficient but has little effect on the corresponding g-coefficient.

3.3 Composites: Parallel Connection

If the two phases lie in layers perpendicular to the electrode (Figure 6b), again for the one-dimensional case and neglecting transverse coupling, the composite piezoelectric coefficient is

$$\bar{d}_{33} = \frac{{}^1_v {}^1_d {}^2_{s_{33}} + {}^2_v {}^2_d {}^1_{s_{33}}}{{}^1_v {}^2_{s_{33}} + {}^2_v {}^1_{s_{33}}} \quad (3)$$

where ${}^1_{s_{33}}$ and ${}^2_{s_{33}}$ are the elastic compliances for stresses normal to the electrodes. For the voltage coefficient,

$$\bar{g}_{33} = \frac{{}^1_v {}^1_d {}^2_{s_{33}} + {}^2_v {}^2_d {}^1_{s_{33}}}{({}^1_v {}^2_{s_{33}} + {}^2_v {}^1_{s_{33}})({}^1_v {}^1_{\epsilon_{33}} + {}^2_v {}^2_{\epsilon_{33}})} \quad (4)$$

A composite of interest here is that of an elastically compliant nonpiezoelectric in parallel with a stiff piezoelectric. In this case ${}^1_{d_{33}} \gg {}^2_{d_{33}}$, ${}^1_{s_{33}} \ll {}^2_{s_{33}}$, ${}^1_v = {}^2_v = 1/2$ then $\bar{d}_{33} \approx {}^1_{d_{33}}$, and if ${}^1_{\epsilon_{33}} \gg {}^2_{\epsilon_{33}}$, then $\bar{g}_{33} \approx {}^1_{g_{33}}$, and for smaller volume fractions of the piezoelectric phase, the g-coefficient is correspondingly amplified. It is this case which accounts for the highly successful performance of the replamineform transducer structure described in a later paper. The structure also has considerable hydrostatic sensitivity.

3.4 Hydrostatic Sensitivity

A problem arises when one attempts to use solid PZT as a hydrostatic sensor because d_{33} is approximately equal to $-2d_{31}$, resulting in a low piezoelectric

response to hydrostatic pressure change. Since sizable \bar{d}_{33} coefficients can be obtained for composites with parallel connection, it is interesting to inquire into the hydrostatic sensitivity of this type of connectivity (2).

To evaluate the effective hydrostatic sensitivity for parallel connection, it is necessary to evaluate the transverse piezoelectric coefficient \bar{d}_{31} since $P_3 = -p(\bar{d}_{33} + 2\bar{d}_{31})$ where p is the applied hydrostatic pressure. Since the PZT rods are connected in series in the lateral directions it can be shown that $\bar{d}_{31} \approx {}^1_v {}^1_d d_{31} + {}^2_v {}^2_d d_{31}$. This leads to a hydrostatic piezoelectric coefficient

$$\bar{d}_h = \bar{d}_{33} + 2\bar{d}_{31} \approx \frac{{}^1_v {}^1_d d_{33} {}^2_s s_{33} + {}^2_v {}^2_d d_{33} {}^1_s s_{11}}{{}^1_v {}^2_s s_{33} + {}^2_v {}^1_s s_{33}} + 2({}^1_v {}^1_d d_{31} + {}^2_v {}^2_d d_{31})$$

Suppose for the composite we choose equal volumes of piezoelectric PZT (phase 1) and a soft elastomer (phase 2) such that ${}^1_v = {}^2_v = \frac{1}{2}$, ${}^1_s \ll {}^2_s$, ${}^2_s s_{33}$, ${}^1_d d_{33} \gg {}^2_d d_{33}$, and ${}^1_d d_{33} \approx -2{}^1_d d_{31}$. For the composite $\bar{d}_{31} \approx \frac{1}{2} {}^1_d d_{31}$ and $\bar{d}_{33} \approx {}^1_d d_{33}$, giving $\bar{d}_h \approx \frac{1}{2} {}^1_d d_{33}$.

This is a considerable improvement over single phase performance. Since the hydrophones used under hydrostatic conditions are normally voltage generators, the further favorable enhancement of the voltage coefficient \bar{g}_h can also be exploited: $\bar{g}_h = \bar{d}_h / \bar{\epsilon}_{33}$. Lowering the permittivity $\bar{\epsilon}_{33}$ increases the sensitivity to small pressure changes by raising \bar{g}_h .

4. Piezoelectric Composites with 3-1 Connectivity

Considering the parallel connectivity described above, the ideal three dimensional case is one of PZT rods embedded in a continuous polymer phase, that is, 3-1 connectivity (section 2.2). According to this equal strain composite theory, \bar{d}_{33} should not be a function of the volume fraction of PZT in the composite. This assumes an idealized situation in which the

polymer phase is far more compliant than PZT, causing all the stress on the polymer to be transferred to the PZT rods. That is, as the volume fraction of PZT decreases, the stress on the rods increases proportionally, so that the charge per unit area of the composite is constant. For pressure sensors, it is not necessary that \bar{d}_{33} be large in order to enhance the \bar{d}_h coefficient of the composite. If, as the volume fraction of PZT is decreased, \bar{d}_{31} decreases more rapidly than \bar{d}_{33} , then \bar{d}_h will be increased. Likewise, if \bar{g}_{33} decreases more rapidly than \bar{g}_h , as the volume fraction PZT decreases, then \bar{g}_h will be enhanced.

4.1 Fabrication Method

The thin PZT rods required for 3-1 composites must be sintered to near theoretical density (7900 kgm^{-3}) before they can be poled. For the composite transducers described here, the rods are formed by extrusion of a PZT-organic binder slip (18).

Ninety weight percent PZT is mixed with a solution of 2% polyvinyl alcohol and 8% water, and the mixture ball milled for 16 hours to homogenize the slip. Further homogenization is achieved by repeatedly extruding the slip through a one mm diameter die. The PZT rods are then extruded onto a moving glass plate, dried for ten hours at 120°C , cut into 3 cm lengths and heated at 550°C for 30 minutes to burn out the binder. Sintering is carried out at 1300°C for 30 minutes in the presence of a PbO vapor source composed of 97 mole % PZT and 3 mole % PbO to compensate for lead loss. To reduce porosity and improve their dielectric breakdown strength, the sintered rods are refired in a hot isostatic press (HIP) for one hour at 1300°C under 20 MPa argon pressure. Use of the HIP unit increases the relative density of the rods from 0.94 to about 0.98. PZT rods ranging between 200 and 840 μm in diameter have been used in the composites.

A fixture consisting of two brass discs, each with an array of holes, is used to align the rods (Figure 7). Several hole patterns have been drilled for each of the rod sizes so that composites of 50, 40, 30, 20 and 10 volume % PZT can be prepared. When a rack has been filled with rods it is placed in a plastic tube and the tube filled under vacuum with the appropriate epoxy resin, thus ensuring complete investment of the rods by the polymer. The epoxy is cured at 70°C for sixteen hours, and segments 1, 2, 3 and 4 mm in thickness are cut from the slug (Figure 7) with a diamond saw. The excess epoxy around the composite is trimmed off so that a uniform composite remains.

Air-dry silver electrodes were applied and the samples poled in a 75°C oil bath for five minutes using a field of 2.2 MVm^{-1} . Permittivity was measured at 1 kHz using a capacitance bridge, and the piezoelectric coefficient determined with a d_{33} -meter using two rounded rams. The hydrostatic piezoelectric coefficient (d_h) was measured by altering pressure in an oil chamber at a rate of 3.5 MPas^{-1} and collecting the charge with an electrometer connected in a feedback integration mode which maintain constant electric field conditions.

4.2 Piezoelectric Coefficients

To provide a better understanding of piezoelectric composites, the following factors have been varied: volume fraction PZT, rod diameter, and sample thickness. Specifying the rod diameter and volume fraction PZT automatically fixes a fourth factor: the distance between rods. Obviously, if the stress on the polymer is to be transferred to the PZT rods, the distance from a particular point in the polymer to the nearest rod is important. For a given volume fraction of PZT, the rods are much closer together in composites with

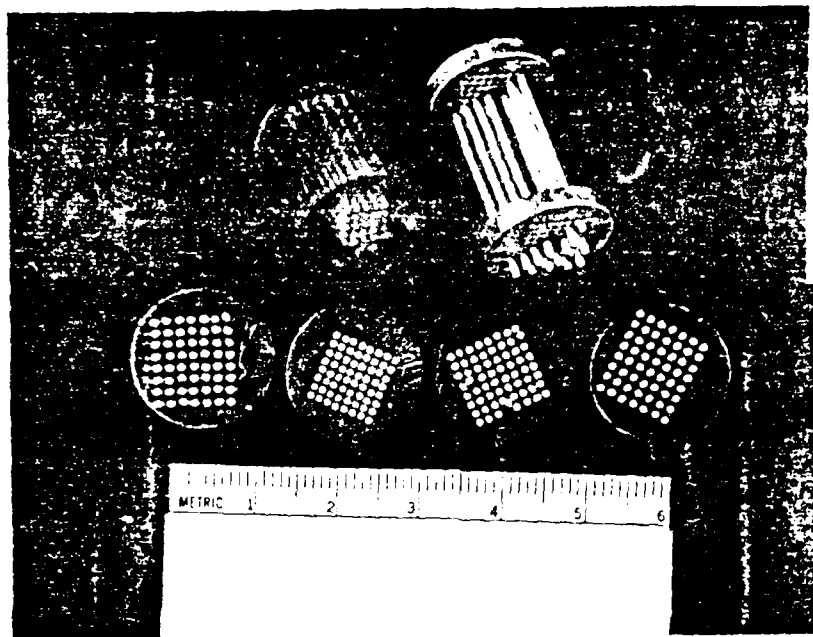


Figure 7. Fabrication of 3-1 composites with PZT rods and an epoxy.

small rod diameters, and with closely-spaced rods, the composite becomes more piezoelectrically homogeneous.

Figure 8 shows that for PZT volume percentages down to 40% the \bar{d}_{33} coefficients are comparable to the value of d_{33} for solid PZT, about 400 pC/N^{-1} . Below 40% PZT, the \bar{d}_{33} values decrease, but even at 10% are still greater than half the value for pure PZT.

The data shown in Figure 8 were measured on composites 4 mm thick. \bar{d}_{33} values for composites of 3, 2 and 1 mm thickness were also measured, and a thickness effect was observed. For all composites the \bar{d}_{33} coefficients decreased with increasing thickness. The magnitude of the thickness effect was a function of rod diameter, volume fraction PZT and separation between the rods.

4.3 Permittivity and Voltage Coefficient

The dielectric constant of a 3-1 composite can be estimated from a model based on two capacitors connected in parallel. The value of $\bar{\epsilon}_{33}$ varies linearly with volume fraction, and since the dielectric constant of PZT is about 1600, and that of the epoxy is about 7, the value of $\bar{\epsilon}_{33}$ may be approximately as $1600v$, where v is the volume fraction of PZT. Experimental values of $\bar{\epsilon}_{33}$ agree well with the theoretical values, as shown in Figure 9.

The piezoelectric voltage coefficient under uniaxial loading is defined as $g_{33} = d_{33}/\epsilon_0$. The g_{33} coefficient of solid PZT is approximately $29 \times 10^{-3} \text{ VmN}^{-1}$. Figure 10 shows the dependence of \bar{g}_{33} on volume fraction of PZT and on rod diameter for composite samples 4 mm thick. While there is little dependence on rod diameter, the magnitude of \bar{g}_{33} is greatly affected by volume fraction. A composite of 254 μm diameter rods with a volume fraction of 0.025 PZT has a piezoelectric voltage coefficient nearly nine times greater

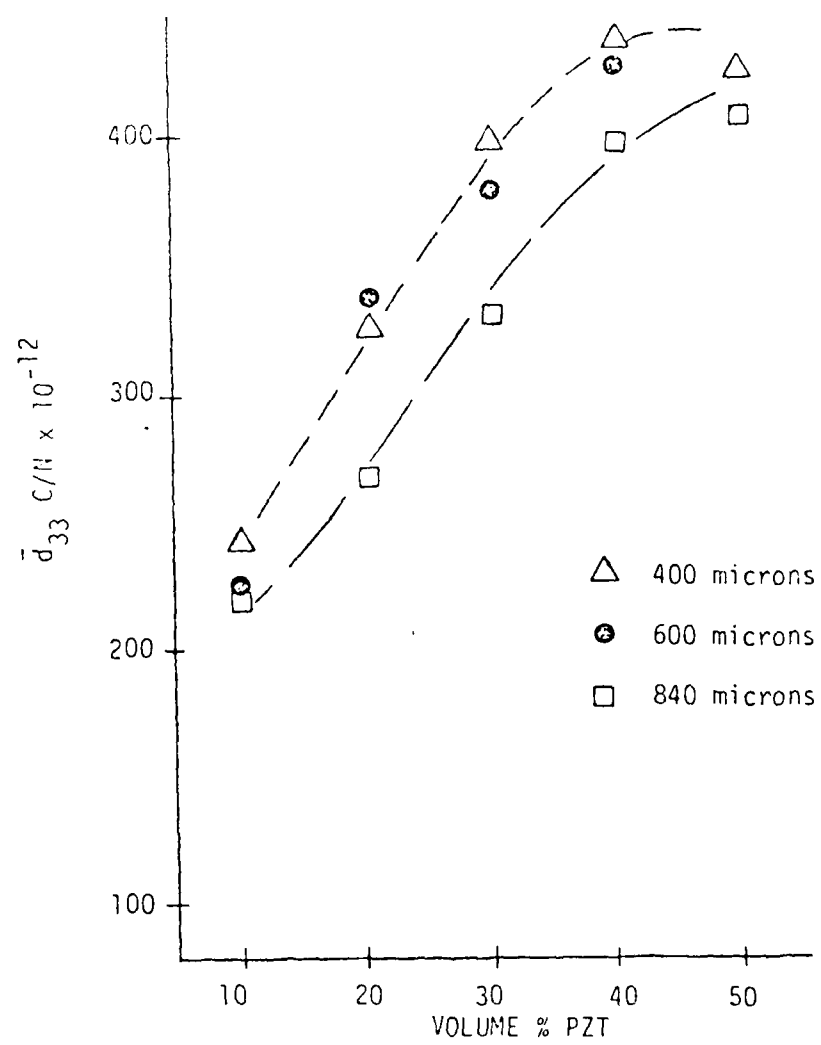


Figure 8. \bar{d}_{33} vs volume % PZT.

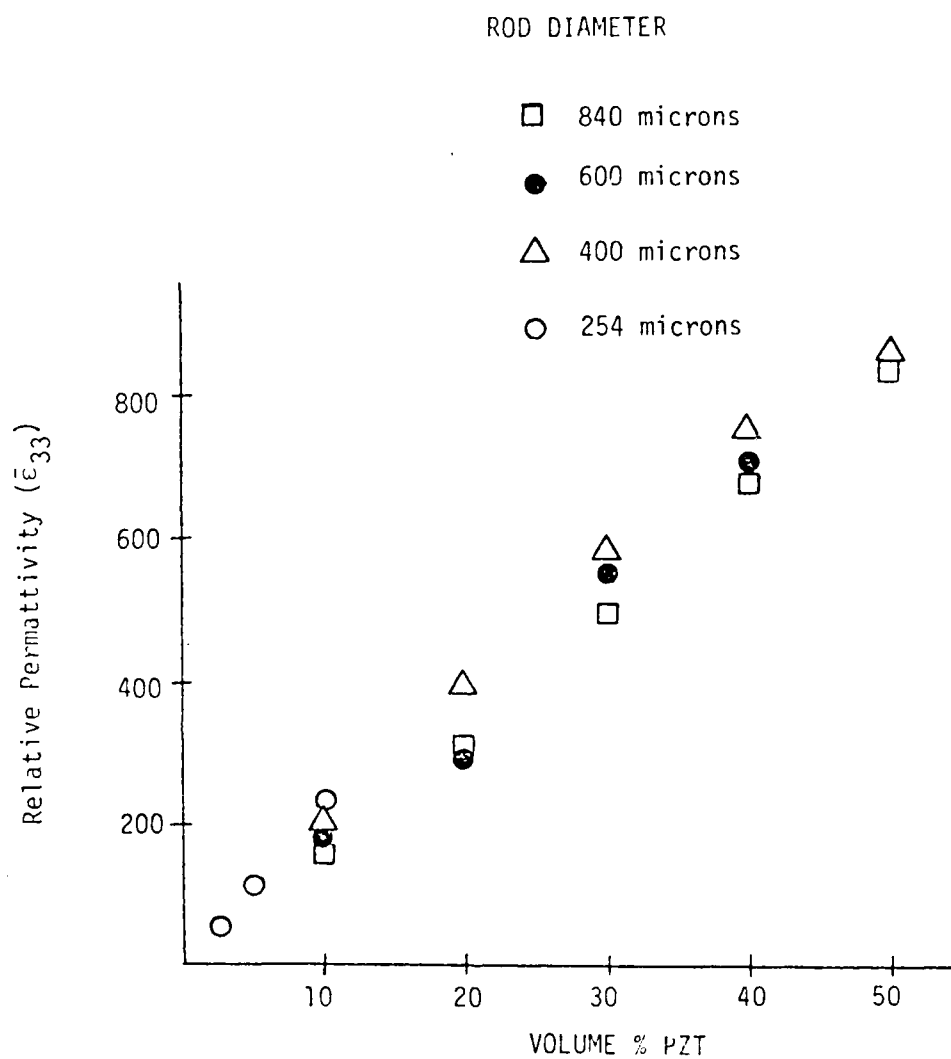


Figure 9. Relative permittivity as a function of volume % PZT.

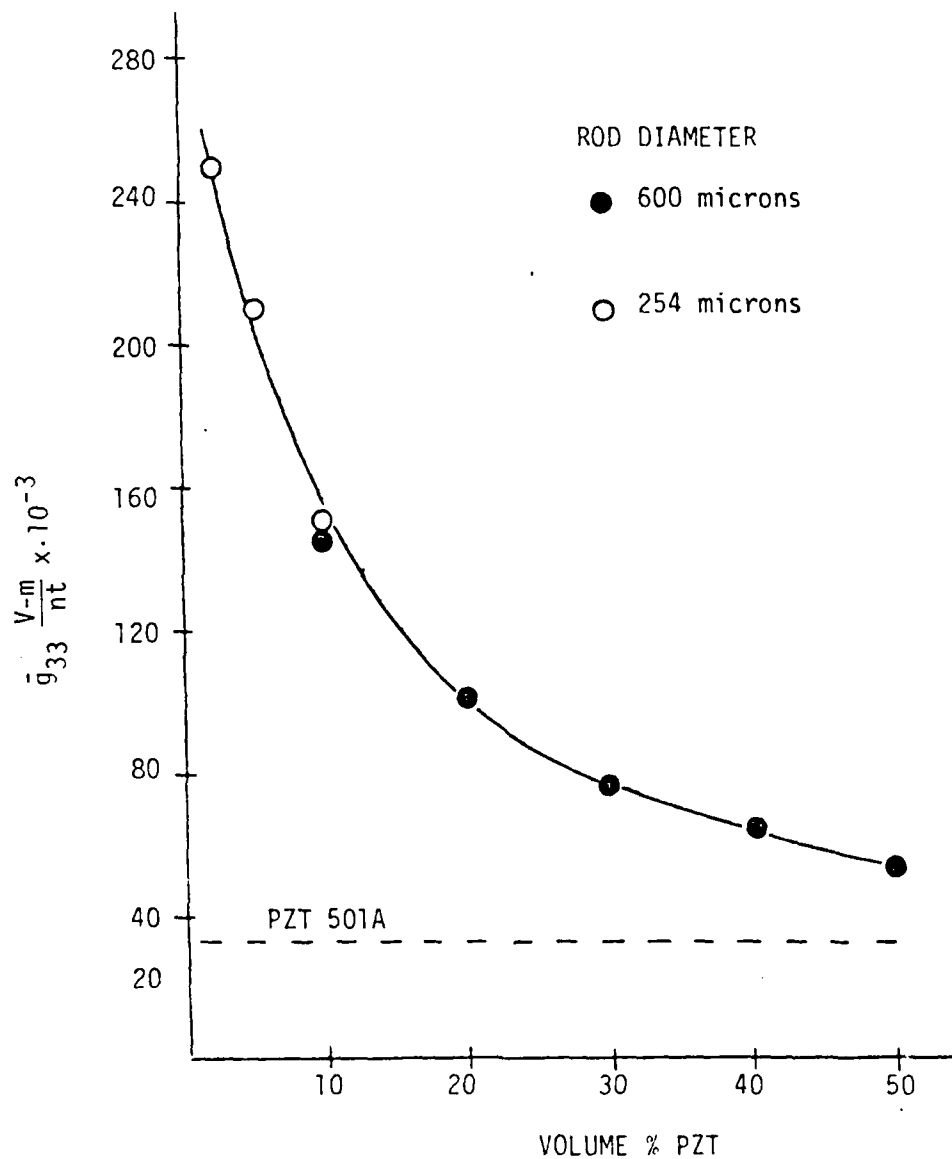


Figure 10. \bar{g}_{33} as a function of volume % PZT.

than that of pure PZT. All the 3-1 composites have larger g_{33} coefficients than solid PZT.

4.4 Hydrostatic Piezoelectric Effects

In figures 11-13, \bar{d}_h is plotted as a function of composite thickness, rod diameter and volume % PZT. As observed in the \bar{d}_{33} measurements, the hydrostatic piezoelectric coefficient is a function of sample thickness. For most of the composites, the \bar{d}_h values are substantially larger than that of pure PZT. Solid ceramic pellets identical in composition with the PZT rods have an average d_h of 31 pCN^{-1} .

As predicted, composites with lower volume fractions of PZT have higher values of \bar{d}_h . Theory (2) indicates that \bar{d}_{31} should decrease linearly with the volume fraction of PZT while \bar{d}_{33} remains constant. If this were true, \bar{d}_h should increase linearly as the volume fraction of PZT decreases. However, the measurements indicate that \bar{d}_{33} decreases when the volume fraction of PZT drops below 40% PZT. If both \bar{d}_{31} and \bar{d}_{33} decreased with PZT content, then \bar{d}_h might decrease, or increase, or remain constant as the volume % PZT decreased. As shown in Figure 12 all of these occur. In composites made with 840 micron diameter rods, \bar{d}_h decreases with volume fraction PZT. For composites containing 600 micron rods, \bar{d}_h is nearly constant from 50% to 20% PZT, while the composites made with 400 micron rods show an increase in \bar{d}_h over the same range. Although the 10% composites have the lowest \bar{d}_h coefficients for all the rod sizes, these samples show the largest increases in \bar{d}_h with each reduction in rod diameter. From the data it appears that if the rod diameter could be further reduced, the 10% composites would have the largest hydrostatic piezoelectric coefficient. The fact that the composites with the lowest volume fraction of PZT have the highest \bar{d}_h is consistent with theory, but the magnitude of the experimental

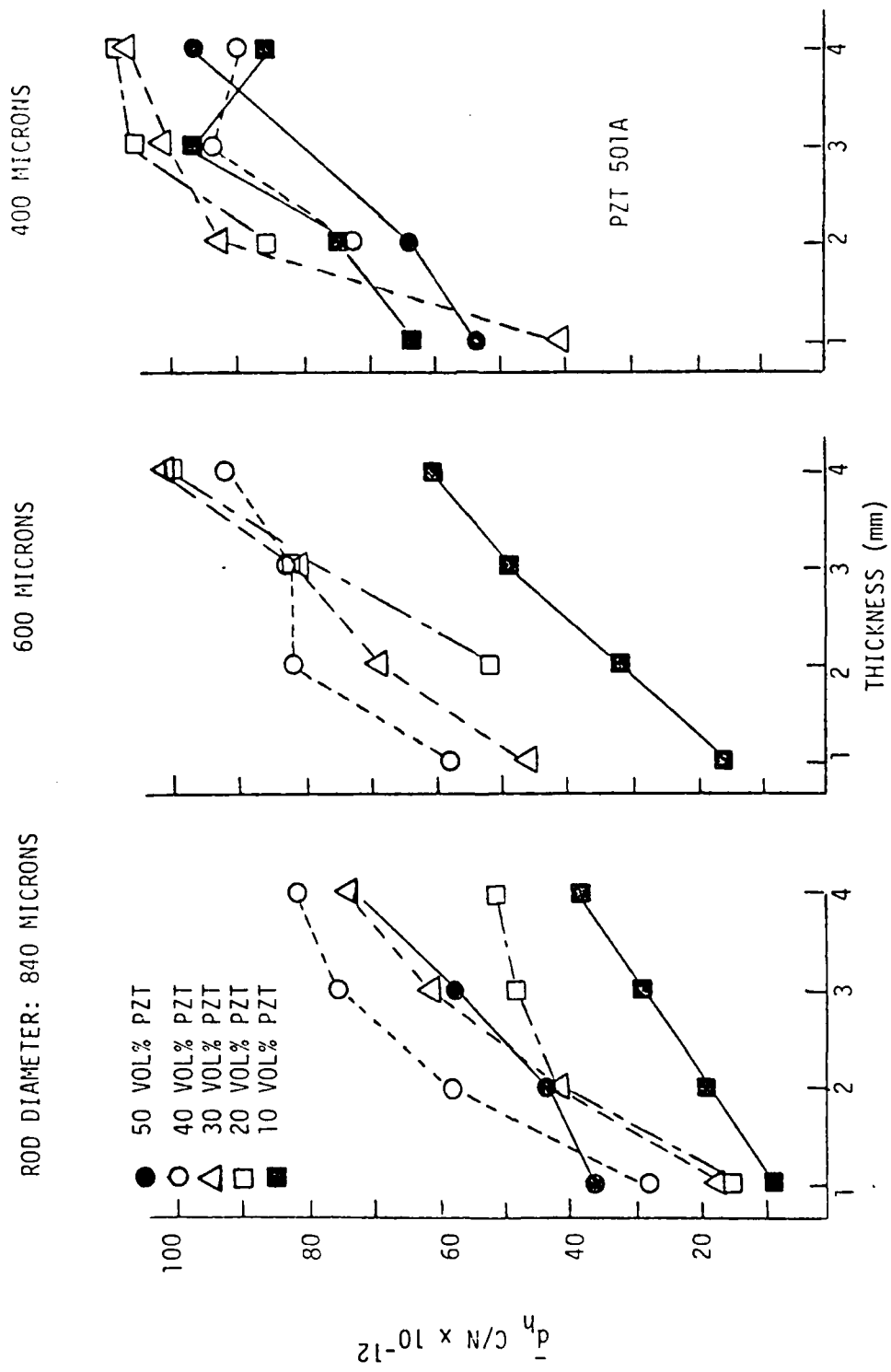


Figure 11. \bar{d}_h as a function of volume % PZT, rod diameter and composite thickness.

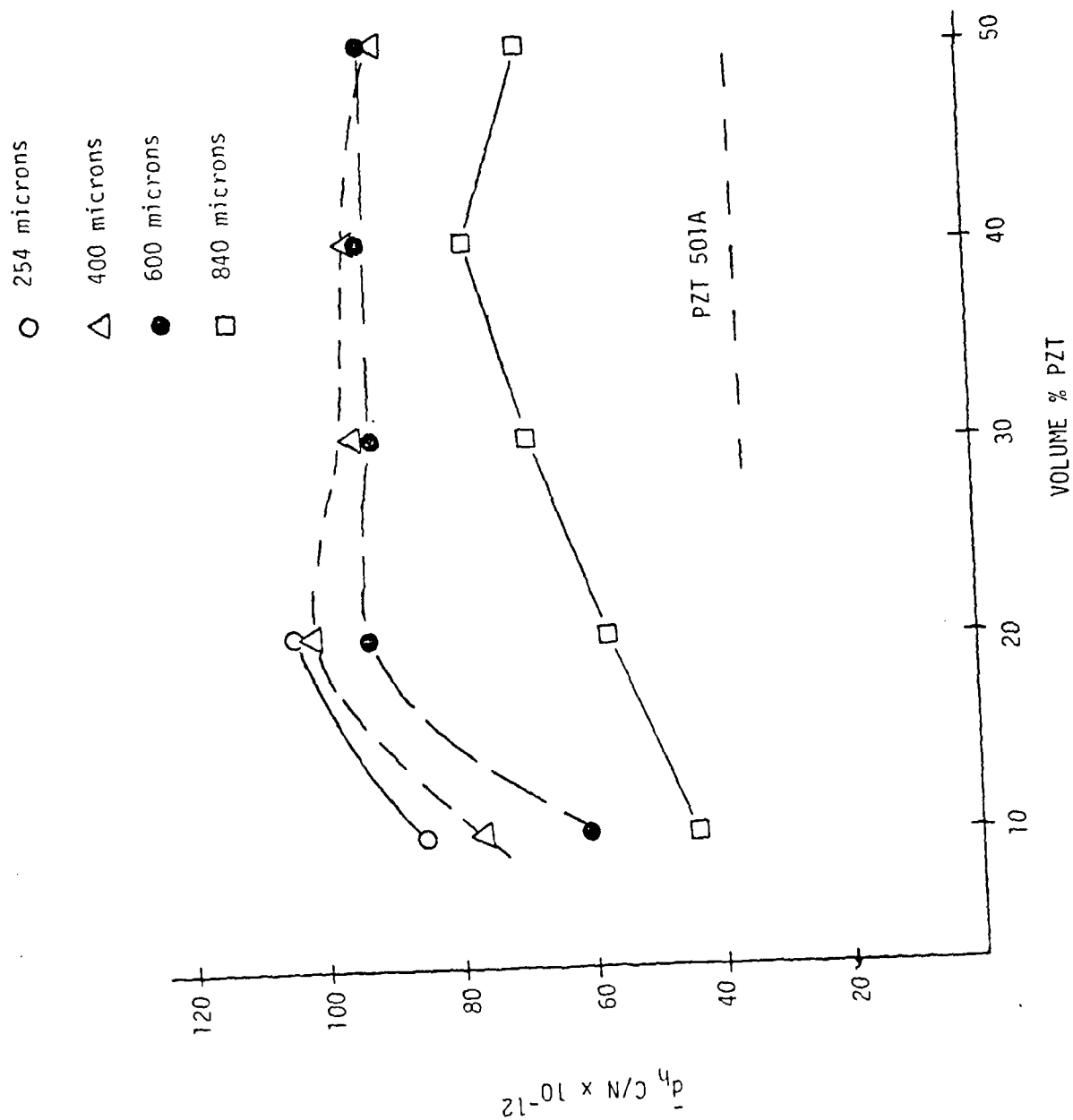


Figure 12. \bar{d}_h as a function of volume % PZT and rod diameter (sample thickness 4 mm).

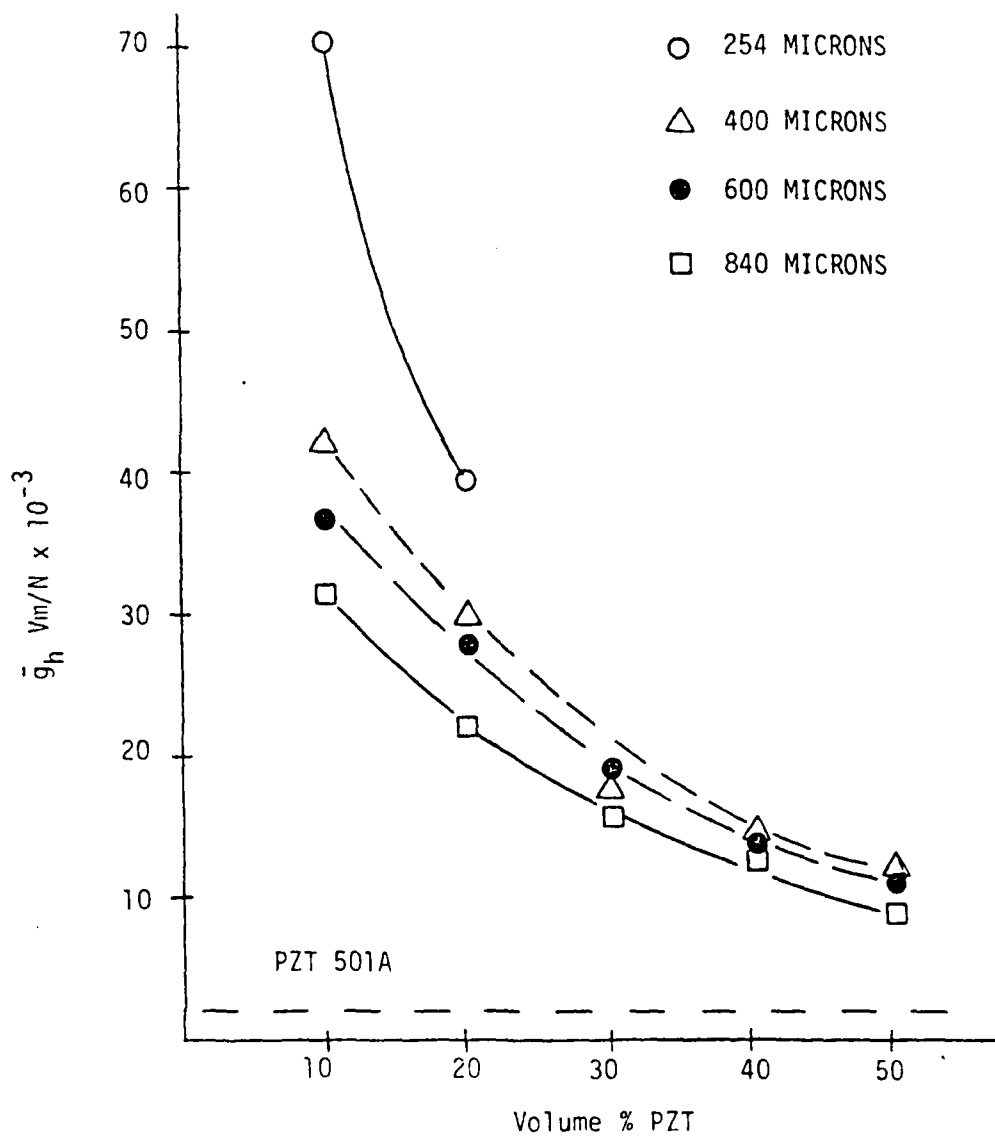


Figure 13. \bar{g}_h as a function of volume % PZT.

\bar{d}_h values are less than one third the theoretical values. It must be remembered that the theory called for a second phase which was much more compliant than the piezoelectric phase, and since epoxy is a stiff polymer, better agreement with the theory is expected when an elastomer is used as the second phase.

The hydrostatic voltage coefficient \bar{g}_h is equal to \bar{d}_h divided by $\bar{\epsilon}_{33}$, the composite permittivity measured in the poling direction. Composites with substantial values of \bar{d}_h and small volume fractions of PZT, have extremely large hydrostatic voltage coefficients. Figure 13 shows a plot of \bar{g}_h for the data shown in Figures 9 and 12. The dotted line in Figure 13 is the value of \bar{g}_h for solid PZT. A 10% PZT composite made from 254 micron rods has a voltage coefficient more than twenty-five times that of the solid PZT. Although use of a more compliant matrix would not appreciably effect $\bar{\epsilon}_{33}$, the resulting enhancement of \bar{d}_h would cause a corresponding increase in \bar{g}_h .

4.5 Specific Gravity

The density of a composite transducer is important because of weight considerations and acoustic impedance matching to the load. Density and acoustic velocity differences between the transducer and the surrounding medium cause reflection losses due to mismatch in acoustic impedances. Reducing the density of the transducer to a value near that of water may help to minimize these losses, at least in the quasi-static case.

The density of the composite can be adjusted between the density of PZT ($7,900 \text{ kgm}^{-3}$) and that of the epoxy (about 1000 kgm^{-3}). It is important to note that the greatest values of \bar{d}_h , \bar{g}_h , and \bar{g}_{33} are all found in the composites with low volume fractions of PZT. Therefore the desired properties of low density and large piezoelectric coefficients are obtained with the same composites.

4.6 Other Fabrication Methods

The production of 3-1 composites is not limited to the use of extruded rods. Rods, bars, fibers, or other small PZT elements may be made by other techniques such as dicing a sintered PZT ceramic, dipping cloth thread in a PZT slip or solution, or spraying a thread with PZT slip and then burning out the thread and sintering the PZT. A sintered PZT slug might be cut in a criss-cross manner with a diamond saw to produce an array of PZT columns of desired dimension and spacing. The manner in which the rods are produced is not important. Neither is the technique in which the rods are aligned. We have aligned rods by moving the discs of the alignment rack close together so that rods aligned in the rack protrude several millimeters beyond the end of the rack. By positioning the array upright in a shallow dish, a single composite may be made by pouring epoxy into the dish to the depth of the desired composite thickness. This technique is especially useful when making composites with an elastomer matrix.

Composites may be made with a matrix other than epoxy. A matrix of a polyester resin results in \bar{d}_{33} , \bar{g}_{33} , \bar{d}_h , and \bar{g}_h coefficients comparable to those obtained with epoxy composites. Composites have been made with elastomers such as silicone rubber and polyurethane. Transducers made with these elastomers are mechanically flexible. Because of the difficulty of cutting or sawing elastomer composites without breaking the PZT rods, such composites must be cast to size as just described.

4.7 Continuous Poling of PZT Fibers

With normal fabrication procedures, the composite thickness is limited by the size of the electric field required to pole the piezoelectric component. At 2.2 MVm^{-1} poling field, 10kV power supply restricts the

thickness of PZT-polymer composites to about 5 mm. The continuous poling technique developed by Gururaja (19) eliminates this problem by using pre-poled PZT rods of any length. The pre-poled rods can also be used to fabricate composites in which rods are aligned in many different patterns, making new transducer designs feasible.

The continuous poling technique utilizes the idea of gradually advancing a rod between two electrical contacts maintained at the required potential difference. Electrical contact to the PZT rods is achieved in two ways.

In the first method, the wetting behavior of a low-melting solder with copper is utilized to form a molten film of solder over a circular hole (2-4 mm in diameter) in a copper plate (2 mm thick). The entire system is immersed in an oil bath maintained at 150°C. The surface tension and the upward thrust of the heated oil keep the molten film stable. A second copper plate is positioned 2-4 mm away from the first plate to provide the second electrical contact.

In the second method, conductive carbon foam is attached to both the top and bottom copper plates using a conductive epoxy. The PZT rods are pulled through the foam attached to the copper plates, in an oil bath maintained at 80°C. The separation between the two electrodes and the pulling rate are the same as in the molten-solder method. An electric field of $1.6-1.8 \text{ MVm}^{-1}$ is required to pole the rods to saturation because the poling temperature is only 80°C.

4.8 PZT Spheres

Initial work on PZT-polymer composites undertaken by Harrison and co-workers (17) utilized coarse granules of sintered PZT rather than PZT rods. A schematic drawing of this PZT-loaded polymer film is shown in Figure 5b. Silicone rubber was used as the matrix material because of its flexibility over a

wide temperature range. The piezoelectric properties were optimized by adjusting the size of the granules and the volume fraction of PZT. Typical values were given in Table 2.

PZT granules of irregular shape assume a variety of orientations with respect to the parallel surface of the composite and thus grinding does not expose every granule to the electroded surface. For poling of the PZT elements to occur, these elements must be in electrical contact with both electroded surfaces. Therefore, composites fabricated from irregular granules are likely to contain unpoled regions which are piezoelectrically "dead". The inactive PZT fragments not only detract from piezoelectric response of the composite but also increase the density and decrease the flexibility unnecessarily.

Similar composites have been fabricated by Safari and Bowen (20) using PZT spheres instead of irregular granules. Spheres offer several potential advantages over irregularly shaped particles. Composites are easily fabricated by pouring the spheres into a pan to form a monolayer, and then covering them with the polymer phase. A light sanding exposes the PZT, allowing contact to both electrodes. This results in excellent poling and piezoelectric activity.

There is the possibility of stress modification in the PZT sphere composites since the compressive stress is born primarily by the small regions at the top and bottom exposed to the electroded surface, resulting in a tensile orthogonal stress. The sign of d_{31} is thus reversed near the perimeter of the spheres, where the ceramic is under tension, and d_{33} may be enhanced (section 3.4). Piezoelectric voltage coefficients \bar{g}_{33} and \bar{g}_h may also be enhanced because of the low permittivity.

TABLE 2 Hydrostatic Mode Materials

	K_{33}	d_h pCN^{-1}	g_h 10^{-3}VmN^{-1}	$d_h g_h$ $10^{-15} \text{M}^2 \text{N}^{-1}$
Ceramics				
PZT Type I	1300	45.9	4	180
PZT Type II	1700	30.0	2	60
PbNb_2O_6	225	67.6	34	2300
Flexible Composites				
PZT Particles in a Silicone Rubber Matrix	100	28.3	32	900
PZT Replamine in a Silicone Rubber Matrix	50	35.8	80	2800
PZT Cubes in a Silicone Rubber Matrix	715	25.2	4	100
PZT Rods in an Epoxy Matrix (3-1 Connectivity)	200	77.6	40.4	3138
Polymer				
PVF_2	12	11.5	108	1246

5. Piezoelectric Composites with 3-3 Connectivity

As shown in the previous section, a composite with 3-1 connectivity makes an effective piezoelectric transducer. Since, however, in firing the ceramic fibers one must maintain this orientation, some interconnections between the rods are helpful; i.e. partial 3-3 character is required. In a 3-3 template, both phases are continuously connected in all three dimensions. This type of structure is exhibited by certain polymer foams, some diphasic glasses, three-dimensionally woven materials, and by biological substances such as wood and coral.

5.1 Replamine Process

Coral skeletons are characterized by a structure with the following features: (i) a narrow pore size distribution; (ii) a pore volume approximately equal to the solid phase volume, and (iii) complete pore interconnectivity making every pore accessible from all other pores. The dimensions of the pores vary from species to species, but within one species the size range is quite narrow. Different species of coral have various degrees of anisotropy in their structure ranging from a 3-1 connectivity of nearly parallel tubes to highly isotropic 3-3 structures. Figure 4 shows a micrograph cube of the calcium carbonate skeleton of the coral species *goniopora* which we have used as a structural template for making composite transducers. The replicating technique, known as the replamineform process, was developed at the Materials Research Laboratory at Penn State for producing prosthetic materials (9). We chose the replamineform process for reproducing the 3-3 connectivity type because of past experience with this procedure, although other preparation

techniques may be more practical.

The first step of the replamine process (Figure 14) is to shape the coral, which is easily machinable, to the desired geometry. The coral template is then vacuum-impregnated with a casting wax and the wax allowed to harden, after which the calcium carbonate coral skeleton is leached away in hydrochloric acid leaving a wax negative of the original coral template. The negative is reinvested with a PZT slip (average grain size $\sim 2 \mu\text{m}$) containing PZT, water, and poly(vinyl alcohol). Investment is carried out by vacuum impregnation with vibratory action to render the thixotropic PZT slip fluid. The wax negative is burned off leaving a coral-type structure of PZT which is then sintered for one hour at 1300°C . A 13% linear shrinkage is observed in the replicas, but the replicated pore structure is maintained. The PZT replica is back-filled with a suitable polymer such as a high purity silicone rubber, and, after the surface has been cleaned, a silver-loaded silicone rubber electrode is applied. The composite is then poled at a field strength of 1.4 MVm^{-1} for 5 minutes at 100°C . Relative permittivity of the unbroken composite, as determined with a capacitance bridge, is about 100. The average longitudinal piezoelectric coefficient \bar{d}_{33} obtained for the unbroken composite is approximately 160 pCn^{-1} . As poled, the replamine replica is still a rigid structure because of the three-dimensional connectivity of the ceramic phase. If, however, the body is now crushed to break the ceramic connectivity, an extremely flexible piezoelectric composite results (Figure 15). Crushing is carried out by reducing the sample height to about 80% of its original value and simultaneously shearing the sample 20% of the sample height about an axis perpendicular to the crushing force direction.

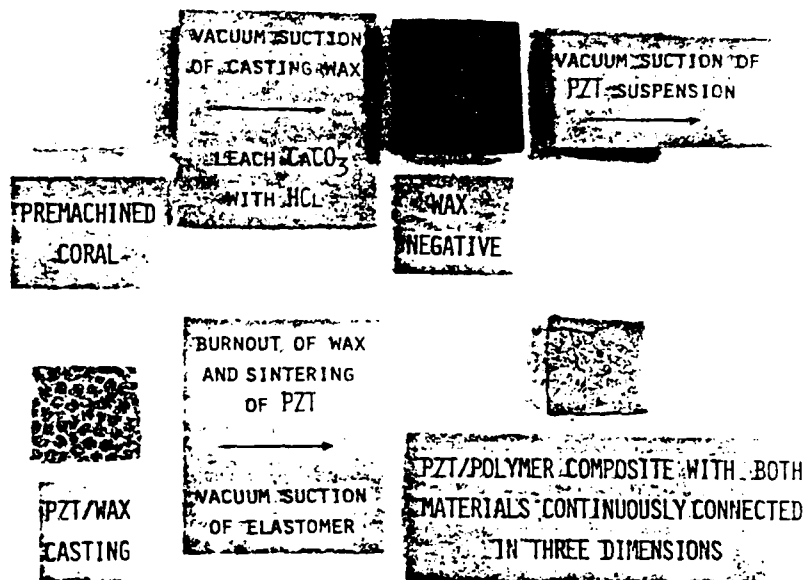


Figure 14. The replamine "lost-wax" fabrication process.



Figure 15. Flexibility in a PZT/silicone rubber composite fabricated using the Replamine process.

By breaking the poled ceramic the easy electric flux path through the poled piezoelectric is interrupted, thus lowering the permittivity. The pieces of poled piezoelectric are still held in position by the polymer matrix and will therefore still transmit stress. As a result, the \bar{d}_{33} coefficient remains high while the permittivity is reduced and thus the longitudinal piezoelectric voltage coefficient, $\bar{g}_{33}(=\bar{d}_{33}/\bar{\epsilon}_{33})$, is greatly enhanced with respect to the g value of a homogeneous ceramic piezoelectric.

After disrupting the connectivity of the PZT phase by crushing the sample, the relative permittivity is reduced to about 40, while \bar{d}_{33} is only reduced to about 100 pC/N . Hence, the \bar{g}_{33} values of these flexible composites are approximately $300 \times 10^{-3} \text{ V/mN}$, which is fifteen times better than a homogeneous PZT transducer. Table 2 contains a comparison of transducer characteristics, from which it is obvious that the replamine composite of PZT and silicone rubber compares very favorably with homogeneous transducer materials for passive device applications. The compliance of the composite is large compared to solid PZT, imparting mechanical shock resistance.

5.2 Alternative Fabrication Methods

Several alternative methods of making 3-3 transducer composites have been suggested (1,2,3), utilizing simpler fabrication techniques than the coral replamine process.

The method proposed by Shrout (21), involves the use of a volatile phase in the fabrication procedure. Commercially available PZT powder is mixed with polymethyl methacrylate (PMM) spheres (50 to 150 μm diameter) in a 30/70 volume ratio. The mixture is die-pressed using poly(vinyl alcohol) as a binder and the binder and PMM spheres volatilized out by very slowly heating the pressed pellet to 400°C . After sintering at

1300°C for 0.5 hours the cold highly porous pellets are vacuum impregnated with a suitable polymer: after a flexible silicone rubber elastomer or a stiff epoxy resin.

SEM micrographs of the PZT-epoxy composite are shown in Figure 16. A similar microstructure is observed in the PZT/silicone rubber composites. It is clearly seen that the two phases are randomly interconnected. The size of the PZT phase regions ranges from a few microns to 100 microns, whereas the polymer regions range from 20 to 120 μm and are quite spherical in nature. The replamine microstructure is somewhat more open with polymer regions in the order of 500 μm in diameter interspersed with PZT regions of about 200 μm diameter. Piezoelectric properties are similar to the replamine materials. When filled with silicone rubber, \bar{d}_{33} is about 200 pC N^{-1} and \bar{g}_{33} about $170 \times 10^{-3} \text{ V m N}^{-1}$. The piezoelectric coefficients are somewhat lower with an epoxy filling: $\bar{d}_{33} \sim 90 \text{ pC N}^{-1}$, $\bar{g}_{33} \sim 90 \times 10^{-3} \text{ V m N}^{-1}$. The principal advantage of this method is that it is readily adapted to mass production.

Interconnected PZT-polymer composites have also been made by Nagata and co-workers (22). Using an undisclosed powder preparation technique, porous $\text{Pb}(\text{Zr}_{0.53}\text{Ti}_{0.47})\text{O}_3$ ceramics were conventionally sintered to a volume fraction of 48%. Silicone rubber was injected to fill the pore channels giving 3-3 connectivity. Volume fractions are about 50% for the two phases, and skeletal diameters about 20 μm . Poled specimens exhibit \bar{g}_{33} coefficients of $130 \times 10^{-3} \text{ V m N}^{-1}$, increasing the hydrophone sensitivity to nearly four times that of solid PZT ceramics.

Miyashita, Takano and Toda (1979) have synthesized a more regular PZT-polymer composite resembling a ladder structure made from thin strips of PZT. Specimens with porosity levels in the 40 to 60% range have good \bar{g}_{33} coefficients of $90 \times 10^{-3} \text{ V m N}^{-1}$.

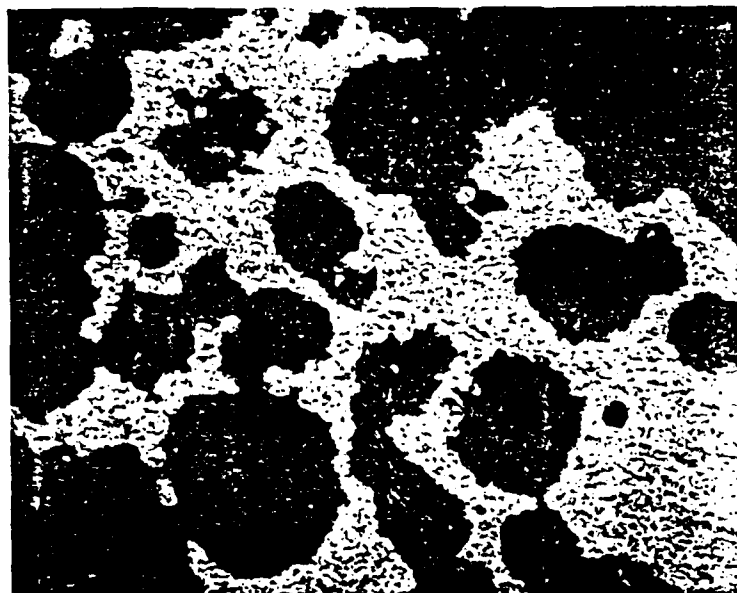


Figure 16. PZT-epoxy composite fabricated by mixing organic spheres with the PZT prior to sintering (Light grey phase is PZT).

6. Piezoelectric Composites with 2-2 Connectivity

Piezoelectric composites with multilayer structures (2-2 connectivity) have been fabricated to give (i) enhanced electromechanical coupling under high driving fields, (ii) high stability electrical filters and (iii) improved impedance matching.

6.1 Tape-cast Composites

Tape-casting provides a convenient way of making thin ceramic layers, approximately 250 μm thick (24). In the tape-casting process, a ceramic powder is mixed with a liquid organic binder to form a homogeneous slurry, which is then spread in a thin continuous layer onto a moving glass substrate. The thickness and uniformity of the sheet are controlled by a series of knife edges set parallel to the surface of the glass plate and a fixed distance above it. After drying, the organic binder hardens to give a flexible plastic tape impregnated with ceramic powder. The tape can be cut to size and sintered in the normal way. Green density and sintering characteristics can be modified by a post casting pressing operation so that materials which normally would sinter at different rates can be fired together without problems arising from uneven shrinkage. To fabricate multilayer composites, the component layers are stacked alternately and pressed together at about 50°C to obtain a firm bond before firing (25).

Using this technique, lamellar heterogeneous devices comprised of layers of a commercial soft ferroelectric (modified PZT) and an anti-ferroelectric (modified PZSnT) have been produced (26). The purpose of the antiferroelectric layers is to prevent depoling of the soft ferroelectric phase under high electric fields, since the antiferroelectric has a large coercive field. Series model calculations show that a high piezoelectric coefficient can be obtained if a high permittivity anti-

ferroelectric phase is employed. By selecting a temperature (90°C) at which the antiferroelectric had maximum coercive field, it was shown that antiferroelectric-ferroelectric composites were dielectrically more stable (harder) under high field cycling than a typical commercially used hard PZT.

In another 2-2 connected composite, layers of lead magnesium niobate $\text{Pb}_3\text{MgNb}_2\text{O}_9$ alternated with layers of $0.8\text{Pb}_3\text{MgNb}_2\text{O}_9-0.2\text{PbTiO}_3$ have been used to form a temperature-stable resonator for electrical filter applications (27). These two materials have compensating positive and negative temperature coefficients of elastic compliance. As a result, changes of less than 60 ppm/°C in the radial resonant frequency over a temperature range between -10°C and 80°C have been obtained.

In a third application, multilayered composites of poled PZT incorporating platinum metal internal electrodes have been developed for applications where electrical impedance matching is important (28). The basic electrode configuration used in the piezoelectric devices is similar to that employed in multilayer capacitors. In such a device the poling of alternate layers is of opposite direction but the responses are additive in either a driven or driver mode. Thus, the voltage required to produce a given displacement is found to be greatly reduced compared to homogeneous devices of the same PZT composition, and the measured direct \bar{d}_{33} is increased by a factor approximately equal to the number of internal electrodes employed. Resonant properties are unaffected by the presence of the internal electrodes (28). Consequently, internal electrodes can be incorporated into piezoelectric transformers in order to increase their step-up ratio. Here the transformer ratio is multiplied by the number of layers introduced into the primary end of a conventional bar-shaped transformer (29). A second advantage is that the ends of the internal electrodes, which act

as the low side of the secondary circuit allow a more uniform poling and larger electrode area, thereby increasing the current capacity and hence the power of the secondary. If DC isolation of the primary and secondary is required, a thin section of strip electrodes may be included as the low side of the secondary circuit.

6.2 High Frequency Applications

Piezoelectric composites are not limited to low frequency applications. A 2-2 connected temperature-compensated resonator material composed of lead magnesium niobate and lead titanate has already been described (Section 6.1). Another high frequency application involves bandwidth modification in electrical filters.

Electrical circuits operating at high frequency often require some form of frequency control to limit the pass band of frequencies. This control can take the form of piezoelectric crystal or ceramic component shaped so that the frequency range of interest coincides with a resonance frequency of the piezoelectric element. At resonance the piezoelectric filter has minimum impedance, several orders of magnitude lower than its nonresonant impedance. Consequently, the element readily passes signals at frequencies close to its resonant frequency, the width of the pass band usually being defined by the mechanical Q of the device as $Q = \frac{f}{\Delta f_{3dB}}$ for $Q > 10.0$. Here f is the center frequency and Δf_{3dB} is the (power) 3 decibel pass band. For ceramic piezoelectrics the mechanical Q is typically in the range 50 - 1000, giving 3dB bandwidths in the range 0.1 - 2% of the center frequency. Using composite devices, it is possible to reduce or widen the bandwidth of a piezoelectric material by combining several active piezoelectric elements mechanically in series or in parallel respectively.

A reduction in bandwidth can be obtained by carefully grinding several piezoelectric discs to the same thickness and bonding them together in a series configuration using an electrically conducting epoxy resin, as shown in Figure 17(a). For the fundamental thickness mode of a single disc, the resonant frequency is governed by the equation:

$$f_L = \frac{1}{2L} \frac{1}{\sqrt{\rho s}},$$

where ρ is the density and s the elastic compliance.

The disc thickness L is equal to half the acoustic wavelength. Therefore, since the sign of the stress changes every half wavelength, in order to resonate in phase the polarity of adjacent discs must be reversed. Acoustic wave transmission occurs only at frequencies very close to f_L and consequently the bandwidth is reduced. Using one PZT disc as a driver or "primary" Figure 17(a), the output from the "secondary" (Figures 18(a) and 18(b) is reduced in bandwidth and increased in amplitude compared to a single disc of the same material. The increase in amplitude arises because the device also acts as a piezoelectric transformer (29).

A similar composite device, capable of operation at microwave frequencies, has been developed (30) using cadmium sulfide as the active piezoelectric element. The CdS layers are separated by inactive half-wavelength-thick films of silicon monoxide so that polarity reversal is unnecessary.

One problem associated with series multilayer transducer designs is the extremely accurate dimensional tolerances which must be achieved if constructive interference is to be achieved (31). Moreover in many applications, the reduction in bandwidth and increase in amplitude are simply trade-offs, and do not result in an overall increase in conversion efficiency (32). Since narrow bandwidth materials are abundant ($Q > 10^5$

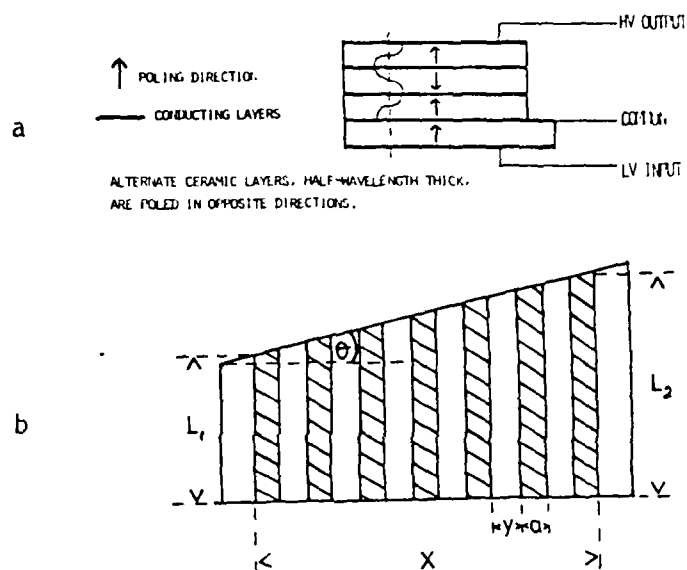
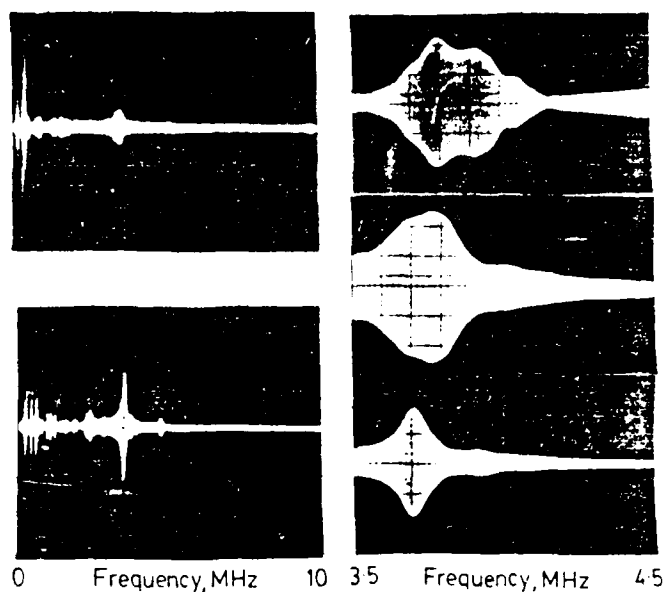


Figure 17(a). Series resonant device for band-width reduction, composed of half-wavelength thick piezoelectric layers separated by electrically-conducting epoxy.

Figure 17(b). Parallel resonant device for broadband applications. Piezoelectric layers (shaded) are decoupled mechanically by an inactive, low Q polymer.



0 Frequency, MHz 10 35 Frequency, MHz 45

a b

Figure 18(a). Increase in amplitude of thickness mode resonance for series, connected resonant composites (3 layers thick).

Figure 18(b). Decrease in bandwidth of thickness mode. From Top: single layer, 2 layer, 3 layer case).

for quartz), it seems likely that series-connected multilayer filters will find only limited applications.

Although narrow band pass filters are readily available for most frequency ranges of interest, broadband filters, in which bandwidths up to 50% of the center frequency are required, are more difficult to produce. Apart from electrical filters, broadband devices are being employed in acoustic imaging, especially for noninvasive medical uses, and nondestructive flaw detection (33-36). Ultrasonic imaging has an advantage over its optical counterpart of improved contrast, since it relies for contrast on elastic discontinuities which are generally of greater magnitude than changes in refractive index, particularly in biological tissue. In acoustic imaging the piezoelectric element acts as both source and detector in a "pulse-echo" operational mode (37,38). At present the image is built up by mechanically scanning a single transducer over the area of interest, and integrating its output to form a coherent picture (39). Typical commercial broadband transducers for biomedical applications are shown in Figure 19.

Previously, bandwidth has been increased (39,40) by: (i) electrically connecting narrow bandwidth filters with slightly different resonance frequencies in parallel, (ii) damping the resonance of a low Q piezoelectric element in order to spread the resonance peak over a wider frequency range, or (iii) impedance matching piezoelectric transducers to the load with quarter-wave acoustic transformers. Methods (i) and (iii) have the disadvantages of extreme complexity, and in method (ii) much of the input energy is wasted by damping.

Based on the equation for f_L , it is possible to fabricate a broad bandwidth electromechanical transducer from a single piezoelectric element by forming the element into a wedge shape of varying thickness and driving

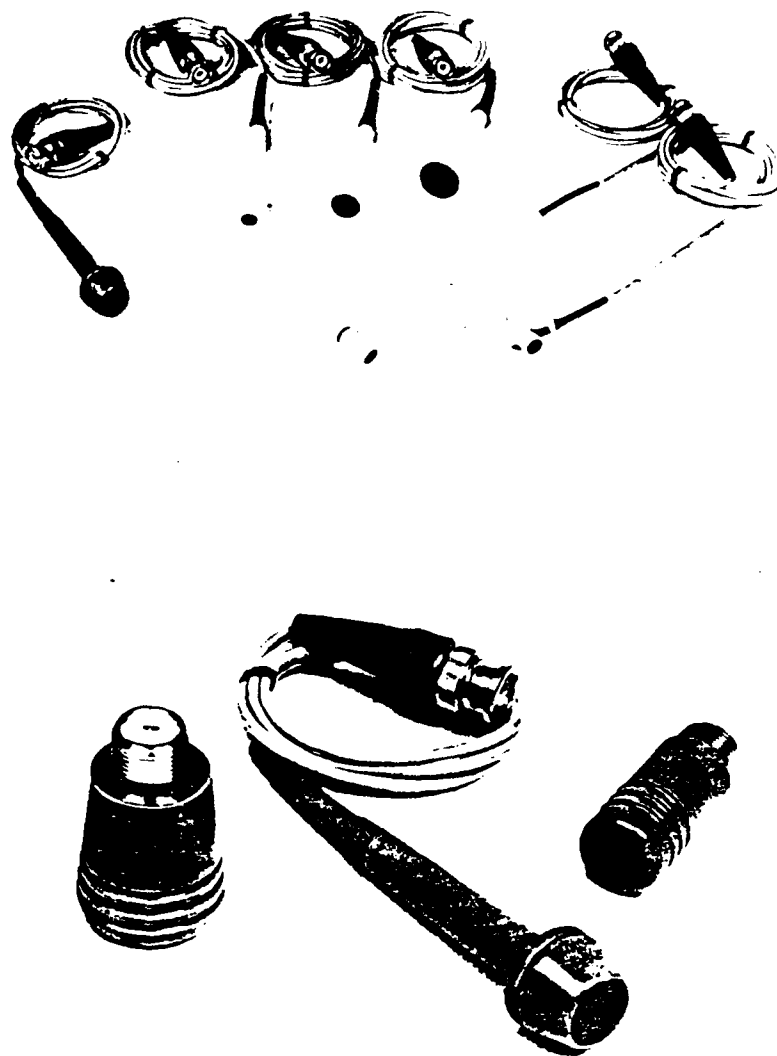


Figure 19. Ultrasonic transducers for medical diagnostic applications in echocardiography and two-dimensional imaging.

(Photographs courtesy of KB-Aerotech, Lewistown, Pa.)

it at frequencies corresponding to resonance of the thickness dimensions. In this case the thickness mode resonance encompasses a range of frequencies governed by its maximum and minimum dimensions. However, since the element is strongly mechanically coupled at all points, destructive mechanical interference occurs between regions of different thickness resonating at different frequencies, and low efficiency results.

Connecting piezoelectric ceramic elements in parallel with a mechanically lossy polymer can overcome the shortcomings of the wedge configuration, and produce an efficient broadband device. In this application many piezoelectric elements with different dimensions are used to provide a wide pass band, but the elements are combined into a single array using an inactive, low Q polymer which decouples the elements mechanically and prevents interference. The device consists of sheets of piezoelectric material, e.g. PZT, laminated with sheets of polymer so that the active elements are separated by sufficient polymer that most of the mechanical coupling between the elements is removed (see Figure 17(b)). The slope of the device, $\tan \theta$, defines its bandwidth according to the relationship:

$$\Delta f = \frac{x \tan \theta \cdot f_1 f_2}{N}$$

where Δf is the bandwidth in Hz, x is the width of the device, and f_1 and f_2 are the resonance frequencies of elements of length L_1 and L_2 , respectively, and N is the longitudinal mode frequency constant of the piezoelectric material used. The bandwidth can be increased by increasing θ as far as the natural mechanical Q of the PZT will allow.

The above concept has been verified experimentally by substituting for the 2-2 connected lamellar composite a composite of soft PZT ceramic fibers embedded in epoxy, similar to those described in Section 4.1. This material

has the advantage of accepting any surface profile, thus providing a greater versatility in applications. In principle, the pass band of this composite can be tailored to provide a frequency spectrum of any shape.

Figures 20(a) and 20(b) compare the frequency spectra from 0 to 1 MHz for 30 volume % PZT fiber composites with their opposite faces inclined at 2° and 10° respectively. The 6dB bandwidth has been increased from 7% for a composite with faces ground parallel, to 11% for the 2° composite, and to 45% for the device with faces inclined at 10° .

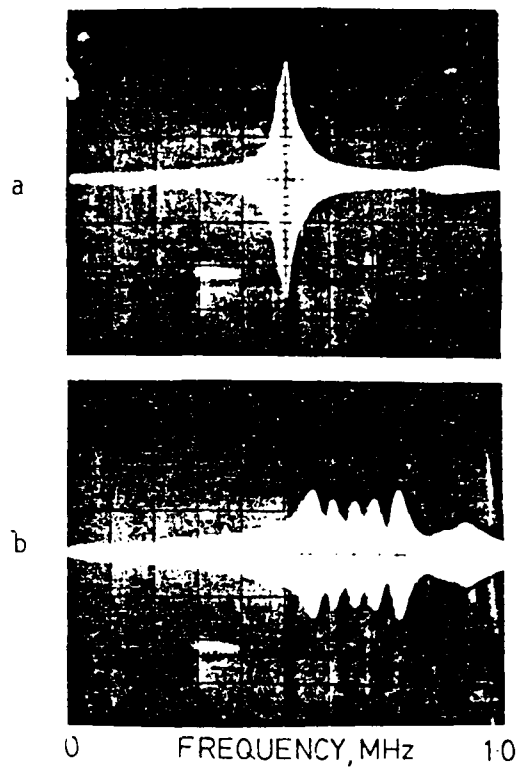


Figure 20(a). Bandwidth broadening in parallel connected resonant composites.
(a) $Q = 2^\circ$

Figure 20(b). $Q = 10^\circ$
Vertical scale = amplitude
Horizontal scale = frequency

SUMMARY AND CONCLUSIONS

Composite piezoelectric elements form an interesting family of materials which highlight the major advantages composite structures afford in improving coupled properties in solids for transduction applications. By careful consideration of the crystal symmetry, macrosymmetry, and possible modes of phase interconnection (connectivity) which can be realized by modern processing technologies, it is possible to design new composite transducers with property combinations tailored for specific device requirements.

For electromechanical applications at low frequencies where the acoustic signal has a wavelength λ much larger than the scale of the macrostructure, it is shown that ceramic:plastic composites can be designed which have mean piezoelectric voltage coefficients \bar{g}_{33} and \bar{g}_h which are orders of magnitude larger than those of the active ceramic phase. Such materials have obvious application in hydrophones and other listening devices.

Composites in other geometries can be designed so as to modify the poling and depoling characteristics of the active ceramic PZT phase, and thus to effectively stiffen the electrical characteristics against depoling under high stresses.

By prepoling ceramic PZT fibers before the composite is assembled, it is possible to construct new types of polar solid with interpenetrating polar axes and property combinations which would be impossible in the simple single phase solid.

For high frequency applications where λ is comparable to the scale of the composite macrostructure, the full potential of composite structures begins to become apparent. In such systems impedance, bandwidth, and radiation pattern can be controlled in a sophisticated manner which is impossible in single phase systems. For transducer arrays which could be used in focusing and scanning modes, the potential for composite structures

is clear.

We believe that the composite materials offer a new versatility in property combinations, and it will be most interesting to observe how this is taken up and exploited in subsequent generations of piezoelectric devices.

8. References

1. R. E. Newnham, D. P. Skinner, and L. E. Cross, Mat. Res. Bull. 13 525 (1978).
2. D. P. Skinner, R. E. Newnham, and L. E. Cross, Mat. Res. Bull. 13 599 (1978).
3. R. E. Newnham, D. P. Skinner, K. A. Klicker, A. S. Bhalla, B. Hardiman and T. R. Gururaja, Ferroelectrics, vol. 3, p. 49 (1980).
4. J. van Suchtelen, Philips Res. Rpts. 27, 28 (1972).
5. J. L. Broutman and R. H. Krock, Modern Composite Materials, Addison-Wesley Publ. Co., Reading, Mass. (1967).
6. J. van den Boomgaard, D. R. Terrell, R. A. J. Born and H. F. J. I. Giller, J. Mat. Sci. 9, 1705 (1974).
7. A. M. J. G. van Run, D. R. Terrell and J. H. Scholing, J. Mat. Sci. 9, 1710 (1974).
8. J. F. Nye, Physical Properties of Crystals, Oxford University Press, London (1957).
9. R. A. White, J. N. Weber and E. W. White, Science 176, 922 (1972).
10. D. A. Payne, "The Role of Internal Boundaries Upon the Dielectric Properties of Polycrystalline Ferroelectric Materials." Ph.D. Dissertation in Solid State Science, The Pennsylvania State University, March 1973.
11. T. Furukawa, K. Fugino and E. Fukada, Japan. J. Appl. Phys. 15, 2119 (1976).
12. Landolt-Bornstein Tables on Elastic, Piezoelectric, Piezooptic and Electrooptic Constants of Crystals. Vols. II, 1 (1966) and II, 2 (1969). Springer Verlag, Berlin.
13. H. Kawai, Japan. J. Appl. Phys. 8, 975 (1969).
14. H. Burkard and G. Pfister, J. Appl. Phys. 45, 3360 (1974).
15. S. Edelman, Proceedings of the Workshop on Sonar Transducer Materials, Naval Research Laboratory (Feb. 1976).
16. Y. Wada and R. Hayakawa, Japan. J. Appl. Phys. 15, 2041 (1976).
17. W. B. Harrison, Proceedings of the Workshop on Sonar Transducer Materials, Naval Research Laboratory (Feb. 1976).

18. K. A. Klicker, J. V. Biggers, and R. E. Newnham, J. Amer. Ceram. Soc. (accepted).
19. T. R. Gururaja, R. E. Newnham and L. E. Cross. Amer. Ceram. Soc. Bulletin. (accepted).
20. A. Safari and L. Bowen, Private Comm.
21. T. R. Shrout, W. A. Schulze, and J. V. Biggers, J. Amer. Ceram. Soc. (in press).
22. K. Nagata, H. Igarashi, K. Okazaki, and R. C. Bradt, Japan. J. Appl. Phys. 19, L37-40 (1980).
23. M. Miyashita, K. Takano, and T. Toda Proc. Int. I.E.E.E. Symp. on Appl. of Ferroelectrics, Minneapolis, June 13-15 (1979) (to be published in Ferroelectrics).
24. J. C. Williams, "Doctor-Blade Process," Treatise on Materials Science and Technology, vol. 9 (Ceramic Fabrication Processes), F. Y. Wang, editor; p. 173, Academic Press, 1976.
25. J. V. Biggers, T. R. Shrout and W. A. Schulze, Bull. Amer. Ceram. Soc. 58, 516 (1979).
26. T. R. Shrout, W. A. Schulze and J. V. Biggers, Ferroelectrics (to be published).
27. T. R. Shrout, W. A. Schulze and J. V. Biggers, Ferroelectrics (to be published).
28. L. J. Bowen, T. R. Shrout, W. A. Schulze and J. V. Biggers, Ferroelectrics (to be published).
29. H. W. Katz, "Solid State Magnetic and Dielectric Devices", Wiley, 1959, Chapter 5.
30. J. de Klerk, P. A. Klemens and E. F. Kelly, Appl. Phys. Lett., 7, 265 (1965).
31. R. Holland and E. P. EerNisse, "Design of Resonant Piezoelectric Devices", Research Monograph No 50, MIT Press, 1969, p.89.
32. E. K. Sittig, IEEE Transactions on Sonics and Ultrasonics, Su-14, (4), 167 (1967).
33. A. Wade, IEEE Transactions on Sonics and Ultrasonics, Su-22, 385 (1975).
34. K. R. Erikson, F. J. Pry and J. P. Jones, IEEE Transactions on Sonics and Ultrasonics, SU-21, 144 (1974).
35. A. Nemet, Phil. Trans. R. Soc. Lond. A.292, 137 (1979).
36. R. S. Sharpe, Phil. Trans. R. Soc. Lond. A292, 163 (1979).
37. B. T. Khuri, — Yakub and G. S. Kino, Appl. Phys. Lett., 30, (1977).

38. K. R. Erikson, IEEE Transactions on Sonics and Ultrasonics, Vol SU-26, 7 (1979).
39. A. de Sterke, "Advances in the Technology of Mechanized Ultrasonic Testing", Phil. Trans. R. Soc. Lond. A292, 207-221, 1979.
40. W. P. Mason, "Physical Acoustics", Vol 1A, 384, Academic Press, 1964.
41. J. H. Goll, "The Design of Broad-Band Fluid-Loaded Ultrasonic Transducers", IEEE Transactions on Sonics and Ultrasonics, SU-26, (6), 385-393, 1979.

List of Figures

1. Curve of History
2. Flow chart
3. Connectivity Patterns
4. Four examples of conn. Patt.
5. PZT/polymer composites
6. Series and Parallel models
7. Klicker 3-1 composites (photo)
8. d_{33} curves
9. ϵ_{33} curves
10. g_{33} curves
11. Thickness curves for d_h
12. Rod diam curves for d_h
13. g_h vs PZT vol %
14. Replamine processing steps
15. Fingers bending replamine
16. Shrout BURPS micrograph
17. High freq. device config.
18. High freq. spectra

APPENDIX 39

T.R. Gururaja, R.E. Newnham, K.A. Klicker, S.Y. Lynn, W.A. Schulze,
T.R. Shrout, L.J. Bowen. Composite Piezoelectric Transducers. IEEE
Ultrasonics Symposium, Nov. 5-7, 1980, Boston, MA. (accepted).

COMPOSITE PIEZOELECTRIC TRANSDUCERS

T.R. Gururaja, R.E. Newnham, K.A. Klicker, S.Y. Lynn, W.A. Schulze, T.R. Shrout and L.J. Bowen

Materials Research Laboratory
The Pennsylvania State University
University Park, Pennsylvania 16802

Abstract

Consideration of macrosymmetry and interphase connectivity has been used to explore possible macrostructures of interest as piezoelectric composites. Based on these design considerations, ceramic polymer composites have been fabricated with 3-3, 3-1, and 1-3 phase connectivity. In general these composites yield a lower permittivity, higher hydrostatic charge coefficient (d_h) and voltage coefficient (g_h), and in some cases increased thickness coupling coefficient (k_t). These composites can be used to construct hydrophones, broad band filters, and deformable mirror base. The composites can be made flexible and conformal using an elastomer as the second phase.

1. Introduction

Progress in materials science—like progress in most fields—follows the curve of history (Fig.1). When a new effect such as ferroelectricity is discovered, scientific development is rather slow at first, until its importance is recognized. Then follows a period of rapid growth when practical applications and many new materials are discovered. Rapid changes take place in selecting the "best" material for each application. Eventually the field matures as the choices are made, and the curve of history saturates.

We see this saturation effect in many fields of materials science. Lead zirconate titanate (PZT) has been the best transducer material for 25 years. BaTiO₃ has been the best high dielectric capacitor material for 30 years. Similar trends can be noted in magnetic materials, semiconductors, and superconductors. Despite intensive search for new compounds, relatively little progress has been made in the past ten or twenty years.

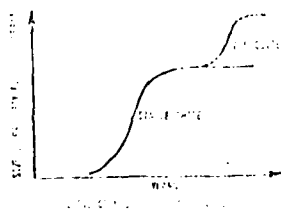


Figure 1

Recent years have witnessed the growth of materials engineering with the optimization of specific properties by carefully patterned inhomogeneous solids such as semiconductor integrated circuits, fiber reinforced metals, and barrier layer ferroelectric capacitors. In heterogeneous systems, there are generally several phases involved and a number of material parameters to be optimized.

The present case of designing an electromechanical transducer for towed array hydrophone application requires a combination of properties such as large hydrostatic piezoelectric coefficient (d_h) and voltage coefficient (g_h), low density, and high mechanical flexibility. The figure of merit for a hydrophone material is given by the product $d_h g_h$.

PZT solid solutions which are currently used in many transducer applications have low d_h and g_h coefficients. The low coefficients are a result of coupling of the d_{33} and d_{31} coefficients. Specifically $d_h = d_{33} + 2d_{31}$. In PZT $d_{33} \approx -2d_{31}$ resulting in a very low d_h (~ 30 pC/N). The hydrostatic voltage coefficient $g_h = \frac{d_h}{\epsilon_{33}}$ is also low ($\sim 3 \times 10^{-3}$ Vm/N)

because of the low d_h and high permittivity (ϵ_{33}) of PZT.

For the past few years we have been investigating piezoelectric composites made from polymers and ferroelectric ceramics, attempting to decouple d_{33} and d_{31} , and lower the permittivity to give improved values of d_h and g_h (1,2,3,4). The polymer phase also lowers the density, and by using an elastomer the composite can be made flexible.

The properties of the composites are influenced by the connectivity of the components of the composites. Connectivity is defined as the number of dimensions in which each phase is continuous. There are ten connectivity patterns in diphasic solids, ranging from a 0-0 unconnected checkerboard pattern in which both phases are three dimensionally connected (1). A composite with 3-1 connectivity has a one-dimensionally connected phase embedded in a three dimensional matrix phase. This paper summarizes our work on composites with several interesting connectivity patterns. A number of other research groups are also investigating the properties of ferroelectric composites with 3-0, 3-1, and 3-3 connectivity patterns (5,6,7).

2. Piezoelectric Composites with 3-1 Connectivity

These composites consist of thin PZT rods (phase 1) embedded in a polymer matrix (phase 2) with the rods oriented perpendicular to the transducer electrode (Fig. 2).

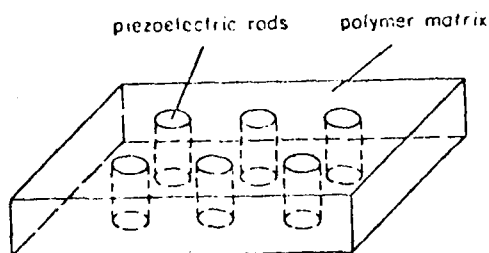


Figure 2 - Composite with 3-1 connectivity

Theoretical expressions for the piezoelectric response of composites with 3-1 connectivity (2) are as follows.

$$\bar{d}_{33} = \frac{1_V 1_{d_{33}} S_{33} + 2_V 2_{d_{33}} 1_{S_{33}}}{1_V 2_{S_{33}} + 2_V 1_{S_{33}}} \quad (1)$$

$$\bar{d}_{31} = 1_V 1_{d_{31}} + 2_V 2_{d_{31}} \quad (2)$$

$$\bar{\epsilon}_{33} = 1_V 1_{\epsilon_{33}} + 2_V 2_{\epsilon_{33}} \quad (3)$$

where 1_V , $1_{d_{33}}$, $1_{d_{31}}$, $1_{S_{33}}$, and $1_{\epsilon_{33}}$ are respectively the volume fraction, piezoelectric coefficients, elastic compliance and permittivity of phase 1. The average coefficients for the composites are \bar{d}_{33} , \bar{d}_{31} , and $\bar{\epsilon}_{33}$. For the PZT polymer composite, if we assume that

$$1_{d_{33}} \gg 2_{d_{33}}, \quad 1_{S_{33}} \ll 2_{S_{33}}, \quad \text{and} \quad 1_{\epsilon_{33}} \gg 2_{\epsilon_{33}},$$

then \bar{d}_{33} does not depend on the volume fraction of PZT in the composite. This is based on the ideal situation in which the polymer is much more compliant than the PZT phase and that all the stress on the polymer is transferred to the PZT. According to equations (2) and (3), \bar{d}_{31} and $\bar{\epsilon}_{33}$ decrease linearly with volume fraction PZT. As a result, \bar{d}_{31} and \bar{g}_h will be enhanced. Theoretical calculations indicate that ideally the figure of merit ($\bar{d}_{31}\bar{g}_h$) for composites with 5 volume% PZT is about $300,000 \times 10^{-15} \text{ m}^2/\text{N}$, more than a thousand times larger than solid PZT.

PZT rods are made by extrusion of PZT 501A slip followed by drying, firing, and hot isostatic pressing. After aligning the sintered rods in a metal rack, they are placed in a cup and covered with spurr epoxy (Earnest E. Fullum Inc., Schenectady, NY) and then poled along the length of the rods (4). To provide a better understanding of the composites, PZT rods of diameters 840, 600, 400, and 254 μm were used to fabricate piezoelectric composites with 10 to 50 volume percent PZT for each rod size. Piezo-

electric measurements are done on samples of different thicknesses ranging from 1 to 4 mm. For a given volume fraction PZT, a composite with very thin rods and close rod spacing behaves like a homogeneous piezoelectric medium.

Electric permittivities of the composites were measured at 1 KHz and \bar{d}_{33} was measured using a Berlincourt \bar{d}_{33} meter at 100 Hz. The hydrostatic piezoelectric coefficient was measured by changing the pressure in an oil chamber at the rate of 50 psi/sec and collecting the charge with an electrometer.

The \bar{d}_{33} value of the composites down to 40 volume % PZT were comparable to the value of \bar{d}_{33} for solid PZT 501A of 400 pC/N. Below 40%, the values decreased, but even at 10 volume % PZT \bar{d}_{33} exceeded 220 pC/N, indicating that much of the stress on the polymer phase is being transferred to the PZT. The \bar{d}_{33} coefficients of the composites increased with increasing thickness because of improved stress transfer.

The permittivity ($\bar{\epsilon}_{33}$) showed a linear decrease with volume fraction of PZT, as predicted by eq (3) piezoelectric voltage coefficient $\bar{g}_{33} = \bar{d}_{33}/\bar{\epsilon}_{31}$ of the composites increase rapidly at low volume fraction of PZT because of the decrease in permittivity. A composite made from 254 μm rods with a volume fraction of 0.025 PZT has a \bar{g}_{33} coefficient of $250 \times 10^{-3} \text{ Vm/N}$, about nine times greater than that of solid PZT.

Most of the composites, regardless of thickness, rod diameter, or volume percent PZT, had higher \bar{d}_{31} values than that of solid PZT. Only composites made from 840 μm rods showed a decrease of \bar{d}_{31} as volume % PZT decreases. Composites with thinner rods showed either nearly constant values or increased \bar{d}_{31} at lower volume fractions. At 10 volume percent the \bar{d}_{31} values were the lowest for all rod sizes, but these composites showed the largest increases in \bar{d}_{31} with each reduction in rod diameter indicating that if the rod diameter could be further reduced, the 10 volume % composites would have the largest \bar{d}_{31} , as predicted by theory. Some composites show \bar{d}_{31} values exceeding 80 pC/N, three times that of solid PZT.

Decreases in $\bar{\epsilon}_{33}$ with volume fraction of PZT resulted in large increases of the hydrostatic voltage coefficient \bar{g}_h . Figure 3 shows figure of merit $\bar{d}_{31}\bar{g}_h$ plotted as a function of volume % PZT. The $\bar{d}_{31}\bar{g}_h$ products obtained with composites made from thin PZT fibers at low volume fractions were more than an order of magnitude higher than the $\bar{d}_{31}\bar{g}_h$ product for solid PZT.

The magnitude of the $\bar{d}_{31}\bar{g}_h$ product is large, but is far less than the theoretical value. This is partly because the theory requires that the non-piezoelectric phase be much more compliant than the piezoelectric phase. Since the epoxy is a stiff polymer, better agreement with the theory may be expected when an elastomer is used as the matrix phase. After careful consideration, a highly flexible polyurethane (Flexane 94 from Devcon Corp., Danvers, MA) was chosen to provide the required stress amplification on the PZT rods.



Figure 3. \bar{d}_h as a function of volume percent PZT and rod diameter

Elastomers, like polyurethane, have a high poisson ratio which makes them virtually incompressible under hydrostatic loading. However, the poisson ratio of a polymer can be greatly reduced by introducing porosity into the polymer. The fabrication of 3-1 composites with porous polyurethane was developed by Klicker (8).

In this composite the pores constitute a third phase which is unconnected, and the composite can therefore be designated as having 3-1-0 connectivity. A conductive polyurethane cured directly to the porous polyurethane was used as electrodes for these composites.

Introduction of porosity into the matrix phase had a dramatic effect on \bar{d}_h . Measurements were carried out at a static hydrostatic pressure of 100 psi. Composites with greater than 30% porosity have \bar{d}_h values more than ten times greater than those of similar composites with non-porous matrices. g_h coefficients of the porous composites were as high as $400-500 \times 10^{-3}$ Vm/N. Composites made with 4 volume % PZT rods 240 μ m in diameter in a foamed polyurethane with 45% porosity had a $\bar{d}_h \bar{g}_h$ product close to $100,000 \times 10^{-15}$ m²/N. This value is more than an order of magnitude greater than the $\bar{d}_h \bar{g}_h$ product of composites with a non-porous epoxy matrix.

The \bar{d}_h values of composites made with a matrix of foamed polyurethane are very pressure dependent over 200 psi. This may be due to buckling of the walls between the pores, causing rapid compression of the matrix phase.

Composites formed with epoxy matrices have lower \bar{d}_h values, but are nearly pressure independent. Porosity may also be introduced into epoxy to increase the mechanical compliance and lower Poisson's ratio, thereby enhancing \bar{d}_h . This work has been done by Lynn (9) using a three component foamed epoxy system from REN plastics. Composites with 4 volume % of 280 μ m diameter rods showed a three-fold increase in \bar{d}_h when foamed. During

hydrostatic testing, the composites sometimes absorbed oil from the hydrostatic cell into the pore structure of the epoxy. To prevent this, the porosity was introduced in the form of hollow glass spheres. The hollow spheres (Emerson and Cumins, Inc (Canton, MA) have an average diameter of 80 μ m and wall thickness of 2 μ m. Composites in which the epoxy matrix is filled with approximately 50 volume percent spheres have \bar{d}_h values intermediate between composites made with porous epoxy and those with non-porous epoxy matrices.

Gururaja (10) has developed a continuous poling technique to pole long PZT rods. Prepoled rods can be used to fabricate composites in which rods are aligned in many different patterns making new transducer design feasible.

An alternate processing for making 3-1 composites involves slicing a fired PZT slug with a diamond saw to produce an array of rectangular pillars (11). The inter-pillar spaces were filled with Spurr epoxy. These composites had \bar{d}_h and \bar{g}_{33} values comparable to those made with extruded rods. \bar{d}_h and \bar{g}_{33} of composites with higher percent PZT (>50%) approached the values of solid PZT, consistent with the theory (1).

3. Composites with 3-3 Connectivity

As shown in the previous section a composite with 3-1 connectivity makes an excellent piezoelectric transducer for hydrophone applications. But 3-3 connectivity offers certain advantages in sample preparation; interconnections between the PZT rods maintain the rod orientation during the ceramic processing steps. In a 3-3 composite, both phases are self-connected in all three directions. Microstructures of this type occur in foams, phase separated glasses, wood, and coral.

Ceramic-polymer composites with 3-3 connectivity have been fabricated by the replication of coral structure using a lost wax casting technique (2).

As poled, the PZT-rubber replica is mechanically rigid, but flexing the composite fractures the ceramic skeleton and improves the piezoelectric properties. Shearing the structure lowers the permittivity without appreciably affecting the piezoelectric d coefficient. As a result the longitudinal voltage coefficient g_{33} is greatly enhanced.

Measured values are $\bar{K}_{33} = 40$, $\bar{d}_{33} = 100 \times 10^{-12}$ C/N, and $g_{33} = 300 \times 10^{-3}$ Vm/N, about fifteen times better than a solid PZT ceramic of similar composition. The $\bar{d}_h \bar{g}_h$ product for this composite was 2800×10^{-15} m²/N, about an order of magnitude better than solid PZT.

An alternate method of making 3-3 transducer composites was proposed by Shrout (12,13). The method involves the use of a volatile phase in the fabrication procedure. Commercially available PZT powder is mixed with 20 to 70 volume % polymethyl methacrylate (PMMA) spheres about 100 μ m in diameter. The mixture is die pressed using polyvinyl alcohol as a binder and the binder and PMMA spheres volatilized by slowly heating the

pressed pellets to 400°C. After sintering at 1300°C for 0.5 hour, the highly porous pellets are vacuum impregnated with a suitable polymer such as a silicone rubber elastomer or a stiff epoxy.

Piezoelectric properties of composites with 30% PZT in a silicone rubber matrix were similar to the coral replamine composites. \bar{d}_{33} was about 200 pC/N and g_{33} about 170×10^{-3} Vm/N. The hydrophone figure of merit peaked to a value of $25,000 \times 10^{-15}$ m²/N around 50 volume percent silicone rubber, an order of magnitude larger than the coral replamine composite. The piezoelectric coefficients are somewhat lower with an epoxy filling: $\bar{d}_{33} \sim 150$ pC/N, $g_{33} \sim 90 \times 10^{-3}$ Vm/N for 30% PZT. The \bar{d}_{hgh} product with epoxy filling also peaked around 50 volume % PZT to 4000×10^{-15} m²/N. An added advantage of this method is that it is readily adapted to mass production.

4. High Frequency Application of 3-1 Composites

Piezoelectric composites are not limited to low frequency applications. At high frequencies, 3-1 connected composites show good potential for broad band transducer applications such as ultrasonic imaging.

For a bar shaped specimen, the fundamental frequency of a dilatational mode is given by $f_L = \frac{1}{2L} \sqrt{\frac{Y}{\rho}}$ where L is the governing dimension, ρ the density, and Y the appropriate Young's modulus. In such a transducer, the width of the 3dB pass band (Δf_{3dB}) at resonance frequency (f) is limited by the mechanical Q of the material. Q is given by $f/\Delta f_{3dB}$ for $Q > 10$. For ceramic piezoelectrics, Q is typically in the range 50-1000 giving a 3dB bandwidth of 0.1 to 2% of center frequency.

However, based on the equation for f_L , it is possible to fabricate a broad bandwidth electro-mechanical transducer from a single piezoelectric element by forming the element into a wedge of varying thickness and driving it in thickness resonance. In this case the resonance mode encompasses a range of frequencies governed by the maximum and minimum thickness of the wedge. However, since the vibrating elements are strongly mechanically coupled, destructive interference occurs between regions of different thickness resonating out of phase, and low efficiency results.

Connecting piezoelectric ceramic elements in parallel with a mechanically lossy polymer can overcome the shortcomings of the wedge configuration and produce an efficient broad band device (14). In this application many piezoelectric elements with different dimensions are used to provide a wide pass band, but the elements are combined into a single array using an inactive, low Q polymer which decouples the elements mechanically and prevents interference. The device consists of sheets of piezoelectric material, e.g. PZT, laminated with polymer layers so that the active elements are separated by sufficient polymer to reduce the mechanical coupling. The slope of the device ($\tan \theta$) defines its bandwidth according to the relationship

$$\Delta f = \frac{x \tan \theta f_1 f_2}{N} \quad (5)$$

where Δf is the bandwidth in Hz, x is the width of the device, and f_1 and f_2 are the maximum and minimum resonant frequencies corresponding to elements of length L_1 and L_2 in Fig. 4. N is the longitudinal mode frequency constant of the piezoelectric material used in the composite. The bandwidth can be increased by increasing θ as far as the natural mechanical Q of PZT will allow.

The above concept has been verified experimentally by substituting for the 2-2 connected lamellar composite, a composite of soft PZT ceramic rods embedded in epoxy, similar to those described in Section 2. This material has the advantage of accepting any surface profile, thus providing greater versatility. In principle, the pass band of this composite can be tailored to provide a frequency spectrum of any shape.

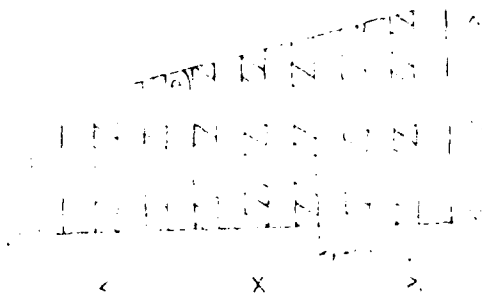


Figure 4 - Parallel resonant device for broadband applications, Piezoelectric layers (shaded) are decoupled mechanically by an inactive, low Q polymer.

Figure 5 (a, b, c) compares the frequency spectra from 0 to 1 MHz for 30 volume % PZT fiber composites with opposite faces inclined at 20, 70 and 10° respectively. The 6dB bandwidth has been increased from 7% for a composite with parallel faces to 11% for 20° composite, and to 45% for the device with faces inclined at 10°.

5. Composites with 1-3 Connectivity

Here, one dimensionally connected polymer is embedded in three dimensionally continuous PZT. The PZT was prepared by Corning Centre in the shape of a honeycomb by extrusion (Fig. 6). The sintered ceramic had a wall thickness of 180-130 μ m and square tubular voids ~ 1.1 mm on a side. Impregnation of this structure with polymer resulted in a composite with 26 volume percent PZT (15).

Relative permittivity agreed with theoretical calculations whereas d_h was somewhat reduced. Resonance measurements indicated that the thickness coupling coefficient (k_t) was 25% greater than that of homogeneous PZT while the planar coupling coefficient was reduced drastically along with the

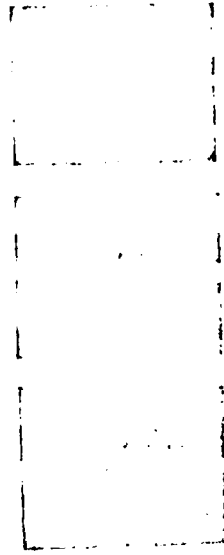


Figure 5 - Bandwidth broadening in parallel connected resonant composites. (a) $0=20^\circ$; (b) $0=70^\circ$; (c) $0=100^\circ$. Vertical scale = amplitude. Horizontal scale = frequencies 1 to 1 MHz

mechanical Q . This composite can also be used for wide bandwidth applications by shaping it into a wedge. 6dB bandwidth has been increased to over 50% of the center frequency for the composite ground to a θ value of 20° .

The enhancement in k_t can be explained by considering equation (6):

$$k_t = e_{33} / \sqrt{\epsilon_{33}^S c_{33}^D} \quad (6)$$

where e_{33} is the piezoelectric constant which relates stress to field, ϵ_{33}^S the clamped permittivity, and c_{33}^D the elastic stiffness at constant charge density. Substituting into equation (6) the relationship $e_{33} = d_{33} c_{33}^E$ (16), results in

$$k_t = \frac{d_{33} c_{33}^E}{\sqrt{\epsilon_{33}^S c_{33}^D}} \quad (7)$$

Given that $\epsilon_{33}^E = c_{33}^D (1 - k_t^2)$ and $\epsilon_{33}^S = \epsilon_{33}^T (1 - k_t^2) (1 - k_p^2)$ equation (7) becomes

$$\frac{k_t^2}{(1 - k_t^2)} = \frac{d_{33}^2 c_{33}^D}{\epsilon_{33}^T (1 - k_p^2)} \quad (8)$$

i.e.,

$$k_t = \left[\frac{\epsilon_{33}^T (1 - k_p^2)}{d_{33}^2 c_{33}^D} + 1 \right]^{-1/2} \quad (9)$$

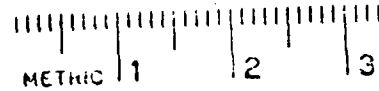


Figure 6 - Extruded PZT honeycomb material

Terms in the righthand side of equation (9) are not expected to change in a compensating manner 1. geometrical differences arising from phase connectivity. Permittivity (ϵ_{33}^T) is always a linear function of the area fraction of piezoelectric in a parallel composite because it is a pure electrical term and does not rely on coupling between the phases. However, in a dynamical situation, e.g., at resonance or at frequencies greater than the mechanical relaxation time of the polymer, the electromechanical terms d_{33} , c_{33}^D , and k_p are expected to approximate those of single phase PZT (16). Little energy transfer between PZT and polymer is possible because a large acoustic impedance discontinuity exists between them. As a result, a net enhancement of k_t , inversely proportional to ϵ_{33}^T , is expected. In practice, this relationship will not be followed exactly due to some dependence of k_p on connectivity.

In the case of 3-1 composites, mentioned earlier, where the polymer is three-dimensionally connected k_p should be lower and the k_t enhancement should be even more pronounced. Planar and thickness coupling coefficients of 19 and 67 percent respectively have been measured for these composites in agreement with this general prediction. One possible "static" application for 1-3 connected honeycomb material is as a deformable mirror (17). In this application a mirror is bonded to a sectioned honeycomb transducer (with or without polymer phase) and, by driving the transducer through piezoelectric d_{31} with a voltage applied across the PZT wall thickness. The ability to individually address small regions of the honeycomb material coupled with low operating voltages makes for potential application as an active optic device in communication. The ability to distort sections of a thin mirror can eliminate phase differences from an incoming optical wave front distorted by atmospheric turbulence (18).

References

1. R.E. Newnham, D.P. Skinner and L.E. Cross, Mat. Res. Bull. 12, 525 (1978).
2. D.P. Skinner, R.E. Newnham and L.E. Cross, Mat. Res. Bull. 13, 599 (1978).
3. R.E. Newnham, D.P. Skinner, K.A. Klicker, A.S. Bhalla, B. Hardiman and T.R. Gururaja, Ferroelectrics 27, 49 (1980).
4. K.A. Klicker, J.V. Biggers and R.E. Newnham, J. Amer. Ceram. Soc. (accepted).
5. W.B. Harrison, Proceedings of the Workshop on Sonar Transducer Materials, Naval Research Laboratory (Feb. 1976).
6. K. Nagata, H. Igarashi, K. Okazaki and R.C. Bradt, Japan. J. Appl. Phys. 19, L37-40 (1980).
7. M. Miyashita, K. Takano and T. Toda. Ferroelectrics 28, 397 (1980).
8. K.A. Klicker, Ph.D. Thesis, Solid State Science, The Pennsylvania State University (1980).
9. S.Y. Lynn, M.S. Thesis, Solid State Science, The Pennsylvania State University (1980).
10. T.R. Gururaja, L.E. Cross and R.E. Newnham, Bull. Amer. Ceram. Soc. (accepted).
11. H.P. Savakus, K.A. Klicker and R.E. Newnham, Phys. Stat. Sol. (submitted).
12. T.R. Shrout, W.A. Schulze and J.V. Biggers, Mat. Res. Bull. 14, 1533 (1979).
13. K. Rittenmyer, T.R. Shrout and R.E. Newnham (to be published).
14. L.J. Bowen and T.R. Gururaja, J. Appl. Phys. (accepted).
15. T.R. Shrout, L.J. Bowen and W.A. Schulze, Mat. Res. Bull. (Nov 1980).
16. D. Berlincourt, Ultrasonic Transducer Materials, O.E. Mattiat (Ed.), Plenum Press, NY (1971).
17. K. Uchino, S. Nomura, L.E. Cross and R.E. Newnham, Proc. 2nd Soviet-Japanese Symposium on Ferroelectricity (Sept 1980), J. Phys. Soc. Japan (Sup) (submitted).
18. R.E. Aldrich, Ferroelectrics 27, 19 (1980).

AD-A096 451

PENNSYLVANIA STATE UNIV UNIVERSITY PARK MATERIALS RE--ETC F/G 9/1
TARGETED BASIC STUDIES OF FERROELECTRIC AND FERROELASTIC MATERI--ETC(U)
DEC 80 L E CROSS, R E NEWNHAM, G R BARSCH N00014-78-C-0291

UNCLASSIFIED

NL

4 of 7
88-011



11111

11111

11111

11111

11111

11111

11111

APPENDIX 40

T.R. Shrout, L.J. Bowen, W.A. Schulze. Extruded PZT/Polymer Composites for Electromechanical Transducer Applications. Mat. Res. Bull. 15, 1371 (1980).

EXTRUDED PZT/POLYMER COMPOSITES FOR ELECTROMECHANICAL TRANSDUCER APPLICATIONS

T. R. Shrout, L. J. Bowen, and W. A. Schulze
Materials Research Laboratory
The Pennsylvania State University
University Park, Pennsylvania 16802

(Received May 14, 1980; Refereed)

ABSTRACT

PZT/polymer composites having a 1-3 parallel connectivity were fabricated by impregnating a sintered, extruded honeycomb configuration of PZT with various polymers. The resultant composites were found to have densities less than 2900 kg/m^3 , a dielectric constant of ~ 500 and a piezoelectric d_{33} of $\sim 300 \times 10^{-12} \text{ C/N}$. The 1-3 connectivity increases the piezoelectric voltage coefficient (g_{33}) from $22 \times 10^{-3} \text{ Vm/N}$ (solid PZT) to $\sim 70 \times 10^{-3} \text{ Vm/N}$.

The composites have thickness mode electromechanical coupling coefficients (k_t) which are $\sim 25\%$ greater than that of homogeneous PZT, and are readily adaptable for broad bandwidth operation. This combination of electromechanical properties makes these composites ideal for low voltage displacement and pulse echo applications.

Introduction

Over the past few years, several researchers (1-6) have utilized the concept of phase connectivity (3) in designing piezoelectric/polymer transducers with improved electromechanical properties over those of present-day homogeneous piezoelectric materials. Specifically, diphasic composites of modified PZT (lead zirconate titanate), ceramic and various epoxy resins and elastomers have a low density and exhibit an enhanced piezoelectric voltage coefficient, referred to as the g -coefficient, making them useful for transducer applications, e.g., hydrophones, acoustic imaging, etc. The g -coefficient is defined in equation [1] as the piezoelectric strain coefficient d_{ijk} divided by the appropriate permittivity coefficient ϵ_{ij} :

$$g_{ijk} = \frac{d_{ijk}}{\epsilon_{ij}} . \quad [1]$$

The basis of the enhanced g -coefficient lies in the theoretical expression developed by Newnham (3) for a parallel connected diphasic composite, e.g., a 3-1 connectivity in which rods of PZT (phase 1, normal to the electrode surface) are embedded in a three-dimensional continuous polymer. The theoretical

equation for \bar{g}_{33} (composite g_{33}) is given as

$$\bar{g}_{33} = \frac{{}^1V {}^1d_{33} {}^2S_{33} + {}^2V {}^2d_{33} {}^1S_{33}}{({}^1V {}^2S_{33} + {}^2V {}^1S_{33})({}^1V {}^1\epsilon_{33} + {}^2V {}^2\epsilon_{33})} \quad [2]$$

where V , d_{33} , S_{33} , and ϵ_{33} are, respectively, the volume fraction, piezoelectric strain coefficient, elastic compliance and permittivity of the appropriate phase (note: shortened tensor notation used for compliance and piezoelectric coefficient). Given a composite comprised of a mechanically stiff piezoelectric (phase 1) where ${}^1d_{33} \gg {}^2d_{33}$, ${}^1S_{33} \ll {}^2S_{33}$, ${}^1\epsilon_{33} \gg {}^2\epsilon_{33}$ yields

$$\bar{g}_{33} \approx \frac{{}^1d_{33}}{2 {}^1V {}^1\epsilon_{33}}.$$

Thus the voltage coefficient of the composite can easily exceed that of the solid piezoelectric. For smaller volume fractions of the piezoelectric phase, the g coefficient is amplified even further.

It is the intention of this work to investigate a 1-3 parallel connected composite¹ in which a PZT phase is three-dimensionally connected with a polymer connected in one-dimension. PZT/polymer composites having a 1-3 connectivity are fabricated by impregnating a sintered, extruded honeycomb configuration of PZT with a polymer (see Figure 1).

Electromechanical and physical properties measured on the composites are compared to those of the homogeneous piezoelectric material. Possible applications for honeycomb 1-3 connected transducers are discussed.

Experimental Procedure

Sample Preparation

The extruded PZT honeycomb material was made by Dr. Irwin Lachman of the Corning Research Center, using a commercially available PZT powder². The extruded material was placed on a Pt foil and sintered in closed high-purity alumina crucibles with lead zirconate added as a source of PbO. A silicon carbide resistance furnace with a programmable controller was used, the heating rate being 200°C/hr. with a soak temperature of 1300°C for a period of 0.5 hrs.

Due to inhomogeneity in the fired density, samples were refired in a hot isostatic press (HIP) for one hour at 1300°C and 20 MPa argon pressure. Use of the HIP was found to increase the fired density from ~93% to >97% of theoretical density. Details of the HIP process for pressure sintering the extruded Corning honeycomb materials and improving its dielectric breakdown strength can be found in Reference 7.

The highly open honeycomb structure allowed easy impregnation with polymer. In this investigation two types of polymers were used: a stiff vinylcyclo-

¹Note: Although no strict distinction can be made between 1-3 and 3-1 connectivity, this paper designates the first digit to represent the polymer connectivity.

²Ultrasonic Powder PZT-501A. Ultrasonics Powders, Inc., 2383 S. Clinton Avenue, South Plainfield, NJ 07080.

hexane dioxide epoxy³ (Spurrs) and a medium soft (high viscosity) flexible elastomer⁴ (Flexane). Approximately 30 millimeter long by 17 millimeter diameter sections of sintered extruded material were placed in slightly larger plastic tubes which were closed at one end. After pouring the polymer and evacuating to remove trapped air, the polymers were cured at 70°C for at least eight hours. The PZT component of the composites made up about 26% of the total volume.

For electromechanical measurements, disks were cut perpendicular to the composite axis, and polished parallel using ~ 25 micron SiC paper. The surfaces were then cleaned with alcohol and electrodes of air-dry silver applied.

Measurements.

The composites were poled in a stirred oil bath at 80°C by applying a DC field ranging from 15-20 MV/m for at least two minutes. The completeness of poling was checked by measuring the piezoelectric d_{33} coefficient using a Berlincourt d_{33} meter⁵. Dielectric permittivity and loss ($\tan \delta$) were measured using an automatic capacitance bridge at 1 kHz. Measurements were made both before and 24 hours after poling.

Hydrostatic piezoelectric coefficient, d_h , was determined by a pseudo-static method. Pressure was changed at the rate of 3.5 MPa/sec., while charge was collected by a Keithley Electrometer⁷ in the feedback charge integration mode.

A resonance testing apparatus, based on the IRE Standards on Piezoelectric Crystals (8), was used to measure electromechanical coupling factors, Young's modulus, frequency constants, and the mechanical quality factor Q . Measurements were made 24 hours after poling.

Results and Discussion

Macrostructure

Typical macrostructures of the honeycomb material and a sectioned 1-3 connected PZT/Spurrs composite are shown in Fig. 1. These photographs also

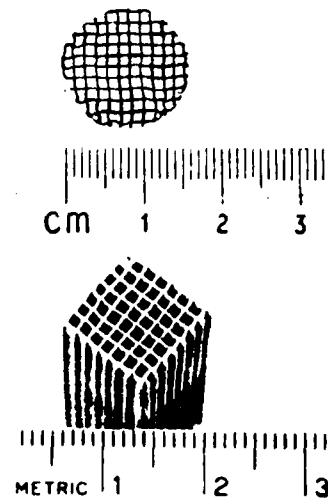


FIG. 1

Photographs of PZT Spurrs "honeycomb" composite.

³Spurrs Low-Viscosity Embedding Media, No. 5135, Polysciences, Inc., Washington, PA 18976.

⁴Devon Flexane #60, Nocen Industries, Inc., 502 Railroad St., Jersey Shore, PA 17740.

⁵Berlincourt (Model 333) d_{33} meter, Channel Products, Inc., 16722 Park Circle Drive, Chagrin Falls, OH 44020.

⁶Hewlett Packard (Model 4270A) Automatic Capacitance Bridge, Hewlett Packard, 1-59-1 Yoyogi, Tokyo, Japan 151.

⁷Keithley (Model 616) Digital Electrometer, Keithley Instruments, Inc., Cleveland, OH.

TABLE 1
Electromechanical and Physical Properties of PZT/Polymer Composites

Property	Homogeneous PZT 501A ^{a,b}	1-3 Composites	
		PZT/Spurrs	PZT/Flexane
density (kg/m ³)	7900	2900	2600
dielectric constant (K)	2000 (1800) ^b	(unpoled) 340-370 (poled) 450-500	390-460 480-520
tan δ	0.014	0.017	0.025
piezo d_{33} ($\times 10^{-12}$ C/N)	400	240-300	260-340
piezo d_h ($\times 10^{-12}$ C/N)	50	10-20	15-20
piezo d_{31} ($\times 10^{-12}$ C/N)	175	115-140	120-160
voltage coef. g_{33} ($\times 10^{-3}$ Vm/N)	22	60-70	60-70
voltage coef. g_{31} ($\times 10^{-3}$ Vm/N)	10	29-32	28-35

^aUltrasonic Powder, Inc., "Piezoelectric Powders" data sheet.

^bProperties measured on PZT-50A disks were found to be in good agreement with expected values. However typical values of dielectric constants were found to be lower ~1800:10%.

TABLE 2
Electromechanical and Physical Properties Determined by Resonance

Property	Homogeneous PZT-501A ^{a,b}	1-3 Composites	
		PZT/Spurrs	PZT/Flexane
Frequency constant $N_{\text{thickness}}$ (Hz·m)	1740	1600	1600
Elastic stiffness C_{33}^D (G Pa)	96	81	81
Thickness coupling coefficient, k_t (%)	45	55-65	55-58
Planar coupling coefficient, k_p (%)	63	35	---

^cNote: The PZT/Flexane composites did not give distinct planar mode resonances due to difficulties in processing uniform disks.

typify the macrostructure of PZT/Flexane composite except that the Flexane is black. It is clearly seen that the PZT phase is three-dimensionally interconnected with the polymer one-dimensionally connected. The deformations present in the PZT structure arise from imperfections in the green extruded material, such as non-uniform wall thickness. The wall thickness of the PZT ranged from 180 μm to 350 μm (~ 7 to ~ 13 mils), with approximately 1.1 mm interspacings. Excess polymer around the edge of the specimen gives additional mechanical strength but means that the polymer phase is partially three-dimensionally connected.

Electromechanical and Physical Data

Electromechanical and physical properties are reported in Tables 1 and 2, with Table 2 representing properties as determined by resonance.

The densities of the PZT/Spurrs composites were found to be $\sim 2900 \text{ Kg/m}^3$. A reduction of density from 2900 to 2600 Kg/m^3 in the PZT/Flexane composites was the result of bubbles in the polymer.

Values of the dielectric constant (\bar{K}) were found to be around 500 for both the PZT/Spurrs and PZT/Flexane composites. The predicted value of \bar{K} , calculated for the parallel model equation [3]:

$$\bar{K}_{(\text{composite})} = {}^1V {}^1K_{(\text{PZT})} + {}^2V {}^2K_{(\text{polymer})} \quad [3]$$

given 1V and 1K are 26 volume % PZT and ~ 1800 , respectively, and 2V and 2K are 74 volume % polymer and 6 is approximately 470. The predicted value of the dielectric constant was within 10 percent of the experimental values. Dielectric constants of the Spurrs epoxy and Flexane elastomer were 6 and 8, respectively.

According to the theory developed by Newnham (3), the piezoelectric constant \bar{d}_{33} for a parallel connected model would not be a function of the volume fraction of PZT in the composite, assuming that the polymer phase is much more compliant than the PZT and that all the stress is transferred to the PZT. Composite values of piezoelectric \bar{d}_{33} are somewhat lower than expected assuming an ideal parallel model, indicating that not all the stress is transferred to the PZT phase. The values of \bar{d}_{33} are also found to vary considerably from point to point, as determined using the Berlincourt d_{33} Meter. The d_{33} Meter measures the charge developed on a sample due to stress from two rounded rams. As reported by Klicker (5,6), if the rams happen to be in direct physical contact of PZT, then the force on the PZT is transmitted directly by the rams and not to the PZT phase via the polymer phase. Values of piezoelectric d_{33} taken at points near or on the PZT phase are considerably higher ($>400 \times 10^{-12}$ C/N) than values taken more on the polymer phase. It is for this reason that the reported values, found in Table 1, are the average values of at least ten random point measurements.

Since PZT is the three-dimensionally connected phase it is to be expected that the piezoelectric \bar{d}_{31} coefficient should also be largely unaffected by the volume fraction. Values of piezoelectric \bar{d}_{31} found in Table 1, determined from the measured \bar{d}_{33} and \bar{d}_h using the following relationship:

$$\bar{d}_h = 2\bar{d}_{31} + \bar{d}_{33},$$

are also found to be somewhat lower than expected, assuming \bar{d}_{31} independent of volume fraction. The piezoelectric \bar{g}_{33} and \bar{g}_{31} values reported were computed from the measured \bar{d}_{33} and calculated \bar{d}_{31} values and from the permittivities. The \bar{g} values were found to be up to three times the value for homogeneous PZT, as expected from permittivity considerations (equations 1 and 3).

A resonance spectrum for 1-3 composites is shown in Fig. 2. A weak planar mode resonance signal (lower left corner) and a very broad thickness mode signal are shown. Other possible spurious resonances appear to have been suppressed, possibly due to the very low mechanical Q of the composites. Mechanical Q measurements appear to show some dependence on specimen connectivity, but are inconclusive and require further investigation.

In Table 2, measured resonant properties for the composites are compared to those for homogeneous PZT. Interestingly, the fundamental thickness mode frequency constants (N_t) are identical for both types of composites and are similar to that of solid PZT, indicating that the polymer has very little effect on resonant properties in this direction. This observation is in agreement with previous work on 3-1 composites and has been explained elsewhere (9). Both planar and thickness mode coupling coefficients are reported in Table 2. The planar coupling coefficient (k_p) is considerably larger for homogeneous PZT than for the PZT/Spurrs composite, which may be expected considering the partial series connectivity of the polymer in this direction. A measured value of 45 percent for the thickness coupling

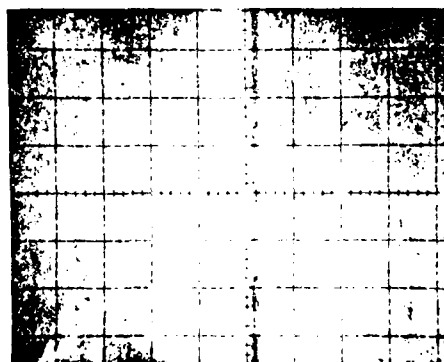


FIG. 2

Resonance spectra for PZT/polymer composite. Horizontal scale is 0-1.4 MHz.

coefficient (k_t) for homogeneous PZT is typical of those for commonly used PZT's (hard and soft) which normally fall in the range from 30 to 51 percent (10). However, for both types of 1-3 connected composites k_t is higher by 20 to 30 percent than the homogeneous PZT value. It appears, therefore, that the composite connectivity enhances the thickness mode coupling coefficient.

The enhancement can be explained by considering equation [4]:

$$k_t = e_{33} / \sqrt{\epsilon_{33}^S C_{33}^D} \quad [4]$$

where e_{33} is the piezoelectric constant which relates stress to field, ϵ_{33}^S the clamped permittivity, and C_{33}^D the elastic stiffness at constant charge density. Substituting into equation [4] the relationship $e_{33} = d_{33} C_{33}^E$ (9), results in

$$k_t = \frac{d_{33} C_{33}^E}{\sqrt{\epsilon_{33}^S C_{33}^D}} \quad [5]$$

Given that $C_{33}^E = C_{33}^D (1 - k_t^2)$ and $\epsilon_{33}^S = \epsilon_{33}^T (1 - k_t^2) (1 - k_p^2)$ (8), equation [5] becomes

$$\frac{k_t^2}{(1 - k_t^2)} = \frac{d_{33}^2 C_{33}^D}{\epsilon_{33}^T (1 - k_p^2)} \quad [6]$$

$$\text{i.e., } k_t = \left[\frac{\epsilon_{33}^T (1 - k_p^2)}{d_{33}^2 C_{33}^D} + 1 \right]^{-1/2} \quad [7]$$

Terms in the right hand side of equation [7] are not expected to change in a compensating manner to geometrical differences arising from phase connectivity. Permittivity (ϵ_{33}^T) is always a linear function of the area fraction of piezoelectric in a parallel composite because it is a pure electrical term and does not rely on coupling between the phases. However, in a dynamical situation, e.g., at resonance or at frequencies greater than the mechanical relaxation time of the polymer, the electromechanical terms d_{33} , C_{33}^D , and k_p are expected to approximate to those of single phase PZT (9). Little energy transfer between PZT and polymer is possible because a large acoustic impedance discontinuity exists between them. As a result, a net enhancement of k_t , inversely proportional to $\sqrt{\epsilon_{33}^T}$ is expected. In practice, this relationship will not be followed exactly due to some dependence of k_p on connectivity.

In the case of 3-1 composites, mentioned earlier, where the polymer is three-dimensionally connected k_p should be lower and the k_t enhancement should be even more pronounced. Planar and thickness coupling coefficients of 19 and 67 percent respectively, have been measured for these composites⁸, in agreement with this general prediction.

Applications

Possible transducer applications for the honeycomb 1-3 connected com-

⁸Note: The 3-1 composite coupling coefficients were made on thin disks (19 mm in diameter) comprised of 0.5 mm diameter rods of PZT embedded in 3-dimensionally connected Spurr's polymer. The volume fraction of PZT was 0.2.

posites fall into two main categories: low frequency (static) uses and high frequency (resonant) applications.

For high frequency applications, the honeycomb composite's low mechanical Q , low density, improved piezoelectric g_{33} , and enhanced k_t make it a promising candidate for ultrasonic imaging, especially for non-destructive testing and in biomedical acoustics (11,12). The composite material also offers versatility in shape capability, making possible extremely wide bandwidths, a prerequisite for pulse-echo applications (13). Broad bandwidth is essential for obtaining rapid rise time and ring down in pulse reproduction. Adaptation to broad bandwidth applications of 3-1 connected composite transducers has been described in references (9 and 14) and in principle the procedure for the 1-3 connected honeycomb composite is the same. Basically, the composite is driven at its thickness mode resonance frequency and this frequency is spread by inclining the faces normal to the thickness at an angle θ . The device consists of a series of piezoelectric elements with different lengths (or thicknesses) resonating over a range of frequencies. The elements are mechanically decoupled by the polymer phase so that destructive interference does not occur. Figures 3(a-c) compare the frequency/amplitude spectra for 1-3 (PZT/Spurrs) honeycomb composites ground at θ values of 0° , 1° , and 2° , respectively. The resonance spectra are transmission measurements obtained using a circuit described in reference (15). Comparison to the spectra in Fig. 3 indicates that the 6 dB bandwidth has been increased to over 50% of the center frequency for the composite ground to a θ value of 2° while the signal amplitude is reduced only 18% as compared to that of the parallel ground composite ($\theta = 0^\circ$).

One possible "static" application for 1-3 connected honeycomb material is as a deformable mirror bending material (16). In this application a mirror is bonded to a sectioned honeycomb transducer (with or without the polymer phase) (Fig. 4), and, by driving the transducer through piezoelectric d_{31} with a voltage applied across the PZT wall thickness, the mirror surface can be subjected to small controlled deformations. To reduce the large hysteretic strain/field effects associated with a "soft" PZT, a "hard" PZT or electrostrictive material (driven through the electrostrictive Q_{12} coefficient) can be used (17). The ability to individually address small regions of the honeycomb material coupled with low operating voltages arising from the PZT (or electrostrictive material) wall thinness, makes for potential application as an active optic device in astronomy for eliminating phase differences from an incoming

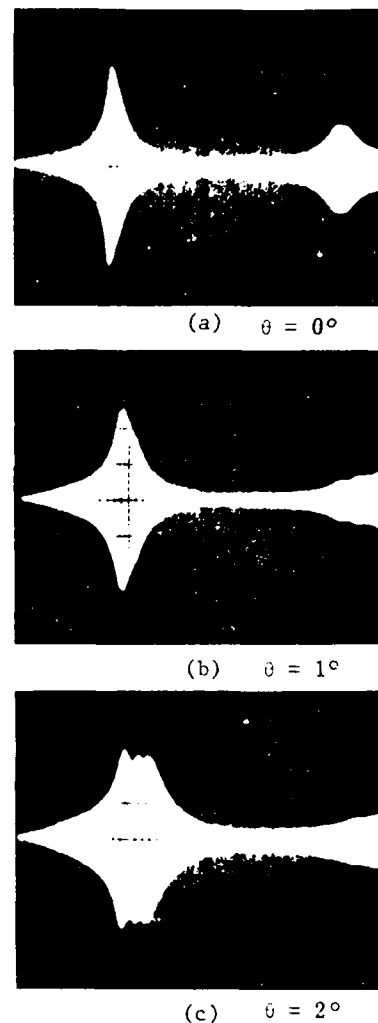
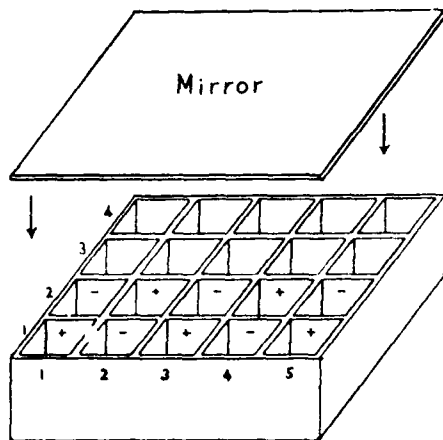


FIG. 3

Frequency amplitude spectra for 1-3 PZT/Spurrs composite. Horizontal scale is 0-3 MHz.



-FIG. 4

Honeycomb-type transducer as a low voltage deformable mirror backing material.

optical wavefront caused by atmospheric turbulence (18).

Summary and Conclusions

PZT/polymer composites having a 1-3 connectivity were fabricated by impregnating a sintered extruded honeycomb configuration of PZT with a polymer. The resultant composites had low densities ($<2900 \text{ kg/m}^3$) and high piezoelectric voltage coefficients, as expected from reduction in their permittivity. More importantly, the composites were found to have enhanced thickness mode electro-mechanical coupling coefficient (k_t) compared to homogeneous PZT. It is postulated that the enhancement of k_t arose from the low composite permittivity which was not compensated for by a corresponding reduction in the relevant mechanical coefficients, such as stiffness and piezoelectric coefficient.

The ability to extrude large quantities of the honeycomb material in various lengths and diameters makes this process simple and practical for fabrication of composite transducer materials. A PZT honeycomb extruded with a lower volume percent PZT and with thinner walls and narrower openings should result in a more piezoelectrically homogeneous composite with further enhanced piezoelectric coefficients. Couple with the ability to individually address small regions of the composite, and to use low driving voltages, these devices are potentially useful for displacement applications.

The combination of low driving voltage, high k_t , and high piezoelectric voltage coefficient make 1-3 connected composites ideal for pulse-echo applications. Varying the composite thickness broad bandwidths, over 50% of the center frequency, can be readily obtained.

Acknowledgement

We wish to thank Corning Research Center for supplying the extruded material and Philips Laboratory for their support of this work through Purchase Order No. 961815.

References

1. D. P. Skinner, R. E. Newnham, and L. E. Cross, *Mat. Res. Bull.* **13**, 525 (1978).
2. W. Harrison, *Proceedings of the Workshop on Sonar Transducer Materials*; F. Smith and R. Pohanka (Eds.), Naval Research Laboratory, Washington, DC (Feb. 1976).
3. R. E. Newnham, D. P. Skinner, and L. E. Cross, *Mat. Res. Bull.* **13**, 525 (1978).
4. T. R. ShROUT, W. A. Schulze, and J. V. Biggers, *Mat. Res. Bull.* **14**, 1553 (1979).

5. K. A. Klicker, J. V. Biggers, and R. E. Newnham, Am. Ceram. Soc. Bull. (submitted).
6. K. A. Klicker, Ph.D. Thesis, Solid State Science, The Pennsylvania State University (1980).
7. L. J. Bowen, W. A. Schulze, and J. V. Biggers, Powder Met. Int. (accepted).
8. B. Jaffee, W. R. Cook, Jr., and H. Jaffee, Piezoelectric Ceramics, Academic Press, London and New York (1971).
9. L. J. Bowen, J. Appl. Phys. (submitted).
10. Don Berlincourt, Ultrasonic Transducer Materials, O. E. Mattiat (Ed.), Plenum Press, NY (1971).
11. K. R. Enkron, F. J. Fry, and J. P. Jones, IEEE Trans. on Sonics and Ultrasonics SU-21, 144 (1974).
12. A. deSterke, Phil. Trans. Royal Soc. Lond. A292, 207 (1979).
13. H. J. McSkimin, Physical Acoustics, Vol. 1A, W. P. Mason (Ed.), Academic Press (1964).
14. R. E. Newnham, L. E. Cross, L. J. Bowen, and K. Klicker, Int. J. Mat. Eng. Appl. (submitted).
15. T. R. Shrout, W. A. Schulze, J. V. Biggers, and L. J. Bowen, Mat. Res. Bull. (in print).
16. K. Uchino, S. Nomura, L. E. Cross, and R. E. Newnham, Proc. 2nd Soviet-Japanese Symposium on Ferroelectricity (Sept. 1980), J. Phys. Soc. Japan (Sup) (submitted).
17. W. A. Schulze, T. R. Shrout, S. Jang, S. Sharp, and L. E. Cross, Am. Ceram. Soc. Bull. (submitted).
18. R. E. Aldrich, Ferroelectrics (accepted).

APPENDIX 41

L.J. Bowen, T. Gururaja. High Frequency Electromechanical Properties of Ceramic/Polymer Composites in Broadband Applications. J. Appl. Phys. (accepted).

High-frequency electromechanical properties of piezoelectric ceramic/polymer composites in broadband applications

Leslie J. Bowen and Turuvekere R. Gururaja

Materials Research Laboratory, The Pennsylvania State University, University Park, Pennsylvania 16802

(Received 19 May 1980; accepted for publication 5 August 1980)

Composites of piezoelectric ceramic (lead zirconate titanate) rods aligned in an epoxy resin matrix have been evaluated for broadband transducer applications. The rods are driven at their longitudinal mode resonance frequency and bandwidth is increased by fabricating the composite in a wedge configuration. The passband can be tailored as required by altering the surface profile of the device, and in principle bandwidths of almost 100% are possible. Dimensional parameters governing the design and performance of the device are presented. The attenuation properties of the polymer phase are of prime importance in mechanically decoupling adjacent piezoelectric elements. Acoustic signal attenuation in the polymer is accomplished by the series combination of acoustic impedance mismatch and classical transmission line attenuation. Experimental and theoretical considerations suggest the mechanical Q of the polymer is so low that the active elements are insignificantly damped. As a corollary, linear theory is not reliable for the prediction of dynamic mechanical properties of piezoelectric composites.

PACS numbers: 43.88.Fx, 43.35.Mr, 43.80.Vj

INTRODUCTION

Electrical circuits operating at high frequency often require some form of frequency control to limit the passband of frequencies. This control can take the form of a piezoelectric crystal or ceramic component shaped so that the frequency range of interest coincides with a resonance frequency of the piezoelectric element. At resonance, the piezoelectric filter has minimum impedance several orders of magnitude lower than its nonresonant impedance. Consequently, the element readily passes signals at frequencies close to its resonant frequency, the width of the passband usually being defined by the mechanical Q of the device as¹

$$Q = \frac{f}{\Delta f_{3\text{dB}}}, \quad \text{for } Q > 10, \quad (1)$$

where f is the center frequency and $\Delta f_{3\text{dB}}$ is the three decibel (power) passband. For ceramic piezoelectrics the mechanical Q is typically in the range 50–1000, whereas for quartz it can be higher than 100 000. Therefore, while narrow passband filters are readily available, broadband filters, in which bandwidths up to 50% of the center frequency are required, are more difficult to produce.

Broad bandwidth devices are finding extensive uses in acoustic imaging, especially for nondestructive testing and biomedical applications.^{2–5} Usually the transducers are operated in a pulse-echo arrangement. Here, wide bandwidth offers fast pulse rise time because the frequency response is significantly higher than the center frequency, and low ringing because these transducers generally have low mechanical Q .

Previously, the transducer bandwidth has been increased in several ways, including (a) Connecting an inductor in series with the piezoelectric element in order to match its electrical Q with the detection circuit.⁶ (b) Electrically connecting narrow bandwidth elements with slightly different resonance frequencies in parallel.⁶ (c) Mechanically

damping the resonance of a low Q piezoelectric element with a well-matched backing layer in order to spread the resonance peak over a wider frequency range.⁷ (d) Using matching transformers of quarter wave thickness between the transducer and the load in order to minimize acoustic impedance discontinuity.^{7,8}

Methods (c) and (d) are now widely favored, although in method (c) much of the input energy is wasted by damping, and in (d) a lack of transformer materials with the correct acoustic impedance necessitates the use of complex transformer configurations. Nevertheless, by employing three matching transformers with a suitable backing material and electrical impedance matching, Goll⁷ has produced efficient transducers with 3 dB bandwidths up to 76% of the center frequency.

In this paper a new type of broad bandwidth device is described. By combining resonant piezoelectric elements mechanically in parallel with a low mechanical Q polymer, a monolithic, low loss transducer with a widely variable bandwidth has been developed. Critical factors governing the physical dimensions of the device are presented, along with details of the role of the polymer in attenuating acoustic signals between adjacent piezoelectric elements.

THE TRANSDUCER DESIGN

Resonance behavior is critically dependent on the dimensions of the resonance specimen. For a bar-shaped specimen the frequency of a fundamental dilatational mode resonance is given by

$$f = \frac{1}{2L} \left(\frac{Y}{\rho} \right)^{1/2}, \quad (2)$$

where L is the governing dimension, ρ the density, and Y the appropriate Young's modulus. Equation (2) holds provided the dimensions of the bar are sufficiently different (usually by a factor of three (Ref. 9)) that mode coupling through

Poisson's ratio is not encountered. Also, it is important for a clean resonance that the opposite faces of the specimen, determining L , be accurately parallel.

In such a transducer, the bandwidth is determined by the mechanical Q and as such is a material property. However, it is possible in principle to broaden the bandwidth by forming a single piezoelectric element into a shape which has varying thickness (e.g., a wedge) and driving the element at frequencies corresponding to resonance of the thickness dimensions. In this case the thickness mode resonance encompasses a range of frequencies governed by its maximum and minimum dimensions. Unfortunately, since the element is strongly mechanically coupled at all points, destructive mechanical interference occurs between regions of different thickness resonating at different frequencies, and low efficiency results.

In the new device many piezoelectric elements with different dimensions are used to provide a wide passband, but the elements are combined into a monolithic array using an inactive, low Q polymer which decouples the elements mechanically and so prevents interference. The device, shown diagrammatically in Fig. 1(a), consists of sheets of piezoelectric material, e.g., lead zirconate titanate (PZT), laminated with the sheets of polymer so that the active elements are separated by sufficient polymer that most of the mechanical coupling between elements is removed. The piezoelectric is arranged with its polar axis parallel to the polymer interface and in the direction governing the desired resonance frequency. The composite is then ground to form a wedge, the slope of which, $\tan\theta$, defines its bandwidth according to the relationship

$$\Delta f = X \tan\theta f_1 f_2 / N, \quad (3)$$

where X is the spacing between the first and last active elements, f_1 and f_2 are the resonance frequencies of these ele-

ments, and N is the longitudinal mode frequency constant (product of resonance frequency and its governing dimension) of the piezoelectric material used.

The maximum value of θ is limited by the natural bandwidth of the piezoelectric and is determined from

$$\tan\theta_{\max} = (\Delta f/f)(\bar{L}/a), \quad (4)$$

where $(\Delta f/f)$ is the natural bandwidth of the active piezoelectric (within a given signal level, say 3 dB), \bar{L} is the mean length of an element, and a is its width. Thus at high θ values a clean resonance will not be obtained owing to the variation in length of each element. Also, the active elements must be sufficiently closely spaced that the resonance frequencies of individual elements overlap to provide a smooth continuous passband.

EXPERIMENTAL

Although the concept outlined above describes sheets of piezoelectric ceramic laminated with polymer, the actual experimental work has been conducted on composites of PZT fibers in an epoxy resin matrix. The form of these composites is already well known in hydrophone applications,^{10,11} and their fabrication has been described elsewhere.¹² This composite has the advantage over the lamellar composite described previously of accepting any surface profile and thus provides greater versatility for passband modification.

In principle, the passband of the composite can be tailored to provide a frequency spectrum of any shape. The device can even be fabricated in a "convex mirror" configuration to permit acoustic focusing over a wide range of frequencies.

Composites containing 10, 20, 30, 40, and 50 Vol % PZT (Ultrasonic Powders, Inc., South Plainfield, N.J. 07080, Type 501A) fibers embedded in Spurr's epoxy resin (Ernest F. Fullam, Inc., Schenectady, N.Y. No. 5132) were cut and ground to 3.2 mm thickness so that their opposite faces (perpendicular to the fiber axis) were accurately parallel ($\pm 3 \mu\text{m}$). The fiber diameter a was kept constant at 0.63 mm and the interfiber spacing y was computed from the mean of at least ten measurements on each composite. The thickness of the composites governed the length of the fibers and their resonance frequency, and was maintained at least three times as long as the fiber diameter to avoid mode coupling. With these dimensions, the longitudinal mode resonance frequency for the fibers was approximately 500 kHz.

To obtain resonance data, the parallel faces of the specimen were electroded with sputtered gold and loosely held between platinum wire contacts. Measurements fell into two categories:

(a) Amplitude/frequency measurements to obtain information about the acoustic attenuation mechanism of the polymer and determine the optimum volume fraction of fibers. The signal transfer between adjacent rows of fibers was obtained using the electrode configuration shown in Fig. 1(b) by driving one row of three fibers at resonance and using the next as a detector. It was assumed that the fiber rows approximated to the planar configuration described earlier.

(b) Impedance/frequency spectra for the composites

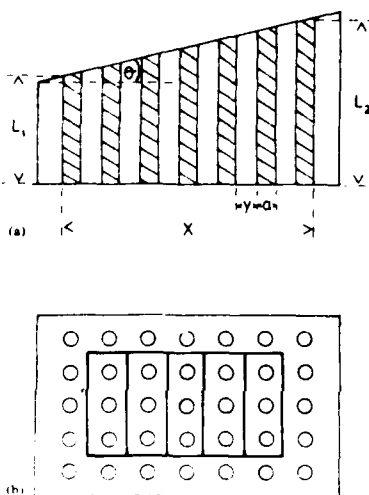


FIG. 1 (a) Broadband transducer configuration showing the spatial relationships between active elements (shaded) and polymer matrix. (b) Horizontal section through the fiber composite showing the electrode pattern. Thick lines denote breaks in the electrode. For bandwidth determination the whole central 5×3 matrix of fibers was employed. Attenuation data were obtained between adjacent 1×3 fiber matrices.

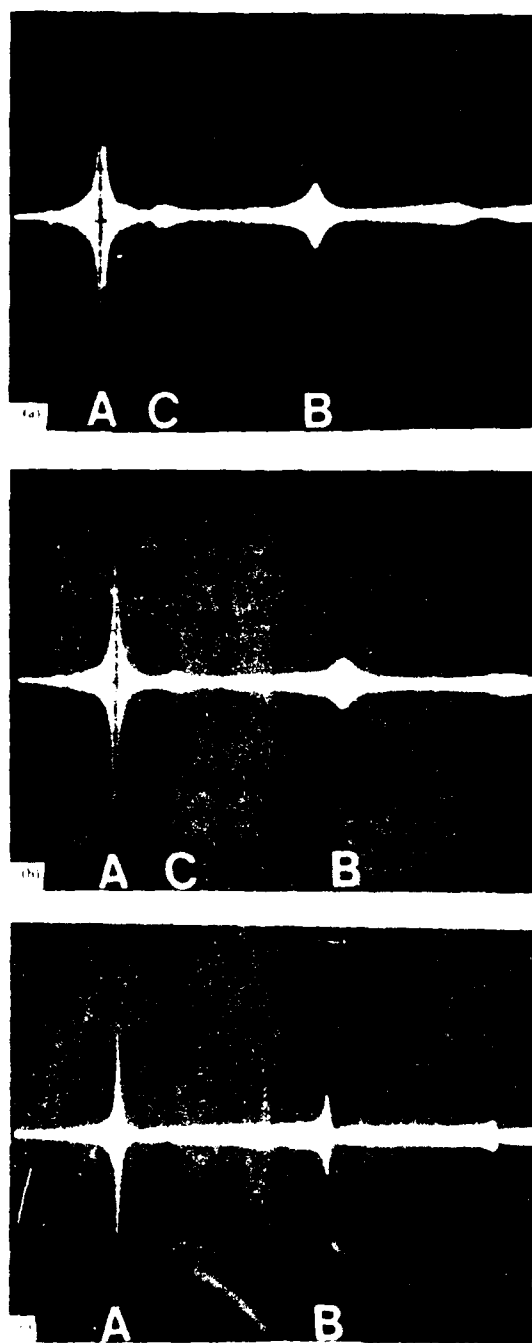


FIG. 2. Amplitude/frequency spectra for (a) 30 Vol % PZT composite with faces parallel ground and electrodes extending to the edges of the device. (b) The same composite with the outermost row of fibers removed from the electrical circuit. (c) A single PZT fiber removed from a parallel ground composite. [Horizontal scale—frequency (0–3 MHz); vertical scale—amplitude of transmitted voltage.]

were obtained over the required range of frequencies (usually 0–1 MHz) in transmission using a circuit described elsewhere.¹¹ In most cases a 5×3 matrix of fibers was employed. The faces were completely electroded and the angle between them varied in steps of 0, 1, 2, 2.6, 5, 7, and 10° in order to increase the bandwidth.

The resonance spectrum for a 30 vol % PZT composite with parallel ground faces, which was typical of all the composites, is shown in Figs. 2(a) and 2(b). In Fig. 2(a) the electrodes extended to the very edge of the specimen, and the resonance peaks were found to be split into doublets. This was probably due to lowering of the resonance frequency of the outermost fibers by the adjacent acoustic impedance discontinuity. When the outermost row of fibers was removed from the circuit by reducing the area of the electrodes a much cleaner resonance spectrum was obtained [Fig. 2(b)]. Only two peaks other than the fundamental thickness mode resonance *A* were observed. One corresponded to the third harmonic *B* and the other minor peak at *C* may have been a composite resonance or resonance of the epoxy resin. No radial mode resonances corresponding to the diameter of the fibers were detected, indicative of strong damping by the polymer in all directions perpendicular to the fiber length. The resonance spectrum of a single fiber without epoxy resin [Fig. 2(c)] showed close similarity in resonance frequency and peak width with that of the 30% composite [Fig. 2(b)] and with spectra for the other composites.

RESULTS AND DISCUSSION

Bandwidth broadening

In Table I, 6-dB bandwidth data for the various composites are given for θ values from 0 to 10°. For the 10% PZT composite the bandwidth rapidly broadened with increasing θ owing to the wide interfiber spacing y and consequently could not be kept within a 6 dB tolerance. Attenuation data for the 50% composites showed considerable scatter (see the next section) and consequently bandwidths were not determined. Also shown in the table are 6 dB bandwidth and resonance frequencies for PZT rods of identical length to those in the composites.

Comparing the resonance behavior of the 20, 30, 40, and 50% composites with that of the PZT rods, there is no consistent change in the resonance frequency or bandwidth at $\theta = 0^\circ$. The implication is that the resonance behavior of a rod embedded in a composite closely resembles that of a "free" rod. Considering the acoustic impedance discontinuity between the polymer and the ceramic, and the higher mechanical Q of the latter (see later section), this behavior is to be expected.⁷

The data in Table I show a large increase in bandwidth with increasing θ . Equation (3) predicts that the bandwidth should be linearly dependent on $X \tan \theta$ and this is indeed the case, as Fig. 3 demonstrates. In Fig. 4 the 6 dB bandwidths and the change in amplitude of the resonance peaks are shown as a function of θ for the 20, 30, and 40% PZT composites. For all these devices a reduction in amplitude is observed until θ is sufficiently large that peak separation occurs on the resonance spectra (at approximately 7°), whereupon no further reduction in amplitude takes place. The constant amplitude at high θ indicates that the θ limit set by Eq. (4) has not been exceeded. However, at very high θ values peak separation can be sufficient to exceed the bandwidth tolerance. Bandwidth broadening is shown in Fig. 5 for a 30% PZT composite ground to θ values of 2, 7, and 10°.

TABLE I. 6 dB bandwidth data for various composites with θ values from 0° to 10°

Specimen (Vol % PZT)	v (mm)	Fundamental longitudinal mode resonance frequency (kHz)	0°	1°	2	% Bandwidth (6 dB) 2.6°	5°	7°	10°
10	1.23	495	N.D.	14	20	Very broad	Very broad	Very broad	Very broad
20	0.66	460	6.4	6.2	8.0	10.4	16	30	56
30	0.46	490	7.3	6.9	11.0	9.0	16	36	46
40	0.31	510	6.6	5.3	6.6	7.1	12	30	38
50	0.19	520	5.8	N.D.	N.D.	N.D.	N.D.	N.D.	N.D.
PZT rods	...	490	6.5 (average of ten)

Bandpass tolerances are usually set at 3 dB for most filter applications, but in the present work the 6 dB level has been employed. This is because only fifteen fibers have been used to evaluate each composite, leading to problems with resolution. It must be remembered that using a sufficiently large number of active elements enables the composites to be trimmed to almost any desired tolerance and makes extremely wide bandwidths feasible.

ATTENUATION IN THE POLYMER MATRIX

The purpose of the polymer matrix is to mechanically decouple the PZT fibers without significantly affecting their individual resonance behavior. From the previous section, the Spurr's epoxy resin appears to fulfill both requirements. However, it is necessary to determine the factors governing the attenuation characteristics of the polymer in order to minimize the interfiber spacing and obtain high piezoelectric element density, without compromising mechanical decoupling.

Two attenuation mechanisms are possible in the composites. First, an acoustic impedance discontinuity exists at the PZT/polymer interface which can reduce signal transmission into and out of the polymer. This must be the case since the fibers are free to resonate with little damping by the

polymer (Table I), and also because the calculated acoustic impedances differ by a factor of ≈ 10 assuming a value of 3000 ms^{-1} for the acoustic velocity of a typical polymer.⁴ Consider an acoustic signal of amplitude η_0 incident normally across unit area of interface. The total signal transmission across two PZT/polymer interfaces can be estimated using the relationship

$$T = 4Z / (Z^2 + 2Z + 1), \quad (5)$$

where T is the overall transmission coefficient and

$$Z = Z_c / Z_p = \rho_c V_c / \rho_p V_p, \quad (6)$$

where Z_c , Z_p , V_c , and V_p are the acoustic impedances and velocities of the ceramic and polymer, respectively. Plotting T against Z (Fig. 6), for $Z > 1$, the overall transmission coefficient falls rapidly with increasing Z , up to $Z \approx 10$, whereupon further increases in Z have only a limited effect on T . Since most polymer/PZT combinations have calculated Z values greater than ten, it is to be expected that many polymers can fulfill the impedance discontinuity requirements for high signal attenuation.

The second attenuation mechanism involves acoustic energy absorption within the polymer, which can arise from both internal friction and phase shift mechanisms.¹ If the

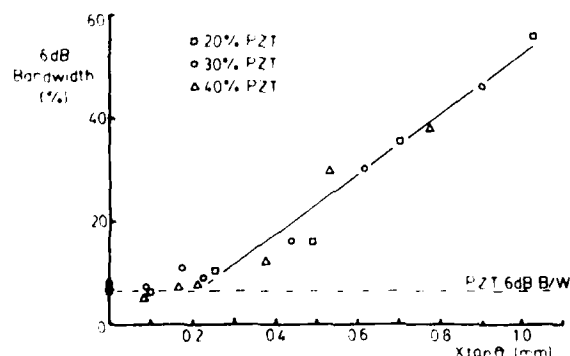
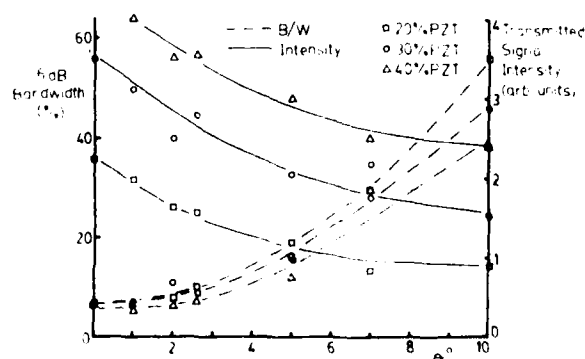


FIG. 3. Bandwidth dependence on composite geometry

FIG. 4. Effect of θ on bandwidth and signal intensity for composites containing 20, 30, and 40 Vol % PZT fibers

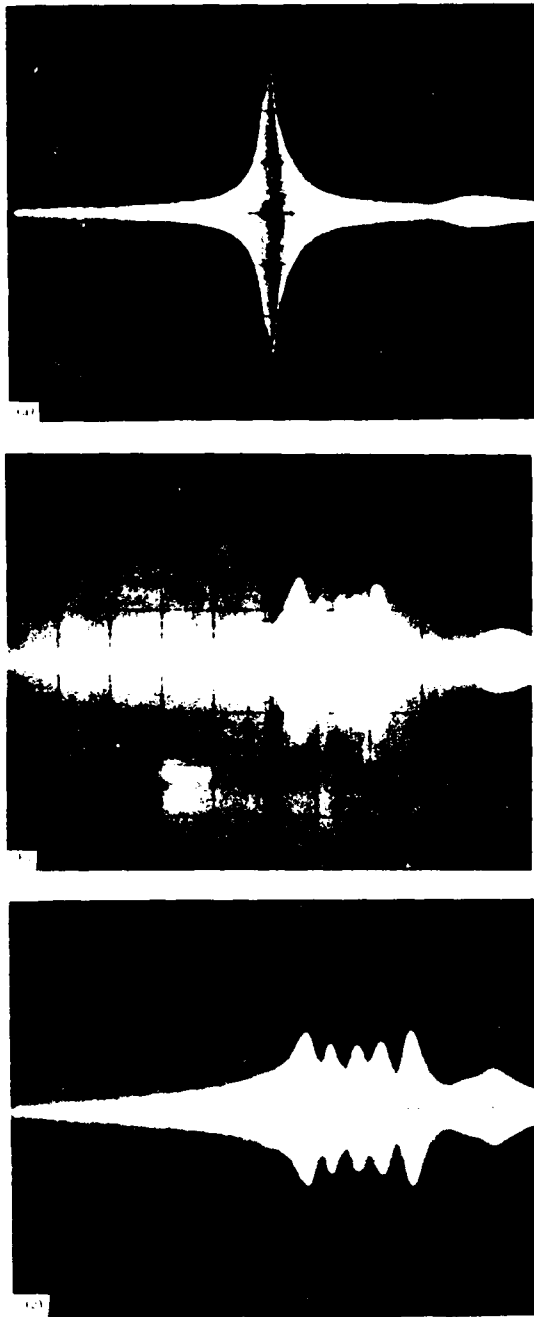


FIG. 5. Bandwidth broadening in composites containing 30 Vol % PZT ground to θ values of (a) 2° , (b) 7° , and (c) 10° . [Horizontal scale—frequency (0–1 MHz); vertical scale—transmitted voltage amplitude on the same linear scale as Fig. 2(b)]

polymer is considered to be a transmission line of infinite length, a one-dimensional treatment can be applied, governed by the wave equation

$$Y^* \frac{d^2 \eta}{dy^2} = \rho \frac{d^2 y}{dt^2}, \quad (7)$$

where η is the particle displacement, y is a distance parameter, t is time, and Y^* is the complex Young's modulus defined by

$$Y^* = Y' + iY'', \quad (8)$$

The solution for Eq. (7) has the form

$$\eta = \eta_0 e^{i(\omega t - \phi)}, \quad (9)$$

where ω has its usual meaning and ϕ , the propagation constant, includes both real (internal friction) and imaginary (phase shift) attenuation terms and is given by

$$\phi = i\omega(\rho/Y^*)^{1/2}. \quad (10)$$

Rearranging Eq. (10) and substituting for $|Y^*|^2$ from Eq. (8) yields

$$1 + \frac{|Y''|^2}{|Y'|^2} = \frac{\omega^4 \rho^2}{\phi^4 |Y'|^2}. \quad (11)$$

Substituting $Q = |Y'/Y''|$ into Eq. (10) gives

$$\phi = \omega H \left(\frac{\rho}{Y'} \right)^{1/2}, \quad \text{where } H = \left(\frac{Q^2}{Q^2 + 1} \right)^{1/4} \quad (12)$$

(H is the overall attenuation coefficient) and the attenuation equation can be rewritten as:

$$\ln(\eta/\eta_0) = i\omega t - \omega y H (\rho/Y')^{1/2}. \quad (13)$$

Plotting H as a function of Q (Fig. 7), the effect of the mechanical Q of the polymer can be seen to be small unless its value is less than unity.

The applicability of Eq. (12) to the present work has been tested by plotting $-\ln \eta/\eta_0$ against ωy for the composites (Fig. 8). Each point on this graph corresponds to an amplitude ratio measurement between adjacent rows in the appropriate composite. The relationship is linear for the 10, 20, and 30% materials and extrapolates approximately through the origin. For PZT volume fractions above 30% the data deviate from the form expected and the attenuation ratio becomes approximately constant at 0.21. Scatter is noticeably greater in the 50% case, which may be due to geometrical factors since the fibers are spaced less than 200 μm apart.

The attenuation minimum in Fig. 8 probably represents a limit set by superimposed attenuation due to the impedance discontinuity at the PZT/polymer interface. Bhalla¹⁴ has estimated the acoustic velocity in Spurr's epoxy resin to be 2400 ms^{-1} by the pulse-echo method. Using this value for V_p and assuming the density to be 1100 kg m^{-3} the Z ratio

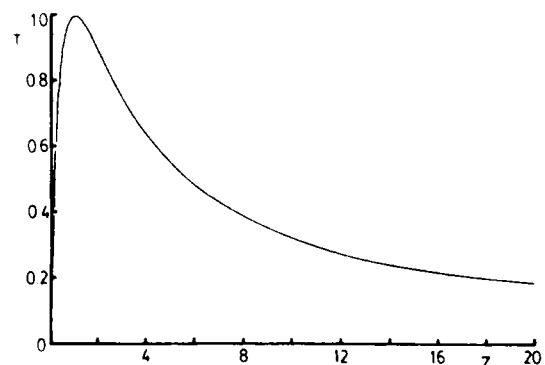
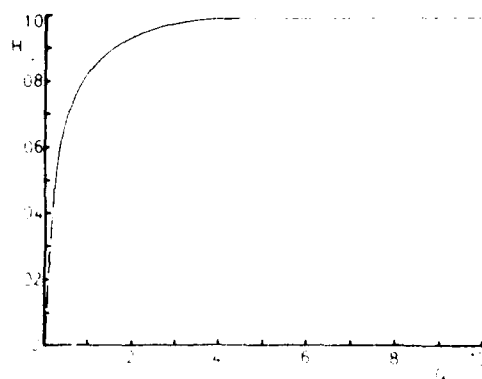


FIG. 6. Influence of acoustic impedance discontinuity Z on the fraction T of the force amplitude transmitted between adjacent piezoelectric elements.

FIG. 7. Effect of mechanical Q on the overall attenuation coefficient H .

for PZT and Spurr's is approximately 14. Thus from Eq. (5) the calculated overall transmission coefficient is 0.26, in good agreement with the value of 0.21 obtained from Fig. 8.

Pseudostatic Young's modulus Y' has been estimated by Klicker¹² for Spurr's as $3 \times 10^9 \text{ Nm}^{-2}$. Substituting this value and the slope of Fig. 8 into Eq. (13) (corrected for attenuation by acoustic impedance mismatch) yields a Q value for the polymer of 0.3. While this value may seem extremely low by solid state, inorganic material standards, it is typical for polymers near their glass transition temperature.¹⁵ At sufficiently high frequencies ($> 10 \text{ MHz}$) the complex Young's modulus attains a constant value independent of frequency as the polymer assumes glasslike character.¹⁶

Although the attenuation data for the 10, 20, and 30% PZT composites appear to be a good fit to classical attenuation theory, there are some reservations. In the first place, the theory is developed for a transmission medium which is long compared to the wavelength, clearly not the case for these composites. However, it seems probable that the polymer phase is so highly attenuating that interference from reflection at the end of the transmission line is insignificant. Secondly, the lateral dimensions of the composites may approach the acoustic wavelength in some cases and cause velocity dispersion.¹⁷ In general, however, the attainable accuracy for polymeric materials does not warrant the complexity of making Rayleigh type corrections.¹

The acoustic attenuation mechanism of the polymer is thus a series combination of acoustic impedance discontinuity effects, internal friction, and phase shift. Since 75–80% of the attenuation occurs at the PZT/polymer interface, it may be expected that high PZT volume fractions can be utilized without encountering problems due to mechanical interference between adjacent piezoelectric elements.

CONCLUSIONS

Monolithic composite transducers consisting of active piezoelectric elements dispersed in an inactive polymer matrix have been investigated for broadband applications, such as acoustic imaging. The active elements are PZT ceramic rods aligned perpendicular to the thickness dimension of the composite and made to resonate in their length mode. Other modes are suppressed by the low mechanical Q polymer matrix. The composite is made broadband by varying its thick-

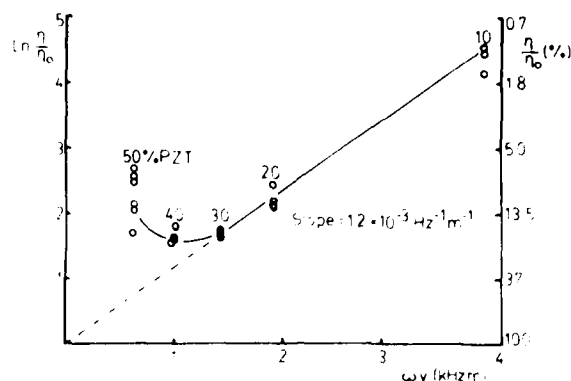


FIG. 8. Experimental data fit to the attenuation equation.

ness, and shows sufficient versatility that the passband can be tailored to almost any desired shape.

Crosstalk between adjacent piezoelectric elements resonating at different frequencies is minimized by the highly attenuating nature of the polymer matrix. Attenuation takes place by a series combination of reflection at the PZT/polymer acoustic impedance discontinuity and transmission attenuation within the polymer itself. Important design parameters pertaining to bandwidth broadening and crosstalk elimination are outlined for the composites.

ACKNOWLEDGMENTS

Processing procedures for the fiber composites were developed by Dr. K. Klicker at the Materials Research Laboratory. The authors thank Professor R. E. Newnham of MRL and Professor B. Auld of Stanford University for their helpful comments and Professor L. E. Cross of MRL for his interest and for reviewing the manuscript.

- ¹H. J. McSkimin, in *Physical Acoustics*, edited by W. P. Mason (Academic, New York, 1964), Vol. 1A, Chap. 4, pp. 271–334.
- ²K. R. Enkron, F. T. Fry, and J. P. Jones, *IEEE Trans. Sonics Ultrason.* SU-21, 144 (1974).
- ³R. S. Sharpe, *Philos. Trans. R. Soc. Lond. Ser. A* **292**, 163 (1979).
- ⁴A. deSterke, *Philos. Trans. R. Soc. London Ser. A* **292**, 207 (1979).
- ⁵P. N. T. Wells, *Philos. Trans. R. Soc. London Ser. A* **292**, 187 (1979).
- ⁶W. P. Mason, in *Physical Acoustics*, edited by W. P. Mason (Academic, New York, 1964), Vol. 1A, Chap. 5, pp. 335–415.
- ⁷J. H. Goll, *IEEE Trans. Sonics Ultrason.* SU-26, 385 (1979).
- ⁸C. S. Desilets, *IEEE Trans. Sonics Ultrason.* SU-25, 115 (1978).
- ⁹*Proc. IRE* **46**, 764 (1958).
- ¹⁰R. E. Newnham, D. P. Skinner, and L. E. Cross, *Mater. Res. Bull.* **13**, 525 (1978).
- ¹¹D. P. Skinner, R. E. Newnham, and L. E. Cross, *Mater. Res. Bull.* **13**, 509 (1978).
- ¹²K. Klicker, Ph.D. thesis, The Pennsylvania State University, 1980.
- ¹³T. R. Shrout, W. A. Schulze, J. V. Biggers, and L. J. Bowen, *Mater. Res. Bull.* **15**, 551 (1980).
- ¹⁴A. Bhalla (private communication).
- ¹⁵T. F. Nielsen, *Mechanical Properties of Polymers and Composites* (Dekker, New York, 1974), Vol. 1, Chap. 1, pp. 1–37.
- ¹⁶D. J. Williams, *Polymer Science and Engineering* (Prentice-Hall, New Jersey, 1971), Chap. 11, pp. 293–339.
- ¹⁷H. Kolsky, *Stress Waves in Solids* (Clarendon, Oxford, 1953), Chap. 3, pp. 41–86.

APPENDIX 42

T.R. Shrout, W.A. Schulze, J.V. Biggers, L.J. Bowen. Resonance Behavior of Internally Electroded PZT Devices. Mat. Res. Bull. 15, 551 (1980).

RESONANCE BEHAVIOR OF INTERNALLY ELECTRODED PZT DEVICES

T. R. Shrout, W. A. Schulze, J. V. Biggers and L. J. Bowen
Materials Research Laboratory
The Pennsylvania State University
University Park, Pennsylvania 16802

(Received January 29, 1980; Refereed)

ABSTRACT

Preparation and resonant properties of hard and soft internally electroded PZT bars are described. The presence of cofired platinum internal electrodes is shown to have little effect on the resonance behavior of hard PZT. Piezoelectric transformers having internally electroded primaries and secondaries are compared with conventional devices and show improved transformer ratio and power handling capability.

Introduction

In a previous paper (1) the authors described the use of cofired platinum internal electrodes for impedance modification of lead zirconate-lead titanate (PZT) electromechanical transducers. By incorporating the internal electrodes into the PZT in a multilayer configuration (2) reduced voltage/strain ratios were obtained. Electrical properties (relative permittivity, dissipation factor, piezoelectric coefficients, and mechanical losses) were largely unaffected by the presence of internal electrodes.

This paper will describe the preparation and high frequency (resonant) electromechanical properties of multilayer transducers made from commercial PZT formulations and utilizing platinum internal electrodes. Improvements in piezoelectric transformer performance by the use of internal electroding will be demonstrated.

Experimental

Device Configurations

The device configurations used to study the effects of internal electrodes on electromechanical properties have already been described (1). The device that offers greatest potential in transducer applications is based on a multilayer capacitor internal electrode configuration. Alternate internal electrodes are connected together by an external electrode applied after firing. During

poling an electric field is applied to the external electrodes so that adjacent PZT layers are poled in opposite directions, but a driving field on these external electrodes excites in phase strain.

Internally electroded multilayer capacitors are produced (2) by applying metal electrode ink onto thin tapecast sheets of high dielectric constant material (such as barium titanate), assembling the electroded tape into the required device configuration, and firing to form a dense body. The resulting composite has greatly enhanced capacitance-to-volume ratio for a given operating voltage and has the additional advantage of high dielectric breakdown strength arising from the thinness of the insulating ceramic layers (3).

Two other device configurations were employed as controls for characterizing the piezoelectric properties of plain and internally electroded PZT. These consisted of bars ground from plain PZT and PZT with cofired internal electrodes. In the latter case, the plane of the internal electrode was parallel to the largest dimensions of the bar and the poling direction extended throughout its whole thickness. In most cases four internal electrodes were employed. Mode coupling was minimized by careful choice of specimen dimensions (4).

Device Preparation

Three commercial* grades of PZT powders were used: a soft PZT (501A), an intermediate grade (401), and a high mechanical Q material designated 401-888. Manufacturers' specifications for sintered specimens of these materials are given in Table 1. The device fabrication process is shown diagrammatically in Figure 1. PZT powder mixed with liquid organic binder is tapecast (5) 0.25 mm thick, dried, cut into 25 mm squares, and electroded with platinum paste** by screen printing. The tape pieces are then stacked in the appropriate configuration, warm pressed at 30 MNm^{-2} and 50°C to form a coherent device structure, and the binder burned out in flowing air at 700°C over a 30-hour period. Firing in the presence of a lead zirconate PbO source at 1300°C for 90 minutes results in specimens over 95% dense. After grinding the fired specimens to expose the

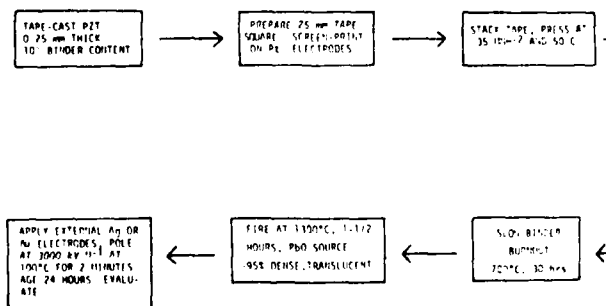


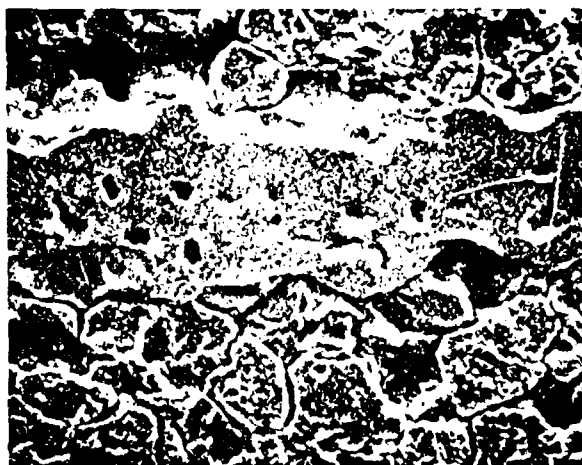
FIG. 1
Device fabrication route

*Ultrasonic Powders, Inc., South Plainfield, NJ 07080.

**Engelhard Industries, East Newark, NJ 07029, Type E-305-A.

Table 1

Material	Relative Permittivity	$\tan \delta$ (1 KHz)	K_1	d_{33} $\text{CN}^{-1} \times 10^{-12}$	N_1 (Gauss)	K_2 (Hzm)	Q_m
501A	2000	0.014	0.63	400	1866	1740	80
401	1350	0.004	0.62	290	1540	1670	500
401-888	1000	0.003	0.50	215	1640	1970	1000



— 10 μm —

FIG. 2

Micrograph showing a platinum electrode in an internally electroded specimen.

internal electrodes as required, external electrodes are applied as fired on silver paste*, and electrical connections made by soldering on 0.2 mm diameter silver wire. To prevent delamination, careful control of the internal electrode thickness and the warm-pressing conditions is necessary. Separation at the final grinding stage can be avoided by making the platinum layers as thin as possible, consistent with a continuous electrode film. In addition, it is important that the organic binder be completely burned out prior to sintering.

Figure 2 is a scanning electron micrograph of a sectioned 501A multilayer specimen. This sample has been etched in a dilute aqueous mixture of hydrofluoric and hydrochloric acids to expose the grain boundaries. The platinum electrode is incompletely sintered but fully coherent, and it appears from the etched features to be bonded to the surrounding ceramic by an intermediate second phase. In all the specimens examined the internal electrodes appeared to be continuous.

*Dupont Electronic Products, Wilmington, DE, 16898, Type 7095.

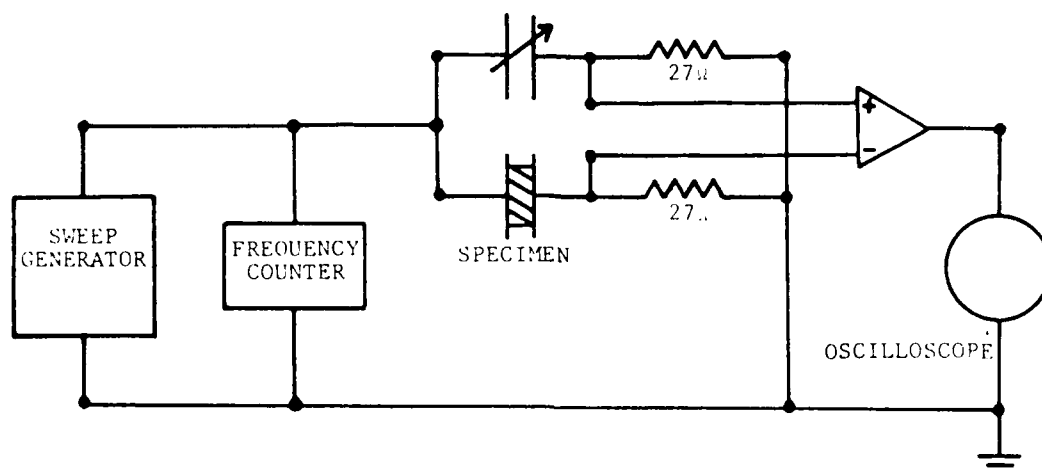


FIG. 3(a)
Resonance detecting circuit

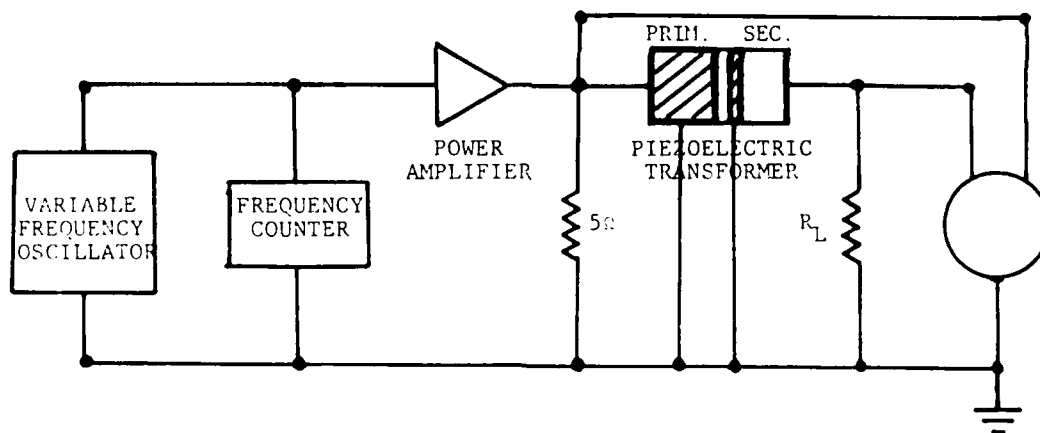


FIG. 3(b)
Transformer evaluation circuit

Resonance spectra for bar-shaped specimens of plain and internally electroded PZT were obtained using the circuit shown in Figure 3(a). The variable capacitor and differential amplifier were used to subtract out the base capacitance of the sample to allow observation of the resonance peaks at higher frequencies without distortion.

Performance characteristics of the piezoelectric transformers were analyzed using the circuit in Figure 3(b). The load resistance, R_L , was varied from 10^3 to $10^7 \Omega$. The output impedance of the oscillator was lowered to provide a stable supply voltage for the low input impedance multilayer transformers at resonance.

Results

Effect of Internal Electrodes on Resonant Properties

Resonance spectra, obtained using the circuit shown in Figure 3(a) for three types of commercial PZT (501A, 401, and 401-888) with and without internal electrodes, are compared in Figure 4(a), (b), and (c). The data are for frequencies in the range 0-3 MHz, above which no major resonances could be detected. The spectra contain resonances corresponding to the three dilatational modes for which the frequency constant, N , is given by:

$$N = \frac{1}{2\sqrt{\rho s}} \quad [1]$$

where ρ = density and s = elastic compliance. Other resonances probably arise from harmonics, shear modes, and mode coupling. For the harder piezoelectrics (401 and 401-888), several closely spaced resonances are seen rather than a single one corresponding to each mode. This may have been caused by a slightly wedge-shaped specimen geometry owing to difficulty experienced in obtaining perfectly parallel opposite faces on the resonance bars during grinding. In the thickness mode, peak broadening is especially evident since accurate dimensional tolerances are more difficult to achieve and mode coupling is a major problem (4).

Comparing the spectra of plain and internally electroded specimens prepared from each PZT, the most obvious feature is their similarity. For each resonance in the plain specimens, the corresponding resonance in the internally electroded ones has a similar amplitude and frequency. This suggests that acoustic losses at the internal electrode/PZT interfaces are quite small, which is indicative of good bonding and low acoustic impedance mismatch.

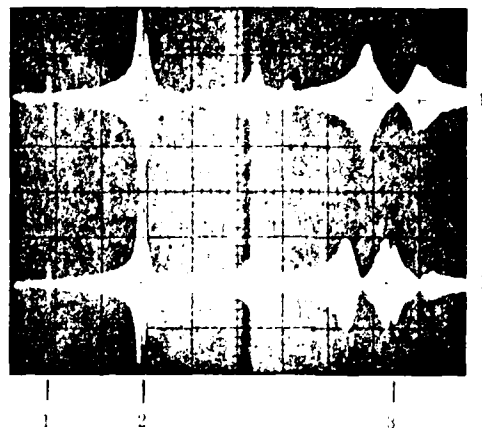


FIG. 4(a)

501A. 1=long mode; 2=width mode; 3=thickness mode. Horizontal scale = frequency; P = plain; I = internally electroded.

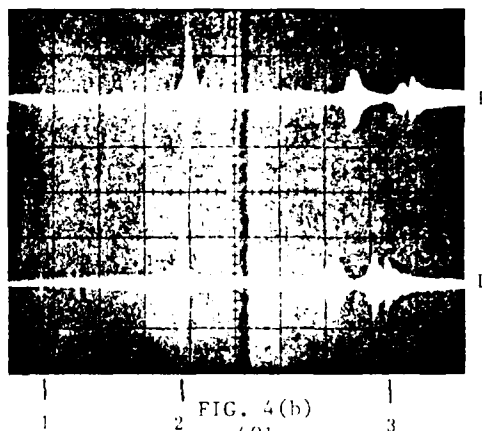


FIG. 4(b)

401

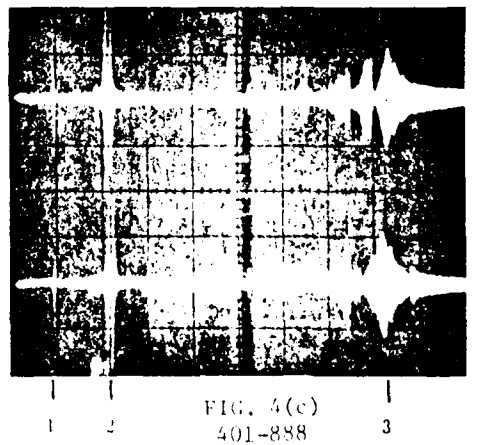


FIG. 4(c)

401-888

Values of frequency constant for dilatational mode resonances in the different specimens are given in Table 2. In all cases, differences in the frequency constants between plain and corresponding internally electroded specimens are less than 5% except for the thickness mode vibrations in the softer 501A and 401 materials. For these, the resonance frequencies are respectively 10% and 7% lower in the internally electroded than in the plain devices. It is possible that in the softer materials the presence of equipotential planes (internal electrodes) can affect the internal field distributions and influence domain wall motion, thus increasing the elastic compliance and reducing the resonance frequency (equation 1). This effect would not be as pronounced in the harder 401-888 PZT where the domain structure is more stable and, indeed, the thickness mode resonance frequencies for the plain and internally electroded 401-888 agree to within 2%.

Table 2

Specimen	Frequency Constant		
	Longitudinal Mode	Width Mode	Thickness Mode
501A Plain	1390	1450	2190
501A Internally electroded	1380	1440	1970
401 Plain	1670	1690	2220
401 Internally electroded	1620	1610	2070
401-888 Plain	1750	1880	2230
401-888 Internally electroded	1740	1750	2200

Considering that eight platinum/PZT interfaces exist within the internally electroded specimens, it is reasonable to expect that the influence of the electrodes on the resonance spectra should be far greater than that observed, at least in the thickness mode. Some insight into the relative insignificance of internal electrodes in hard PZT can be obtained by assuming the material to be a series linked composite, in which case the mean elastic compliance (\bar{S}) can be estimated using the equation:

$$\bar{S} = \frac{P_{tL} P_{tS} + P_{ZTL} P_{ZTS}}{P_{tL} + P_{ZTL}} \quad [2]$$

where L is the thickness of the appropriate layer.

In the present devices, $P_{ZTL}/P_{tL} \approx 20$, $P_{ZTS}^E = 8.3 \times 10^{-12} \text{ m}^2 \text{ N}^{-1}$. The average density for a composite containing four internal electrodes is $8,260 \text{ kg m}^{-3}$ assuming densities of 7600 and 21500 kg m^{-3} for PZT and platinum respectively. Hence the calculated frequency constant values are 1990 Hzm for the plain 401-888 and 1935 Hzm for the internally electroded material, a difference of only 2.7%. Values of the mean elastic compliance and mean density derived from this model show a reduction and an increase respectively over the values for pure PZT

and therefore compensate to some extent. In addition, for composites having a large ceramic-to-metal layer thickness ratio, the series model predicts only small changes in frequency constant. As a corollary, it should be possible by tailoring the densities, elastic compliances and relative thicknesses of the ceramic and metal phases, to employ a wide range of internal electrode materials without influencing resonance behavior.

Piezoelectric Transformer

Conventional piezoelectric transformers (6) consist of a long thin piezoelectric ceramic bar, the primary end of which is thickness poled, while the secondary end is longitudinally poled as shown in Figure 5(a). When operated at the longitudinal mode fundamental resonance frequency, the secondary d_{33} piezoelectric coefficient is driven efficiently by the primary d_{31} piezoelectric coefficient. The voltage step-up capability is determined by the relative lengths of the poled regions and by the driving and loading conditions (7).

In the present work an internally electroded primary has been employed to obtain an improvement in step-up ratio over the conventional design. The actual device configuration used is shown in Figure 5(b). The primary is a nine internal electrode multilayer linked to a 401-888 PZT secondary by a separate internally electroded region which acts as one of the secondary electrodes. This arrangement is intended to provide increased secondary electrode area, thus permitting more uniform poling and greater charge collection capacity than is possible with the conventional secondary configuration. Furthermore, D.C. isolation is possible since secondary electrodes are isolated from the input. The overall dimensions of the device are 15 x 16 x 1.5 mm and the operating frequency is approximately 100 kHz.

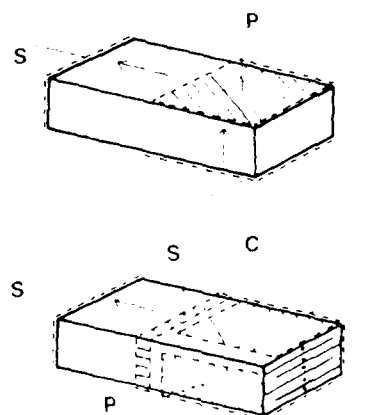


FIG. 5

(a) conventional; (b) multilayer input/high output transformer configurations. P - Primary electrodes
S - Secondary electrodes
C - Common

Figure 6 compares the voltage step-up ratio and its variation with load resistance, for four types of transformer: (A) conventional; (B) conventional with high output secondary electrodes; (C) multilayer input/low output secondary electrodes, and (D) multilayer input/high output secondary electrodes. Data presented are for transformers of similar size driven at their fundamental resonant frequency, using the circuit shown in Figure 3(b). All voltages are measured peak-to-peak and the input peak field is constant. In all the transformers an increase in voltage step-up ratio with increasing load resistance is seen. However, the transformers equipped with a multilayer primary have a greatly improved step-up ratio compared to those having a conventional input. Some dependence of step-up ratio on input field is evident, especially for the internally electroded devices. More experimental work is necessary to explain this observation.

In Figure 7 the output power of the four transformer configurations is plotted as a function of load resistance. The power output curves have a bimodal

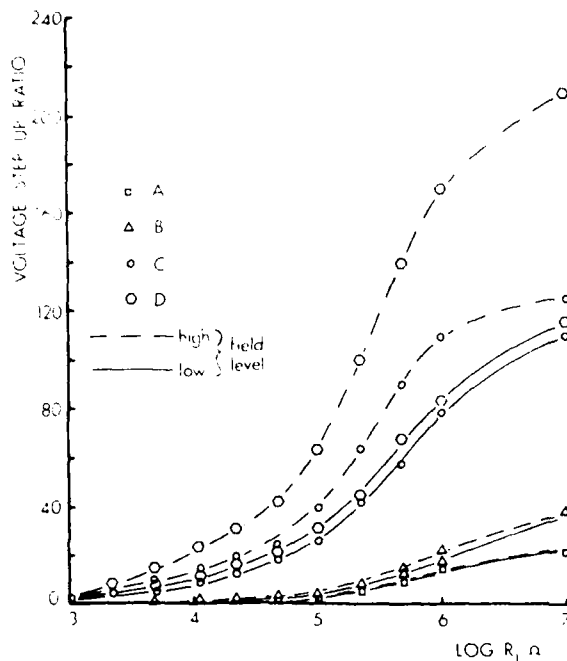


FIG. 6

Transformation ratio as a function of load resistance for the four piezoelectric transformer configurations (maximum field level used = 0.02 MV/m^{-1}).

shape which is consistent with previously published work (7). Figure 7 shows that the transformers with a high output secondary (B and D) are capable of handling up to three times more power than those with a conventional secondary.

Conclusions

Platinum internal electrodes have been incorporated into PZT by a conventional multilayer capacitor processing technique. Resonance measurements show that the electrodes have little influence on the frequency constants of sintered PZT, especially for hard PZT compositions.

Piezoelectric transformers with internal electrodes can readily be fabricated using a tapecasting approach. Transformers equipped with a multilayer primary show enhanced voltage step-up ratio compared to conventional devices. In addition, the power handling capability of the transformers can be greatly increased by the incorporation of internal electrodes into the common secondary electrode.

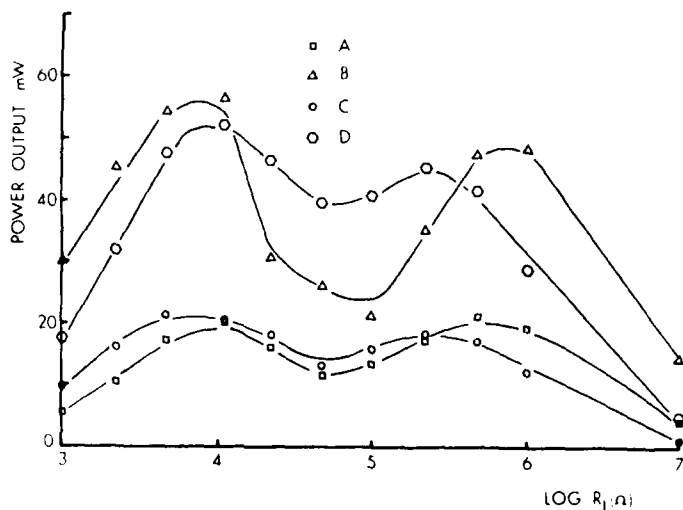


FIG. 7

Power handling capability of the various transformer configurations.

Acknowledgment

The authors wish to acknowledge the technical assistance of Susan Sharp and Daniel Cross. This work was supported by the Office of Naval Research under Contract No. N00014-78-C-0291.

References

1. L. J. Bowen, T. R. Shrout, W. A. Schulze and J. V. Biggers, "Piezoelectric Properties of Internally Electroded PZT Multilayers," to be published in *Ferroelectrics*.
2. J. C. Williams, "Doctor-Blade Process," *Treatise on Materials Science and Technology*, Vol. 9, (Ceramic Fabrication Processes), F. Y. Wang, editor, 173, Academic Press 1976.
3. W. D. Kingery, H. K. Bowen and D. R. Uhlmann, "Introduction to Ceramics," 2nd ed., 960-963, Wiley 1976.
4. "IRE Standards on Piezoelectric Crystals: Determination of the Elastic, Piezoelectric and Dielectric Constants - The Electromechanical Coupling Factor," 1958, *Proc. IRE*, 46, p. 764-78.
5. J. V. Biggers, T. R. Shrout and W. A. Schulze, "Densification of PZT Cast Tape by Pressing," *American Ceramic Society Bulletin*, 58, (5), 516-521, 1979.
6. H. W. Katz, "Solid State Magnetic and Dielectric Devices," Wiley 1959, Chapter 5.
7. W. B. Harrison and U. Bonne, "Relationship of Piezoelectric Properties to High Voltage Transformer Performance." Paper presented at American Ceramic Society Annual Meeting (Electronic Division), Dallas, 1978.

APPENDIX 43

T.R. Gururaja, L.E. Cross, R.E. Newnham. Continuous Poling Technique for PZT Fibers. Bull. Amer. Ceram. Soc. (accepted).

Submitted as Note for Bulletin of The
American Ceramic Society

CONTINUOUS POLING TECHNIQUE
FOR PZT FIBERS

T. R. Gururaja, L. E. Cross* and R. E. Newnham*

Materials Research Laboratory
Pennsylvania State University
University Park, Pa., 16802

* Member, American Ceramic Society

Supported by the Office of Naval Research
under contract No. N00014-78-C-0291.

/

In recent years, ferroelectric composites with several different connectivity patterns have been synthesized for transducer applications.¹⁻³ Epoxy - PZT composites with 3-1 connectivity pattern have shown remarkable improvement of hydrostatic piezoelectric coefficients (d_h) and voltage coefficients (g_h) over solid PZT ceramics.⁴ The composites consist of parallel PZT rods embedded in a three-dimensionally connected polymer matrix, as illustrated schematically in Fig. 1. PZT rods ranging from 200 to 800 μm , in diameter have been used to fabricate composites with 10-50 volume percent PZT. Composites with \bar{d}_h three times that of solid PZT-501A* and \bar{g}_h at least thirty times greater were obtained in this way.

A detailed procedure for fabricating composites with 3-1 connectivity has been reported by Klicker et.al.⁴ In essence, PZT rods were extruded and fired, and then were epoxied in the arrangement shown in Fig. 1. Samples of thicknesses 1-4 mm were cut from longer composites and poled in a 75°C oil bath with a field of 22 kV/cm for five minutes. Using a 10 kV power supply, this method of poling limits the thickness of the composites to about 4mm.

Further enhancement of the voltage coefficient and the hydrostatic piezoelectric coefficient can be achieved by arranging the rods in other patterns. A triple-pillar composite with rods oriented in three perpendicular directions is one such example. Poling complex composites is difficult by conventional techniques. Since it is easier to work with pre-poled fibers, a continuous poling technique for long PZT rods has been developed which overcomes the limitations on size and geometrical arrangement encountered in the direct poling of composites.

The continuous poling technique utilizes the idea of gradually advancing the rods through two electrical contacts maintained at the required potential difference. Electrical contact to the PZT rods was achieved in two ways.

*Ultra Sonics Powders, Inc., South Plainfield, NJ

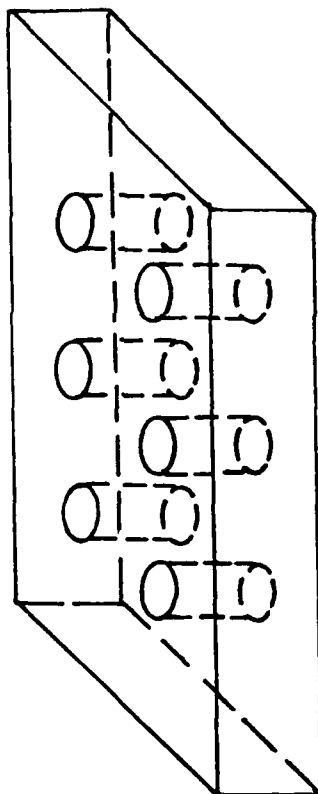


Fig. 1. Composite transducers with 3-1 connectivity. Ferroelectric ceramic rods embedded in a polymer matrix give sizeable piezoelectric effects.

In the first method, the wetting behavior of a low-melting solder* with copper was utilized to form a molten film of solder over a circular hole (2-4mm in diameter) in a copper plate (2mm thick). The entire system was immersed in an oil bath maintained at 150°C. The surface tension and the upward thrust of the heated oil kept the molten film reasonably stable. A second copper plate was positioned 2-4mm away from the first plate to provide the second electrical contact (Fig. 2a).

PZT rods were pulled through the two solder films at a slow rate of 0.5mm/minute. An electric field of about 14 kV/cm was applied between the copper plates. The solder did not wet the PZT rods and was not pulled along with the rod. Hence the problem of shorting the two plates was not encountered.

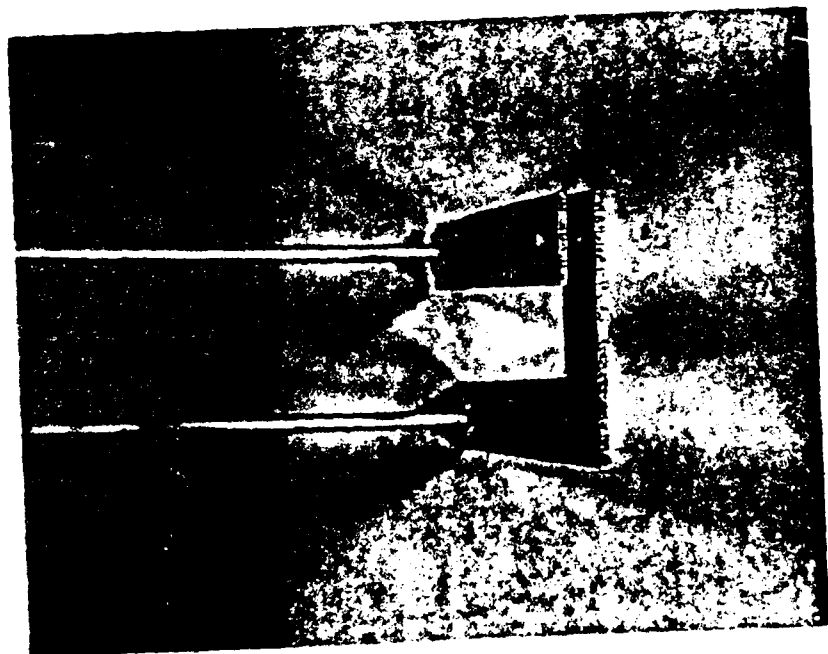
PZT-501A rods 200-600 μm in diameter and several cm long were poled using this technique. Piezoelectric d_{33} coefficients of the PZT rods were measured with a d_{33} meter.† Values of $400-450 \times 10^{-12}$ C/N were achieved consistently which compares favorably with the d_{33} values reported for PZT-501A ceramic disks (~ 380 pC/N).

The molten solder film proved to be rather delicate to work with, however, making large scale production difficult. To pole large numbers of PZT rods for composites, an alternate way of providing the contacts was developed.

In the second method, conductive carbon foam was attached to both the top and bottom copper plates using a conductive epoxy (Fig. 2b). The PZT rods were pulled through the foam attached to the copper plates. The oil bath was maintained at 80°C. The separation between the two electrodes and the pulling rate were the same as in the molten-solder method. An electric field of 16-18 kV/cm was required to pole the rods to saturation because the poling temperature was only 80°C.

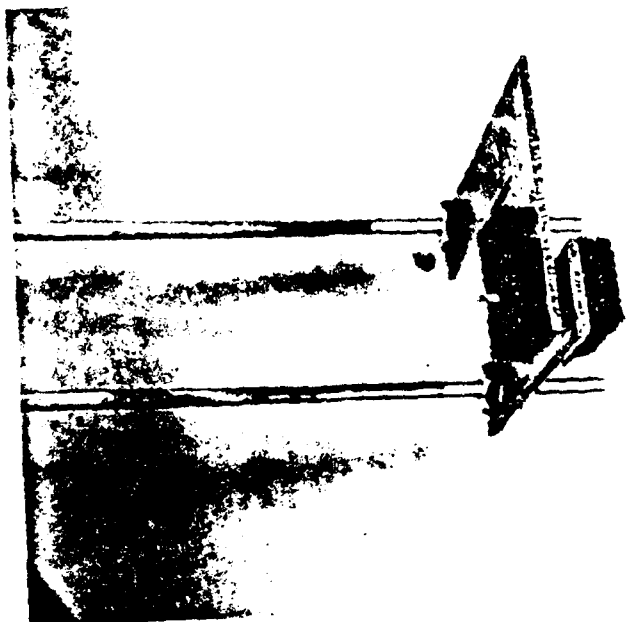
* Lead-Bismuth eutectic alloy from Indium Corporation.

† Channel products, Chesterland, Ohio, Model CPDT 3300.



2a

Fig. 2. Jig for the continuous poling technique



2b

APPENDIX 44

L.J. Bowen, T.R. Shrout, S. Venkataramani, J.V. Biggers. Inhomogeneous
Densification During Sintering of PZT. J. Amer. Ceram. Soc. (submitted).

Inhomogeneous Densification During Sintering of PZT

L.J. Bowen[†]*, T.R. Shrout*, S. Venkataramani* and J.V. Biggers*

Materials Research Laboratory
The Pennsylvania State University
University Park, Pennsylvania 16802

Abstract

Densification during sintering in lead zirconate titanate (PZT) shows anomalies not predicted by conventional sintering theory, e.g. a linear dependence of the fired density on the green density and an influence of the external powder compact geometry on sintered density. Microstructural observations of density variations within partially sintered PZT powder compacts indicate that densification during sintering takes place inhomogeneously. Chemical heterogeneity arising from incomplete calcining of the oxide precursors PbO, TiO₂, and ZrO₂ appears to be one factor which adversely affects sintering uniformity.

Introduction

The elimination of porosity in electrical ceramics is important for close control of their bulk dielectric properties (1), especially for the enhancement of dielectric breakdown strength since most piezoelectric ceramics must be subjected to high electric fields during poling. In lead zirconate titanate (PZT) complete pore removal during sintering is difficult, and densities between 95 and 97% of theoretical ($7,900 \text{ kgm}^{-3}$) are usually attained. Attempts to improve the density of ceramics have included hot pressing (2) and hot isostatic pressing (3,4). Kim and Hart (5) claim that niobia-doped PZT can be pressureless sintered in oxygen to theoretical density if powder processing is adequately controlled.

[†]Now at GTE Labs, Inc., 40 Sylvan Road, Waltham, MA 02154.

*Member, American Ceramic Society.

Recently, other workers (6) have observed anomalies in the sintering behavior of PZT that are not predicted by conventional sintering models. Specifically, cold-pressed PZT tape sinters to high density at temperatures 100°C lower than die pressed discs of comparable green density, and the fired density of the pressed tape is linearly dependent on its green density over a wide range of sintering temperatures. No difference that could explain these sintering effects could be established between the physical characteristics of the PZT powders used for tape casting or die pressing.

In the following, further sintering data are presented which highlight deviations in PZT from ideal sintering behavior. Shrinkage and microstructural data are not consistent with existing sintering models and a tentative explanation for the anomalous sintering behavior is offered in terms of inhomogeneous densification. Possible origins of inhomogeneous densification in practical powder compacts are reviewed and compared to observations in PZT sintering.

Background

The development of sintering theory since the pioneering work of Kuczynski (7) in 1949 can be approximately classified chronologically as the formulation of two-sphere models to describe densification processes atomistically, acknowledgment that two or more of these processes can be acting simultaneously (8), followed by the more recent recognition that these models are often only an approximation to the situation in actual powder compacts. Despite this realization, many researchers still apply theoretical sintering models to experimental shrinkage data without taking into account the practical limitations of the models. Direct application of the two-sphere models requires a three dimensional array of monosized spheres, preferably packed in a simple cubic array so that external shrinkage can readily be related to the interpenetration of the spheres.

Greskovich (9) defines a typical quantitative diffusional creep model by

the equation:

$$\frac{\Delta L}{L_0} = \left(\frac{cD\gamma\Omega t}{kTr^n} \right)^m \quad (1)$$

where $\Delta L/L_0$ is the linear fractional shrinkage, c , m , and n are numerical constants dependent on model geometry and sintering mechanism; t , r , γ , Ω , D and kT are time, initial sphere radius, surface energy, atomic volume, self-diffusion coefficient and thermal energy, respectively. c , D , r , m , and n are all functions of model geometry and change during sintering, especially at the closed porosity stage (approximately 0.90 relative density). The driving force for densification is assumed to arise only from surface energy reduction due to the uniform penetration of two spheres. No dependence of shrinkage rate on green density, internal powder compact geometry fluctuations or chemical heterogeneity can be interpreted from equation (1). Yet all of these factors are known (9-16) to influence densification during sintering in a practical powder compact, leading to inhomogeneous densification.

Inhomogeneous densification can result in the formation of pore concentrations or large closed pores for which the shrinkage driving force can be very low or even negative (15,17). The presence of non-diffusible gases within these pores further reduces their ability to shrink during sintering (18,19). Palmour and colleagues have shown in a series of publications (20) that controlling shrinkage rates during densification can prevent early pore closure in high density regions within a powder compact, leading to more uniform microstructures with finer grain size than conventional sintering. Non-Arrhenian kinetics are claimed (21) for alumina sintered under rate-controlled conditions, at variance with the predictions of the two-sphere models. Generally, the distribution of pore sizes in a compact reflects the particle size distribution (22) and is therefore influenced by powder morphology. Particle aggregation and agglomeration in the starting powders are well known (23) to influence sintering behavior by locally

enhancing densification. Exner and colleagues (12,13) have demonstrated that aggregation can be enhanced during sintering in two dimensional arrays of spherical particles and is strongly influenced by local interparticle coordination number variations.

Considering the interpenetration of two particles in contact under the sintering driving force, the center to center approach between the particles must influence and be influenced by the surrounding environment. Therefore it would appear that inhomogeneous densification arises from local variations in the powder compact geometry. In a more general case, non-uniform densification is better represented in terms of local variations in driving force, since this approach can take into account both physical and chemical effects. Possible causes of local fluctuations in driving force can include:

1. Wide particle size distribution, since the driving force for densification arises from a chemical potential gradient across the neck between particles, which is strongly influenced by neck geometry.

2. "Free" internal surface within the powder compact due to particle packing flaws introduced during processing. This internal surface can occur as large pores formed by bridging between agglomerates (14), lamellar flaws introduced during pressing or large pores remaining after removal of an inhomogeneously distributed, fugitive binder phase during sintering (24). The effects of a bimodal pore size distribution on densification have been described by Onoda and Messing (25) and Exner (12). Nonspherical large pores introduced during processing must tend to spheroidize on sintering with a possible increase in volume if the pore surface area remains approximately constant.

3. Heterogeneous particle coordination number distribution (N). To obtain an estimate of the magnitude of this effect on densification, consider regions

of hexagonal close packing ($N=12$) and simple cubic packing ($N=6$) of monosized spheres, each forming unit area of "free" surface in an array. From simple geometrical calculations, assuming equal compressive stress during sintering at each interparticle contact, the total stress normal to the area of surface is three times greater for the hexagonal close packed array compared to simple cubic packing. Note that in random packing of uniform spheres extreme coordination numbers ranging from 1 to as high as 13.4 (26) can be encountered. This effect is further exaggerated by particle size distribution but is an effect present in almost all ceramics.

4. Chemical inhomogeneity arising from incomplete calcining prior to sintering can enhance local sintering driving forces by a reactive sintering mechanism. Chaklader (27) has observed that enhanced densification occurs in powder systems which undergo chemical reaction or phase transformation during sintering or hot pressing. The enhanced sinterability may arise from the formation and reactivity of freshly formed, extremely fine crystallites or from enhancement of the surface energy driving force by chemical free energy (28). Paulus (29) notes that chemical reactivity and homogeneity have a pronounced effect on sintering in ferrites where shrinkage behavior is further complicated by the formation of Kirkendall porosity during multicomponent sintering.

In summary, it is to be expected that shrinkage can occur away from regions of low coordination number and free internal surface, just as shrinkage occurs away from the external surface of a powder compact. As a corollary, the median pore size in an inhomogeneously densifying powder compact need not decrease until all the fine porosity has been eliminated and particle rearrangement has ceased, or unless a large external driving force, e.g. pressure, is available. Increases in the median pore size during sintering have been demonstrated in several systems (10-13,30-32).

Experimental

Microstructural details of the PZT powders and the tape casting and post casting pressing procedures have been published elsewhere (6). The PZT powder

used for most of the experimental work was a commercial "morphotropic phase boundary" composition designated 401 by the manufacturer*, in which the principal dopant was Fe^{3+} . This was ball milled with a surface active organic binder** for 48 hours to disperse the powder and prevent flocculation during tape casting. Particle size and surface area measurements on as-received PZT powder and powder used for tape casting have shown that the additional ball milling step has little influence on morphology (6). Isothermal sintering was achieved by placing the specimens in a preheated furnace and air quenching after the specified time. The sintering atmosphere was maintained lead oxide rich using lead zirconate powder. PZT tapes used for obtaining green density/fired density data were heated to the sintering temperature at $200^{\circ}\text{C}/\text{hour}$ and were therefore not fired under ideal isothermal conditions, especially for the higher temperatures.

Polished sections for microstructural work were difficult to prepare because of the tendency in PZT for grain pullouts during polishing. This problem was avoided by vacuum impregnating the specimens with liquid epoxy resin, grinding with fixed abrasives to $<40\ \mu\text{m}$ silicon carbide, and polishing for twelve hours with $1\ \mu\text{m}$ diamond on a hard paper lap.

Results and Discussion

Figure 1 is a plot of green relative density versus fired relative density for cold pressed and sintered PZT cast tape. Sintering data have been obtained at four firing temperatures over the range 1220 to 1325°C with soak times at temperature of 1.5 hours. Except for the 1325°C data, for which the slope of the graph is comparable to the scatter in the data, a linear relationship is

*Ultrasonic Powders, Inc., South Plainfield, NJ 07080.

**Cladan Binder B62, Cladan Inc., San Diego, CA.

evident. The straight lines have been fitted to the data by least squares.

Apart from the linearity of the fired density/green density plot, a further interesting feature of Figure 1 is the tendency of the data to converge at a fired density maximum of 96% theoretical density. This convergence is not in itself particularly remarkable since the densification rate for a sintering process normally decreases with increasing relative density. However, the maximum attainable relative density of 0.96 suggests that this represents a sintered density limit for PZT, regardless of the green density and sintering temperature. Other sintering work is in agreement with this observation (4,5).

The existence of a sintered density limit implies that a change in sintering geometry, e.g. discontinuous grain growth, is preventing the attainment of theoretical density by hindering the elimination of closed porosity. In Figure 2 the grain size distribution for the as-received PZT powder is compared with the distribution for tape cast material sintered at the extreme conditions of 1325°C for 1.5 hours. Grain size distributions were obtained by quantitative SEM (33) on freeze-dried, dispersed powder specimens and random, polished, etched sections of sintered specimens. The average grain size has increased from 4 to 6 μm on sintering while maintaining a narrow size distribution. Observations of pores trapped within grains by grain growth are rare; thus, discontinuous grain growth is probably not responsible for the observed endpoint density in PZT.

An alternative possibility is the formation of gross porosity due to inhomogeneous densification during sintering, for which several possible mechanisms have already been described. Fired density/green density linearity has been observed elsewhere (24,34,35) and attributed to inhomogeneous densification.

Onoda (24) has attempted to explain this linearity by postulating the existence of a bimodal particle and pore size distribution within the powder compact. During sintering the compact shrinks by elimination of the fine porosity giving rise to the relationship:

$$\rho_{sc} = \frac{\rho_{sf}}{\rho_{gf}} \rho_{gc} \quad (2)$$

where ρ is density and subscripts f, c, g, and s denote fines, compact, green density, and sintered density, respectively. Unfortunately, Onoda's derivation requires that the large pores shrink as the fine ones are eliminated because the compact shrinks as a whole. This is the case for a purely parallel connected pore model, but in practice some series connectivity exists. Therefore, the median coarse pore diameter can remain constant, or even increase, and yet allow a net shrinkage of the body. This phenomenon has been observed in several sintering systems (10-13, 30-32). However, the present authors would agree with Onoda in that green density/fired density linearity is probably associated with non-ideal pore elimination during sintering.

Previous data (6) indicated that tape cast and pressed PZT sinters more readily under a given set of conditions than identical cold pressed powder. To demonstrate that powder processing was not responsible for these observed differences in sintering rate, identical PZT specimens were prepared by either cold pressing powder or tape casting and fired for various times at 1150°C. At this temperature densification was sufficiently slow that isothermal conditions were readily attained. Density/time curves, shown in Figure 3, were very similar for both types of specimen up to 83% of theoretical density, the maximum attained in 4 hours at this temperature, indicating a similar shrinkage mechanism, little influenced by differences in processing conditions.

Since tape casting inherently produces specimens thinner than cold pressed discs, the possibility exists that external specimen geometry may influence the sintering behavior. Accordingly, discs of from one to ten layers of PZT cast tape were warm-pressed together at 50°C using sufficient pressure to provide a firm bond and obtain the same green density, and fired at 1200°C for times ranging from 1/2 to 3 hours. The results, shown in Figure 4, indicate a consistent trend towards reduced shrinkage (measured radially for greater accuracy) for the thicker tape specimens. Conventional sintering models do not predict this dependence of shrinkage on specimen geometry, and again the implication is that sintering in this system is non-ideal. In an inhomogeneously densifying system it is possible that early pore closure can attenuate shrinkage owing to the presence of non-diffusible gases within pores (18,19). When the specimens are very thin, as in the case of cast tapes, most of the porosity may remain open to the surface, even at a late stage in densification. Wiens and Cahn (22) and Kingery et al. (36) report that the behavior of voids during sintering can be influenced by their proximity to the exterior surface. Thus, if non-uniform densification occurs in a sintering system, the external specimen geometry might be expected to exert some influence on shrinkage behavior.

Microstructural evidence for the occurrence of inhomogeneous densification during sintering of PZT cast tape is presented in Figures 5 and 6, which are scanning electron micrographs of polished sections through single layers of tape fired at 1200°C to 0.80-0.90 relative density. (In all cases the porous regions are filled with epoxy resin introduced before polishing by vacuum impregnation, and accurately represent the pore structure in the original microstructure.) Figure 5 demonstrates that a porosity gradient exists across the fired tape thickness. This is probably associated with segregation of PZT and liquid organic binder during drying. In the higher density regions inhomogeneous

densification is shown in relation to the average grain size, which is around 4 μm and has a narrow distribution, consistent with the data in Figure 2. The high density regions within these specimens are on the order of ten grain diameters across and are usually associated with a large single pore or group of pores which are somewhat larger than the average grain size.

Although the experimental data suggest that sintering takes place inhomogeneously in PZT, the actual origin of inhomogeneous densification is not clear. Particle size distribution effects should not be a major factor influencing densification homogeneity, since the size distribution is narrow in both the starting powder and the sintered product and little discontinuous grain growth has occurred. Processing flaws are also unlikely to be of importance. The tape casting fabrication approach minimizes agglomeration because the powder is well dispersed in a surface-active, liquid organic binder which also acts as a lubricant during subsequent pressing operations.

The possibility remains that chemical inhomogeneity can affect sintering in PZT. To investigate its effects, reagent grade component oxides PbO , ZrO_2 , and TiO_2 were mixed as described elsewhere (37) in a composition equivalent to $\text{PbZr}_{0.6}\text{Ti}_{0.4}\text{O}_3$. Part of the mixture was calcined twice (with an intermediate comminution step) to complete reaction (determined by x-ray analysis), ball-milled, cold-pressed without binder and sintered at various temperatures in the range 1000–1300°C. The specimens were heated at 200°C per hour and removed from the furnace immediately upon reaching the desired temperature. The remainder of the oxide mixture was processed under identical conditions but without the calcining operation. After impregnation with epoxy resin the specimens were carefully polished so as to preserve their pore structure.

Figure 7 shows the microstructures of the uncalcined specimens sintered at 1000, 1100, and 1300°C. At 1000°C inhomogeneous densification is very prominent.

Although the average grain size is around 1 μm diameter, large aggregates up to 10 μm across have formed (Figure 7a) and are themselves showing signs of inhomogeneous sintering (Figure 7b). Large pores of 20-30 μm across are present between the aggregates. By this sintering temperature chemical reaction to form PZT should already be completed, according to x-ray analysis (37). At temperatures between 1000 and 1100°C grain growth occurs within the aggregates forming crystallites approximately 5 μm in diameter. Higher sintering temperatures up to 1300°C lead to little further inhomogeneous sintering or grain growth. In the control specimens calcined prior to sintering, no aggregation or inhomogeneous sintering is observable even after one hour at 1300°C (Figure 8).

The implication is that chemical inhomogeneity arising from incomplete calcining can influence sintering in PZT and may cause inhomogeneous sintering. This does not preclude the possibility that other deleterious factors, e.g. powder agglomeration, may be present. Further work on the interaction between chemical heterogeneity and sintering in PZT is necessary to resolve this question. Elimination of inhomogeneous densification in PZT may permit lower sintering temperatures and avoid end point densities.

Conclusions

Microstructural data indicate that densification during sintering in pressed, tape cast PZT occurs inhomogeneously. Characteristics of inhomogeneous sintering include a linear dependence of fired density on green density and some influence from external specimen geometry on shrinkage during sintering. Neither of these effects is predicted by existing sintering theory.

Inhomogeneous sintering can be a consequence of local geometry variations or chemical heterogeneity in powder compacts, both of which can lead to driving force imbalance between sintering particles. In PZT, chemical inhomogeneity

arising from incomplete calcining has been shown to be one factor hindering uniform densification during sintering.

Acknowledgments

The authors wish to thank Professor G. Messing of the Ceramics Department, The Pennsylvania State University, for reviewing the manuscript. This work was supported by the Office of Naval Research, Contract No. N00014-78-C-0291.

References

1. K. Okazaki and K. Nagata, "Effects of Density and Grain Size on Elastic and Piezoelectric Properties of $\text{Pb}(\text{Zr-Ti})\text{O}_3$ Ceramics," *Mech. Behav. Mater., Proc. Int. Conf. Ist*, 4, 404-412 (1972).
2. V.L. Balkevich and C.M. Flidlider, "Hot Pressing of Piezoelectric Ceramics In the PZT System," *Ceram. Int.* 2(2), 81-87 (1976).
3. K.H. Hårdtl, "A Simplified Method fot the Hot Isostatic Pressing of Ceramics," *Philips Technical Review* 35, 65-72 (1975).
4. L.J. Bowen, W.A. Schulze and J.V. Biggers, "Hot-Isostatic Pressing of PZT Materials," *Powder Met. Int.* 12(2), 92-95 (1980).
5. Y.S. Kim and R.J. Hart, "High Density Piezoelectric Ceramic Compositions," *Materials Science Research*, Vol. II, Eds. H. Palmour, R.F. Davis and T.M. Hare, 323-333, Plenum Press, NY (1978).
6. J.V. Biggers, T.A. Shrout and W.A. Schulze, "Densification of PZT Cast Tape by Pressing," *Bull. Amer. Ceram. Soc.* 58(5), 516-521 (1979).
7. G.C. Kuczynski, "Self-Diffusion in Sintering of Metallic Particles," *Trans. AIME* 185(2), 169-178 (1949).
8. D. Lynn Johnson, "New Method of Obtaining Volume, Grain-Boundary and Surface Diffusion Coefficients from Sintering Data," *J. Appl. Phys.* 40, 192-200 (1969).
9. C. Greskovich, "Effect of Green Density on the Initial Sintering of Alumina," *Physics of Sintering* 4(1), 33-46 (1972).
10. K. Asaga, M. Daimon, R. Kondo and K. Hamano, "Changes in Pore Structure in the Sintering Processes of Al_2O_3 ," *Proc. Int. Symp. on Factors in Densification and Sintering of Oxide + Non Oxide Ceramics*, Eds. S. Somiya and S. Saito, 110-118, Gakujutsu Bunken Fukyu-Kai, Tokyo (1979).

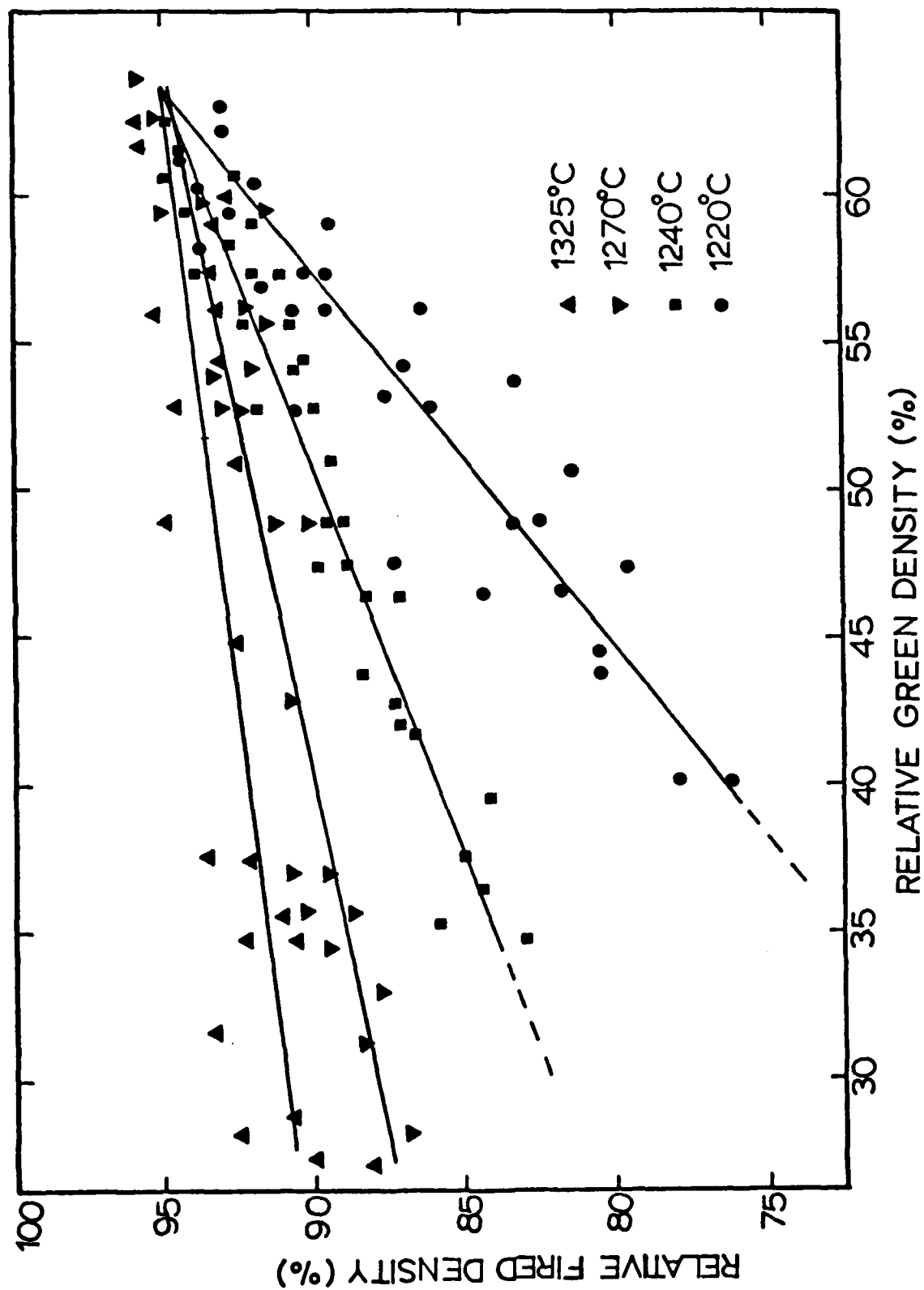
11. T. Shinohira, A. Makishima, K. Kotami, M. Wakakuwa, "Sintering of Mono-dispersed Amorphous Silica Particles," *ibid* 119-127.
12. H.E. Exner, G. Petzow, P. Wellner, "Problems in the Extension of Sintering Theories to Real Systems," *Mat. Sci. Res.* 6, 351-362, Ed. G.C. Kuczynski, Plenum Press, NY (1973).
13. H.E. Exner and G. Petzow, "Shrinkage and Rearrangement during Sintering of Glass Spheres," *Mat. Sci. Res.* 10, Ed. G.C. Kuczynski, 279-293, Plenum Press, NY (1975).
14. C. Greskovich, "Milling," *Treatise on Mat. Sci. and Technology* 9 (Ceramic Fabrication Processes), Ed. F.Y. Wang, 15-33, Academic Press, NY (1976).
15. W.D. Kingery and B. Francois, "The Sintering of Crystalline Oxides, I. Interactions between Grain Boundaries and Pores," *Sintering and Related Phenomena, Proc. 2nd Conf. Notre Dame*, Eds. G.C. Kuczynski, N.A. Hooton and C.F. Gibbon, Gordon And Breach, NY, 471-498 (1967).
16. T. Nomura and T. Yamaguchi, "Characterization of Ferrite Raw Material Powders," *Proc. Int. Symp. on Factors in Densification and Sintering of Oxide and Non Oxide Ceramics*, 1978, Japan, Eds. S. Somiya and S. Saito, 110-118, Gakujutsu Bunken Fukyu-Kai (1979).
17. J.A. Pask and C.E. Hoge, "Thermodynamic Aspects of Solid State Sintering," *Mat. Sci. Res.* 10, Ed. G.C. Kuczynski, 229-238, Plenum Press, NY (1975).
18. I. Amato, "On the Effect of Gas Trapped on Sintering," *Phys. of Sintering* Ed. M.M. Ristić, 5(2), 51-62 (1973).
19. R.A. Abbott, C.W. Tally, A.A. Solomon, "The Effects of Internal Gas Pressure on the Microstructure and Dimensional Stability of Ceramics," *Ceramic Microstructures 1976*, Eds. R.M. Fulrath and J.A. Pask, 320-329, West-view Press, Boulder, CO (1977).

20. For example: H. Palmour III, M.L. Huckabee and T.M. Hare, "Microstructural Development during Optimized Rate Controlled Sintering," *ibid.* 308-319.
21. H. Palmour III and M.L. Huckabee, "Studies in Densification Dynamics," *Mat. Sci. Res.* 6, Ed. G.C. Kuczynski, 275-282, Plenum Press, NY (1973).
22. J.J. Weins and J.W. Cahn, "The Effects of Size and Distribution of Second Phase Particles and Voids on Sintering," *Mat. Sci. Res.* 6, 151-163, Ed. G.C. Kuczynski, Plenum Press, NY (1973).
23. For example: J.S. Reed, T. Carbone, C. Scott, "Some Effects of Aggregates and Agglomerates in the Fabrication of Fine Grained Ceramics," *Mat. Sci. Res.* 11, Eds. H. Palmour III, R.F. Davis, T.M. Hare, 171-180, Plenum Press, NY (1978).
24. G.Y. Onoda, Jr., "Green Body Characteristics and their Relationship to Finished Microstructures," *Ceramic Microstructures 1976*, Eds. R.M. Fulrath and J.A. Pask, 184-195, Westview Press, Boulder, CO (1977).
25. (a) G.L. Messing and G.Y. Onoda, Jr., "Inhomogeneity-Packing Density Relations in Binary Powders," *J. Amer. Ceram. Soc.* 61(1-2), 1-5 (1978).
(b) G.L. Messing and G.Y. Onoda, Jr., "Inhomogeneity-Packing Density Relations in Binary Powders," *J. Amer. Ceram. Soc.* 61(7-8), 363-366 (1978).
26. D.W. Budworth, "A Random Packing Geometrical Model of Sintering," *Ceramic Microstructures 1976*, Eds. R.M. Fulrath and J.A. Pask, 255-260, Westview Press, Boulder, CO (1977).
27. A.C.D. Chaklader, "Transformation Plasticity in Ceramic Systems and Reactive Hot Pressing," *Proc. Brit. Ceram. Soc.* 15, 225-245 (1970).
28. L.J. Bowen, T.G. Carruthers and R.J. Brook, "Hot-Pressing of Si_3N_4 with Y_2O_3 and Li_2O as Additives," *J. Amer. Ceram. Soc.* 61(7-8), 335-339 (1978).

29. M. Paulus, "Relationship between Densification, Crystal Growth and Mechanisms of Formation in Ceramics," *Mat. Sci. Res.* 6, 225-245, Ed. G.C. Kuczynski, Plenum Press, NY (1973).
30. L.K. Barrett and C.S. Yust, "Progressive Shape Changes of the Void during Sintering," *Trans. AIME* 239, 1172-1180 (1967).
31. N.A.L. Mansour and J. White, "Causes of Residual Porosity in Sintered Uranium Dioxide," *Powder Met.* 12, 108-121 (1963).
32. C.A. Bruch, "Sintering Kinetics for the High Density Alumina Process," *Bull. Amer. Ceram. Soc.* 41(12), 799-806 (1962).
33. J. Lebedzik, R.G. Bouke, S. Troutman, G.G. Johnson, JR. and E.W. White, "New Methods for Quantitative Characterization of Multiphase Particulate Materials including Thickness Measurement," pp 121-28 in *Proc. 6th Ann. Scanning Electron Microscope Symp.* Ed. O. Johari and I. Corvin, IIT Research Institute, Chicago (1973).
34. C. Gorin and A. Metzger, "Characterization of MgO Powders Obtained by Thermolysis of $MgCl_2$," *Ceramic Microstructures 1976*, Eds. R.M. Fulrath and J.A. Pask, 184-195, Westview Press, Boulder, CO (1977).
35. P.E.D. Morgan, "Importance of Green Densification," paper presented at the Annual American Ceramic Society Meeting, Chicago, May, 1980.
36. W.D. Kingery, H.K. Bowen, D.R. Uhlmann, "Introduction to Ceramics," 2nd edn., 485, Wiley, NY (1976).
37. D.L. Hankey, "Calcination Reaction Mechanisms and Kinetics in $PbO-TiO_2-ZrO_2$ Powder Compacts," Ph.D. dissertation, The Pennsylvania State University, University Park, PA 16802 (1980).

Figure Captions

- Fig. 1 Influence of green density on fired density showing an approximately linear relationship over a wide range of firing temperatures.
- Fig. 2 Particle size distributions for (a) as-received and (b) sintered commercial PZT.
- Fig. 3 Densification curves for die pressed and pressed tape cast PZT isothermally sintered at 1150°C.
- Fig. 4 Influence of specimen thickness on shrinkage for pressed PZT tape isothermally sintered at 1200°C.
- Fig. 5 Scanning electron micrographs of partially sintered PZT cast tape showing inhomogeneous sintering and the porosity gradient arising from PZT/binder segregation during drying.
- Fig. 6 Inhomogeneous densification in PZT cast tape sintered at 1200°C.
- Fig. 7 Microstructures of sintered, uncalcined $\text{PbZr}_{0.6}\text{Ti}_{0.4}\text{O}_3$ specimens heated at 200°C per hour to (a) 1000°C, (b) 1000°C, (c) 1100°C, (d) 1300°C.
- Fig. 8 (a) Uncalcined; (b) calcined PZT sintered by heating at 200°C per hour to 1100°C (magnification 400X).



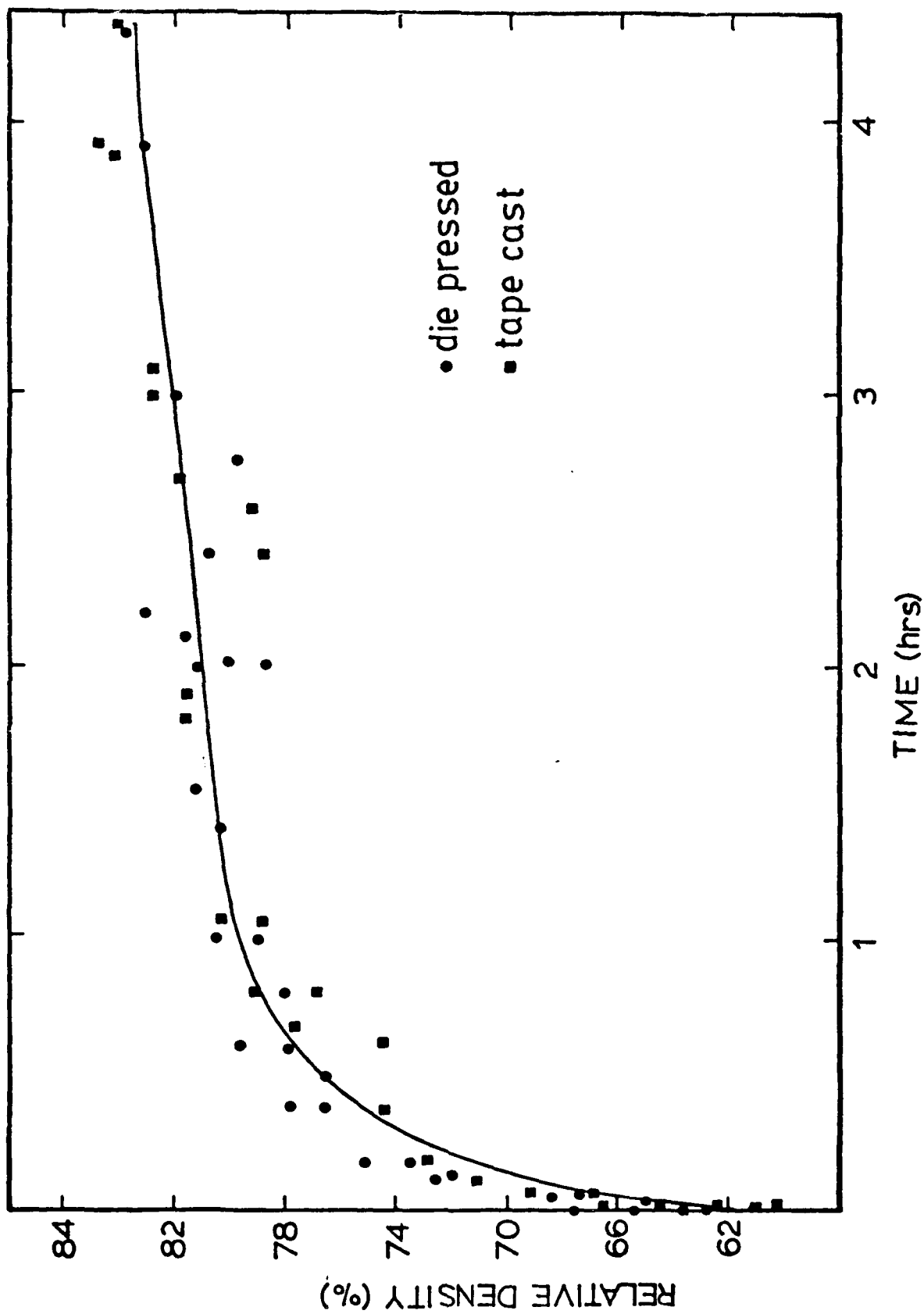
Average diameter distribution						
Class	0	1	2	3	4	5
limit	0	1	2	3	4	5
(μm)	-----	0-----	0-----	0-----	0-----	0-----
						Class(%)
0.25	[0.00
0.40	[0.00
0.63	[0.21
1.00	[**					3.10
1.60	[*****					12.27
2.50	[*****					27.36
4.00	[*****					35.05
6.30	[*****					19.53
10.00	[*					2.33
16.00	[0.07
25.00	[0.07

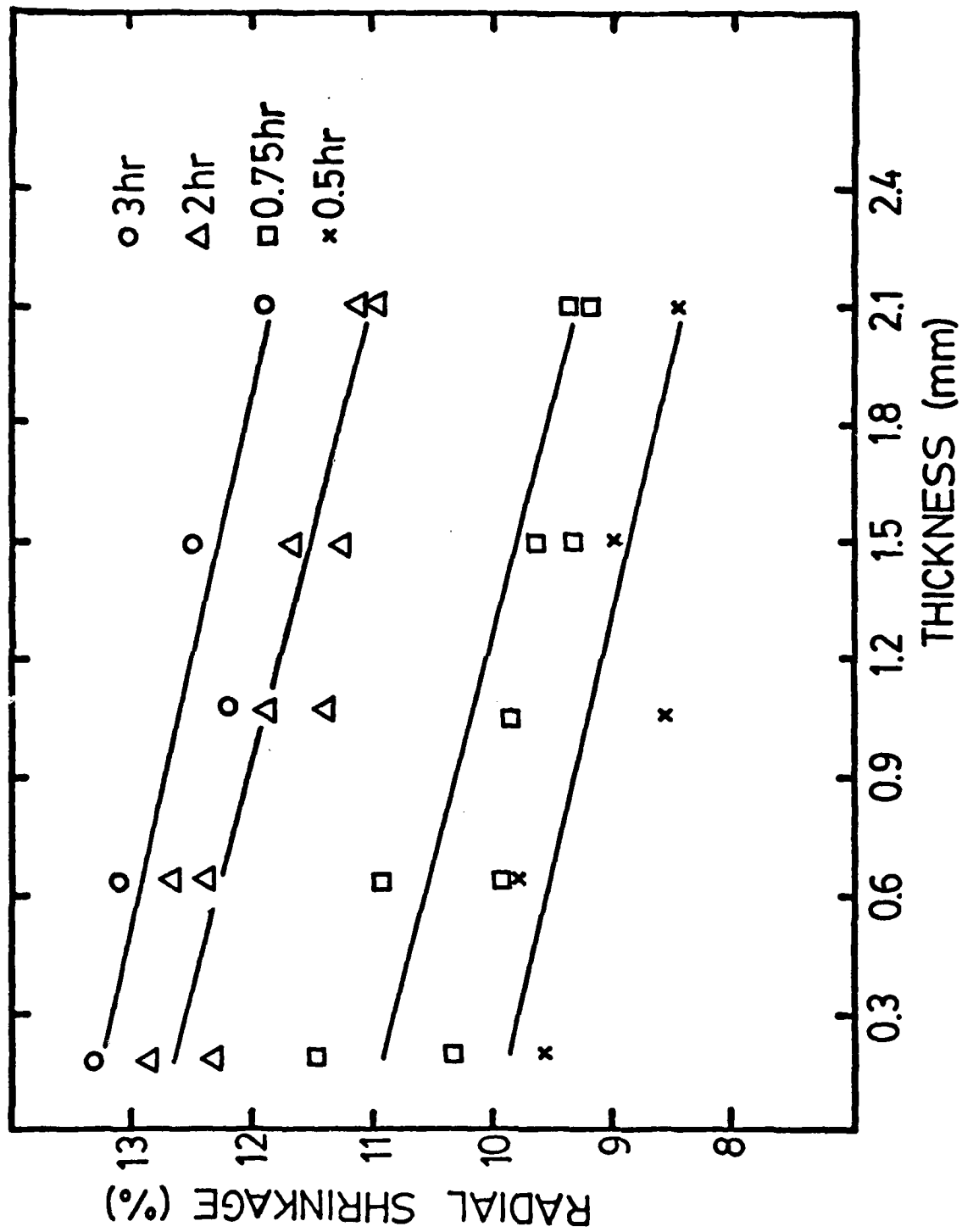
(a)

Average diameter distribution						
Class	0	1	2	3	4	5
limit	0	1	2	3	4	5
(μm)	-----	0-----	0-----	0-----	0-----	0-----
						Class (%)
0.25	[0.00
0.40	[0.10
0.63	[0.21
1.00	[0.31
1.60	[*					2.30
2.50	[****					8.47
4.00	[*****					29.18
6.30	[*****					49.69
10.00	[*****					9.62
16.00	[0.10
25.00	[0.00

(b)

Figure 2





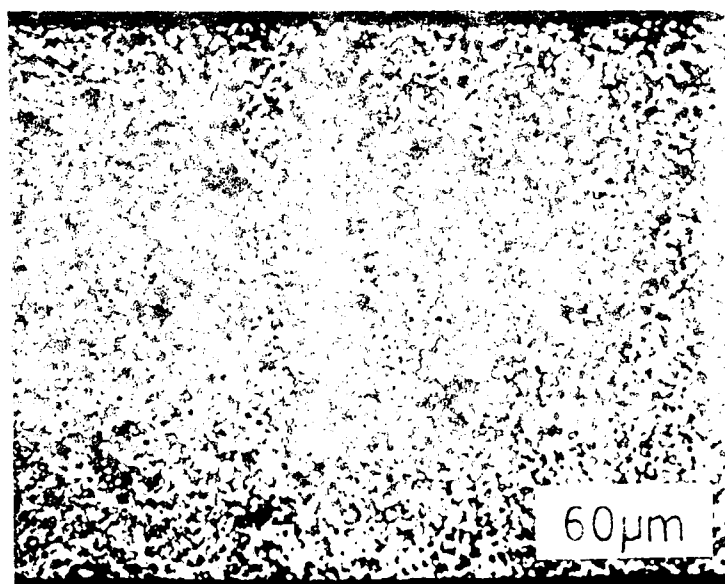
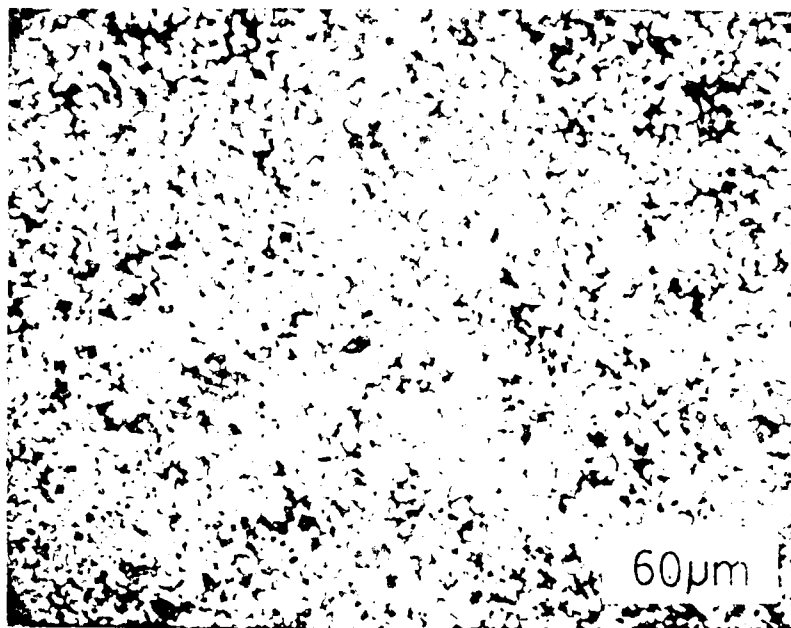


Figure 5

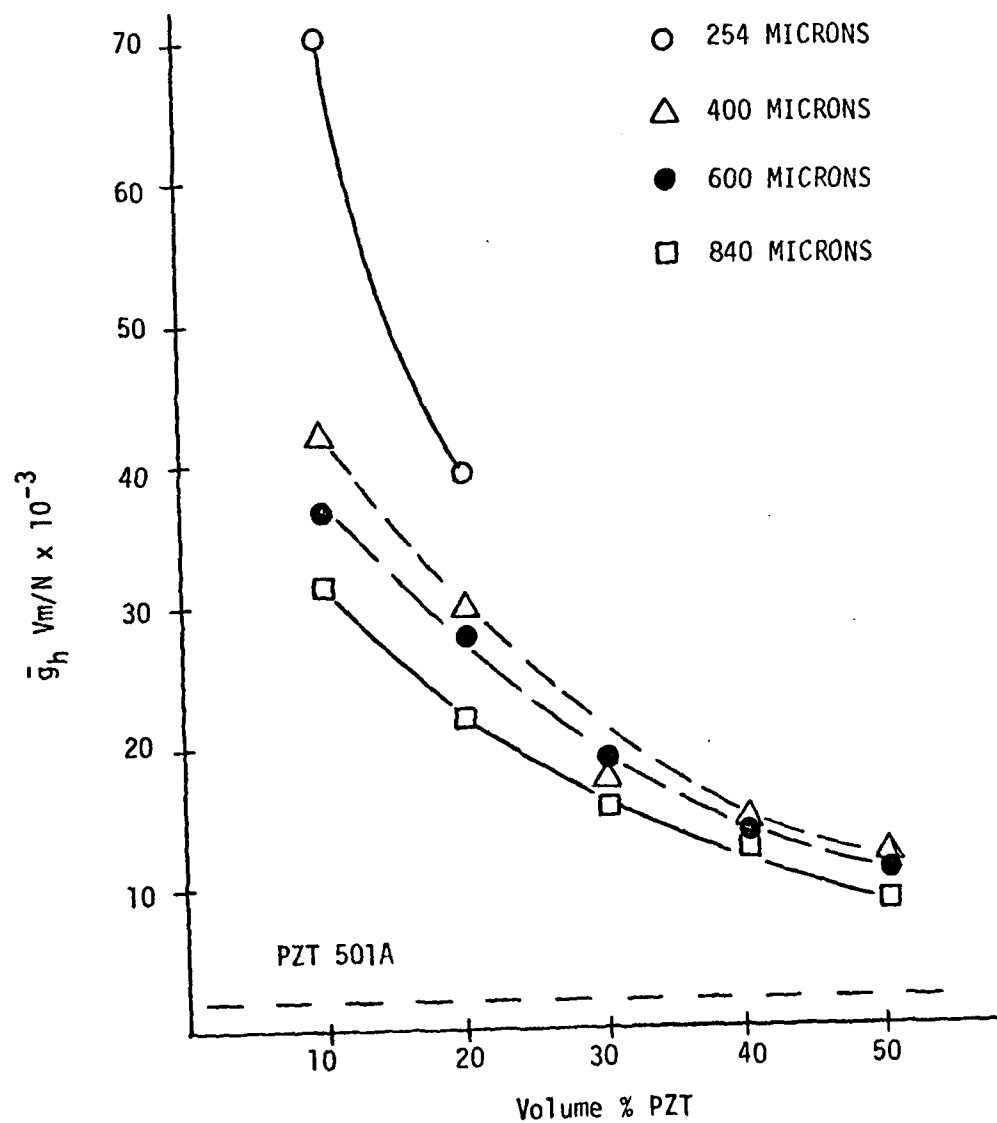


Figure 8. \bar{g}_h as a function of volume % PZT.

APPENDIX 45

H.P. Savakus, K.A. Klicker, R.E. Newnham. PZT:Epoxy Piezoelectric Transducers: A Simplified Fabrication Procedure. Phys. Stat. Sol. (submitted).

PZT-EPOXY PIEZOELECTRIC TRANSDUCERS: A SIMPLIFIED
FABRICATION PROCEDURE

H.P. Savakus, K.A. Klicker and R.E. Newnham

Materials Research Laboratory
The Pennsylvania State University
University Park, Pennsylvania 16802

ABSTRACT

Composite piezoelectric transducers have been constructed by partially dicing PZT ceramics and back-filling with epoxy. Piezoelectric properties are compared with solid PZT and with 3-1 composites made by extrusion.

Introduction

For the past twenty-five years piezoelectric transducers have been made from poled PZT ceramics with compositions near $\text{PbZr}_{0.5}\text{Ti}_{0.5}\text{O}_3$. In many ways PZT is superior to other piezoelectrics, but the hydrostatic piezoelectric coefficient ($d_h = d_{33} + 2d_{31}$) is too small and the dielectric constant is too large. These problems can be largely eliminated by combining PZT and polymers in composites with 3-1 connectivity (1-4). The composites consist of thin PZT fibers embedded in a polymer matrix with the fibers oriented perpendicular to the transducer electrodes and extending from electrode to electrode. The fibers are made by extrusion of PZT slip followed by drying, firing, and hot isostatic pressing. After aligning the sintered rods in the metal rack, they are placed in a cup, covered with epoxy or polyurethane, and then poled. The process is rather delicate and time consuming because of the necessity of handling large numbers of fragile ceramic fibers. In this paper we describe an alternative processing method in which solid PZT disks are diced with a diamond saw and then back-filled with epoxy.

Composite Fabrication

Ceramic disks of PZT 501A* were prepared by conventional powder processing methods (5) and sintered to a density of 7.9 g/cm^3 . Using Crystal Bond epoxy, the ceramic disk was cemented to an aluminum block and mounted on a high-speed saw. Diamond-impregnated saw blades ranging in width from 0.3 to 1.1 mm were used in slicing the ceramic. Parallel cuts about 1 cm deep were made in ceramic, leaving a 2 mm solid base for support. The PZT was then removed from aluminum block and cleaned ultrasonically to remove residual particles from the cut

*Ultrasonic Powders, Inc., South Plainfield, N.J.

surfaces. After drying, the parallel cuts were filled with Spurr's* low viscosity embedding medium. This is a clear hard epoxy which is easily machined after curing.

After grinding off the excess epoxy, the composite was remounted on the diamond saw and a second series of parallel cuts were made at 90° to the first set, again leaving a solid 2 mm base. The cuts were cleaned and filled with epoxy and then sliced into two 4 mm disks, discarding the solid base. Figure 1 shows the 3-1 PZT/epoxy transducer prior to electroding. A number of such composites were prepared with different pillar diameters and separations.

After trimming and polishing, the composites were electroded with air-dry silver paint and then poled for five minutes in a 75°C oil bath with an electric field of 22 kV/cm. A Berlincourt d_{33} -meter was used to assess the degree of poling.

Piezoelectric Properties

The piezoelectric and dielectric properties of the composites were measured using the same testing procedures used previously on piezoelectric composites. To determine the dielectric constant, capacitance measurements were made at 1 KHz using a Hewlett Packard 4270A capacitance bridge. The experimental values followed the mixing rule for parallel connection

$$\bar{K} = 1_v 1_K + 2_v 2_K$$

where 1_K and 2_K are the dielectric constants of PZT and polymer, and 1_v and 2_v are the respective volume fractions. Numerically, \bar{K} ranged from about 200 for a sample containing 15 volume percent PZT to 1000 for one containing 70% PZT.

The longitudinal piezoelectric coefficient \bar{d}_{33} was measured with the Berlincourt d_{33} -meter. An average was taken from ten different readings since

*Ernest F. Fullum Inc, Schenectady, N.Y.

the values depend on how the force head is positioned with respect to the PZT pillars. As shown in Figure 2, the \bar{d}_{33} coefficients of the composites are comparable to that of solid PZT 501 (about 400×10^{12} C/N) because of the stress transfer from polymer to PZT. For a given volume fraction PZT, \bar{d}_{33} is largest for the thinnest ceramic pillars where stress transfer is best.

The hydrostatic piezoelectric coefficient \bar{d}_h was measured under near-static conditions. Oil pressure within the test cell was changed at a rate of 50 psi/sec ($35 \text{ kN/m}^2 - \text{sec}$), and the resulting piezoelectric charge collected with a Keithley 616 Digital Electrometer. Hydrostatic piezoelectric coefficients for the 3-1 composites (Figure 3) compare favorably with solid PZT (about 50×10^{-12} C/N) and with composites of similar dimensions prepared from extruded PZT rods (5). Composites with the thinnest pillars have the largest d_h coefficients. Unfortunately it is difficult to produce extremely thin pillars by conventional sawing methods.

The piezoelectric voltage coefficients of the composites are extremely good because of their relatively low dielectric constants. Diced and back-filled composites are also of interest as longitudinal acoustic wave generators. By decoupling the PZT elements with polymer, it is possible to suppress the radial vibration mode without appreciably affecting the longitudinal mode.

Acknowledgments

This work was sponsored by the Office of Naval Research under Contract No. N00014-78-C-0291. We wish to thank Prof. L. E. Cross, Dr. W. A. Schulze and Dr. J. V. Biggers for several useful discussions.

References

- ¹ R. E. Newnham, D. P. Skinner, and L. E. Cross. Connectivity and Piezoelectric-Pyroelectric Composites. *Mat. Res. Bull.* 13 525-536 (1978).
- ² R. E. Newnham, D. P. Skinner, K. A. Klicker, A. S. Bhalla, B. Hardiman and T. R. Gururaja. Ferroelectric Ceramic-Plastic Composites for Piezoelectric and Pyroelectric Applications. *Ferroelectrics* 27 49-55 (1980).
- ³ K. A. Klicker. Piezoelectric Composites with 3-1 Connectivity for Transducer Applications. Ph.D. Thesis, Pennsylvania State University, 1980.
- ⁴ K. A. Klicker, J. V. Biggers and R. E. Newnham. Composites of PZT and Epoxy for Hydrostatic Transducer Applications. *J. Amer. Ceram. Soc.* (in press).
- ⁵ K. A. Klicker. Control of PbO Partial Pressure During the Sintering of PZT Ceramics. M. S. Thesis, Pennsylvania State University, 1979.

Figure Captions

Fig. 1. PZT-epoxy composites with 3-1 connectivity prepared by dicing solid ceramics and backfilling with polymer. The width of the composite transducers is approximately 1 cm, and the thickness about 4 mm.

Fig. 2. Piezoelectric coefficients d_{33} and d_h plotted as function of volume fraction PZT for five different pillar widths.

Fig. 3. Hydrostatic piezoelectric coefficient d_h plotted as a function of volume fraction PZT for five different pillar widths. The smallest pillars (745 μm) were made by extrusion rather than dicing.

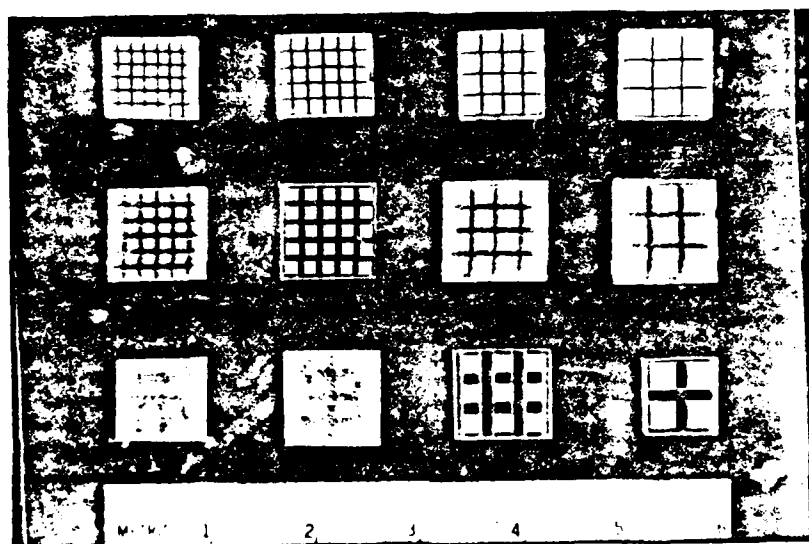


Figure 1

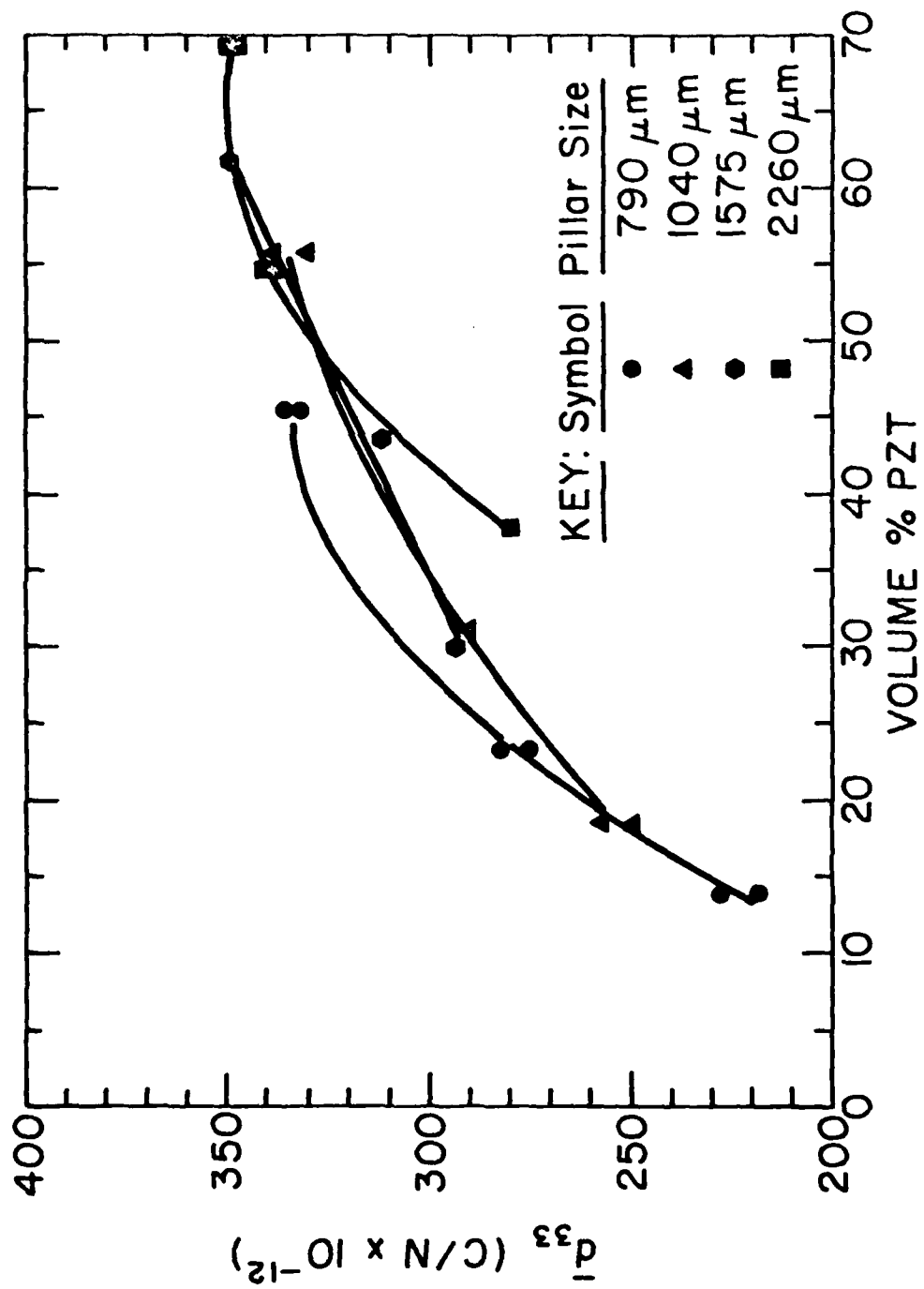


Figure 2

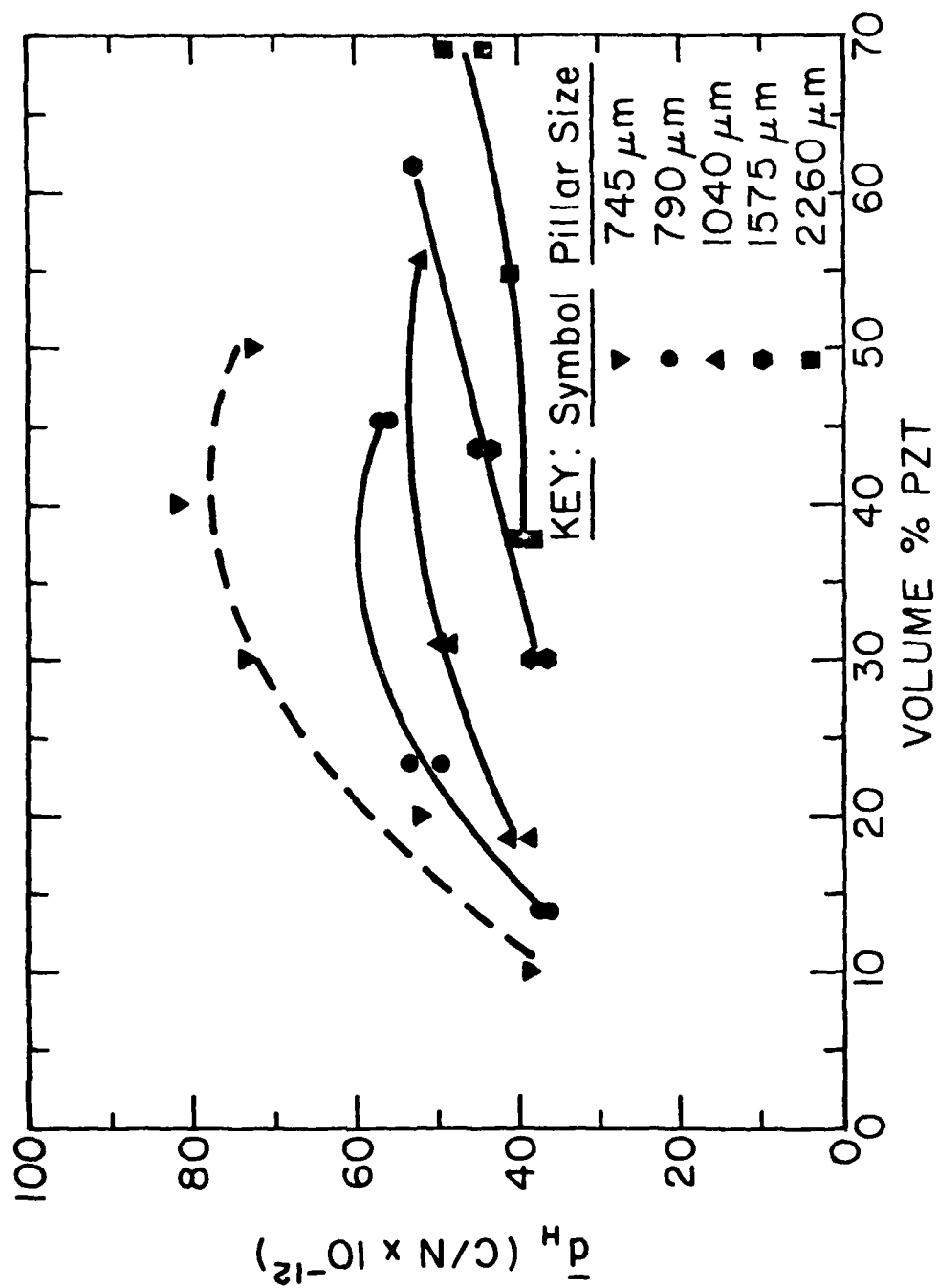


Figure 3

APPENDIX 46

K.A. Klicker, J.V. Biggers, R.E. Newnham. Composites of PZT and Epoxy
for Hydrostatic Transducer Applications. J. Amer. Ceram. Soc. (submitted).

COMPOSITES OF PZT AND EPOXY FOR HYDROSTATIC TRANSDUCER APPLICATIONS

K.A. Klicker, J.V. Biggers, R.E. Newnham

Materials Research Laboratory
The Pennsylvania State University
University Park, Pennsylvania 16802

ABSTRACT

Composites with 3-1 connectivity for transducer applications have been made by embedding extruded PZT rods in an epoxy matrix. The effect of rod diameter, volume fraction of PZT, and composite thickness on the hydrostatic properties of the composites was determined. Due to decoupling of the \bar{d}_{33} and \bar{d}_{31} coefficients in a composite with 3-1 connectivity, the \bar{d}_h may be enhanced even in composites of low volume fractions of PZT. Composites with low volume fractions of PZT also have a low dielectric permittivity. The combination of high \bar{d}_h values and low $\bar{\epsilon}_r$ value results in a greatly enhanced \bar{g}_h . Composites with 10 volume % PZT have been made with values of \bar{d}_h and \bar{g}_h which are respectively two times ($>80 \times 10^{-12}$ C/N) and twenty-five times ($>70 \times 10^{-3} \frac{V-m}{N}$) the solid PZT values.

COMPOSITES OF PZT AND EPOXY FOR HYDROSTATIC TRANSDUCER APPLICATIONS

K.A. Klicker, J.V. Biggers, R.E. Newnham

Materials Research Laboratory
The Pennsylvania State University
University Park, Pennsylvania 16802

Introduction

Lead Zirconate titanate solid solutions (PZT) are currently used in many transducer applications. They have, however, limited utility in transducers used under hydrostatic conditions because their low hydrostatic piezoelectric coefficients (d_h) and voltage coefficient (g_h). The low coefficients are a result of the coupling of the d_{33} and d_{31} coefficients. Specifically

$$d_h = d_{33} + 2d_{31}$$

In PZT's \bar{d}_{33} is about twice the magnitude and of opposite sign of d_{31} resulting in a very low value of d_h . The voltage coefficient (g_h) is related to d_h by

$$g_h = \frac{d_h}{\epsilon_{33}}$$

and is also low because of the low d_h and high permittivity (ϵ_{33}) of PZT.

It is possible that a properly designed composite material of PZT and a polymer phase might decouple d_{33} and d_{31} and lower the permittivity resulting in improved values of d_h and g_h . In this paper we will describe a technique of producing composites of extruded and fired PZT rods embedded in a compliant polymer matrix.

Composites have been made using PZT particles bound in a matrix of silicon rubber.¹ These composites were not only flexible, but also exhibited good sensitivity to low frequency sound. Density of the composites varied from 6.2 - 3.9 g/cc depending on percent silicon rubber in the composite and the density of the PZT particles. Composites of polymer and PZT have also been prepared by use of the "replamine technique".² Using coral as a template, composites in which both the PZT and the polymer are three dimensionally connected have been made. These transducers also have low density and good sensitivity.

The properties of a composite are influenced by the connectivity³ of the components of the composite. Connectivity is defined as the number of dimensions in which each phase is continuous. In the composite made by the replicate technique, for example, both the polymer and the PZT are continuous in all three dimensions and therefore the composite has 3-3 connectivity. A composite with 3-1 connectivity is shown in Figure 1. A theory for piezoelectric response has been developed⁴ for composites of 3-1 connectivity in which rods of PZT (phase 1) are embedded in a three dimensionally continuous polymer. The PZT rods are poled along their length and therefore the 3 direction of the composite, as shown by Figure 1, is along the direction in which the rods are aligned. The theoretical equations for a composite with 3-1 connectivity are as follows:

$$\bar{d}_{33} = \frac{{}^1V {}^1d_{33} {}^2S_{33} + {}^2V {}^2d_{33} {}^1S_{33}}{{}^1V {}^2S_{33} + {}^2V {}^1S_{33}} \quad (1)$$

$$\bar{d}_{31} = {}^1V {}^1d_{31} + {}^2V {}^2d_{31} \quad (2)$$

$$\bar{\epsilon}_{33} = {}^1V {}^1\epsilon_{33} + {}^2V {}^2\epsilon_{33} \quad (3)$$

where 1V , ${}^1d_{33}$, ${}^1d_{31}$, ${}^1\epsilon_{33}$ and ${}^1S_{33}$ are respectively the volume fraction, piezoelectric coefficients, elastic compliance and permittivity of phase one. The average coefficients for the composite are \bar{d}_{33} , \bar{d}_{31} and $\bar{\epsilon}_{33}$.

If the following conditions are assumed:

$${}^1V = {}^2V = 0.5$$

$${}^1d_{33} \gg {}^2d_{33}$$

$${}^1S_{33} \ll {}^2S_{33}$$

$${}^1\epsilon_{33} \gg {}^2\epsilon_{33}$$

the theoretical results are:

$$\bar{d}_{33} \approx {}^1d_{33} \quad (4)$$

$$\bar{d}_{31} \approx 0.5 {}^1d_{31} \quad (5)$$

$$\bar{\epsilon}_{33} \approx 0.5 {}^1\epsilon_{33} \quad (6)$$

The piezoelectric response to hydrostatic pressure (d_h) is defined as

$$d_h = d_{33} + 2d_{31} \quad (7)$$

The \bar{d}_h coefficient for solid PZT is small because $d_{33} \approx -2d_{31}$. If however a reduction in \bar{d}_{31} is accompanied by either a smaller reduction in \bar{d}_{33} or no reduction at all, then the value of d_h will be greater than that for solid PZT. Substitution of equations (4) and (5) into equation (7) will have the result of

$$\bar{d}_h = \bar{d}_{33} + 2\bar{d}_{31} = {}^1d_{33} + 2(0.5 {}^1d_{31}) \quad (8)$$

This theoretical value of \bar{d}_h for the composite of 50 vol % PZT is greater than the d_h of solid PZT. Re-examination of equations (1), (2) and (7) shows that as the volume fraction of PZT is reduced from the value of 0.5 used above, \bar{d}_{33} is constant but \bar{d}_{31} will be further reduced and \bar{d}_h will become even greater.

Another piezoelectric coefficient of interest is the hydrostatic voltage coefficient (g_h) which is defined as

$$\bar{g}_h = \frac{\bar{d}_h}{\bar{\epsilon}_{33}} \quad (9)$$

If the permittivity of phase one is much larger than the permittivity of phase two, equation (3) may be written as

$$\bar{\epsilon}_{33} \approx {}^1\epsilon_{33} {}^1V \quad (10)$$

If the conditions assumed above are used equation (10) becomes

$$\bar{\epsilon}_{33} \approx 0.5({}^1\epsilon_{33}) \quad (11)$$

The theoretical value of \bar{d}_h for a composite of 50 vol % has been shown to be greater than d_h of solid PZT (Equation 8) and $\bar{\epsilon}_{33}$ is one half of ϵ_{33} (Equation 11). From equation (9), \bar{g}_h will be much larger than g_h for solid PZT.

According to the theory, \bar{d}_{33} is not a function of volume % PZT because the rods bear all the load in the 3 direction. If this is not strictly true, d_{33} will also be a function of volume % PZT. Figure 2 illustrates the theoretical behavior of \bar{d}_h as a function of volume % PZT. Also shown is the behavior in a general case where \bar{d}_{33} is a function of volume % PZT but to a lesser degree than d_{31} , and the case where both d_{33} and d_{31} are strictly a function of volume % PZT.

2. Procedure

Ninety weight percent PZT 501A* was mixed by hand in a plastic jar with a solution of 20 weight percent PVA and 80 weight percent water. After mixing the jar was tightly capped and put onto a ball mill rack and allowed to spin for 16 hours. The spinning helped to homogenize the batch. Further homogenization is done by extruding the batch through a 1 mm die several times. PZT rods are then extruded onto a moving glass plate. The rods are dried on the glass plates for ten hours at 120°C. Dried rods are cut into 3 cm lengths, laid on a platinum sheet and the binder is burned out at 550°C for 1/2 hour. Sintering takes place in a sealed alumina crucible at 1300°C for one half hour. A PbO vapor source of composition 97 mole % 501A and 3 mole % PbO is included in the crucible.⁵

In the larger extruded rods, porosity exists probably due to the multiple extrusions carried out to homogenize the batch before the final extrusion. To reduce this porosity, all sintered rods were re-fired in a hot isostatic press (HIP)⁶ for one hour at 1300°C under a pressure of two hundred atmospheres of argon. Use of the HIP increases the average density

*Ultrasonics Powders, Inc., South Plainfield, NJ (PZT 501A).

of the rods from 7.45 to 7.7 - 7.8 gm/cc. Finished rods of diameters 840, 600, 400, and 254 μm were made.

A fixture consisting of two brass discs in which an array of holes is drilled is used to align the rods. Several were made for each of the rod sizes so that composites of 50, 40, 30, 20 and 10 volume % PZT could be made. The polymer used in this work was an epoxy.* Once a rack had been filled with rods, the rack was placed in a plastic tube with two closed ends. The tube had a slot cut into one side so that the epoxy could be poured around the rods. To assure that complete investment of the rods by the epoxy would not be hindered by air bubbles trapped between the rods, an apparatus was used which placed the plastic tube and its contents under vacuum while the epoxy was poured into the plastic tube. The epoxy was cured at 70°C for sixteen hours. Parts of thickness 1, 2, 3 and 4 mm were cut from the slug with a diamond saw. Some of these parts are seen in Figure 3. The excess epoxy around the composite was cut off so that only the composite volume remained.

Air dry silver electrodes were applied and the parts were poled in a 75°C oil bath with a field of 22 kv/cm for five minutes. Permittivity was measured at 1 KHZ. \bar{d}_{33} was measured with a d_{33} meter** using the two rounded rams. The hydrostatic piezoelectric coefficient (d_h) was measured by changing pressure in an oil chamber at the rate of 500 psi/sec and collecting the charge with an electrometer in the feedback intergration mode which maintains nearly zero sample potential. Because of the possible influence of irreversible polarization and current effects, the values recorded are from many runs utilizing both increasing and decreasing pressure.

* Ernest F. Fullum, Inc., Schenectady, NY No. 5135

** Channel Products, Chesterland, Ohio, Model CPDT 3300.

3. Results and Discussion

According to the theory already described, \bar{d}_{33} would not be a function of the volume fraction of PZT in the composite. This assumes an ideal situation in which the polymer phase is much more compliant than the PZT and that all the stress on the polymer phase is transferred to the PZT. That is, as the volume % PZT decreases, the pressure on the PZT increases proportionally so that the charge per unit area of the composite is constant. It is not necessary that \bar{d}_{33} of the composite be constant with respect to volume % PZT for d_h to be enhanced in the composite. If, as the volume % PZT is decreased \bar{d}_{31} decreases more rapidly than \bar{d}_{33} , then \bar{d}_h will be enhanced. Likewise, if $\bar{\epsilon}_{33}$ decreases more rapidly than \bar{d}_h , as the volume % PZT is decreased, then \bar{g}_h will be enhanced.

3.1 \bar{d}_{33} of the composites

In this work the following factors were varied: volume % PZT, diameter of PZT rods and sample thickness. The combination of the factors of rod diameter and volume % PZT brings in a fourth factor: the separation between the rods. Obviously, if the stress on the polymer is to be transferred to the PZT rods, the distance from a particular unit of load bearing polymer to the nearest rod is important. In the composites with the smaller rods at a fixed volume % PZT, the rods are much closer together. For this reason a point measurement of d_{33} on the composites should become more constant with respect to position on the composite surface at constant volume % PZT. Thus, if the rod diameter is decreased, the composite becomes more piezoelectrically homogeneous.

Figure 4.A shows that for volume fractions down to 40 volume % PZT the values of \bar{d}_{33} are comparable to the value of d_{33} for solid PZT 501A of 400. Below 40 vol% PZT, the \bar{d}_{33} values of all the composites decrease

but it is significant to note that the \bar{d}_{33} of all the composites at 10 vol % are still greater than 220×10^{-12} c/N. If \bar{d}_{33} had decreased strictly as a function of volume % PZT because the PZT rods were not bearing any part of the load on the polymer, the calculated \bar{d}_{33} would be 10% of solid PZT or $\sim 40 \times 10^{-12}$ c/N. The method in which these \bar{d}_{33} values were measured has somewhat affected the way \bar{d}_{33} has varied as a function of volume fraction and rod diameter. The d_{33} meter measures the charge developed on a sample due to a stress from two rounded rams which stress the sample from the top and bottom. Whether or not the piezoelectric response of composites becomes more homogenous is hard to determine due to the size of these rounded rams with regard to the separation of the rods. If the rams are in physical contact with the rods then the force on the rods is transmitted directly by the ram and not to the rods via the polymer phase. It would not be justified to expect a similar \bar{d}_{33} value when the composite is stressed hydrostatically by a fluid and a sizeable percentage of force (equal to the volume % of polymer) will fall directly on the polymer. For this reason the \bar{d}_{33} values for lower volume fractions of PZT where the rams of the d_{33} meter may stress the polymer alone are probably closer to the true \bar{d}_{33} of these composites. Each of the data points on Figure 4.A are an average of at least fifteen values measured at random over the electroded surface of the composite. The standard deviation of these values are shown in Figure 4.B. The piezoelectric response has indeed become more homogeneous as the rod diameters and the distance between piezoelectric elements are decreased. All the values shown in Figure 4 were measured on composites with a 4 mm thickness. The \bar{d}_{33} of composites of 3, 2 and 1 mm thickness were also measured. A thickness effect was found. For all composites the \bar{d}_{33} decreased as the composite thickness increased. This thickness effect was also a function of rod diameter and volume % PZT. \bar{d}_{33} decreased as the separation between the rods increased.

3.2 \bar{d}_h of the composites

In Figure 5, \bar{d}_h is plotted as a function of composite thickness, rod diameter and volume % PZT. As was found with the measurements on the d_{33} meter, \bar{d}_h is a function of composite thickness. This effect is least noticeable for the 400 micron rods. It should be noted that for most of the composites measured, regardless of composite thickness, rod diameter or volume % PZT, the \bar{d}_h of the composite is greater than that for solid PZT 501A. PZT 501A pellets were cold pressed, sintered and fired in the HIP along with the rods used in the composites. An average \bar{d}_h value of $30 - 32 \text{ c/N} \times 10^{-12}$ was measured on these pellets. Composites of the same PZT but with much lower volume fractions of PZT have higher values of \bar{d}_h . The theory (Figure 2) predicted that \bar{d}_{33} would be constant and that \bar{d}_{31} would decrease linearly with the volume fraction PZT. If this were true, \bar{d}_h would increase linearly as the volume fraction of PZT was decreased. However, point probing indicates that \bar{d}_{33} for all the composites decreased as the volume fraction of PZT decreased below 40 vol % PZT. If \bar{d}_{31} decreased as the theory predicts and \bar{d}_{33} decreased at a slower rate then \bar{d}_h could either decrease, increase or be constant as the volume % PZT decreased. As shown by Figure 6, all of these occur. All the data in Figure 6 were measured on composites with a thickness of 4 mm. The composites of rods of 840 micron diameter show a decrease of \bar{d}_h as volume % PZT decreases. From a volume fraction of 0.4 to a volume fraction of 0.1 its volume % PZT has decreased 75% but the \bar{d}_h has decreased only 50%. For the composites of 600 micron rods \bar{d}_h is nearly constant from 50 vol % down to 20 vol %. The composites of 400 micron rods actually show an increase of \bar{d}_h going from 50 vol % down to 20 vol %. Although \bar{d}_h at 10 vol % is the lowest for all the rod sizes these composites shown the largest increases in \bar{d}_h with each reduction in rod

diameter. It appears that if the rod diameter could be further reduced, the 10 vol % composite would eventually have the greatest \bar{d}_h . That the composite with the lowest volume fraction of PZT would have the highest \bar{d}_h is predicted by the theory but the magnitude of the experimental \bar{d}_h value are less than one third theoretical value. It must be remembered that the theory called for a phase 2 which was much more compliant than phase 1. As the epoxy is a stiff polymer, better agreement with the theory may be found when an elastomer is used as the phase two.

3.3 Effects on $\bar{\epsilon}_{33}$ and \bar{g}_h

The calculation of $\bar{\epsilon}_{33}$ uses the equation for two capacitors in parallel and the value of $\bar{\epsilon}_{33}$ varies linearly with the volume fractions of the two phases present. Since ϵ of the PZT is ~ 1600 and that of the epoxy is ~ 7 , the value of $\bar{\epsilon}_{33}$ may be approximated as $1600 \times \text{volume \% PZT}$. The experimental values of ϵ_{33} agree with calculated levels, as shown by Figure 7. Since \bar{g}_h equals \bar{d}_h divided by $\bar{\epsilon}_{33}$, constant or increasing values of \bar{d}_h with decreasing volume % PZT result in large increases in the value of \bar{g}_h . Figure 8 is a plot of the \bar{g}_h for the data shown in Figures 6 and 7. The dotted line in Figure 8 represents the \bar{g}_h of solid PZT 501A. The 10 vol % composite of 254 micron rods has a \bar{g}_h of better than twenty-five times that of the solid PZT. Although use of a more compliant matter would not appreciably affect $\bar{\epsilon}_{33}$, its enhancement of \bar{d}_h would naturally cause a corresponding increase in \bar{g}_h .

Conclusions

1. A technique has been developed for fabrication of composites of extruded PZT rods and an epoxy matrix. These composites have 3-1 connectivity.

2. The values of \bar{d}_h and \bar{g}_h of such a composite have been found to be a function of the diameter of the PZT rods, the spacing between the PZT rods and the thickness of the composite.

3. \bar{d}_h and \bar{g}_h are probably also a function of the difference in the mechanical compliances of the PZT and the epoxy.

4. Composites with high values of \bar{d}_h and \bar{g}_h have bulk densities of less than 1.8 gm/cc.

5. Composites have been developed with a \bar{d}_h three times that of PZT 501A and a \bar{g}_h at least twenty-five times greater.

Acknowledgment

This work was supported by the Office of Naval Research under Contracts N00014-76-C-0515 and N00014-78-C-0291

References

1. W. Harrison. Proceedings of the Workshop on Sonar Transducer Materials.
Edited by P. Smith and R. Pohanka, Naval Research Laboratory,
Washington, DC, 1976, pp. 257-268.
2. D.P. Skinner. Diphasic Piezoelectric Transducers. Ph.D. Thesis, The
Pennsylvania State University, 1980.
3. R.E. Newnham, D.P. Skinner and L.E. Cross. Connectivity and Piezoelectric-
Pyroelectric Composites. Mat. Res. Bull. 13, 525 (1978).
4. D.P. Skinner, R.E. Newnham and L.E. Cross. Flexible Composite Transducers.
Mat. Res. Bull. 13, 599 (1978).
5. K.A. Klicker. Control of PbO Partial Pressure During the Sintering of
PZT Ceramics. M.S. Thesis, The Pennsylvania State University, 1979.
6. L.J. Bowen, W.A. Schulze and J.V. Biggers. Hot Isostatic Pressing of
Lamellar Heterogeneous Piezoelectric Devices. Electronics Division
and IEEE Ferroelectrics Subcommittee, Fall Meeting, Dallas, TX,
Sept. 1978.

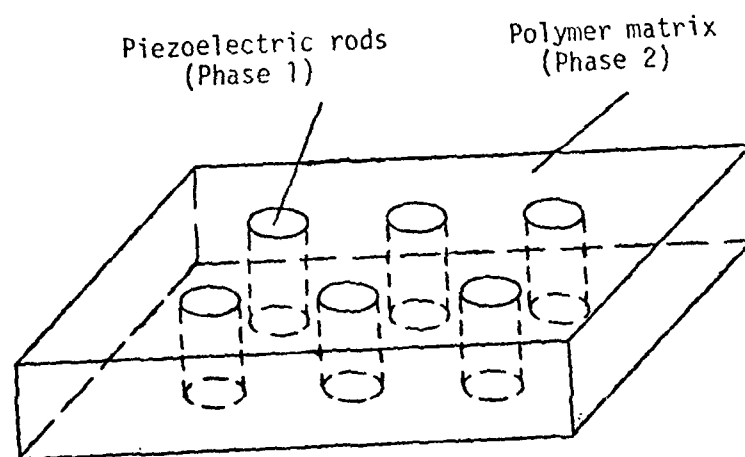


Figure 1. Composite with 3-1 connectivity.

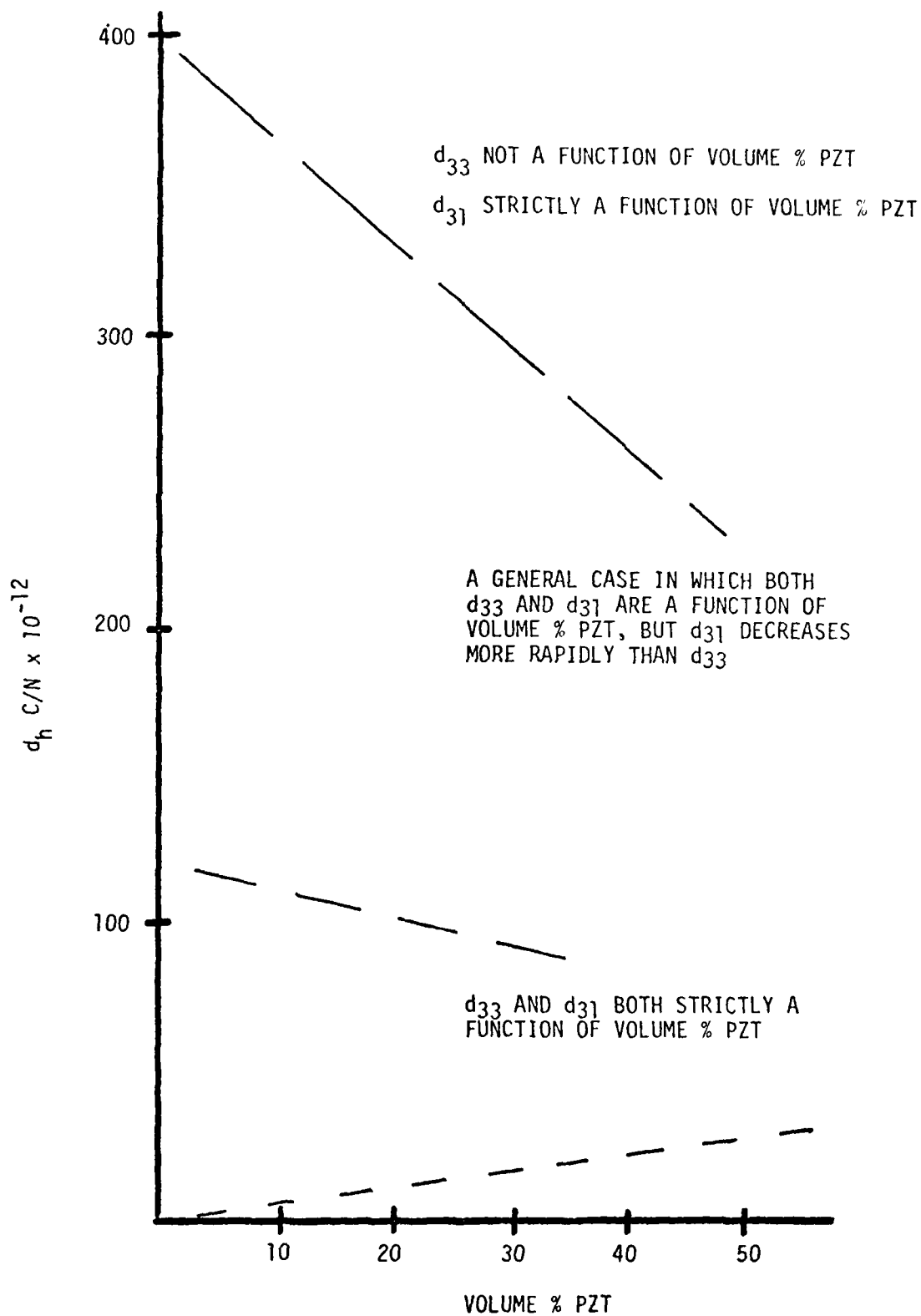


Figure 2. d_h AS A FUNCTION OF VOLUME % PZT, ASSUMING SEVERAL RELATIONS OF d_{33} AND d_{31} TO VOLUME % PZT.

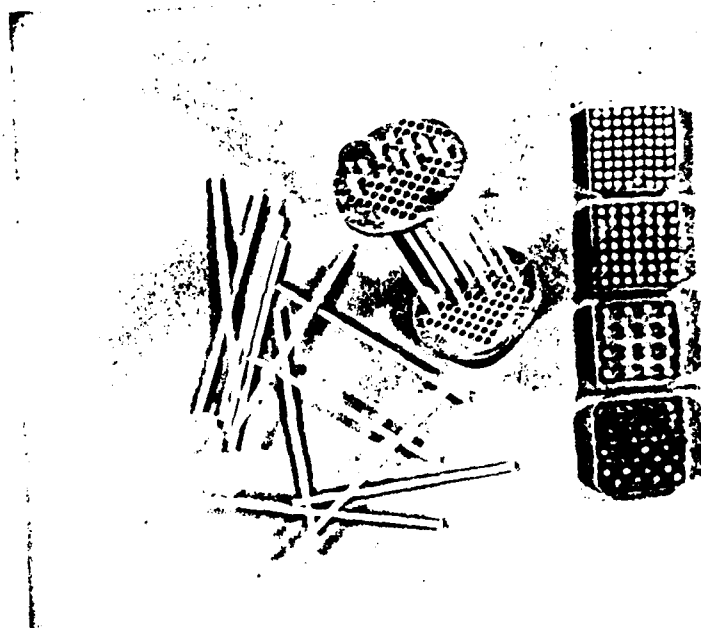


FIGURE 3. FIXTURE USED TO ALIGN RODS FOR INVESTMENT IN EPOXY AND COMPOSITES WHICH HAVE BEEN SLICED FROM THE CURED SLUG.

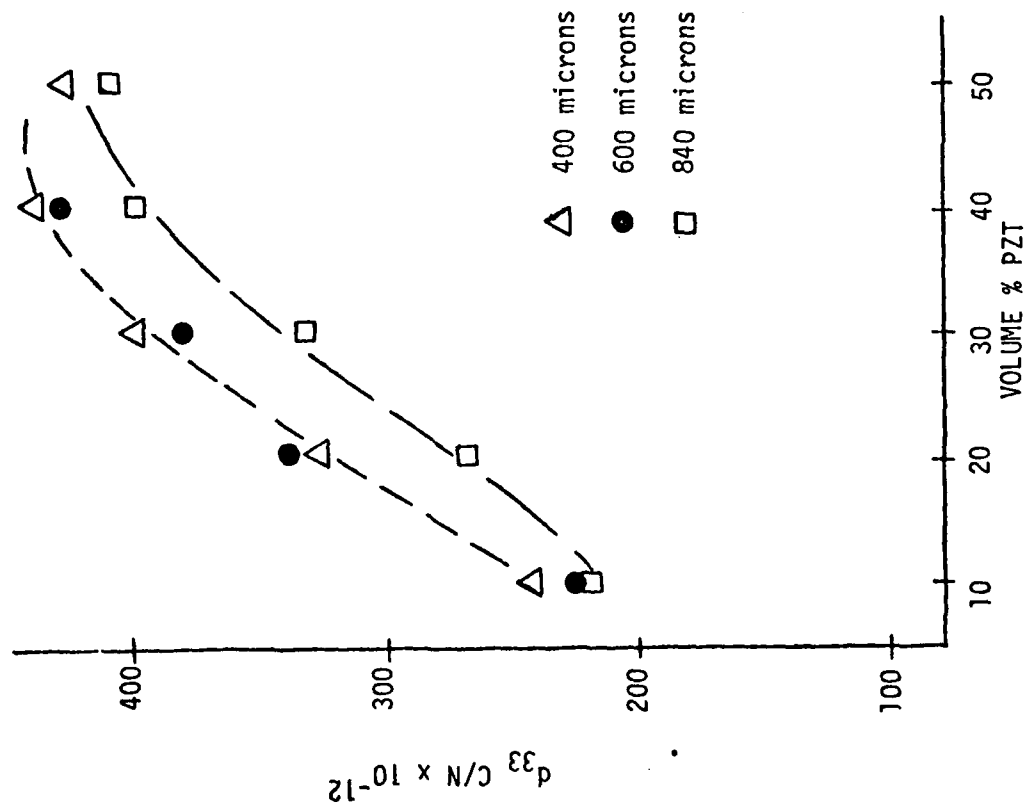


Figure 4a. d_{33} vs volume % PZT.

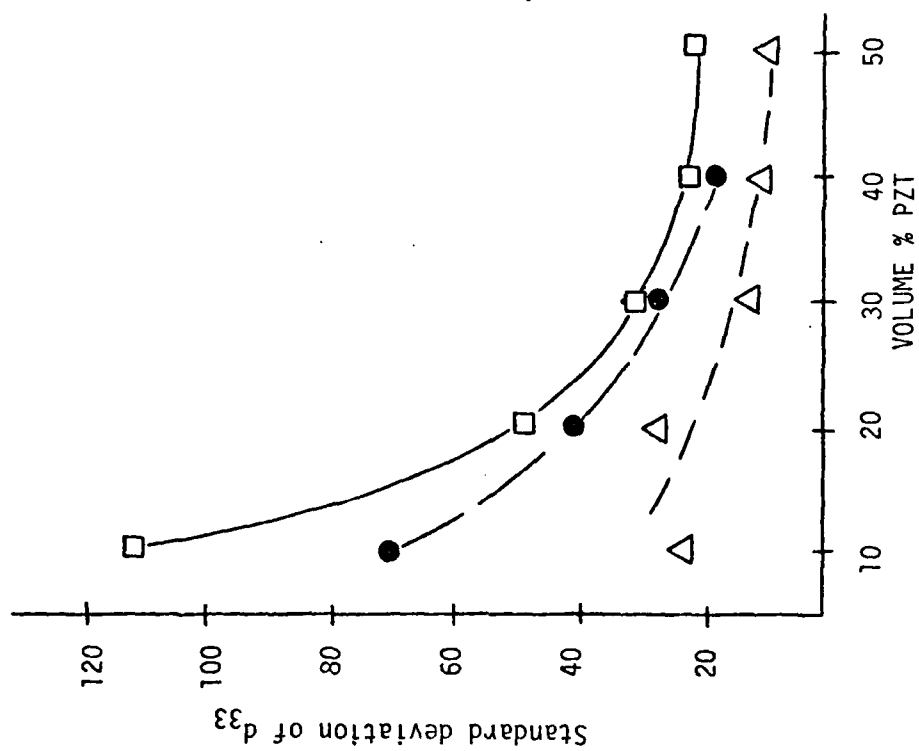


Figure 4b. Standard deviation of d_{33} values as a function of volume % PZT.

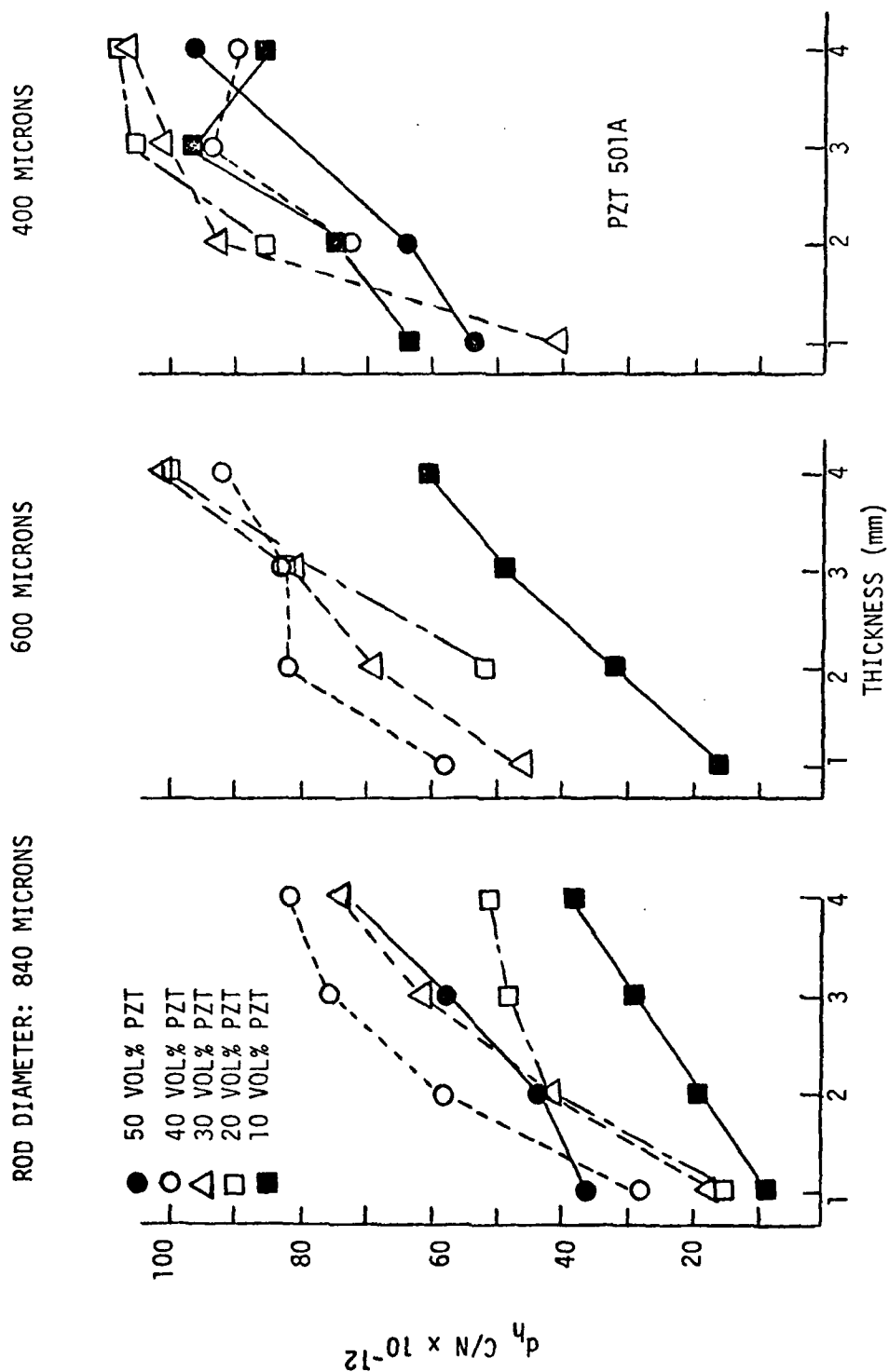


Figure 5. d_h as a function of volume % PZT, rod diameter and composite thickness.

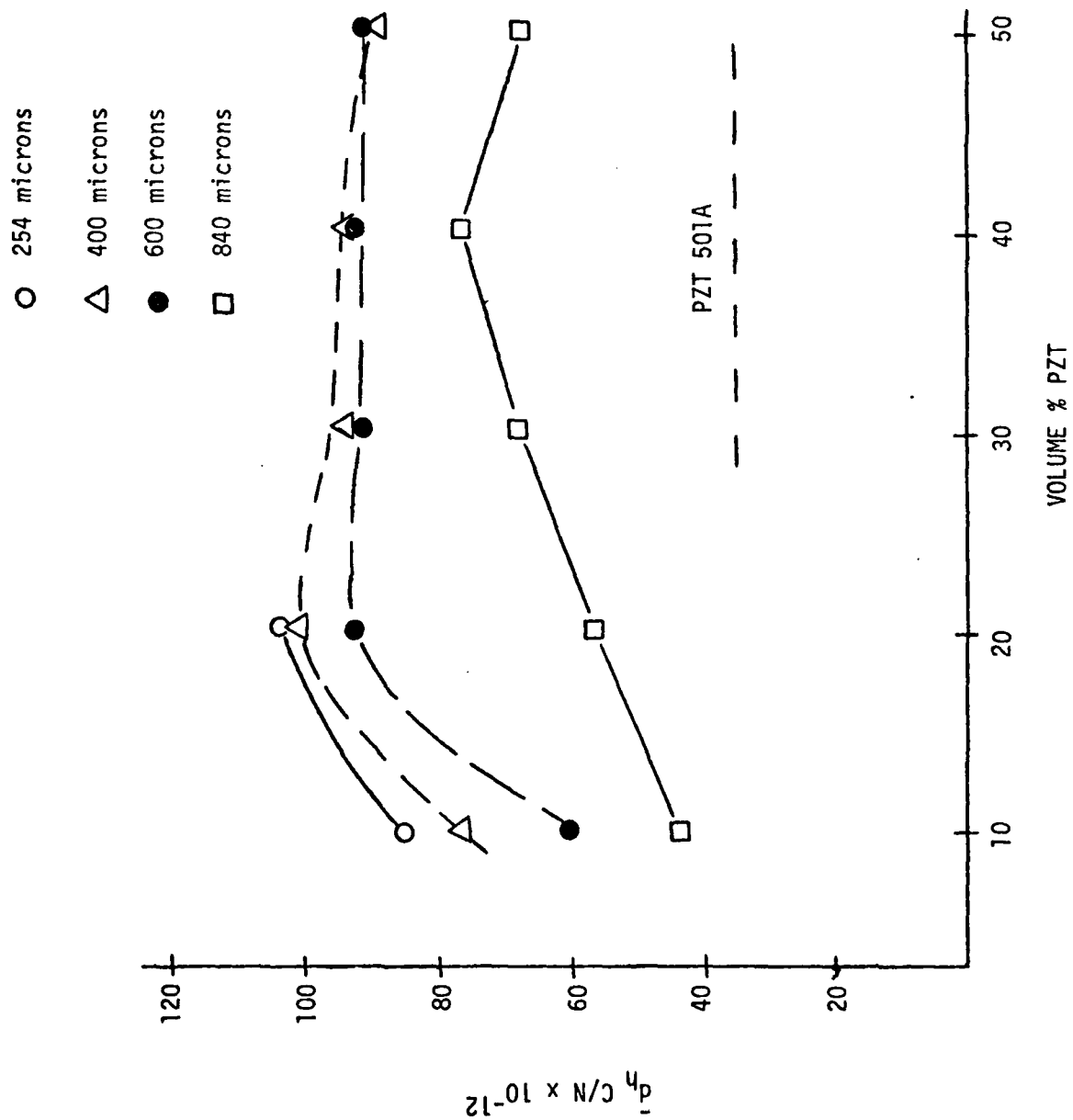


Figure 6. \bar{d}_h as a function of volume % PZT and rod diameter (sample thickness 4 mm).

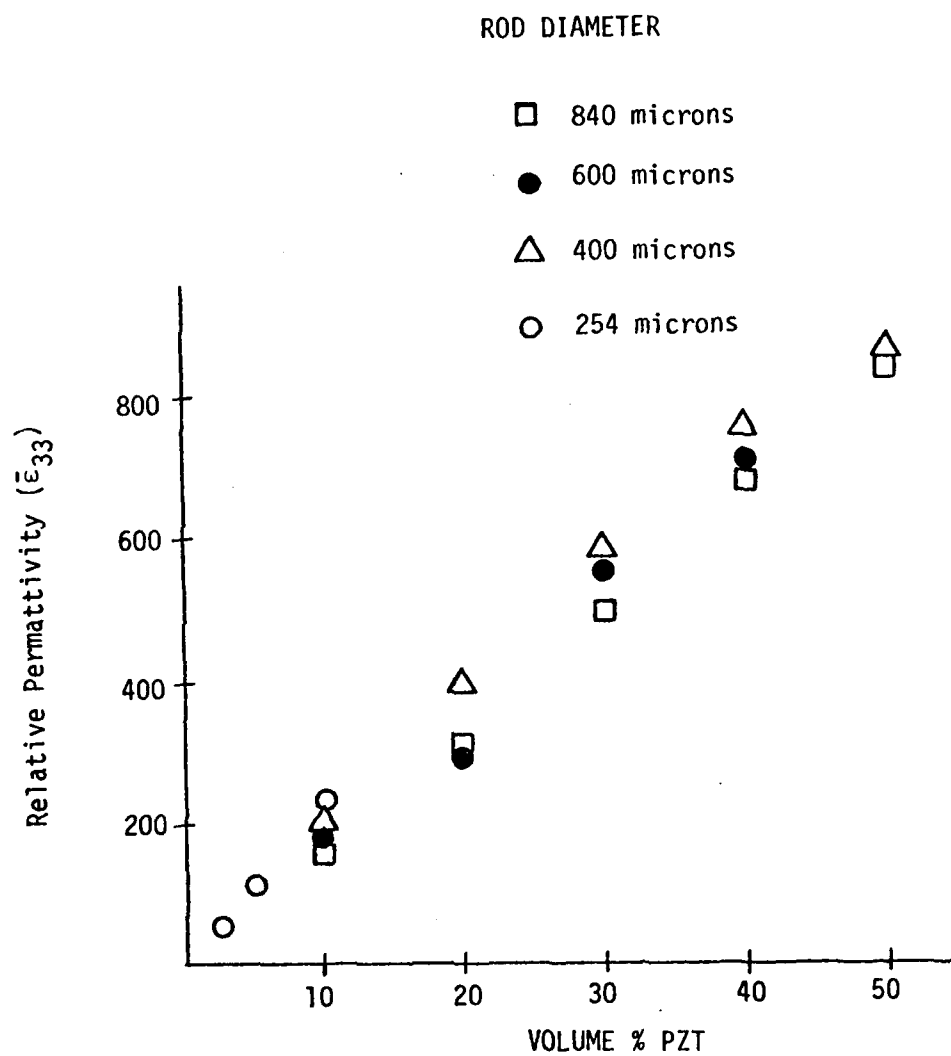


Figure 7. Relative permittivity as a function of volume % PZT.

4b respectively. The orthorhombic state is again metastable at all field levels and has therefore been omitted. The ratio of the total polarization at 100 kv/cm to the spontaneous polarization at 0 kv/cm is plotted versus composition in Figures 5a and 5b for the two orientations of the applied electric field.

4. DISCUSSION

The analysis of the effect of hydrostatic pressure on the phase stability of morphotropic PZT compositions shows some expected results. The rhombohedral-tetragonal phase boundary (MPB) is rather sensitive to changes in the elastic boundary conditions. A rhombohedral-tetragonal phase transition can be induced in the morphotropic PZT compositions by the application of a relatively low hydrostatic pressure. This is not a surprising conclusion, since most of the lead containing perovskites are known to have low elastic stiffness coefficients, and therefore are elastically soft materials. The Gibbs free energy difference between stable and metastable phases at the PbTiO_3 composition agrees well with that proposed by Henning and Härdtl [6] on empirical grounds, though from our calculations the free energies themselves are not linear functions of compositions. In a future study we intend to use the opposed diamond anvil-high pressure cell to examine morphotropic PZT compositions at high hydrostatic pressures by means of x-ray diffraction, and to explore the morphotropic phase boundary shifts as a function of pressure.

On the other hand, the effect of electric boundary condition changes on phase stability shows some unexpected and interesting results. It can be seen from Figures 4a and 4b that it is rather easy to field

force the rhombohedral state to the tetragonal state. However, in the tetragonal phase even the most favorable orientation field along [111] will not force changes to rhombohedral state. We believe that this may be part of the reason there is a rapid escalation of coercivity against poling in tetragonal phase compositions.

Acknowledgment

This work was supported by the Office of Naval Research, Contract No. N00014-78-C-0291.

References

1. B. JAFFE, W.J. COOK and H. JAFFE, Piezoelectric Ceramics, Academic Press, London, 1971.
2. A. AMIN, B. BADGER, H. MCKINSTRY and L.E. CROSS, J. Appl. Phys. (submitted).
3. V. GINSBURG, J. Exp. Theor. Phys. SSSR 15 (1945) 739.
4. A.F. DEVONSHIRE, Phil. Mag. 40 (1949) 1040.
5. H. LANDOLT and B. BORNSTEIN, Ferroelectric and Antiferroelectric Substances, second edition 9, edited by K. Hellwege, Springer-Verlag Berlin, 1975.
6. D. HENNING and H.K. HÄRDTL, Proc. Int. Conf. Science of Ceramics, Baden, W. Germany, 1971.

Figure Captions

Fig. 1 $\text{PbZrO}_3\text{-PbTiO}_3$ phase diagram [1].

Fig. 2 Elastic Gibbs free energy under high hydrostatic pressure at 25°C for compositions close to the morphotropic boundary in the PZT system. (a) Positive pressure
(b) Negative pressure

Fig. 3 Predicted shift of the morphotropic phase boundary as a function of hydrostatic pressure at 25°C.

Fig. 4 Elastic Gibbs free energy under dc field at 25°C for compositions close to morphotropy in the PZT system.
(a) Field along [001] cubic direction
(b) Field along [111] cubic direction

Fig. 5 Predicted compositional dependence of $P_S(100 \text{ kv/cm})/P_S(0)$.
(a) Field along [001] cubic direction
(b) Field along [111] cubic direction

Appearance of Figures

Figure 1 in Section 1.

Figures 2a, 2b, and 3 in Section 2.

Figures 4a, 4b, 5a, and 5b in Section 3.

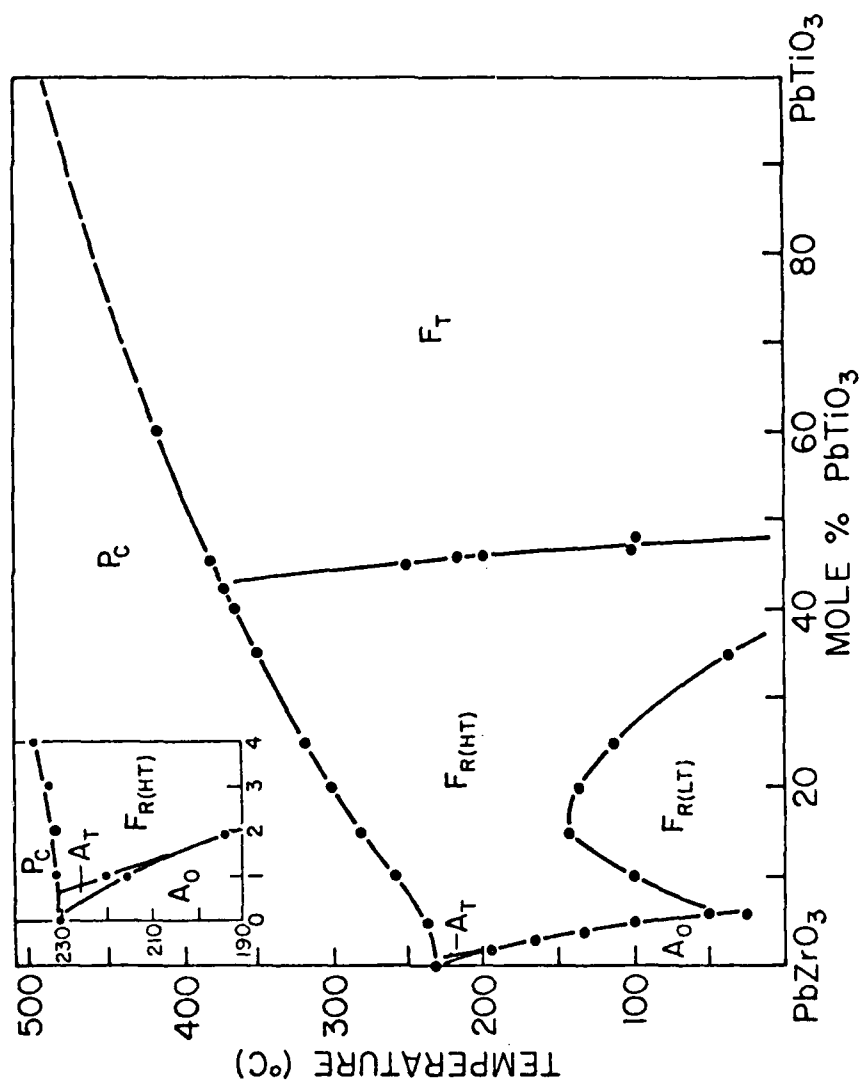


Fig. 1

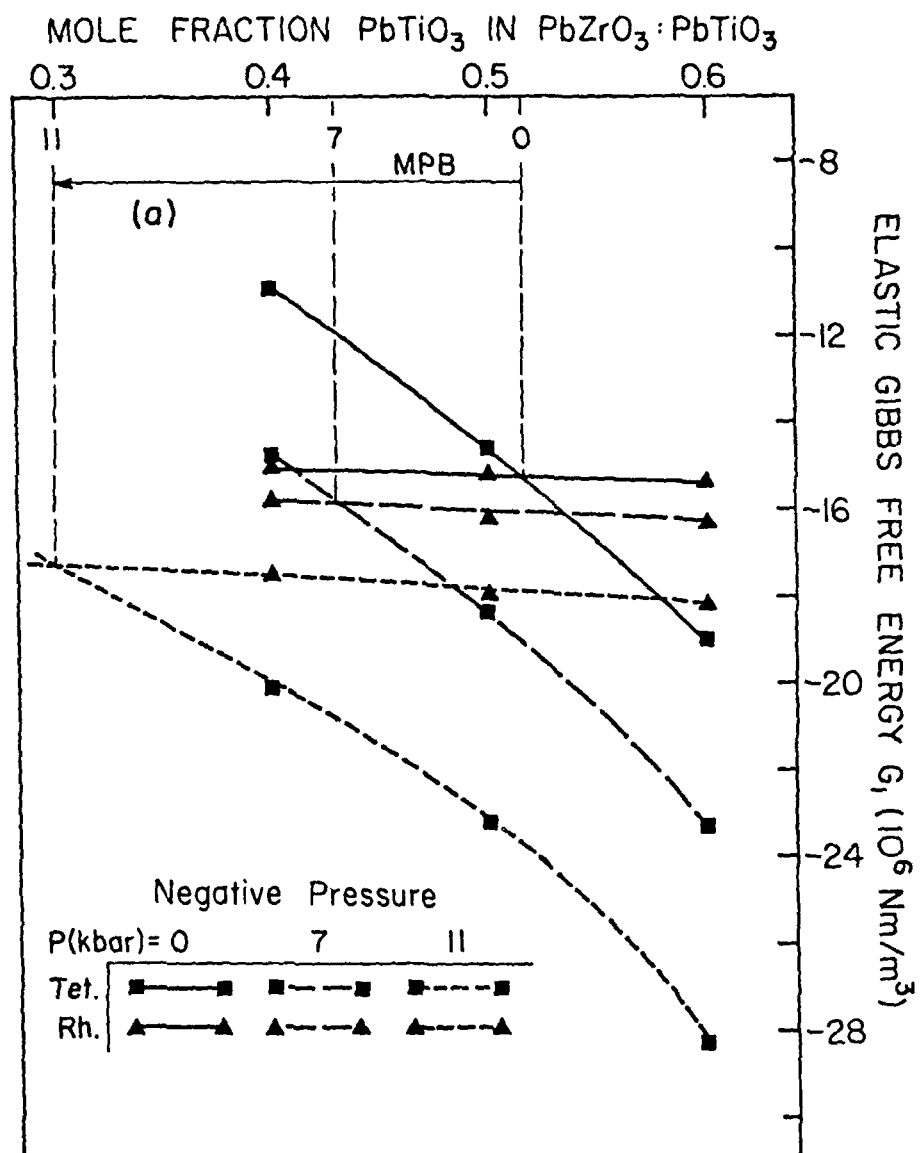


Fig. 2 (a)

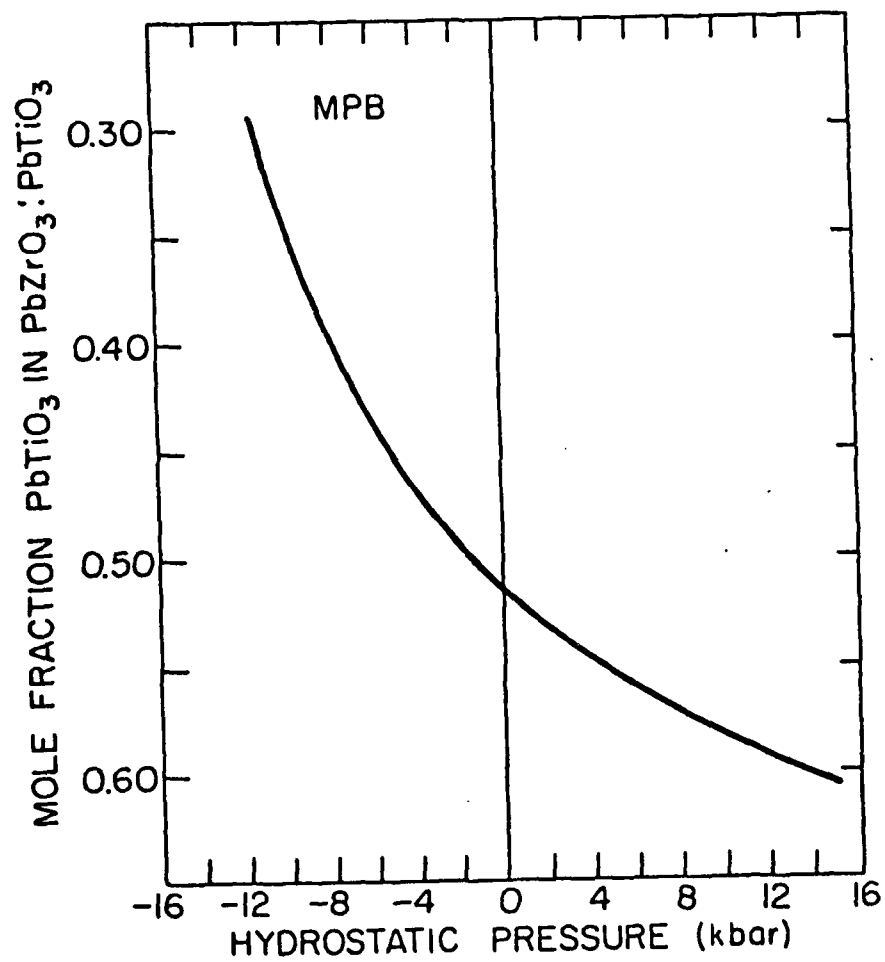


Fig. 3

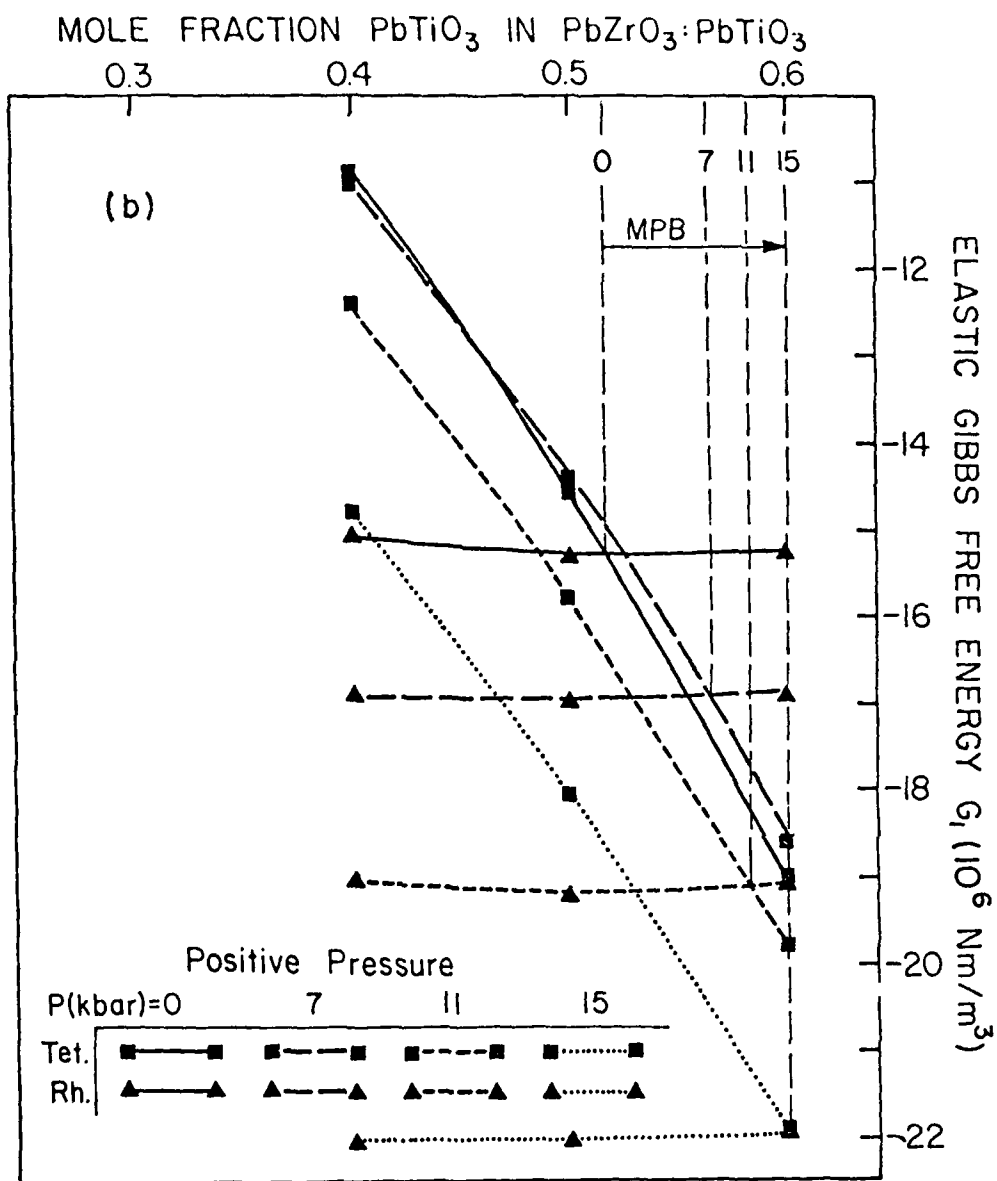


Fig. 2(b)

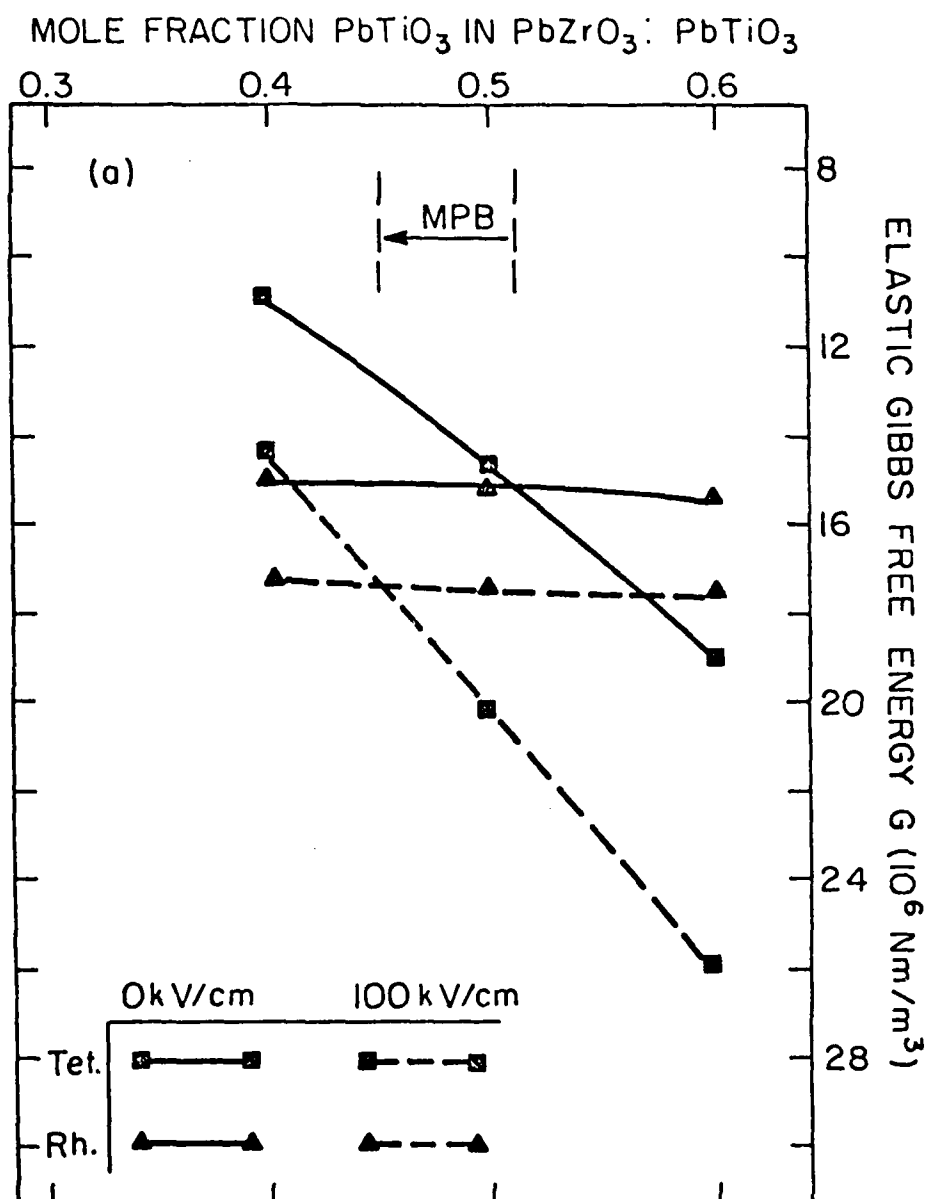


Fig. 4 (a)

AD-A096 451

PENNSYLVANIA STATE UNIV UNIVERSITY PARK MATERIALS RE--ETC F/G 9/1
TARGETED BASIC STUDIES OF FERROELECTRIC AND FERROELASTIC MATERI--ETC(U)
DEC 80 L E CROSS, R E NEWNHAM, G R BARSCH N00014-78-C-0291

UNCLASSIFIED

NL

500
70-41



70-41

END

DATE

4-8-81

DTIC

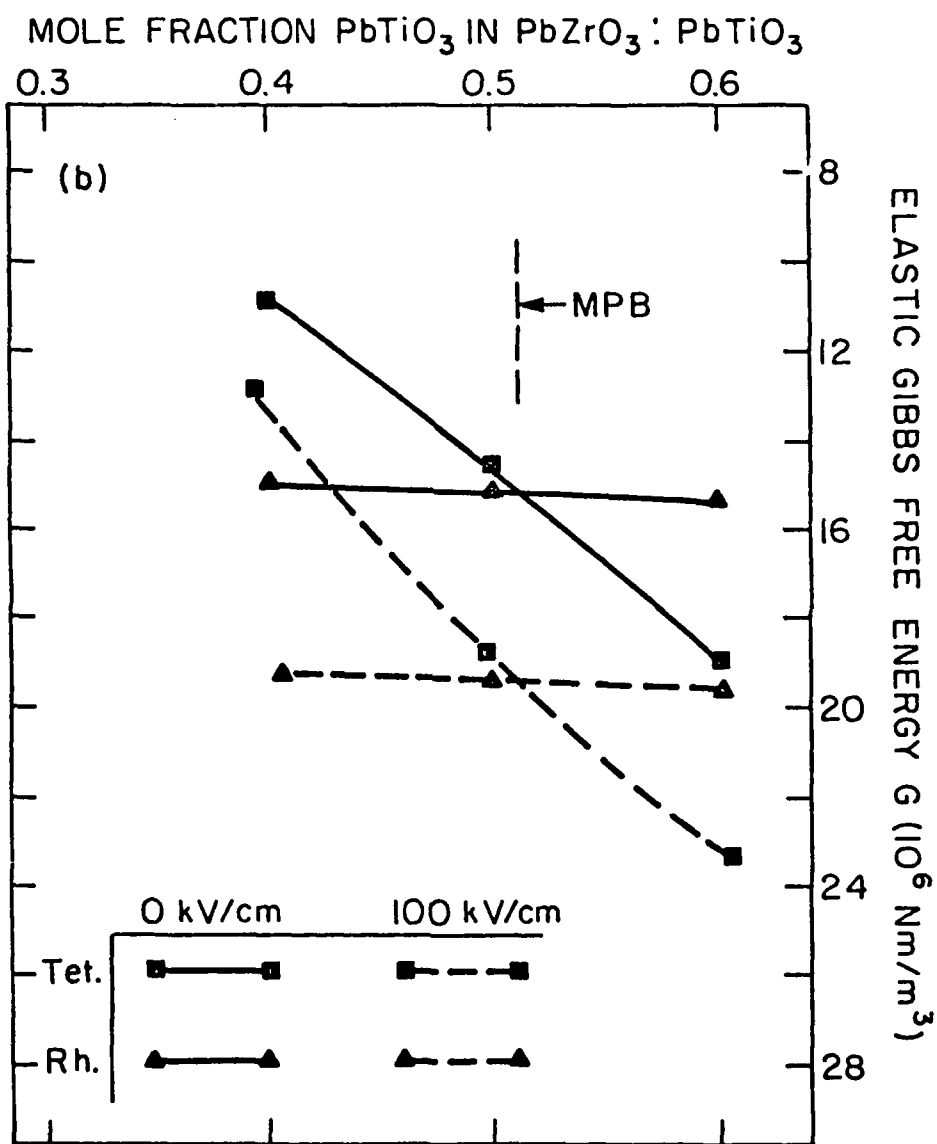


Fig. 4 (b)

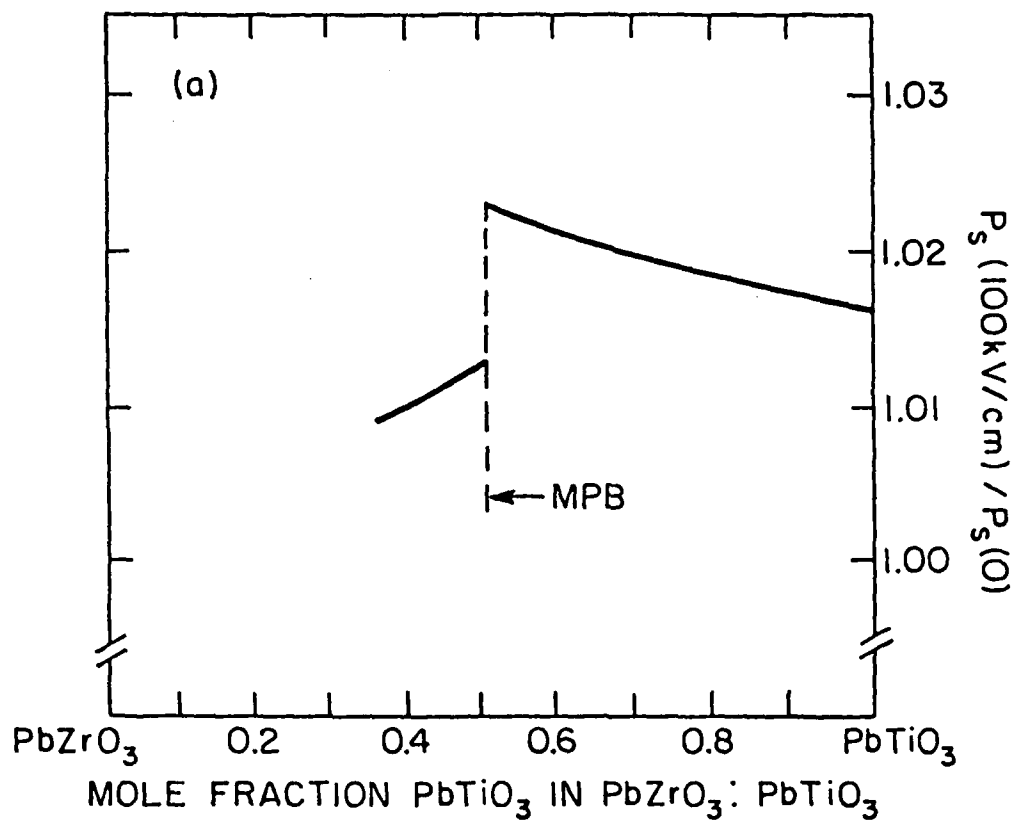


Fig. 5(a)

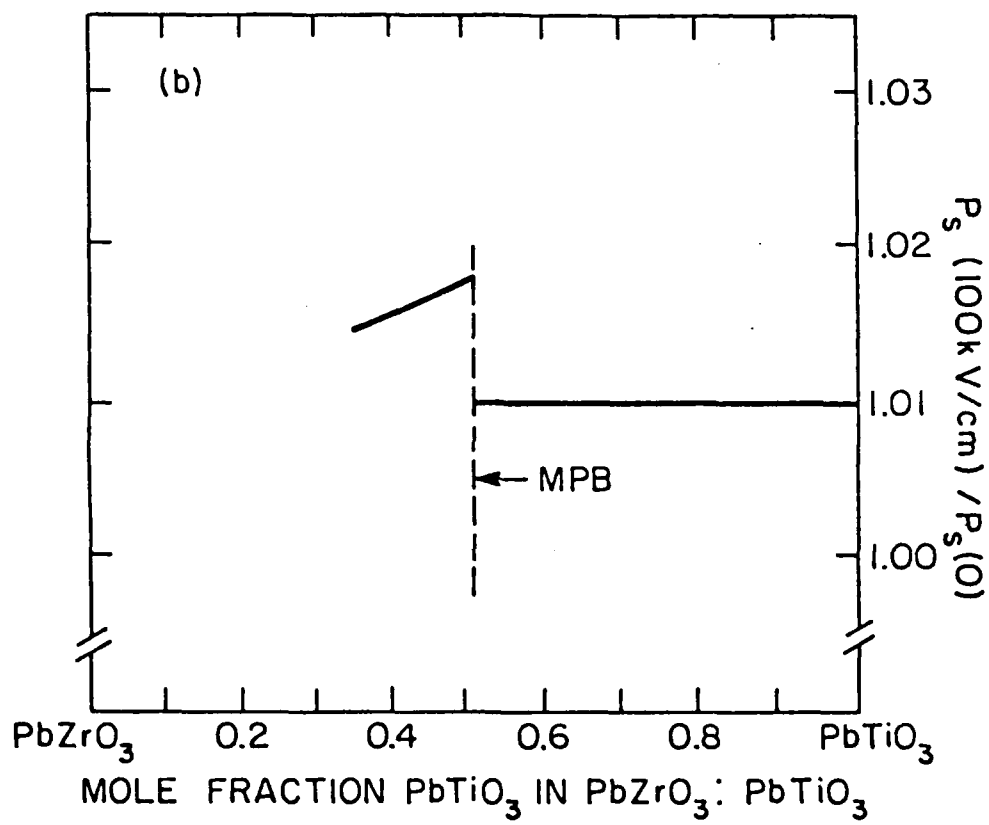


Fig. 5(b)

APPENDIX 47

M. Granahan, M. Holmes, W.A. Schulze, R.E. Newnham. Grain-Oriented PbNb_2O_6 Ceramics. J. Amer. Ceram. Soc. (submitted).

GRAIN-ORIENTED PbNb_2O_6 CERAMICS

M. Granahan, M. Holmes, W. A. Schulze and R. E. Newnham

Materials Research Laboratory
 Pennsylvania State University
 University Park, Pa., 16802

ABSTRACT

Grain-oriented ceramics of ferroelectric lead metaniobate have been prepared by molten salt synthesis of anisotropic crystallites followed by doctor blade casting. The sintered ceramics have an orthorhombic texture with elongated c-axis grains parallel to the casting direction. This allows efficient poling in directions perpendicular to the tape.

In recent years novel fabrication techniques have made possible the production of ceramics with textured microstructures. The earlier applications were in the production of magnetic ceramics¹. More recently hot-forging techniques have produced grain-oriented ferroelectrics², primarily directed toward maximizing piezoelectric properties. The most recent and possibly simplest technique is a combination of molten salt syntheses of anisotropic crystallites and conventional doctor blade casting³. This system has been shown to produce highly oriented ceramics for the layer structures $\text{Bi}_4\text{Ti}_3\text{O}_{12}$ and Bi_2WO_6 .

In this note we present preliminary data demonstrating that the molten-salt-tape-casting method can produce ceramic that is more than just oriented in the sheet of the casting but is actually orthorhombic in texture and electrical properties. The oxide chosen for study is lead metaniobate

which is used commercially as a piezoelectric transducer because of three outstanding properties⁵: a very high Curie point (570°C), a very low mechanical Q (about 10), and a large d_{33}/d_{31} ratio. The large ratio results in a large hydrostatic piezoelectric effect $d_h = d_{33} + 2d_{31}$. For this reason, PbNb_2O_6 is preferred over PZT for hydrostatic pressure detectors. The lower dielectric constant of PbNb_2O_6 is also an advantage because it increases the voltage sensitivity. Grain alignment is expected to improve some of its properties.

The techniques used to produce the powder and green ceramic were exactly as described by Holmes^{3,4}. The specific conditions used to produce the stoichiometric PbNb_2O_6 acicular crystallites and ceramic shown in Figure 1a were: (a) use of an equimolar NaCl-KCl flux; (b) reaction of equal weights of flux and component oxides at 800°C - 1 hr then 1050°C - 5 hr; (c) in tape casting, PbNb_2O_6 was 63% of the total weight; (d) casting height was 0.013 inches; (e) tape was pressed at 60°C, 25 Kpsi for three minutes; (f) fired in air at 1260°C for 1 hr. The resulting ceramic had a density of 5.4 gr/cc and its microstructure can be compared to the starting powder in Figure 1b.

The orthorhombic nature of the unpoled ceramic can be demonstrated by comparing the x-ray intensities in Figure 2. Each pattern has been normalized to its most intense peak. The nomenclature used in this paper assigns the x direction to the tape casting direction, z as normal to the sheet, and y as the axis in the sheet perpendicular to the casting direction. The action of tape casting causes the acicular crystallites to lie with the long axis (c or [001] axis) in the sheet. Additional orientation occurs within the plane, where the crystals show a tendency to orient parallel to the casting direction. In the x-ray patterns, this is evident from the very intense

002 peak in the z plane, a moderate peak in the x plane, and the absence of the reflection in the diffraction pattern obtained from the y plane.

The orthorhombic nature is, however, not as apparent in the unpoled relative permittivity which is 355 in the sheet and 260 in the z direction. But after poling, the difference in the three axes becomes more obvious. Under moderate poling conditions (26 kV/cm, 140°C for 10 minutes), a d_{33} value of 110×10^{-12} C/N was developed along the z axis. Along y the value was 90×10^{-12} C/N, and only 75×10^{-12} could be induced along the x axis or the casting direction. These results are consistent with the x-ray data which show that for most grains the c axis lies in the z plane, with many oriented parallel to the casting (x) direction. The polar axis in ferroelectric PbNb_2O_6 is in the plane perpendicular to the c axis, or radial for the acicular crystallites. This means that the remanent polarization and piezoelectric coefficient should be largest perpendicular to the tape and smallest parallel to the casting direction, as observed.

Table 1 gives the permittivity of the poled ceramic and its resonance characteristics. The coupling factors listed have been corrected by the figure of merit⁴ and are true k_{31} values, except for measurements in the poling direction which are k effective values. The coupling factors are less than maximum since the d_{33} coefficients are not at saturation levels. A saturation d_{33} was found to be 145×10^{-12} C/N in the z direction when poled at 40 kV/cm for thin samples.

In summary, the molten salt production of acicular crystallites combined with tape casting can produce PbNb_2O_6 ceramic with pseudo-orthorhombic symmetry and the fabrication should be applicable to many other systems in which asymmetric crystallites can be produced. The grain oriented PbNb_2O_6

Table 1. Electrical properties of poled grain-oriented lead niobate ceramics. K is the relative permittivity, k the coupling factor, Q the mechanical quality factor, and N the frequency constant in Hz.m (constant displacement).

Poling Direction	Direction of Property Measurement or Vibration			
		x	y	z
x	K	340	---	310
	k	0.20	---	0.20
	Q	19	---	25
	N	1850	---	1550
y	K	---	300	320
	k	---	0.22	0.24
	Q	---	25	24
	N	---	1900	1460
z	K	390	410	260
	k	0.23	0.29	0.33
	Q	26	20	20
	N	1690	1670	1870

should produce a ceramic with a significantly higher d_{33} and possibly lower permittivity than is presently available. It is hoped that the ongoing study of this material will increase the understanding of the unusually low Q and low planar coupling found in conventional PbNb_2O_6 piezoelectric ceramics.

References

- ¹ R. H. Arendt "The Molten Salt Synthesis of Single Magnetic Domain Barium Iron Oxide ($\text{BaFe}_{12}\text{O}_{19}$) and Strontium Iron Oxide ($\text{SrFe}_{12}\text{O}_{19}$) Ceramics" J. Solid State Chem. 8 [4] 339-347 (1973).
- ² H. Igarashi, K. Matsunaga, T. Taniai and K. Okazaki, "Dielectric and Piezoelectric Properties of Grain-Oriented $\text{PbBi}_2\text{Nb}_2\text{O}_9$ Ceramics" Am. Ceram. Soc. Bull. [9] 815-817 (1978).
- ³ M. Holmes, R. E. Newnham and L. E. Cross "Grain-Oriented Ferroelectric Ceramics" Amer. Ceramic Soc. Bull. 58 [9] 872 (1979).
- ⁴ M. Holmes "Grain-Oriented Ferroelectric Ceramics" M.S. Thesis in Ceramic Science, Pennsylvania State University, 1980.
- ⁵ G. Goodman "Ferroelectric Properties of Lead Metaniobate" Amer. Ceram. Soc. Journal 36 [11] 368-372 (1953).



Figure 1a



Figure 1b

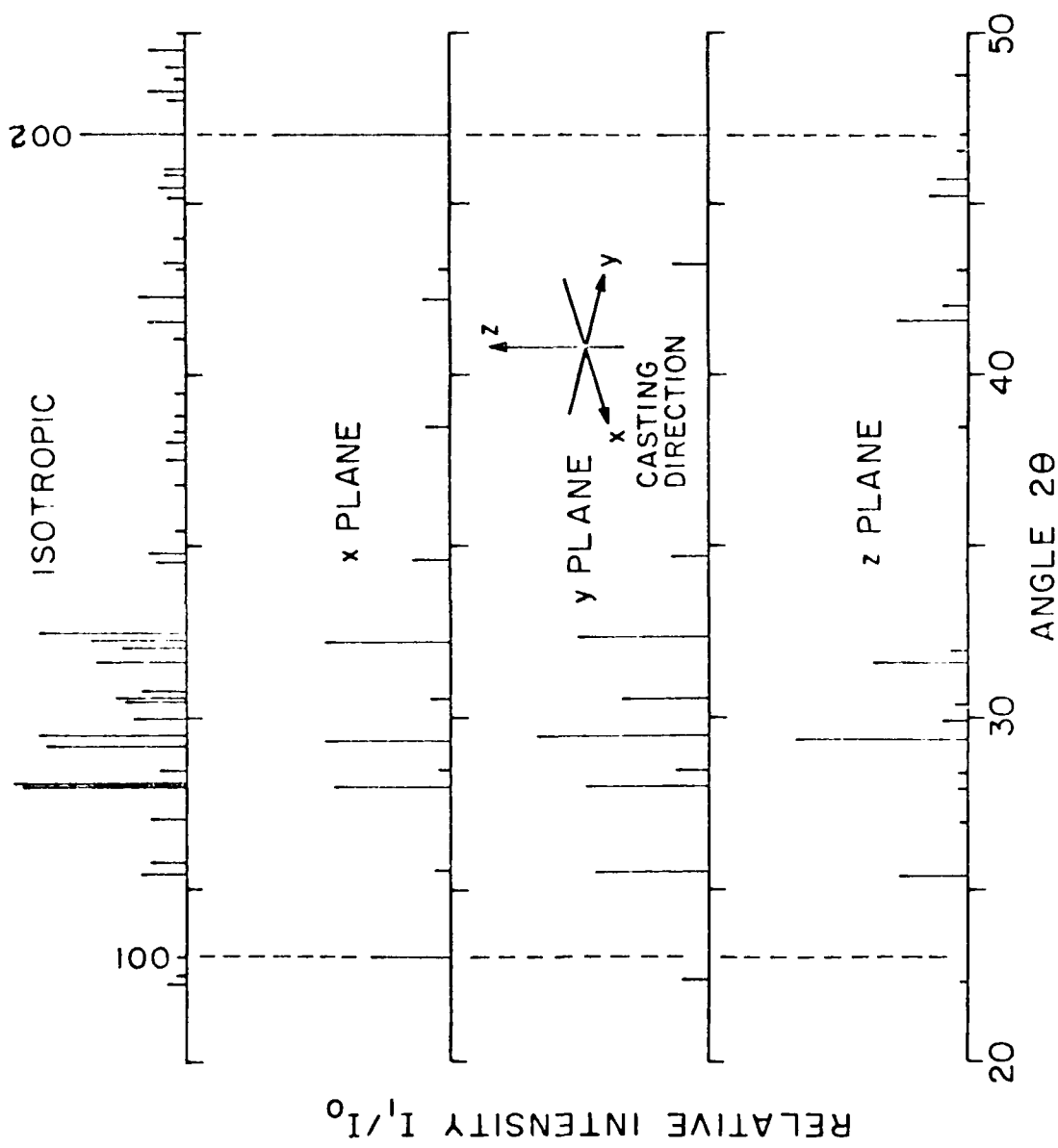


Figure 2

APPENDIX 48

A. Amin, R.E. Newnham, L.E. Cross. Atom Shifts, Polarization Levels, and Curie Temperatures in Ferroelectric $\text{PbZrO}_3\text{:PbTiO}_3$ Solid Solutions. Mat. Res. Bull. 15, 721 (1980).

ATOM SHIFTS, POLARIZATION LEVELS, AND CURIE TEMPERATURES
IN FERROELECTRIC PbZrO_3 : PbTiO_3 SOLID SOLUTIONS

A. Amin, R. E. Newnham and L. E. Cross
Materials Research Laboratory
The Pennsylvania State University
University Park, Pennsylvania 16802

(Received February 26, 1980; Refereed)

ABSTRACT

New data concerning the atomic shifts and polarization levels in some solid solutions in the Lead Zirconate: Lead Titanate system have been used to re-examine the empirical relations of Abrahams et al. for displacive ferroelectrics. It is shown that the relation between P_s and the homopolar atom shift δz is well followed, with a correlation coefficient of $2.51(7) \text{ C/m}^2 - \text{\AA}$. The second relation between T_c and δz , which is explicable on the Landau-Ginsburg-Devonshire theory if the transitions are near second order appears, however, to require different values of the correlation coefficient in the different ferroelectric structures.

Introduction

Based on a survey of ten different displacive ferroelectrics, Abrahams et al. (1) observed that the spontaneous polarization P_s is linearly related to the homopolar atom shift δz (\AA) by the relation

$$P_s = k \delta z \quad \text{C/m}^2 \quad [1]$$

where $k = 2.58(9) \text{ C/m}^2 - \text{\AA}$. In addition they found a second relationship between the Curie temperature T_c and $(\delta z)^2$

$$T_c = 2.00(9) \times 10^4 (\delta z)^2 \quad [2]$$

Since most of the technologically important ferroelectric materials are ceramics, Eqs. [1,2] are very useful, especially when good single crystals are unavailable for P_s measurements. The homopolar atom shift δz , and the Curie temperature T_c can be determined accurately from ceramic samples. Since these two parameters are identical in ceramic and single crystal forms, P_s can be determined from Eq. [1].

In this paper we discuss the origin of these relationships and their application to the technologically important PZT system, the perovskite solid solution between PbZrO_3 and PbTiO_3 . The first of the Abrahams et al. relationships can be understood on the basis of a point charge model for $\text{A}^{2+}\text{B}^{4+}\text{O}_3^{2-}$ perovskites, and the second relationship by the Landau-Ginsburg-Devonshire theory of second order phase transition. Some recent results on the PZT system are used to verify the relationships.

Relationships in the PZT System

The $(\text{Zr}/\text{Ti})^{4+}$ and Pb^{2+} atom shifts determined by neutron diffraction and the spontaneous polarization values are listed in Table 1. The experimental values of $\delta z(\text{Zr}/\text{Ti})^{4+}$ and P_s are shown in Figure 1. These points have been fitted by the method of least squares. In the fitting procedure, each δz value was weighted by the inverse of its variance. The least squares line equation is given by

$$P_s = k \delta z \quad [3]$$

where $k = 2.51(7) \text{ C/m}^2 - \text{\AA}$ which agrees well with the value obtained by Abrahams and coworkers. Figure 2 shows the compositional dependence of the room temperature value of $P_s - (\text{Zr}/\text{Ti})^{4+}$ atom shifts as determined from Eq. [3]. Note the continuous variation of these two parameters as a function of composition in both the tetragonal and rhombohedral regions, with a discontinuity at the morphotropic phase boundary.

The experimental values of $\delta z(\text{Zr}/\text{Ti})^{4+}$ and $\delta z(\text{Pb})^{2+}$ are shown in Figure 3. These points have been fitted to a straight line by the method of least squares. In the fitting procedure, each δz value was weighted by the inverse of its variance. The least squares line equation is given by

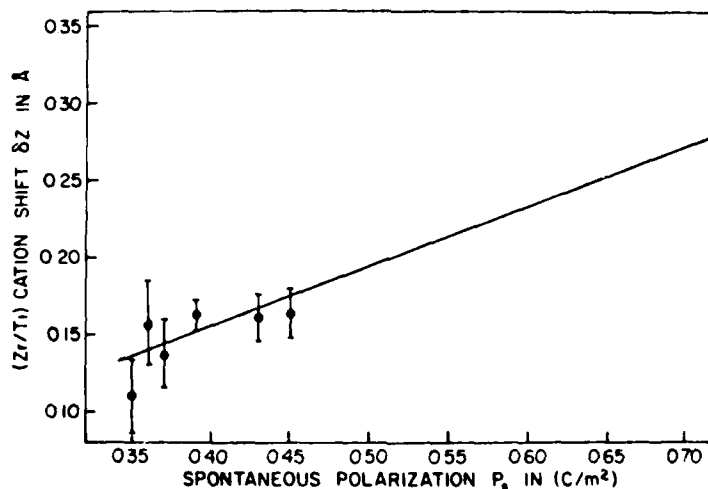


FIG. 1

Experimental (Zr/Ti) shifts versus P_s

TABLE 1
Experimental cation shifts (neutron diffraction) and spontaneous
polarizations for $\text{PbZr}_x\text{Ti}_{1-x}\text{O}_3$

Composition x	$T(^{\circ}\text{C})$	Space Group	$(\text{Zr}/\text{Ti})^{4+}$ Shift (\AA)	Pb^{2+} Shift (\AA)	Ref.	$P_s (\text{C}/\text{m}^2)$	$P_s (\text{C}/\text{m}^2)$ from Eq. [3]
0.90	25	R3c	0.164(16)	0.46(1)	Glazer et al. (3)	0.45 ⁺	0.41(4)
	60	"	0.161(14)	0.44(1)	"	0.43 ⁺	0.40(4)
	100	"	0.137(23)	0.38(2)	"	0.37 ⁺	0.34(5)
	150	R3m	0.111(23)	0.37(2)	"	0.35 ⁺	0.28(5)
	200	"	0.104(19)**	0.26(2)	"	0.35 ⁺	0.26(5)
	235	"	0.030(68)**	0.21(3)	"	0.26 ⁺	0.08(18)
0.60	-263	R3c	0.162(7)	0.49(1)	Amin et al. (2)	0.39*	0.41(2)
	-73	R3m	0.157(27)	0.49(2)	"	0.36*	0.39(6)
0.58	25	"	0.154(9)**	0.44(1)	"	0.34*	0.39(3)
	25	R3m	0.13(?)**	0.23(?)	Michel et al. (4)	0.34*	0.33
	-183	P4mm	0.325**	0.492	Glazer et al. (10)	0.77*	0.81(3)
(PbTiO ₃)	-115	"	0.308**	0.479	"	0.74*	0.77(2)
	25	"	0.311**	0.473	"	0.75 ⁺	0.78(2)
	25	"	0.299(40)	0.465	Shirane et al. (6)		0.75(9)

⁺ Glazer et al. (3).

* Amin et al. (9).

[†] Gavril'yachenko et al. (8).

** Not used in the least squares fit.

Numbers in parentheses represent the standard deviation in the least significant digit.

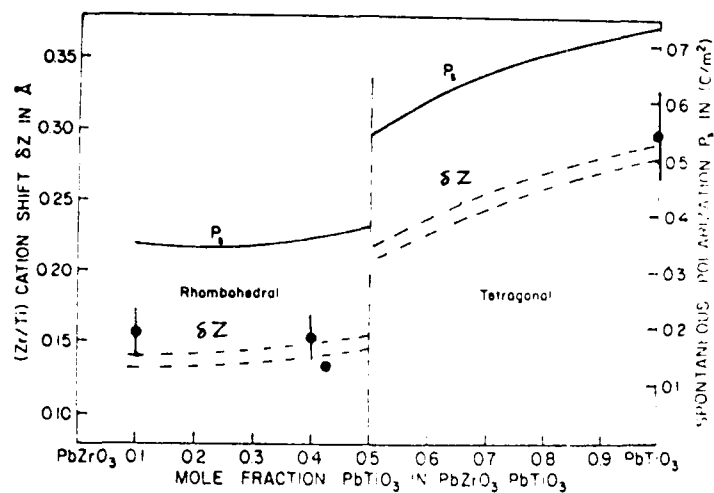


FIG. 2

Compositional dependence of single domain P_s at 25°C (9) and calculated (Zr/Ti) shifts δz . Filled circles represent experimental shifts.

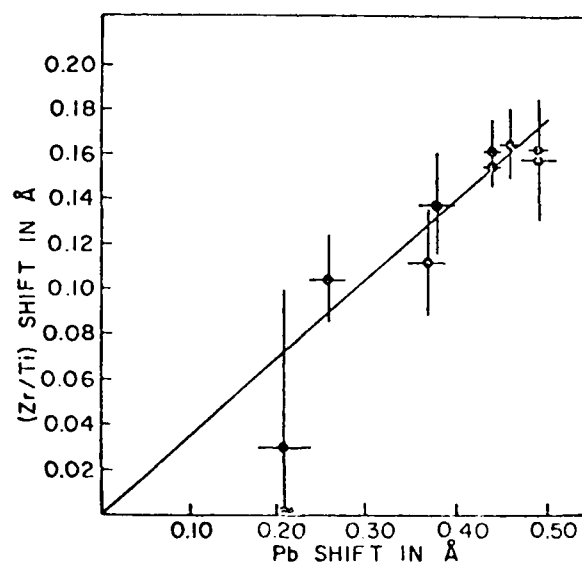


FIG. 3

Experimental (Zr/Ti) shifts versus Pb shifts for R3c and R3m PZT compositions.

$$\delta z(\text{Pb})^{2+} = k' \delta z(\text{Zr}/\text{Ti})^{4+} \quad [4]$$

where $k' = 2.87(7)$. It must be noted that during the structure refinement of $\text{PbZr}_{0.6}\text{Ti}_{0.4}\text{O}_3$ (2) the Pb and (Zr/Ti) atom shifts were highly correlated. The same high correlation was observed in the refinement of $\text{PbZr}_{0.9}\text{Ti}_{0.1}\text{O}_3$ (3).

It is interesting to note that, a similar correlation between A-cation ($A = \text{Pb}, \text{Bi}$, or Li) displacement and B-cation ($B = \text{Ti}, \text{Zr}, \text{Fe}, \text{Nb}$, or Ta) displacement for several rhombohedral ABO_3 perovskites was observed by Michel et al. (4). The correlation coefficient being equal to 2.95 is close to that given by Eq. [4] for the rhombohedral compositions in the PbZrO_3 - PbTiO_3 solid solution system. However, Megaw et al. (5) observed that for NaNbO_3 -(N) phase and KNbO_3 , the A and B displacements deviate from that suggested by Michel et al. In the following paragraph, we examine the point charge model for $\text{A}^{2+}\text{B}^{4+}\text{O}_3^{2-}$ perovskites, imposing the constraint given by Eq. [4].

The point charge model provides a very simple way of calculating the single domain spontaneous polarization P_s along the polar axis. Assuming complete ionicity, P_s can be written as

$$P_s = N \sum_{i=1}^N n_i e \delta z_i \quad [5]$$

where N is the number of unit cells/unit volume, n_i the i^{th} ion valency, e the electronic charge, δz_i the i^{th} ion displacement along the polar axis. The summation in Eq. [5] is taken over all the ions N in the unit cell. Relative to an origin taken at the O^{2-} anions in the ferroelectric state, and assuming rigid BO_6 octahedra, the spontaneous polarization P_s can be written as

$$P_s = \frac{64}{V} [\delta z(B) + 0.5 \delta z(A)] \text{ C/m}^2 \quad [6]$$

where $\delta z(B)$ and $\delta z(A)$ are the B^{4+} and A^{2+} cation shifts \AA along the polar axis in the ferroelectric state from their high symmetry position, and V is the unit cell volume \AA^3 . Substituting for $\delta z(A)$ from Eq. [4] in Eq. [6]

$$P_s = \frac{156 \pm 2}{V} \delta z(B) \text{ C/m}^2 \quad [7]$$

It is clear from Eq. [7] that the spontaneous polarization P_s is linearly related to the homopolar atom shift $\delta z(B)$ in agreement with the survey of Abrahams et al.

Numerical results for PbTiO_3 , $\text{PbZr}_{0.9}\text{Ti}_{0.1}\text{O}_3$, and $\text{PbZr}_{0.6}\text{Ti}_{0.4}\text{O}_3$ are now considered. The room temperature crystal structure of ferroelectric PbTiO_3 is given by Shirane et al. (6). The Ti atom shift $\delta z(\text{Ti})$ is given in Table 1, the unit cell volume $V = 67.3 \text{\AA}^3$. Substituting for $\delta z(\text{Ti})$ and V in Eq. [7] we obtain $P_s = 0.69(9) \text{ C/m}^2$. The literature room temperature value of P_s for PbTiO_3 vary from 0.51 - 0.81 C/m^2 (7). However, a more reliable value^s of 0.75 C/m^2 was reported by Gavril'yachenko et al. (8). The room temperature crystal structure of ferroelectric $\text{PbZr}_{0.9}\text{Ti}_{0.1}\text{O}_3$ is given by Glazer et al. (3). The (Zr/Ti) atom shift $\delta z(\text{Zr}/\text{Ti})$ is given in Table 1, the unit cell volume $V = 70.9 \text{\AA}^3$. Substituting for $\delta z(\text{Zr}/\text{Ti})$ and V in Eq. [7] we obtain $P_s = 0.36(4) \text{ C/m}^2$. For ferroelectric $\text{PbZr}_{0.6}\text{Ti}_{0.4}\text{O}_3$, the room temperature (Zr/Ti) atom shift is given in Table 1, the unit cell volume $V = 67.9 \text{\AA}^3$. Substituting for $\delta z(\text{Zr}/\text{Ti})$ and V in Eq. [7] gives $P_s = 0.35(2) \text{ C/m}^2$. The single crystal P_s values at room temperature for these two compositions are listed in Table 1.

Phenomenological Basis of the $T_c - \delta z$ Relationship

When applied to simple proper ferroelectric, the elastic Gibbs free energy function is treated as an analytical function of the spontaneous polarization, and in its most simple form as an expansion in even powers of P_s .

$$\Delta G = AP_s^2 + BP_s^4 + \dots \quad [8]$$

Minimizing with respect to P_s

$$\frac{\delta \Delta G}{\delta P} = E = 2AP_s + 4BP_s^3 = 0 \quad [9]$$

Eq. [9] leads to the following solutions

$$\text{Paraelectric solution, } P_s = 0 \quad [10]$$

$$\text{Ferroelectric solution, } P_s^2 = -\frac{2A}{4B} = -\text{constant (T-9)} \quad [11]$$

For a second order phase transition the Curie-Weiss temperature θ and the phase transition temperature T_c are identical. Therefore, Eq. [11] may be expressed for temperatures far below T_c as

$$P_s^2 = \text{const. } T_c \quad [12]$$

From Eq. [3] we have

$$P_s^2 = \text{const. } \delta z^2 \quad [13]$$

From Eqs. [12] and [13] one obtains

$$T_c = \text{const. } \delta z^2 \quad [14]$$

Which is the second of Abrahams et al. relationships.

Unfortunately, the experimental data on the composition dependence of the homopolar (Zr/Ti) atom shifts δz in the PZT system are rather sparse. However, it can be seen from Figure 1 that the calculated room temperature (Zr/Ti) shifts agree reasonably well with the experimentally determined values. Therefore, we decided to use the compositional dependence of the calculated shifts (Eq. [3]) to see if they were correlated to the Curie temperature T_c as suggested by Eq. [14]. The square of the calculated (Zr/Ti) shifts at room temperature for several PZT compositions in the tetragonal phase field was found to be linearly correlated to their Curie temperature T_c by

$$T_c = 1.04(6) \times 10^4 (\delta z)^2 \quad K \quad [15]$$

whereas for the rhombohedral phase field compositions, the Curie temperature is related to the (Zr/Ti) shifts by

$$T_c = 3.3(2) \times 10^4 (\delta z)^2 \quad K \quad [16]$$

Table 2 lists the experimental T_c values for several PZT compositions (12), δz (Zr/Ti) as calculated from Eq. [3], and the calculated Curie temperature from Eqs. [15] and [16] for the tetragonal and rhombohedral compositions respectively.

TABLE 2
Calculated (Zr/Ti) Shift and Curie Temperature
for $\text{PbZr}_x\text{Ti}_{1-x}\text{O}_3$

Composition x	T_C (K) Exp.	δz (Zr/Ti) Å Calc.	T_C (K) Calc.
PbTiO_3	765	0.282(8)	827(48)
0.1	750	0.279(7)	809(47)
0.2	732	0.276(7)	792(46)
0.3	713	0.259(7)	698(39)
0.4	692	0.239(7)	594(33)
0.5	667	0.210(10)	459(26)
0.6	638	0.131(4)	561(34)
0.7	608	0.135(4)	601(36)
0.8	573	0.135(4)	601(36)
0.9	531	0.135(4)	601(36)

Summary and Conclusions

Some recent results on the mixed perovskite solid solutions between ferroelectric PbTiO_3 and antiferroelectric PbZrO_3 have been used to examine Abrahams et al. relationships for displacive type ferroelectrics. The first of the two relationships, i.e., the linear correlation between the homopolar atom shift δz and P_s was found to hold reasonably well for the PZT system. The correlation coefficient being equal to $2.51(7) \text{ C/m}^2 - \text{\AA}$ is in good agreement with the value $2.53(9) \text{ C/m}^2 - \text{\AA}$ determined previously. It is also shown that, if the first relation is true, then the relationship between the Curie temperature T_C and the homopolar atom shifts $(\delta z)^2$ must be satisfied according to the Landau-Ginsburg-Devonshire theory of second order phase transition. It is quite possible that the correlation coefficient between P_s and δz is almost the same for all displacive type ferroelectrics. However, this argument cannot be extended to the correlation coefficient between T_C and $(\delta z)^2$. For example, in the $\text{PbZrO}_3 - \text{PbTiO}_3$ system two correlation coefficients (depending on symmetry) were found between T_C and $(\delta z)^2$ for several compositions across the phase diagram. Another exception is bismuth tungstate. The structure of ferroelectric Bi_2WO_6 consists of alternate layers of BiO_2 and perovskite like units (11). The predicted Curie temperature from the homopolar atom shift is 1250°C , well above its melting point. Thus, the correlation coefficient between T_C and $(\delta z)^2$ is not sufficiently general to be useful in practice.

Acknowledgments

This work was supported by the Office of Naval Research through Contract number N00014-78-0291.

References

1. S. C. Abrahams, S. K. Kurtz and P. B. Jamieson, *Phys. Rev.*, 172 (2), 551 (1968).
2. A. Amin, R. E. Newnham, L. E. Cross and D. E. Cox, *J. Solid State Chem.* (Submitted).
3. A. M. Glazer, S. A. Mabud and R. Clarke, *Acta Cryst.* B34, 1060 (1978).
4. C. Michel, J. M. Moreau, G. D. Achenbach, R. Gerson and W. J. James, *Solid State Commun.* 1, 865 (1969).
5. H. D. Megaw and C. N. W. Darlington, *Acta Cryst.* A31, 161 (1975).
6. G. Shirane, R. Pepinsky and B. C. Frazer, *Acta Cryst.* 9, 131 (1956).
7. *Ferroelectric and Antiferroelectric Substances*. Landolt Bornstein (New Series). Vol. IX, Springer-Verlag, New York (1975).
8. V. G. Gavrilyachenko, R. I. Spinko and R. Martynenko, *Soviet Phys. - Solid State* 12, 1203 (1970).
9. A. Amin, B. Badger, H. McKinstry and L. E. Cross, *J. Appl. Phys.* (Submitted).
10. A. M. Glazer and S. A. Mabud, *Acta Cryst.* B34, 1065 (1978).
11. R. W. Wolf, R. E. Newnham and M. I. Kay, *Solid State Commun.* 1, 1797 (1969).
12. B. Jaffe, W. R. Cook, Jr. and H. Jaffe, *Piezoelectric Ceramics*, Academic Press, London and New York (1971).

APPENDIX 49

A. Amin, L.E. Cross, R.E. Newnham. Effects of Elastic and Electric Boundary Conditions on the Morphotropic Phase Boundary in PZT. J. Mat. Sci. (accepted).

Effect of Elastic and Electric Boundary Conditions
on the Morphotropic Phase Boundary in PZT

A. Amin, L.E. Cross, R.E. Newnham

Materials Research Laboratory
The Pennsylvania State University
University Park, Pennsylvania 16802

ABSTRACT

The Gibbs free energy function has been used to calculate the influence of elastic and electric boundary conditions on the relative phase stabilities and single domain properties for PZT compositions close to the Zr:Ti=1:1 ratio. Free energy-composition phase diagrams under hydrostatic pressure and applied dc fields are discussed in terms of the morphotropic phase boundary behavior.

Effect of Elastic and Electric Boundary Conditions
on the Morphotropic Phase Boundary in PZT

A. Amin, L.E. Cross, R.E. Newnham

Materials Research Laboratory
 The Pennsylvania State University
 University Park, Pennsylvania 16802

1. INTRODUCTION

The PZT perovskite solid solution between antiferroelectric lead zirconate (PbZrO_3) and ferroelectric lead titanate (PbTiO_3) contains a number of extremely important compositions (Figure 1) used in the electronics industry [1]. Piezoelectric devices such as sonar transmitters and detectors are made of poled PZT ceramics with compositions near the morphotropic phase boundary MPB ($\text{Zr}:\text{Ti} \sim 1:1$) where the dielectric constant, and piezoelectric coupling coefficients are unusually high.

In this work an elastic Gibbs function derived earlier by computer graphic fitting techniques [2] is used to calculate the influence of some postulated elastic and electrical boundary conditions upon the relative phase stabilities and the single domain properties for compositions close to the $\text{Zr}:\text{Ti}=1:1$ ratio required for morphotropy at zero stress and field.

Consider the free energy function for a simple proper ferroelectric derived from a prototypic phase of symmetry $\text{Pm}3\text{m}$. For Brillouin zone center modes, the free energy may be written as a power series [3,4] in dielectric polarization P_i ($i=1,2,3$).

$$G = \alpha_1^X (P_1^2 + P_2^2 + P_3^2) + \alpha_{11}^X (P_1^4 + P_2^4 + P_3^4) \\
+ \alpha_{12}^X (P_1^2 P_2^2 + P_2^2 P_3^2 + P_3^2 P_1^2) + \alpha_{111}^X (P_1^6 + P_2^6 + P_3^6)$$

$$\begin{aligned}
& + \alpha_{112}^X (P_1^4 (P_2^2 + P_3^2) + P_2^4 (P_3^2 + P_1^2) + P_3^4 (P_1^2 + P_2^2)) \\
& + \alpha_{123}^X P_1^2 P_2^2 P_3^2 - 1/2 s_{11}^P (X_1^2 + X_2^2 + X_3^2) \\
& - s_{12}^P (X_1 X_2 + X_2 X_3 + X_3 X_1) - 1/2 s_{44}^P (X_4^2 + X_5^2 + X_6^2) \\
& - Q_{11} (X_1 P_1^2 + X_2 P_2^2 + X_3 P_3^2) \\
& - Q_{12} (X_1 (P_2^2 + P_3^2) + X_2 (P_3^2 + P_1^2) + X_3 (P_1^2 + P_2^2)) \\
& - Q_{44} (X_4 P_2 P_3 + X_5 P_3 P_1 + X_6 P_1 P_2)
\end{aligned} \tag{1}$$

where α_1^X , α_{ij}^X , α_{ijk}^X are related to dielectric stiffness and higher order stiffness coefficients; s_{11}^P , s_{12}^P , s_{44}^P are the elastic compliances measured at constant polarization; and Q_{11} , Q_{12} , Q_{44} are the electrostriction constants written in polarization notation. The expression is complete up to all six power terms in polarization, but contains only first order terms in electrostrictive and elastic behavior.

Adjustable parameters in the free energy function (1) which fit the observed PbZrO_3 - PbTiO_3 phase diagram and the observed physical properties (dielectric and piezoelectric coupling coefficients) have previously been determined [2]. In the computation of phase stability and properties [2] it was assumed that in equation (1) all stresses are absent ($X_{ij}=0$). Under zero stress, morphotropy with coexisting rhombohedral and tetragonal phases was obtained with the following parameters:

$$\alpha_1^X = \chi_0 (T - \theta), \quad \chi_0 = 1/2 \epsilon_0 C,$$

$$\phi = \alpha_{12}^X / \alpha_{11}^X = -1.20 \text{ in } \text{PbZrO}_3 \text{ changing}$$

linearly with composition to 0.80 in PbTiO_3 ,

$$\alpha_{112}^X = 8000/\epsilon_0 C,$$

$$\alpha_{123}^X = -45000/\epsilon_0 C \text{ in } \text{PbZrO}_3 \text{ changing linearly with composition to } 20000/\epsilon_0 C \text{ in } \text{PbTiO}_3,$$

where C is the Curie-Weiss constant and ϵ_0 is the permittivity of free space.

2. INFLUENCE OF HYDROSTATIC PRESSURE

To assess the phase stability and physical properties under static stress systems, it is necessary to consider various X_{ij} values and their effect on the energy function. For a hydrostatic pressure p

$$X_{11} = X_{22} = X_{33} = -p.$$

$$X_{12} = X_{23} = X_{31} = 0.$$

Under these conditions the free energy equation (1) takes the form:

$$\begin{aligned} G = & - \left(\frac{3s_{11}^P + 6s_{12}^P}{2} \right) p^2 + [\alpha_1^X (Q_{11} + 2Q_{12}) p] (P_1^2 + P_2^2 + P_3^2) \\ & + \alpha_{11}^X (P_1^4 + P_2^4 + P_3^4) + \alpha_{12}^X (P_1^2 P_2^2 + P_2^2 P_3^2 + P_3^2 P_1^2) \\ & + \alpha_{111}^X (P_1^6 + P_2^6 + P_3^6) \\ & + \alpha_{112}^X \{ P_1^4 (P_2^2 + P_3^2) + P_2^4 (P_3^2 + P_1^2) + P_3^4 (P_1^2 + P_2^2) \} \\ & + \alpha_{123}^X P_1^2 P_2^2 P_3^2 \end{aligned} \quad (2)$$

The first partial derivative equations give the electric field components

$$\left(\frac{\partial G}{\partial P_i} \right) = E_i \quad (i=1,2,3) \quad (3)$$

The dielectric reciprocal susceptibilities (dielectric stiffnesses) are given by the second partial derivatives of the free energy function

$$\frac{\partial^2 G}{\partial P_i \partial P_j} = \frac{1}{\chi_{ij}} \quad (i, j=1, 2, 3) \quad (4)$$

The piezoelectric coefficients are given by

$$d_{mkl} = \chi_{mj}(\epsilon_o) Q_{ijkl} P_i \quad (5)$$

Choosing an appropriate value for p (hydrostatic pressure), the first derivative equations $(\frac{\partial G}{\partial P_i}) = E_i = 0$ ($i=1, 2, 3$) are solved to give new values of the polarization P_i under stress, which can then be reinserted in equation (2) to delineate G as a function of composition, temperature, and applied stress. In the computational procedure the following values were used: $Q_{11} = .065 \text{ m}^4/\text{C}^2$, $Q_{12} = -0.032 \text{ m}^4/\text{C}^2$, $s_{11}^P = 6.785 \times 10^{-12} \text{ m}^2/\text{N}$, $s_{12}^P = -2.5 \times 10^{-12} \text{ m}^2/\text{N}$ [2,5].

For compositions near the morphotropic phase boundary, the resulting free energies at 0, 7, and 11 kbar pressure are shown in Figure 2a, and for 0, 7, 11, and 15 kbar tension in Figure 2b. The orthorhombic state is metastable at all pressures for all single cell compositions. Therefore, the orthorhombic free energies have been omitted from Figures 2a and 2b for clarity. From results similar to these at many intermediate pressures, the composition at the morphotropic boundary has been calculated as a function of stress and is given in Figure 3.

3. EFFECT OF ELECTRIC FIELD

Various electric boundary conditions have also been studied. The way in which applied dc fields affect phase stability and physical

properties is of interest, since in a polycrystalline PZT ceramic the electric boundary conditions vary considerably. In addition, since all the piezoceramic compositions (Zr:Ti ~1:1) are electrically poled at temperatures near the Curie temperature T_c , it is interesting to know what effect the poling field has on morphotropic compositions.

For an applied dc field E_i , the free energy function takes the form

$$\begin{aligned}
 G = & \alpha_1^X (P_1^2 + P_2^2 + P_3^2) + \alpha_{11}^X (P_1^4 + P_2^4 + P_3^4) \\
 & + \alpha_{12}^X (P_1^2 P_2^2 + P_2^2 P_3^2 + P_3^2 P_1^2) + \alpha_{111}^X (P_1^6 + P_2^6 + P_3^6) \\
 & + \alpha_{112}^X (P_1^4 (P_2^2 + P_3^2) + P_2^4 (P_3^2 + P_1^2) + P_3^4 (P_1^2 + P_2^2)) \\
 & + \alpha_{123}^X (P_1^2 P_2^2 P_3^2 - (E_1 P_1 + E_2 P_2 + E_3 P_3))
 \end{aligned} \tag{6}$$

The dielectric reciprocal susceptibilities and the piezoelectric moduli for the cubic, tetragonal, rhombohedral, and orthorhombic states are given by a set of equations similar to those given in Section 2.

Choosing an arbitrary value and orientation for E (applied electric field), the first partial derivative equation $(\frac{\partial G}{\partial P_i}) = E_i \neq 0$ ($i=1,2,3$) are solved to give new values of the polarization P_i under applied electric field. These values can then be reinserted in equation (6) to delineate G as a function of composition, temperature, and applied electric field.

The free energy-composition phase diagram for dc fields applied along the cubic [001] and [111] directions are shown in Figures 4a and

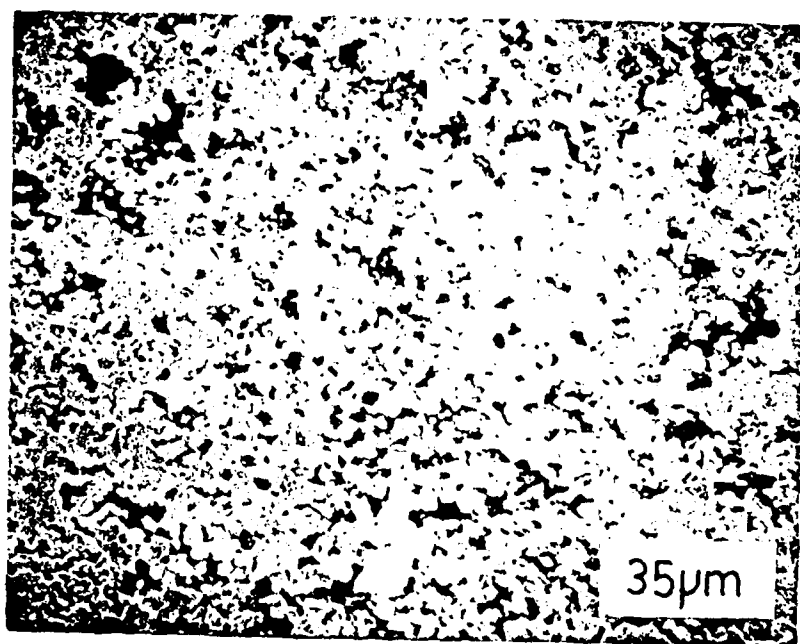
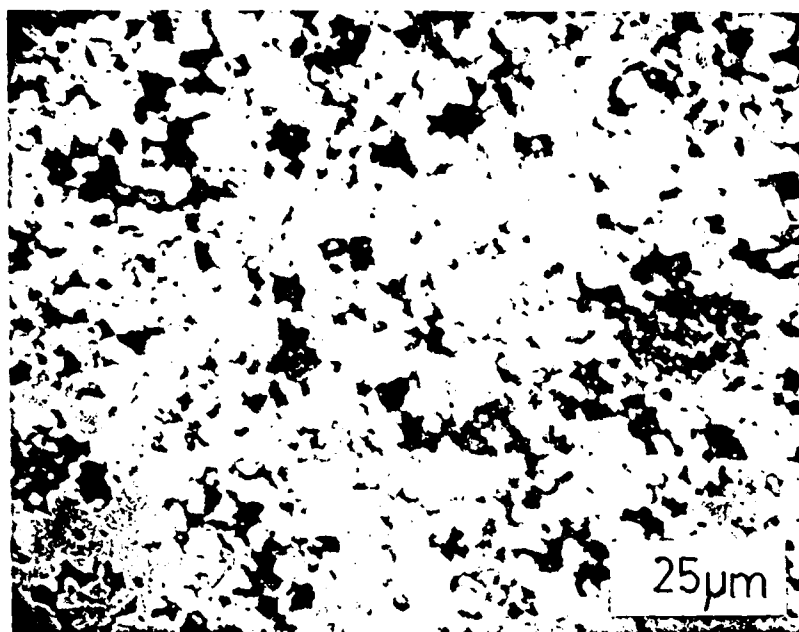
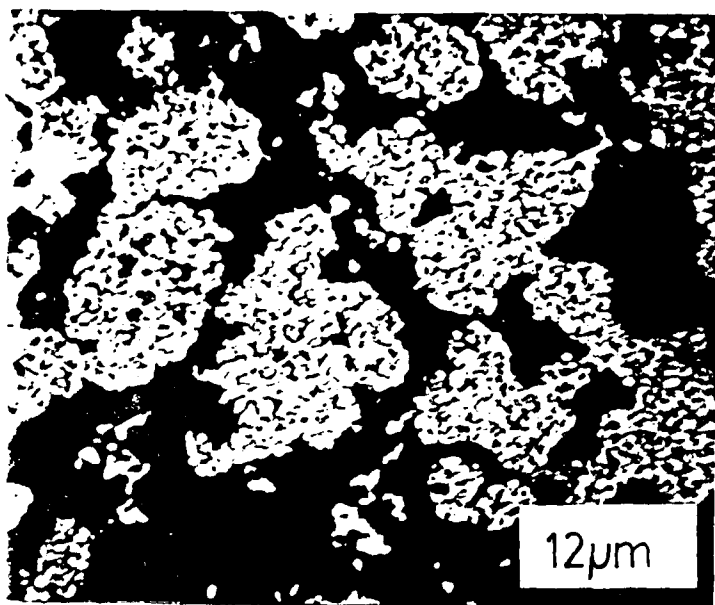
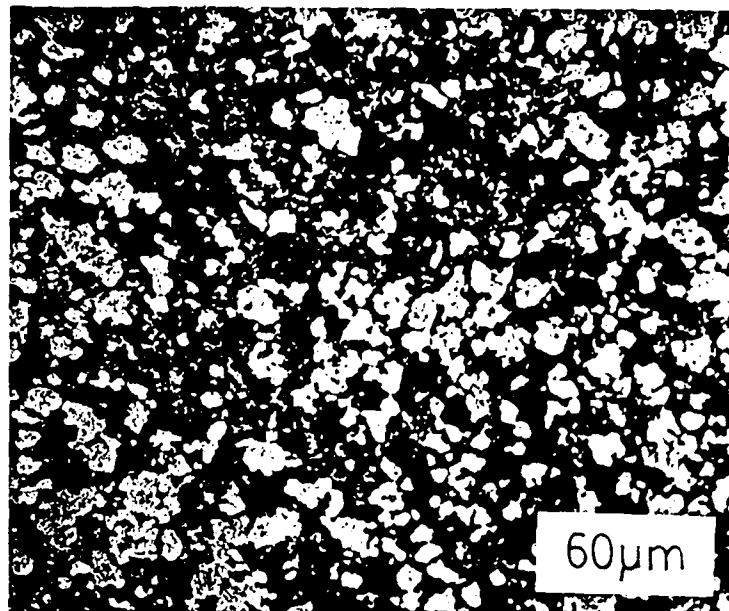


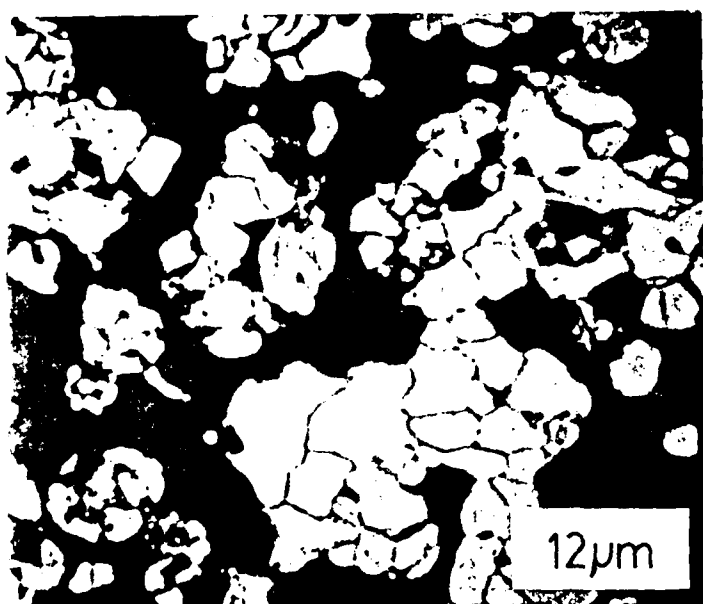
Figure 6



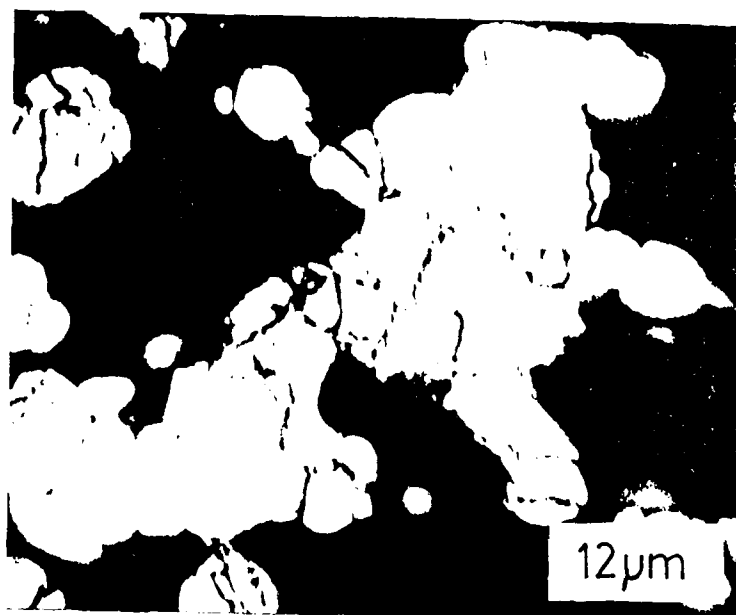
(a)



(b)

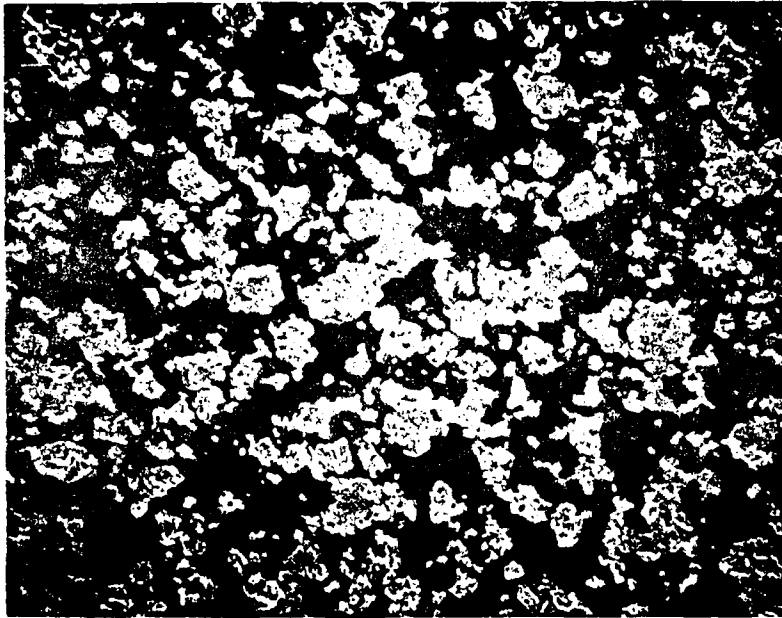


(c)



(d)

Figure 7



(a)

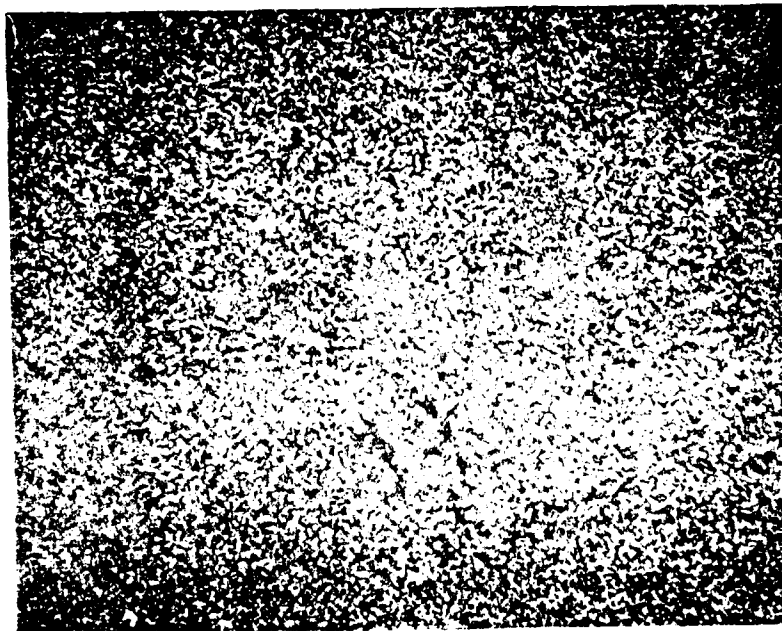


Figure 8

APPENDIX 50

L.E. Cross, K.H. Hardtl. Ferroelectrics. Kirk Othmer Encyclopedia of Chemical Technology, Vol. 10, 1980, John Wiley and Sons, NY.

F

Continued

FERROELECTRICS

The term *ferroelectric* was first used by Valasek (1) to emphasize the analogy between the nonlinear hysteretic dielectric properties of Rochelle salt [304-59-6] (sodium potassium tartrate tetrahydrate, $\text{NaKC}_4\text{H}_4\text{O}_6 \cdot 4\text{H}_2\text{O}$) and the magnetic behavior of ferromagnetic iron. More recently (2-3) the concept has been generalized and the term *ferroic* has been used to describe all materials that exhibit one or more phases showing a twin or domain structure in which the individual domain states may be reoriented by applied magnetic, electric, or elastic stress fields or combinations of such fields (see Magnetic materials).

The parameters, the state shifts, and the resulting hysteretic responses for the primary *ferroic* ferromagnets, *ferroelectrics*, and *ferroelastics* are shown in Figure 1. It is evident that in the ferroelectric the domain states differ in orientation of spontaneous electric polarization, and that the ferroelectric character is established when it is evident that the states can be transformed one to another by a suitably directed electric field. Spontaneous polarization (P_s), remanent polarization (P_r), and coercive field (E_c) are defined by analogy with corresponding magnetic quantities. Clearly, it is the reorientability of the domain state polarizations that distinguishes ferroelectrics as a subgroup from the larger class of pyroelectric crystals in the 10 polar-point symmetries (4).

For many years it appeared that ferroelectricity was a rare and unusual phenomenon, and Rochelle salt a strange accident of nature. However, with the discovery of the simple perovskite ferroelectric barium titanate [120-17-27-7], BaTiO_3 , in the early 1940s and the development of important practical applications, much more effort was focused on the problem, and by the late 1950s and early 1960s many other compounds in different structural families were shown to have ferroelectric phases.

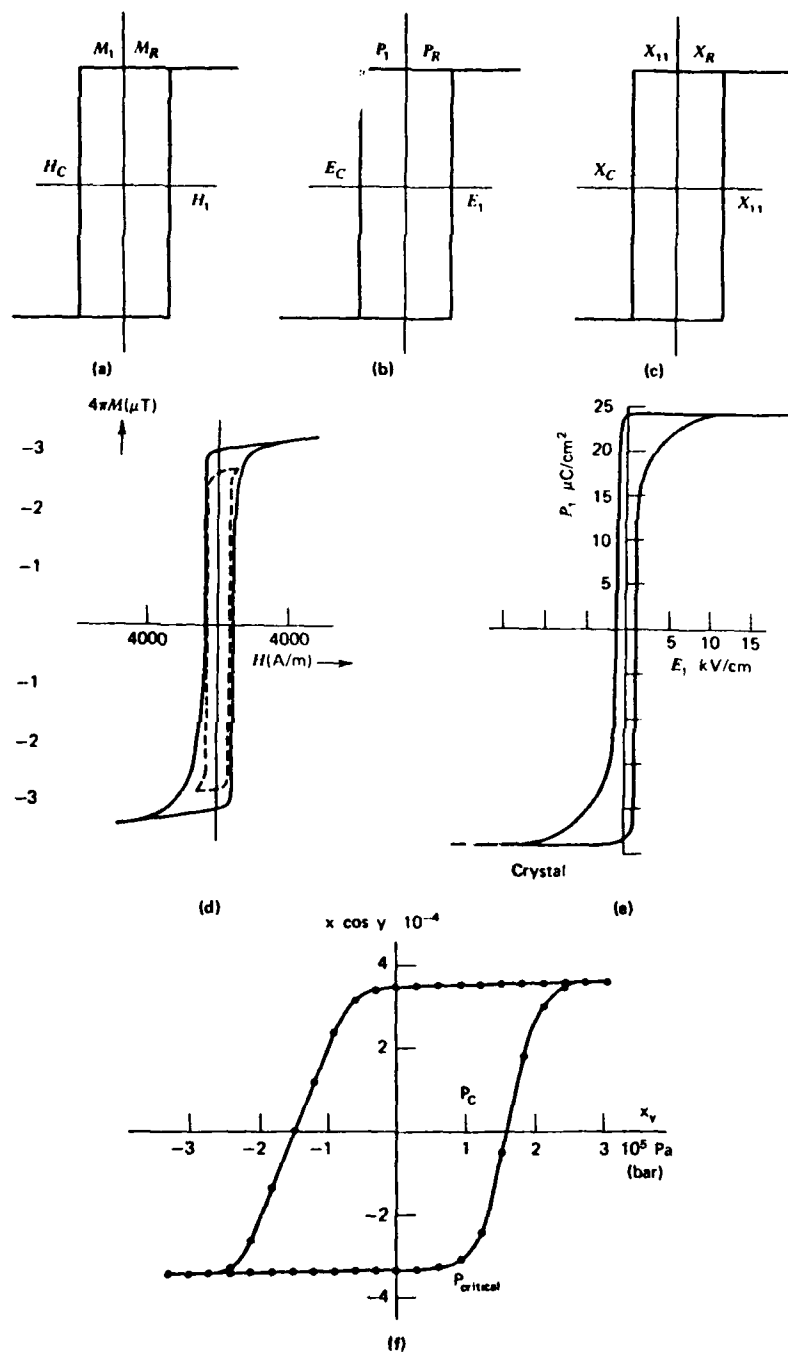


Figure 1. Primary ferroics. (a) ferromagnetic; (b) ferroelectric; (c) ferroelastic; (d) ceramic; $Co_{0.1}Fe(II)_{0.9}Fe_2O_4$, 25°C; (e) single crystal, $BaTiO_3$, 25°C; (f) single crystal, $Pb_3P_{1.6}V_{0.4}O_{10}$, 25°C. To convert tesla to gauss, divide by 10^{-4} ; to convert A/m to oersted, divide by 79.58.

At present there are more than 38 different structural families of ferroelectrics. As an example, within the perovskite, in addition to barium titanate, there are more than 60 ferroelectric compounds, and crystalline solid solutions between more than 150 of these different end-member compositions have been explored.

An excellent compendium of experimental information on ferroelectric crystals is given by Landolt-Börnstein (5-6). The listing of materials is complete up to 1973, and the experimental data have been screened by authors of international repute.

Recent theoretical developments in the field of ferroelectricity have been admirably covered in a text that also reviews application of the single crystals to pyroelectric and electrooptic devices (7).

Oxide ferroelectrics and their applications in ceramic form for piezoelectric devices are also described in considerable detail in ref. 8.

Properties

In many (not all) ferroelectrics the domain state spontaneous polarization is a decreasing function of temperature, going to zero at a phase transition temperature T_c which is called the Curie point. Above T_c a number of ferroelectrics exhibit very high, temperature-dependent dielectric susceptibility (η) such that one component of the susceptibility tensor follows a Curie-Weiss law

$$\eta_{ii} = \frac{C}{T - \theta}$$

where C is called the Curie constant and θ the Curie-Weiss temperature. Again, the terminology is taken directly from the magnetic analogy. It must be noted, however, that for the dielectric case the Curie constant C is ca 5 to 7 orders of magnitude larger than in the ferromagnet. In practice this means that very high useful dielectric susceptibilities (permittivities) persist for a wide range of temperature above T_c in the paraelectric phase. In fact, it is this high intrinsic "softness" in the dielectric response that is the phenomenon most used in the practical application of ferroelectrics, and polycrystalline ceramic ferroelectric dielectrics with relative permittivities ranging up to 10,000 are very widely used in compact disk, tubular, and multilayer capacitors (see Dielectrics below).

Although the intrinsic coupling between changes of polarization and lattice deformation (strain) through the piezoelectric or electrostrictive effects (the a_{ij} , b_{ij} , or Q_{ijkl} constants) of the paraelectric or prototype structure are quite normal, the large spontaneous polarizations of the domains in many ferroelectrics lead to substantial spontaneous strains (ca 1% in BaTiO₃ at room temperature), and it is not surprising to find that a number of ferroelectric crystals are also full or partial ferroelastics such that all, or just some, of the electric domain states may be reoriented by uniform elastic stress. Perhaps of more practical importance is the fact that the very high polarizability of the ferroelectric gives large polarization changes at low fields, so that the field-related piezoelectric and electrostriction constants (d_{ij} , e_{ij} , and M_{ijkl}) are also very large. Thus a second major area of application uses this high electromechanical coupling for efficient transduction between electrical and mechanical signals, in sonics and ultrasonics (qv), NDE (non-destructive evaluation), acceleration and pressure sensing, fusing and spark ignition, and many other transducer applications.

Ferroelectric piezoelectrics are also used extensively for broad-band filter ap-

4 FERROELECTRICS

plication, but not as yet for critical frequency control. A current challenge in ferroelectricity is to find materials with temperature-compensated elastic properties so that the strong electromechanical coupling coefficients may be used to fabricate precisely tuned bulk and surface acoustic wave filters and signal processing devices.

In ferroelectrics both P_r and P_s are strong functions of temperature, particularly at temperatures close to T_c , thus these crystals and poled ceramics have very high pyroelectric coefficients and may be applied in thermometry and in bolometric sensing devices (point detectors) of infrared radiation. A large research effort is at present focused on extending the application of pyroelectrics to long wavelength ir imaging using both vidicon and detector array schemes (see Infrared technology; Temperature measurement).

Since many ferroelectrics are high-band-gap insulating crystals, they can have good transparency in both the visible and near ir spectral regions. Qualitatively, it may be expected that the large dielectric polarizability will lead to an ability to modify the refractive index ellipsoid (indicatrix) under electric fields, and thus to high linear and quadratic electrooptic coefficients. There is much current research seeking to develop effective broad-band modulation and switching techniques for both bulk and guided optical waves by using ferroelectric electrooptic structures. Recently, polycrystalline ceramic ferroelectrics have been processed to very high densities and good optical transparency. These materials possess new parameter combinations for modulation and imaging devices.

In the single-domain state, many ferroelectric crystals also exhibit high optical nonlinearity and this, coupled to the large standing optical anisotropies (birefringences) that are often available, makes the ferroelectrics interesting candidates for phase-matched optical second harmonic generation (SHG).

Finally, a most important area of application utilizes the interaction between the dielectric polarization and the electrical transport processes in ferroelectrics. In single crystals the effects of the domain polarizations upon the drift and retrapping of photogenerated carriers give most interesting photoferroelectric effects. Of more immediate applicability, however, are the large effects of the dielectric changes at the ferroelectric phase transition upon the potential barriers at grain boundaries in suitably prepared semiconducting ceramic ferroelectrics (see Semiconductors). These barium titanate-based compositions show very strong positive temperature coefficients of resistivity (PTC effects) and are finding wide application in temperature and current control for domestic, industrial, and automotive applications (see Semiconducting PTC Materials).

Classifications

A ferroelectric crystal is a material that exhibits one or more ferroelectric phases in a realizable range of temperature and pressure. In the ferroelectric phase, the crystal is spontaneously electrically polarized and the polarization has more than one possible equilibrium orientation. To establish ferroelectricity it must be demonstrated that the polarization can be reoriented between orientation states by a realizable electric field.

Two facets of this rigorous definition can lead to practical difficulty: (1) it is often difficult to demonstrate that the persistent electrical polarizations in a crystal are an equilibrium property of the material, and not just long-lived induced electret states;

and (2) the requirement of reorientability leads to a conditional definition, which hinges on the interpretation of what should be a realizable field for any given insulator.

Since the conditions for dielectric breakdown are often difficult to establish and impossible to calculate, there must be a "fuzziness" at the edges of the subject for certain materials. This problem is severely compounded if the crystal is semiconducting or conducting, or if the structure is complex so that individual domains are difficult to identify.

There is some debate as to whether certain liquid crystal systems and polymers such as the poly(vinylidene difluorides) should be included in the class of ferroelectrics, and the problems are essentially in each case related to these facets of the definition.

Symmetry Classification. A comprehensive classification of all possible ferroelectrics has been given on symmetry grounds (9-10). It has been shown that the family of rotation and rotation/inversion operations required to get from each domain state to all other domain states, taken with the domain symmetry in the ferroelectric crystal, defines a prototype symmetry from which the spontaneous deformation parameters of the domain state can be unequivocally deduced. Conversely, for each possible prototypic point symmetry, the consequences of the appearance of spontaneous (switchable) polarization can be tabulated, so that all possible ferroelectric species accessible from a given prototype point symmetry are immediately evident.

An example of the derivation for a prototype of $4/mmm$ (D_{4h}) point symmetry is given in Figure 2, and the resultant ferroelectric species are tabulated in Table 1 using the notation of Shuvalov (10).

In many ferroelectrics it is intuitively obvious how to define P_s , since the prototype is unpolarized and thus all polarization is switchable. For ferroelectrics derived from polar prototypes, however, the definition of spontaneous polarization is not so simple and the concept of a prototype is more important. For ferroelastic crystals a similar tabulation has been given (11-12) and here the definition of the prototype is vital since spontaneous strain has no meaning without reference to the prototypic form.

It may be noted that similar symmetry-based compilations have now been given for all ferromagnetic species (13) and recently, in general, for all possible ferroic species (14-15).

Other Classification Schemes. Hard-Soft Ferroelectrics. In the earlier ferroelectric literature a classification based on the qualitative elastic properties is often suggested. Hard materials like the ceramic oxides with perovskite, pyrochlore, tungsten bronze, and bismuth oxide layer structures were contrasted with the softer organic and water-soluble compounds like Rochelle salt, potassium dihydrogen phosphate [7778-77-0] and other ferroelectric phosphates, arsenates, sulfates, nitrates, and nitrites.

Unfortunately, however, in these systems the dielectric properties are not commensurate with the mechanical properties, and the oxides are in general much softer dielectrically (Curie constant C ca 10^5 vs C ca 10^3 in water-soluble crystals). With the evolution of the subject and the development of many new materials with intermediate properties, this classification has now largely fallen into disuse.

Improper or Extrinsic Ferroelectrics. In most ferroelectric crystals, the parameter that characterizes the phase transition into the ferroelectric form (the primary order parameter for the transition) is the electric polarization, P . Elastic, piezoelectric,

6 FERROELECTRICS

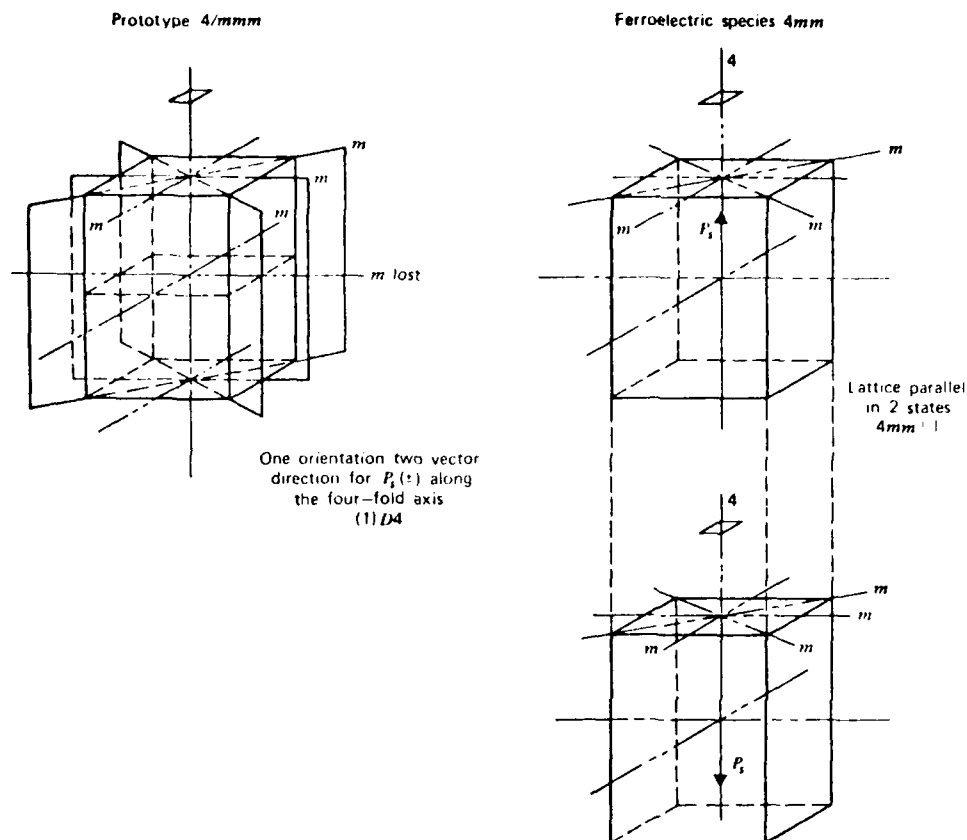


Figure 2. Pictorial representation of Shuvalov species $4/mmm(1)D4F4mm$.

optical, and thermal changes that occur may be regarded as essentially secondary consequences of the appearance of the nonzero P vector.

Recently, it has become apparent from studies of dielectrics in the gadolinium molybdate [14985-14-9] ($Gd_2(MoO_4)_3$) (16-18) and langbeinite [67320-08-5] ($Cd_2(NH_4)_2(SO_4)_3$) (19) families that ferroelectricity itself might arise as a secondary consequence in a phase change dominated by a completely different order parameter. If, as is the case in the examples quoted above, the order parameter is of different symmetry from the polarization, the dielectric properties in the prototypic phase might be quite normal and Curie-Weiss behavior entirely absent. Crystals in these families where the temperature-dependent P_s is not accompanied by high dielectric permittivity are efficient pyroelectric voltage generators and are under intensive study for pyroelectric imaging applications (20) (see Electrophotography).

Antiferroelectrics. In view of the analogy with magnetic materials, it is natural to inquire whether in dielectrics there are systems that exhibit antipolar ordering of elementary electric dipoles and thus could be considered analogous to the antiferromagnets. Unfortunately, however, in viewing almost any ionic crystal with a centric structure, sets of antipolar dipoles can be picked out and in this simple sense the classification is not meaningful.

Table 1. Shuvalov Species for Point Symmetry $4/mmm^{a,b}$

Syngony of initial phase	Kind of transition, kind of ferroelectric phase	Number of subtypes	Corresponding simple form of initial phase	Order of transition
tetragonal	$4/mmm(1)D4F4mm\parallel$	2	pinacoid	II
	$4/mmm(2)D2Fmm2\parallel$		tetragonal prism	II
	$4/mmm(4)A4Fm\parallel$	2	ditetragonal prism	I
	$4/mmm(4)A2Fn\parallel$		tetragonal bipyramid	I
	$4/mmm(8)A1F1\parallel$		ditetragonal bipyramid	I

^a Ref. 10.

^b In the Shuvalov notation the first group of symbols gives the prototype symmetry ($4/mmm$). Parentheses enclose the number of orientations; twice this number is the number of vector directions for P_r . The symbol D indicates the orientations are definite or A , arbitrary, with respect to the following axis or plane. The symbol F indicates a ferroic species, and the final block of symbols the point symmetry of the domain state. The symbol \parallel indicates that the lattices of domain states are parallel. If the symbol is absent they are mutually tilted. Simple forms are the corresponding solid figures whose faces are normal to the vector directions of P_r . The final column indicates whether the transition into the ferroic state can be continuous, II, or must be discontinuous (first-order), I.

There are, however, within a number of the ferroelectric structure families, crystals that exhibit phase changes into ferroelastic forms in which the volume of the primitive unit cell is an integral multiple of that in the prototype structure and appears to be well described as a superlattice of two interpenetrating but compensating ferroelectric-like displacement systems.

For several of these structures the similarity is further reinforced by the fact that the structure may be switched to a strongly polar ferroelectric form by a suitably oriented high electric field, and it may be demonstrated by x-ray analysis that the superlattice is now eliminated.

The term antiferroelectric is now reserved for such crystals. It is recognized that the dielectric anomalies at the phase change in these crystals are a characteristic of what would be a lower temperature ferroelectric form which has been frustrated by the slightly more stable antipolar arrangement occurring first.

The phenomenon of doubled, or split hysteresis, which occurs at the field-induced antiferroelectric-ferroelectric transitions driven by cyclic fields is an expected consequence of the phase change, but is in no way definitive without corroborating structural evidence. Similar looking double loops can occur in normal ferroelectrics, owing to defect dipoles pinning a stable domain structure, and at paraelectric-ferroelectric transitions when the behavior is markedly first order.

Domains and Switching

An internal structure of spontaneously electrically polarized domains is a characteristic feature of the ferroelectric phase, so that for most practical applications of ferroelectrics it is necessary to ascertain how this domain structure will modify the required properties and, often, how it may be controlled or eliminated to optimize performance.

The planes along which individual domains conjoin are termed domain walls, and the process of polarization reversal or reorientation under high fields is accomplished by the motion of existing walls, or by the creation and motion of new domain walls.

For each ferroelectric species, conditions for the permitted orientations of P_s in the domain structure are dictated by the prototype symmetry, which also determines whether the state will be fully, partially, or nonferroelastic. If contiguous domains are strain-distinct, the conjoining ferroelectric-ferroelastic wall has only a limited family of possible orientations which are rigorously prescribed by the conditions for dimensional compatibility between the two domains along the wall plane. Usually (but not always) the permitted wall is a common high-symmetry plane in the prototype, which was lost on the appearance of P_s . Conditions of compatibility have been generally formulated for all ferroelastic-ferroelectric walls (21-22). These ferroelastic domains in transparent ferroelectric crystals are readily observed in the polarizing microscope. Domains that are distinct in strain, a second-rank polar tensor property, must also be distinct in all other second-rank polar tensor properties, and are thus necessarily distinct in optical permeability. Examples for several different species are given in Figure 3.

The switching behavior of ferroelastic-ferroelectric walls depends markedly on the magnitude and the nature of the spontaneous domain strains, which can vary widely even between ferroelectrics in the same structure family. In cases where the strains are large, switching that is not carefully controlled can cause stress concentrations sufficient to crack the crystal, and fatigue effects are often evidenced on repeated switching. The problem is most acute in polycrystalline ceramic ferroelectrics, which have to be poled to a high saturation remanence for piezoelectric applications (see under Applications). In these systems both the elastic and electrical boundary conditions on the individual crystallites are complex functions of the crystallite size, size distribution, ferroelectric phase assemblage, minor phase additions, and poling conditions. Residual stresses left after poling do cause slow continuing changes in the domain assemblage and the continuous aging which is an undesirable feature in the properties of these ceramics.

For nonferroelastic domains, i.e., antipolar domain structures originating from centric prototypes, all conjoining planes are elastically compatible and wall structures generally appear more tortuous. Generally, planes parallel to P_s appear to be preferred and would be expected to be so since the normal component of displacement across such planes is preserved. Figure 3c and d show typical antipolar structures in BaTiO_3 , and in triglycine sulfate [513-29-1], $(\text{NH}_2\text{CH}_2\text{COOH})_3\text{H}_2\text{SO}_4$ (TGS).

Theoretical calculations (23-24) and experimental observation (25-26) confirm that the width of such simple ferroelectric walls is exceedingly narrow, with the polarization changing abruptly across only a few unit cells of the structure.

Very extensive studies have been made of the switching behavior of simple antipolar ferroelectric domains for BaTiO_3 (27), TGS (28), and other simple ferroelectrics (29). The kinetics can be described by measuring the time taken for reversal of the polarization under different levels of d-c driving field E and has been shown to follow an equation of the form

$$t_s \propto \exp(\alpha/E)$$

where t_s is the time required for switchings, α is a constant with the dimensions of a field (called the activation field), and E is the applied driving field.

The equation is valid for several materials over quite a wide range of fields, but at very high field levels the timing appears to change over to a power law of the form

$$t_s \propto E^{-n}$$

where n varies from 1 to 7 in different systems (30).

In BaTiO_3 the bulk switching relation has been effectively correlated to the individual domain wall motion which appears to follow a relation (31)

$$v = v_{\infty} \exp(-\delta/E)$$

where the constant δ appears to depend somewhat on the defect concentration in the crystal, v is the wall velocity under driving field E , and v_{∞} a constant for the crystal.

It was noted quite early (32) that since the domain wall is very narrow, the energy gained by moving the wall just one lattice constant is necessarily very much smaller than the wall energy itself, and thus true continuous sidewise motion of the wall, as occurs for many magnetic domain walls, is most unlikely.

The model that does appear to explain the behavior is that the apparent sidewise motion of walls is caused by the nucleation and growth of step-like protrusions on existing 180° walls. An analysis of this model was given (33) to explain the exponential behavior in the low field region. The model was then extended (34) to account for the power law behavior, and a more recent general formulation covering both regimes has been published (35).

The narrow domain wall has most important consequences in the major practical application of ferroelectrics in capacitor dielectrics. Since critical size nuclei occur only very infrequently at low fields, reversible wall motion does not contribute in a major way to the dielectric response, and the capacitor engineer must manipulate the soft single-domain ferroelectric and the paraelectric permittivity to satisfy system requirements.

Similarly, the device engineer who wishes to exploit the apparent bistability of the dielectric hysteresis must be aware that the ferroelectric coercivity is due to the "knee" on an exponential curve, and that given time or frequent reverse pulsing, the ferroelectric may change polarization state for fields much below the apparent 60 Hz coercivity.

Ferroelectric Materials

Perovskites. The simple cubic perovskite structure, which is the high temperature form for many mixed oxides of the ABO_3 type, was one of the first simple structures to exhibit compounds with ferroelectric properties and is still probably the most important ferroelectric prototype.

The very simple cubic structure (point symmetry $m3m$) (Fig. 4) is made up of a regular array of corner-sharing oxygen octahedra with smaller highly charged cations like Ti, Sn, Zr, Nb, Ta, W, etc, occupying the central octahedral B site, and lower-charged larger cations like Na, K, Rb, Ca, Sr, Ba, Pb, etc, filling the interstices between octahedra in the larger 12-coordinated A sites.

The simple ABO_3 compounds, BaTiO_3 [12060-00-3], PbTiO_3 [12060-01-4], NaNbO_3 [12031-09-2], KNbO_3 [12030-85-2], AgNbO_3 [12309-96-5], WO_3 [1314-35-8], have interesting high temperature ferroelectric or antiferroelectric phases. The perovskite structure is, however, also tolerant of a very wide range of multiple cation substitution on both A and B sites, so that many more complex compounds such as $(\text{K}_{1/2}\text{Bi}_{1/2})\text{TiO}_3$, $\text{Pb}(\text{Fe}_{1/2}\text{Ta}_{1/2})\text{O}_3$, $\text{Pb}(\text{Co}_{1/4}\text{Mn}_{1/4}\text{W}_{1/2})\text{O}_3$ can be prepared.

Barium titanate was the first perovskite-type compound shown to be ferroelectric

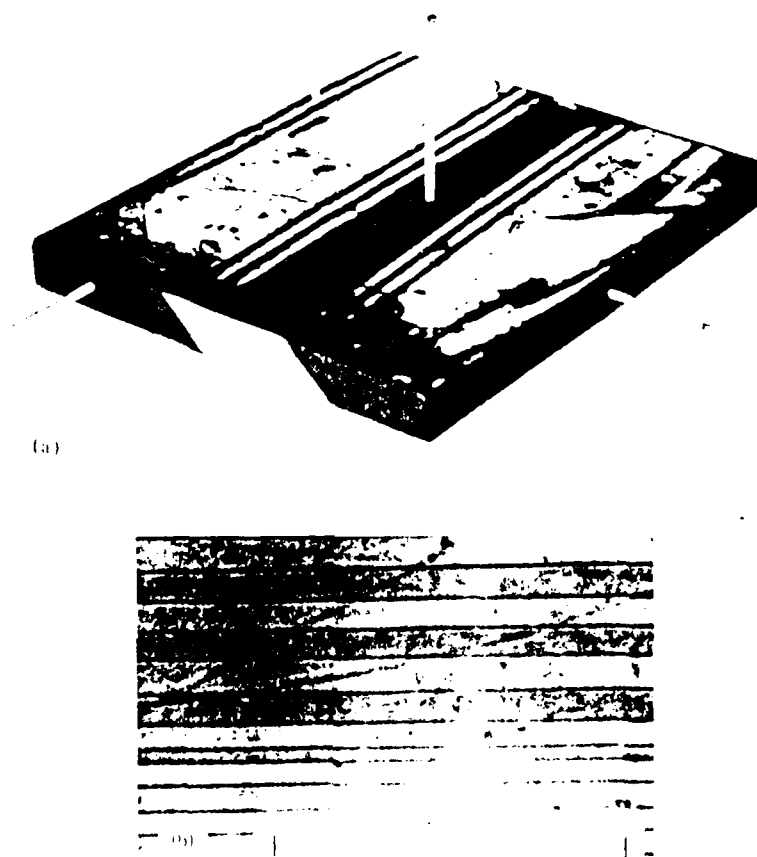


Figure 3. Examples of ferroelastic-ferroelectric and antiparallel domains. (a) Ferroelastic-ferroelectric 90 domains in BaTiO_3 . Crystal dimensions are ca $0.7 \times 0.7 \times 0.05$ mm. Polarized NaD light. Pins indicate orientations of tetragonal c axis. (b) Ferroelastic-ferroelectric domains in gadolinium molybdate $\text{Gd}_2(\text{MoO}_4)_3$. ($\times 50$) (c) Antiparallel domains in triglycine sulfate. Top and bottom surface of a plate cut perpendicular to the polar b axis, etched in water to reveal the structure. (d) Antiparallel domain in BaTiO_3 , c domain crystal revealed by etching in HF.

(ca 1943) and is to date the most thoroughly investigated ferroelectric material (36). This is essentially a consequence of its relatively simple lattice structure (see Fig. 4), allowing, by means of simple models, an understanding of ferroelectric phenomena. In addition, BaTiO_3 proved to be ideal in applications because its electrical properties can be controlled within a wide range by means of mixed crystal formation and doping.

The characteristic feature of the BaTiO_3 unit cell (Fig. 4) is the TiO_6 -octahedra, which because of their high polarizability, essentially determine the dielectric prop-

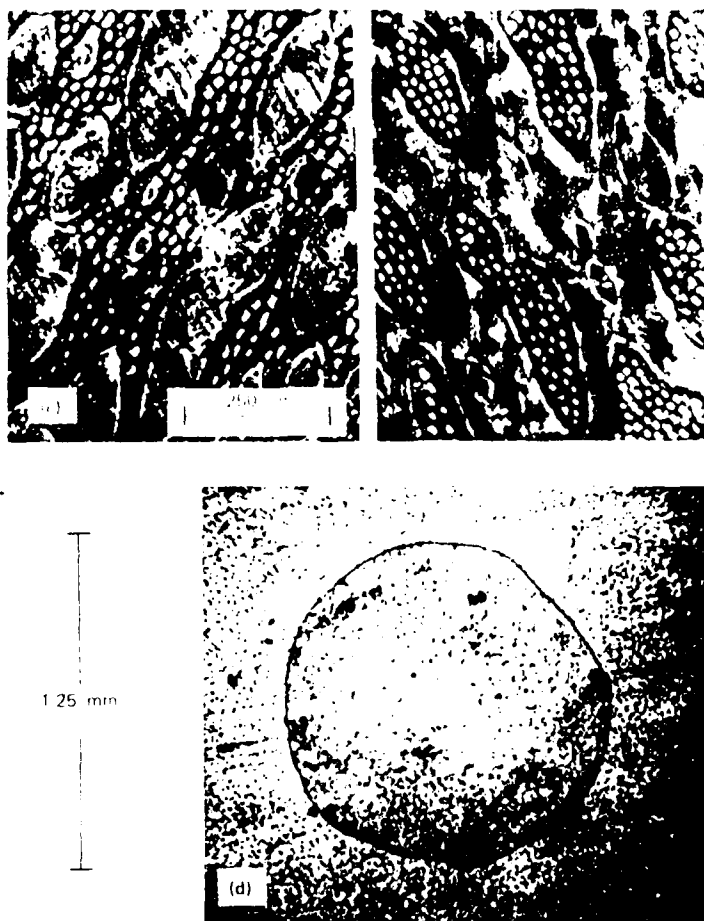


Figure 3. (Continued)

erties. The high polarizability is due to the fact that the small Ti^{4+} ions have relatively more space within the oxygen octahedra. The cubic unit-cell of Figure 4 with the Ti^{4+} ion in the center of the oxygen octahedron is, however, stable only above the Curie point T_c of about 130°C . Below T_c the Ti^{4+} ions occupy off-center positions. This transition to the off-center position at T_c results in a series of important physical consequences (Fig. 5). The crystal structure changes from cubic ($T > 130^\circ\text{C}$) via tetragonal ($+5^\circ\text{C} < T < +130^\circ\text{C}$; $c/a = 1.01$) and orthorhombic ($-90^\circ\text{C} < T < +5^\circ\text{C}$) to rhombohedral ($T < -90^\circ\text{C}$). At the same time a spontaneous polarization P_s ($26 \mu\text{C}/\text{cm}^2$ at room temperature) appears, the direction of which is in the tetragonal phase along one of the 6 edges, in the orthorhombic phase along one of the 12 surface diagonals, and in the rhombohedral phase along one of the 8 space diagonals of the ideal cubic unit cell. The direction of P_s can be switched by high electrical field (ca $1\text{--}2 \text{ kV}/\text{cm}$) between the different crystallographic allowed positions which are characteristic in each ferroelectric phase.

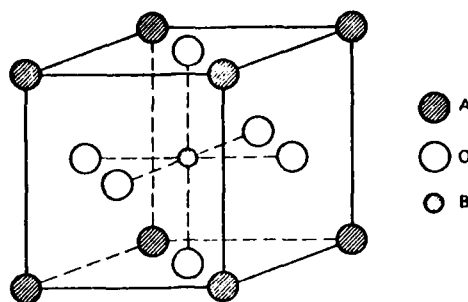


Figure 4. Cubic ($m\bar{3}m$) prototype structure of perovskite-type ABO_3 compounds. For $BaTiO_3$, A = Ba^{2+} , B = Ti^{4+} , and O = O^{2-} .

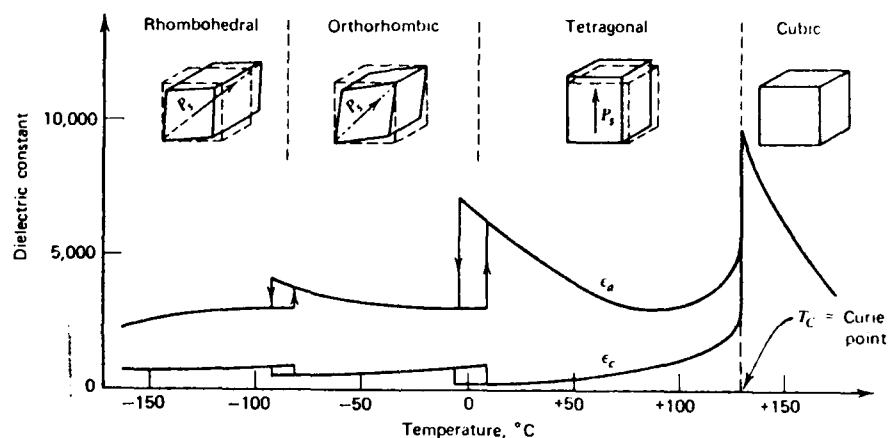


Figure 5. Crystal structure; lattice distortion of the unit cell and direction of spontaneous polarization; dielectric constant in dependence on temperature for a $BaTiO_3$ single crystal. The subscripts a and c relate to orientations parallel and perpendicular to the tetragonal axis, respectively.

At the temperatures of the phase transitions, maxima of the dielectric constant up to 10,000 are found. Moreover, in the ferroelectric state below T_c the material becomes pyroelectric and shows high piezoelectric activity.

Perovskite-type compounds and especially $BaTiO_3$ have the ability to form extensive solid solutions. By this means a wide variety of materials with continuously changing electrical properties can be produced in the polycrystalline ceramic state. By substituting Ba^{2+} ions with Pb^{2+} ions, T_c can be increased linearly up to 490°C for a 100% Pb substitution. In the same manner, T_c can be continuously decreased by the substitution of Ba^{2+} with Sr^{2+} or of Ti^{4+} with Zr^{4+} or Sn^{4+} (Fig. 6). Simultaneously with the change of T_c by formation of solid solutions, the low temperature phase transitions between the tetragonal orthorhombic and orthorhombic-rhombohedral phases are shifted in a rather complex manner.

PbZrO₃-PbTiO₃-Based Materials. Since the middle of the 1950s, solid solutions of $PbZrO_3$ - $PbTiO_3$ ceramics with perovskite structure have gained rising interest because of their superior piezoelectric properties (8,37-38). The phase diagram of the

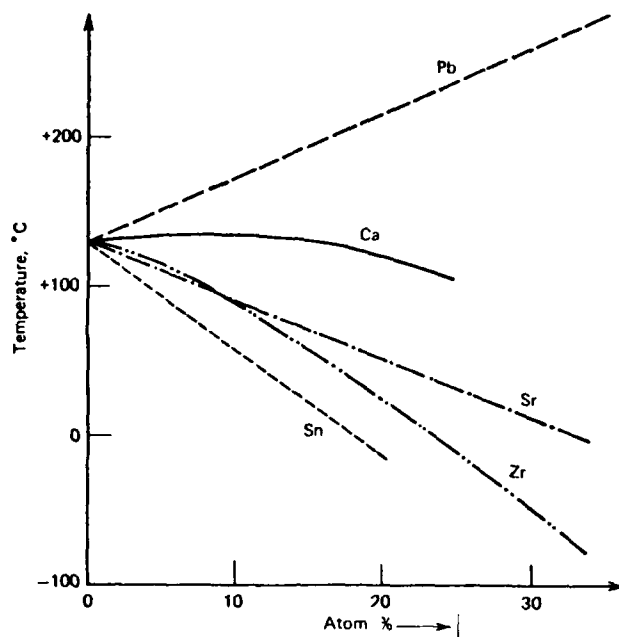


Figure 6. Shift of the Curie point of BaTiO_3 by substitution of Ba^{2+} ions by Pb^{2+} , Ca^{2+} , or Sr^{2+} ions, or of Ti^{4+} ions by Zr^{4+} or Sn^{4+} ions (8).

$\text{Pb}(\text{Zr}_x\text{Ti}_{1-x})\text{O}_3$ system is shown in Figure 7. At high temperatures above T_c , the ideal cubic paraelectric structure is stable, where no ferroelectric phenomena such as spontaneous polarization appear. At room temperature the materials are ferroelectric and show, for Ti-rich compositions ($0 \leq x \leq 0.52$), a tetragonal distortion of the unit cell, whereas compositions with lower Ti content ($0.52 \leq x \leq 0.94$) have rhombohedrally distorted unit cells. Both phases are separated by a morphotropic phase boundary at $x = 0.48$. Compositions near the Zr side of the system ($0.94 \leq x \leq 1$) are antiferroelectric with orthorhombic structure. The direction of the spontaneous polarization P_s is along one of the edges of the unit cell for tetragonal distorted compositions and along one of the space diagonals for rhombohedral distorted compositions.

Today a third or even a fourth and fifth phase of a complex perovskite as, for example, $\text{Pb}(\text{Mg}_{1/3}\text{Nb}_{2/3})\text{O}_3$ is added in addition to PbTiO_3 and PbZrO_3 when forming the solid solution (39). In the same manner ca 20 different elements with similar ionic radii can be substituted in place of Mg or Nb, leading to a huge number of possible combinations and a multitude of compositions having, however, generally comparable properties. At low concentrations of a complex perovskite addition, the phase relationships of the quasi-binary composition are maintained. Increasing amounts of a complex perovskite reduces T_c and pseudocubic phases begin to appear.

Taken together with the fact that there is often a wide range of crystalline solid solubility between end-member compositions, and that the ferroelectric and antiferroelectric Curie temperatures and consequent properties appear to mutate continuously with fractional cation substitution, the perovskite system has the desired

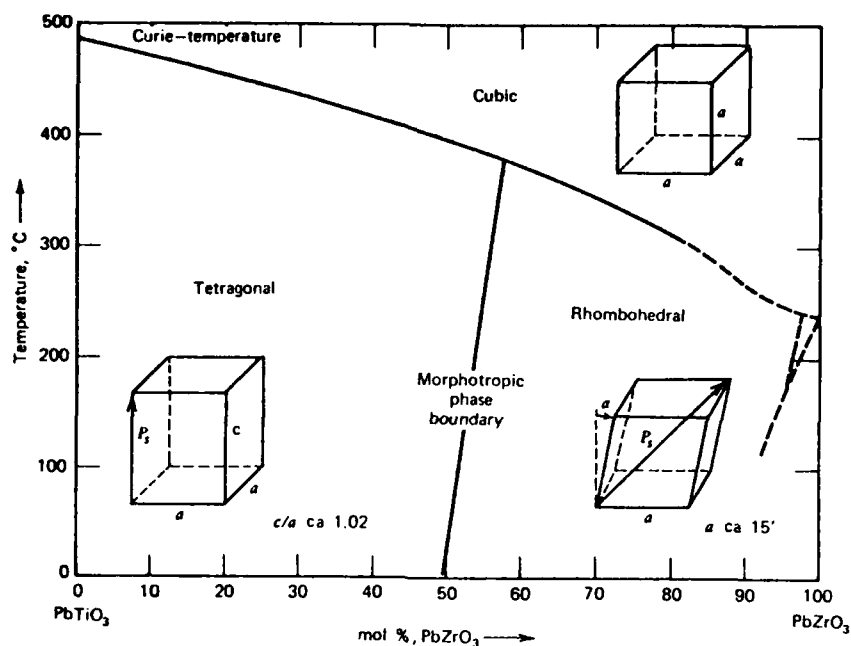


Figure 7. Phase diagram of the $\text{Pb}(\text{Zr,Ti})\text{O}_3$ system.

versatility for the very extensive applications discussed in the following sections on ferroelectric ceramics.

Perovskite-Related Octahedral Structures. Lithium Niobate. LiNbO_3 [12031-63-9] and LiTaO_3 [12031-66-2] have a structure related to the perovskites, but of lower symmetry ($3m$), due to the fact that the oxygen octahedra share edges (Fig. 8). In sequence along the trigonal c axis in the low temperature ferroelectric phase, the octahedra are occupied in the sequence Nb(Ta), vacancy, Li, Nb(Ta), vacancy, and Li (41).

Because of the very high Curie temperatures (ca 1200 $^{\circ}\text{C}$ in LiNbO_3 , 620 $^{\circ}\text{C}$ for LiTaO_3), the prototypic character has not been well established in the niobate, but judging from the tantalate it does appear that the Nb ion is in the center of the oxygen octahedron, whereas the lithium ion is in dynamical equilibrium between displaced positions above and below the triangular ring of oxygens (40).

The ion displacements in the ferroelectric phase are exceedingly large, corresponding to the observed spontaneous polarizations of 50 $\mu\text{C}/\text{cm}^2$ in the tantalate and ca 70 $\mu\text{C}/\text{cm}^2$ in the niobate. Because of these large displacements, poling is usually carried out at elevated temperatures (42), and switching at room temperature was only recently demonstrated with very high pulsed fields. (43).

Lithium niobate is widely used in the single-domain form for both piezoelectric (44) and electrooptic devices (45). The tantalate has a wide application in simple pyroelectric point detectors (46) and, more recently, for acoustic wave devices (47).

Tungsten Bronze Structures. The tungsten bronze family has an oxygen octahedral framework structure that is much more open than the simpler perovskite structure (Fig. 9). The basic tetragonal unit cell (Fig. 9) contains 10 BO_6 octahedra corner-linked

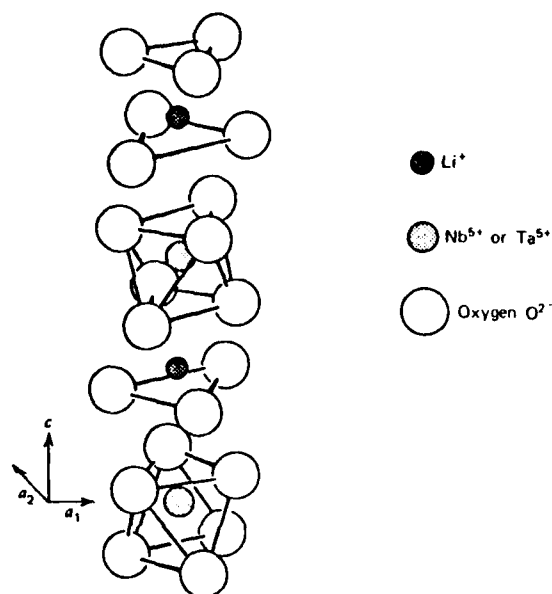


Figure 8. Structure of ferroelectric LiNbO_3 and LiTaO_3 (40).

to form square, triangular, and pentagonal tunnels that extend through the structure along the 4-fold symmetry (c) axis (48). The c axis linkage is regular, but in the a and b directions the linkage is markedly puckered (see also Copper alloys).

There are two types of A sites (A_1, A_2) that can be occupied by large monovalent, divalent, or trivalent ions, two different B sites (B_1, B_2) that are usually occupied by smaller, highly charged cations (Nb, Ta, W, Ti), and a small C site which may be vacant or occupied by Li (49-51).

Lead metaniobate [12034-88-7], PbNb_2O_6 (52), and metatantalate [12065-68-8], PbTa_2O_6 (53), appear to be anomalous as bronzes, and in both these useful ferroelectrics the bronze form is a metastable structure at room temperature (54).

In general, the bronzes appear to be solid solutions of at least two components, and a certain degree of disorder appears conducive to stabilizing the structure.

Among compounds of interest besides PbNb_2O_6 and PbTa_2O_6 are $\text{Ba}_x\text{Sr}_{1-x}\text{Nb}_2\text{O}_6$ and $\text{Ba}_2\text{NaNb}_5\text{O}_{15}$ [12323-03-4]. The metaniobate is still widely used in poled ceramic form as a low Q piezoelectric transducer (55-56) the $\text{Ba}_{0.5}\text{Sr}_{0.5}\text{Nb}_2\text{O}_6$ [37185-09-4] composition in single-crystal form in pyroelectric point detectors (57-58), and the barium sodium niobate and various similar derivative compositions for their very high nonlinear optical properties (59-60).

Bismuth Oxide Layer Structures. The structural arrangements in these materials are typified by $\text{PbBi}_2\text{Nb}_2\text{O}_9$ [12431-20-8] (Fig. 10). The structure may be visualized simply as a stacking of regular perovskite-like $(\text{PbNb}_2\text{O}_7)^{2-}$ double sheets of corner-linked NbO_6 octahedra interleaved by $(\text{Bi}_2\text{O}_2)^{2+}$ layers along the tetragonal 4-fold axis. It appears possible to develop structures of this character with single (Bi_2WO_6) [13595-86-3], double $(\text{PbBi}_2\text{Nb}_2\text{O}_9)$, triple $(\text{Bi}_4\text{Ti}_3\text{O}_{12})$ [12010-77-4], and up to five perovskite layers interleaving the bismuth oxide sheets (61). Extensive cation replacement appears possible within the perovskite layers, though the conditions are

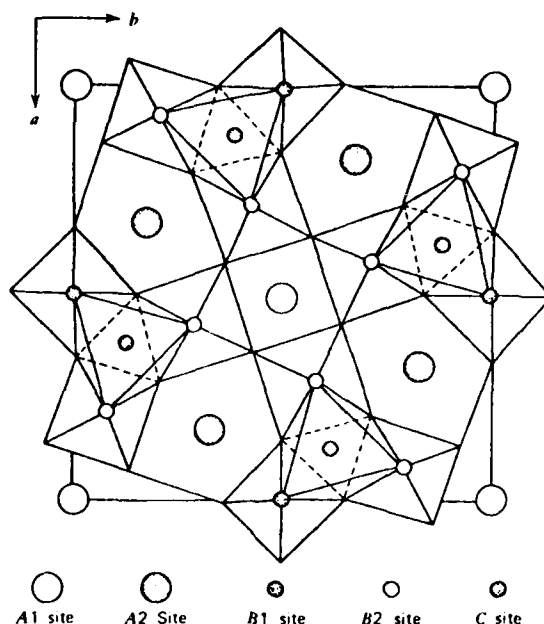


Figure 9. Projection of the tungsten bronze structure looking down the tetragonal c axis (48).

rather more restrictive than in pure perovskites (62), but bismuth cannot be replaced by any comparable trivalent ion in the $(\text{Bi}_2\text{O}_2)^{2+}$ sheets (63).

In almost all these sheet structures, the ferroelectric phases have spontaneous polarizations that lie in the plane of the perovskite sheets, and the ferroelectric symmetry is $mm2$ (64).

Bismuth titanate is unique in transforming directly at 675°C to a low-symmetry monoclinic ferroelectric phase (65) in which the domain states have a polarization vector tilted slightly ($\text{ca } 4^\circ$) out of the plane of the sheet (66).

This tilted vector gives a very small monoclinic shear to the unit cell (less than 2 minutes of arc) but a major tilt to the optical indicatrix ($\text{ca } 60^\circ$) (67). The very unusual optical situation in this crystal has been used for optical image storage (68-69) and to develop an optical page composer for holographic information storage (70) (see Holography).

Pyrochlore Structures. Ferroelectricity was first discovered in $\text{Cd}_2\text{Nb}_2\text{O}_7$ [12187-14-3] in 1952 (71). The structure is again based upon a corner-sharing arrangement of NbO_6 octahedra with the larger Cd^{2+} ions and the extra set of oxygens occupying the interstices. A projection of the structure onto the $[110]$ plane is shown in Figure 11. This family, like the lithium niobate family, is very restricted in the cation substitutions that can be made, and similar properties have been found only in the $\text{Cd}_2\text{Ta}_2\text{O}_7$ [12050-35-0] and corresponding lead compounds $\text{Pb}_2\text{Ta}_2\text{O}_7$ [12065-68-8], $\text{Pb}_2\text{Nb}_2\text{O}_7$ [12059-64-2]. In all cases the Curie temperatures are low, below 200 K (72).

Very recently, very strong ferroelectric behavior ($T_c > 1300^\circ\text{C}$) in $\text{Sr}_2\text{Nb}_2\text{O}_7$ [12201-67-1] has been observed (73), but the structure type is monoclinic and more complex than the cubic pyrochlore.

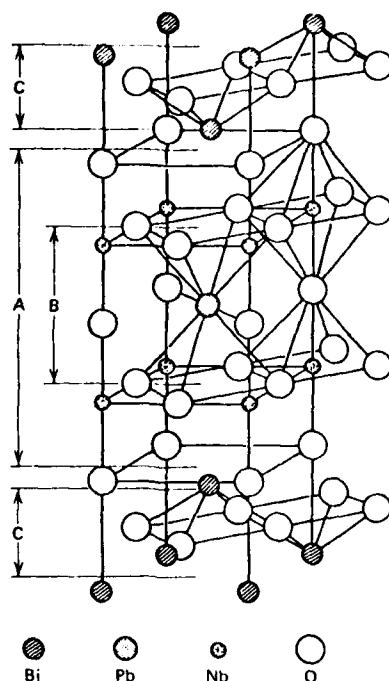


Figure 10. One-half of the tetragonal ($4/mmm$) unit cell of $\text{PbBi}_2\text{Nb}_2\text{O}_9$. A denotes the perovskite layer (PbNb_2O_7) $^{2-}$; B denotes the unit of a hypothetical PbNbO_3 ; C denotes the $(\text{Bi}_2\text{O}_2)^{2+}$ layers.

KDP Family. Potassium dihydrogen phosphate and the isomorphous rubidium and cesium phosphates RbH_2PO_4 [13774-16-8], CsH_2PO_4 [18649-05-3], and arsenates (RbH_2AsO_4 [13464-57-8], CsH_2AsO_4 [16331-85-4]) were the first major family of ferroelectrics to be discovered (74-75). The structure is relatively simple (Fig. 12), being based on an arrangement of PO_4 tetrahedra in layers so that the upper corners of the tetrahedra in one layer are hydrogen bonded to the lower corners of the tetrahedra in the next successive layer. The PO_4 tetrahedra alternate with potassium atoms at distances $c/2$ apart in the tetragonal unit cell (76).

It is of interest that the hydrogen bonds which play a major role in the ferroelectric ordering, lie in planes orthogonal to what becomes the polar axis of the ferroelectric orthorhombic phase. The symmetry above T_c is $\bar{4}2m$ and in the prototypic structure the protons are tunneling between off-center positions along the bond direction.

In the single-domain ferroelectric phase, the protons order along the bonds in such a manner that they are all near upper or lower oxygens of the tetrahedral phosphate groups, and it is this coupling that pushes the phosphorus and potassium from the high-symmetry positions giving rise to a switchable moment along the c axis.

The key role of the hydrogen bonds in the transition leads, as expected, to a strong dependence of the phase transition temperature upon deuteration (77) and DKDP, KD_2PO_4 [13761-79-0], is used in some electrooptic devices (78) because of its larger longitudinal electrooptic coefficients in the paraelectric phase.

In fact, all major applications of KDP family materials use properties in the

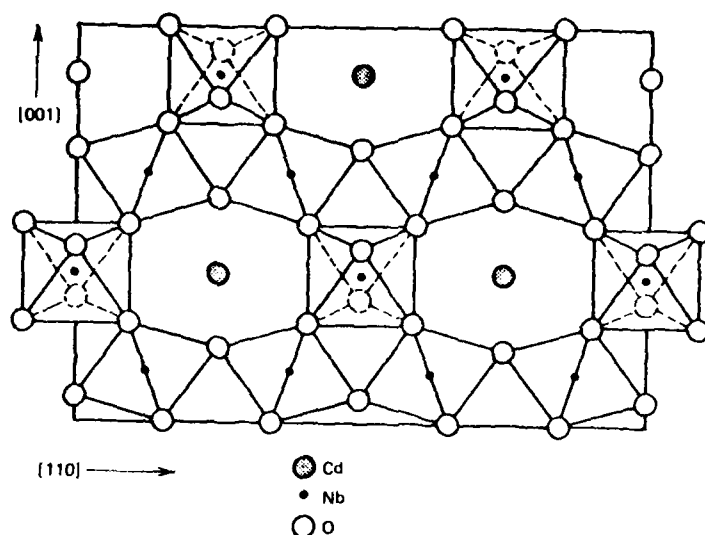


Figure 11. Schematic projection of the cubic ($m\bar{3}m$) structure of the $\text{Cd}_2\text{Nb}_2\text{O}_7$ on $[110]$ plane. The Cd ions that overlap the Nb ions at $(1/8, 1/8)$ etc, and the seventh set of oxygens that are located above and below the Cd ions are not shown.

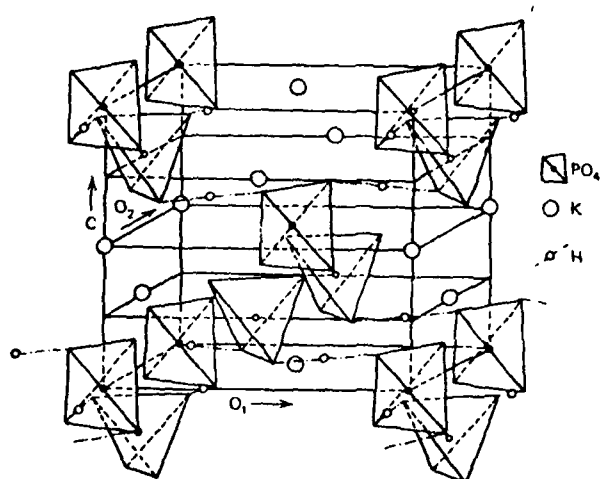


Figure 12. Unit cell of KH_2PO_4 in tetragonal 4_2m prototype structure (76).

paraelectric prototypic form. Frequently, the properties are far from ideal, but the tractable water solution growth of KDP has permitted large crystals of excellent quality, which are difficult if not impossible to duplicate in the more desirable refractory oxides.

Triglycine Sulfate. Strictly speaking, triglycine sulfate (79-80) (TGS) is not representative of a wide range of isomorphous structures, although the isomorphous

selenate [920-25-2] (81) and fluoroberyllate [2396-72-7] (82) do have similar prototypic structures. There is, however, a much wider range of glycine-containing ferroelectrics (5,6) in which the glycinium molecule plays a major role and (TGS) is suitably illustrative.

A projection of the TGS structure along the c axis of the monoclinic unit cell is shown in Figure 13. The unit cell contains three inequivalent glycine molecules labeled I, II, and III, and all participate to some extent in the development of the ferroelectric moment which is confined to the b direction ($\pm P_b$). A major part of this moment does, however, appear associated with the planar glycinium ion which makes an angle of 12.5° with the plane at $b = 1/4$. Above T_c this plane (and the corresponding plane at $b = 3/4$) become mirror planes owing to random statistical distribution of the glycinium I ions, which order at the Curie temperature (79).

TGS has a near second-order phase change to the ferroelectric form at 49°C , and exhibits a spontaneous polarization P_s ca $4 \mu\text{C}/\text{cm}^2$ at room temperature (80). The convenient location of T_c and the easy water solution growth of very perfect TGS crystals make this a popular single crystal material for pyroelectric detectors (81), and particularly for the demanding application in pyroelectric vidicon systems (82).

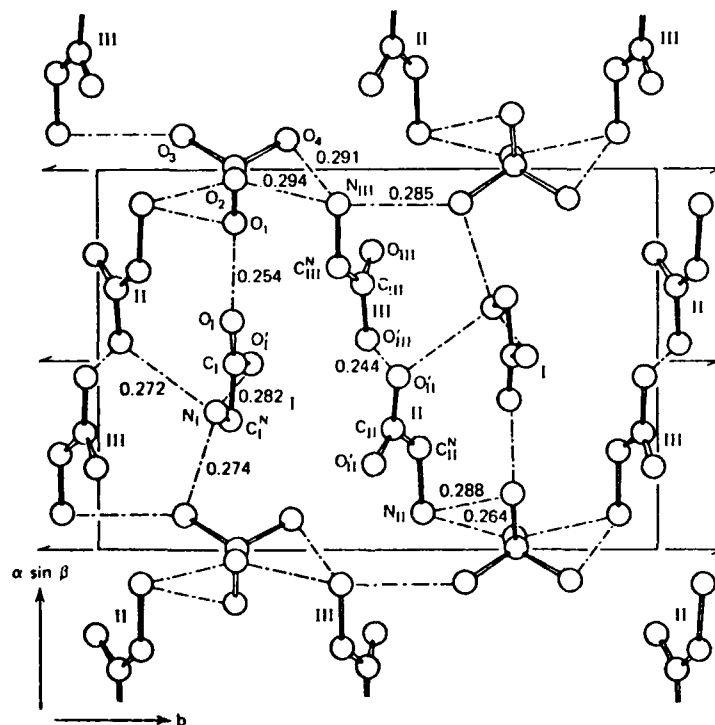


Figure 13. Projection of the structure of triglycine sulfate along the monoclinic c axis (81). Bond lengths are shown in nanometers.

Preparation of Ferroelectric Ceramics

Ferroelectric ceramics are composed of oxide compounds having generally the perovskite structure (Fig. 4), eg, BaTiO_3 or $\text{Pb}(\text{Zr,Ti})\text{O}_3$. They are produced in successive steps as follows (see also Ceramics).

Powder Preparation. Conventional (Mixed Oxide) Methods. As raw materials, mostly oxides (TiO_2 , ZrO_2 , PbO) or carbonates (BaCO_3 , SrCO_3 , CaCO_3) are used which have to meet certain application-dependent specifications with respect to purity and grain size distribution. The final powder product with perovskite structure is formed by a solid state reaction (calcination) of these starting raw materials (8,83). A typical example is



Usually the required product is a fully homogeneous compound having perovskite structure with small particle size ($<1\ \mu\text{m}$). The solid-state reaction occurs by solid state diffusion with a relatively slow diffusion rate. Therefore, small diffusion distances or high calcination temperatures are necessary to complete the reaction. Since, however, high calcination temperatures will result in coarse-grained powders having unsuitable sintering properties, the diffusion distance must be minimized. This can be achieved by intimate mixing or milling procedures (dry or wet using water, alcohol etc) of the ingredients. Mixing and milling times are also limited, however, because long times lead to increasing impurity concentrations by mechanical abrasion of the milling equipment.

The powder preparation usually proceeds with due regard to the principal facts just mentioned, as follows: (1) weighing of the raw materials; (2) intimate mixing or milling (dry or wet) for 1 to 10 h using porcelain, SiO_2 , or Al_2O_3 materials for equipment; (3) calcination 1 to 10 h, 1050 to 1200°C (800 to 900°C for Pb-containing materials); and (4) again intimate mixing or milling (dry or wet) for 1 to 10 h for a further homogenization and for crushing of agglomerates.

Wet Chemical Methods. Preparation by wet chemical methods affords a modern means for achieving high homogenization on the atomic scale during calcination of the different elements that form the perovskite compound. Moreover, these methods include the possibility of producing very pure materials.

Currently several methods for wet chemical preparation of ferroelectric ceramics are used (mostly on laboratory scale):

(1) Thermolysis of compounds consisting of the critical elements in an exactly defined stoichiometric ratio in a closely packed arrangement on the atomic scale. Examples are: preparation of LaFeO_3 [12022-43-4] from $\text{La}[\text{Fe}(\text{CN})_6]$ (84) or of BaTiO_3 from $\text{BaTiO}(\text{C}_2\text{O}_4)_2 \cdot 4\text{H}_2\text{O}$ (85).

(2) The homogeneous distribution of the different ions in a liquid solution that is nearly ideal, even on an atomic scale, can be transferred into the solid state by proper chemical processes: coprecipitation of the different ions from aqueous solutions (eg, preparation of $\text{Pb}(\text{Zr,Ti})\text{O}_3$ (86); precipitation from metal alcoholates by hydrolysis (eg, BaTiO_3) (87) and $(\text{Pb,Lu})(\text{Zr,Ti})\text{O}_3$ (88) (see Alkoxides, metal); precipitation from aqueous solutions by spraying into a liquid in which there is no solubility (eg, preparation of BaTiO_3 by spraying an aqueous Ba-Ti-citrate solution into concentrated ethanol) (89); reaction of an aqueous citrate solution with a polyhydric alcohol (eg, ethylene glycol) to form an organic glass (polyester resin) (90).

The preparation methods according to (1) are restricted to the existence of a suitable compound and are not suited for the preparation of mixed crystals or doped materials. The last two methods according to (2) seem to be most universally applicable.

The formation of the perovskite compound again occurs by a calcination process that works at much lower temperatures if compared with the conventional mixed-oxide methods.

Shaping. Various amounts of binders (mostly organic compounds) are added to the powders for better rheological properties. "Green" ceramic bodies (density ca 50-60%) can then be easily shaped by a large variety of conventional ceramic processes such as pressing (disks), extrusion (tubes), rolling, and slip casting. Thin sheets (<50 μm) are made by pouring a controlled thickness of special slip onto a polished metal belt, then the slip is dried and stripped.

Sintering. The green ferroelectric ceramics are sintered at high temperatures for 1-10 h to achieve a high density, 95-100% of the theoretical. After sintering, the ceramic body is built up of closely packed grains with randomly distributed crystallographic orientation and with grain diameters in the 1-100 μm range. Proper sintering is most important for the quality of the final products and is generally carried out in electric furnaces for a better control of temperature and atmosphere. BaTiO_3 -type materials are normally sintered at 1300-1450°C. $\text{Pb}(\text{Zr},\text{Ti})\text{O}_3$ -bodies typically sinter in the 1150-1300°C range. These latter ceramics may lose PbO , which can be prevented by maintaining a partial pressure of this oxide in the ware, eg, by including pellets of PbZrO_3 in a refractory enclosure in which the ware is fired.

The whole sintering cycle (rising, holding, cooling time, temperature, atmosphere) determines in a rather complex way the microstructure of the finished ceramics and this, in turn, influences strongly the resulting ferroelectric properties.

For certain applications (eg, electrooptic and SAW (surface acoustic wave) devices) fully dense ceramics without residual pores are necessary. The usual way to achieve such full density is by hot pressing, which means sintering with the application of uniaxial or isostatic pressure (91-92). This can be done by using a high temperature mold of refractory oxides or metal and a source of heat (resistance wire or induction heating). Problems usually arise from the reaction of the powder to be compacted with the refractory oxides or metal of the mold. The temperature of operation is typically about 100°C lower than that required in the absence of pressure. The pressure range is typically about 10-50 MPa (100-500 atm).

Device Fabrication. The geometrical shape of the sintered ceramics corresponds in many cases to the shape of the final products (eg, disks). Frequently, however, where close dimensional tolerances are required, the final shape has to be achieved by cutting, sawing, and lapping with diamond tools that might contribute considerably to the production costs (see Abrasives).

Since the ferroelectric ceramics will be operated as electronic devices, they have to be furnished with electrically conductive electrodes. A series of different techniques for the application of the electrodes are used, all of them having their own special merits and drawbacks: (1) screening techniques such as forming a layer of metallic silver (applied in dispersed liquid or paste form and sintered at about 800°C to give a continuous conductive layer intimately bonded to the ceramic surface); (2) vacuum evaporation of gold or copper (see Film deposition techniques); (3) application of electroless nickel or gold plating (see Electroless plating). If necessary, leads are soldered or clamped to the electrodes (see also Electrical connectors).

22 FERROELECTRICS

After electroding, many devices have to be adjusted to their proper electrical specifications. This may be done (eg, in ceramic capacitors) by sandblasting part of the electrodes to adjust to the proper capacitance value or by reducing the geometrical shape of an electromechanical resonator to achieve the proper resonance frequency.

The last step in the device fabrication is encapsulation (eg, dipping a ceramic capacitor in an organic paste) to protect the device against moisture, dust, or mechanical damage and to prevent electrical breakdown (see Microencapsulation).

Economic Aspects

Table 2 shows the estimated world production in pieces per year and world turnover in dollars per year of ferroelectric ceramics for 1978. The trend is increasing production for all three types of applications.

The prices of the different devices are highly variable and range from the 1 cent region for a simple disk or miniature chip capacitor up near the 1 dollar region for encapsulated large-capacitance multilayer capacitors, PTC degaussing units, or large piezoceramic rings for ultrasound generation.

The overall price of a device depends on the cost of the different production steps: raw materials, powder preparation, preparation of ceramic specimens, and device fabrication. Because of the very different qualities of the finished products, it is impossible to give exact figures for the price fraction of the different production steps. It is, however, obvious that the larger the amount of ceramic material in a ferroelectric device, the higher the price fraction of the first production steps, and the lower the amount of ceramic the higher the price fraction of the last production steps. Therefore, only very rough order-of-magnitude estimates of the price fraction can be made for typical products:

<i>Production stage</i>	<i>Fraction of total cost, %</i>
raw materials	0.1-10; typically 1%
powder preparation	0.1-10; typically 2%
specimen preparation	5-50; typically 20%
device fabrication	40-90; typically 75%

Applications

Piezoelectric. Immediately after sintering, ferroelectric ceramics exhibit no piezoelectric effect. To exploit the latent piezoelectric properties of these ceramics, the originally isotropic spread of orientations of the spontaneous polarization within the

Table 2. Estimated World Production of Ferroelectric Ceramics for 1978

	Pieces/y	10 ⁶ \$/y
piezoceramics		50
all ceramic capacitors	24 × 10 ⁹	750
multilayer capacitors	1.5 × 10 ⁹	250
PTC ceramics	150 × 10 ⁶	50

various grains has to be aligned by a so-called poling process. Poling is accomplished by applying a large electrical field (higher than the coercive field E_c) at elevated temperatures (100–200°C) and cooling to room temperature with the field applied. By this means, piezoelectric response in a ceramic (inherently isotropic) material is achieved through the reorientability of P_s , which is characteristic of a ferroelectric.

The piezoelectric activity induced by the poling process is directly proportional to the degree of orientation of the grains which come up to the maximum attainable value (80–90% of the single-crystal value) for $\text{Pb}(\text{Zr,Ti})\text{O}_3$ materials with rhombohedral structure. For $\text{Pb}(\text{Zr,Ti})\text{O}_3$ materials with tetragonal structure, ca 50% orientation is characteristic. A large degree of orientation, F , high spontaneous polarization P_s , combined with high remanent polarization P_r , $P_r \approx F \cdot P_s$, and high dielectric constant, are the basic requirements for maximum piezoelectric activity (93–94).

In this respect $\text{Pb}(\text{Zr,Ti})\text{O}_3$ ceramics have much superior properties to the earlier BaTiO_3 -based piezoceramic materials. However, high piezoelectric properties in the $\text{Pb}(\text{Zr,Ti})\text{O}_3$ system (expressed by the electromechanical coupling factor k ; the square of k can be used as a figure of merit) are found only for compositions near the morphotropic phase boundary (38,95) (Fig. 14). The reason for this is the high dielectric constant ϵ_{33}^T and the relatively large remanent polarization P_r which are attainable in this composition region.

Moreover, $\text{Pb}(\text{Zr,Ti})\text{O}_3$ ceramics show the big advantage that their material parameters can be optimized for specific application by a controlled doping, and currently only such doped ceramics are produced. There exists a multitude of different doping ions that can be classified into three groups:

(1) Donor dopants, eg, La, Nb, Sb, or W, which are incorporated at a lattice site

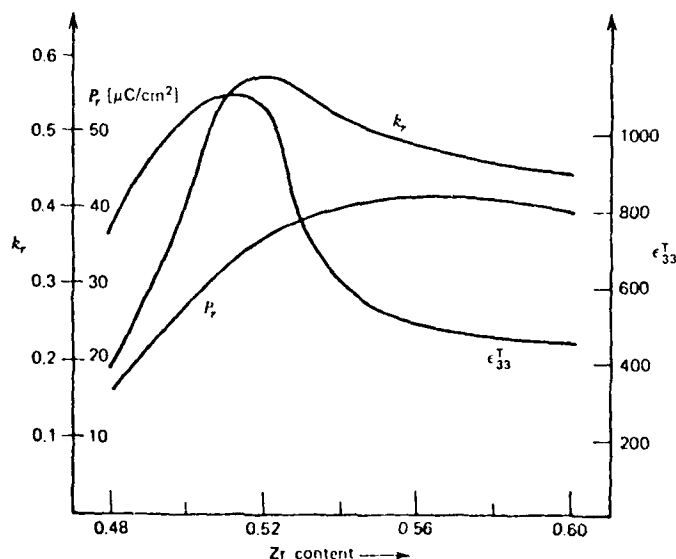


Figure 14. Planar coupling factor k_r , dielectric constant ϵ_{33}^T (measured with electrical field along poling direction and at 16 kHz below resonance frequency) and remanent polarization P_r of undoped ceramic $\text{Pb}(\text{Zr,Ti}_{1-x})\text{O}_3$ samples.

of lower valency (eg, La^{3+} at Pb^{2+} sites). These donor dopings lead to the so-called soft materials exhibiting increased coupling factors (up to 0.7) and dielectric constants (up to 3000) but also increased electrical and mechanical losses (94,96).

(2) The second group of doping ions is formed by the transition metals, eg, Fe, Mn, Ni, Co, which are incorporated at a lattice site of higher valency (eg, Fe^{3+} at Ti^{4+} sites), thus showing acceptor character. These acceptor dopants have an effect just opposite to the above donors. They reduce the dielectric constant, the coupling factor and also reduce the losses and improve the aging properties. Moreover, they increase the stability of the ceramics with respect to electrical or mechanical depolarization. Therefore, these acceptor-doped ceramics are called hard materials (94,96-100).

(3) On transgressing the solubility limit of the doping species, eg, at high concentrations of Mn, or if one dopes with ions that barely dissolve into the perovskite lattice, eg, Al, then a second phase is formed at the grain boundaries and this, by means of space-charge effects, also increases the stability of the ceramics (101-103).

Piezoelectric ceramics (piezoceramics) are used as piezoelectric devices in a multitude of compositions and geometrical shapes for a large variety of different applications (8,83,104-105).

As transducers, piezoceramics become increasingly useful at higher frequencies, and therefore, they are applied in the field of acoustics and especially in the field of ultrasonics (qv), transforming electrical into mechanical energy or vice versa. They are well adapted to receive or transmit elastic energy into liquids (sonar and medical applications, ultrasonic cleaning) or solids (ultrasonic welding, soldering, delamination) that are comparable in density to the piezoelectric body, but they require mechanical transformer systems such as horns to match well into low density media like air. For all transducer-type applications, a hard acceptor-doped (mostly Fe) $\text{Pb}(\text{Zr},\text{Ti})\text{O}_3$ is used which can be operated up to high power levels at elevated temperatures without depolarization.

Acceptor-doped hard solid solutions of $\text{Pb}(\text{TiO}_3-\text{PbZrO}_3)$ -complex perovskite (eg, $\text{Pb}(\text{Mn}_{1-x}\text{Nb}_x)\text{O}_3$) are used mostly for ignition applications. Large stresses applied in the poling direction of piezoelectric slugs generate sparks in the voltage range up to 20 kV/cm for ignition of natural gas in space heaters, cooking stoves, or in cigarette lighters. Owing to the acceptor dopant, the stresses (impact and squeeze) that are used can be applied thousands of times without serious degradation in the form of depolarization (106).

Piezoceramics also have major applications as resonators in devices determining or limiting the operating frequency of electrical networks. Contrary to transducer or ignition applications, resonators are operated at low driving levels. The problems in this area involve low mechanical losses (equivalent to high mechanical quality factors) and low temperature and time dependence (aging) of the resonance frequency. Optimum properties are obtained with Mn-doped $\text{Pb}(\text{TiO}_3-\text{PbZrO}_3)$ -complex perovskite (eg, $\text{Pb}(\text{Zn}_{1/20}\text{Nb}_{9/20})\text{O}_3$ ceramics of tetragonal crystal structure).

The ceramic resonators are frequently in the form of bandpass filters having high bandwidths of up to 10% of the central frequency and are possible because of the large coupling factors of the materials. Today they are widely used in large quantities in the intermediate frequency stage of AM and FM radio receivers (452 kHz and 10 MHz) (107).

The direct piezoelectric effect is exploited in phonograph pickup elements where a mechanical force is converted to an electrical charge. Highest conversion ratios are

obtained with donor-doped soft materials showing high coupling factors and high dielectric constants. In the same type of materials, the inverse piezoelectric effect is utilized for "actuators" where an electrical field is converted into a change of the geometrical dimensions (8).

Dielectrics. Owing to their ferroelectric nature, BaTiO_3 -based ceramics show high dielectric constants and therefore these materials are suited for and widely used in capacitor applications. The biggest advantage of the ceramic capacitor is compactness owing to the high capacitance per unit volume.

However, like single crystals (See Fig. 5), the dielectric constant of BaTiO_3 ceramics has a strong temperature dependence and a pronounced maximum at the Curie point (Fig. 15). By a partial substitution of Ba by Sr or Ca or of Ti by Zr or Sn (Fig. 6), the Curie point can be shifted to room temperature, resulting in materials with a maximum of the dielectric constant of 10,000 to 15,000 at this temperature (Fig. 15). Unfortunately, however, these simple materials suffer from high dielectric losses and show large temperature and field dependences, which worsen for high dielectric constant compositions. These unfavorable properties can be suppressed to a certain degree by: (1) optimum doping; (2) proper mixed crystal formation; and (3) exact control of the microstructure.

By doping with transition metal ions such as Fe or Mn, it is possible to stabilize the domain walls and to reduce the dielectric losses (108). Besides a shift of the Curie point to desired temperature regions, mixed crystal formation broadens the peak of the dielectric constant (Fig. 15), and thus reduces the strong temperature dependence (109-110).

As demonstrated in Figure 15, a change of the microstructure is an important means of influencing and controlling the electrical characteristics of a ferroelectric ceramic. Owing to the difference in microstructure, dielectric constants of about 1500

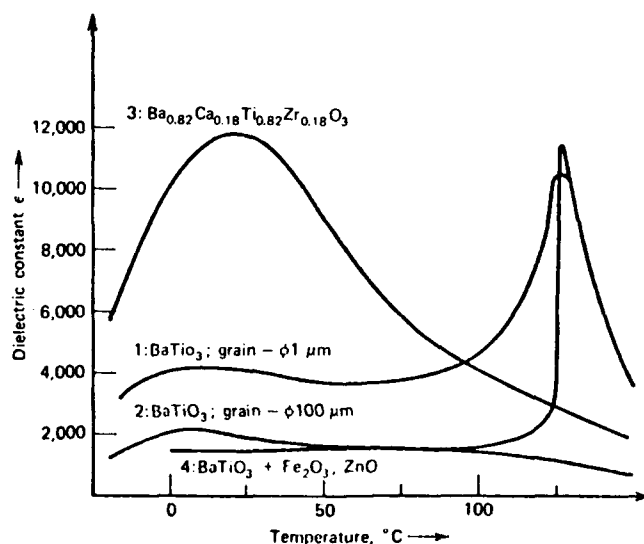


Figure 15. Temperature of dependence the dielectric constant of different BaTiO_3 -based ceramics for capacitor applications. ϕ = mean grain diameter.

are found for coarse-grained (mean grain diameter 100 μm) and of about 3500 for fine-grained (mean grain diameter 1 μm) ceramic specimens. Moreover, the Curie peak of fine-grained specimens is broadened with respect to the coarse-grained sample (111).

It is quite likely that optimum improvements in the dielectric characteristics can be achieved by combining all three effects. By adding relatively large amounts of Fe_2O_3 and ZnO (112) to BaTiO_3 (resulting in extremely fine-grained doped ceramic materials and with second phases finely dispersed at the grain boundaries), the Curie peak can be fully suppressed (Fig. 15).

Extremely high dielectric constants can be obtained if the so-called intergranular layer capacitors are used. They consist of semiconducting grains divided by high-resistance barrier layers at each grain boundary. In that case the electric field concentrates in the barrier layers and the true thickness of the dielectric consists only of the sum of these high-resistance barrier layers, resulting in effective dielectric constants up to 100,000. There are, however, large losses and strong temperature and field dependences (113–114).

From these various materials ceramic capacitors are produced ranging from the pF to the μF region in a multitude of geometrical shapes and different applications (83). The most important are disk capacitors, tube capacitors, miniature chip capacitors, and multilayer capacitors.

Disk capacitors are generally produced by pressing the powder together with some binder in a disk-shaped die. Depending on operating voltage and capacitance value, the geometrical shape of the disk generally varies between 0.5 mm and 4 mm in thicknesses and between 4 and 10 mm in diameter. Since it is difficult to produce disk capacitors having a thickness below 0.5 mm, their capacitance values are relatively low, but they are suitable for large operating voltages (≥ 250 V). Screen-printed silver normally serves as electrode material.

Tube capacitors are produced by extrusion. The geometrical dimensions range from 2 to 4 mm in diameter and from 8 to ca 40 mm in length. Normally, the electrodes are screen-printed silver.

The advantage of miniature chip capacitors is their low thickness (0.1–0.3 mm) resulting in a high capacitance per surface area at reduced operating voltages (typically 60 V). The thin ceramic sheet of this capacitor type is generally produced by rolling techniques from which rectangular chips are punched or cut out. Evaporated copper is often used as electrodes.

During recent years the multilayer capacitor has gained increasing importance (115). With this capacitor type, high capacitances per unit volume can be achieved by piling up several thin (20–50 μm) ceramic foils. These foils are produced by casting techniques. They are provided with screened metal electrodes in the "green" unsintered state, then laminated, pressed, and sintered together with the metal electrodes (Fig. 16). Because the dielectric materials require sintering temperatures of about 1300°C and atmospheres of oxygen or air to attain good dielectric properties, noble metal electrodes, mainly palladium, have to be used. The capacitance range of multilayer capacitors is 100 nF–1 μF .

Semiconducting—Positive Temperature Coefficient (PTC) Materials. By substituting some 0.1–0.4 mol % of Ba^{2+} ions by La^{3+} ions, or Ti^{4+} ions by Sb^{5+} or Nb^{5+} ions, BaTiO_3 can be transferred into an n-type semiconductor with a resistivity of about 10 $\Omega\text{-cm}$ at room temperature. However, as shown in Fig. 17, the resistivity rises very

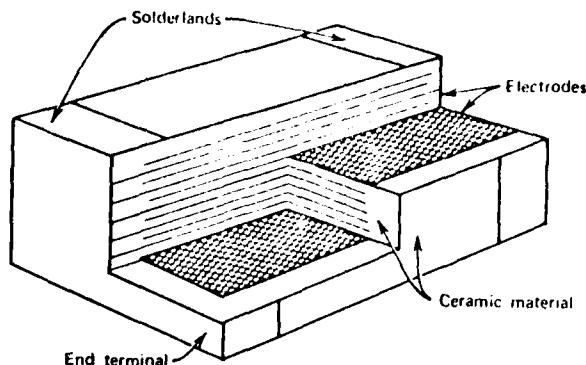


Figure 16. Schematic representation of a multilayer capacitor.

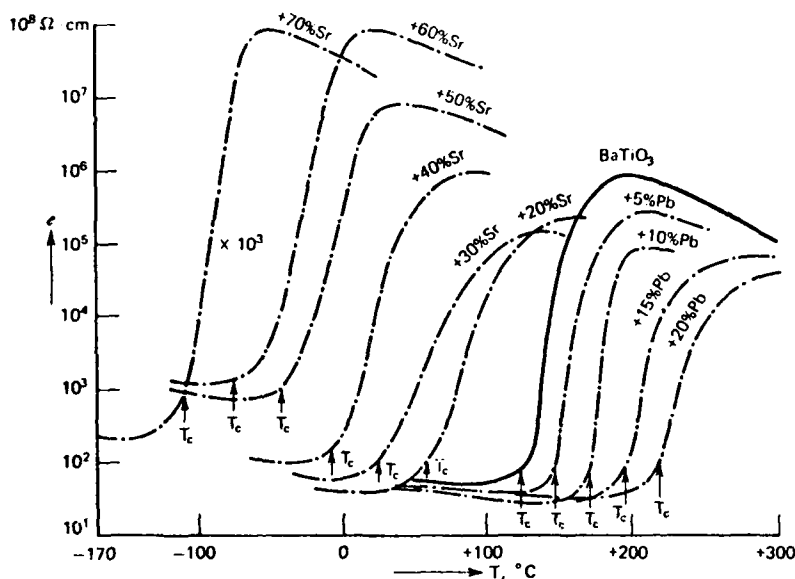


Figure 17. Temperature dependence of the resistivity of semiconducting BaTiO_3 and of mixed crystals of $(\text{Ba,Sr})\text{TiO}_3$ and $(\text{Ba,Pb})\text{TiO}_3$ after doping with 0.3 mol % Sb. The arrows mark the Curie point T_c of the respective compositions.

rapidly (up to $60\%/^{\circ}\text{C}$) just at the Curie point T_c , thus forming a resistor material with a large positive temperature coefficient (PTC effect) (116). The range of the PTC effect can be continuously shifted to the desired temperature region by mixed crystal formation (see Figs. 6 and 17) (117).

This rather uncommon PTC behavior is caused by barrier layers at the grain boundaries. They originate from defects with acceptor character at the grain boundaries which trap conduction electrons and thus form a depletion layer with a high-resistance potential barrier (118–120). The height of the potential barrier is governed by the ferroelectric properties of BaTiO_3 . Below T_c the spontaneous po-

larization P_s compensates partially or fully for the defects (depending on their concentration) and removes the depletion layer, so that the potential barrier is not fully effective, resulting in high conductivity. Above T_c , where no spontaneous polarization exists, the depletion layer and the potential barrier at the grain boundary become fully effective. The height of the potential barrier is dependent on the reciprocal of the dielectric constant which, according to the Curie-Weiss law, falls with increasing temperature. Consequently, the potential barrier increases with rising temperature and the resistivity, owing to the exponential dependence of the resistivity on the barrier height, increases by several orders of magnitude.

PTC ceramics are normally produced in disks or rectangular bars which are supplied with low-resistance electrodes with or without soldered beam leads. The devices are used in a wide variety of controlling or measuring applications such as current limiters, degaussing units in color television sets, self-controlling heating elements, for overload protection or for temperature measurement and control.

BIBLIOGRAPHY

"Ferroelectrics" in *ECT* 2nd ed., Vol. 9, pp. 1-25, by Edward C. Henry, General Electric Company.

1. J. Valasek, *Phys. Rev.* **17**, 475 (1921).
2. R. E. Newnham and L. E. Cross, *Mater. Res. Bull.* **9**, 927 (1974).
3. *Ibid.*, 1021 (1974).
4. J. F. Nye, *Physical Properties of Crystals*, Clarendon Press, Oxford, 1957.
5. Landolt-Börnstein, *Ferroelectric and Antiferroelectric Substances*, Vol. 3, New Series Group III, Springer Verlag, Berlin, 1969.
6. Landolt-Börnstein, *Ferroelectric and Antiferroelectric Substances*, Vol. 9, New Series Group III, Springer Verlag, Berlin, 1975.
7. A. Glass and M. E. Lines, *Principles and Applications of Ferroelectrics and Related Materials*, Clarendon Press, Oxford, 1977.
8. B. Jaffe, W. R. Cooke, Jr., and H. Jaffe, *Piezoelectric Ceramics*, Academic Press, New York, 1971.
9. K. Aizu, *J. Phys. Soc. Jpn.* **20**, 959 (1965); *Phys. Rev.* **146**, 423 (1966).
10. L. A. Shuvalov, *J. Phys. Soc. Jpn.* **28S**, 38 (1970).
11. K. Aizu, *J. Phys. Soc. Jpn.* **27**, 387 (1969).
12. K. Aizu, *J. Phys. Soc. Jpn.* **28**, 706 (1970).
13. K. Aizu, *Phys. Rev.* **B2**, 754 (1970).
14. K. Aizu, *J. Phys. Soc. Jpn.* **32**, 1287 (1972).
15. K. Aizu, *J. Phys. Soc. Jpn.* **34**, 121 (1973).
16. H. L. Borchardt and P. E. Bierstedt, *J. Appl. Phys.* **38**, 2057 (1967).
17. L. E. Cross, A. Fouskova, and S. E. Cummins, *Phys. Rev. Lett.* **21**, 812 (1968).
18. V. Dvorak, *Phys. Status Solidi* **46B**, 763 (1971).
19. V. Dvorak, *Phys. Status Solidi* **52B**, 93 (1972).
20. B. Singer, "Theory and Performance Characteristics of Pyroelectric Imaging Tubes" in *Advances in Image Pickup and Display*, Vol. 13, Academic Press, London, 1977.
21. J. Fousek and V. Janovec, *J. Appl. Phys.* **40**, 135 (1969).
22. J. Fousek, *Czech. J. Phys.* **21**, 955 (1971).
23. V. A. Zhirnov, *Sov. Phys. JETP* **8**, 882 (1959).
24. W. Kinase and H. Takahashi, *J. Phys. Soc. Jpn.* **12**, 464 (1957).
25. T. Yatohashi, G. Honjo, and M. Tanaka, *J. Phys. Soc. Jpn.* **28**, 386 (1970).
26. M. Tanaka and G. Honjo, *J. Phys. Soc. Jpn.* **19**, 954 (1964).
27. W. J. Merz, *Phys. Rev.* **95**, 690 (1954).
28. E. Fatuzzo and W. J. Merz, *Phys. Rev.* **116**, 61 (1959).
29. E. Fatuzzo and W. J. Merz, *Ferroelectricity*, North Holland Press, Amsterdam, 1967, p. 197.
30. I. Hatta and A. Sawada, *Jpn. J. Appl. Phys.* **4**, 389 (1965).
31. R. C. Miller and A. J. Savage, *J. Appl. Phys.* **31**, 632 (1960).
32. R. Landauer, *J. Appl. Phys.* **28**, 227 (1957).

33. K. C. Miller and G. Weinreich, *Phys. Rev.* **117**, 1460 (1960).
34. H. I. Stadler and P. J. Zachmanidis, *J. Appl. Phys.* **34**, 3255 (1963).
35. M. Hayashi, *J. Phys. Soc. Jpn.* **33**, 616 (1972).
36. F. Jona and G. Shirane, *Ferroelectric Crystals*, Pergamon Press, New York, 1962, p. 108.
37. E. Sawaguchi, *J. Phys. Soc. Jpn.* **8**, 615 (1953).
38. B. Jaffe, R. S. Roth, and S. Marzullo, *J. Res. Nat. Bur. Stand.* **55**, 239 (1955).
39. H. Ouchi, K. Nagano, and S. Hayakawa, *J. Am. Ceram. Soc.* **48**, 630 (1965).
40. S. C. Abrahams and co-workers, *J. Phys. Chem. Solids* **34**, 521 (1973).
41. S. C. Abrahams, W. C. Hamilton, and A. Sequeira, *J. Phys. Chem. Solids* **28**, 1693 (1967).
42. K. Nassau, *J. Phys. Chem. Solids* **27**, 983 (1966).
43. I. Camlibel, *J. Appl. Phys.* **40**, 1690 (1969).
44. A. J. Slabodnik, Jr., *Proc. IEEE* **64**, 581 (1976).
45. I. P. Kaminow, *Ferroelectrics* **10**, 247 (1976).
46. S. T. Liu, *Ferroelectrics* **10**, 83 (1976).
47. F. W. Ainger, *Ferroelectrics* **10**, 75 (1976).
48. P. B. Jamieson, S. C. Abrahams, and J. L. Bernstein, *J. Chem. Phys.* **48**, 5048 (1968).
49. L. G. Van'tert and co-workers, *Mater. Res. Bull.* **3**, 47 (1968).
50. S. C. Abrahams, P. B. Jamieson, and J. L. Bernstein, *J. Chem. Phys.* **54**, 2355 (1971).
51. B. A. Scott and co-workers, *Mater. Res. Bull.* **5**, 47 (1970).
52. G. Goodman, *J. Am. Ceram. Soc.* **36**, 368 (1953).
53. G. A. Smolensky and A. I. Agranovskaya, *Dokl. Akad. Nauk SSSR* **97**, 237 (1954).
54. M. B. Francombe, *Acta Crystallogr.* **13**, 131 (1960).
55. U.S. Pat. 2,805,165 (Apr. 25, 1955), G. Goodman (to General Electric Company).
56. B. Lewis and L. A. Thomas, *Proc. Int. Conf. Solid State Electronics Brussels* **4**, 883 (1960).
57. A. M. Glass, *J. Appl. Phys.* **40**, 4699 (1969).
58. R. B. Maciolek and S. T. Liu, *J. Electron. Mater.* **2**, 191 (1973).
59. J. E. Geusic and co-workers, *Appl. Phys. Lett.* **11**, 269 (1968).
60. R. G. Smith, *J. Appl. Phys.* **39**, 4030 (1968).
61. R. E. Newnham, R. W. Wolfe, and J. F. Dorrian, *Mater. Res. Bull.* **6**, 1029 (1971).
62. R. E. Newnham and R. W. Wolfe, *J. Electrochem. Soc.* **116**, 832 (1969).
63. R. A. Armstrong and R. E. Newnham, *Mater. Res. Bull.* **7**, 1025 (1972).
64. L. E. Cross and R. Pohanka, *Mater. Res. Bull.* **6**, 939 (1971).
65. S. E. Cummins and L. E. Cross, *J. Appl. Phys.* **39**, 3268 (1968).
66. S. E. Cummins and T. E. Luke, *Ferroelectrics* **3**, 125 (1972).
67. S. E. Cummins, *J. Appl. Phys.* **37**, 2510 (1966).
68. S. E. Cummins and T. E. Luke, *IEEE Trans. Electron Devices* **ED18**, 761 (1971).
69. S. E. Cummins and B. H. Hill, *Proc. IEEE* **58**, 938 (1970).
70. S. E. Kenneman and co-workers, *Appl. Phys. Lett.* **17**, 173 (1970).
71. W. R. Cook, Jr. and H. Jaffe, *Phys. Rev.* **88**, 1426 (1952).
72. V. A. Isupov, *Izv. Akad. Nauk SSSR, Ser. Fiz.* **21**, 402 (1957).
73. S. Nanamatsu, M. Kimura, and T. Kawamura, *J. Phys. Soc. Jpn.* **38**, 817 (1975).
74. G. Busch and P. Scherrer, *Naturwissenschaften* **23**, 737 (1935).
75. G. Busch, *Helv. Phys. Acta* **11**, 269 (1938).
76. J. West, *Z. Krist.* **74**, 306 (1930).
77. W. Baulte, *Helv. Phys. Acta* **15**, 373 (1942).
78. G. Morie, *Ferroelectrics* **10**, 9 (1976).
79. B. T. Matthias, C. E. Miller, and J. P. Remeika, *Phys. Rev.* **104**, 849 (1956).
80. S. Triebwasser, *IBM J. Res. Dev.* **2**, 212 (1958).
81. S. Hoshino and co-workers, *Phys. Rev.* **107**, 1255 (1957).
82. R. Pepinsky, Y. Okaya, and F. Jona, *Bull. Am. Phys. Soc.* **2**, 220 (1957).
83. A. Bauer and co-workers, *Technologie und Anwendungen von Ferroelektrika*, Akademische Verlagsgesellschaft Geest & Portig K.-G., Leipzig, 1976.
84. P. K. Gallagher, *Mater. Res. Bull.* **3**, 225 (1968).
85. W. S. Clabaugh, E. M. Swiggard, and R. Gilchrist, *J. Res. NBS, Res. Paper* **2677**, 289 (1956).
86. V. M. McNamara, *J. Can. Ceram. Soc.* **34**, 103 (1965).
87. K. S. Mazdiyasn, R. T. Dollot, and J. S. Smith H. *J. Am. Ceram. Soc.* **52**, 523 (1969).
88. G. H. Haertling, *J. Am. Ceram. Soc.* **54**, 303 (1971).
89. B. I. Mulder, *Am. Ceram. Soc. Bull.* **49**, 990 (1970).

90. U.S. Pat. 3,330,697 (Aug. 26, 1963), M. P. Pechini (to Sprague Electric Company).
91. G. Haertling, *Am. Ceram. Soc. Bull.* **43**, 875 (1964).
92. K. H. Hardtl, *Am. Ceram. Soc. Bull.* **54**, 201 (1975).
93. K. Carl and K. H. Hardtl, *Phys. Status Solidi A* **8**, 87 (1971).
94. K. H. Hardtl, *Ferroelectrics* **12**, 9 (1976).
95. D. Berlincourt, C. Smolik, and H. Jaffe, *Proc. IRE* **48**, 220 (1960).
96. F. Kulcsar, *J. Am. Ceram. Soc.* **42**, 343 (1959).
97. H. Thomann, *Z. Angew. Phys.* **20**, 554 (1966).
98. T. B. Weston, A. H. Webster, and V. M. McNamara, *J. Am. Ceram. Soc.* **52**, 253 (1969).
99. N. Uchida and T. Ikeda, *Jpn. J. Appl. Phys.* **6**, 1292 (1967).
100. K. Carl and K. H. Hardtl, *Ferroelectrics* **17**, 473 (1978).
101. K. Okazaki and K. Sakata, *Electrotech. J. Jpn.* **7**, 13 (1962).
102. S. Takahashi and M. Takahashi, *Jpn. J. Appl. Phys.* **11**, 31 (1971).
103. H. Thomann, *Ferroelectrics* **4**, 141 (1972).
104. H. Jaffe, *Proceedings on Electron Devices, IEEE ED-16*, 557 (1969).
105. W. P. Mason, ed., *Handbook on Physical Acoustics*, Vol. 1, Part A, Academic Press, New York, 1964, Chapt. III.
106. Y. Kodama and M. Osada, *Sumitomo Electric Techn. Rev.* **10**, 102 (1967).
107. H. H. Schüssler, *Proceedings on Sonics and Ultrasonics, IEEE SU-21*, 257 (1974).
108. H.-J. Hagemann, *J. Phys. C* **11**, 3333 (1978).
109. V. V. Kirilov and V. A. Isupov, *Ferroelectrics* **5**, 3 (1975).
110. A. J. Burggraaf and K. Keizer, *Mater. Res. Bull.* **10**, 521 (1975).
111. W. R. Buessem, L. E. Cross, and A. K. Goswami, *J. Am. Ceram. Soc.* **49**, 33 (1966).
112. H. Thomann and H. Heydrich, *Ferroelectrics* **7**, 357 (1974).
113. S. Waku, *Rev. Electr. Comm. Lab.* **5**, 689 (1967).
114. H. Brauer, *Z. Angew. Phys.* **29**, 282 (1970).
115. V. F. Capozzi, *Multilayer Ceramic Capacitor Materials and Manufacture*, Oxy Metal Industries Corp., Nutley, N.J., 1975.
116. Ger. Pat. 929,350 (1955), P. W. Haayman, R. W. Dam, and H. A. Klasens.
117. E. Andrich and K. H. Hardtl, *Philips Tech. Rev.* **26**, 119 (1965).
118. W. Heywang, *Solid State Electron.* **3**, 51 (1961).
119. G. H. Jonker, *Solid State Electron.* **7**, 895 (1964).
120. J. Daniels and co-workers, *Philips Res. Rep.* **31**, 487 (1976).

L. E. CROSS
The Pennsylvania State University

K. H. HÄRDTL
Philips Forschungslaboratorium Aachen GmbH

BASIC DISTRIBUTION LIST

Technical and Summary Reports

November 1979

<u>Organization</u>	<u>Copies</u>	<u>Organization</u>	<u>Copies</u>
Defense Documentation Center Cameron Station Alexandria, VA 22314	12	Naval Air Propulsion Test Center Trenton, NJ 08628 ATTN: Library	1
Office of Naval Research Department of the Navy 800 M. Quincy Street Arlington, VA 22217 ATTN: Code 471 Code 470	1 1	Naval Construction Battalion Civil Engineering Laboratory Port Hueneme, CA 93043 ATTN: Materials Division	1
Commanding Officer Office of Naval Research Branch Office Building 114, Section D 666 Summer Street Boston, MA 02210	1	Naval Electronics Laboratory San Diego, CA 92152 ATTN: Electron Materials Sciences Division	1
Commanding Officer Office of Naval Research Branch Office 536 South Clark Street Chicago, IL 60605	1	Naval Missile Center Materials Consultant Code 3312-1 Point Mugu, CA 92041	1
Office of Naval Research San Francisco Area Office One Hallidie Plaza Suite 601 San Francisco, CA 94102	1	Commanding Officer Naval Surface Weapons Center White Oak Laboratory Silver Spring, MD 20910 ATTN: Library	1
Naval Research Laboratory Washington, DC 20375 ATTN: Codes 6000 6100 6300 2627	1 1 1 1	Commander David W. Taylor Naval Ship Research and Development Center Bethesda, MD 20084	1
Naval Air Development Center Code 606 Warminster, PA 18974 ATTN: Mr. F. S. Williams	1	Naval Oceans Systems Center San Diego, CA 92132 ATTN: Library	1
		Naval Underwater System Center Newport, RI 02840 ATTN: Library	1
		Naval Postgraduate School Monterey, CA 93940 ATTN: Mechanical Engineering Department	1
		Naval Weapons Center China Lake, CA 93555 ATTN: Library	1

BASIC DISTRIBUTION LIST (cont'd)

<u>Organization</u>	<u>Copies</u>	<u>Organization</u>	<u>Copies</u>
Naval Air Systems Command Washington, DC 20360 ATTN: Codes 52031 52032	1 1	NASA Lewis Research Center 21000 Brookpark Road Cleveland, OH 44135 ATTN: Library	1
Naval Sea System Command Washington, DC 20362 ATTN: Code 05R	1	National Bureau of Standards Washington, DC 20234 ATTN: Metals Science and Standards Division	1
Naval Facilities Engineering Command Alexandria, VA 22331 ATTN: Code 03	1	Ceramics Glass and Solid State Science Division Fracture and Deformation Division	1 1
Scientific Advisor Commandant of the Marine Corps Washington, DC 20380 ATTN: Code AX	1	Director Applied Physics Laboratory University of Washington 1013 Northeast Fortthieth Street Seattle, WA 98105	1
Army Research Office P. O. Box 12211 Triangle Park, NC 27709 ATTN: Metallurgy & Ceramics Program	1	Defense Metals and Ceramics Information Center Battelle Memorial Institute 505 King Avenue Columbus, OH 43201	1
Army Materials and Mechanics Research Center Watertown, MA 02172 ATTN: Research Programs Office		Metals and Ceramics Division Oak Ridge National Laboratory P. O. Box X Oak Ridge, TN 37380	1
Air Force Office of Scientific Research/NE Building 410 Bolling Air Force Base Washington, DC 20332 ATTN: Chemical Science Directorate Electronics & Materials Sciences Directorate	1 1	Los Alamos Scientific Laboratory P. O. Box 1663 Los Alamos, NM 87544 ATTN: Report Librarian	1
Air Force Materials Laboratory Wright-Patterson AFB Dayton, OH 45433	1	Argonne National Laboratory Metallurgy Division P. O. Box 229 Lemont, IL 60439	1
Library Building 50, Room 134 Lawrence Radiation Laboratory Berkeley, CA	1	Brookhaven National Laboratory Technical Information Division Upton, Long Island New York 11973 ATTN: Research Library	1
NASA Headquarters Washington, DC 20546 ATTN: Code RRM	1	Office of Naval Research Branch Office 1030 East Green Street Pasadena, CA 91106	1

SUPPLEMENTARY DISTRIBUTION LIST A
Electronic, Magnetic, and Optical Ceramics

032
June 1980

Advanced Research Projects Agency
Materials Science Director
1400 Wilson Boulevard
Arlington, VA 22209

Dr. Don Berlincourt
Channel Products
16722 Park Circle Drive W.
Chagrin Falls, OH 44022

Dr. J. V. Biggers
Pennsylvania State University
Materials Research Laboratory
University Park, PA 16802

Mr. George Boyer
Sensor Systems Program
Office of Naval Research
Code 222
Arlington, VA 22217

Professor R. Bradt
Ceramics Section
Materials Sciences Department
The Pennsylvania State University
University Park, PA 16802

Dr. Dean Buckner
Piezo Products Division
Gulton Industries
P. O. Box 4300
Fullerton, CA 92634

Dr. Robert Callahan
Channel Industries
839 Ward Drive
Box 3680
Santa Barbara, CA 93105

Professor L. E. Cross
The Pennsylvania State University
Materials Research Laboratory
University Park, PA 16802

Mr. N. Coda
Vice President for Engineering
Erie Technological Products
West College Avenue
State College, PA 16802

Dr. Gene Haertling
Motorola Corporation
3434 Vassar, NE
Albuquerque, NM 87107

Dr. W. B. Harrison
Honeywell Ceramics Center
1885 Douglas Drive
Golden Valley, MN 55422

Dr. C. M. Stickley, V. P.
The BDM Corporation
7915 Jones Branch Drive
McLean, VA 22102

Dr. L. L. Hench
Department of Metallurgy
University of Florida
Gainesville, FL 32603

Dr. B. F. Rider
Rockwell International
400 Collins Road NE
Cedar Rapids, IA 52406

Dr. F. Robert Hill
Marine Resources
755 Highway 17 & 92
Fern Park, FL 32730

Dr. Bernard Jaffe
232 Forbes Road
Bedford, OH 44146

Dr. B. G. Koepke
Honeywell, Inc.
Corporate Research Center
10701 Lyndale Avenue South
Bloomington, MN 55420

Dr. R. Lapetina
Edo Western Corporation
2645 South 300 West
Salt Lake City, UT 84115

Mr. C. LeBlanc
Naval Underwater Systems Center
TD 121
Newport, RI 02840

Dr. N. Perrone
Code 474
Office of Naval Research
800 N. Quincy Street
Arlington, VA 22217

Dr. Frank Recny
General Electric Company
Court Street
Plant Building C
Box 1122
Syracuse, NY 13201

Dr. J. H. Rosolowski
General Electric Company
Research and Development Center
P. O. Box 8
Schenectady, NY 02301

Dr. P. L. Smith
Naval Research Laboratory
Code 6361
Washington, DC 20375

Dr. R. W. Timme
Naval Research Laboratory
Code 8275
Underwater Sound Reference Division
P. O. Box 8337
Orlando, FL 32806

Dr. Charles C. Walker
Naval Sea Systems Command
National Center #3
2531 Jefferson Davis Highway
Arlington, VA 20390

Dr. Paul D. Wilcox
Sandia Laboratories
Division 2521
Albuquerque, NM 87115

The State University of New York
at Alfred
Material Sciences Division
Alfred, NY

Dr. R. Rice
Naval Research Laboratory
Code 6360
Washington, DC 20375

Professor R. Roy
The Pennsylvania State University
Materials Research Laboratory
University Park, PA 16802

Dr. N. Tallan
AFML Wright-Patterson AFB
Dayton, OH 45433

Dr. H. E. Bennett
Naval Weapons Center
Code 3818
China Lake, CA 93555

Dr. Michael Bell
Inorganic Materials Division
National Bureau of Standards
Washington, DC 20234

Dr. R. Bratton
Westinghouse Research Laboratory
Pittsburgh, PA 15235

Dr. Joe Dougherty, Dir. Engr.
Gulton Industries
212 Durham Avenue
Metuchen, NJ 08840

Dr. James Pappis
Raytheon Co., Research Division
28 Seyon Street
Waltham, MA 02154

Dr. Perry A. Miles
Raytheon Co., Research Division
28 Seyon Street
Waltham, MA 02154

Dr. P. E. D. Morgan
Rockwell Science Center
1049 Camino Dos Rios
P. O. Box 1085
Thousand Oaks, CA 91360

Dr. G. Ewell
MS6-D163
Hughes Aircraft Company
Centinela & Teale Streets
Culver City, CA 90230

Dr. David C. Hill
Member Technical Staff
Texas Instruments, Inc.
Attleboro, MA 02703

Dr. S. K. Kurtz, V. P.
Clairol, Inc.
2 Blachley Road
Stamford, CT 06902

Dr. Herb Moss
RCA Laboratories
Princeton, NJ 08540

Dr. R. E. Newnham
Materials Research Laboratory
The Pennsylvania State University
University Park, PA 16802

Dr. Charles S. Sahagian, Chief
EM Technology Branch, SSS Division
HQ Rome Air Dev. Center (AFSC)
Deputy for Electronic Technology
Hanscom AFB, MA 01731

Dr. J. Smith
GTE Sylvania
100 Endicott Street
Danvers, MA 01923

Dr. Wallace A. Smith
North American Philips Laboratories
345 Scarborough Road
Briarcliff Manor, NY 10510

Mr. Raymond E. Sparks
Technology Library R220
Delco Electronics Division/GMC
P. O. Box 1104
Kokomo, IN 46901

Dr. Manfred Kahn
Senior Scientist, Prod. Dev.
AVX Ceramics, P. O. Box 867
Myrtle Beach, SC 29577

Mr. G. Goodman, Manager
Corporation of Applied Research Group
Globe-Union Inc.
5757 North Green Bay Avenue
Milwaukee, WI 53201

Dr. George W. Taylor
Princeton Resources, Inc.
P. O. Box 211
Princeton, NJ 08540

Mr. John J. Thiermann
Physics International
2700 Merced Street
San Leandro, CA 94577

Dr. D. Carson
Code 7122
Naval Ocean Systems Center
San Diego, CA 92152

Dr. C. Hicks
Code 631
Naval Ocean Systems Center
San Diego, CA 92152

Dr. R. Smith
Code 7122
Naval Ocean Systems Center
San Diego, CA 92152

Professor R. Buchanan
Department of Ceramic Engineering
University of Illinois
Urbana, Illinois 61801

Professor B. A. Auld
Stanford University
W. W. Hansen Laboratories of Physics
Stanford, CA 94306

Dr. S. Musikant
General Electric Co.
3188 Chestnut Street
Philadelphia, PA 19101

Dr. A. Gentile
Hughes Research Laboratories
3011 Malibu Canyon Road
Malibu, CA 90265

Dr. J. Harrington
Hughes Research Laboratories
3011 Malibu Canyon Road
Malibu, CA 90265

Professor G. Kino
Stanford University
Stanford, CA 94305

Dr. A. E. Clark
Naval Surface Weapons Center
White Oak Laboratory
Silver Spring, MD 20910

Dr. Gordon Martin
2627 Burgener
San Diego CA 92110

Eric Udd
McDonnell Douglas Astronautics
5301 Bolsa Ave
Huntington Beach CA 92647

Director
Applied Research Lab
The Pennsylvania State Univ.
University Park, PA 16802

Army Research Office
Box CM, Duke Station
Attn: Met. & Ceram. Div.
Durham, NC 27706

National Bur. Standards
Inorganic Mats. Division
Washington DC 20234

National Bur. Standards
Metallurgy Division
Washington DC 20234

Naval Air Systems Comm.
Code 320
Washington DC 20360

Pacific Missile Test Center
Materials Consultant
Code 4121
Pt. Mugu, CA 93042

Naval Research Lab
Code 6400
Washington DC 20390

Naval Sea System Command
Code 035
Washington DC 20362

Naval Ship Engr. Center
Code 6101, CTR BG #2
3700 East-West Highway
Prince Georges Plaza
Hyattsville, MD 20782

Office of Naval Research
Department of the Navy
Code 102
Arlington, VA 22217

Dr. G. Bansal
Battelle Laboratories
505 King Avenue
Columbus, OH 43201

Dr. George Benthien
Naval Ocean Systems Center
Code 212
San Diego, CA 92152

Mr. N. Coda, VP Engr.
Erie Technol. Products
Res. and Dev.
Erie, PA 16512

Dr. G. Denman, Code LPJ
AFML, Wright-Patterson AFB
Dayton, OH 45433

Sheldon Detwiler, Disp. Mgr.
Adv. Technol. Laboratories
13208 Northrup Way, PO Box 6639
Bellevue, WA 98007

Dr. W.G.D. Frederick
AFML, Wright-Patterson AFB
Dayton, OH 45433

Dr. P. Gielisse
University of Rhode Island
Kingston, RI 02881

Mr. G. Hayes
Naval Weapons Center
China Lake, CA 93555

Dr. R.N. Katz
Army Materials and Mechanics
Research Center
Watertown, MA 02171

Dr. P.L. Lall
Office of Naval Research
666 Summer Street
Boston, MA 02210

Dr. P. Land
AFML, Wright-Patterson AFB
Dayton, OH 45433

Dr. F.F. Lange
Rockwell International
PO Box 1085
1049 Camino Dos Rios
Thousand Oaks, CA 91360

Dr. Eugene A. Larson, Pres.
Blue River Laboratories
PO Box 442
Lewistown, PA 17044

Mr. K. Letson
Redstone Arsenal
Huntsville, AL 35809

Dr. N. Macmillan
Materials Research Laboratory
The Pennsylvania State Univ.
University Park, PA 16802

Mr. F. Markarian
Naval Weapons Center
China Lake, CA 93555

Mr. K.D. McHenry
Yoneywell Corp. Tech. Center
10701 Lyndale Avenue South
Bloomington, MN 55420

Dr. R.R. Neurgaonkar
Rockwell International Science Center
1049 Camino Dos Rios
PO Box 1085
Thousand Oaks, CA 91360

Norton Company - Library
Industrial Ceramics Division
Worcester, MA 01606

James W. Pell
Manager of Development
Rohe Scientific Corporation
2722 S. Fairview Street
Santa Ana, CA 92704

Dr. R.C. Pohanka
Room 619, Ballston Tower
800 N. Quincy Street
Arlington, VA 22217

Dr. R.A. Queeney
126 Hammond Building
The Pennsylvania State Univ.
University Park, PA 16802

J.J. Rasmussen, Manager
Applied Research Division
Montana Energy and MHD R&D
PO Box 3809
Butte, Montana 59701

Dr. R. Ruh
AFML, Wright-Patterson AFB
Dayton, OH 45433

James Runt
313 Steidle Bldg
The Pennsylvania State Univ.
University Park, PA 16802

Mr. G. Schmitt
AFML, Wright-Patterson AFB
Dayton, OH 45433

Dr. T. Sentementes
GTE Sylvania
100 Endicott Street
Danvers, MA 01923

State University of New York
College of Ceramics
Alfred University
Attn: Library
Alfred, NY 14802

Dr. R.E. Tressler
Ceramic Science Section
226 Steidle Building
The Pennsylvania State Univ.
University Park, PA 16802

Eric Udd
McDonnell Douglas Astron.
5301 Bolsa Avenue
Huntington Beach, CA 92647

Dr. T. Vasilos
AVCO R & Adv. Dev. Division
201 Lowell Street
Wilmington, MA 01887

Mr. J.D. Walton
Engineering Experiment Station
Georgia Institute of Technology
Atlanta, GA 30332

Mr. L.B. Weckesser
Applied Physics Laboratory
Johns Hopkins Road
Laurel, MD 20810

DATE
ILME